

ABSTRACT

Title of Dissertation: **EXPERIMENTAL MEASUREMENTS AND ANALYSIS OF RELATIVISTIC THOMSON SCATTERING PRODUCED BY INTENSE LASERS**

Calvin Z. He
Doctor of Philosophy, 2023

Dissertation Directed by: Professor Wendell T. Hill, III
Institute for Physical Science and Technology

The viability of using relativistic Thomson scattering (RTS) as an intensity gauge of intense ($I \gtrsim 2 \times 10^{18} \text{ W/cm}^2$) lasers is explored. Theory motivating measurement of the RTS second harmonic spectrum as well as angular distribution as possible diagnostics of the laser intensity are developed and presented. Experiments conducted at the Centro de Láseres Pulsados (CLPU) laser facility in Salamanca, Spain measuring the second harmonic spectrum radiated along E as well as the angular distribution along the E-k plane are described and their results summarized. We conclude that measurements of the second harmonic spectrum provide a means for determining the laser peak intensity via the corresponding Doppler shifted onset wavelength, provided that the intensity is in the range of $\sim 10^{18}$ to $\sim 10^{19} \text{ W/cm}^2$. Measurement of the angular distribution along the E-k plane, on the other hand, does not provide features that are useful for indicating laser intensity. Possible paths forward in the study of RTS are discussed.

**EXPERIMENTAL MEASUREMENTS AND ANALYSIS OF
RELATIVISTIC THOMSON SCATTERING
PRODUCED BY INTENSE LASERS**

by

Calvin Z. He

Dissertation submitted to the Faculty of the Graduate School of the
University of Maryland, College Park in partial fulfillment
of the requirements for the degree of
Doctor of Philosophy
2023

Advisory Committee:

Professor Wendell T. Hill, III, Chair/Advisor
Adjunct Professor Charles W. Clark
Professor Julius Goldhar
Professor Ki-Yong Kim
Professor Phillip A. Sprangle

© Copyright by
Calvin Z. He
2023

Acknowledgments

First, I would like to thank my advisor, Wendell T. Hill, III, for overseeing my Ph.D., taking on the responsibilities in being my advisor as well as principal investigator of the experiments in this thesis.

Next, I would like to thank my committee members Professors Charles Clark, Julius Goldhar, Ki-Yong Kim, and Phillip Sprangle. Their feedback was helpful in constructing a more comprehensive thesis. I also would like to thank Trey Porto, who was in my committee for advancement to candidacy.

I would next like to acknowledge the funding sources that have enabled the work in thesis to be done. They include: **National Science Foundation** (PHY2010392, PHY1806584), **Natural Sciences and Engineering Research Council of Canada** (RGPIN-2014-05736), **Ministerio de Ciencia, Innovaciòn y Universidades** (FIS2016-81056-R), **LaserLab Europe IV** (654148), and **Consolidated Research Unit, Consejería de Educación, Junta de Castilla y León** (167).

This thesis would not have been possible without the collaborators and group members that I have worked with in these experiments. I therefore would like to thank Andrew Longman, Professor Robert Fedosejevs, former director of the Centro de Láseres Pulsados (CLPU) Professor Luis Roso, and Smrithan Ravichandran.

I would like to thank the personnel from the CLPU facility who provided the much needed assistance during our experiments. **Experiment 1 (2018):** Jose Perez-Hernández, Massimo de

Marco, Carlos Salgado, and Ghassan Zeraouli. **Experiment 2 (2019):** Jose Perez-Hernández, Jon Apiñaniz, and Massimo de Marco. **Experiment 3 (2022):** Marine Huault and Robert Matellanes.

Engineering and Technical Support: Diego de Luis Blanco, Juan Hernández, Jose Miguel García Mata, Diego Arana Nieto, and Ruben Hernández Martín. **Laser Crew:** Cruz Mendez, Enrique Garcia, and Jose Barcina. **Administrative Support:** Luis Roso, Luca Volpe, Giancarlo Gatti, Sara Sanchez, and Ana Santa Cruz.

Back at UMD, the IPST staff have been critical in the planning and preparation of the experiments. I therefore would like to thank Teri Schuler, Stacey Bremerman, and Johnathan Long have processed a countless amount orders on our behalf. Furthermore, the Chemical Physics program coordinators Souad Nejjar and Deborah Jenkins have been helpful in providing resources and advice regarding the meeting academic requirements for the Ph.D. program.

I would like to thank Lester Putnam for his working in machining the side arc and teaching me a great deal about machining and fabrication. The staff and volunteers at the Terrapin Works Instructional Fabrication Lab are credited for providing me structured education and hands-on training on machining in a way that is accessible. I thank Alessandro Restelli for his assistance solving various problems I've encountered in electronics as well as the knowledge I've gained through working with him.

I thank students that I have worked with in Wendell Hill's group for their help in analysis, planning as well as general lab assistance. They include Max Szostak and Emma McMillian, Sara Negussie, Lucas Smith, Nathan McLane, and Rohan Mahnot.

Communicating with representatives from Thorlabs, Edmund Optics, Hamamatsu, Andor, Newport, Grainger, McMaster-Carr, Zaber, Amplitude Laser, and others were critical for understanding the technical properties of their products, and I thank them for their insight and the

technical information they provided.

I would like to thank Professor Amy Mullin for granting me the opportunity to work with her group as part of my second lab rotation and her then students, Hannah Ogden and Tara Michael for introducing me to the world of physical chemistry.

I want to thank the graduate students that I studied with during the challenging graduate courses and for the qualifying exam. They include Angela Small, Rahul Gaur, Zachary Short, Qingfeng Wang, Junheng Tao, Jacob Fortner, Renjie Zhao, Peiyin Lee, and Yalun Yu. I also want to thank my landlord, Pedro Paz, who had been very friendly and easy to deal with throughout my time in Maryland.

Going back to when I was an undergraduate, I thank Professor Eric Hudson for providing me an opportunity to work as an undergraduate researcher in his lab and his group members Justin Christensen and David Hucul for sharing their knowledge and enthusiasm for science, along with Professor Wesley Campbell and his group members that I had worked with.

I want to thank my high school physics teacher Dean Papadakis, for making my first experience with physics fun to learn and showing a demonstrating for every topic in the class. I would like to thank my long time friends from high school who given me a sense of community and whom I still keep in touch with today. They include Devan Nichols, Juan Acevedo, and Matt Willing.

I would like to thank my family, including my mom, Lucy Huang, and my dad, Samuel He, for their support. My uncle Tim He introduced me to the computer while I was young. My younger brother Warren He told me about his experience working with Ph.D. students while I was still in community college and provided a window into graduate level education.

There are many people that have been a positive influence for me that I have not named.

They include the many professors I have taken courses with, the students and TAs I've interacted with in class, labs, as well as extracurriculars, and the people I served with in the US Army Reserves. I would like to thank them as well.

Lastly, I would like to thank the reader, for taking the time to read this thesis. I hope you will find something useful among its contents that you may apply to your own research or elsewhere.

Table of Contents

Acknowledgements	ii
Table of Contents	vi
List of Tables	x
List of Figures	xii
List of Abbreviations	xix
Chapter 1: Introduction and Literature Review	1
1.1 High Power Laser Facilities	1
1.2 The Need for <i>in situ</i> Laser Diagnostics	12
1.3 Relativistic Thomson scattering (RTS) as an Intensity Gauge	13
1.4 Coordinate System	14
1.5 Experimental Measurements of RTS	18
Chapter 2: Physics of Relativistic Thomson Scattering	20
2.1 Overview	20
2.2 Linear Thomson scattering	21
2.2.1 Equations of motion	21
2.3 Nonlinear (relativistic) Thomson scattering	25
2.3.1 The normalized vector potential	26
2.3.2 Electron Motion in the Lab Frame	28
2.3.3 Electron Motion in the Drift Frame	37
2.3.4 Radiation and Harmonic Generation	42
2.3.5 Relativistic Doppler Shift	57
2.3.6 Radiation Pattern (Numerical)	63
2.3.7 Radiation Pattern (Analytical)	72
2.3.8 Radiation Pattern Dip	77
2.3.9 Ionization and Electron Birth Conditions	78
Chapter 3: Overview of Experiments using VEGA at CLPU	84
3.1 The VEGA Laser System	84
3.2 Experimental Campaigns on RTS at CLPU	88
3.2.1 The Target Area	88
3.2.2 RTS Detectors and Gas Source	90

Chapter 4: Experiment 1: Second Harmonic Spectrum	93
4.1 VEGA-2 Laser Focal Region	94
4.1.1 Spatial Calibration	95
4.1.2 Spatial Distribution	98
4.2 VEGA-2 Temporal and Spectral Characteristics	105
4.3 Indirect Estimation of VEGA-2 Intensity	106
4.4 Microscope Objectives for RTS Detection	110
4.5 Imaging Beam Paths	111
4.6 Scattered Light Mitigation	113
4.7 Alignment of Detection Optics	113
4.8 Gas (Electron) Source	114
4.9 Image Readout	117
4.10 Spectrum Measurement	121
4.10.1 Physics of Diffraction Gratings	123
4.10.2 Spatial Calibration	132
4.10.3 Wavelength Calibration	138
4.10.4 Recombination Spectra	144
4.10.5 Temporal Gating	146
4.11 Results and Analysis	150
4.11.1 Comparison with Indirect Method	154
4.12 Discussion and Conclusion	155
Chapter 5: Experiment 2: Angular Distribution	157
5.1 VEGA-2 Characteristics	158
5.2 The All-Around Radiation Collector (AARC)	162
5.3 Fiber Optic Detectors	165
5.3.1 Coupling to Spectrometer	166
5.3.2 Wavelength Calibration	167
5.3.3 Alignment of Detection Optics	168
5.4 Scattered Light Mitigation	170
5.5 Gas (Electron) Source	171
5.6 Experimental Procedure	172
5.7 Analysis	172
5.7.1 Image Processing	172
5.7.2 Region of Interest	175
5.8 Results	176
5.9 Discussion	179
5.10 Conclusions	180
Chapter 6: Experiment 3: High Resolution Angular Distribution	182
6.1 VEGA-3 Characteristics	183
6.1.1 Focal Scan	184
6.1.2 Temporal and Spectral Measurements (Wizzler)	188
6.1.3 Energy and Temporal Measurements (Live Shots)	190
6.1.4 Peak Intensity Estimation	197

6.2	The Side Arc	199
6.3	Fiber Optic Detectors	201
6.4	Alignment of Detectors	202
6.4.1	Fiber Alignment to AARC Center	202
6.4.2	AARC Alignment to Laser Focus	211
6.5	Reimaging of Fiber Array	214
6.5.1	Signal Bleeding and Ghosting	222
6.6	Measuring Temporally Resolved Signals with the Streak Camera	224
6.6.1	Streak Camera Timing	225
6.7	Experimental Procedure	238
6.8	Results and Analysis	239
6.9	Discussion and Conclusion	245
Chapter 7:	Modeling Relativistic Thomson Scattering for Realistic Laser Beams	247
7.1	Gaussian Beams	247
7.2	Maxwell-Consistent Fields	248
7.3	Ponderomotive Scattering	249
7.4	Plane Wave Solutions Convolved with Gaussian Laser Distribution	256
Chapter 8:	Conclusion	264
8.1	Summary of Thesis	264
8.2	Conclusions from Results	266
8.3	Future Research Possibilities on RTS	267
8.3.1	Verification of Spectral Analysis of Second Harmonic	267
8.3.2	Spectral Analysis of Third Harmonic RTS	268
8.3.3	Spectral Analysis of Fundamental RTS	269
8.3.4	RTS from Protons	269
8.3.5	Further Studies of RTS Angular Distribution	270
Chapter A:	Formula Derivations	271
A.1	Angular Distribution of Radiation in Component Form	271
Appendix B:	Units and Physical Constants	275
B.1	Conversion of Electric Charge and Fields between cgs and SI	275
B.2	Conversion of Radiation Expressions from cgs to SI	279
B.3	Dimensional Analysis of Radiation Expressions	281
Appendix C:	MATLAB Code (Numerical Calculations) from Chapter 2	284
C.1	A Note on Double Precision	284
C.2	Electron Motion under Lorentz Force by an Infinite Plane Wave	285
C.3	Electron Motion under Lorentz Force by a Gaussian Temporal Pulse	287
C.4	Electron Motion in the Drift Frame via Lorentz Transform	289
C.5	Electron Motion in the Drift Frame from Analytical Expressions	291
C.6	Radiation Spectrum at $\theta = 90^\circ$	293
C.7	Total Energy Angular Distribution	294

C.8 Energy Angular Distribution over a Spectral Band	296
Appendix D: MATLAB Code (Data Analysis)	299
D.1 Calibration using USAF Test Pattern (Experiment 3)	299
Appendix E: MATLAB Code (Numerical Calculations) from Chapter 7	303
E.1 Electron Motion under Lorentz Force by a Focused Pulse	303
E.2 Volume-Weight Distribution vs. a for a Focused Gaussian Beam (peak = a_0)	306
E.3 Angular Distribution Convolved with Gaussian Beam	307
Appendix F: Gas Nozzle Simulations	311
F.1 Gas Nozzle Simulations for a 1 mm Orifice	311

List of Tables

1.1	Petawatt class lasers (including ones being planned or developed) in the North American and Asian regions, from the ICUIL world map [1] as of 2023.	10
1.2	Petawatt class lasers (including ones being planned or developed) in the European region, from the ICUIL world map [1] as of 2023.	11
2.1	Values of the transverse excursion amplitude, x_{exc} , the longitudinal periodic excursion length, z_{exc} , and the electron interaction cycle, T_{RTS} , for various values of a_0 and intensity, I	37
2.2	Table of ionization energies and appearance intensities for atomic nitrogen and argon.	81
3.1	Summary of experimental parameters of the laser.	90
3.2	Summary of experimental parameters of the detectors and gas source.	92
4.1	Measurements of the FWHM of the horizontal (H) and vertical (V) average profiles of the subset of focal spot images with the smallest spot sizes captured by the direct and wedge imaging systems (5 images from each imaging system).	97
4.2	List of molecular densities, ρ_{mol} , at various gas pressures P_{gas} , assuming an ideal gas.	117
4.3	Table of the y-pixel locations of the troughs (local minima), y_{min} , in the vertical profiles of the imaged 1 mm grid paper strip along with the differences between adjacent troughs, Δy_{min}	134
4.4	Table of the fit results of the horizontal spatial calibration of the spectrometer based on the slit width.	136
4.5	Table of the pixel positions, x , of select Hg emission lines measured by the spectrometer, their corresponding wavelengths from the NIST tables of strong lines [2], λ_N	140
4.6	Results of the linear fits to the NIST wavelengths, λ_i , as a function of measured x pixel positions, x_i , for a given central wavelength setting, λ_c	142
4.7	The residuals between the calibrated wavelengths, λ , and NIST tabulated wavelengths, λ_N , defined by $\Delta_\lambda \equiv \lambda - \lambda_N$	143
4.8	Summary values for the selected helium (He) recombination lines measured by the spectrometer.	146
4.9	Summary of the results of the second harmonic spectrum onset wavelength determined versus pulse energy on target, U	154
6.1	Spatial calibration results determined from each lineout.	188

6.2	Table summarizing the measured energy, measured pulse duration, and corrected pulse duration.	196
6.3	Values involved in the estimate of the peak intensity using the focal spot images, and measured energy and pulse duration.	198
6.4	Table of delays (from Hamamatsu spec sheet as well as experimental settings, recorded on 3/23/2022) versus sweep duration.	236
6.5	Summary statistical parameters of the fits to the angular distribution data, for various angular ranges.	244
D.1	Positions of the element line edges determined from finding the intersection between the lineout and threshold values fo Group 6 Element 2.	300
D.2	Values of element line widths determined from taking the difference between adjacent edges.	300
D.3	Chart of line pairs per mm for the corresponding Group and Element in a 1951 USAF resolution test target.	301
F.1	List of molecular densities, ρ_{mol} , at various gas pressures P_{gas} , assuming an ideal gas, along with the average interparticle spacing, $\overline{\Delta r} \equiv \rho_{mol}^{-1/3}$, and mean free path, l_p , calculated for molecular nitrogen.	312

List of Figures

1.1	Plot of record peak intensities over time.	3
1.2	Diagram illustrating the Schwinger effect.	5
1.3	Plots of ultra-intense laser facilities worldwide.	8
1.4	Diagram showing the coordinate system used in this thesis.	15
1.5	Plots showing the physical picture of relativistic Thomson scattering.	18
2.1	Diagrams illustrating the linear Thomson scattering radiation pattern.	24
2.2	The donut shaped pattern of the scattered power oriented with respect to the laser for an oscillating dipole.	25
2.3	Plots of the electron path of motion in space for $a_0 = 1$ from solving the Lorentz force differential equation for an infinite plane wave, with force components and momentum at various times superimposed.	32
2.4	Plots of electron motion in the lab frame due to interaction with a plane electromagnetic wave over a single cycle.	33
2.5	Plots of the electron position and electromagnetic wave profile at various snapshots in time for $a_0 = 1$	35
2.6	Plots of the electron position and electromagnetic wave profile at various snapshots in time for $a_0 = 3/2$	36
2.7	Plots showing the transformation of the lab frame electron motion to the average drift frame.	39
2.8	Detailed plots of the drift frame figure-8 motion.	41
2.9	Plots of electron motion in the average drift frame due to interaction with a plane electromagnetic wave over a single cycle.	42
2.10	Diagram illustrating the vectors involved in describing an electron in relativistic motion and its observed radiation.	45
2.11	Plots showing the components of electron motion in the lab frame involved in describing its radiation along with their Fourier transforms.	50
2.12	Plots showing the components of electron motion in the drift frame involved in describing its radiation along with their Fourier transforms.	51
2.13	Fourier decomposition of the electron motion.	52
2.14	Plots of radiated spectra along select directions for an electron interacting with an infinite plane electromagnetic wave.	54
2.15	Plots showing the results of electron motion due to a Gaussian temporal pulse.	56
2.16	Diagram clarifying the derivation of the relativistic Doppler effect, showing an observer moving at a speed v directly away from a source.	57

2.17	Diagram clarifying the derivation of the relativistic Doppler effect for an arbitrary direction, showing an observer moving at a speed v in a direction with an angle θ relative to the line connecting the source and observer.	59
2.18	Diagram illustrating the directional dependence of the Doppler effect.	61
2.19	Plots of spectra, calculated for a 30 fs intensity FWHM Gaussian temporal pulse and observed in the direction $\theta = 90^\circ$ and $\phi = 0^\circ$ at various intensities.	62
2.20	Plot of onset wavelength as a function of intensity for various values of observation angle θ	63
2.21	Diagram of showing the definitions of the angles θ_1 , θ_2 , α_1 , and α_2 based on the vectors β , $\dot{\beta}$, and \hat{n} for two cases concerning the value of θ_1 for the convention used in this section.	64
2.22	Polar plots of the instantaneous radiation distribution of $ \mathbf{E}_{\text{rad}} $ as a function of $\theta_1 = \angle(\hat{n}, \beta)$ (with β directed towards 0°).	66
2.23	Plots illustrating the instantaneous RTS radiation pattern for various points along the electron path.	67
2.24	Plots of the directionally-resolved total radiated energy distribution per unit solid angle.	69
2.25	Plots of the directionally-resolved radiated energy distribution in the 400 to 700 nm band per unit solid angle.	71
2.26	Plots of the analytical directionally-resolved average radiated power distribution per unit solid angle of the first harmonic ($n = 1$).	74
2.27	Plots of the analytical directionally-resolved average radiated power distribution per unit solid angle of the second harmonic ($n = 2$).	75
2.28	Plots of the analytical directionally-resolved average radiated power distribution per unit solid angle of the third harmonic ($n = 3$).	76
2.29	Plots of the RTS angular distribution in the E-k plane calculated numerically and analytically, with their dip locations compared.	78
2.30	Diagram showing barrier suppression ionization for nitrogen.	79
2.31	Plot showing the appearance intensities at various ionization stages of nitrogen and argon.	82
2.32	Zoomed-in plots of the instantaneous intensity temporal profile of a Gaussian pulse plotted against various nitrogen appearance intensities.	83
3.1	Schematics of the main components of the VEGA laser system [3].	85
3.2	Diagrams of the VEGA laser system and its diagnostics in the CLPU laser bay.	86
3.3	Diagram of the VEGA-2 beamline in the target area.	88
3.4	Diagrams of the VEGA-3 target chamber.	89
3.5	Diagrams of detectors from a) experiment 1, b) experiment 2, and c) experiment 3.	91
4.1	Diagram of the experimental layout around the focal region.	95
4.2	Diagram of the focal spot imaging and spatial calibration system.	96
4.3	Focal scan images captured by the NIR microscope objective coaxial with the wedge-reflected beam at various offsets, z , relative to the best focus, $z = 0$	99
4.4	Plots showing the image processing steps taken of the focal spot images to produce the final intensity map.	101

4.5	Plots showing the processed focal spot image and the characterization of the spot size.	103
4.6	Plots of the Wizzler reconstructed temporal profile, phase, as well as measured spectrum.	106
4.7	Plots of the intensity per unit pulse energy based on the processed focal spot image at best focus.	110
4.8	Annotated photo of the internal layout of the VEGA-2 target chamber.	112
4.9	Annotated photo of the layout outside of the VEGA-2 target chamber.	112
4.10	Photo of the alignment tip at the focal region with the RTS detection microscopes and brass gas nozzle.	114
4.11	Plot of predicted gas density per unit reservoir density as a function of position from the nozzle. This is based on Eq. 4.13, which is determined from Monte Carlo simulations described in Appendix section F.1. The shaded region includes the 95% confidence interval for the best fit parameter of R_f	116
4.12	Images of the focal region captured during live shots by the $E_{ }$ objective under varying conditions.	118
4.13	Images of the focal region captured during live shots by the E_{\perp} objective at various conditions.	120
4.14	Cropped taken during the live shots emphasizing the location of the laser beam. .	121
4.15	Diagrams of the Oriel MS260i spectrometer showing a) exterior photo and b) schematics of internal optics, which is based on the Czerny-Turner design [4]. .	123
4.16	Diagram of a) the ray geometry of a blazed diffraction grating and b) photo of the physical diffraction gratings used in the experiment.	124
4.17	Diagrams showing the coordinate system used in the Fresnel-Kirchoff integral from two perspectives.	126
4.18	Diagrams of the coordinate system used in the Fresnel-Kirchoff integral applied to a diffraction grating.	129
4.19	Plots of $H(N, kdp/2)$ for a) two different values of N and b) two wavelengths differing by $\delta\lambda$	130
4.20	Diagrams showing the calibration of the entrance slit to the spectrometer.	133
4.21	Images of the laser-illuminated entrance slit captured by the spectrometer readout camera at varying slit widths and their horizontal profiles.	135
4.22	Plot of the data and linear fits to the slit width, w_{real} , based on the micrometer reading as a function the width of the horizontal profile, Δx , from the slit image captured by the spectrometer readout camera.	136
4.23	Diagrams illustrating the orientation of the laser and field polarizations as they are images onto the entrance slit.	138
4.24	Spectrum images (1024 wide by 255 high) of mercury emission lines from a) - c) a UV lamp at various central wavelength, λ_c , settings of the spectrometer and of d) the room lights.	139
4.25	Plots of the NIST tabulated wavelengths as a function of the measured pixel positions, x , of mercury (Hg) strong lines, at various central wavelengths, λ_c	141
4.26	Recombination spectra of a) helium (w/ 1% nitrogen mix), b) argon, and c) nitrogen.	145
4.27	Diagrams of illustrating the intensified CCD camera and its gating operation.	147

4.28	RTS spectra (background-subtracted) taken using the E_{\perp} objective over subsequently smaller gate durations, τ_{gate}	148
4.29	RTS spectra taken using the E_{\perp} objective with $\tau_{gate} = 5$ ns over various gate delay offsets, Δt_{delay} as well as a background spectrum.	149
4.30	Spectrum images captured during the live laser shots by the E_{\perp} -objective (a-b) on 07/11/2018 a) with and b) without the use of a BG39 filter.	151
4.31	Plots of spectral profiles of the spectrum images for three values of pulse energy: a) 2.	153
4.32	Plot comparing the predicted peak intensities from measurement of the second harmonic spectrum onset wavelengths (data points) to the peak intensities estimated from the focal spot images.	155
5.1	Diagram of experimental layout, with the target chamber viewed from the top.	158
5.2	Plots of diagnostic measurements of the VEGA-2 beam from the laser bay metrology bench.	159
5.3	Annotated photo of the interior of the vacuum chamber containing experimental components, including the focal spot imaging system.	160
5.4	Images showing the focal spot and spatial calibration method.	162
5.5	Models of the AARC showing an isometric (left) and front (right) view.	163
5.6	Plot of the mapping between $(\theta_{Arc}, \phi_{Arc})$ and (θ, ϕ)	165
5.7	Exploded diagram of the fiber-based detection optics.	166
5.8	Photos of a) the fiber connected to a vacuum fiber feedthrough, b) bare fibers coupled into the spectrometer input via a 3D printed mount.	167
5.9	Spectrometer image of the mercury (Hg) room lights captured by two optical fiber lines from the detectors mounted in the AARC.	168
5.10	Photo, a), of the AARC assembly with a blue diode laser illuminating the glass bead mounted on the alignment tip, and b) the signal of the illuminated bead captured by the fiber detectors and spectrometer system.	169
5.11	Photos of a) the beam dump consisting of an array of ND filters glued to an aluminum frame and b) the beam dump chamber with the beam dump mounted at Brewster's angle relative to the beam.	170
5.12	Photo of a) the gas nozzle and b) the reservoir chamber.	171
5.13	Spectrometer images showing the image processing steps.	173
5.14	Cropped image of the RTS spectrum captured by the fiber mounted at $\phi_{Arc} = 0$	176
5.15	Plots showing the results of the angular distribution measurement.	178
6.1	Diagram of the experimental layout for the 2022 RTS experiment.	183
6.2	Top view of the CAD model of the VEGA-3 target area.	184
6.3	Schematic (not drawn to scale) of the two focal spot imaging systems.	185
6.4	Images of the focal spot captured by the wedge imaging system at various offsets from the plane of best focus.	186
6.5	Images (labeled Im1 to Im4) of various groups and elements of the USAF test pattern used.	187
6.6	Plots of the lineouts sampled from the images of the USAF test pattern images.	187

6.7	Plots of the pattern line widths calculated from taking the difference between the locations of the pattern line edges determined from their intersections with various threshold values (within the horizontal dotted lines in Fig.	188
6.8	Plots of a) the reconstructed temporal pulse shape and phase and b) the spectrum measured from the VEGA-3 laser by the Wizzler at the laser bay metrology bench.	189
6.9	Laser energy (last shot of run) and autocorrelator-measured pulse duration data (averaged over each run) for each run number for the runs operating at 2 J nominal energy, 8 shots per run at 1 Hz.	191
6.10	Laser energy (last shot of run) and autocorrelator-measured pulse duration data (averaged over each run) for each run number for the runs operating at 6 J nominal energy, 8 shots per run at 1 Hz.	192
6.11	Laser energy (last shot of run) and autocorrelator-measured pulse duration data (averaged over each run) for each run number for the runs operating at 10 J nominal energy, 8 shots per run at 1 Hz.	193
6.12	Laser energy and autocorrelator-measured pulse duration data for each run number for the runs operating at 30 J nominal energy, single-shot.	194
6.13	Plot of the Δt versus GDD curve along with measured and corrected values of pulse duration.	197
6.14	Plot of the estimated peak intensity (left vertical axis) versus energy on target as well as the pulse duration (right vertical axis) versus energy on target.	198
6.15	CAD images of the side arc assembly mounted on the rotary base in isometric view and side view.	200
6.16	Transmission curves of a) the shortpass 725 nm filter, b) the bandpass 600-650 nm filter, and the combined (shortpass 725 nm and bandpass 600-650 nm) filter set plotted in log scale.	202
6.17	Photo of the setup used for detector alignment.	203
6.18	Images of the bead at maximum excursion to the left and right of the image out of a set of images captured every 10° over a full rotation of the rotary base.	204
6.19	Photos showing the profiles of the back illuminated light from the fibers at different locations.	205
6.20	Images of the bead (in focus) and projection of the back illuminated fiber light for each of the four detectors mounted at different positions on the side AARC.	205
6.21	Photos of the aluminum foil shims at different stages of the application process for ever-so-slight pointing adjustment of the detector toward the desired direction.	206
6.22	Images of the alignment tip (bead missing) and projected back illuminated fiber light after these detectors have been shimmed.	207
6.23	Images showing two types of detector holders.	208
6.24	Diagram of the placement of the inspection imaging system during alignment.	211
6.25	Images captured by the microscope objective imaging system oriented along the main beam during alignment.	213
6.26	Diagram of the reimaging system used for coupling the output fibers onto the input slit of the streak camera, showing the geometric quantities used for calculating coupling efficiency.	215
6.27	Photos showing the setup used for measuring image distance s_o versus object distance s_i of the reimaging lens.	217

6.28 Plots of a) the image distance versus object distance datasets taken over two different days along with a fit over the combined dataset and b) same as a) but with the magnification measurements included.	217
6.29 Plot of the overall efficiency versus magnification from the dataset as well as the curve based on the fit parameters.	218
6.30 Photo showing initial prototyping of a system for holding mounting multiple bare fibers.	219
6.31 Photos showing the final assembly used to mount the output fibers.	220
6.32 Diagram of the full assembly for output fiber mounting and reimaging.	221
6.33 Images of the reimaged fibers along with ambient light collected at the input slit of the streak camera.	222
6.34 Images of individual illuminated fibers and their of ghost images, captured by the streak camera.	223
6.35 Plots of the lineouts of the illuminated fiber ends (top four images) and that of their corresponding ghost spots (bottom four images).	224
6.36 Diagram of components in a streak camera for converting temporal light signals into streak images.	225
6.37 Timing diagram for normal mode operation.	226
6.38 Timing diagram for trigger mode.	227
6.39 Diagram of trigger network for the streak camera in the target area.	228
6.40 Scope image showing oscillator train and streak monitor out.	229
6.41 Diagram of the trigger sources in the laser bay.	230
6.42 Scope image showing two triggers synchronized with the laser shots, CH2: V3-2 (blue) and CH4: V3-1 (green).	231
6.43 Streak camera images captured manually subsequently in time showing the evidence of jitter with jumps between adjacent oscillator pulses in the laser bay. . . .	232
6.44 Centroids averaged over the four fiber detectors from the streak camera images at a 500 ps streak duration, taken during the live runs of the angular RTS scans at different energies.	233
6.45 Streaked images from air breakdown from the laser at low power (3 mJ) at different streak times.	234
6.46 Streaked images from 6 J laser interaction with gas on (800 mbar reservoir pressure) at different streak times.	235
6.47 Image of fiber face on the readout camera in focus mode, as well as a vertical lineout of one of the fiber spots.	237
6.48 An example image of the streaked fibers (labeled from left to right: F1, F2, F3, F4) taken with a streak duration of 500 ps.	240
6.49 Plots of the angular distribution measurement data taken at different energies for both the F3 and F4 detectors in log scale.	241
6.50 Plots of the angular distribution data in linear scale at various pulse energies along with parabolic fits over the data points in the angular range of 50° to 90°.	242

6.51 Plots of a) the parabola vertex position, θ_{min} , from the fits to the angular distribution data using various ranges of angles (details in Table 6.5) and b) the forward skewing factor, S_f , for each angular distribution dataset defined as the ratio between the average of the signals in the angular range of 50° to 60° to that in the angular of 80° to 90° (see Eq.	243
7.1 Plots of the electron motion born at $z(t_0) = 0$, $y(t_0) = 0$, and various locations in $x(t_0)$ from $x(t_0) = 0$ to $x(t_0) = w_0$, where $w_0 = 20 \mu\text{m}$ for a_0 values of 1 (a and e), 2 (b and f), and 3 (c and g).	252
7.2 Plots of a traveling focused pulse ($w_0 = 20 \mu\text{m}$, $a_0 = 2$) and the resulting scattered electrons born at focus.	255
7.3 Plots of a) contour lines and b) surface contours of constant a for a Gaussian spatial distribution.	258
7.4 Plots of the weight distributions, $\frac{\Delta V}{\Delta a}(a; a_0)$, calculated numerically for various values of a_0	259
7.5 Plots of the total angular distribution of photons rate per unit solid angle in the second harmonic, $\frac{d\Gamma^{(2)}}{d\Omega}$, calculated from the weighted sum of plane wave solutions.	261
7.6 Plots of the total angular distribution of photon rate per unit solid angle in the second harmonic, $\frac{d\Gamma_{tot}^{(2)}}{d\Omega}$, from calculating the weighted sum of the plane wave solutions looking along the E-k plane.	262
A.1 Diagrams of a unit sphere with grid lines which are mapped to a rectilinear 2D grid in θ and ϕ	274
C.1 Plot of eps (precision) as a function of the \log_{10} value.	285
D.1 Plots used to illustrate an example of the spatial calibration using a USAF test pattern.	300
F.1 Plots of the initial position and velocity distribution of particles used in the simulation.	314
F.2 Plots of the position distribution, shown in isometric as well as top view, of the simulated particles at various times.	315
F.3 Plots of single variable as well as two-variable histograms of simulated particle numbers.	318
F.4 Plots of histograms averaged over 10 simulation runs.	319

List of Abbreviations

AARC	All-Around Radiation Collector
AC	Alternating Current
ADK	Ammosove-Delone-Krainov
as	Attosecond
BP	Bandpass
BSI	Barrier Suppression Ionization
CAD	Computer-aided Design
CCD	Charge-Coupled Device
CDF	Cumulative Distribution Function
CEP	Carrier-envelope Phase
cgs	Centimeters-grams-seconds
CH	Channel
CLPU	Centro de Láseres Pulsados
CMOS	Complementary Metal-Oxide Semiconductor
CNC	Computer Numeric Control
CPA	Chirped Pulse Amplification
CW	Continuous Wave
DC	Direct Current
ELI	Extreme Light Infrastructure
ELWD	Extremely Long Working Distance
eps	Epsilon of the Machine
eV	Electron-volt
EW	Exawatt
f/#	F-number
FF	Far-field
FOV	Field of View
FPGA	Field-programmable Gate Array
FROG	Frequency-resolved Optical Gating
fs	Femtosecond

FWHM	Full-width at Half-maximum
GDD	Group Delay Dispersion
GVD	Group Velocity Dispersion
HeNe	Helium-Neon
Hg	Mercury
HWHM	Half-width at Half-maximum
HV	High Vacuum
ICUIL	International Committee on Ultra-High Intensity Lasers
ID	Inner Diameter
ICCD	Intensified Charge-Coupled Device
InGaAs	Indium Gallium Arsenide
IPST	Institute for Physical Science and Technology
LG	Laguerre-Gaussian
LLNL	Lawrence Livermore National Laboratory
LP	Longpass
LTS	Linear Thomson Scattering
LW	Liénard-Wiechert
MCP	Microchannel Plate
MP	Mega-pixel
NA	Numerical Aperture
ND	Neutral Density
Nd:Glass	Neodymium-doped Glass
NF	Near-field
NIF	National Ignition Facility
NIR	Near Infrared
NIST	National Institute of Standards and Technology
NOA	Norland Optical Adhesive
NLTS	Nonlinear Thomson Scattering
ns	Nanosecond
OAP	Off-axis Parabola
OD	Outer Diameter
ODE	Ordinary Differential Equation
PP	Principal Plane

PW	Petawatt
ps	Picosecond
QED	Quantum Electrodynamics
QFT	Quantum Field Theory
ROI	Region of Interest
RMS	Root Mean Square
RTS	Relativistic Thomson Scattering
SI	International System of Units
SLAC	Stanford Linear Accelerator Center
SMA	SubMiniature Version A
SP	Shortpass
SWIR	Short Wave Infrared
TCC	Target Chamber Center
Ti:Sa	Titanium-doped Sapphire
TTL	Transistor-Transistor Logic
TW	Terawatt
UHV	Ultra-high Vacuum
UMD	University of Maryland
UV	Ultraviolet
VIS	Visible
WD	Working Distance

List of Common Symbols

a_0 Normalized Vector Potential

A Vector Potential

A Area

A_0 Vector Potential Amplitude

B Magnetic Field

B_0 Magnetic Field Amplitude

β Normalized Velocity

β Normalized Speed

c Vacuum Speed of Light

χ^2 Chi-squared

e Elementary Charge

E Electric Field

E_0 Electric Field Amplitude

ϵ_0 Permittivity of Free Space

f Focal Length or Function or Frequency

F Force

γ Lorentz Factor

γ_0 Average Oscillatory Lorentz Factor

γ_D Lorentz Factor of Drift Velocity

Γ Rate

I Intensity

I_0 Peak Intensity

I_{pk} Peak Intensity

k Propagation Vector

k Wavenumber

λ Wavelength

λ_0	Incident Laser Wavelength
λ_r	Onset Wavelength
m	Mass
m_e	Electron Mass
m_p	Proton Mass
M	Magnification
μ_0	Permeability of Free Space
n	Harmonic Number
$\hat{\mathbf{n}}$	Unit Observation Direction Vector
n_e	Electron Density
N	Number of Particles
N_e	Number of Electrons
ω	Angular Frequency
ω_0	Incident Laser Angular Frequency
Ω	Solid Angle
$d\Omega$	Differential Solid Angle
\mathbf{p}	Momentum
p	Magnitude of Momentum
P	Power
P_{pk}	Peak Power
ϕ	Azimuthal Angle or Spectral Phase
Φ	Electrostatic Potential
\mathbf{r}	Radial Vector or Electron Position
r	Radial Distance or Electron Distance
r_0	Classical Electron Radius
\mathbf{S}	Poynting Vector
s_i	Image Distance
s_o	Object Distance
t	Time
Δt	Pulse Duration (FWHM)
T	Period or Temperature
τ	$\exp(-1)$ Pulse Duration
θ	Polar Angle

U Energy

V Potential or Volume

\mathbf{v} Electron Velocity

v Electron Speed

w_0 Beam Waist

\mathbf{x} Observation Position

$\hat{\mathbf{x}}$ Unit Vector along x axis

$\hat{\mathbf{y}}$ Unit Vector along y axis

z_R Rayleigh Length

$\hat{\mathbf{z}}$ Unit Vector along z axis

Z Ionization Stage

Chapter 1

Introduction and Literature Review

Objective of Research

This thesis is motivated by the technological development of the world's most powerful lasers, which can be focused to intensities $\gtrsim 10^{18} \text{ W/cm}^2$, and are also known as ultraintense lasers. As the intensity of these lasers reach ever higher regimes (due to not only advances in technology but also establishment of programs for constructing petawatt laser facilities), opportunities for experimentally testing new physics have emerged along with a need for laser diagnostics that have not kept up with the growth in laser output. Relativistic Thomson scattering (RTS), also known as nonlinear Thomson scattering, is a phenomenon that occurs readily in ultraintense laser facilities, specifically due to the scattering of free electrons by a low frequency (e.g., 800 nm infrared) laser at focus, and have recurrently been proposed as a viable diagnostic for laser intensity. It therefore follows that the objective for the research discussed in this thesis is to experimentally explore the feasibility of using RTS as an intensity gauge, and in doing so, also perform novel measurements of RTS that have not previously been accomplished.

1.1 High Power Laser Facilities

Since the invention of the laser, first conceptualized in 1958 [5] and demonstrated in 1960 [6], followed by methods for generating shorts pulses down to the nanosecond (ns) regime, where 1 ns is equal to 10^{-9} seconds (s), via Q-switching [7] (1963) and later the picosecond (ps) regime,

with 1 ps being equal to 10^{-12} s, via modelocking [8] (1964), the record for the peak focused intensities would grow at an exponential rate analogous to Moore's law [9]. It eventually hit a plateau, as shown in Fig. 1.1, as a result of the difficulty in amplifying short pulses without undesired effects, such as damage to optics [10]. The plateau was finally broken in 1985 following the invention of chirped pulse amplification (CPA) [11], originally based on neodymium-doped glass (Nd:Glass) [12, 13], that allowed short pulses to be amplified by first temporally stretching the pulse, effectively reducing their peak intensity before being amplified by a gain medium, and finally compressed without damage to optics. This method was later applied to titanium-doped sapphire (Ti:Sapphire) crystals [14] and, with the invention of Ti:Sapphire Kerr lens mode locking (KLM) [10, 15], pulse durations were brought down to the fs regime. These technologies enabled broad commercial development of intense lasers as well as global construction of nationally and multi-nationally funded laboratories housing the world's most powerful lasers.

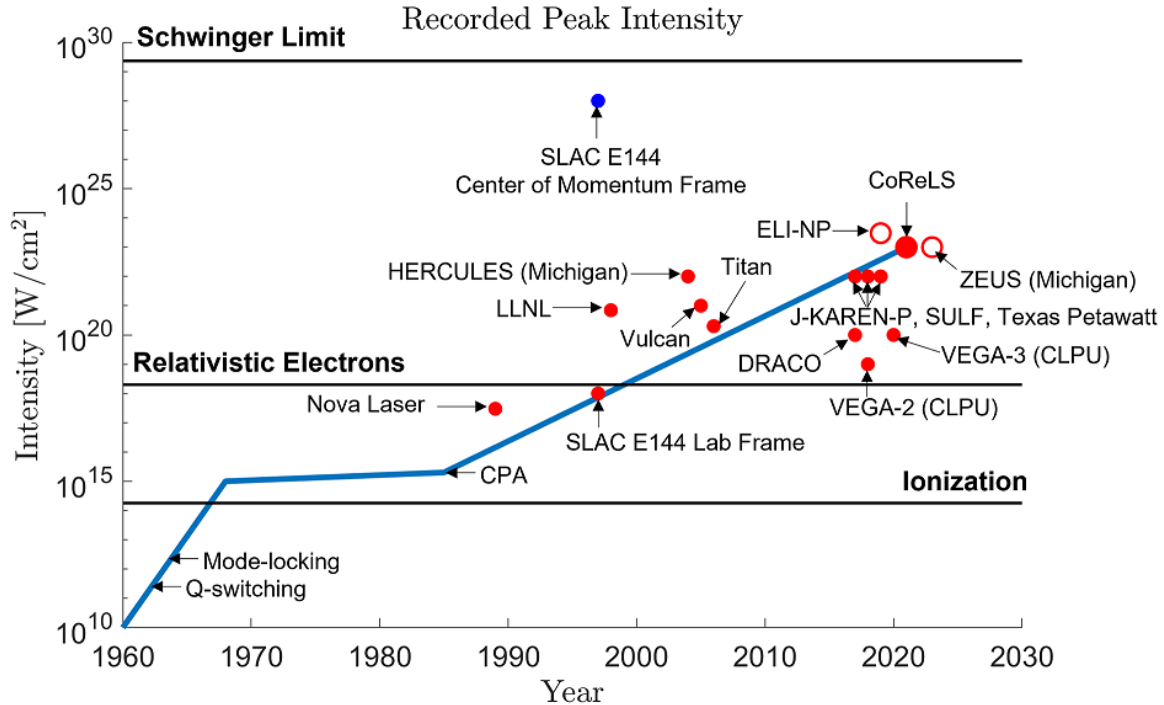


Figure 1.1: Plot of record peak intensities over time. This is an updated replotting of Fig. 1.3 in [9]. The red dots include demonstrated peak intensities [3, 16–23], of which today CoReLS holds the record (10^{23} W/cm^2). The blue dot corresponds to intensity seen at the center of momentum frame of a relativistic electron beam during the SLAC E144 experiment [24–26]. The first open red circle corresponds to the intensity of the ELI-NP facility, which has current record demonstrated peak power [27], if it was focused to a $1 \mu\text{m}$ spot (not yet demonstrated). The second red circle corresponds to the ZEUS laser, which has begun operation and promises peak intensities of 10^{23} W/cm^2 .

New record intensities enable new frontiers in physics research. In the early beginnings of the laser, experiments were conducted on the transitions between electronic bound states of atoms and molecules. Shortly after the invention of ultrashort pulse lasers, peak intensities reached levels large enough to ionize atoms and molecules with low frequency photons via multiphoton processes, and the field of strong field laser physics emerged to study dynamics of ionization and molecular dissociation at ultrafast time scales [28–31]. For example, molecular nitrogen ionizes at an electron appearance intensity of $I \approx 2 \times 10^{14} \text{ W/cm}^2$, based on a model which is discussed in section 2.3.9. Furthermore, new frontiers in nonlinear optics opened up to study

harmonic generation from such lasers [32, 33]. At intensities sufficient to accelerate an electron to relativistic speeds in a single cycle, new experiments become possible in exploring the properties of the relativistic electrons scattered by the laser, including the radiated light known as relativistic Thomson scattering (RTS), which is the focus of this thesis with a literature review provided in sections 1.3 and 1.5. This regime of so-called relativistic intensities occur at $I \approx 2 \times 10^{18} \text{ W/cm}^2$, corresponding to a normalized vector potential, discussed later in section 2.3.1, of $a_0 = 1$.

At ultrarelativistic intensities, where $I \gg 10^{21} \text{ W/cm}^2$, it would be possible to test for radiation reaction [34, 35], Unruh radiation [36], and theories in quantum electrodynamics (QED) associated with positron-electron pair production [37–41] by an intense field. Radiation reaction is the phenomenon in which a charged particle emitting radiation experiences non-negligible recoil as a result of energy and momentum conservation in the radiation process. Unruh radiation is a generalization of Hawking radiation, which we briefly explain here. In 1975, Hawking predicted that particles accelerated by the strong gravitational fields of a black hole at the event horizon can radiate like a blackbody as a result of quantum mechanical effects, a process that led to the famous idea of black hole evaporation [42]. Unruh later generalized this process for particles undergoing any form acceleration [43]. Although these phenomena are theoretical and have not been directly observed, it is believed that ultraintense lasers may be able to produce conditions necessary to create Unruh radiation, due to the violent accelerations imparted by the lasers upon electrons.

Pair production can be understood from the Dirac sea model, in which space is occupied by an infinite sea of electrons obeying the Pauli exclusion principle having energy states consistent with the negative solutions in the equation: $U = \pm\sqrt{(pc)^2 + (m_e c^2)^2}$. According to Euler and Heisenberg [44, 45], an electric field, E_0 , on the order of or larger than the Schwinger critical

electric field $E_s = \frac{m_e^2 c^3}{e\hbar}$ distorts the energy spectrum in space, as shown in Fig. 1.2, such that an electron with energy $-m_e c^2$ has a substantial probability $\approx \exp(-\pi E_s/E_0)$ to tunnel into the energy level corresponding to an electron with energy $m_e c^2$. This transition results in an electron being created and leaves a "hole" in the Dirac sea which behaves physically like an electron with positive charge. Modern physics considers this hole as a particle called the positron. The Schwinger electric field is defined as the field required to accelerate an electron to a kinetic energy equal to its rest mass, $m_e c^2$, over a distance equal to the reduced Compton wavelength, $\bar{\lambda}_c = \frac{\hbar}{m_e c} \approx 382$ femtometers (fm), where 1 fm is equal to 10^{-15} m and the reduced Compton wavelength is equal to the Compton wavelength, λ_c , divided by 2π . This condition is achieved at an electric field strength of 1.3×10^{18} V/m and an intensity of $\approx 10^{29}$ W/cm².

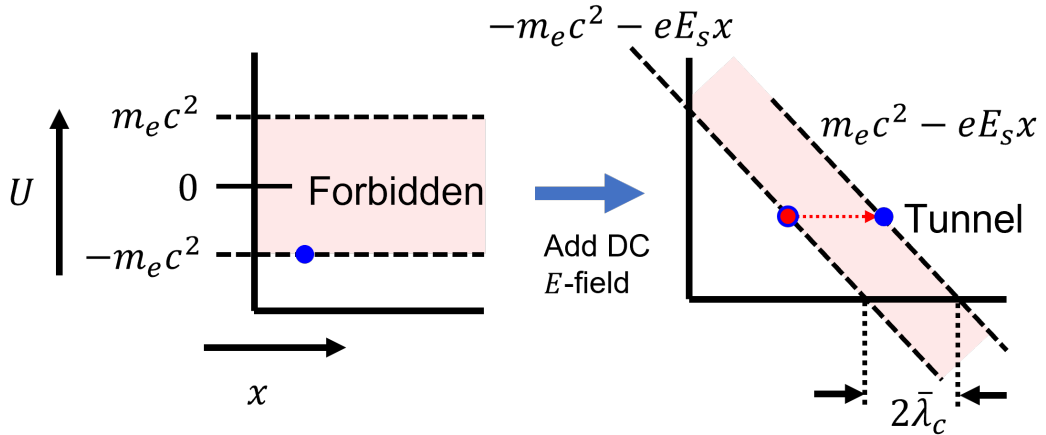


Figure 1.2: Diagram illustrating the Schwinger effect. Energy diagrams over space show the energy levels corresponding to an electron at rest, $m_e c^2$, as well as an electron occupying the first negative solution to $U = \pm\sqrt{(pc)^2 + (m_e c^2)^2}$, namely $U = -m_e c^2$. When a static electric field is applied over space, the energy spectrum in space is distorted so that an electron occupying the $-m_e c^2$ energy level may tunnel through the forbidden region into the $m_e c^2$ energy level. This diagram is based on Fig. 1 in [44, 45].

Although pair production has been observed in the SLAC E-144 experiment at a laser intensity of only $\sim 10^{18}$ W/cm² [26], this relied on the use of a relativistic electron beam in which the observed laser field strength is enhanced in the electron rest frame. In order to generate the

Schwinger electric field in the laboratory frame, it would be necessary for laser peak intensities to increase by at least 6 orders of magnitude compared to what is available today. The previously mentioned research areas in the relativistic and ultrarelativistic regimes are certainly not exhaustive of all of the possibilities created by ultraintense lasers. A number of publications, such as the 2022 Multi-Petawatt Physics Prioritization (MP3) Workshop report [46], the 2019 Brightest Light Initiative Workshop report [47], the 2018 consensus study report by the National Academies of Sciences [9], as well as review papers on the field of ultraintense lasers [10, 48, 49] have cataloged the many research opportunities and applications enabled by ultraintense lasers, to include laser wakefield generation, light source generation, high energy density science, radiation therapy, and manufacturing.

Pulsed lasers are characterized by their peak power, P_{pk} , which is roughly equal to the pulse energy, U , divided by the pulse duration Δt . When focused, pulsed lasers reach high peak intensities, I_{pk} , roughly equal to the peak power divided by the area of the beam profile at the focal plane, approximated as a circular disc with a radius equal to the beam waist, w_0 .

$$I_{\text{pk}} \approx \frac{P_{\text{pk}}}{\pi w_0^2} \approx \frac{U}{\Delta t \pi w_0^2} \quad (1.1)$$

Ultraintense laser pulses typically have Δt on the order of tens of fs ($1 \text{ fs} = 10^{-15} \text{ s}$) in duration. Although the shortest duration are lasers pulses are on the order of ~ 40 attoseconds ($1 \text{ as} = 10^{-18} \text{ s} = 10^{-3} \text{ fs}$), these lasers are typically weak. Relativistic intensities ($I_{\text{pk}} \gtrsim 10^{18} \text{ W/cm}^2$) are achievable for $P_{\text{pk}} \sim 10 \text{ TW}$ ($U \sim 0.5 \text{ J}$) lasers, where 1 TW is equal to 10^{12} W , that are tightly focused (e.g., f/3 or $w_0 \sim 2 \mu\text{m}$) and for $\sim 100 \text{ TW}$ ($\sim 5 \text{ J}$) lasers that are focused with a more relaxed geometry (e.g., f/10 or $w_0 \sim 20 \mu\text{m}$). Petawatt class lasers ($1 \text{ PW} = 10^{15}$

$W = 10^3$ TW) are able to take peak intensities to $\sim 10^{20}$ W/cm² and beyond. Manufacturing of ultraintense lasers are lead by the companies Thales Group and Amplitude Laser, providing entire laser systems as well as components for home-made ultraintense lasers. Figure 1.3 shows the geographical distribution of high-peak-power lasers as of 2023.

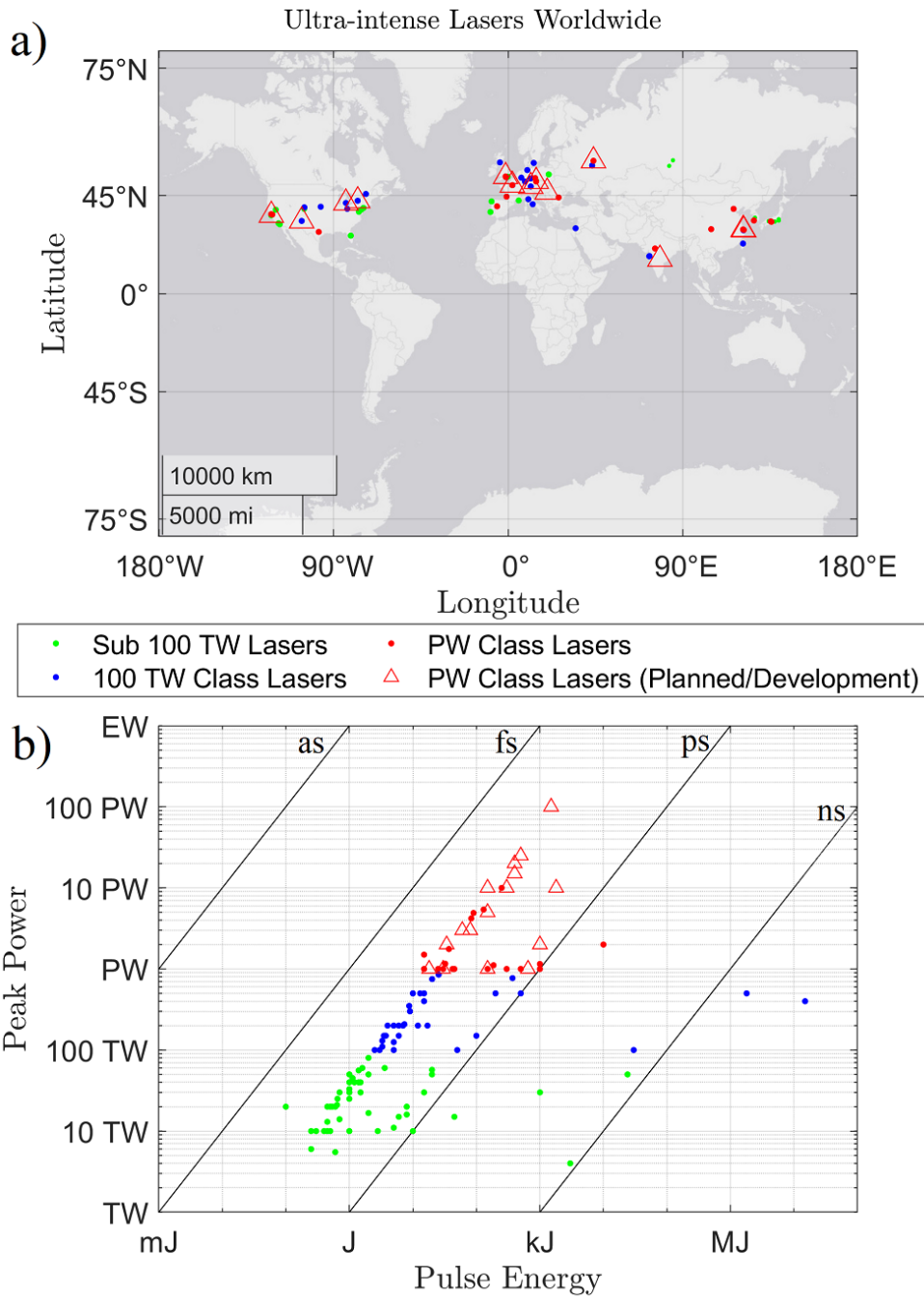


Figure 1.3: Plots of ultra-intense laser facilities worldwide. Shown are a) geographic locations of and b) the peak power vs. pulse energy with contours of constant pulse duration of laser systems from the dataset obtained from the ICUIL world map [1]. This dataset includes an up-to-date list of laser systems known to ICUIL either in excess of 10 TW peak power or capable of being focused to at least 10^{19} W/cm².

The highest peak powers today are achieved by lasers that have a duration \sim 20 fs and pulse energies \sim 100 J. Although the most energetic lasers have pulse energies on the order of a MJ, such as the National Ignition Facility (NIF) at the Lawrence Livermore National Laboratory (LLNL) or the Laser MégaJoule (LMJ) at the Centre D'etudes Scientifiques et Techniques D'aquitaine (CESTA) in France, the energies of these lasers are spread out over an order of a few nanoseconds, reaching peak intensities of only \sim 500 TW. As of writing (2023), the current record holder for highest demonstrated peak power is the Center for Relativistic Laser Science (CoReLS), Institute for Basic Science in the Republic of Korea, having demonstrated in 2020 a pulse intensity of over 10^{23} W/cm² [23] with a laser reportedly operating at 2.7 PW peak power on target (67% of the full 4 PW power that the system is capable) and focused using an f/1.1 off-axis parabolic mirror (OAP) to a beam diameter full-width at half-maximum (FWHM) of 1.1 μ m. The record holder for highest demonstrated peak power is the Extreme Light Infrastructure - Nuclear Physics (ELI-NP) facility in Romania, Europe, at just over 10 PW reported in March, 2019 [27].

It is expected over the next decade that there will be further technological advancement towards 100 PW lasers and beyond [49]. A number of 10 PW lasers are currently in development around the world, as well as a 25 PW laser being planned for construction in Rochester, NY [50, 51] and a 100 PW laser in Shanghai, China, as can be seen in the lists of petawatt class lasers in Tables 1.1 and 1.2. Plans to reach exawatt ($1\text{ EW} = 10^3\text{ PW} = 10^{18}\text{ W}$) class lasers and beyond have also been discussed [48, 49].

Table 1.1: Petawatt class lasers (including ones being planned or developed) in the North American and Asian regions, from the ICUIL world map [1] as of 2023. The list is organized geographically.

Laser	Status	Facility	Location	Peak Power [PW]	Pulse Energy [J]	Pulse Duration [fs]
BELLA	Operational	LBNL	Berkeley, CA, US	1	42.2	40
Titan	Operational	LLNL-JLF	Livermore, CA, US	1	300	700 to 20000
MEC	In Development	SLAC	Portola Valley, CA, US	1	150	150
Z-Petawatt	In Development	SNL	Albuquerque, NM, US	1	650	500
Texas Petawatt	Operational	UTex	Austin, TX	1.11	186	167
ZEUS	In Development	UMich	Ann Arbor, MI, US	3	80	25
EP-OPAL	Planned	LLE	Rochester, NY, US	25	500	20
RRCAT PW	Operational	RRCAT	Indore, IN	1	25	25
TIFR-H PW	Planned	TIFR-H	Hyderabad, IN	1	30	25
CAEP 4.9 PW	Operational	CAEP	Mianyang, CN	4.9	90.1	18.6
Xtreme Light - III	Operational	IOP	Beijing, CN	1.16	32.3	27.9
SIOM 1.76 PW	Operational	SIOM	Shanghai, CN	1.76	37	21
SEL 100 PW	Planned	SEL	Shanghai, CN	100	1500	15
Shenguang II UP PW	Operational	SIOM	Shanghai, CN	1	1000	1000 to 10000
SIOM 5 PW	In Development	SIOM	Shanghai, CN	5	1500	15
SULF 5.4 PW	Operational	SULF	Shanghai, CN	5.4	130	24
SULF (Upgrade)	In Development	SULF	Shanghai, CN	10	300	30
CoReLS PW	Operational	CoReLS	Gwangju, KR	4.2	83	19.6
LFEX 2 PW	Operational	ILE-j	Osaka, JP	2	1000	1000 to 20000
J-KAREN-P	Operational	KPSI	Kizugawa, JP	1	30	30

Table 1.2: Petawatt class lasers (including ones being planned or developed) in the European region, from the ICUIL world map [1] as of 2023. The list is organized geographically.

Laser	Status	Facility	Location	Peak Power [PW]	Pulse Energy [J]	Pulse Duration [fs]
Vulcan (Upgraded)	Planned	RAL	Didcot, UK	20	400	20
Vulcan	Operational	RAL	Didcot, UK	1	500	500
Orion	Operational	AWE	Aldermaston, UK	1	500	500
VEGA 3	Operational	CLPU	Salamanca, ES	1	30	30
PETAL	Operational	CESTA	Le Barp, FR	1.15	1000	500
F2	Operational	APOLL	Saclay, FR	1	15	15
F1	In Development	APOLL	Saclay, FR	10	150	15
ATLAS-3000	In Development	CALA	Garching bei München, DE	3	60	20
PENELOPE	Operational	HZDR	Dresden, DE	1	150	150
DRACO	Operational	HZDR	Dresden, DE	1	45	30
Laser 3 HAPLS	Operational	ELI-Cz	Dolní Břežany, CZ	1	30	30
Laser 4 ADBC	In Development	ELI-Cz	Dolní Břežany, CZ	10	1800	150
Laser 2 Amos (stage 2)	In Development	ELI-Cz	Dolní Břežany, CZ	1	18	20
HF - 2 PW arm	In Development	ELI-Hu	Szeged, HU	2	34	17
CETAL Configuration 1	Operational	INFLPR	Bucharest, RO	1	25	25
HPLS	Operational	ELI-NP	Măguerele, RO	10	250	25
PEARL	Operational	IAP	Nizhny Novgorod, RU	1.5	15	10
PEARL-10	In Development	IAP	Nizhny Novgorod, RU	5	150	30
XCELS 15 PW	Planned	XCELS	Nizhny Novgorod, RU	15	400	25
Femta-Ray	Decommissioned	VNIIEF	Sarov, RU	1	70	70

1.2 The Need for *in situ* Laser Diagnostics

As discussed in section 1.1, ultraintense lasers open up a variety of new tests in physics and other applications. There will be many experiments that rely on diagnostics of the focused intensity itself for scientific verification and reproducibility. Furthermore, laser diagnostics goes hand-in-hand with laser control and optimization, in order to enable user facilities to provide high-quality and predictable beams. Laser intensity characterization methods, however, have not kept pace with the advances in laser peak power. High power laser systems also present new challenges to control and optimization, as they tend to suffer more from effects that distort the beam profile, through what is known as spatiotemporal distortions, causing a deviation from the ideal (e.g., Gaussian) and resulting in significant reductions in peak intensity, as discussed in [52, 53]. Current intensity characterization methods, being limited by the damage thresholds of detectors, rely on either sampling a small fraction of the main beam to produce a diagnostic beam for subsequent analysis at a diagnostics bench or performing measurements of the main beam operating at low powers, neither of which are guaranteed to both reproduce the beam exactly at focus and capture effects that scale with the full power intensity.

An *in situ* intensity gauge would provide a means to characterize the behavior of the full power laser at focus. While a full reconstruction of the beam at focus would provide a wealth of information, for many experiments, measurement of the peak intensity would suffice as evidence of having achieved desired intensity thresholds. An ideal *in situ* intensity gauge would be capable of operating single-shot, simultaneously with the physics experiment without intrusion, and thus monitor the shot-to-shot fluctuations and drifts in the laser parameters over time, complementary with the physics measurements being carried out.

1.3 Relativistic Thomson scattering (RTS) as an Intensity Gauge

There are a number of proposed methods for direct characterization of focused intensity, including the measurement of radiation produced by free electrons scattered by the laser, a phenomenon known as relativistic Thomson scattering (RTS) [54–60], which is the topic of this dissertation. All three measurements can be applied to the case where gas molecules are ionized by the laser radiation, liberating electrons from their parent ions. While electron beams may also be used for producing RTS [61–64], such methods focus on the generation of high frequency photons, add a layer of experimental complexity involving the use of particle acceleration schemes, and are thus not explored in this dissertation. Instead, this dissertation focuses on electrons produced from ionization of molecules and atoms from a low-density gas by the laser. The interaction is therefore treated as a single particle, with an effectively negligible initial velocity, interacting classically with an electromagnetic wave (typically IR, e.g., $\lambda_0 \approx 800$ nm). The resulting particle motion produces harmonic light in the visible band predominantly from the second harmonic (e.g., $\lambda_{\text{RTS}} \gtrsim 400$ nm).

This remaining parts of this section provide a brief review of theoretical papers on RTS radiation produced in intense field conditions, including proposals for using RTS as an intensity diagnostic. In 1962, Vachaspati derived expressions for the fundamental and second harmonic RTS differential cross section and showing that at high intensities, the second harmonic has a magnitude comparable to the fundamental [54]. In 1970, Sarachik and Schappert wrote a comprehensive classical treatment of relativistic Thomson scattering radiation, produced by intense lasers. Their paper derived analytical expressions for the electron motion and radiated angular distribution of power and frequency of generated harmonics, as functions of the intensity, for the

case of the plane wave approximating the conditions at peak of a laser pulse. Later, during 2004 - 2015, papers presenting numerical calculations of the electron trajectory, angular distribution, and spectra using a Gaussian temporal and spatial envelope would emerge [56–58, 60], revealing the spectrum broadening and ponderomotive scattering effects associated with a real laser pulse. In 2012, Paredes calculated the angular distribution of the second and third harmonic by convolving the plane wave results from Sarachik and Schappert of varying intensities with a Gaussian spatial profile [59], an approach that - although neglects ponderomotive effects - provides insight on how the laser corona modifies the plane wave angular distribution, while having the advantage of primarily being an analytical approach. These theoretical approaches, while illustrative of many important ideas, would need to be refined and carried out using parameters consistent with experiment in order to support experimental validation of an intensity gauge.

1.4 Coordinate System

Before moving on, we define the coordinate system, illustrated in Fig. 1.4 which will be used throughout this thesis. We are interested in a laser with propagation vector \mathbf{k} whose magnitude is the wavenumber, $k = \frac{2\pi}{\lambda}$, where λ is the wavelength. We adopt the convention such that \mathbf{k} is oriented along the z axis. Furthermore, we consider a linearly polarized wave, such that the electric field, \mathbf{E} , is oriented along the x axis and the magnetic field, \mathbf{B} , is oriented along the y axis.

For a given position in space defined by the vector \mathbf{r} , the vector crosses the unit sphere at

point P and has a corresponding unit vector, $\hat{\mathbf{r}}$, given by:

$$\hat{\mathbf{r}} = \sin \theta \cos \phi \hat{\mathbf{x}} + \sin \theta \sin \phi \hat{\mathbf{y}} + \cos \theta \hat{\mathbf{z}} \quad (1.2)$$

where $\hat{\mathbf{x}}$, $\hat{\mathbf{y}}$, are the $\hat{\mathbf{z}}$ unit vectors along the positive x , y , and z axes respectively, θ is the polar angle relative to the positive z axis, and ϕ is the azimuthal angle which rotates about the z axis relative to the half-plane containing the positive x axis in the x - z plane.

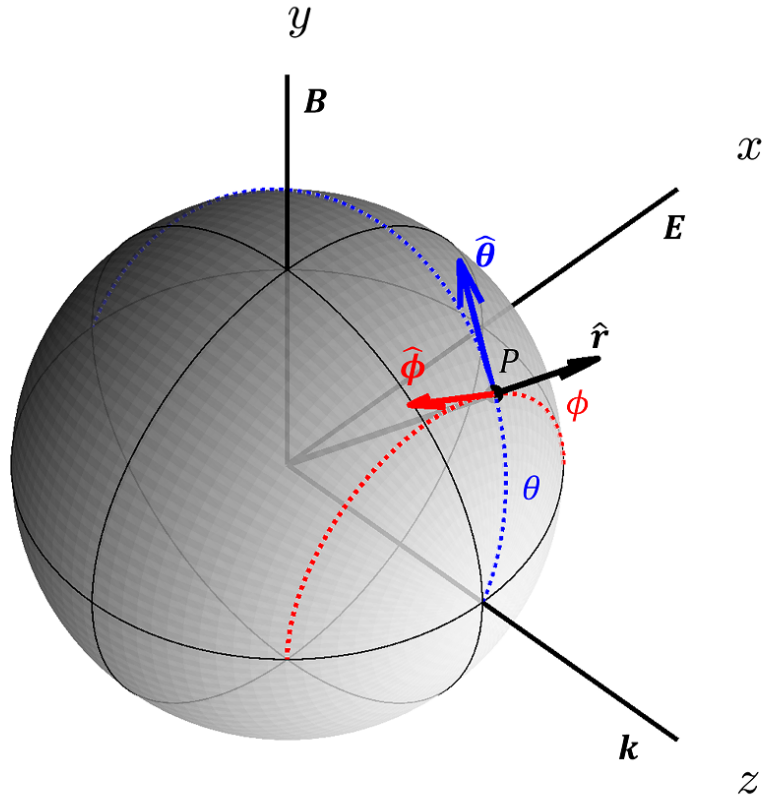


Figure 1.4: Diagram showing the coordinate system used in this thesis. Shown is a sphere whose pole is oriented along the z axis, with θ being the polar angle, and ϕ being the azimuthal angle relative to the half-plane containing the positive x axis in the x - z plane. The orientation of the laser propagation vector, \mathbf{k} , in this coordinate system is also established, along with the electric and magnetic fields, \mathbf{E} and \mathbf{B} respectively. The unit vectors $\hat{\mathbf{r}}$ defined in Eq. 1.2, as well as $\hat{\theta}$ and $\hat{\phi}$, defined in Eq. 1.3 and 1.4, are also shown.

We also define the unit vectors $\hat{\theta}$ and $\hat{\phi}$ based on the convention in [65] as:

$$\hat{\theta} = \cos \theta \cos \phi \hat{x} + \cos \theta \sin \phi \hat{y} - \sin \theta \hat{z} \quad (1.3)$$

$$\hat{\phi} = -\sin \phi \hat{x} + \cos \phi \hat{y} \quad (1.4)$$

The vectors $\hat{\theta}$ and $\hat{\phi}$ may be understood to be the vectors tangent to the surface of the sphere at point P , with $\hat{\theta}$ oriented towards the negative z axis, and $\hat{\phi}$ oriented perpendicular to the z axis according to the right hand rule (with the positive z axis being the thumb, and $\hat{\phi}$ being the curled fingers). Analogous to geography, if the intersection between the positive z axis and the unit sphere is called the "north pole" and that between the negative z axis and the unit sphere is called the "south pole", then $\hat{\theta}$ is always oriented "south" wherever P is on the unit sphere, while $\hat{\phi}$ is always oriented "east". One can see that these vectors also satisfy $\hat{\theta} \times \hat{\phi} = \hat{r}$.

The differential solid angle, $d\Omega$, is defined from θ and ϕ using the standard expression:

$$d\Omega = \sin \theta d\theta d\phi \quad (1.5)$$

so that the total solid angle Ω for θ from θ_1 to θ_2 and ϕ from ϕ_1 to ϕ_2 is defined via a double integral:

$$\Omega = \iint d\Omega = \int_{\phi_1}^{\phi_2} \int_{\theta_1}^{\theta_2} \sin \theta d\theta d\phi \quad (1.6)$$

It is common to consider the total solid angle associated with a cone with half-angle θ_{HA} , which is simply a special case of Eq. 1.6 where ϕ is integrated from 0 to 2π and θ is integrated from 0

to θ_{HA} :

$$\Omega_{\text{cone}} = \int_0^{2\pi} \int_0^{\theta_{\text{HA}}} \sin \theta d\theta d\phi = 2\pi (1 - \cos \theta_{\text{HA}}) \quad (1.7)$$

If there is some quantity, say power per unit steradian, $\frac{dP}{d\Omega}(\theta, \phi)$, which depends on θ and ϕ , and we are interested in the power radiated over a solid angle, Ω , defined by θ from θ_1 to θ_2 and ϕ from ϕ_1 to ϕ_2 , then we simply integrate $\frac{dP}{d\Omega}(\theta, \phi)$ over the solid angle:

$$P = \int_{\phi_1}^{\phi_2} \int_{\theta_1}^{\theta_2} \frac{dP}{d\Omega}(\theta, \phi) \sin \theta d\theta d\phi \quad (1.8)$$

Lastly, we provide some cautionary notes. In general, the solid angle may be computed with respect to an arbitrary direction \hat{n} , in which case we define a polar angle, $\theta_{\hat{n}}$, and azimuth angle $\phi_{\hat{n}}$ relative to \hat{n} and perform calculations of $d\Omega$ and Ω accordingly. However, this calculation requires a change between two spherical coordinate systems, such as the one carried out for a specific case in section 5.2, which is complicated and not carried out in this thesis. Also, the notation \mathbf{r} will be used for defining the electron position, whereas the notation \mathbf{x} relative to the origin and unit vector \hat{n} being defined as the unit vector pointing from the electron to the observer position (see Fig. 1.5). The polar coordinates, θ and ϕ , will typically refer to the observer position, rather than the electron.

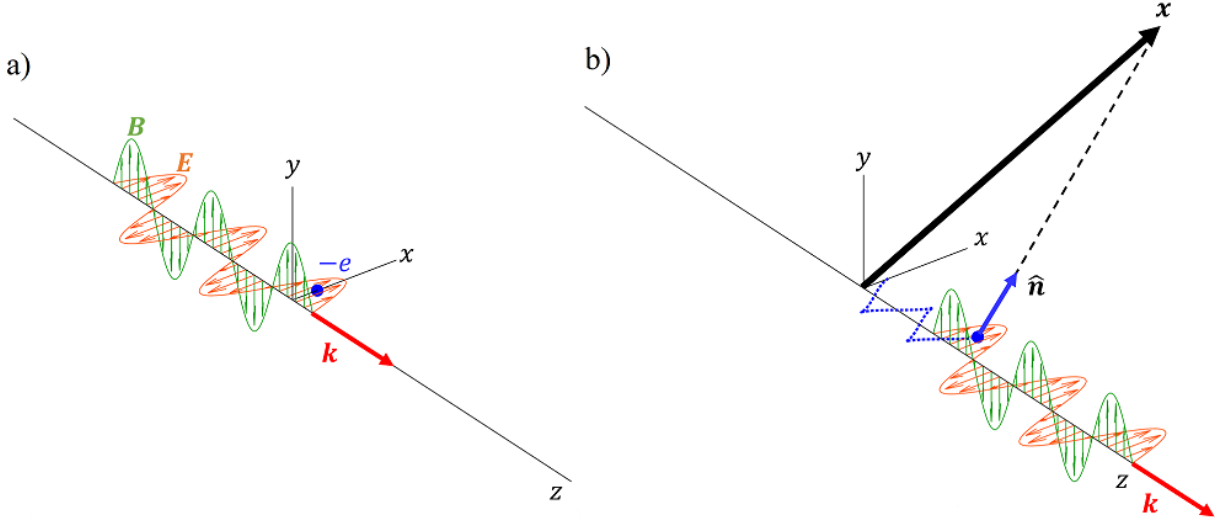


Figure 1.5: Plots showing the physical picture of relativistic Thomson scattering. An electron sees an electromagnetic plane wave a) and experiences a force that causes the electron to move along a path shown in the blue dotted lines in b). The motion of the electron produces radiation that propagates along in the direction \hat{n} and is observed at a position x from the origin.

1.5 Experimental Measurements of RTS

Overall, there have not been very many experiments attempting to resolve the details of relativistic Thomson scattering radiation, nor explore its viability as an *in situ* intensity characterization diagnostic. Prior to Sarachik and Schappert's paper, Thomson scattering had been observed in plasma experiments and used, for example, to determine the electron temperature via the Doppler shifted spectrum of the fundamental harmonic (see Peacock 1969 [66]). One of the earliest accounts of observing the second harmonic of relativistic Thomson scattering in the lab was the experiment conducted by Englert and Rinehart in 1983 [67], taking coincidence measurements of second harmonic photons emitted perpendicular to the beam of a 1 ps, Nd:Glass, 1060 nm pulsed laser at $1.7 \times 10^{14} \text{ W/cm}^2$ counter-propagating with an electron beam at 500 and 1600 eV. The first experiment to resolve the angular distribution of RTS harmonics was done by

Chen et al in 1998 [68] using 1053 nm wavelength, 400 fs laser pulses focused to an intensity of $\sim 3 \times 10^{18} \text{ W/cm}^2$ into helium gas, producing electrons through photoionization. These measurements were taken for the second and third harmonics over a range of values in ϕ (defined as in section 1.4) from 0° to 180° , for two fixed values of θ , namely 90° and 51° .

In 2018, our group performed a commissioning experiment measuring the spectra of the second harmonic of RTS using the VEGA-2 laser at the Centro de Láseres Pulsados (CLPU) facility in Spain, which was a linearly polarized, 800 nm, Ti:Sapphire chirp-pulse amplifier (CPA) type laser with 30 fs pulses, focused to a range of intensities from $\sim 10^{18} - 10^{19} \text{ W/cm}^2$ with an $f/13$ off-axis parabola (OAP) [69]. This was, to our knowledge, the first such RTS measurement using a laser of this class. We later followed up with another experiment in 2019, again using the VEGA-2 laser, to measure the angular distribution of RTS over varying values of θ , and observed the existence of a dip in radiation intensity, for second harmonic light. A third experiment in 2022 was done using the VEGA-3 laser to quantify the location of the dip as a function of laser intensity in a range of 10^{18} to 10^{20} W/cm^2 , alongside experiments investigating alternative *in situ* approaches to intensity characterization including ion and electron detection. During this same period from 2018 to 2022, the Peatross group and collaborators at Brigham Young University had made angular distribution measurements of RTS (over a range of values in ϕ for $\theta = 90^\circ$) with detectors resolving the radiated polarization along $\hat{\phi}$ and $\hat{\theta}$ separately, corresponding respectively to the electron's transverse and longitudinal motion relative to the propagating beam [70, 71].

Chapter 2

Physics of Relativistic Thomson Scattering

2.1 Overview

This chapter will be devoted to explaining the physical behavior of free electrons as they interact with incident electromagnetic radiation. The mathematical expressions throughout this chapter will be in SI units as opposed to Gaussian. Equations taken from sources using Gaussian (cgs) units have been converted into SI as explained in Appendix C. We will discuss two regimes of Thomson scattering - linear Thomson scattering (LTS) and nonlinear, relativistic Thomson scattering (RTS) - with a focus on how RTS may be exploited as an intensity gauge for relativistic intensities.

The distinction between linear and nonlinear, relativistic Thomson scattering can be seen by taking the limits in which $v/c \ll 1$ and $v/c \rightarrow 1$ respectively, where v is the electron speed, and c is the speed of light in vacuum. At low intensity, the magnetic force on the electron can be ignored, because $|ev \times B| \ll |eE|$, where E and B are the electric and magnetic fields respectively. The electron oscillates in phase with the electric field with speed $v \ll c$, and emits (dipole) radiation, at the incident laser frequency. At high intensity, $v \rightarrow c$, so that the magnetic force must be included and the electron motion becomes more complicated. Relativistic speeds also lead to strong Doppler effects which modify the frequency spectrum of the emitted radiation. In this discussion, we consider incident radiation that is linearly polarized and generated by Ti:Sapphire lasers with a central wavelength of 800 nm. This chapter will be primarily focused on the electron

response to an infinite plane wave, but will also explore the case where the wave has a Gaussian temporal profile representing a pulse. The effects of a nonuniform intensity distribution due to a focused beam is left for Chapter 7 to discuss.

2.2 Linear Thomson scattering

2.2.1 Equations of motion

We begin with the the Lorentz force equation for an electron with charge $-e$ (where e is positive with value of $1.602\ 176\ 634 \times 10^{-19}$ C as defined by the current SI standard, and C is the coulomb):

$$\mathbf{F} = -e(\mathbf{E} + \mathbf{v} \times \mathbf{B}). \quad (2.1)$$

For an electromagnetic wave propagating in vacuum, $E/B = c$, where $E = |\mathbf{E}|$, $B = |\mathbf{B}|$. We write the right hand side of Eq. 2.1 in the more suggestive form

$$\mathbf{F} = -eE\hat{\mathbf{E}} - eE\beta (\hat{\mathbf{v}} \times \hat{\mathbf{B}}) = \mathbf{F}_E + \mathbf{F}_B, \quad (2.2)$$

where $\hat{\mathbf{E}}$, $\hat{\mathbf{B}}$, and $\hat{\mathbf{v}}$ are unit vectors in the directions of \mathbf{E} , \mathbf{B} , and \mathbf{v} respectively and $\beta = v/c$. The Lorentz force is separated into an electrical component, $\mathbf{F}_E \equiv -eE\hat{\mathbf{E}}$, and a magnetic component, $\mathbf{F}_B \equiv -eE\beta (\hat{\mathbf{v}} \times \hat{\mathbf{B}})$, whose magnitudes are $|\mathbf{F}_E| = eE$ and $|\mathbf{F}_B| \leq eE\beta$. It can be shown that for low intensities ($I \ll 10^{18}$ W/cm² or equivalently), $\beta \leq 0.01$. The motion of the electron remains nonrelativistic.

For an infinite plane electromagnetic wave with angular frequency ω propagating in the \hat{z} direction, with the electric field polarized in the \hat{x} direction, the electric force on the electron can

be written as:

$$\mathbf{F}_E = -eE_0 \cos(kz - \omega t) \hat{\mathbf{x}}, \quad (2.3)$$

where E_0 is the electric field amplitude of the wave, $k = 2\pi/\lambda$ is the wavenumber. Here, we assume the electron is stationary when it encounters the wave and consequently its z coordinate stays fixed over time. We also assume that the electron is born during time $t = 0$ at $z = 0$, although in general, there may be a transverse drift that depends on the laser phase the electron sees during birth. For an electron born at the peak of the pulse, this drift is 0. For nonrelativistic motion, the Lorentz factor $\gamma = 1/\sqrt{1 - \beta^2}$ is approximately 1, so that $\mathbf{F} = \frac{d\mathbf{p}}{dt} \approx m\mathbf{a}$, where $\mathbf{p} = \gamma m\mathbf{v} \approx m\mathbf{v}$ is the momentum, and $\mathbf{a} = \frac{d\mathbf{v}}{dt}$ is the acceleration. Equation 2.3 can then be rewritten as:

$$\mathbf{a}(t) = -\frac{eE_0}{m_e} \cos(kz - \omega t) \hat{\mathbf{x}} \quad (2.4)$$

and then integrated over time to determine the electron position and velocity:

$$\mathbf{v}(t) = -\frac{eE_0}{m_e \omega} \sin(\omega t) \hat{\mathbf{x}}. \quad (2.5)$$

$$\mathbf{r}(t) = \frac{eE_0}{m_e \omega} \left[\frac{1}{\omega} \cos(\omega t) \right] \hat{\mathbf{x}}, \quad (2.6)$$

Equations 2.6 and 2.5 tells us that the electron motion is harmonic and undergoes *dipole oscillation*.

The electromagnetic waves radiated by a nonrelativistic electron, as observed at some po-

sition \mathbf{x} relative to the electron, is described by:

$$\mathbf{E}_{\text{rad}}(\mathbf{x}, t) = -\frac{e}{4\pi\epsilon_0 c} \left[\frac{\hat{\mathbf{n}} \times (\hat{\mathbf{n}} \times \dot{\beta})}{R} \right]_{\text{ret}} \quad (2.7)$$

where $\hat{\mathbf{n}}$ is the observation direction unit vector, $\dot{\beta} = \mathbf{a}/c$ is the acceleration normalized to c , R is the distance from the electron to the observer, and the subscript ret indicates that the quantities in brackets, are to be evaluated at the retarded time, $t_{\text{ret}} = t - R/c$. Equation 2.7 is determined by taking the nonrelativistic limit of Eq. 2.66 (see section 2.3.4 for an outline of the derivation based on Jackson [72]). Other texts, such as Griffiths (see Eq. 11.74 in [65]) also derive the same result. Since we are considering an observer far away, we can approximate the quantities $\hat{\mathbf{n}}$ and R as constant over time, so that the retarded time, t_{ret} is just t shifted by a constant and we may as well drop the ret subscript. Equation 2.7 is more intuitively understood by defining the observation angle $\theta_{\hat{\mathbf{x}}}$ subtended by $\hat{\mathbf{n}}$ from $\hat{\mathbf{x}}$, so that Eq. 2.7 can be written as:

$$\mathbf{E}_{\text{rad}} = -\frac{e}{4\pi\epsilon_0 c R} \dot{\beta} \sin \theta_{\hat{\mathbf{x}}} \hat{\epsilon} \quad (2.8)$$

where $\dot{\beta}$ is the magnitude of $\dot{\beta}$, and $\hat{\epsilon}$ is the polarization unit vector which is in the plane defined by the component of $\dot{\beta}$ perpendicular to $\hat{\mathbf{n}}$ (see Fig. 2.1).

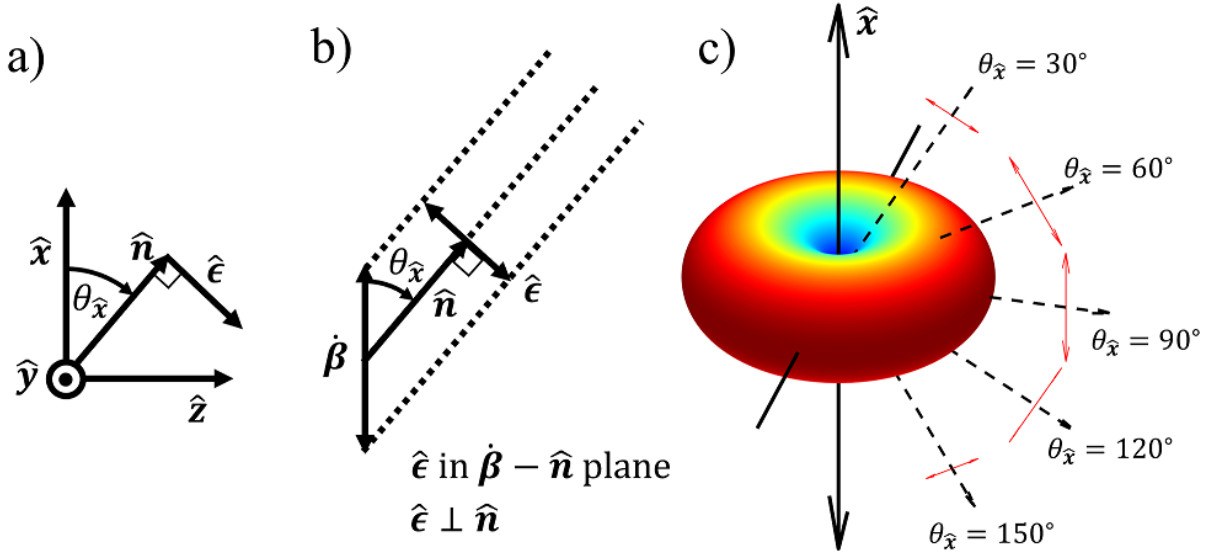


Figure 2.1: Diagrams illustrating the linear Thomson scattering radiation pattern. Shown are a) the Cartesian axes along with the observation direction \hat{n} , together with \hat{x} defines the angle $\theta_{\hat{x}}$ and polarization vector $\hat{\epsilon}$, b) the polarization direction defined by component of $\dot{\beta} \perp \hat{n}$, and c) a 3D diagram of the radiated power distribution as well as electric field vectors for various values of $\theta_{\hat{x}}$. The strength and polarization of radiated light in the far-field and nonrelativistic approximation is determined solely by the component of $\dot{\beta} \perp \hat{n}$, and does not consist any contribution by the component of $\dot{\beta} \parallel \hat{n}$.

The radiation pattern is that of an oscillating dipole (the electron is essentially an antenna), whose power is given by:

$$\frac{dP}{d\Omega} = \frac{e^2}{16\pi^2\epsilon_0 c^3} |\dot{v}|^2 \sin^2 \theta_{\hat{x}}. \quad (2.9)$$

after substitution of $v(t)$ with Eq. 2.5, giving the expression for the donut pattern. The strongest emission occurs in the direction perpendicular to the direction of dipole oscillation and vanishes along the direction of the dipole oscillation. If \dot{v} is taken to be along the x axis, we may write our expression in terms of the polar coordinates θ and ϕ defined in section 1.4, that is $\sin^2 \theta_{\hat{x}} = 1 - \sin^2 \theta \cos^2 \phi$, so that the radiation pattern oriented relative to the laser polarization and propagation vectors is as shown in Fig. 2.2.

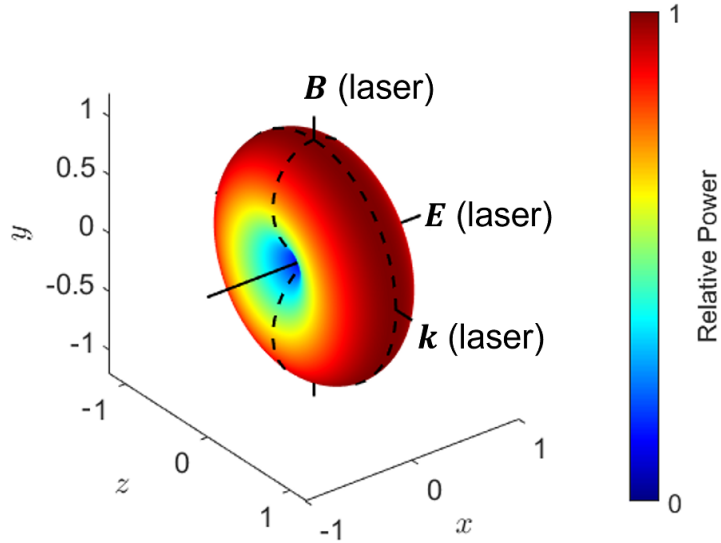


Figure 2.2: The donut shaped pattern of the scattered power oriented with respect to the laser for an oscillating dipole. The oscillating dipole is located at the origin (Eq. 2.9), and the dipole motion is oriented along the laser E field. A unique point on the surface defines corresponds to a unique direction, and the distance between that point and the origin represents the relative emitted power (also color coded).

The power scattered per electron per unit steradian for Thomson scattering can also be obtained from the Thomson Scattering differential cross section [73],

$$\frac{d\sigma_T}{d\Omega} = r_0^2(1 - \sin^2 \theta \cos^2 \phi), \quad (2.10)$$

where $r_0 = e^2/4\pi\epsilon_0 m_e c^3 \approx 2.82$ fm is the classical electron radius. To do so, we simply multiply

$\frac{d\sigma_T}{d\Omega}$ by the incident power flux per unit area P_{in}/A :

$$\frac{dP_T}{d\Omega} = \frac{P_{in}}{A} \frac{d\sigma_T}{d\Omega}. \quad (2.11)$$

Since $\frac{d\sigma_T}{d\Omega}$ does not depend on the input power, the emitted power scales linearly with P_{in} .

2.3 Nonlinear (relativistic) Thomson scattering

As mentioned in Chapter 1, a classical treatment of Thomson Scattering in the relativistic regime for plane waves was formulated in 1970 by Sarachik and Schappert [55], which forms the

cornerstone of the theory of relativistic Thomson scattering in this thesis. The book by Gibbon [74] provides an alternate perspective on the same topic which is also a source of many of the analytical formulas for electron motion in this chapter. The equations for the radiation by a point charge moving in an arbitrary motion at relativistic speeds comes primarily from Jackson [72], which we will also refer to.

2.3.1 The normalized vector potential

Before discussing the details of relativistic Thomson scattering, it is useful to define a parameter that scales with the laser electric field strength, which tells us when the accelerated electrons are relativistic. We can derive such a parameter, which is typically called a_0 , through the following analysis. We start with the canonical momentum, \mathbf{p}_{can} , for a system with an electron interacting with an electromagnetic field:

$$\mathbf{p}_{\text{can}} = \mathbf{p} - e\mathbf{A}. \quad (2.12)$$

Here, \mathbf{p} is the kinetic momentum, and \mathbf{A} is the vector potential. In the case of plane electromagnetic wave propagating in the $\hat{\mathbf{z}}$ direction, \mathbf{A} , which is a function of $kz - \omega t$, depends on the particle's position only through the variable z . Hence, one can see from either the Euler-Lagrange equation ($\frac{dp_{\text{can},k}}{dt} = \frac{\partial L}{\partial q_k}$) or Hamilton's equations of motion ($\frac{dp_{\text{can},k}}{dt} = -\frac{\partial H}{\partial q_k}$) that the x and y components of \mathbf{p}_{can} are conserved. The respective components in the quantity $-e\mathbf{A}$ can be thought of collectively as a "potential momentum," and those of \mathbf{A} as the potential momentum per unit charge (see section 10.1.4 in [65]).

To simplify our analysis, we ignore the z components in Eq. 2.12, since the transverse motion of the electron becomes relativistic before the longitudinal component does. We analyze the situation in which $\mathbf{p}_{\text{can}} = 0$ (which means there are only oscillations and no drift) and can

solve for the kinetic momentum ($\mathbf{p} = e\mathbf{A}$). Since the electric field is linearly polarized, both \mathbf{p} and \mathbf{A} only have x components and we may simply write:

$$p(t) = eA(t). \quad (2.13)$$

In the next step of our analysis, we note that the motion of the electron becomes relativistic when the momentum approaches $m_e c$. Letting $p = \gamma m_e c$ leads to

$$\frac{p}{m_e c} = \gamma \beta = \frac{\beta}{\sqrt{1 - \beta^2}} \sim 1. \quad (2.14)$$

Solving for β shows that this condition means $\beta \sim 0.71$ and $\gamma \sim 1.4$ which we will take to be the onset of relativistic motion. We could also instead consider the condition where the kinetic energy is equal or greater than the rest mass, or $(\gamma - 1)m_e c^2 \gtrsim m_e c^2$ which gives $\gamma \gtrsim 2$, however, this is not significantly different from the momentum condition and involves a higher speed.

Finally, we are interested in the situation where the motion of the electron, on average, is relativistic, therefore we define a parameter, a_0^2 , to be twice the time average of the square ratio of p to $m_e c$:

$$a_0^2 \equiv 2 \left\langle \left[\frac{p(t)}{m_e c} \right]^2 \right\rangle = 2 \frac{e^2 \langle A(t)^2 \rangle}{m_e^2 c^2} = \left(\frac{eA_0}{m_e c} \right)^2, \quad (2.15)$$

where we have taken the vector potential to be harmonic, i.e., $A(t) = A_0 \cos(\omega t)$. The parameter $a_0 = eA_0/m_e c$ is known as the "normalized vector potential." We note that many sources cite a_0 in Gaussian units, where there is an extra factor of c^2 in the denominator of the expression for a_0^2 in Eq. 2.15.

We are interested in expressing a_0 in a form that can be more readily applied to lasers. To

do this, we start by writing the electromagnetic radiation intensity in terms of A_0 :

$$I = \langle |\mathbf{S}| \rangle = \left\langle \frac{1}{\mu_0 c} |\mathbf{E}|^2 \right\rangle = \frac{\omega^2}{\mu_0 c} A_0^2 \langle \cos^2(\omega t) \rangle = \frac{\omega^2}{2\mu_0 c} A_0^2. \quad (2.16)$$

The normalized vector potential can then be rewritten as:

$$a_0 \approx 0.855 \times \sqrt{I[10^{18} \text{ W/cm}^2]} \times \lambda[\mu\text{m}]. \quad (2.17)$$

For our wavelength of interest at 800 nm, one achieves an a_0 value of 1.00 when $I \approx 2.14 \times 10^{18} \text{ W/cm}^2$. This produces an RMS value for β ($\beta_{\text{rms}} \equiv \sqrt{\langle \beta^2 \rangle}$) of ~ 0.58 (from rewriting the right hand side of Eq. 2.15 in terms of β and solving for β_{rms}). For the purposes of this thesis, we will take $a_0 \gtrsim 1$ to be the condition in which the electron is classified as relativistic.

2.3.2 Electron Motion in the Lab Frame

When the parameter $a_0 \gtrsim 1$, the condition $\beta \ll 1$ no longer holds. The magnetic component in the Lorentz force, $\mathbf{F}_B = -e\mathbf{v} \times \mathbf{B}$ then becomes comparable with the electric component. It turns out that this magnetic force leads to a longitudinal (along \mathbf{k}) acceleration component that is periodic with a frequency double that of its transverse oscillation, leading to, a forward motion of the electron that is modulated with an angular frequency of $2\omega^{(1)}$ where $\omega^{(1)}$ is the electron transverse oscillation angular frequency.

The trajectory of the relativistic electron can be solved numerically by treating the Lorentz force equation as a differential equation, which is accurate up to intensities of around 10^{22} after which the effects of radiation reaction (which is the modification of the electron trajectory due to recoil from radiating photons with energies $\sim m_e c^2$) appear. The Lorentz force equation, $\mathbf{F} = \frac{d\mathbf{p}}{dt} = -e(\mathbf{E} + \mathbf{v} \times \mathbf{B})$, is a differential equation in the sense that electron momentum and

the velocity are related via $\mathbf{p} = \gamma m\mathbf{v}$, and that the electric and magnetic fields are functions of the electron's position, \mathbf{r} in space and in general may have an explicit time dependence - i.e., $\mathbf{E} = \mathbf{E}(\mathbf{r}, t)$ and $\mathbf{B} = \mathbf{B}(\mathbf{r}, t)$ - which is related to the velocity via $\frac{d\mathbf{r}}{dt} = \mathbf{v}$. These relations hold for any fixed value for time, t , so that the variables \mathbf{r} , \mathbf{v} , \mathbf{p} , γ are all functions of time.

As a simple example, we take the fields to be infinite plane waves. This is an approximation applicable for focused lasers at the peak of the pulse, although for tightly focused lasers or short pulses, a more detailed model is required. We define the fields as:

$$\mathbf{E} = E_0 \cos(kz - \omega t + \delta_0) \hat{\mathbf{x}} \quad (2.18)$$

$$\mathbf{B} = \frac{E_0}{c} \cos(kz - \omega t + \delta_0) \hat{\mathbf{y}} \quad (2.19)$$

where the relation $B_0 = E_0/c$ was used and introduced an initial phase parameter δ_0 . Furthermore, the electric field amplitude can be written in terms of the normalized vector potential using $eE_0 = a_0\omega_0 mc$ so that the Lorentz force equation becomes:

$$\frac{d\mathbf{p}}{dt} = -a_0\omega_0 mc(\hat{\mathbf{x}} + \boldsymbol{\beta} \times \hat{\mathbf{y}}) \cos(kz - \omega t + \delta_0) \quad (2.20)$$

We next normalize the variables to their associated natural constants as follows, such that the values of the variables do not differ by many orders of magnitude, which is useful for avoiding

issues related to rounding errors during numerical computation:

$$\mathbf{r}' = k\mathbf{r} \Rightarrow x' = kx, y' = ky, z' = kz \quad (2.21)$$

$$t' = \omega t \quad (2.22)$$

$$\mathbf{p}' = \frac{\mathbf{p}}{mc} \quad (2.23)$$

$$\frac{d\mathbf{p}'}{dt} = \frac{1}{\omega mc} \frac{d\mathbf{p}}{dt} \quad (2.24)$$

$$\mathbf{v}' = \frac{\mathbf{v}}{c} = \boldsymbol{\beta} \quad (2.25)$$

In terms of the normalized variables, we have the following complete equations of motion:

$$\frac{d\mathbf{r}'}{dt'} = \frac{\mathbf{p}'}{\gamma} \quad (2.26)$$

$$\frac{d\mathbf{p}'}{dt'} = -a_0(\hat{\mathbf{x}} + \boldsymbol{\beta} \times \hat{\mathbf{y}}) \cos(z' - t' + \delta_0) \quad (2.27)$$

Carrying out the cross product, $\boldsymbol{\beta} \times \hat{\mathbf{y}} = -\beta_z \hat{\mathbf{x}} + \beta_x \hat{\mathbf{z}}$, we find that the force in the $\hat{\mathbf{y}}$ direction is always, 0. For simplicity, we may take the initial position and velocity of the electron along $\hat{\mathbf{y}}$ to be zero, so that we only need to be concerned with the components along $\hat{\mathbf{x}}$ and $\hat{\mathbf{z}}$. The equations of motion can then be represented as a system of ordinary-differential-equations (ODE) with the x and z components of the position and momenta as variables:

$$\frac{d\mathbf{X}}{dt'}(t') = f(t', \mathbf{X}(t')) \quad (2.28)$$

where

$$\mathbf{X}(t') = \begin{bmatrix} x'(t') \\ z'(t') \\ p'_x(t') \\ p'_z(t') \end{bmatrix} \quad (2.29)$$

$$\frac{d\mathbf{X}}{dt}(t') = \begin{bmatrix} \frac{dx'}{dt}(t') \\ \frac{dz'}{dt}(t') \\ \frac{dp'_x}{dt}(t') \\ \frac{dp'_z}{dt}(t') \end{bmatrix} \quad (2.30)$$

and

$$f(t', \mathbf{X}(t')) = \begin{bmatrix} \frac{p'_x(t')}{\gamma(t')} \\ \frac{p'_z(t')}{\gamma(t')} \\ -a_0 \left(1 - \frac{p'_z(t')}{\gamma(t')}\right) \cos(t' - z'(t') + \delta_0) \\ -a_0 \frac{p'_x(t')}{\gamma(t')} \cos(t' - z'(t') + \delta_0) \end{bmatrix} \quad (2.31)$$

with $\gamma(t') = \sqrt{1 + p'_x(t')^2 + p'_z(t')^2}$.

Given a set of initial conditions:

$$\mathbf{X}(0) = \begin{bmatrix} x'(0) \\ z'(0) \\ p'_x(0) \\ p'_z(0) \end{bmatrix} = \begin{bmatrix} a_0 \\ 0 \\ 0 \\ 0 \end{bmatrix} \quad (2.32)$$

$$\delta_0 = 0 \quad (2.33)$$

the system of ODEs may be solved using a numerical method. The results shown in this section

are solved using MATLAB's ODE89 method. The code is provided in Appendix C.2.

Shown in Fig. 2.3 is the numerically computed path traversed by the electron due to the electromagnetic wave, along with the forces and momenta at select points in time. In space, the electron trajectory contains sharp cusps at the end of its excursions. Analogous to simple harmonic motion, the acceleration is the strongest and the speed is the slowest at these endpoints, whereas the speed is maximum (and acceleration 0) at the half-way crossings between the end-points. We define this inertial reference frame as the "laboratory" frame, or "lab" frame for short.

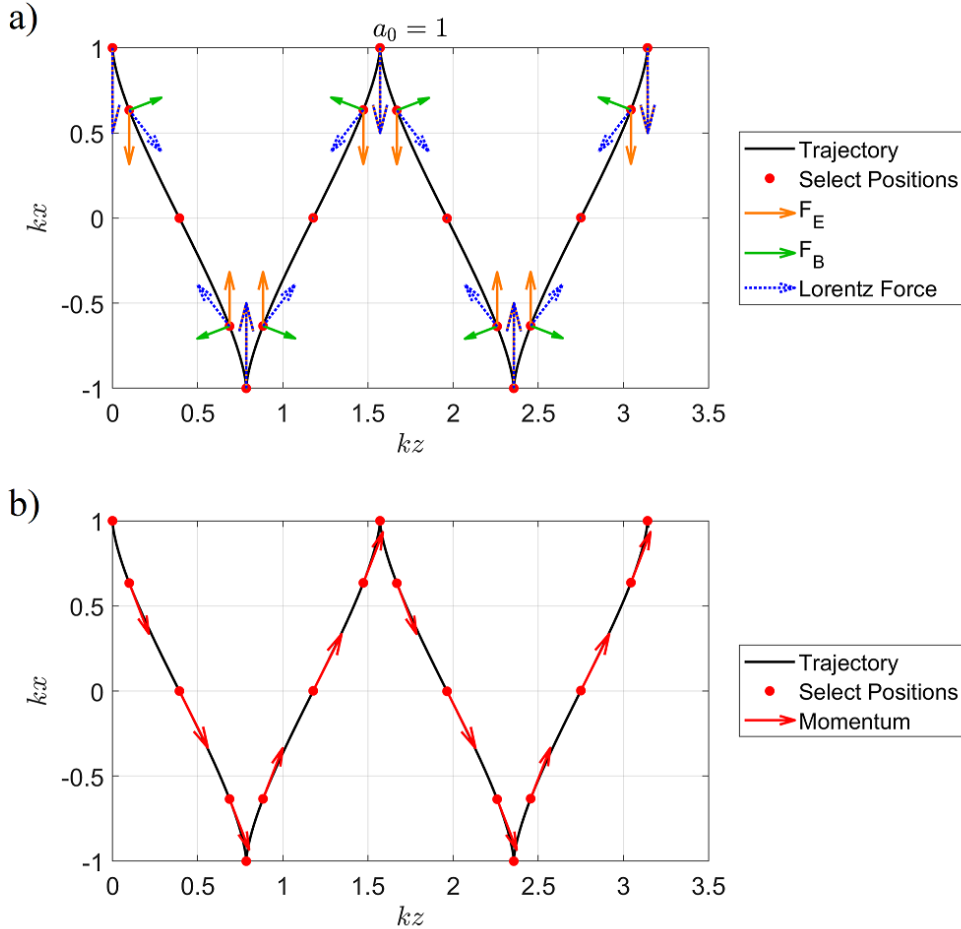


Figure 2.3: Plots of the electron path of motion in space for $a_0 = 1$ from solving the Lorentz force differential equation for an infinite plane wave, with force components and momentum at various times superimposed. See Eq. 2.28-2.33. Plotted on top of the path are select positions along with the a) electric, magnetic, and total Lorentz forces and b) the momentum at those positions. As will be discussed later, the electron oscillates with a transverse excursion amplitude of $kx_{\text{exc}} = a_0$ if born at the peak of the field $\delta_0 = 0$ at rest. The electron at rest at $(kz, kx) = (0, 1)$ is initially accelerated by the electric force along x and gains a velocity which results in a magnetic force pushing the electron forward. At the halfway crossing ($kx = 0$), the electromagnetic wave is 0 and the electron is at maximum speed, after which there is a net force which point in a direction opposing the electron momentum, slowing the electron down until it comes to a stop at $kx = -1$. The electron then follows a mirrored path to complete the second half of the cycle, returning to $kx = 0$ at some offset in kz from the initial position. Two cycles are shown in the plots.

The electron position, momentum, and force over time are shown in Fig. 2.4 for one interaction period. The motion is periodic, with the z component completing two periods per single period in the x component. The z component exhibits a lurching motion, containing both

a linear and periodic component in time. In the frame, the electron never moves backwards along z . From the plots of the z component variables, we can expect second harmonic radiation to be generated along with the fundamental. The shape of the curves deviate from perfect first and second harmonic sinusoids, which would lead to radiation at other frequencies and is discussed in more detail in section 2.3.4.

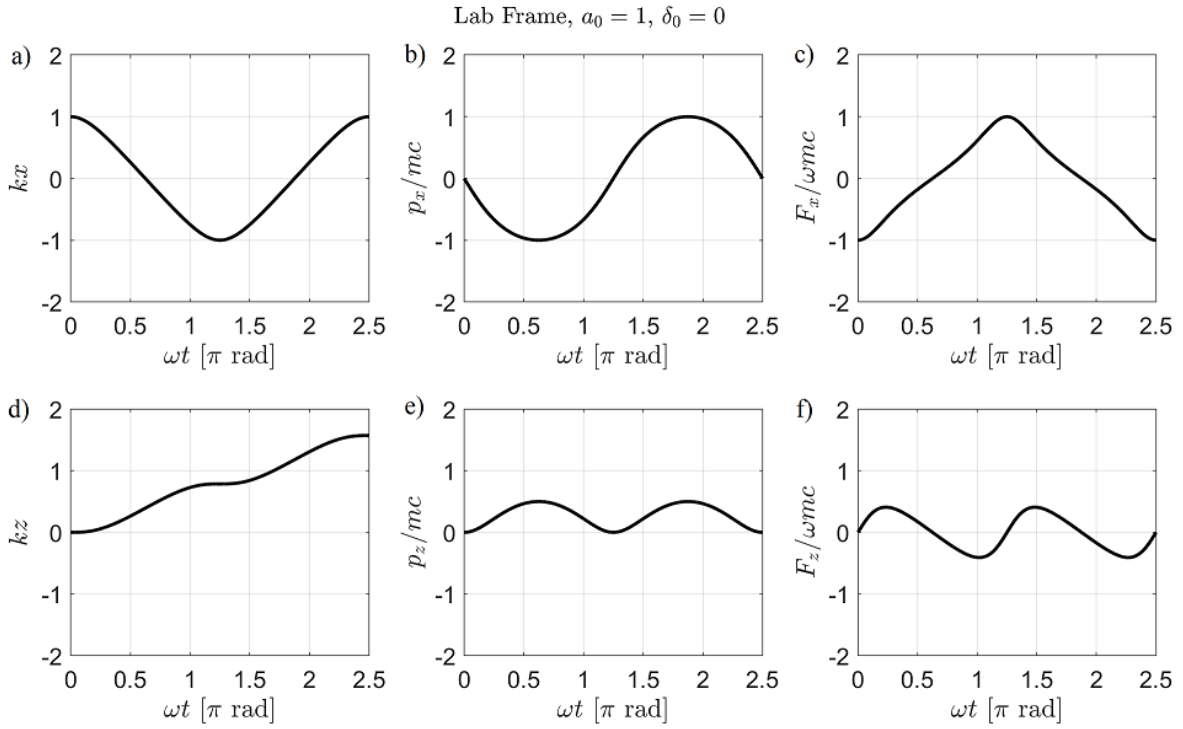


Figure 2.4: Plots of electron motion in the lab frame due to interaction with a plane electromagnetic wave over a single cycle. Shown are the x and z components of the electron position, momentum, and experienced Lorentz force for an electron born at the peak of the wave with $a_0 = 1$.

Analytical expressions for the electron motion for an infinite plane wave (see the derivations in [74] and [55]) provide another perspective on the physics and reveal additional details. For a

linear polarized wave with the electric field along \hat{x} and propagation vector along \hat{z} :

$$\frac{p_z}{mc} = \frac{a_0^2}{2} \{1 - \cos[2(kz - \omega t)]\} \quad (2.34)$$

$$\frac{p_x}{mc} = -a_0 \sin(kz - \omega t) \quad (2.35)$$

$$kz = \frac{a_0^2}{4} \{\sin[2(kz - \omega t)] - (kz - \omega t)\} \quad (2.36)$$

$$kx = -a_0 \cos(kz - \omega t) \quad (2.37)$$

The excursion amplitude, x_{exc} , being proportional to a_0 is seen in Eq. 2.37. In other words,

$$kx_{\text{exc}} = a_0 \Rightarrow x_{\text{exc}} = \frac{a_0}{2\pi} \lambda \quad (2.38)$$

where λ is the laser wavelength in the lab frame. The forward lurching motion (along z) has a periodic excursion which also depends on a_0 , which can be determined as follows. After the electron has interacted with one laser cycle, the phase, $\eta \equiv kz - \omega t$, that the electron sees would have changed by -2π (see Fig. 2.5). The electron would have lurched forward (from setting $\eta = -2\pi$ on the right hand side of Eq. 2.36) by an amount such that:

$$kz_{\text{exc}} = \frac{a_0^2}{4} 2\pi \Rightarrow z_{\text{exc}} = \frac{a_0^2}{4} \lambda \quad (2.39)$$

This occurs over an elapsed time (from plugging kz_{exc} in Eq. 2.39 into $\omega t = kz + 2\pi$) equal to:

$$\omega T_{\text{RTS}} = \left(\frac{a_0^2}{4} + 1 \right) 2\pi \Rightarrow T_{\text{RTS}} = \left(\frac{a_0^2}{4} + 1 \right) T \quad (2.40)$$

where T_{RTS} is the electron interaction period and T is the laser period in the lab frame.

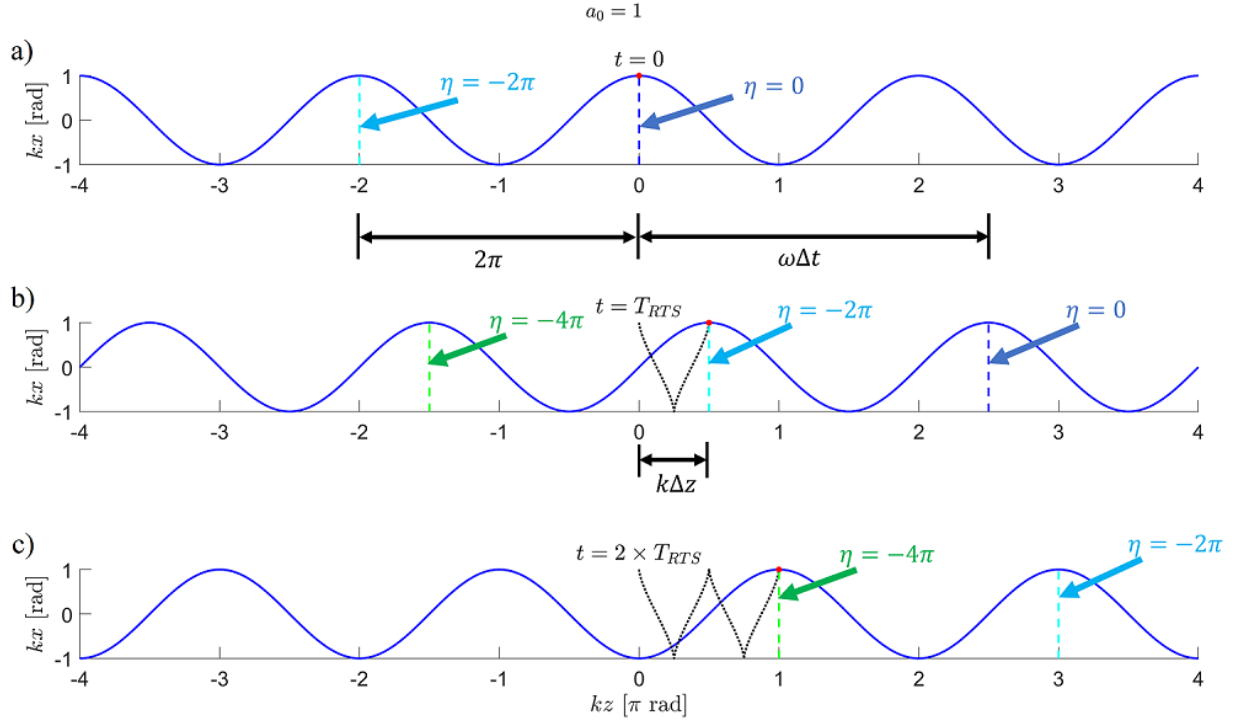


Figure 2.5: Plots of the electron position and electromagnetic wave profile at various snapshots in time for $a_0 = 1$. The times are given by a) $t = 0$, b) $t = T_{RTS}$, and c) $t = 2 \times T_{RTS}$, where T_{RTS} corresponds to an electron oscillation period and given by Eq. 2.40. Annotations indicate the phase at adjacent wave crests, differing by 2π . After one electron oscillation period, the phase front moves by a distance corresponding to $c\Delta t$ (or $\omega\Delta t$ in k_z space), where $\Delta t = T_{RTS}$. Meanwhile, the electron moves forward by a distance corresponding to Δz (or $k\Delta z$ in k_z space), where $\Delta z = z_{exc}$ in Eq. 2.39.

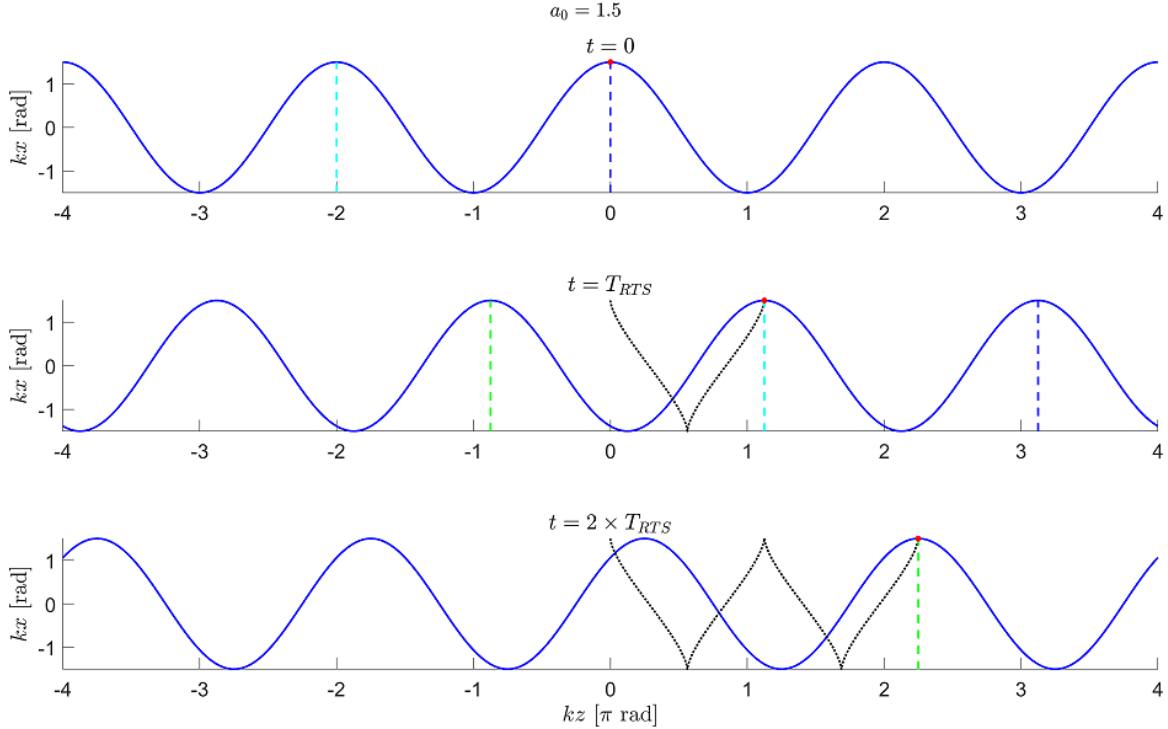


Figure 2.6: Plots of the electron position and electromagnetic wave profile at various snapshots in time for $a_0 = 3/2$. This is the same type of plot as Fig. 2.5, but shows that the electron excursion increases at a larger a_0 value.

To put the excursion lengths and oscillation periods into context, these values given in Table 2.1 for various values of a_0 assuming an 800 nm infinite plane wave. This table shows that $x_{\text{exc}} \ll w_0$ and $z_{\text{exc}} \ll z_R$ up to $a_0 \sim 5$ for f/3 focusing geometry (where $w_0 \sim 1.5 \mu\text{m}$ and $z_R \sim 10 \mu\text{m}$ if diffraction limited). At larger a_0 , the plane wave model which these values are based upon breaks down. If the focusing geometry is relaxed (larger f/#) or non-diffraction limited pulses are considered, both w_0 and z_R get larger so that the electron born at the peak of the field remains well-contained within the high intensity region. We may estimate the total electron interaction time, Δt_{RTS} , with a pulse of duration Δt (typically $\Delta t \sim 30 \text{ fs FWHM}$) by using eq. 2.40, with T replaced by Δt . The drifting electron interacts with the pulse over a stretched amount of time compared to the laser period seen at a fixed point in space. As an extreme case,

for $a_0 = 100$, $z_{\text{exc}} \gg x_{\text{exc}}$ owing to the quadratic dependence of z_{exc} on a_0 , meaning the electron "surfs" with the laser pulse at a speed close to c .

Table 2.1: Values of the transverse excursion amplitude, x_{exc} , the longitudinal periodic excursion length, z_{exc} , and the electron interaction cycle, T_{RTS} , for various values of a_0 and intensity, I . See Eq. 2.38 to 2.40. The electromagnetic wave is a $\lambda = 800$ nm infinite plane wave (with oscillation period $T = 2.7$ fs). Also shown are the effective interaction time, Δt_{RTS} , for a 30 fs square pulse (see previous paragraph).

a_0	$I [10^{18} \text{ W/cm}^2]$	$x_{\text{exc}} [\mu\text{m}]$	$z_{\text{exc}} [\mu\text{m}]$	$T_{\text{RTS}} [\text{fs}]$	Δt_{RTS}
0.1	2e-2	1e-2	2e-3	3	30
1	2	0.1	0.2	3	40
2	9	0.3	0.8	5	60
3	20	0.4	2	9	100
4	30	0.5	3	10	150
5	50	0.6	5	20	200
10	2e2	1	20	70	800
100	2e4	10	2e3	7e3	8e4

2.3.3 Electron Motion in the Drift Frame

The average motion of the electron is a constant drift along the laser propagation direction, with a velocity known as the drift velocity. This drift velocity can be determined by averaging the analytical equations over an interaction cycle and written in terms of a_0 . We begin by rewriting Eq. 2.36 in a more suggestive form where kz can be separated from ωt :

$$kz = \frac{a_0^2}{4 + a_0^2} \{ \sin[2(kz - \omega t)] + \omega t \} \quad (2.41)$$

After one cycle, the phase term in Eq. 2.41 averages to 0 so that the sinusoidal term is vanishes, resulting in the following expression of the average drift velocity:

$$v_D \equiv \left\langle \frac{z}{t} \right\rangle = \frac{a_0^2}{4 + a_0^2} c \quad (2.42)$$

Here, $\omega/k = c$ was identified as the phase velocity of the propagating wave equivalent to the speed of light.

We define the "drift frame" to be the inertial reference frame following the average drift velocity of the electron. The electron path in the drift frame can be obtained by a Lorentz transform to a reference frame moving at v_D . Defining the normalized drift velocity $\beta_D = v_D/c$, the Lorentz transform consists of the following equations:

$$t^{(D)} = \gamma_D(t - \beta_D z) \quad (2.43)$$

$$z^{(D)} = \gamma_D(z - \beta_D t) \quad (2.44)$$

where $t^{(D)}$ and $z^{(D)}$ are the t and z coordinates in the drift frame respectively and $\gamma_D = 1/\sqrt{1 - \beta_D^2}$ is the Lorentz factor associated with β_D . The superscript (D) notation is to distinguish the time, position, and the resulting velocity in the drift frame from the average drift velocity denoted by subscript D . The x coordinate remains unchanged in the drift frame, however it evolves with respect to $t^{(D)}$. Shown in Fig. 2.7 is a plot of the Minkowski diagram and a plot of the electron path in space in both the lab (blue) and drift (red) frames. The lab frame curves were produced from the ODE solutions of the lab frame motion described in section 2.3.2, while the drift frame curves were obtained by applying the Lorentz transform to the lab frame curves.

A change in inertial frames also necessitates a transform of the laser wavelength and frequency. The laser frequency in the average drift frame, $\omega_0^{(D)}$, is related to that in the lab frame, ω_0 , via [72, 75]:

$$\omega_0^{(D)} = \sqrt{\frac{1 - \beta_D}{1 + \beta_D}} \omega_0 = \frac{1}{\sqrt{1 + \frac{a_0^2}{2}}} \omega_0 \quad (2.45)$$

A derivation of this expression is discussed in section 2.3.5. The wavenumber k transforms in the same manner. The wavelength, λ , and observed period T transforms via a multiplication by the reciprocal factor in Eq. 2.45. Applying this correction, one can plot the motion in kz vs. ωt as it applies for k and ω in the average drift frame.

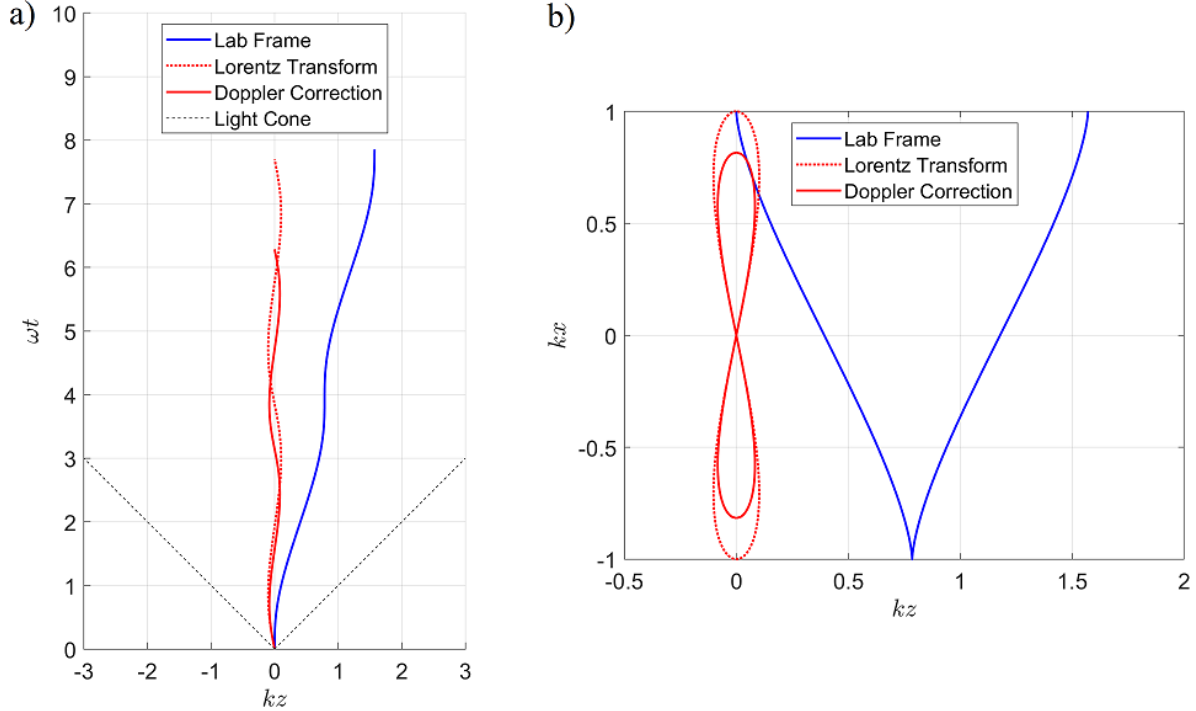


Figure 2.7: Plots showing the transformation of the lab frame electron motion to the average drift frame. Shown are a) the Minkowski diagram showing the electron motion (due to an electromagnetic wave with $a_0 = 1$) along the propagation direction z over time in the lab (blue) and drift frame (red) as well as b) the electron path of motion in the lab and drift frames. In the drift frame, the red dotted line is a plot using the k and ω values of the lab frame. The solid red line (labeled as "Doppler Correction") corresponds to the path using the k and ω values in the average drift frame (Eq. 2.45).

Analytical expressions for the electron motion in the drift frame are given by [74]:

$$\frac{p_z}{mc} = -\frac{a_0^2}{4\sqrt{1 + \frac{a_0^2}{2}}} \cos[2(kz - \omega t)] \quad (2.46)$$

$$\frac{p_x}{mc} = -a_0 \sin(kz - \omega t) \quad (2.47)$$

$$kz = \frac{a_0^2}{4\left(1 + \frac{a_0^2}{2}\right)} \sin[2(kz - \omega t)] \quad (2.48)$$

$$kx = -\frac{a_0}{\sqrt{1 + \frac{a_0^2}{2}}} \cos(kz - \omega t) \quad (2.49)$$

The electron trajectory in the drift is the well-known modified figure-8 given by the equation:

$$16(kz)^2 = (kx)^2 \left[\frac{a_0^2}{1 + \frac{a_0^2}{2}} - (kx)^2 \right] \quad (2.50)$$

which can be determined by eliminating the phase term $kz - \omega t$ in eq. 2.48 and 2.49. In this reference frame, the electron passes through the center of the figure-8 twice per cycle while moving forward, and passes along the outside edges of the figure-8 loops twice per cycle while moving backward, as shown in Fig. 2.8a. As a_0 increases, so does the size of the figure-8 and the proportion of its width relative to its height, as shown in Fig. 2.8b. While in kx vs. kz space the figure-8 reaches a limiting size as $a_0 \rightarrow \infty$, the physical size of the figure-8 would grow without bound as $a_0 \rightarrow \infty$ since the wavelength λ in the drift frame also increases monotonically with a_0 (as discussed previously, the values of k and ω are smaller in the drift frame compare to their analogs in the lab frame due to the Doppler effect). The width and height of the figure-8,

given by

$$\frac{z_{\text{exc}}}{x_{\text{exc}}} = \frac{a_0^2}{4 \left(1 + \frac{a_0^2}{2}\right)} \left(\frac{a_0}{\sqrt{1 + \frac{a_0^2}{2}}} \right)^{-1} = \frac{a_0}{\sqrt{2 + a_0^2}} \frac{\sqrt{2}}{4} \quad (2.51)$$

however, does reach a limiting ratio (as plotted in Fig. 2.8c), namely $\frac{\sqrt{2}}{4} \approx 0.354$.

Over one oscillation period in the drift frame, the electron's z position is unchanged. Only the time has changed by a period $T_{\text{RTS}}^{(D)}$ consistent with $\omega_0^{(D)} T_{\text{RTS}}^{(D)} = 2\pi \Rightarrow T_{\text{RTS}} = T^{(D)}$. This also means that the electron oscillation period and the laser period are the same in the drift frame.

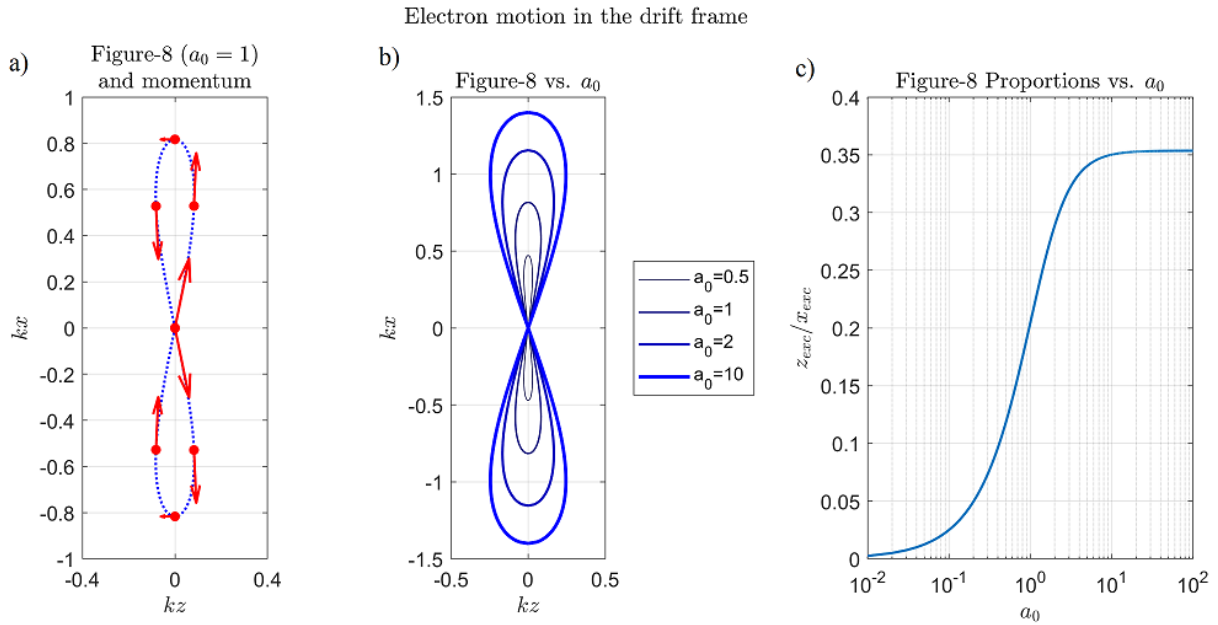


Figure 2.8: Detailed plots of the drift frame figure-8 motion. Shown are a) the electron motion in the drift frame due to an infinite plane electromagnetic wave at various points along the path with its momentum indicated, b) the figure-8 path of the electron at various values of a_0 , and c) the longitudinal to transverse excursion amplitude ratios at various values of a_0 indicating the change in the shape of figure-8. The width of the figure-8 relative to its height changes the fastest near $a_0 = 1$ and the ratio approaches an asymptotic value of $\sqrt{2}/4$ at large a_0 .

The motion in the drift frame can be computed from Eq. 2.46 to 2.49 by treating Eq. 2.48, as a transcendental equation in the variable kz with ωt fixed. A transcendental equation needs to be solved for each value in time, which can be done using a numerical solver to determine kz . The

solution to kz may then be plugged into the other equations from Eq. 2.46 to 2.49 to determine the full set of solutions. The force may also then be computed by numerically differentiating p_z and p_x with respect to time. Figure 2.9 shows the results of the approach described.

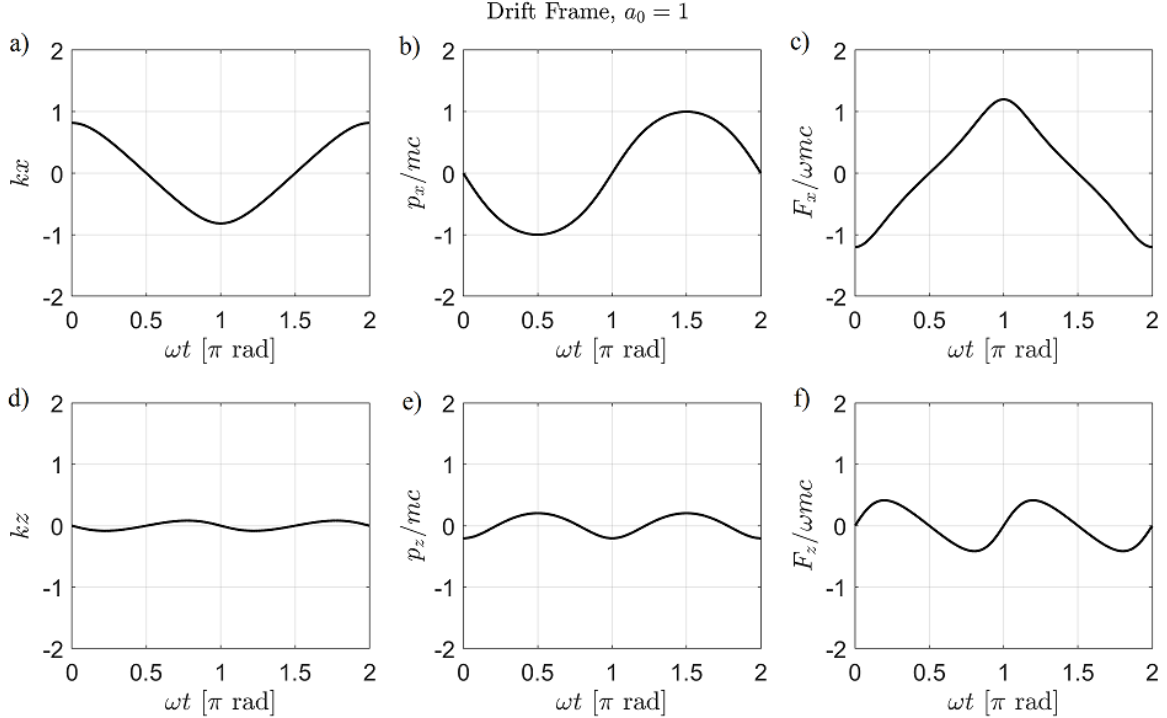


Figure 2.9: Plots of electron motion in the average drift frame due to interaction with a plane electromagnetic wave over a single cycle. Shown are the x and z components of the position, momentum, and experienced force in the drift frame, computed by numerically solving Eq. 2.46 to 2.46 and numerical differentiating the momentum. The values k and ω have been Doppler shifted from their lab frame counterparts via $k \rightarrow k/\sqrt{1+a_0^2/2}$ and $\omega \rightarrow \omega/\sqrt{1+a_0^2/2}$. A phase shift of π had been added to Eq. 2.46 to 2.46 so that the x position begins at the full excursion at $t = 0$.

2.3.4 Radiation and Harmonic Generation

We are interested in the general (relativistic) expressions of the radiation produced by an accelerating electron. We begin by outlining key steps of the derivation taken by Jackson [72] to

reach the desired expressions. We start with the inhomogenous Maxwell Wave Equations:

$$\frac{1}{c^2} \frac{\partial^2 \mathbf{E}}{\partial t^2} - \nabla^2 \mathbf{E} = - \left(\frac{1}{\epsilon_0} \nabla \rho + \mu_0 \frac{\partial \mathbf{J}}{\partial t} \right) \quad (2.52)$$

$$\frac{1}{c^2} \frac{\partial^2 \mathbf{B}}{\partial t^2} - \nabla^2 \mathbf{B} = \mu_0 \nabla \times \mathbf{J} \quad (2.53)$$

where ρ is the charge density per unit volume and \mathbf{J} is the current density per unit area. Solutions to the inhomogeneous equations correspond to radiation produced by free charges described by ρ and \mathbf{J} , while solutions to the homogenous equations correspond to radiation external to said charges. In terms of the potentials Φ and \mathbf{A} , which are related to \mathbf{E} and \mathbf{B} via $\mathbf{E} = -\nabla\Phi - \frac{\partial \mathbf{A}}{\partial t}$ and $\mathbf{B} = \nabla \times \mathbf{A}$, these wave equations become:

$$\nabla^2 \Phi - \frac{1}{c^2} \frac{\partial^2 \Phi}{\partial t^2} = -\frac{\rho}{\epsilon_0} \quad (2.54)$$

$$\nabla^2 \mathbf{A} - \frac{1}{c^2} \frac{\partial^2 \mathbf{A}}{\partial t^2} = -\mu_0 \mathbf{J} \quad (2.55)$$

where the potentials satisfy the Lorentz Gauge:

$$\frac{1}{c^2} \frac{\partial \Phi}{\partial t} + \nabla \cdot \mathbf{A} = 0 \quad (2.56)$$

Solutions for Φ and \mathbf{A} in Eq. 2.54 and 2.55 can be found by finding the Green's function, $G(\mathbf{x}, \mathbf{x}', t, t')$, which is the impulse response function satisfying:

$$\nabla^2 G(\mathbf{x}, \mathbf{x}', t, t') - \frac{1}{c^2} \frac{\partial^2 G}{\partial t^2}(\mathbf{x}, \mathbf{x}', t, t') = \delta^3(\mathbf{x} - \mathbf{x}')\delta(t - t') \quad (2.57)$$

The solutions for Φ and \mathbf{A} can then be written as:

$$\Phi(\mathbf{x}, t) = \frac{1}{\epsilon_0} \iiint G(\mathbf{x}, \mathbf{x}', t, t') \rho(\mathbf{x}', t') d^3 \mathbf{x}' dt' \quad (2.58)$$

$$\mathbf{A}(\mathbf{x}, t) = \mu_0 \iiint G(\mathbf{x}, \mathbf{x}', t, t') \mathbf{J}(\mathbf{x}', t') d^3 \mathbf{x}' dt' \quad (2.59)$$

The charge and current densities for an electron modeled as a point particle with charge $-e$, and whose position in time is given by $\mathbf{r}(t')$ and velocity by $\mathbf{v}(t')$, can be written in terms of delta functions tracking the position of the particle:

$$\rho(\mathbf{x}', t') = -e \delta^3[\mathbf{x}' - \mathbf{r}(t')] \quad (2.60)$$

$$\mathbf{J}(\mathbf{x}', t') = -e \mathbf{v}(t') \delta^3[\mathbf{x}' - \mathbf{r}(t')] \quad (2.61)$$

These may be plugged into Eq. 2.58 and 2.59. With the appropriate expression for $G(\mathbf{x}, \mathbf{x}', t, t')$, which is derived in Jackson [72] but glossed over in this thesis, the resulting potentials are known as the Liénard-Wiechert potentials given by:

$$\Phi_{\text{LW}}(\mathbf{x}, t) = \frac{1}{4\pi\epsilon_0} \left[\frac{-e}{(1 - \boldsymbol{\beta} \cdot \hat{\mathbf{n}})R} \right]_{\text{ret}} \quad (2.62)$$

$$\mathbf{A}_{\text{LW}}(\mathbf{x}, t) = \frac{\mu_0}{4\pi} \left[\frac{-e\boldsymbol{\beta}}{(1 - \boldsymbol{\beta} \cdot \hat{\mathbf{n}})R} \right]_{\text{ret}} \quad (2.63)$$

where \mathbf{x} is the observer position, t is the observer time, $\hat{\mathbf{n}}$ and R are the unit vector and distance respectively from the electron position to the observer position, and the subscript ret indicates that the bracketed quantities are to be evaluated at the retarded time, $t_{\text{ret}} = t - R/c$, relative to observer time. These variables are illustrated in Fig. 2.10.

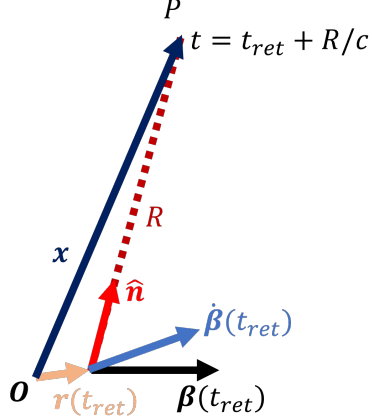


Figure 2.10: Diagram illustrating the vectors involved in describing an electron in relativistic motion and its observed radiation. The electron is located at the head of vector \mathbf{r} from origin O with normalized velocity and acceleration vectors β and $\dot{\beta}$ respectively at time t_{ret} . The electron radiates light in the direction $\hat{\mathbf{n}}$ over a distance R to observation point P located at the head of vector \mathbf{x} from the origin O . The radiation travels at the vacuum speed of light, c , and reaches point P at time $t = t_{ret} + R/c$.

The electric and magnetic fields can be obtained from the Liénard-Wiechert potentials from the definitions [72] [76], $\mathbf{E}_{LW} = \nabla\Phi_{LW} - \frac{\partial\mathbf{A}_{LW}}{\partial t}$ and $\mathbf{B}_{LW} = \nabla \times \mathbf{A}_{LW}$:

$$\mathbf{E}_{LW}(\mathbf{x}, t) = -\frac{e}{4\pi\epsilon_0} \left[\frac{\hat{\mathbf{n}} - \beta}{\gamma^2(1 - \beta \cdot \hat{\mathbf{n}})^3 R^2} \right]_{ret} - \frac{e}{4\pi\epsilon_0 c} \left[\frac{\hat{\mathbf{n}} \times \{(\hat{\mathbf{n}} - \beta) \times \dot{\beta}\}}{(1 - \beta \cdot \hat{\mathbf{n}})^3 R} \right]_{ret} \quad (2.64)$$

$$\mathbf{B}_{LW}(\mathbf{x}, t) = \frac{1}{c} [\hat{\mathbf{n}} \times \mathbf{E}_{LW}]_{ret} \quad (2.65)$$

The fields are separated in terms of their static ($\propto 1/R^2$) and radiated components ($\propto 1/R$).

In experiments, detectors would be located far from the electrons so that the static field becomes

negligible, and we are interested in the radiated components:

$$\mathbf{E}_{\text{rad}}(\mathbf{x}, t) = -\frac{e}{4\pi\epsilon_0 c} \left[\frac{\hat{\mathbf{n}} \times \{(\hat{\mathbf{n}} - \boldsymbol{\beta}) \times \dot{\boldsymbol{\beta}}\}}{(1 - \boldsymbol{\beta} \cdot \hat{\mathbf{n}})^3 R} \right]_{\text{ret}} \quad (2.66)$$

$$\mathbf{B}_{\text{rad}}(\mathbf{x}, t) = \frac{1}{c} [\hat{\mathbf{n}} \times \mathbf{E}_{\text{rad}}]_{\text{ret}} \quad (2.67)$$

Equations 2.66 and 2.67 show that the fields produced by relativistic electrons depend not just on the acceleration, but also the direction and magnitude of the velocity. Furthermore, the direction of strongest radiation is not perpendicular to $\dot{\boldsymbol{\beta}}$, as was the nonrelativistic case, but in a direction that is beamed towards $\boldsymbol{\beta}$, which is discussed further in section 2.3.6.

For an observer far away compared to the spatial extent of the electron motion (e.g., confined over a small region in space with linear dimension $\lesssim 1$ mm), the vector $\hat{\mathbf{n}}$ can be considered constant and equal to the normalized observation vector $\mathbf{x}/|\mathbf{x}|$, assuming the origin \mathcal{O} is situated within the confined region of electron motion. Equations 2.66 and 2.67 provide an expression for the observed instantaneous Poynting vector, $\mathbf{S}(t)$, which, when written in terms of only \mathbf{E}_{rad} has a magnitude

$$|\mathbf{S}(\mathbf{x}, t)| = \frac{1}{\mu_0 c} E_{\text{rad}}^2(\mathbf{x}, t_{\text{ret}}) \quad (2.68)$$

where $E_{\text{rad}}(\mathbf{x}, t)$ is the radiated electric field magnitude. The Poynting vector represents the power radiated per unit area. To convert to power radiated per unit solid angle, the electric field

is to be multiplied with R :

$$\begin{aligned} \frac{dP_{\text{rad}}}{d\Omega}(\hat{\mathbf{n}}, t) &= \frac{1}{\mu_0 c} [RE_{\text{rad}}(\mathbf{x}, t_{\text{ret}})]^2 \\ &= \frac{e^2}{16\pi^2\epsilon_0 c} \left| \frac{\hat{\mathbf{n}} \times \{(\hat{\mathbf{n}} - \beta(t_{\text{ret}})) \times \dot{\beta}(t_{\text{ret}})\}}{(1 - \beta(t_{\text{ret}}) \cdot \hat{\mathbf{n}})^3} \right|^2 \end{aligned} \quad (2.69)$$

The energy radiated per unit solid angle is then:

$$\frac{dU_{\text{rad}}}{d\Omega}(\hat{\mathbf{n}}) = \int_{-\infty}^{\infty} \frac{dP_{\text{rad}}}{d\Omega}(\hat{\mathbf{n}}, t) dt \quad (2.70)$$

The radiated spectrum (in units of energy radiated per unit angular frequency per unit solid angle) is given, via Parseval's theorem, by the square of the Fourier transform of $RE_{\text{rad}}(\mathbf{x}, t_{\text{ret}})$ over the time variable t :

$$\frac{d^2U_{\text{rad}}}{d\omega d\Omega}(\hat{\mathbf{n}}) = \frac{c\epsilon_0}{\pi} \left| \int_{-\infty}^{\infty} R(t_{\text{ret}}) \mathbf{E}_{\text{rad}}(\mathbf{x}, t_{\text{ret}}) \exp(i\omega t) dt \right|^2 \quad (2.71)$$

$$\begin{aligned} &= \frac{e^2}{16\pi^3\epsilon_0 c} \left| \int_{-\infty}^{\infty} \frac{\hat{\mathbf{n}} \times [(\hat{\mathbf{n}} - \beta(t_{\text{ret}})) \times \dot{\beta}(t_{\text{ret}})]}{(1 - \beta(t_{\text{ret}}) \cdot \hat{\mathbf{n}})^2} \exp[i\omega(t_{\text{ret}} - \hat{\mathbf{n}} \cdot \mathbf{r}(t_{\text{ret}})/c)] dt_{\text{ret}} \right|^2 \end{aligned} \quad (2.72)$$

$$= \frac{e^2\omega^2}{16\pi^3\epsilon_0 c} \left| \int_{-\infty}^{\infty} \hat{\mathbf{n}} \times (\hat{\mathbf{n}} \times \beta(t_{\text{ret}})) \exp[i\omega(t_{\text{ret}} - \hat{\mathbf{n}} \cdot \mathbf{r}(t_{\text{ret}})/c)] dt_{\text{ret}} \right|^2 \quad (2.73)$$

Here, a change of variable to the retarded time, $t_{\text{ret}} = t - R(t_{\text{ret}})/c$, was made along with the far-field approximation $R \approx |\mathbf{x}| - \hat{\mathbf{n}} \cdot \mathbf{r}(t_{\text{ret}})$. This leads to $dt_{\text{ret}}(1 - \hat{\mathbf{n}} \cdot \beta(t_{\text{ret}})) = dt$ and a subsequent canceling out of one of the powers of $(1 - \hat{\mathbf{n}} \cdot \beta(t_{\text{ret}}))$ in the denominator along with the conjugate complex exponential factors containing constant phase $|\mathbf{x}|$. Furthermore, Eq. 2.73

is derived from Eq. 2.72 using integration by parts. Lastly, the spectrum per unit wavelength interval is converted from the spectrum per unit frequency interval via the relationship between the intervals $d\lambda = 2\pi c d\omega / \omega^2$, so that:

$$\frac{d^2U}{d\lambda d\Omega} = \frac{\omega^2}{2\pi c} \frac{d^2U}{d\omega d\Omega} \quad (2.74)$$

The purpose of the preceding exercise was twofold:

1. To logically present the expressions from which the radiated angular distribution pattern and spectra may be calculated;
2. To show that the instantaneous radiation, in general, depends on both β and $\dot{\beta}$ (Eq. 2.66);

The radiated spectrum depends on the harmonic composition of β and $\dot{\beta}$ modified with the Doppler effect associated with the term $-\hat{\mathbf{n}} \cdot \mathbf{r}(t_{\text{ret}})/c$ in the complex exponential of the Fourier integral of Eq. 2.73.

The values of β and $\dot{\beta}$ can be computed from the numerical values of the momentum, \mathbf{p} , using $\beta = \mathbf{p}/\gamma(\mathbf{p})mc^2$, followed by numerical differentiation ($\dot{\beta} = d\beta/d\omega t$). The resulting values are shown in Fig. 2.11 for the lab frame and Fig. 2.12 for the drift frame, along with their Fourier transforms. The Fourier transforms are plotted in terms of frequency relative to the fundamental frequency $f^{(1)}$ of the electron interaction cycle for the inertial reference frame analyzed. We use the notation $f^{(n)}$ to specify the n^{th} harmonic frequency, where n is an integer ≥ 1 . As discussed in the previous sections, the fundamental frequency, relative to the electromagnetic wave frequency in the lab frame, f_0 , is $f^{(1)} = f_0/(a_0^2/4 + 1)$ for the lab frame and $f^{(1)} = f_0/\sqrt{1 + a_0^2/2}$ for the drift frame. On top of periodic behavior occurring at the fundamental frequency ($n = 1$)

for the x component and double the fundamental ($n = 2$) at the z component, there are higher order odd harmonics for the x component and even harmonics for the z component. The widths of the peaks in the Fourier transform plots are inversely proportional to the total integrated time in the Fourier integral, which for the plots shown are 20 cycles for the lab frame and 10 cycles for the drift frame.

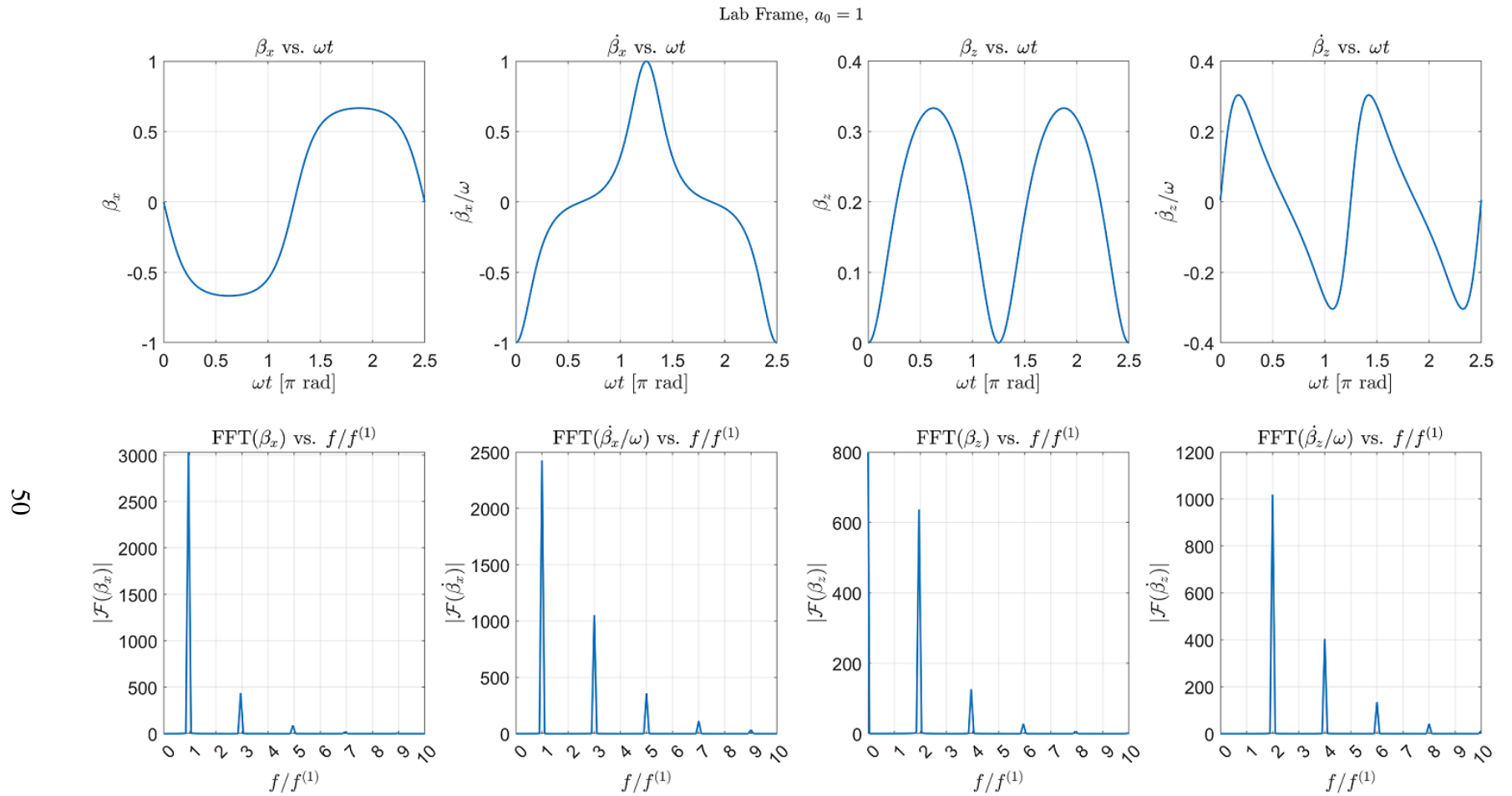


Figure 2.11: Plots showing the components of electron motion in the lab frame involved in describing its radiation along with their Fourier transforms. Shown are the x and z components of β and $\dot{\beta}$ vs. time (top row) for an electron interacting with a plane electromagnetic wave in the lab frame with $a_0 = 1$, and their corresponding Fourier transforms (bottom row). The Fourier transforms were taken for 20 cycles of RTS electron motion. Here, $f^{(1)}$ corresponds to the electron interaction frequency, which is related to the electromagnetic wave frequency, f_0 , via $f^{(1)} = f_0/(a_0^2/4 + 1)$.

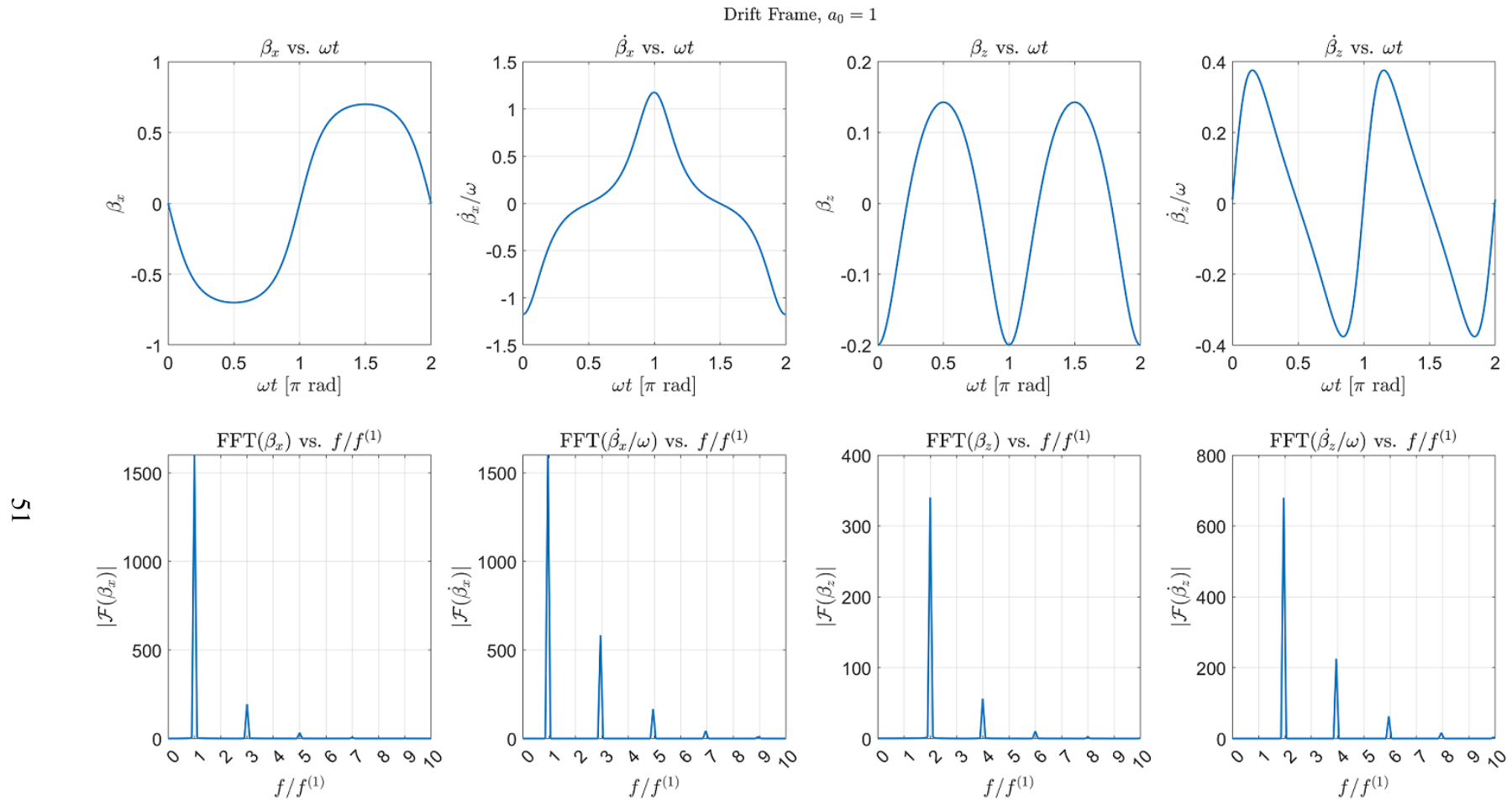


Figure 2.12: Plots showing the components of electron motion in the drift frame involved in describing its radiation along with their Fourier transforms. Shown are the x and z components of β and $\dot{\beta}$ vs. time (top row) for an electron interacting with a plane electromagnetic wave in the drift frame with $a_0 = 1$, and their corresponding Fourier transforms (bottom row). The Fourier transforms were taken for 10 cycles of RTS electron motion. Here, $f^{(1)}$ corresponds to the electron interaction frequency in the drift frame, which is related to the electromagnetic wave frequency in the lab frame, f_0 , via $f^{(1)} = f_0/\sqrt{1 + a_0^2/2}$.

To show that the the x and z components of β and $\dot{\beta}$ indeed consist of integer harmonics, Fig. 2.13 is presented, which shows the Fourier decomposition of Fig. 2.11 and the resulting reconstructed curves.

52

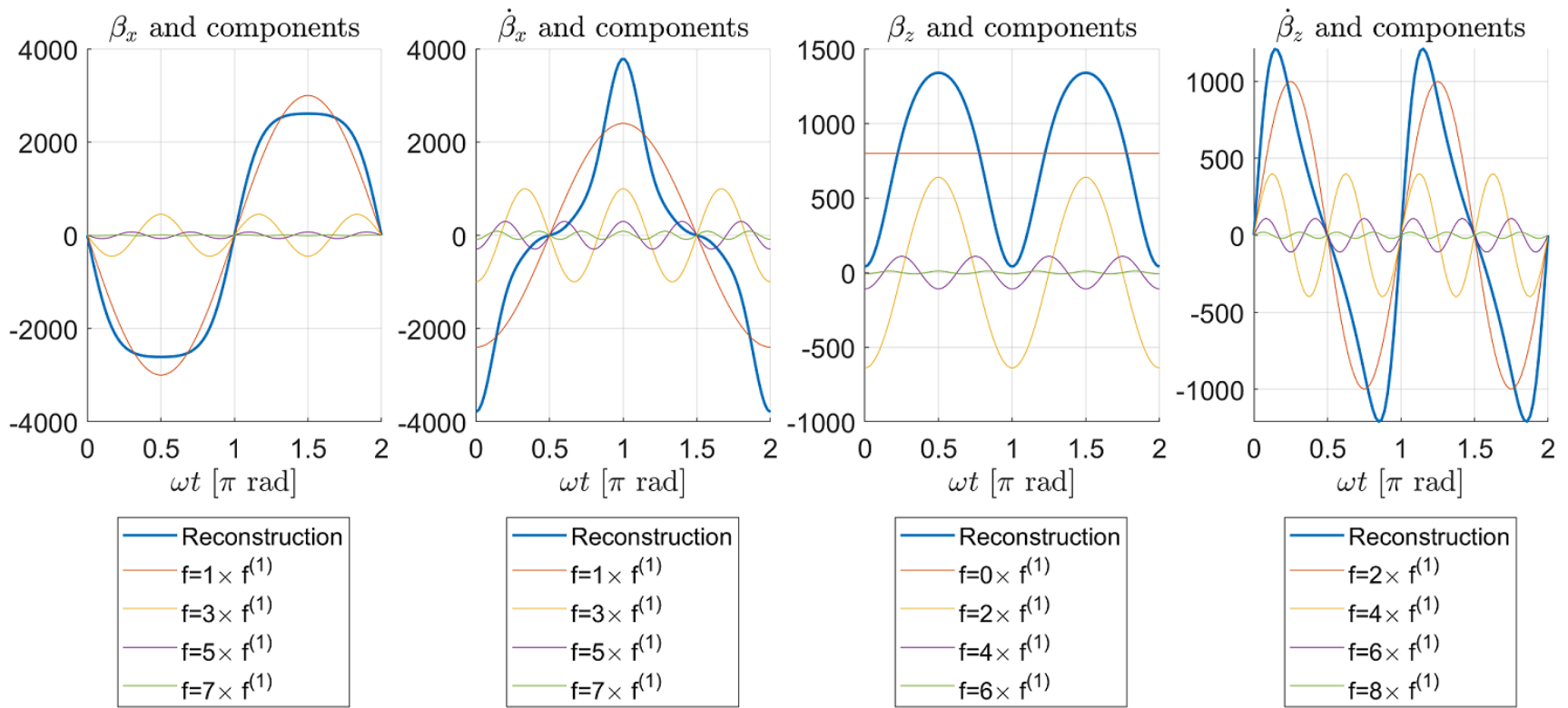


Figure 2.13: Fourier decomposition of the electron motion. Shown are the x and z components of β and $\dot{\beta}$ in the lab frame, reconstructed from weighted summation of sinusoids. Also plotted are the individual sinusoidal components, weighted based on the results of Fourier transforms from Fig. 2.11. Phase shifts of $\pm\pi/2$ or $\pm\pi$ were manually tweaked to produce curves whose crests match in time with Fig. 2.11.

The reason behind the higher harmonics in the motion is equations of motion depending on sinusoidal functions of the phase $kz - \omega t$ rather than just time, which results in, for example, kz appearing in both sides of the equation $kz = \frac{a_0^2}{4+a_0^2} \{\sin[2(kz - \omega t)] + \omega t\} \equiv f_z(kz)$ (Eq. 2.41). The entire expression, $f_z(kz)$, can be recursively plugged into kz to produce a composite of sinusoidal functions which repeat ad infinitum, i.e., $f_z(f_z(\dots f(kz))))$, so that:

$$\begin{aligned}
kz &= \frac{a_0^2}{4 + a_0^2} \{ \sin[2(\\
&\quad \frac{a_0^2}{4 + a_0^2} \{ \sin[2(\\
&\quad \vdots \\
&\quad \frac{a_0^2}{4 + a_0^2} \{ \sin[2(kz - \omega t)] + \omega t \} \\
&\quad \vdots \\
&\quad - \omega t)] + \omega t \} \\
&\quad - \omega t)] + \omega t \} \\
&\quad - \omega t) \} + \omega t \} \tag{2.75}
\end{aligned}$$

The higher harmonic components existing in β and $\dot{\beta}$ implies that the radiated light would also exhibit such harmonics. As an example, we compute Eq. 2.73 using the results for β in the lab frame for two directions: $\hat{\mathbf{n}} \parallel \mathbf{E}$ and $\hat{\mathbf{n}} \perp \mathbf{E}$. This results in the following simplifications for the term inside the Fourier integral:

$$\hat{\mathbf{n}} \parallel \mathbf{E} \Rightarrow \hat{\mathbf{n}} \times (\hat{\mathbf{n}} \times \beta) = -\beta_z \hat{\mathbf{z}} \tag{2.76}$$

$$\hat{\mathbf{n}} \perp \mathbf{E} \Rightarrow \hat{\mathbf{n}} \times (\hat{\mathbf{n}} \times \beta) = \beta_x \hat{\mathbf{x}} - \beta_z \hat{\mathbf{z}} \tag{2.77}$$

where we continue to use the coordinate system such that the electric field polarization is $\parallel \hat{x}$ and the direction of the wave propagation is $\parallel \hat{z}$. These expressions state that light radiated $\parallel E$ consists of only radiation from the β_z motion of the electron, whereas light radiated $\perp E$ contain both the contributions from the β_z and β_x motion, which is expected. The radiation spectra for both directions are plotted in Fig. 2.14 for $a_0 = 1$.

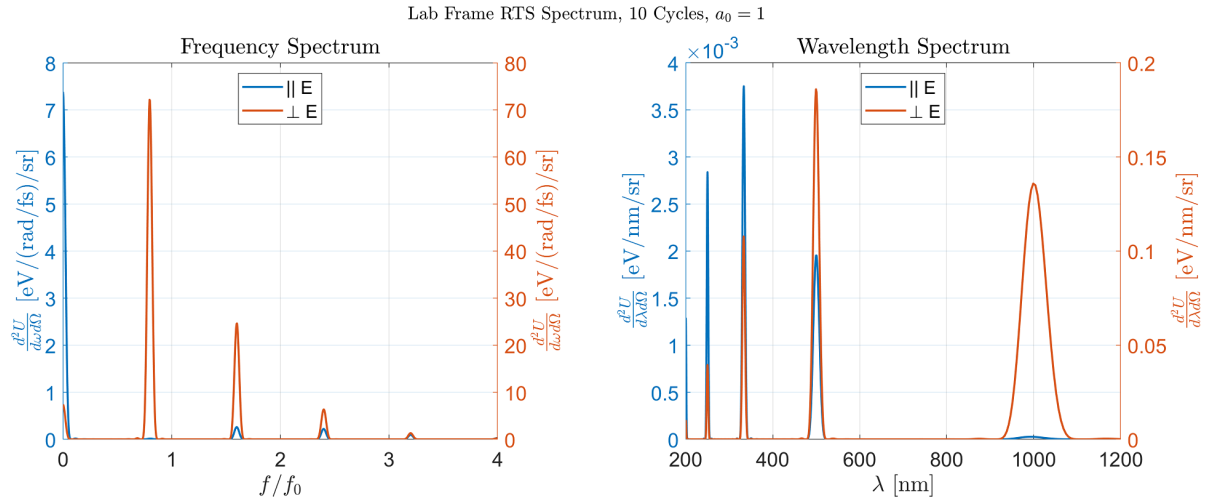


Figure 2.14: Plots of radiated spectra along select directions for an electron interacting with an infinite plane electromagnetic wave. The directions are $\parallel E$ and $\perp E$. The electromagnetic wave has $a_0 = 1$, wavelength $\lambda_0 = 800$ nm, and frequency $f_0 = 375$ THz. These spectra are computed using Eq. 2.73 for electron motion over 10 cycles in a) frequency space and b) wavelength space.

It is apparent from the plots that the radiated spectrum consists of Doppler shifted bands of the electromagnetic wave frequency. The width of the bands are inversely proportional to the number of cycles of the electron oscillation, of which 10 cycles were used. A more realistic situation consisting of a 30 fs Gaussian shaped pulse envelope is presented in Fig. 2.15, which

entails defining the fields of the electromagnetic wave

$$\mathbf{E} = E_0 \cos(kz - \omega t + \delta_0) \exp\left[-\frac{(kz - \omega t)^2}{\tau^2}\right] \hat{\mathbf{x}} \quad (2.78)$$

$$\mathbf{B} = \frac{E_0}{c} \cos(kz - \omega t + \delta_0) \exp\left[-\frac{(kz - \omega t)^2}{\tau^2}\right] \hat{\mathbf{y}} \quad (2.79)$$

where $\tau^2 = \Delta t_{\text{FWHM}}^2 / (2 \ln 2)$ with Δt_{FWHM} being the full width at half-maximum of the intensity profile, set to 30 fs. There are ≈ 10 cycles within this pulse in which the electron experiences $\geq 0.5I_0$, where I_0 is the peak intensity.

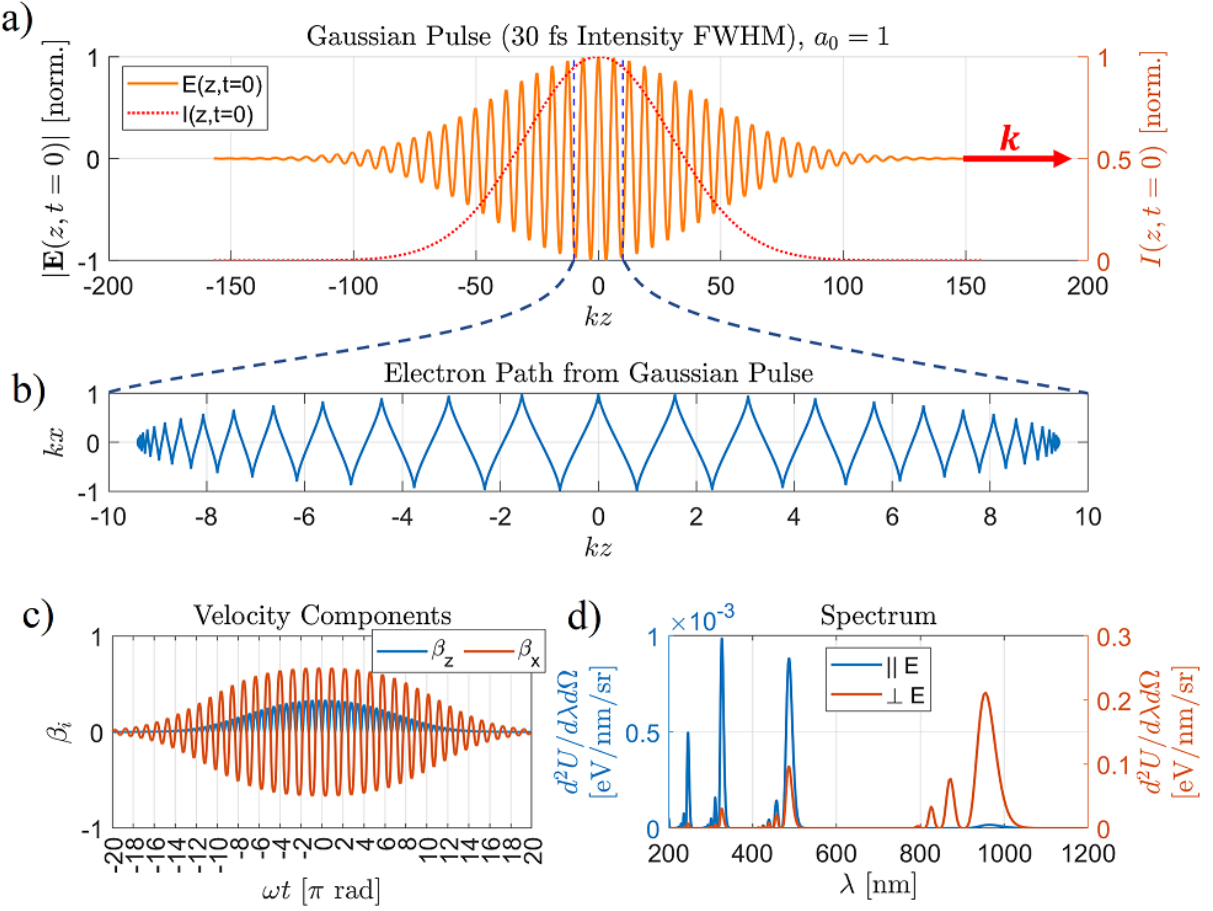


Figure 2.15: Plots showing the results of electron motion due to a Gaussian temporal pulse. Shown are a) the electric field (375 THz carrier frequency, 800 nm central wavelength) with a Gaussian temporal profile (30 fs intensity FWHM) as well as its intensity temporal envelope, b) the electron motion due to the pulse (with peak intensity corresponding to $a_0 = 1$), c) the velocity components, and d) the radiated spectra in the directions $\parallel E$ and $\perp E$. The blue dashed lines show the length scale of the electron drift relative to the pulse for $a_0 = 1$.

The important main difference between the spectra produced by the 30 fs Gaussian pulse with that by the infinite plane wave over 10 cycles is that for the Gaussian pulse, the peaks of the harmonics are less red-shifted, however the onset towards longer wavelengths remain more-or-less unchanged. This can be explained from the fact that the Gaussian pulse is comprised of lower intensity components outside of the peak of the envelope.

The next step would be to take into account the intensity distribution in space for a focused

laser pulse, which is a lot more involved. That exercise is left for Chapter 7. For our purposes here, inclusion of the intensity distribution would primarily add lower intensity contributions to the spectrum, resulting in more energy in the wavelength regions around the central wavelength, λ_0 , of the electromagnetic wave and its harmonics, and less proportional energy in the red-shifted regions. This leaves the wavelength of the red onset, λ_r , of the harmonics to be a possible diagnostic of the laser peak intensity, over an intensity range in which the harmonics are not overlapped as a result of the red shift. This is developed in the section that follows.

2.3.5 Relativistic Doppler Shift

In this section, we derive the expressions for the Lorentz transform of the laser frequency from the lab frame to the electron's average drift frame, followed by a Lorentz transform of the frequency radiated by the electron in the drift frame back into the lab frame. Consider an observer moving at a speed v relative to a source radiating light at frequency f in the source frame, as shown in Fig. 2.16. In the observer frame, the light is traveling towards the observer at the speed of light, c , while the source is traveling away at speed v .

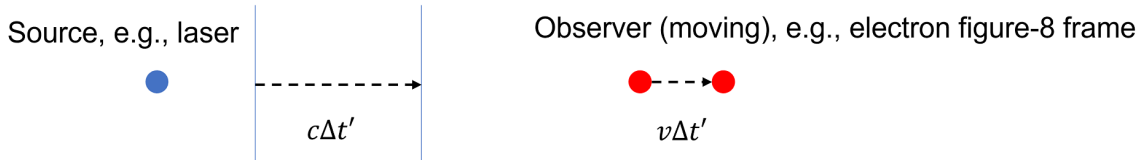


Figure 2.16: Diagram clarifying the derivation of the relativistic Doppler effect, showing an observer moving at a speed v directly away from a source. The source radiates wave fronts traveling at speed c with a period $\Delta t'$ in the observer frame. Over this period, the observer travels a distance of $v\Delta t'$.

The distance between adjacent crests, i.e., the wavelength, seen by the observer is then

given by:

$$\lambda' = c\Delta t' + v\Delta t' \quad (2.80)$$

where $\Delta t'$ is the time difference between adjacent crests radiated by the source as seen in the observer frame. The frequency observed is then given by:

$$f' = \frac{c}{\lambda'} = \frac{1}{(1 + \beta)\Delta t'} \quad (2.81)$$

The time difference between adjacent crests in the source frame is $\Delta t = \frac{1}{f}$ and is related to $\Delta t'$ via a Lorentz transform (i.e., time dilation)

$$\Delta t' = \gamma\Delta t = \frac{\gamma}{f} \quad (2.82)$$

so that the relationship between the frequencies in the two frames is given by:

$$f' = \frac{1}{1 + \beta} \frac{f}{\gamma} = \sqrt{\frac{1 - \beta}{1 + \beta}} f \quad (2.83)$$

Plugging in $\beta_D = \frac{a_0^2}{4+a_0^2}$ for β in Eq. 2.83 results in the relationship for the frequencies between the lab frame and the average drift frame of the scattered electron:

$$\omega_D^{(0)} = \frac{\omega_L^{(0)}}{\sqrt{1 + \frac{a_0^2}{2}}} \quad (2.84)$$

where $\omega_D^{(0)}$ and $\omega_L^{(0)}$ are the angular frequencies of the laser in the drift and lab frame respectively.

This expression is consistent with [55].

In the average drift frame, the electron oscillates at multiple harmonics of the drift frame electromagnetic wave frequency, producing radiation given by $\omega_D^{(n)} = n\omega_D^{(0)}$, where $\omega_D^{(n)}$ is the emitted frequency of the n^{th} harmonic, with n being an integer. For an observer in the drift frame far away, the electron may be considered a stationary point-source radiator. When transforming back into the lab frame, we take into consideration, in general, a direction of observation, θ . Consider an observer moving at a speed v at an angle θ relative to the line connecting the observer and the source, as shown in Fig. 2.17.

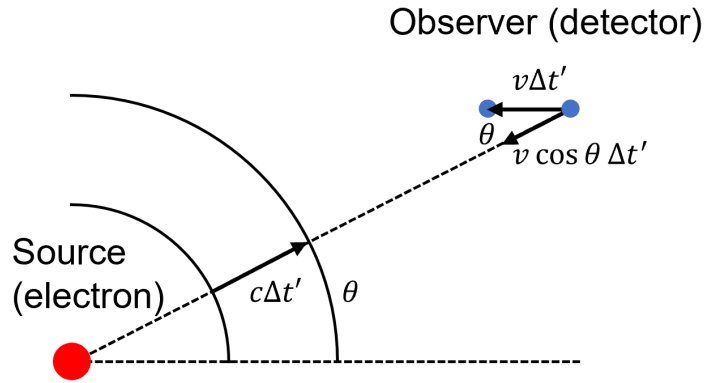


Figure 2.17: Diagram clarifying the derivation of the relativistic Doppler effect for an arbitrary direction, showing an observer moving at a speed v in a direction with an angle θ relative to the line connecting the source and observer. The source radiates spherical wave fronts traveling at speed c with a period $\Delta t'$ in the observer frame. Over this period, the observer travels a distance of $v\Delta t'$, and the change in distance to the source decreases by an amount $v \cos \theta \Delta t'$.

Assuming that the observer is far away so that θ remains unchanged over the time period $\Delta t'$ in which the source in the observer's frame radiates adjacent crests, the wavelength observed is given by:

$$\lambda' = c\Delta t' - v \cos \theta \Delta t' \quad (2.85)$$

so that the observed frequency is:

$$f' = \frac{c}{\lambda'} = \frac{1}{(1 - \beta \cos \theta) \Delta t'} \quad (2.86)$$

The time period $\Delta t'$ is dilated relative to that of the source, so that $\Delta t' = \gamma \Delta t = \gamma/f$. This implies that:

$$f' = \frac{1}{(1 - \beta \cos \theta) \gamma} f = \frac{\sqrt{1 - \beta^2}}{1 - \beta \cos \theta} f \quad (2.87)$$

For the case of transforming from the electron drift frame to the lab frame, we replace f' with $\omega_L^{(n)}$, f with $\omega_D^{(n)}$, and β with $\beta_D = \frac{a_0^2}{4+a_0^2}$, while θ remains as the angle that the detector makes relative to the laser propagation direction in the lab frame. After simplification, and using $\omega_D^{(n)} = n\omega_D^{(0)}$ along with Eq. 2.84, we obtain:

$$\omega_L^{(n)} = \omega_D^{(n)} \frac{\sqrt{1 + \frac{a_0^2}{2}}}{1 + \frac{a_0^2}{2} \sin^2(\frac{\theta}{2})} = \frac{n\omega_D^{(0)}}{1 + \frac{a_0^2}{2} \sin^2(\frac{\theta}{2})}. \quad (2.88)$$

This equation shows that in the lab frame, the radiated n^{th} harmonic frequency decreases with a_0 at a rate which depends on the angle θ (with the exception of $\theta = 0$, where there is no red shift). The angular dependence in the observed radiation may be visualized in the diagram of periodic wave fronts emitted by a moving source shown in Fig. 2.18. The wave fronts are compressed in the direction of motion, and stretched in the direction away from the motion, with intermediate values for directions with components transverse to the motion. In the case of RTS by an infinite plane wave, no Doppler shift occurs in the direction along the particle motion because the blue shift associated with the compressed wave fronts are canceled out with the red shift in the observed electromagnetic wave frequency in the drift frame.

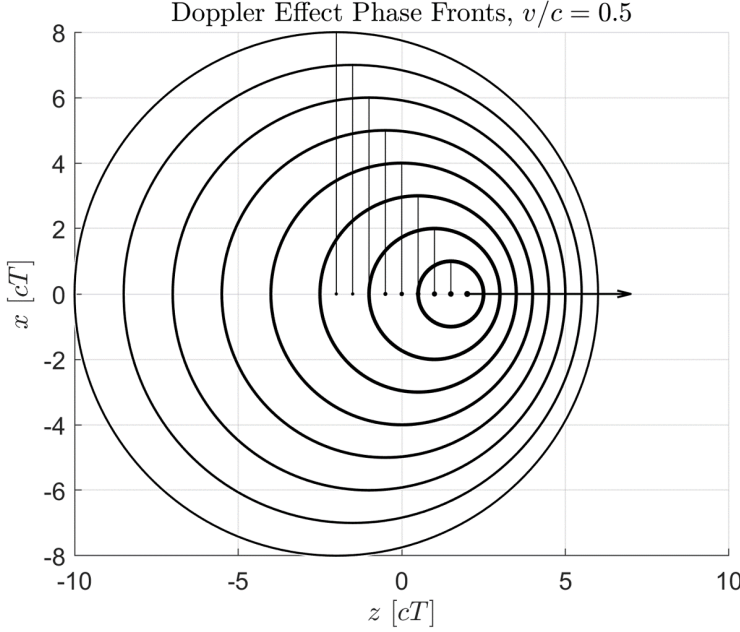


Figure 2.18: Diagram illustrating the directional dependence of the Doppler effect. Shown are phase fronts traveling at c emitted periodically by a source moving at $0.5c$, denoted by the dots which are located the positions during which their corresponding wavefront (indicated with a connecting vertical line) was emitted.

By rewriting 2.88 in terms of wavelength and intensity (instead of frequency and a_0), the wavelength of the n^{th} harmonic emission as a function of I is given by:

$$\lambda^{(n)} = \left[\frac{I r_0 \lambda_0^2 (1 - \cos \theta)}{2\pi m_e c^3} + 1 \right] \frac{\lambda_0}{n}. \quad (2.89)$$

Here, the wavelengths λ_0 and $\lambda^{(n)}$ correspond to the laser and RTS emitted in the n^{th} harmonic respectively, both in the lab frame. There is a one-to-one correspondence between the emitted wavelength and the laser intensity. Solving Eq. 2.89 for I , we obtain:

$$I(\lambda^{(n)}, \theta; n) = \frac{2\pi m_e c^3}{r_0 \lambda_0^2 (1 - \cos \theta)} \left(n \frac{\lambda^{(n)}}{\lambda_0} - 1 \right). \quad (2.90)$$

Calculations of the spectrum for a Gaussian temporal pulse, as shown in Fig. 2.19, show how the onset wavelength, λ_r , shifts with the intensity. The calculated spectra were found to be consistent with Eq. 2.90, as shown in Fig. 2.20. As the intensity increases, the harmonics as well as the

laser band will eventually overlap, and an onset wavelength would no longer be observed. By going to small angles of θ , however, it may be possible to observe the onset wavelength at higher intensities up to around 10^{20} W/cm² for $\theta \approx 25^\circ$. Measuring the intensity using the second harmonic spectrum is explored in Experiment 1 (Chapter 4).

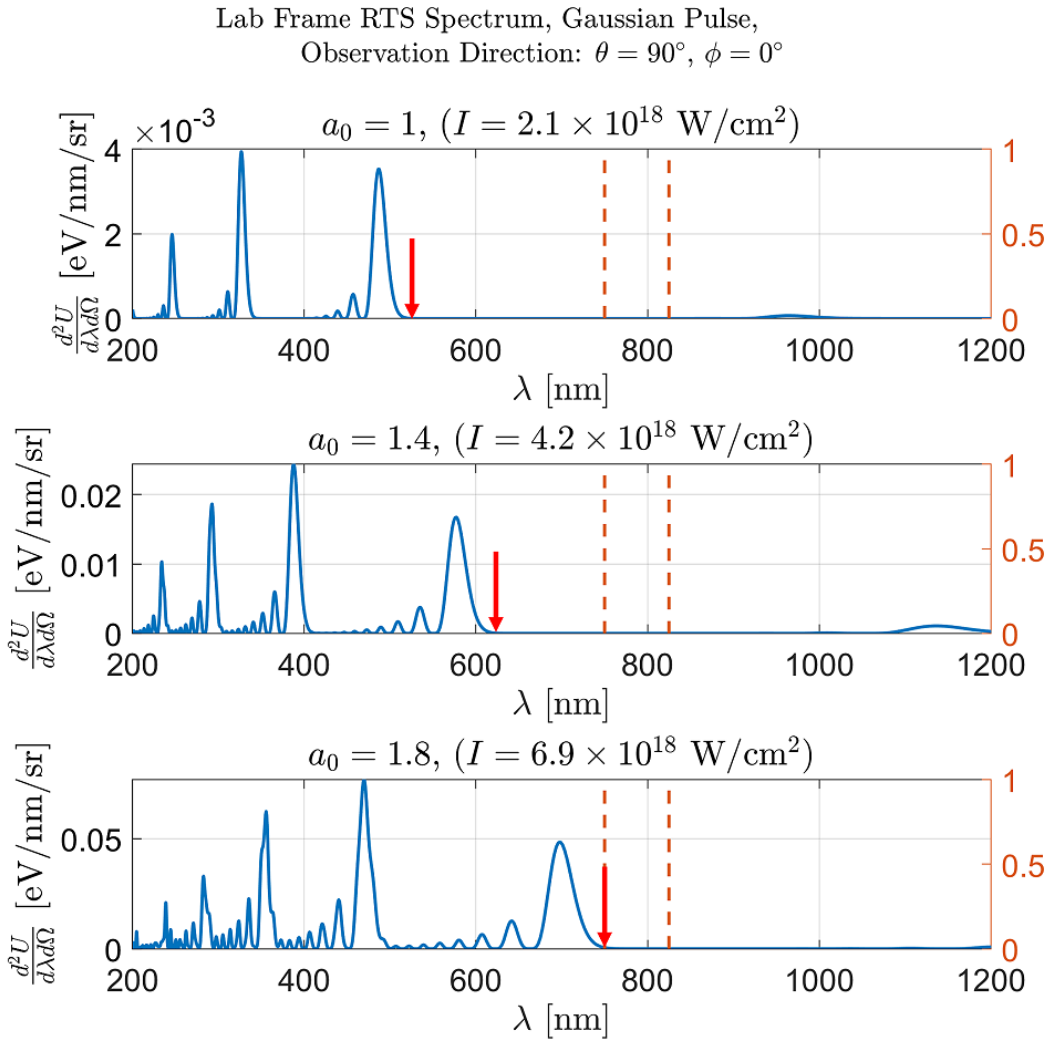


Figure 2.19: Plots of spectra, calculated for a 30 fs intensity FWHM Gaussian temporal pulse and observed in the direction $\theta = 90^\circ$ and $\phi = 0^\circ$ at various intensities. The red arrows in each spectrum indicate the onset wavelength, λ_r , for the second harmonic. The red dashed vertical lines indicate the laser band of a Ti:Sa laser.

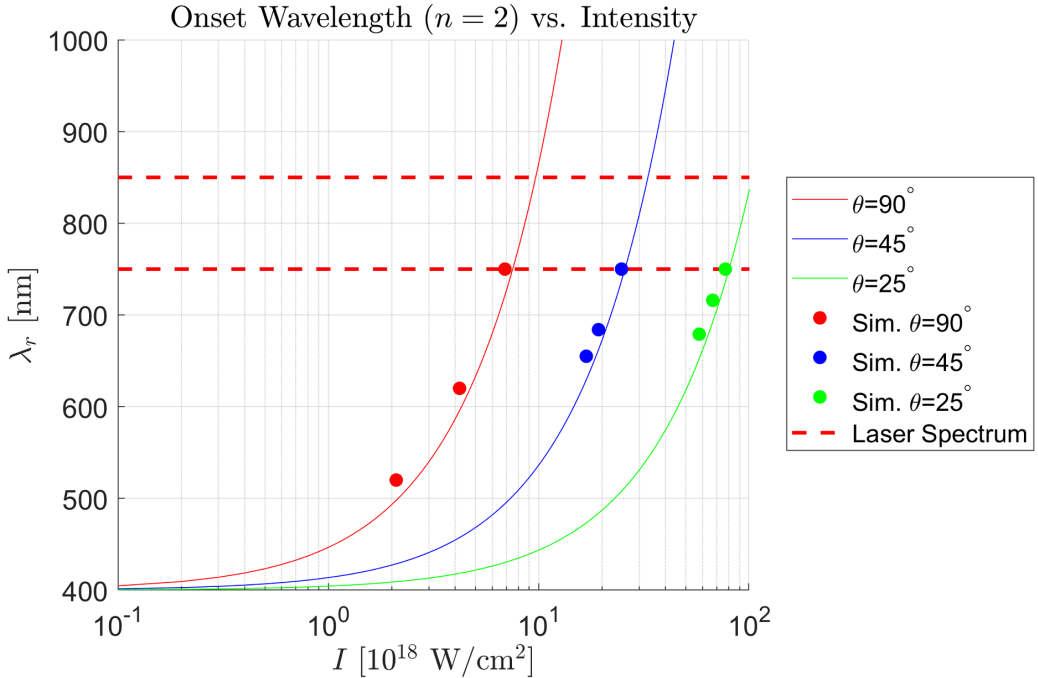


Figure 2.20: Plot of onset wavelength as a function of intensity for various values of observation angle θ . The curves are based on Eq. 2.90. The data points are results from numeric calculations of the spectra (see, for example, Fig. 2.19).

2.3.6 Radiation Pattern (Numerical)

An electron undergoing relativistic Thomson scattering produces an emission pattern which is a modified form of linear Thomson scattering. Due to relativistic aberrations, the donut-shaped emission pattern of linear Thomson Scattering becomes distorted so as to be more forward scattered the stronger the incident laser intensity, as a consequence of a phenomenon known as relativistic beaming. Relativistic beaming is the phenomenon where the radiation generated by a particle moving at relativistic speed is "beamed" towards the direction of motion and is commonly found in experiments involving relativistic electron beams such as synchrotrons [61]. In the case of this thesis topic, where the electron born at rest and subsequently accelerated by an intense field, the radiation pattern is produced from oscillating combined with forward drifting

motion of the electron integrated over time, which leads to a milder overall forward distortion compared to a relativistic particle beam.

To get a sense of how the electron motion contributes to the emission pattern, we will begin with the instantaneous electric field radiated by an electron whose β and $\dot{\beta}$ are confined in the same plane, as is the case for our typical example of an electron interacting with an infinite plane wave, as well as the observation direction \hat{n} . From Eq. 2.66 ($|\mathbf{E}_{\text{rad}}| \propto \left| \frac{\hat{n} \times [(\hat{n} - \beta) \times \dot{\beta}]}{(1 - \beta \cdot \hat{n})^3 R} \right|$), we may define the following angles formed between the vectors (see Fig. 2.21):

$$\theta_1 \equiv \angle(\hat{n}, \beta), \quad \theta_1 \in [0, 2\pi] \quad (2.91)$$

$$\theta_2 \equiv \angle(\dot{\beta}, \beta) \quad (2.92)$$

$$\alpha_1 \equiv \angle(\hat{n} - \beta, -\beta) \quad (2.93)$$

$$\alpha_2 \equiv \angle(\hat{n} - \beta, \dot{\beta}) \quad (2.94)$$

such that θ_1 ranges from 0 to 2π , α_1 is always inside of the triangle formed by \hat{n} , $\hat{n} - \beta$, and β and α_2 is defined separately for Case 1 ($0 \leq \theta_1 \leq \pi$) and Case 2 ($\pi \leq \theta_1 \leq 2\pi$) in Fig. 2.21, while θ_2 remains the same for both cases.

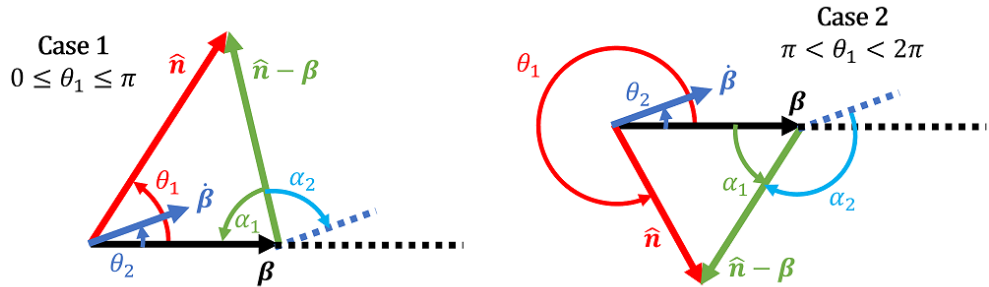


Figure 2.21: Diagram of showing the definitions of the angles θ_1 , θ_2 , α_1 , and α_2 based on the vectors β , $\dot{\beta}$, and \hat{n} for two cases concerning the value of θ_1 for the convention used in this section.

Since we are interested in $|\mathbf{E}_{\text{rad}}|$, we can make the simplification:

$$|\mathbf{E}_{\text{rad}}| \propto \left| \frac{(\hat{\mathbf{n}} - \boldsymbol{\beta}) \times \dot{\boldsymbol{\beta}}}{(1 - \boldsymbol{\beta} \cdot \hat{\mathbf{n}})^3 R} \right| = \frac{|\dot{\boldsymbol{\beta}}| |(\hat{\mathbf{n}} - \boldsymbol{\beta})|}{(1 - \beta \cos \theta_1)^3 R} |\sin \alpha_2| \quad (2.95)$$

From the law of cosines, $|\hat{\mathbf{n}} - \boldsymbol{\beta}| = \sqrt{1 + \beta^2 - 2\beta \cos \theta_1}$. The expression for α_2 was determined, for the two separate cases, as:

$$\alpha_1 = \begin{cases} \pi - \theta_2 - \cos^{-1} \left(\frac{\beta - \cos \theta_1}{\sqrt{1 + \beta^2 - 2\beta \cos \theta_1}} \right) & (\text{Case 1 : } 0 \leq \theta_1 \leq \pi) \\ -\pi + \theta_2 + \cos^{-1} \left(\frac{\beta - \cos \theta_1}{\sqrt{1 + \beta^2 - 2\beta \cos \theta_1}} \right) & (\text{Case 2 : } \pi \leq \theta_1 \leq 2\pi) \end{cases} \quad (2.96)$$

When these results are plugged into Eq. 2.95, $|\mathbf{E}_{\text{rad}}(\theta_1; \beta, |\dot{\boldsymbol{\beta}}|, \theta_2)|$ becomes a function of θ_1 , with β , $|\dot{\boldsymbol{\beta}}|$, and θ_2 as fixed parameters:

$$|\mathbf{E}_{\text{rad}}| \propto \begin{cases} \frac{|\dot{\boldsymbol{\beta}}| \sqrt{1 + \beta^2 - 2\beta \cos \theta_1}}{(1 - \beta \cos \theta_1)^3 R} \left| \sin \left[\pi - \theta_2 - \cos^{-1} \left(\frac{\beta - \cos \theta_1}{\sqrt{1 + \beta^2 - 2\beta \cos \theta_1}} \right) \right] \right| & \text{Case 1} \\ \frac{|\dot{\boldsymbol{\beta}}| \sqrt{1 + \beta^2 - 2\beta \cos \theta_1}}{(1 - \beta \cos \theta_1)^3 R} \left| \sin \left[-\pi + \theta_2 + \cos^{-1} \left(\frac{\beta - \cos \theta_1}{\sqrt{1 + \beta^2 - 2\beta \cos \theta_1}} \right) \right] \right| & \text{Case 2} \end{cases} \quad (2.97)$$

Figure 2.22 shows the radiation patterns plotted as polar functions of $\theta_1 = \angle(\hat{\mathbf{n}}, \boldsymbol{\beta})$, with $\boldsymbol{\beta}$ directed towards 0° , for various values of β and $\theta_2 = \angle(\dot{\boldsymbol{\beta}}, \boldsymbol{\beta})$, with $|\dot{\boldsymbol{\beta}}|$ and R fixed using Eq. 2.97. We can see that the result of increasing β is a distortion and enhancement of the radiation toward the direction of $\boldsymbol{\beta}$.

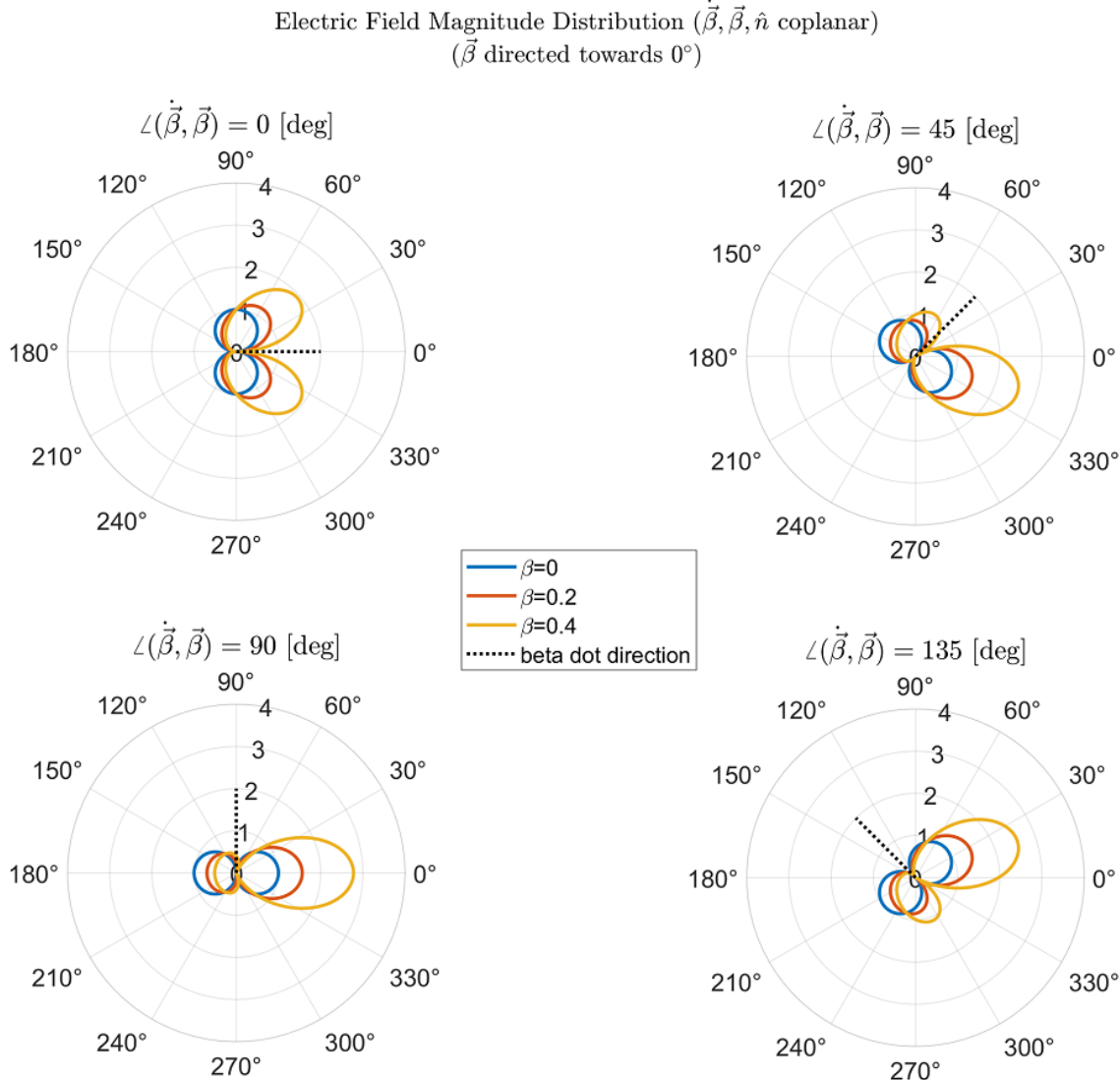


Figure 2.22: Polar plots of the instantaneous radiation distribution of $|E_{rad}|$ as a function of $\theta_1 = \angle(\hat{n}, \dot{\beta})$ (with β directed towards 0°). The plots are based on Eq. 2.97 for various fixed values of β and $\theta_2 = \angle(\dot{\beta}, \beta)$. The values of R and $|\dot{\beta}|$ are fixed throughout.

The next logical step would be to plot $|E_{rad}|$ for various points on the path of an electron undergoing RTS. This is done for $a_0 = 2$ in Fig. 2.23. This figure shows that there is generally little radiation produced at the cusps, where the pattern resembles the classic dipole, compared to the radiation produced near (but not at) the 0 crossings, where the momentum is large and $|\dot{\beta}|$ is nonzero. The direction of strong beaming may be approximated by multiple quantities, one of

which being the minimum electron pitch angle:

$$\tan \theta_{p,\min} = \frac{p_{x,\max}}{p_{z,\max}} = \frac{4}{a_0} \quad (2.98)$$

and the other being the pitch angle of the RMS electron oscillation to the longitudinal drift motion:

$$\tan \theta_{p,\text{avg}} = \frac{\sqrt{p_x^2}}{\bar{p}_z} = \frac{\sqrt{8}}{a_0} \quad (2.99)$$

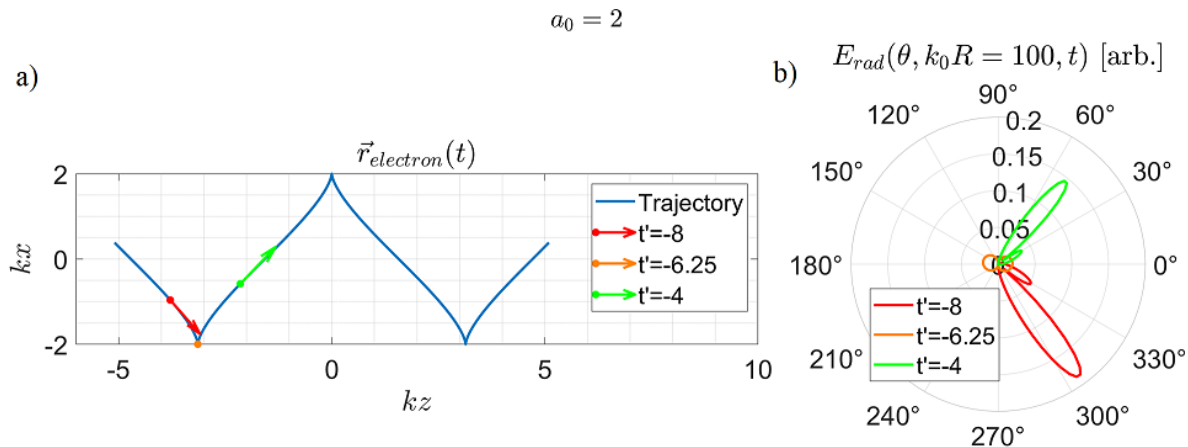


Figure 2.23: Plots illustrating the instantaneous RTS radiation pattern for various points along the electron path. Shown are a) the path of motion of an electron interacting with an infinite plane wave with $a_0 = 2$ along with momentum vectors at various points along the path labeled by their normalized time coordinate $t' = \omega t$, and b) the angular distribution of the instantaneous radiated electric field magnitude relative to the electromagnetic wave propagation direction, 0° , for the select points indicated in a).

The radiation patterns shown can be interpreted as distorted dipole patterns. In an experiment, what's measured is signal integrated over the entire time interval during which RTS takes place. Equation 2.70 allows the total radiated energy distribution per unit steradian to be

calculated. Written in terms of β , $\dot{\beta}$, and $\hat{\mathbf{n}}$, we have:

$$\frac{dU_{\text{rad}}}{d\Omega}(\hat{\mathbf{n}}) = \frac{e^2}{16\pi^2\epsilon_0 c} \int_{-\infty}^{\infty} \left| \frac{\hat{\mathbf{n}} \times [(\hat{\mathbf{n}} - \beta) \times \dot{\beta}]}{(1 - \beta \cdot \hat{\mathbf{n}})^3} \right|_{\text{ret}}^2 dt \quad (2.100)$$

$$= \frac{e^2}{16\pi^2\epsilon_0 c} \int_{-\infty}^{\infty} \left| \frac{\hat{\mathbf{n}} \times [(\hat{\mathbf{n}} - \beta(t_{\text{ret}})) \times \dot{\beta}(t_{\text{ret}})]}{(1 - \beta(t_{\text{ret}}) \cdot \hat{\mathbf{n}})^5} \right|^2 dt_{\text{ret}} \quad (2.101)$$

The calculation of Eq. 2.101 can be carried out numerically for arbitrary motion described by time series of values in β and $\dot{\beta}$. We present a calculation done for RTS due to an infinite plane wave. First, we write the equation in terms of the Cartesian components of \mathbf{n} , β , and $\dot{\beta}$ (n_x , n_y , n_z , etc.). Next, we write the Cartesian components of \mathbf{n} in terms of a 50×50 grid over a sphere based on a rectilinear grid in the spherical coordinates θ and ϕ , as explained in Appendix A.1. The integration is performed by adding the contributions to each grid point from every time step over a time interval consisting of 10 electron oscillations ($\omega\Delta t_{\text{ret}} = 2\pi(1 + \frac{a_0^2}{4}) \times 10$). The results are shown in Fig. 2.24 for RTS motion due to a range of a_0 values from 0.1 to 10. A distortion of the dipole pattern is apparent at $a_0 = 0.5$ and becomes more forward-concentrated as a_0 increases.

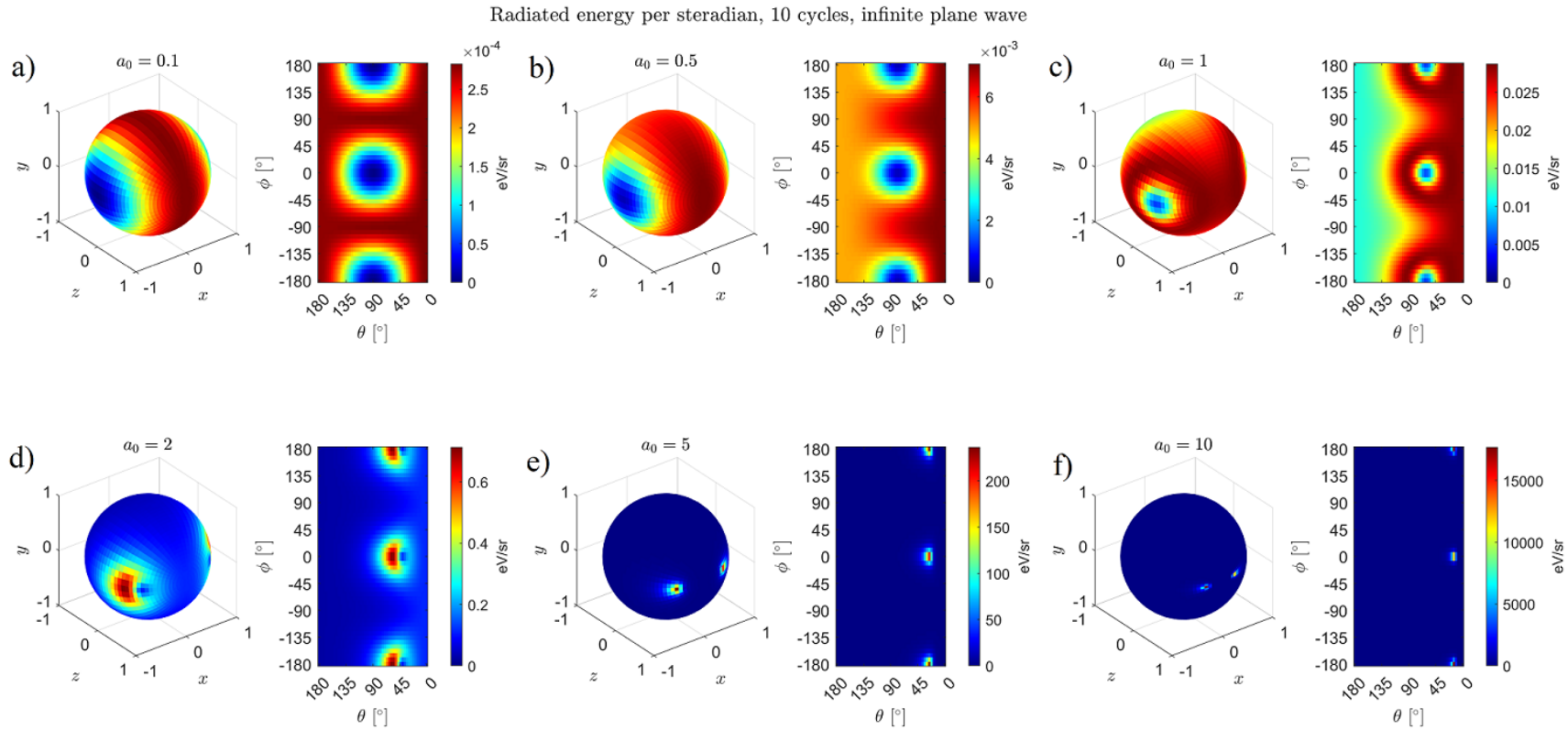


Figure 2.24: Plots of the directionally-resolved total radiated energy distribution per unit solid angle. The direction is parameterized in spherical coordinates. Shown are the distribution around a sphere as well as over rectilinear θ - ϕ space for each a_0 value: a) 0.1, b) 0.5, c) 1, d) 2, e) 5 and f) 10. The electromagnetic wave is an infinite plane wave propagating towards \hat{z} that is linearly polarized with the electric field along x . As a_0 increases, the overall distribution, to include what would have otherwise been the poles along the electron dipole motion at nonrelativistic a_0 ($\ll 1$), becomes distorted and concentrated towards the propagation direction.

What was calculated from Eq. 2.101 is the total radiated energy per unit solid angle that includes all frequencies. In order to isolate the radiation to the visible band where the second harmonic emits, we may take a numerical approach by performing an integration of the energy spectrum per unit solid angle over the desired frequency band, i.e., computing:

$$\frac{d^2U_{\text{rad}}}{d\Omega}(\hat{\mathbf{n}}, \omega) \Bigg|_{\omega_1}^{\omega_2} = \int_{\omega_1}^{\omega_2} \frac{d^2U_{\text{rad}}}{d\omega d\Omega}(\hat{\mathbf{n}}) d\omega \quad (2.102)$$

where ω_1 and ω_2 corresponds to the lower and upper limits of the desired band of angular frequencies and can be defined in terms of the lower and upper limits in wavelength, $\lambda_1 = 2\pi c/\omega_2$ and $\lambda_2 = 2\pi c/\omega_1$. Either of Eq. 2.71 to Eq. 2.73 can be used as the expression for $\frac{d^2U_{\text{rad}}}{d\omega d\Omega}$. We present results of calculations using Eq. 2.73 in Fig. 2.25 performed over a wavelength band from 400 to 700 nm (2.7 rad/fs to 4.7 rad/fs) with 500 uniform angular frequency steps in between.

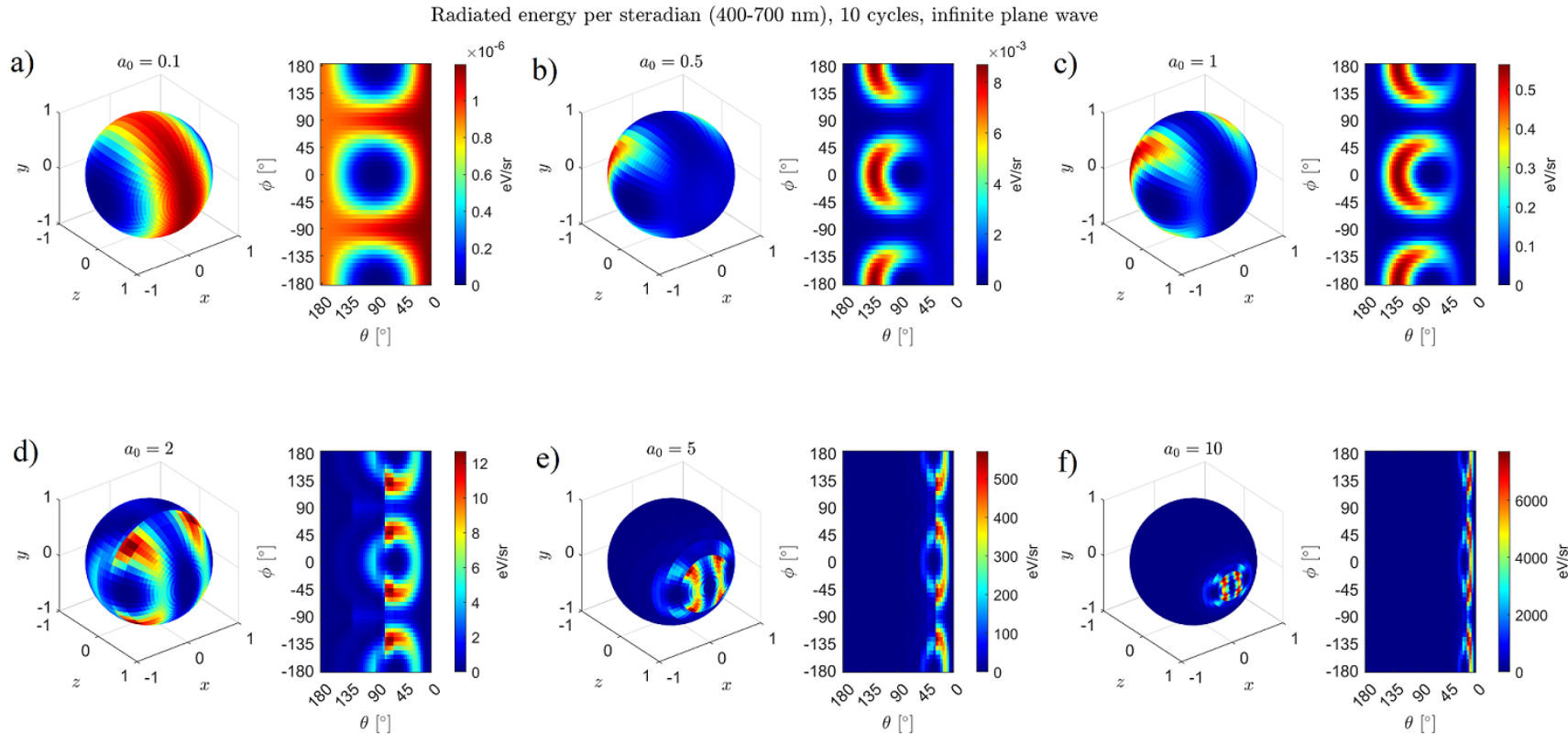


Figure 2.25: Plots of the directionally-resolved radiated energy distribution in the 400 to 700 nm band per unit solid angle. The distribution was calculated using Eq. 2.73, for radiated by 10 cycles of electron oscillation (2001 time steps) from RTS interaction with an infinite plane wave for a_0 equal to a) 0.1, b) 0.5, c) 1, d) 2, e) 5, and f) 10. The integration over the frequency band was done over 500 uniform angular frequency steps from 2.7 rad/fs to 4.7 rad/fs.

The results show that the second harmonic emits in a pattern resembling a pincer closing on its tips as a_0 increases, along with an overall forward concentration of energy. The computation time required to produce these results begin to become a limiting factor due to the fact that solving $\int_{\omega_1}^{\omega_2} \frac{d^2U_{\text{rad}}}{d\omega d\Omega} d\omega$ involves calculating a double integral, one over time, and the other over angular frequency.

2.3.7 Radiation Pattern (Analytical)

An alternative to calculating the second harmonic angular distribution for an electron interacting relativistically with an infinite plane wave would be to use the analytical expressions derived by Sarachik and Schappert (Eq. 4.23 in [55] or Eq. 2 in [59]), which states that the average radiated power per unit steradian of the n th harmonic is proportional to a function of a_0 :

$$\frac{dP^{(n)}}{d\Omega} = \frac{e^2 c}{8\epsilon_0 \lambda_0^2} f^{(n)}(a_0, \theta, \phi) \quad (2.103)$$

The radiation pattern is encoded into the function $f^{(n)}(a_0, \theta, \phi)$, which describes the angular pattern as it is modified by the parameter a_0 , and has the expression:

$$f^{(n)}(a_0, \theta, \phi) = \left(\frac{n^2}{\mathcal{M}^2(a_0, \theta)} \right) \left(\frac{a_0^2 n^2}{\mathcal{M}^4(a_0, \theta)} \right) \left[\left(1 - \frac{\left(1 + \frac{a_0^2}{2} \right) \cos^2 \alpha}{\mathcal{M}^2(a_0, \theta)} \right) (F_1^n(a_0, \theta, \phi))^2 \right. \\ - \frac{a_0 \cos \alpha \left[\cos \theta - \frac{a_0^2}{2} \sin^2(\theta/2) \right]}{2\mathcal{M}^2(a_0, \theta)} F_1^n(a_0, \theta, \phi) F_2^n(a_0, \theta, \phi) \\ \left. + \frac{a_0^2 \sin^2 \theta}{16\mathcal{M}^2(a_0, \theta)} (F_2^n(a_0, \theta, \phi))^2 \right] \quad (2.104)$$

where

$$\mathcal{M}(a_0, \theta) = 1 + \frac{a_0^2}{2} \sin(\theta/2) \quad (2.105)$$

and $\cos \alpha = \sin \theta \cos \phi$ is the directional cosine from $\hat{\mathbf{x}}$. Furthermore, the function $F_s^n(a_0, \theta, \phi)$ is written as a summation of products of Bessel functions:

$$F_s^n(a_0, \theta, \phi) = \sum_{l=-\infty}^{\infty} J_l \left(\frac{n a_0^2 \sin^2(\theta/2)}{4 \mathcal{M}(a_0, \theta)} \right) \left[J_{2l+n+s} \left(\frac{a_0 n \cos \alpha}{\mathcal{M}(a_0, \theta)} \right) + J_{2l+n-s} \left(\frac{a_0 n \cos \alpha}{\mathcal{M}(a_0, \theta)} \right) \right] \quad (2.106)$$

We note that Eq. 2.104 disagrees with [59] in that the leading factor (before the left square bracket) has an extra factor $\frac{n^2}{\mathcal{M}^2(a_0, \theta)}$ (written separate in the equation to stress this point). The original paper [55] states that the leading factor is $A(\omega_L^2) \frac{n^2}{\mathcal{M}^4(a_0, \theta)}$ where $A(\omega_L^2) = \frac{e^2 \omega_L^2 a_0^2}{32 \pi^2 \epsilon_0 c^3}$ and ω_L is the radiated angular frequency in the lab frame which is related to the laser frequency ω_0 via $\omega_L = n \omega_0 / \mathcal{M}(a_0, \theta)$. The assumption in [59] was that $\omega_L = \omega_0$ without any transformation or multiplication by n .

The infinite summation of Bessel functions in Eq. 2.106 may be approximated as a truncated sum, since the arguments of the Bessel functions are bounded. At very high orders, the Bessel functions evaluated at any value within the bounds become vanishingly small. Computing the angular distributions using analytic formulas require much less computing time compared to numerical integration over the two variables t and ω . Figures 2.26 to 2.28 show the computed angular distributions of average radiated power per unit steradian at various a_0 values for the first, second, and third harmonics.

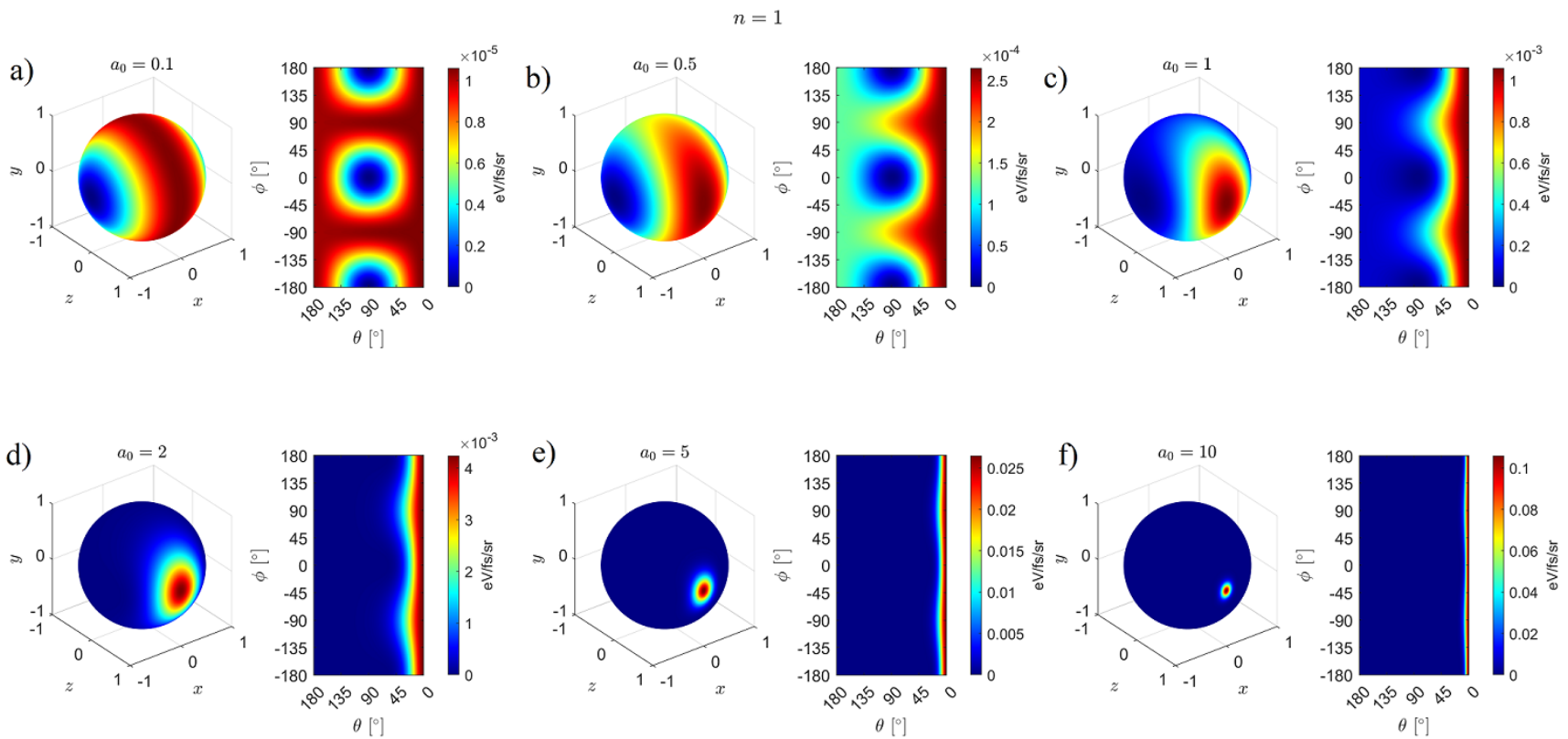


Figure 2.26: Plots of the analytical directionally-resolved average radiated power distribution per unit solid angle of the first harmonic ($n = 1$). The distribution was calculated from the Sarachik analytical expression (Eq. 2.104) for an electron interacting with an infinite plane wave for values of a_0 equal to a) 0.1, b) 0.5, c) 1, d) 2, e) 5, f) 10.

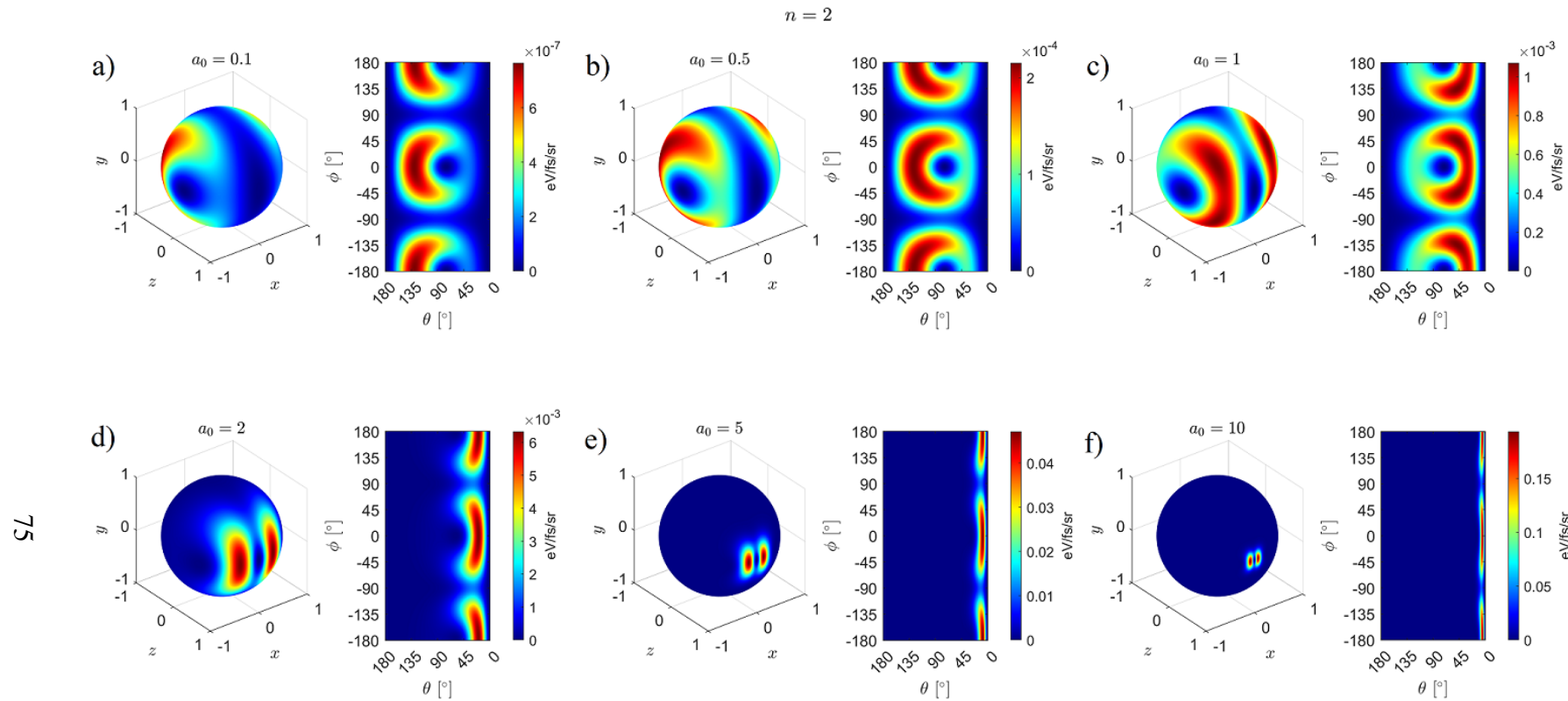


Figure 2.27: Plots of the analytical directionally-resolved average radiated power distribution per unit solid angle of the second harmonic ($n = 2$). The distribution was calculated from the Sarachik analytical expression (Eq. 2.104) for an electron interacting with an infinite plane wave for values of a_0 equal to a) 0.1, b) 0.5, c) 1, d) 2, e) 5, f) 10.

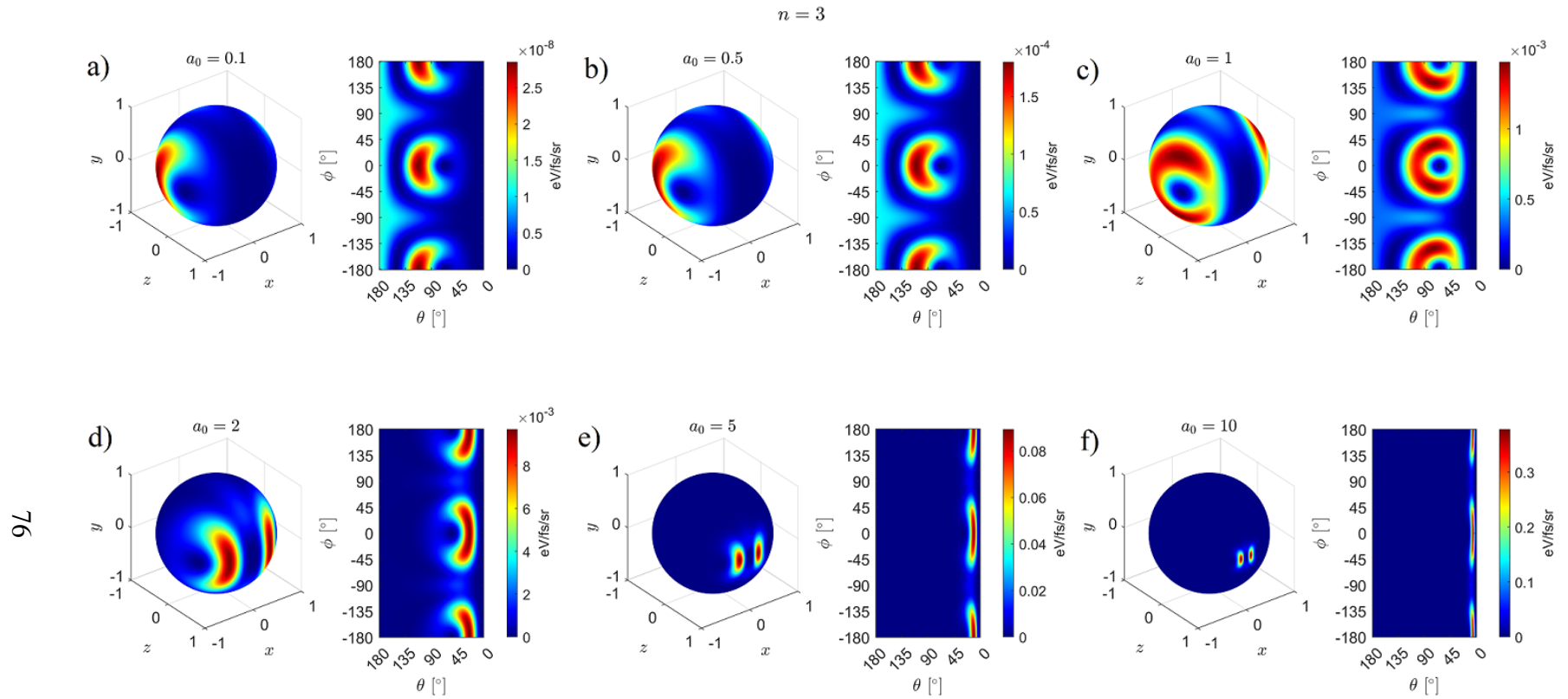


Figure 2.28: Plots of the analytical directionally-resolved average radiated power distribution per unit solid angle of the third harmonic ($n = 3$). The distribution was calculated from the Sarachik analytical expression (Eq. 2.104) for an electron interacting with an infinite plane wave for values of a_0 equal to a) 0.1, b) 0.5, c) 1, d) 2, e) 5, f) 10.

2.3.8 Radiation Pattern Dip

There may be a number of reasons why the numerical calculations (Fig. 2.25) for 400 - 800 nm do not agree exactly with the analytical expressions (Fig. 2.27) for $n = 2$. For one, the 400 - 800 nm band will include contributions from harmonics higher than 2 as the intensity increases. In particular, at $a_0 \approx 1$, the third harmonic will begin to cross the 400 nm mark at $\theta = 180^\circ$ based on Eq. 2.90. There may also be errors in the implementation of the calculations in code as well as assumptions in the mathematical expressions that have been overlooked. A more thorough analysis of the radiation pattern is beyond the scope of this thesis.

Here we focus on specific details in the angular distribution that agree in both calculations and which may be useful for characterizing the laser intensity. One such detail is the location of the pole located in the E-k plane which shift forward with increasing intensity. When the angular distribution is plotted vs. θ in the E-k plane ($\phi = 0$), the pole shows up as a "dip", as shown in Fig. 2.29, whose location θ_{\min} decreases with intensity. Over an intensity range parameterized by $a_0 = 1$ ($2.1 \times 10^{18} \text{ W/cm}^2$) to $a_0 = 2$ ($8.5 \times 10^{18} \text{ W/cm}^2$), the value of θ_{\min} varies linearly from roughly 70° to 60° . This motivates experimental measurements of the angular distribution at various intensities on the order of 10^{18} W/cm^2 . Experiments conducted to test this are discussed in Chapters 5 and 6.

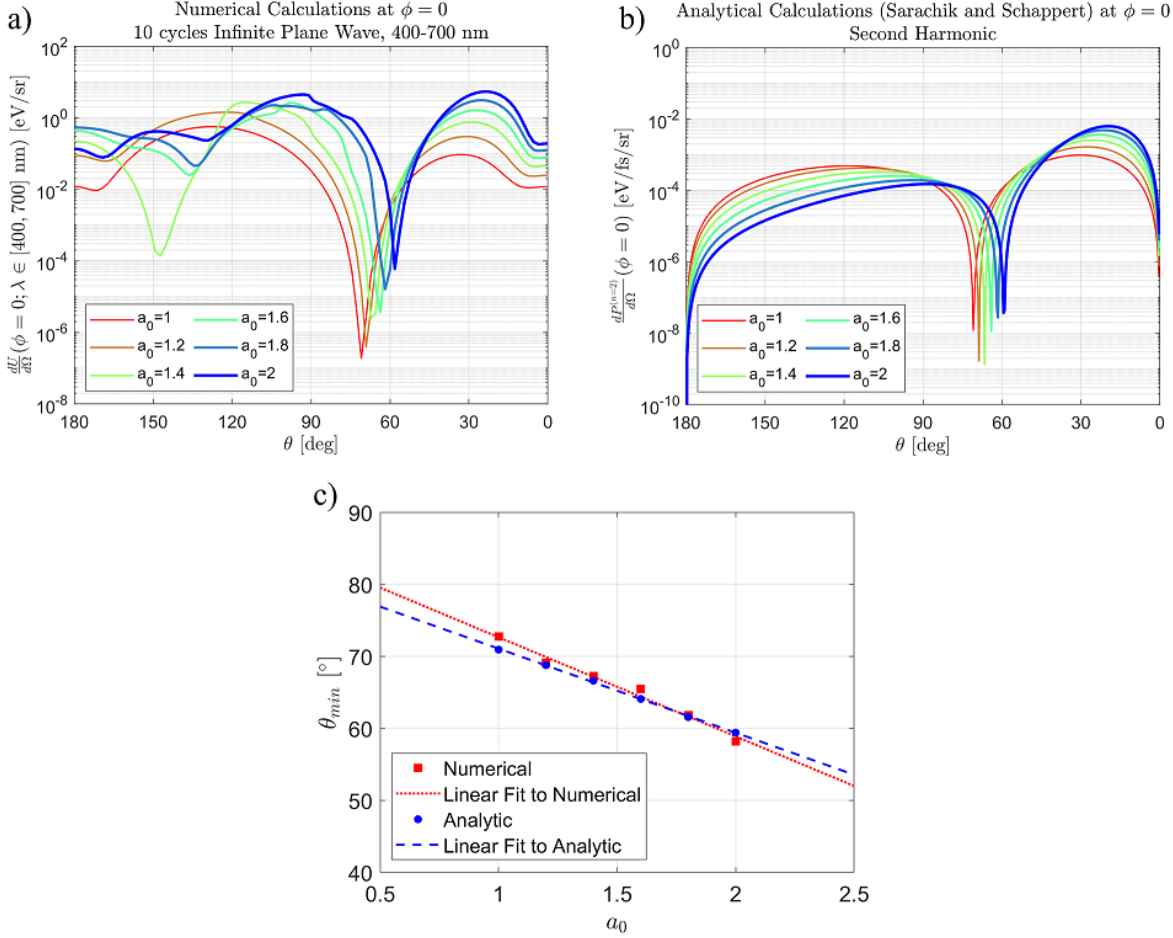


Figure 2.29: Plots of the RTS angular distribution in the E-k plane calculated numerically and analytically, with their dip locations compared. The a) numerical calculations are conducted for the 400 - 700 nm band while the b) analytical expressions were calculated using the Sarachik and Schappert results for $n = 2$. The location in θ of the dip, θ_{\min} as a function of a_0 for both cases are plotted c) along with linear fits. The fit to the numerical data has a slope of $-13.77(2.5)^\circ$ and θ_{\min} -axis intercept of $86.41(3.9)^\circ$, while for the fit to the analytical data, the slope is $-11.67(0.5)^\circ$ and θ_{\min} -axis is $82.73(0.77)^\circ$. The values give in parentheses are the 95% confidence half intervals.

2.3.9 Ionization and Electron Birth Conditions

Producing free electrons at the focus of the laser, whose initial velocities are small (nonrelativistic) compared to their typical velocities when scattered, can be accomplished in a few ways, including ionization directly by the laser from gas molecules as well as preionization through a means such as thermionic emission followed by acceleration onto the laser focus to nonrelativis-

tic speeds. The simplest of these methods to implement is ionization by the laser, requiring only a gas nozzle connected to a pulsed gas source. The ionization by the laser can be modeled using the Barrier Suppression Ionization (BSI) model [74], where the Coulomb potential of the nucleus of the atom is distorted by the laser field such that the peak potential of the barrier falls below the bound electron's energy level, as shown in Fig. 2.30.

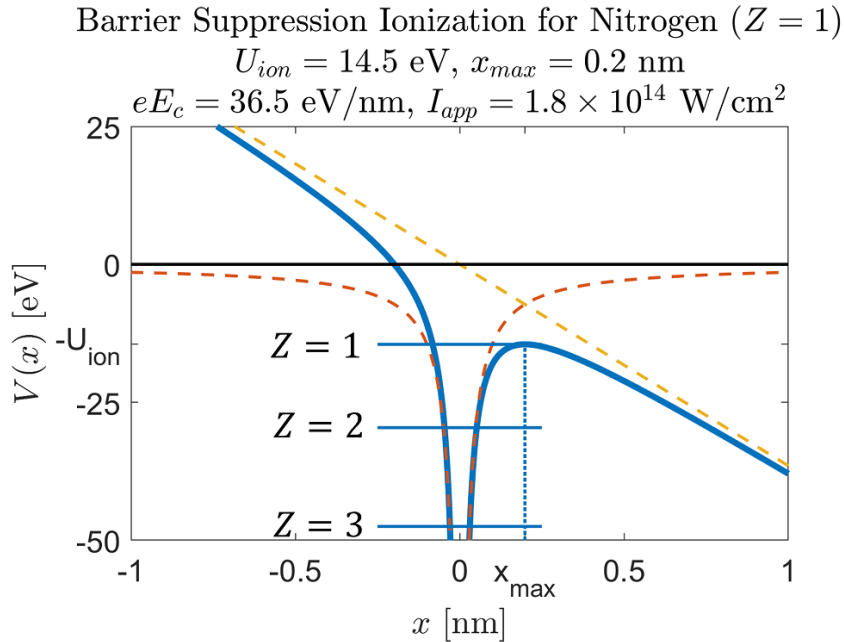


Figure 2.30: Diagram showing barrier suppression ionization for nitrogen. Barrier suppression ionization occurs when the Coulomb field is distorted so that the energy at peak of the barrier located at x_{max} , falls below the energy of the bound electron, $-U_{ion}$.

The potential energy experienced by an electron in a Coulomb potential and a constant electric field E_0 is given (in cgs) by:

$$V(x) = -\frac{Ze^2}{4\pi\epsilon_0 x} - eE_0x \quad (2.107)$$

The location of the peak of the barrier is obtained from differentiating $V(x)$ with respect to x ,

setting the $V'(x)$ to 0, and solving for x :

$$x_{\max} = \sqrt{\frac{Ze}{4\pi\epsilon_0 E_0}} \quad (2.108)$$

Ionization occurs when there is a critical field strength, E_c , potential at the peak of the barrier is equal to the electron's ionization energy, U_{ion} , in other words, $V(x_{\max}) = U_{\text{ion}}$ so that

$$E_c = \frac{\pi\epsilon_0 U_{\text{ion}}^2}{Ze^3} \quad (2.109)$$

The appearance intensity can then be defined in terms of the ionization energy of the electron and ionization state of the atom:

$$I_{\text{app}} = \frac{1}{\mu_0 c} E_c^2 \approx 4 \times 10^9 \left(\frac{U_{\text{ion}}}{\text{eV}} \right)^4 Z^{-2} \text{ W/cm}^2 \quad (2.110)$$

Among the gas species available, nitrogen and argon are both relatively affordable and have more than one electron shell allowing for high maximum appearance intensities, and are therefore suitable for early experiments. Values of the appearance intensities of Nitrogen and Argon are shown in Table 2.2.

Table 2.2: Table of ionization energies and appearance intensities for atomic nitrogen and argon.

Z	Nitrogen		Argon	
	U_{ion} [eV]	I_{app} [W/cm ²]	U_{ion} [eV]	I_{app} [W/cm ²]
1	14.5	1.8e14	15.8	2.5e14
2	29.6	1.2e16	27.6	9.3e15
3	47.5	1.8e17	40.7	9.9e16
4	77.5	2.3e18	59.8	8.2e17
5	97.9	9.2e18	75.0	3.2e18
6	552.1	1.3e22	91.0	9.9e18
7	667.1	3.9e22	124.3	4.7e19
8			143.5	1.1e20
9			422.5	1.0e22
10			478.7	2.1e22

The appearance intensities of nitrogen and argon have spacings which are large (no more than two per decade) and increases with ionization stage. The consequence of this is that there may not be electrons which appear near the peak of the laser, depending on the peak intensity of the laser. Figure 2.31 shows a plot of three Gaussian temporal pulse intensity profiles, with peak intensities of 10^{18} , 10^{19} and 10^{20} W/cm², along with the appearance intensities of nitrogen and argon. It can be seen that the first three ionization stages for both gas species occur early in the laser pulse. As the laser peak intensity increases, higher stage electrons eventually begin to ionize near the peak, however, as the intensity gets even higher, those electrons too will ionized early in the pulse.

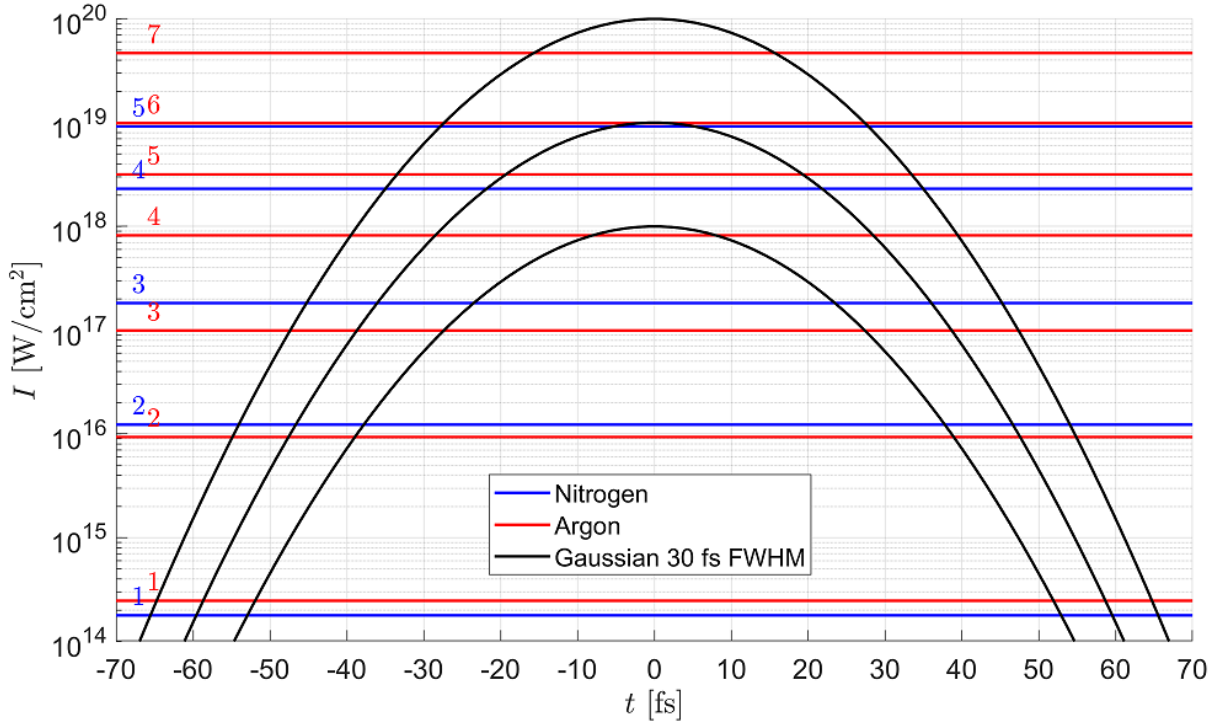


Figure 2.31: Plot showing the appearance intensities at various ionization stages of nitrogen and argon. Three intensity profiles consisting of Gaussian envelopes (30 fs intensity FWHM) over time at different peak intensities of 10^{18} W/cm^2 , 10^{19} W/cm^2 , and 10^{20} W/cm^2 are also plotted to roughly illustrate the ionization time relative to the peak of the pulse.

The moment in time when an electron is born determines its dynamics. Generally speaking, an electron may be born at any time relative to the peak of the laser pulse. This affects its chances of being scattered away from the axis due to the ponderomotive force, which will be discussed in more detail in Chapter 7. This would leave mostly electrons which were born near the central axis to interact at the peak. Furthermore, electrons are typically not ionized exactly at the peak of a laser cycle, but slightly earlier, as shown in Fig. 2.32. This results in transverse momenta added to an electron before it arrives at the peak of the cycle, causing a drift (due to effectively a nonzero value for δ_0 in the equations of motion, e.g., 2.27). Since the offset from the peak is typically small, the drift due to the laser phase of birth is expected to be minor. It is, however, an effect worth noting since it may exacerbate the effect of ponderomotive scattering

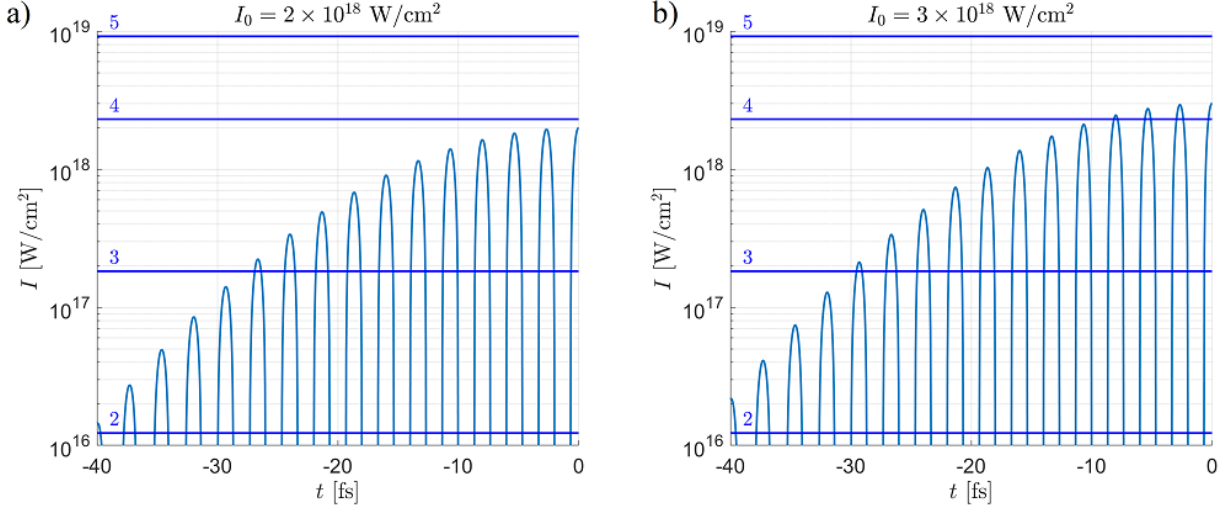


Figure 2.32: Zoomed-in plots of the instantaneous intensity temporal profile of a Gaussian pulse plotted against various nitrogen appearance intensities. The Gaussian profiles are 30 fs intensity FWHM in duration, have a 800 nm central wavelength (375 THz central frequency) and peak intensities of a) $2 \times 10^{18} \text{ W/cm}^2$ and b) $3 \times 10^{18} \text{ W/cm}^2$ along with the appearance intensities of nitrogen near this range.

The Barrier Suppression Ionization model for an atom is sufficient for the purposes of this thesis, however we briefly acknowledge here studies of more precise models. For one, the ADK model [77–79] takes into account quantum tunneling of an electron due to a finite barrier potential, resulting in a nonzero probability of ionization for electrons at intensities lower than I_{app} predicted from BSI. There are also models that use more accurate potentials, such as a "soft" Coulomb potential which have convergent values at $x = 0$, as well as potentials describing molecules, such as the enhanced ionization model for linear diatomic molecules. One would also have to consider the distribution of molecular orientations relative to the field polarization.

Chapter 3

Overview of Experiments using VEGA at CLPU

The three experiments discussed in this thesis took place at the Centro de Láseres Pulsados (CLPU) in Salamanca, Spain, during 2018 - 2022, and utilize the same VEGA laser system. This chapter is dedicated to providing an overview of this system as well as a "birds eye view" of the experiments and their key parameters. Details of the experiments, including design, layout, procedures, results, and analysis are provided in their respective chapters (Chapters 4 to 6).

3.1 The VEGA Laser System

The VEGA laser system at CLPU [3] is a laser manufactured by Amplitude and contains three beamlines and uses a chirp-pulse amplifier (CPA) scheme with Ti:Sapphire as the gain media for the amplification of short pulses that are sent in from an oscillator. The spectrum of this laser system therefore follows the typical Ti:Sapphire curve characterized by a 800 nm center wavelength and 70 nm bandwidth. The first of the three beamlines, named VEGA-1, is used primarily for testing and diagnostics by the laser crew, while the other two beamlines, VEGA-2 and VEGA-3, are designed for users of the facility. VEGA-2 provides a peak power of 200 TW (at 30 fs) at 10 Hz while VEGA-3 provides a peak power of 1 PW (at 30 fs) at up to 1 Hz. At the time of our the recent experiment in March of 2022, the stability of VEGA-3's pulse energy while running at full power and 1 Hz was not yet realized; however, stability for single-shot mode was guaranteed at full power.

As shown in Fig. 3.1, the VEGA system consists of a dual CPA and cross-polarization wave

(XPW) front end for initial amplification of the seed pulses and contrast-enhancement, followed by amplification and compression stages for each beamline at the backend.

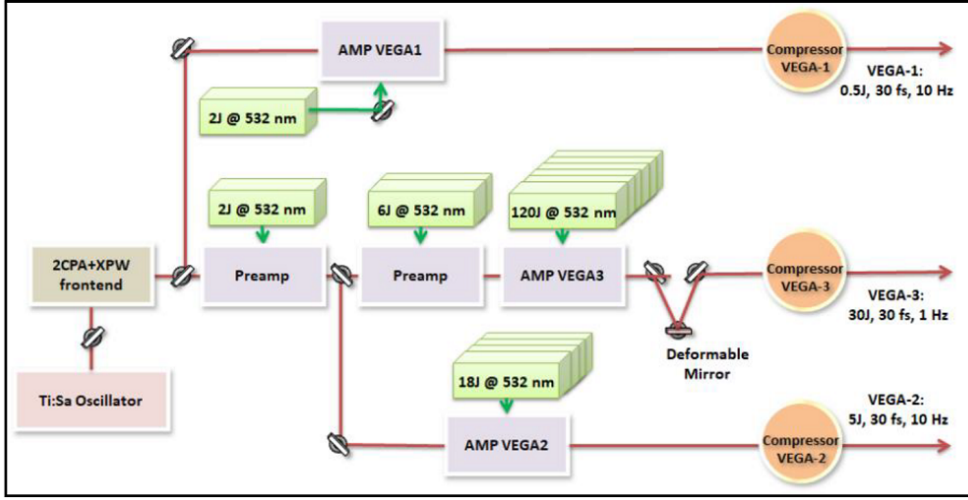


Figure 3.1: Schematics of the main components of the VEGA laser system [3]. Image courtesy of the SPIE digital library and Centro de Láseres Pulsados.

Figure 3.2a shows a more detailed schematic of the VEGA laser system in the laser bay. The laser bay provides a variety of laser diagnostics including, but not limited to: measurements of the pulse energy, pulse duration, and spectrum. Measurement of the pulse energy (Fig. 3.2b) is done before and after the attenuator (Fig 3.2c) by capturing leaked portion of the main beam through back-polished output mirrors using Gentec-eo XLE4 pyroelectric sensors as well as a Basler ace camera. These diagnostics provide shot-to-shot measurement of the laser pulse energy during live runs. The pulse energy arriving at the target chamber is calculated from known transmission losses calibrated from measurements of the pulse energy at target chamber compared with the energy measurements before the compressor at the amplifier.

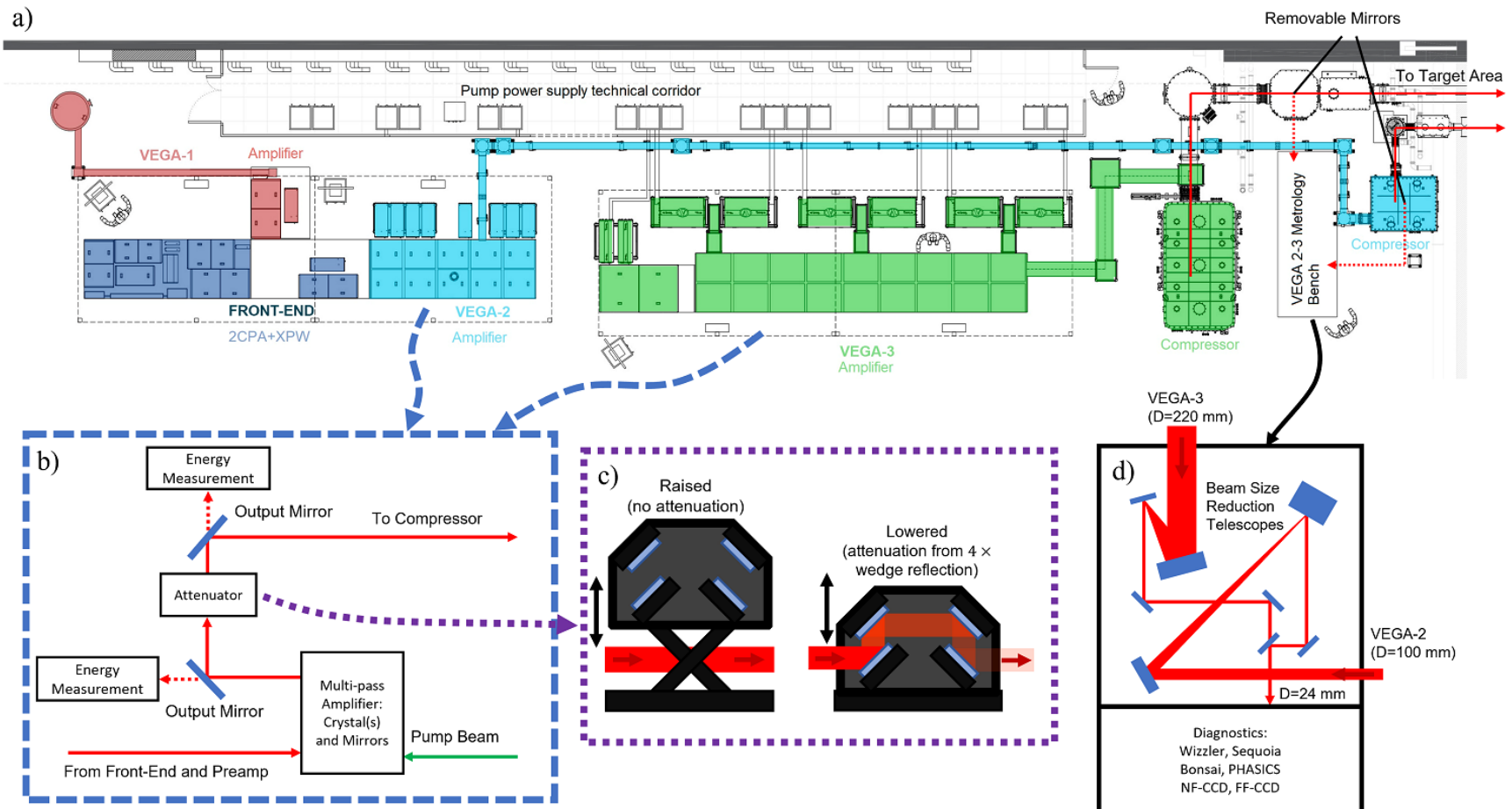


Figure 3.2: Diagrams of the VEGA laser system and its diagnostics in the CLPU laser bay. Shown are a) schematics of the physical layout of the laser bay [80], b) the component layout of an amplifier applicable to both the VEGA-2 and VEGA-3 beamlines, c) diagram of the 4-wedge attenuator (mounted on scissor arms) used to reduce beam power, and d) diagram of the input optics at the metrology bench [3]. Image courtesy of Centro de Láseres Pulsados.

After amplification, the beams are sent to their respective compressors to reduce their temporal duration down to ~ 30 fs. Measurement of the properties of the compressed pulses are conducted at a metrology bench (Fig. 3.2d) at attenuated energies (1 – 4 mJ with the 4-wedge attenuator lowered) using removable mirrors to divert the beams from their otherwise primary paths to the target area. These diagnostics are conducted at the beginning of each day as they cannot be used simultaneously with live shots to the target area. At the metrology bench, the beam sizes are reduced from 100 mm (VEGA-2) and 220 mm (VEGA-3) down to 24 mm using telescopes prior to being sent to various diagnostics. The diagnostics include a Wizzler (which measures the temporal pulse shape and pulse spectrum) [81], a Sequoia (which measures the pulse contrast), a Bonsai autocorrelator (which measures the pulse duration), a PHASICS (which measure the waveform), and two charge-coupled device (CCD) cameras (which measures the near-field, NF, and far-field, FF, profiles). The Wizzler measurements represent the vacuum pulse duration, having accounted for dispersion due to the beam's transmission through a glass window as it exits from the chamber as well as through air.

The backend of VEGA-2 and VEGA-3 are maintained in vacuum at $\sim 10^{-5}$ mbar to mitigate beam dispersion and distortion from scattering. The compressed beams are sent into the target area in the adjacent room as large collimated beams (specifically 11 cm and 22 cm in diameter for VEGA-2 and VEGA-3 respectively) with supergaussian distributions (or roughly a top hat) later to be focused using off-axis parabolic (OAP) mirrors.

3.2 Experimental Campaigns on RTS at CLPU

3.2.1 The Target Area

Three RTS experiments were conducted at CLPU. The first two experiments in 2018 and 2019 utilized the VEGA-2 beam whilst the the third experiment in 2022 utilized the VEGA-3 beam. A long focal length (130 cm) OAP was used with the VEGA-2 beam to focus the beam into the target chamber, which is a cylindrical chamber with a 1.2 m inner diameter and 0.6 height, as shown in Fig. 3.3.

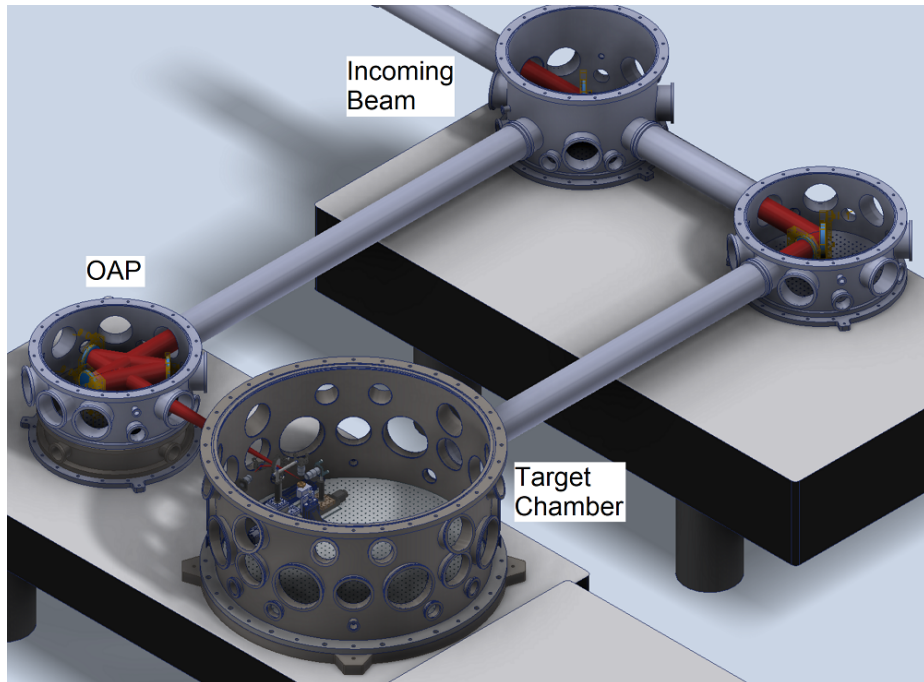


Figure 3.3: Diagram of the VEGA-2 beamline in the target area. The incoming beam from the laser bay is reflected into a chamber containing two turning mirrors and an off-axis parabola (OAP), which focuses the beam into the target chamber. The interior of these chambers were accessed from the top which were covered and sealed before pumping into vacuum. CAD model courtesy of Centro de Láseres Pulsados.

The VEGA-3 beamline is focused by an OAP with focal length of 250 cm into a rectangular target chamber with internal dimensions of $1.5 \text{ cm} \times 1.5 \text{ cm} \times 0.5 \text{ cm}$, as shown in Fig. 3.4. Each

chamber is pumped down to a background pressure of 10^{-5} mbar prior to firing of the laser. The parameters associated with the laser and target chamber during the experiments are summarized in Table 3.1.

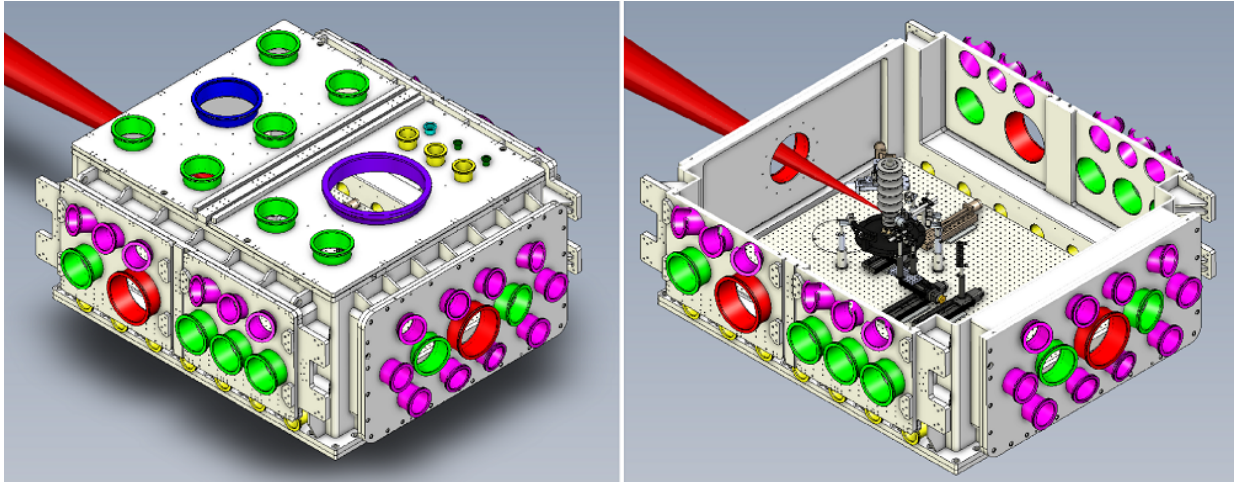


Figure 3.4: Diagrams of the VEGA-3 target chamber. The incoming laser beam was focused from a separate chamber containing an OAP (not included in diagrams). Lateral to the laser axis are four chamber doors which swing open and allow access to the interior. The colors of the flanges (type ISO-K) are codes for their sizes (from largest to smallest): Indigo (DN400), Blue (DN250), Red (DN200), Light Green (DN160), Pink (DN100), Yellow (DN63), Cyan (DN40), and Dark Green (DN25). The DN200 (red) flange, being ~ 20 cm in diameter, on the opposite side of the incoming laser provides sufficient clearance for the expanding laser after focus to pass through. CAD model courtesy of Centro de Láseres Pulsados.

Table 3.1: Summary of experimental parameters of the laser.

	Experiment 1	Experiment 2	Experiment 3
Year	2018	2019	2022
Campaign Duration ^a	14 days	22 days	31 days
Wavelength (Bandwidth)		800(70) nm	
Pulse Duration ^{b,c}		30 fs	
Beamline	VEGA-2		VEGA-3
Entrance Beam Diameter	11 cm		22 cm
OAP Focal Length	130 cm		250 cm
f/#	13		11
Focused Beam Diameter ^c	22 μm		11-13 μm
Repetition Rate	10 Hz		1 Hz / Single Shot
Energy Range ^d	1 – 2.7 J	1.2 – 3.4 J	2 – 20 J
Peak Intensity Range ^{e,f}	$1 - 7 \times 10^{18}$	$2 - 6 \times 10^{18}$	$1 - 10 \times 10^{19}$
Chamber Dimensions	1.2 m (ID) \times 0.6 m (H)		1.5 m \times 1.5 m (LW) \times 0.5 m (H)
Background Pressure		10^{-5} mbar	

^a Including setup time, ^b Nominal, ^c Full-width at half maximum, ^d On target, ^e Estimated, ^f In units of W/cm².

3.2.2 RTS Detectors and Gas Source

In the first experiment, measurements of the second harmonic spectrum were conducted using a pair of microscope objectives looking at the focus. One objective was oriented along the electric field polarization ($\theta = 90^\circ, \phi = 0$) and the other along the magnetic field polarization ($\theta = 90^\circ, \phi = 90^\circ$). The measurements were taken for various laser pulse energies to observe how the Doppler shifted spectrum changes vs. laser peak intensity. In the second and third experiments, the detectors used each consisted of a lens imaging the laser focus from a distance of ~ 13 cm onto a fiber optic cable. These detectors were mounted on an arc-shaped apparatus on a motorized rotation stage, allowing rotation of the positions of the detectors about the \hat{y} axis (parallel to the magnetic field polarization). In the first two experiments, the RTS light was captured through a gated spectrometer with a gate window of 5 ns. In the third experiment, a transition was made to using the streak camera, which for a 0.5 ns gate after accounting for fiber

dispersion. Figure 3.5 show the detectors in their mounting apparatus for the three experiments.

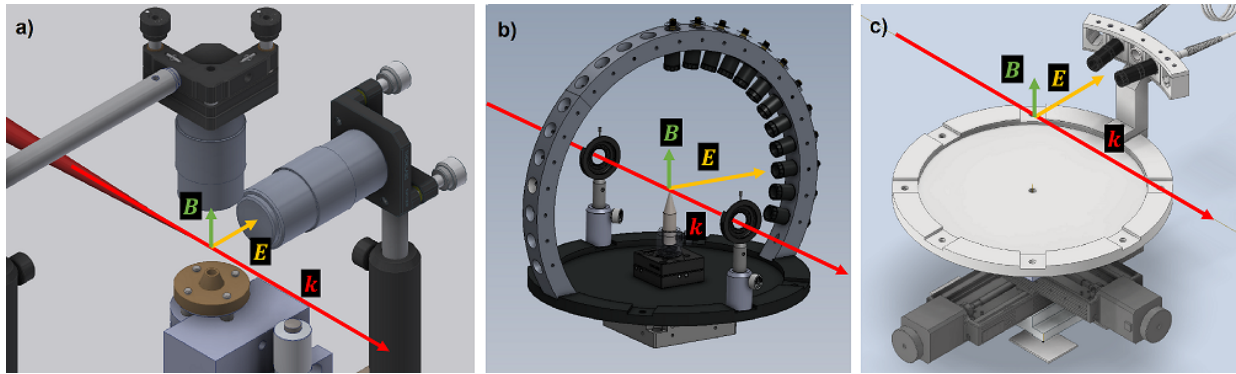


Figure 3.5: Diagrams of detectors from a) experiment 1, b) experiment 2, and c) experiment 3. The detectors from experiment 1 were long working distance, infinity-corrected microscope objectives which imaged the focal region into free-space, to later be focused with a lens. The detectors from experiment 2 were fiber-optic based collection systems mounted along an arc-shaped apparatus designed to rotate about the B axis and collect light over various directions along a sphere. The detectors from experiment 3 were fiber-optic collection systems mounted on an arc oriented along the E-k plane of the laser, which also rotate about the B axis. More details of the detectors are described in the chapters respective to each experiment. Credit: a) CLPU for CAD model of components, b) Andrew Longman for the design and CAD model of the arc assembly, c) Lester Putman for the final design and CAD model of the side arc components.

The gas source for the three experiments generally consisted of molecular nitrogen that was puffed into the chamber via a pulsed gas nozzle. In the first experiment, the nozzle was connected directly to the regulator behind a gas cylinder via a tube. Due to the small size of the tube, this setup resulted in a small drift in the backing pressure as the gas was leaked during shots. This was addressed in later experiments using a reservoir chamber back-filled with gas as the backing source for the gas nozzle. A summary of the parameters associated with the detectors as well as gas source is shown in Table 3.2.

Table 3.2: Summary of experimental parameters of the detectors and gas source.

	Experiment 1	Experiment 2	Experiment 3
Detection Optics	Microscope Objectives	Lens and Fiber Optics	
Object Distance	20 mm ^a	13 cm	
Numerical Aperture	0.28	0.05	
Collection Half-Angle	16°	3°	
Readout Device	Gated Spectrometer	Streak Camera 0.35 ns	
Gate Window ^b	5 ns		
Angular Range	θ $\phi = 0^\circ, 90^\circ$	$30^\circ - 150^\circ$ $\phi_{\text{Arc}}^c = 0^\circ, 50^\circ$	$25^\circ - 120^\circ$ $\phi = 0^\circ$
Gas Species	Molecular Nitrogen		
Pulse Duration	4 ms		
Backing Source	Regulated Cylinder	Reservoir Chamber	
Backing Pressure	10 mbar	200 mbar	800 mbar
Pressure at Focus ^d	10^{-3} mbar	10^{-3} mbar	10^{-2} mbar
Molecular Density ^{d,e}	$3 \times 10^{13} \text{ cm}^{-3}$	$3 \times 10^{13} \text{ cm}^{-3}$	$3 \times 10^{14} \text{ cm}^{-3}$

^a Same as focal length, ^b Duration during which signal is acquired, ^c Refers to azimuthal position on the arc, ^d Estimated, ^e Assuming ideal gas.

Chapter 4

Experiment 1: Second Harmonic Spectrum

Introduction

The premise behind this experiment was to take a spectrum of RTS radiation in the second harmonic and analyze its properties as a function of the laser peak intensity. From the expression for the frequency of radiated RTS based on the Doppler effect in [55], we have derived an expression [69] of the peak intensity as a function of the onset wavelength, $\lambda_r^{(n)}$, given below:

$$I_{\text{pk}}(\lambda_r^{(2)}, \theta) = \frac{2\pi m_e c^3}{r_0 \lambda_0^2 (1 - \cos \theta)} \left(\frac{2\lambda_r^{(2)}}{\lambda_0} - 1 \right) \quad (4.1)$$

where m_e is the electron rest mass, c is the vacuum speed of light, r_0 is the classical electron radius, λ_0 is the laser wavelength, and θ is the polar angle of observation direction relative to the laser propagation direction. This expression assumes that the peak of the laser pulse may be approximated as a plane-wave. Radiation produced from regions in the laser outside of the peak would contribute to wavelengths $\lambda_{\text{RTS}}^{(2)} < \lambda_r^{(2)}$ in the spectrum, so that $\lambda_r^{(2)}$ is associated solely with the peak intensity.

The experimental approach involved using two long working distance (~ 34 mm), infinity-corrected microscope objectives, to image the focal region from two separate directions orthogonal to the propagation direction of the laser, specifically one along the electric field polarization, namely \hat{x} , and the other along the magnetic field polarization, \hat{y} . Light from the imaged region was sent through free-space and, using mirrors, routed out of the chamber to be refocused onto

readout devices. When refocused onto a camera sensor, the focal region’s spatial structure was visualized. Additionally, the spectral measurements were achieved by refocusing the light onto the entrance slit of a spectrometer consisting of an intensified charge-coupled device (ICCD) camera with a gate time of 5 ns.

4.1 VEGA-2 Laser Focal Region

The focus is produced using a f/13 geometry; the incoming 11 cm diameter beam is focused into the target chamber by a 130 cm focal length parabolic mirror onto a spot with a $\sim 22 \mu\text{m}$ FWHM diameter. The spatial characteristics of the focus is estimated using a wedge to pick off a fraction of the beam, as shown in the left on Fig. 4.1, while the beam is operating at low power, and then imaging the reference focus using a Mitutoyo Plan Apo near-infrared (NIR) microscope objective [82] onto a Blackfly PGE 23S6M [83] monochrome complementary-metal-oxide-semiconductor (CMOS) camera sensor. The Blackfly camera has a sensor format of 1/1.2” (more specifically, an area of $11.13 \text{ mm} \times 7.03 \text{ mm}$), a pixel size of $5.86 \mu\text{m} \times 5.86 \mu\text{m}$, and a pixel array of 1920×1200 (horizontal \times vertical) pixels.

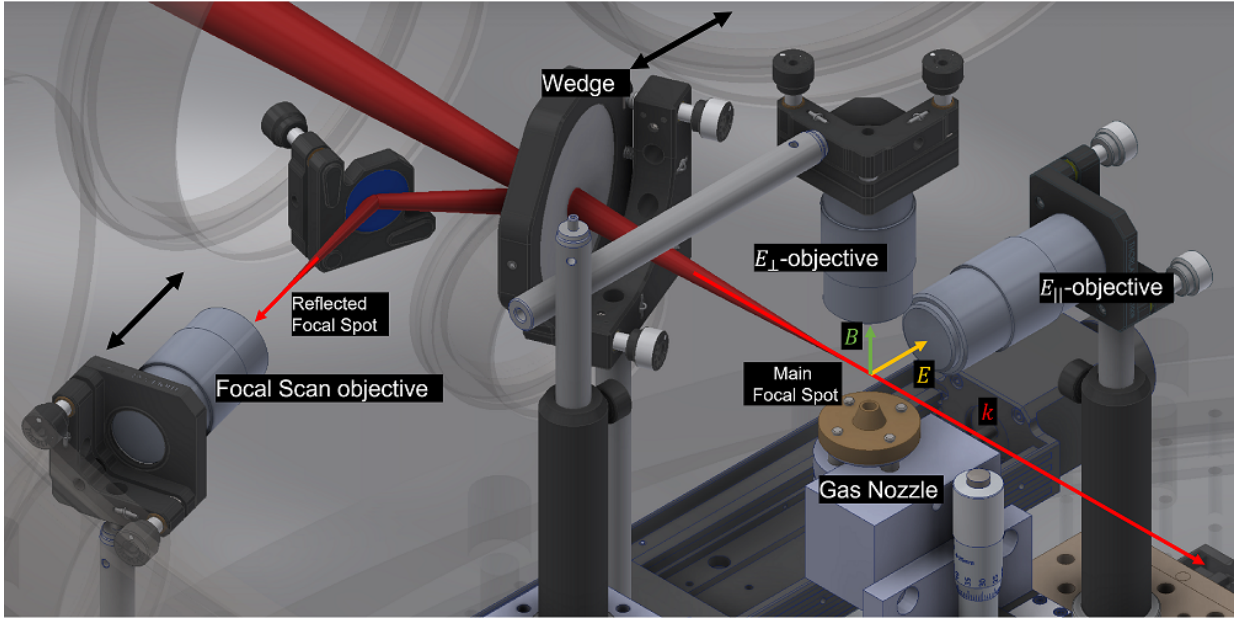


Figure 4.1: Diagram of the experimental layout around the focal region. The VEGA-2 beam is focused onto a spot above the gas nozzle, and imaged with two microscope objectives orthogonal to the propagation vector k , one along the electric field polarization, E , the E_{\parallel} -objective and another orthogonal to the electric field polarization, the E_{\perp} -objective (or equivalently, along the magnetic field polarization B), which is discussed in more detail in section 4.4. A motorized wedge with low reflectivity is moved into the path of the main beam in order to redirect a small fraction of the laser light onto a secondary focus, of which a NIR microscope objective oriented along the propagation of the reflected beam was used to image the laser focal distribution at various offsets from the focal plane. CAD model courtesy of Centro de Láseres Pulsados.

4.1.1 Spatial Calibration

The spatial calibration of this imaging system was conducted by Andrew Longman during the experiment preceding the RTS experiment, which we summarize here and report the results. Focal images were captured directly at the laser focus with a Chameleon charge-coupled device (CCD) camera. The Chameleon has a resolution of 1296×964 with $3.75 \mu\text{m}$ pixels (square sides) and provides a direct measurement of the spatial distribution of the laser. However, unlike the imaging system measuring the reflected beam off the wedge, the Chameleon has low pixel resolution, was more at risk of damage as a result of direct exposure to the unattenuated beam,

and could not be used in vacuum. Its purpose was to provide a spatial reference from which the "wedge" imaging system can be calibrated, while also serving as a wide-view diagnostic of the laser position. Schematics of the two imaging setups are shown in Fig. 4.2, along with example images of the focal spot captured by the Chameleon and Blackfly.

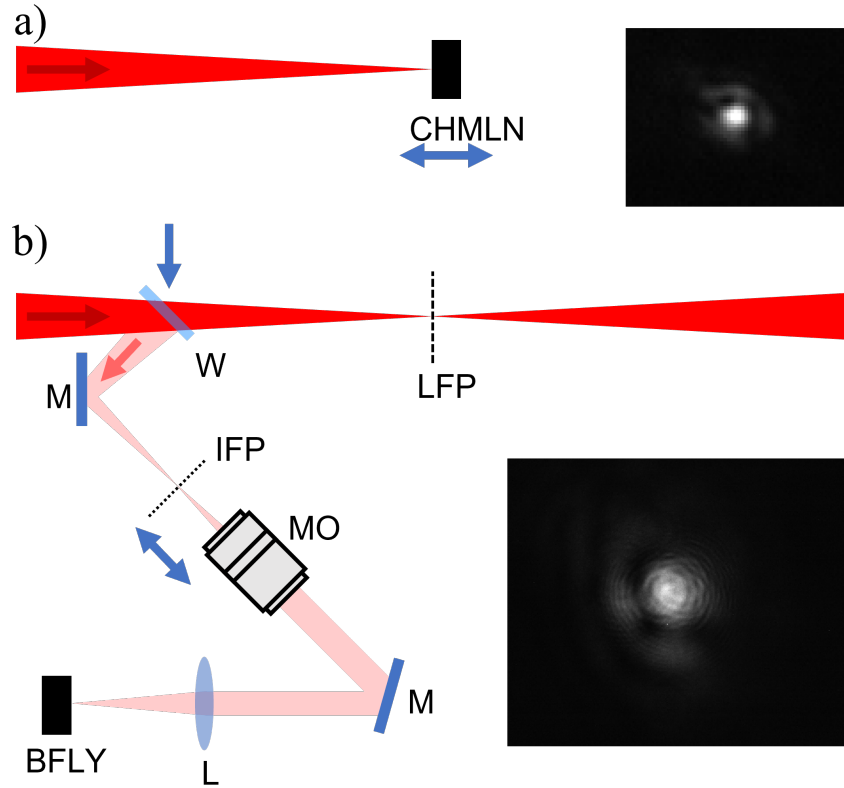


Figure 4.2: Diagram of the focal spot imaging and spatial calibration system. Shown are schematics of a) the laser focal spot imaged by the Chameleon (CHMLN) CCD camera and b) the laser focal spot reflected by a wedge (W) and mirror (M) and imaged at the imaging focal plane (IFP) by an infinity correct microscope objective (MO) and transported to and refocused by a lens (L) onto a Blackfly (BFLY) CCD camera. The captured image is a magnified representation of the laser focal spot at the laser focal plane (LFP). Translating the microscope objective long the imaging axis translates the imaging plane along the reflected beam, corresponding to a translation along the real laser by an equal amount. The images used for the calibration analysis are shown and were taken during a preceding experiment on 06/06/2018.

A set of images were captured by scanning both imaging systems along their respective imaging axis and the 5 images having the smallest focal spot were chosen from each imaging

system for comparison. The width of the focal spot in each image was determined by plotting the average profile horizontally and vertically and finding their FWHM, and are shown in Table 4.1.

Table 4.1: Measurements of the FWHM of the horizontal (H) and vertical (V) average profiles of the subset of focal spot images with the smallest spot sizes captured by the direct and wedge imaging systems (5 images from each imaging system). The mean (standard deviation) of the horizontal and vertical FWHM values for each imaging system are shown in bold. The pixel sizes of the readout cameras are given, although only the Chameleon specifications were used for the calibration

Imaging System	Readout Camera	FWHM (H) [px]	FWHM (V) [px]
Direct	Chameleon (3.75 μm square pixels)	7	6
		8	6
		10	7
		9	6
		9	7
		8.6 (1.0)	6.4 (0.5)
Wedge	Blackfly PGE 23S6M (5.86 μm square pixels)	49	56
		55	69
		51	62
		47	60
		49	56
		50.2 (2.7)	60.6 (4.8)

Given that the FWHM measurements from both imaging systems are measurements of the same object (the laser focal spot), their measurements are an equivalence relation which allow for the spatial calibration, $C_{W,\text{sc}}$, of the wedge imaging system in pixels per μm to be computed for the horizontal and vertical measurements using the equation

$$C_{W,\text{sc}} [\text{px}/\mu\text{m}] = \frac{\Delta_{W,\text{FWHM}}}{\Delta_{D,\text{FWHM}}} \frac{1}{3.75} \quad (4.2)$$

where $\Delta_{W,\text{FWHM}}$ is the measured FWHM in pixels from the wedge imaging system and $\Delta_{D,\text{FWHM}}$ is the measured FWHM in pixels from the direct imaging system. Averaging the results from the

horizontal and vertical measurements, the calibration is calculated to be

$$C_{W,sc} = 2.0 \pm 0.3 \text{ px}/\mu\text{m} \quad (4.3)$$

The uncertainty in the calibration was rather large (17%), suggesting that a better method of calibration was warranted. In later experiments, a 1951 United States Air Force (USAF) resolution test pattern was used for the spatial calibration. For the 2018 experiment discussed in this chapter, however, the calibration previously summarized was the only one available.

4.1.2 Spatial Distribution

Using the spatial calibration, images of focal spot captured by the wedge imaging system can be plotted in spatial dimensions. Figure 4.3 show the focal spot imaged at various offsets from the focal plane as a result of translation of the microscope objective along the optical axis.

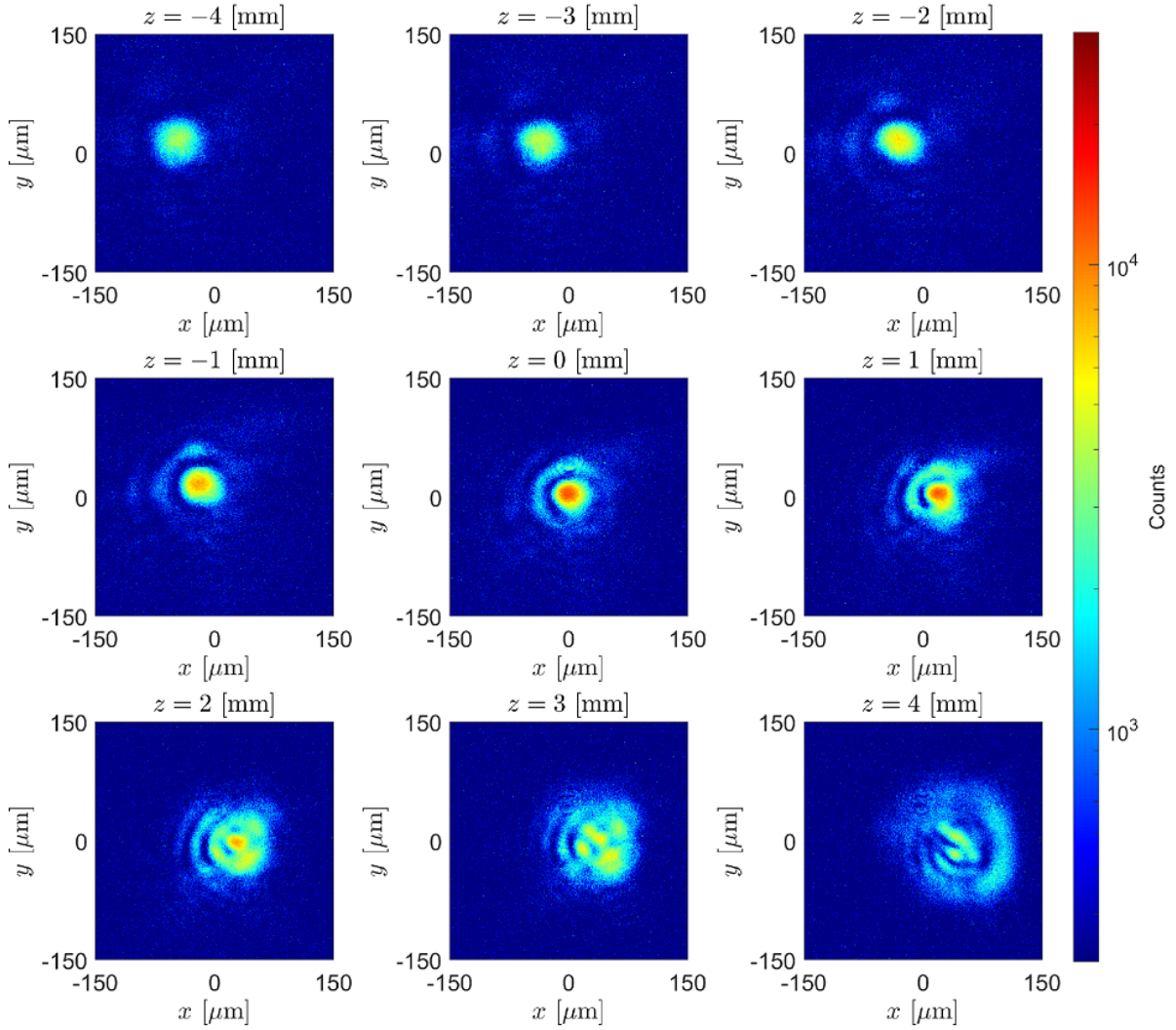


Figure 4.3: Focal scan images captured by the NIR microscope objective coaxial with the wedge-reflected beam at various offsets, z , relative to the best focus, $z = 0$. See Fig. 4.1 for the schematic. Images were captured with the laser at low energy in vacuum, where background pressures $\sim 10^{-5}$ mbar. The laser has a clean profile before focus ($z < 0$) but becomes distorted after focus, possibly due to scattering with the background gas, which, within a cylinder with volume $\pi w_0^2 \times z_R$, where $w_0 \sim 20 \mu\text{m}$ is the beam waist and $z_R \sim 1 \text{ mm}$ is the Rayleigh length, amounts to $\sim 10^5$ molecules, or due to aberration in the collection optics.

In order to characterize the focal spot at best focus, the image is processed with background subtraction and noise filtering, as shown in Fig. 4.4. First, a background value is obtained by taking the 480×300 (horizontal \times vertical pixel) regions at the four corners of the raw image as the representative background and determining the average signal value, which was 2236 counts

with a standard deviation of 341 counts. Next, a median filter was applied to the image, where each pixel was replaced by the median of the 3×3 local region around the pixel. The result of the median filter was the removal of hot pixels. The location of the laser spot center, (x_c, y_c) was determined to be (962, 593) where x ranges from 1 to 1920 and y ranges from 1 to 1200.

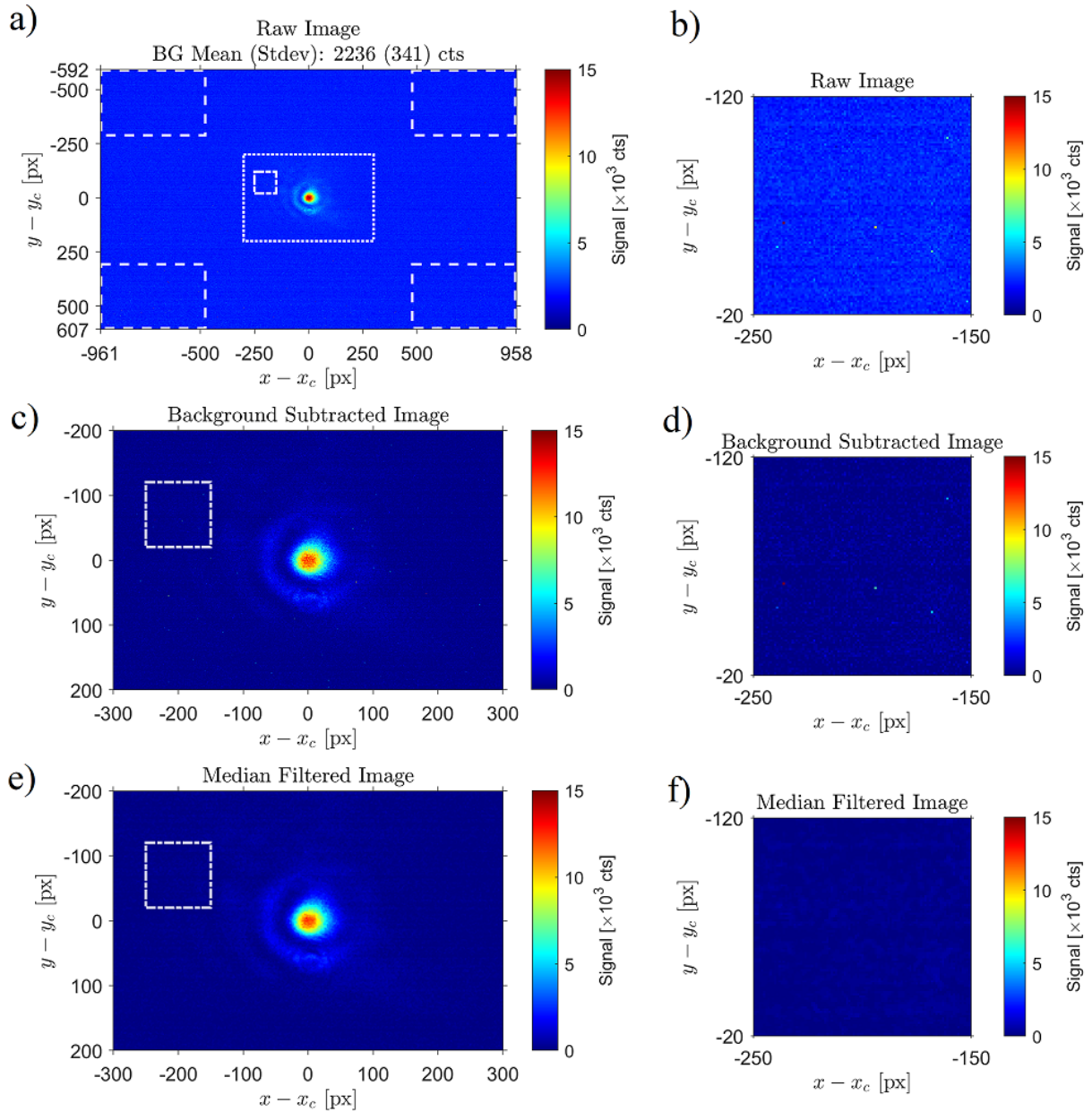


Figure 4.4: Plots showing the image processing steps taken of the focal spot images to produce the final intensity map. Shown are plots of the focal spot at best focus ($z = 0$) at different stages of image processing: a) and b) raw image, c) and d) background subtracted image, and e) and f) median filtered image. In a) the raw image, the boxes with white dashed border indicate the regions used for calculating the background value, while the box with the white dotted border corresponds to the cropped regions shown in plots c) and d). The boxes with the dash-dot border in images a), c) and e) correspond to the cropped region shown in b), d), and f) to show the result of hot pixel removal after using the median filter. The hot pixels in a) and c) are not visible unless the figure is sufficiently zoomed in and may not be representative of the data due to image downscaling.

The spot size was estimated from the processed image, as shown in Fig. 4.5, by averaging the results of two methods. The first method involves calculating the average signal as a function of radial distance from the spot center. The calculation was done by using the image data, which represents the signal strength in a grid of x and y Cartesian coordinates, to interpolate the data into a grid of polar coordinates, (r, θ) , and averaging over the θ dimension for each value of r . The full-width at half-maximum (FWHM) was calculated by taking the maximum signal value at $r = 0$, dividing by 2 to get the half-maximum, and determining the value of r where the signal is closest to the half-maximum, which was determined to be 21 px, and then multiplying by 2 to get a FWHM value of 42 px. The second method involves taking horizontal and vertical lineouts (one dimensional arrays) across the center of the spot of the image (the white dashed lines in Fig. 4.5a), performing a 10th order median filter where each data point in the lineout array was replaced by the median of the 10 local values around the data point. The purpose of the 10th order median filter was to smooth out the signal, particularly at the peak. The peak values of the median filtered arrays were then extracted and divided by two to obtain the half-max values, and the intersection locations of the horizontal lines defined by the half-max values with the median filtered arrays were determined. For each lineout, there are two intersections, one on opposite sides of the peak. The difference between the locations of the two intersects defines the FWHM. The horizontal lineout produced a FWHM of 44 px while the vertical lineout produced a FWHM of 43 px. The mean of the FWHM values determined from the different approaches is 43 px with a standard deviation of 0.8 px. Using the spatial calibration of $0.51 \pm 0.04 \mu\text{m}/\text{px}$, the FWHM of the 43 px focal spot would be $22 \pm 2 \mu\text{m}$.

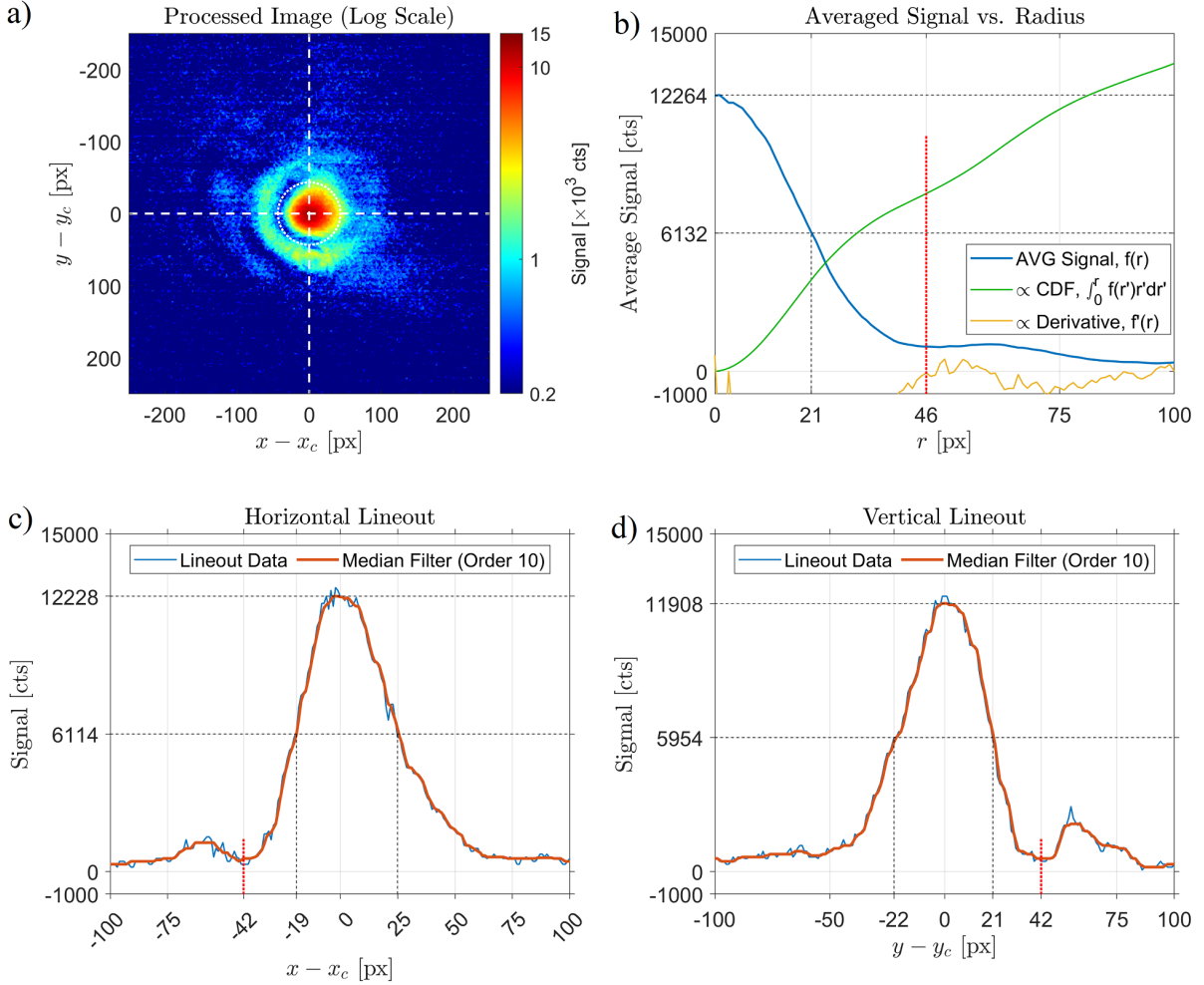


Figure 4.5: Plots showing the processed focal spot image and the characterization of the spot size. Shown are a) the processed focal spot image in a log scale, b) the average signal vs. radial distance from the spot center (peak of the distribution), along with the cumulative distribution function (CDF) and derivative (scaled to fit the plot), c) the horizontal lineout and d) the vertical lineout across the spot center. The white dashed lines in a) mark the locations where the horizontal and vertical lineouts were sample. The white dotted circle in a) marks the location of the first radial node, $r_{\text{airy},0}$, determined from the average value of the set of nodal positions denoted by the vertical red dotted lines in b), c), and d). The black horizontal dashed lines in b), c), and d) demarcate the max and half-max values, while the black vertical dashed lines demarcate the locations of the half-max.

The focal spot is not a Gaussian distribution, but contain airy rings due to diffraction from focusing a top hat distribution by the parabola. Indeed, there is a lack of azimuthal symmetry due to aberrations, and the first radial node is prominent primarily in the left half ($x - x_c \leq 0$) of the

image. As a simple estimation, the central spot can be defined by the circular region consisting of the peak up to the first radial node, which we call $r_{airy,0}$, determined as the mean of the result of three approaches. The first approach is carried out by determining the first local minimum from the average signal vs. radius, as shown in Fig. 4.5b, which coincides with the inflection point of the cumulative distribution, $F(r)$, defined by the integral:

$$F(r) \equiv \int_0^r f(r') r' dr' \quad (4.4)$$

where $f(r')$ is the average signal at radial position r' . The first local minima also coincides with the condition that $f'(r_{airy,0}) = 0$, $f'(r < r_{airy,0}) < 0$, and $f'(r > r_{airy,0}) > 0$, where $f'(r)$ is the first derivative of $f(r)$ with respect to r . In other words, at the local minima, the slope of $f(r)$ changes from negative to positive as r increases. The first local minimum was found to be at 46 px. The second approach involves determining the first local minimum of the horizontal lineout towards the side where there is a prominent airy ring, namely $x - x_c < 0$, which was found to be 42 px in magnitude. The third approach is the same as the second approach but using the vertical lineout, which also determined a value of 42 px. The results of the three approaches results in a mean of 43 px with a standard deviation of 2 px. Using this as the value for $r_{airy,0}$, we integrate the signal over the circular region with radius $r_{airy,0}$ centered at (x_c, y_c) , which is indicated in Fig. 4.5a by the circle with a white dotted border, and divide this value by the integral of the signal over the entire image, which tells us the fraction of the total energy at the focal plane contained in the focal spot. The integral over the central spot was 2.38×10^7 cts, while the integral over the entire image was 6.93×10^7 cts, implying that $\sim 34\%$ of the energy is in the central spot.

4.2 VEGA-2 Temporal and Spectral Characteristics

The VEGA-2 laser's pulse width and spectrum were characterized by the Wizzler as described in section 3.1. While the details of the measurements fluctuated each day, such as the intensity at the shoulders in the temporal measurements or the skewing of the spectrum, the overall characteristics of these measurements stayed the same: The duration of the main pulse is ~ 30 fs and the spectrum has a bandwidth of ~ 70 nm with a central wavelength of ~ 790 nm. An example of the Wizzler measurements is show in Fig. 4.6.

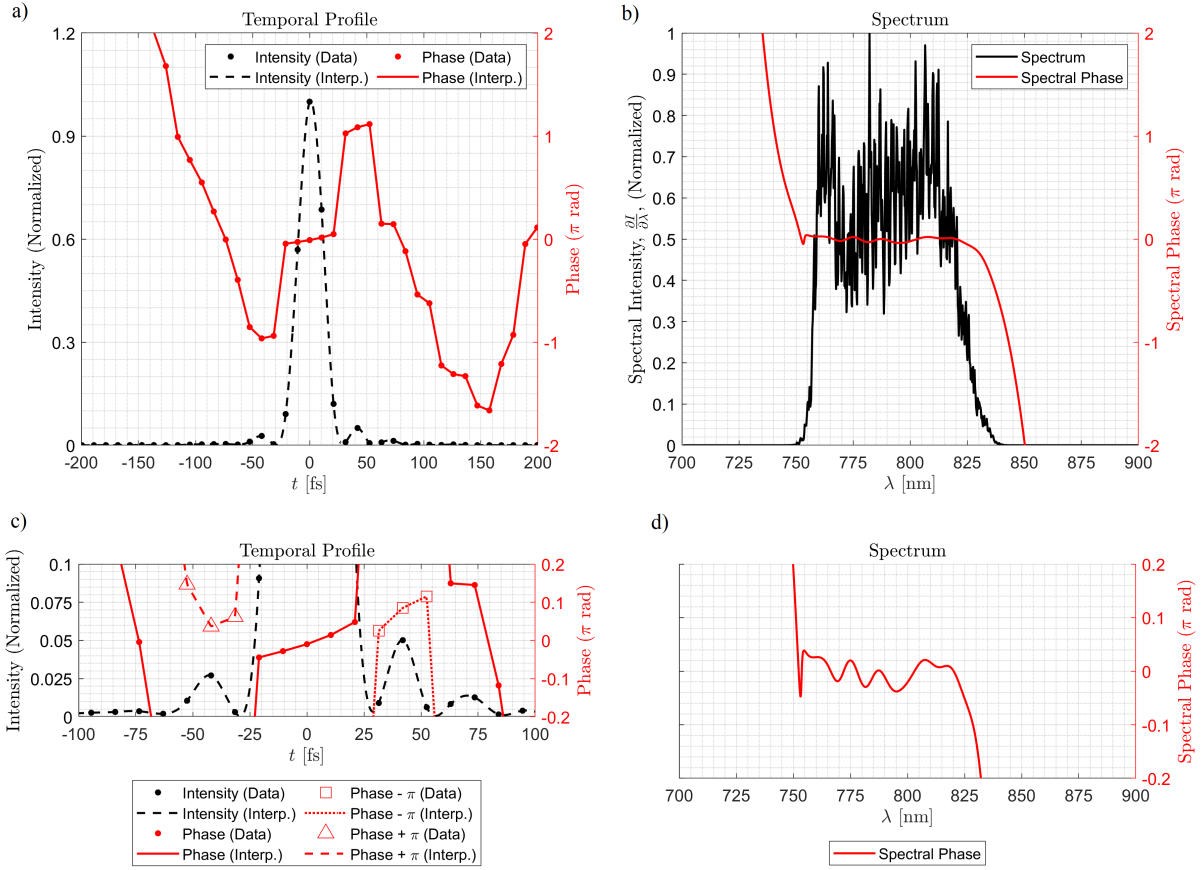


Figure 4.6: Plots of the Wizzler reconstructed temporal profile, phase, as well as measured spectrum. Shown in the top row are: a) temporal intensity and phase profile vs. time and b) spectral intensity and spectral phase vs. wavelength. In the bottom row are zoomed-in plots of: c) intensity and phase and d) spectral phase. For a), the dots indicate the data points measured by the Wizzler, while the curves are interpolated traces (cubic method for the temporal intensity profile, and linear method for the phase) over the data points. As shown in c), the shoulders have intensities which are $\sim 1 - 5\%$ of the peak, while the phase is relatively flat throughout the main peak of the temporal pulse, varying over a range of $\sim 0.1\pi$ radians, as is the case for the two shoulders shown in the phase plots offset by $\pm\pi$. The spectral phase in d) likewise varies over a range of at most about 0.1π radians. These measurements were obtained by the Wizzler in the laser bay on 07/13/2018.

4.3 Indirect Estimation of VEGA-2 Intensity

The images of the laser focal spot show the laser energy distribution (fluence) measured in the focal plane by a camera. Combining this knowledge with the pulse duration and pulse energy

on target, which provided to us by the user facility, we may estimate the peak intensity as well as the intensity distribution at focus using a simple by approximate method. This method requires the assuming that the spatial distribution of the laser is separable from the temporal distribution. A simple formula of the peak intensity and intensity distribution may be derived from the above assumptions and diagnostics.

We begin by considering the intensity distribution at the focal plane of the laser, whose intensity in spatial position (x, y) at time t is given by $I(x, y, t)$. We assume that the spatial and temporal variables can be separated, i.e.,

$$I(x, y, t) = I_0 f(x, y) g(t) \quad (4.5)$$

where I_0 is the peak intensity, $f(x, y)$ is the spatial distribution and $g(t)$ is the temporal distribution, both of whose integrals over infinity are convergent to a finite number. Defined in this manner, both $f(x, y)$ as well as $g(t)$ are equal to unity at the spatial and temporal peaks of the pulse, namely, $f(x_0, y_0) = 1$ and $g(t_0) = 1$ for (x_0, y_0) being the location of the spatial peak and t_0 being the time of the temporal peak. The fluence, $F(x, y)$, is then given by:

$$F(x, y) = \int_{-\infty}^{\infty} I(x, y, t) dt = I_0 f(x, y) \int_{-\infty}^{\infty} g(t) dt \quad (4.6)$$

Integrating the fluence, $F(x, y)$, over all space results in the total laser pulse energy, U , at the focal region.

$$U = \int_{-\infty}^{\infty} \int_{-\infty}^{\infty} F(x, y) dx dy = \int_{-\infty}^{\infty} \int_{-\infty}^{\infty} f(x, y) dx dy \int_{-\infty}^{\infty} g(t) dt \quad (4.7)$$

Assuming that the focal distribution is contained within the image, and the background has been sufficiently removed, we may take the value of $f(x, y)$ outside of the image to be 0, so that the first integral may be approximated as a sum over the image pixels normalized to the counts at the peak of the distribution:

$$\int_{-\infty}^{\infty} \int_{-\infty}^{\infty} f(x, y) dx dy \approx \sum_{i,j}^{N,M} f(x_i, y_j) A_{\text{pix}} \equiv \frac{C_{\text{sum}} A_{\text{pix}}}{C_{\text{pk}}} \quad (4.8)$$

where N and M are the horizontal and vertical dimensions of the image respectively, i and j are the horizontal and vertical image indices respectively, x_i and y_j are the spatial locations represented by the pixel at index values i and j respectively, and A_{pix} is the spatial area represented by a pixel of the focal plane. We define C_{sum} as the sum over the counts over the entire image and C_{pk} as the value of the counts at the peak of the distribution in the image.

The time integral, $\int_{-\infty}^{\infty} g(t) dt$, is equal to some effective time T_{eff} , and depends on the shape of the pulse. For a gaussian temporal shape with pulse duration full-width at half-maximum (FWHM) of Δt , the effective time $T_{\text{eff}} = \sqrt{\pi/\ln 2} \times \Delta t/2 \approx 1.064\Delta t$. Plugging these results into Eq. 4.7, we obtain:

$$U = I_0 \frac{C_{\text{sum}} A_{\text{pix}} T_{\text{eff}}}{C_{\text{pk}}} \quad (4.9)$$

Solving for I_0 and relabeling as $I_{\text{pk}}^{\text{Im}}$, we arrive at the result:

$$I_{\text{pk}}^{\text{Im}} = \frac{U C_{\text{pk}}}{C_{\text{sum}} A_{\text{pix}} T_{\text{eff}}} \quad (4.10)$$

Here, an expression for the peak intensity is given in terms of the pulse energies U , which are values measured by at laser bay and calibrated for the target area (accounting for beam transport

losses), the effective pulse duration T_{eff} , which may be determined by a short pulse temporal diagnostic (in our case, the Wizzler), and parameters which are calculated from the spatially-calibrated and background-subtracted focal spot image: C_{pk} , C_{sum} , and A_{pix} .

The value of C_{pk} is determined by averaging the values of nine pixels in a 3×3 block of pixels near the peak of the focal spot image (see central figure in Fig. 4.3). C_{sum} is simply the total counts summed over the focal spot image, and A_{pix} the area at the focal plane represented by a camera pixel in physical units ($A_{\text{pix}} = 1/C_{W,\text{sc}}^2 = 0.26 \pm 0.04 \mu\text{m}^2$ as discussed in section 4.1.1). The value of T_{eff} is determined by integrating over the Wizzler pulse profile, and multiplying by a rescaling factor $\Delta t/\Delta t_W$, where Δt is the nominal pulse width, and $\Delta t_W = 25.2 \pm 0.4 \text{ fs}$ is the pulse duration measured by the Wizzler. The rescaling is due to the fact that the pulse width measured using an autocorrelator in the target area is larger by $\sim 20\%$, namely $\Delta t_{\text{AC}} = 31.0 \pm 0.4 \text{ fs}$.

Of the quantities in Eq. 4.10 only the energy, U , was deliberately varied during the experiment. While there may be drifts in the pulse duration, the variation is slow compared to the variation of U over subsequent runs. For estimation purposes, we take $\Delta t = 31 \text{ fs}$, and calculate the value for $I_{\text{pk}}^{\text{Im}}/U$ to be $1.9 \times 10^{18} \text{ W/cm}^2/\text{J}$. This value may be plugged into Eq. 4.5 to obtain an expression for the intensity distribution at the temporal peak ($t = t_0$):

$$I(x, y, t_0) = I_{\text{pk}}^{\text{Im}} f(x, y) = (1.9 \times 10^{18} \text{ W/cm}^2/\text{J}) \times U f(x, y) \quad (4.11)$$

Figure 4.7 show surface and contour plots of Eq. 4.11 normalized to the energy from the processed focal spot image at best focus in a linear and log scale.

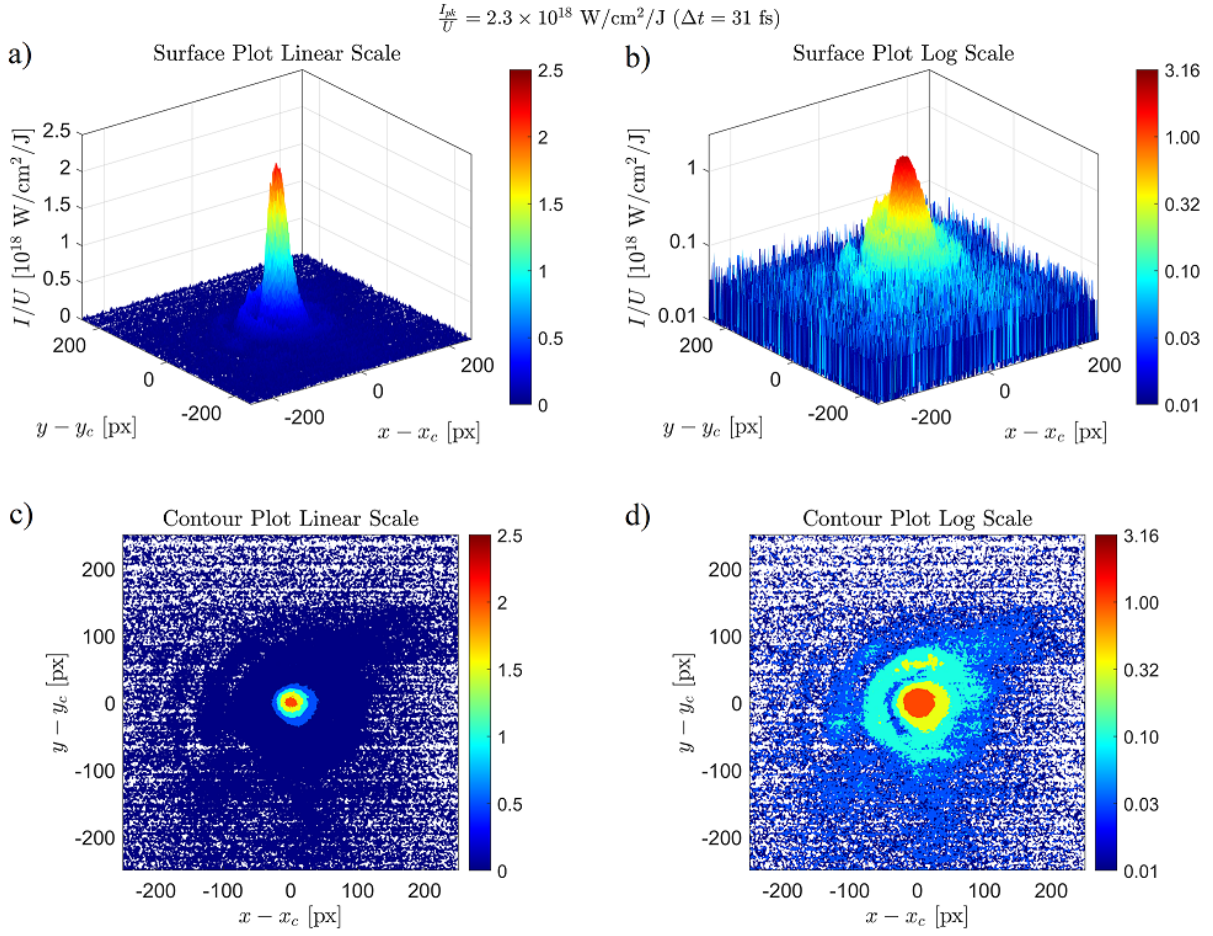


Figure 4.7: Plots of the intensity per unit pulse energy based on the processed focal spot image at best focus. The intensity was calculated based on Eq. 4.11. Shown are a) 3D surface plot in linear scale, b) 3D surface plot in log scale, c) contour plot in linear scale, and d) contour plot in log scale. The colormap values in all plots are in units of $10^{18} \text{ W/cm}^2/\text{J}$.

4.4 Microscope Objectives for RTS Detection

The two microscope objectives used for capturing RTS light are the Mitutoyo 10 \times Plan Apo [84] and the Motic 10 \times Plan Apo [85], both designed for the visible band and having the same focal length ($f_{\text{obj}} = 20 \text{ mm}$), working distance ($d_{\text{wk}} = 34 \text{ mm}$), and numerical aperture (NA = 0.28). They are high-quality off-the-shelf objectives classified as plan apochromats, which are designed to have flat fields and be corrected for aberrations, both spherical and chromatic. The

imaging at infinity allows flexibility in designing the length of the optical path. Upon refocusing into a detector using a lens, the magnification can be calculated via $M = f_{\text{lens}}/f_{\text{obj}}$, where f_{lens} is the focal length of the refocusing lens. In the case of this experiment, $f_{\text{lens}} = 30$ cm, resulting in a magnification of 15. The numerical aperture of 0.28, is equivalent to a $\theta_{\text{acc}} = 16.3^\circ$ acceptance half-angle ($\text{NA} = \sin \theta_{\text{acc}}$). With a small depth of field of 3.50 μm , the laser focus may be imaged while mitigating the collection of background light.

4.5 Imaging Beam Paths

The light captured by the microscope objectives follow paths determined by mirrors. The light from the E_{\perp} objective is taken up along \hat{y} and then parallel to, but offset from, k out of the chamber through a port above the exit port of the laser beam. The light from the $E_{||}$ objective is taken to the side, then parallel to k out through a port at an oblique angle. The imaging paths inside the chamber are shown in Fig. 4.8. Outside of the chamber, light from the E_{\perp} objective is either reflected sideways using a flip mirror and focused onto a camera sensor (Andor DV440-BU2-2492) or sent to the input optics array for the spectrometer (Oriel MS260i). Light from the $E_{||}$ objective is either sent to its own imaging camera a cooled, low-noise CMOS camera (Zyla 4.2 MP PLUS), or redirected upwards using a flip mirror, and then towards the spectrometer. The imaging paths outside of the chamber are shown in Fig. 4.9.

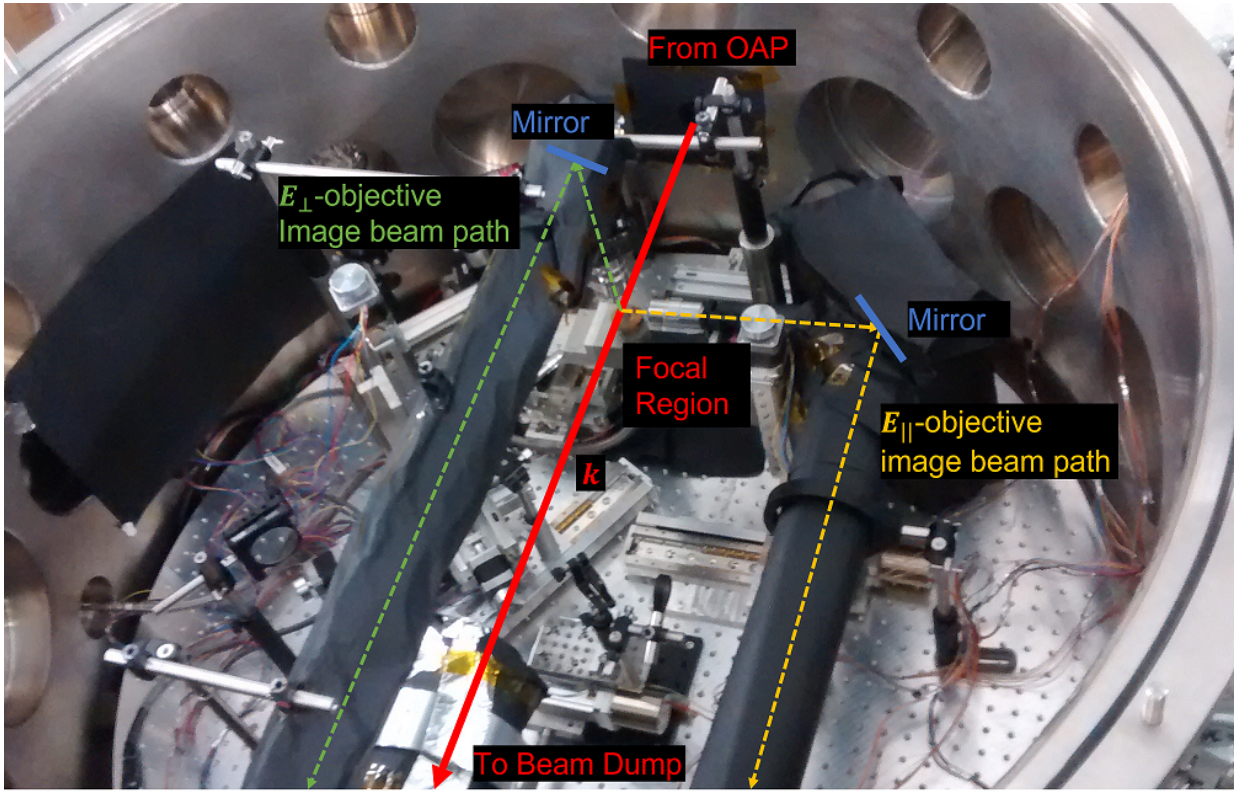


Figure 4.8: Annotated photo of the internal layout of the VEGA-2 target chamber. Shown are the VEGA-2 laser beam, the focal region where RTS light is produced and captured, and the image beam paths captured by the E_{\perp} and E_{\parallel} objectives. To mitigate the capturing of scattered light in the chamber, black-anodized aluminum foil was used to shield the imaging beam paths as well as cover the reflective surfaces in the background of the objectives' fields of view.

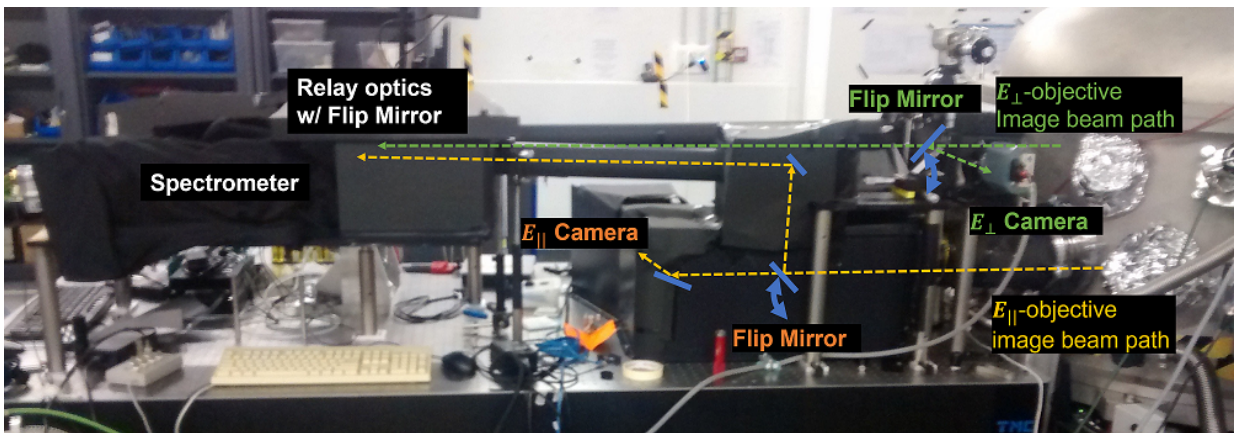


Figure 4.9: Annotated photo of the layout outside of the VEGA-2 target chamber. Shown are the imaging beam paths of the E_{\perp} and E_{\parallel} objectives and their corresponding readout cameras as well as spectrometer. The beam paths are shielded with dark material (construction paper, cloth, and anodized aluminum foil) from ambient light in the room.

4.6 Scattered Light Mitigation

Scattered light from the laser beam off of components inside the vacuum chamber is a major concern for this experiment due to the intense laser beam and relatively weak RTS signal. Multiple reflections of the beam off of surfaces in the chamber can turn the chamber into a big "light bulb." Furthermore, outside of the chamber, there is ambient lighting. The choice of using microscope objectives as well as a temporally gated spectrometer are already themselves means to reduce the collection of background light, however, these factors alone are insufficient, and thus additional measures were taken, as listed below.

- The optical paths of the imaged light were shielded end-to-end using black-anodized aluminum foil.
- Portions of the vacuum chamber were covered in black-anodized aluminum foil in order to reduce the reflectivity off of these surface areas.
- An improvised beam dump, built from black-anodized aluminum foil, was set up behind the exit port of the main beam in order to redirect the beam and confine the scattering inside a separate chamber.

4.7 Alignment of Detection Optics

In order to align the two microscope objectives used for RTS detection (right on Fig. 4.1), a needle tip (Fig. 4.10) mounted on a linear motorized stage is used as a reference of the location of the laser focus. The linear stage facilitates moving the needle into the focal location for alignment, and out of the focal region during the live laser shots. Light from a diode laser is used to illuminate

the tip. The microscope objectives, which are mounted on xy linear translation stages, are moved to bring the illuminated tip into view and into focus. As the chamber is pumped into vacuum, there is a drift in the alignment, therefore real time adjustment of the stages were performed to keep the tip in view and then optimize after the vacuum has reached a steady state.

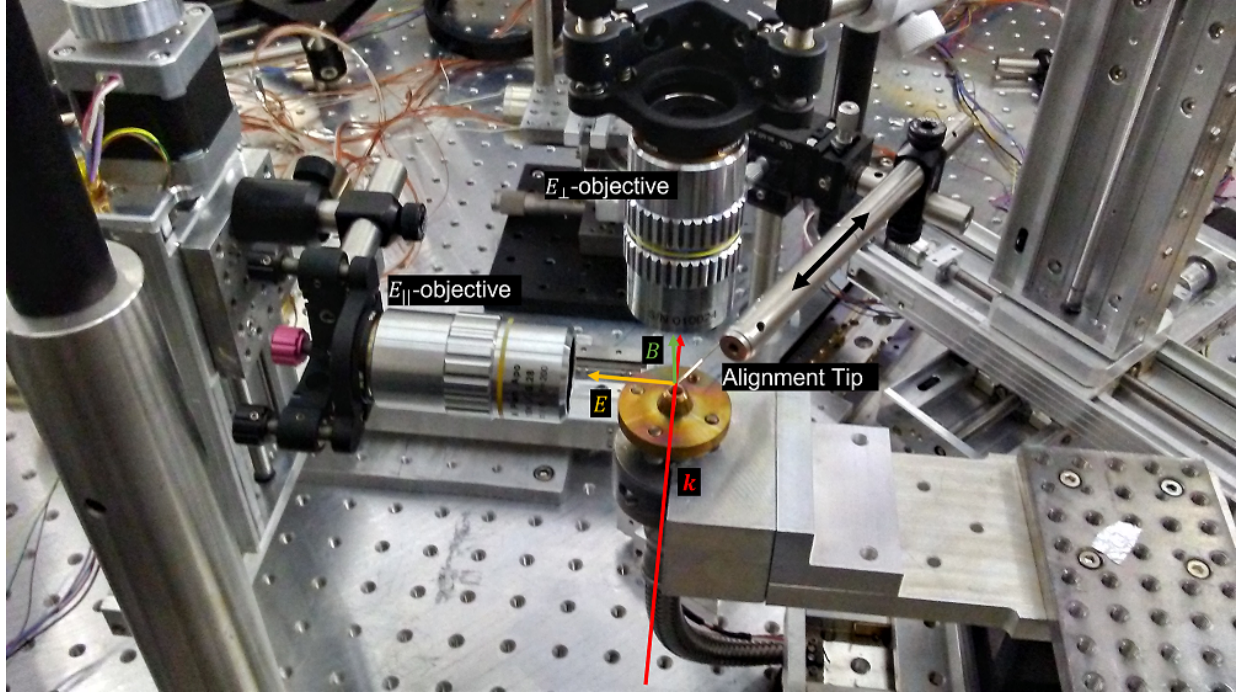


Figure 4.10: Photo of the alignment tip at the focal region with the RTS detection microscopes and brass gas nozzle. The microscopes were mounted on translation stages which allowed for adjustment in their position to find the focal region referenced by the illuminated tip while the tip is in the operating position.

4.8 Gas (Electron) Source

The electrons were produced from laser ionization of nitrogen gas that was puffed into the chamber via a Parker Series 9 Pulsed Valve (model 9S2-A1-P3-9B06) [86] connected to a conical gas nozzle (shown in Fig. 4.10), which was measured by Carlos Salgado using an optical microscope at CLPU to have a 0.8 mm orifice. The laser was focused at a distance ~ 2 mm

above the gas nozzle mouth. The pulsed valve was backfilled using a gas cylinder, connected to a regulator and pressure gauge to control and monitor the backing pressure. The pulsed valve was turned on ~ 2.5 ms prior to the laser pulse and stayed open for 4 ms with each trigger. The regulator was set to output ~ 10 mbar, and needed to be reset after every several shot batches in order to compensate for drift. The gas pressure at focus, after the nozzle opens and releases the gas puff, would necessarily be smaller than the backing pressure of 10 mbar and larger than the background pressure of 10^{-5} mbar.

As an estimation of the gas density at focus, we assume that the backing pressure follows the ideal gas law, which states that:

$$\rho_0 = \frac{P_{gas}}{k_B T} \quad (4.12)$$

where ρ_0 is the molecular density, P_{gas} is the gas pressure, $k_B = 1.38 \times 10^{-23} \text{ m}^2\text{kgs}^{-2}\text{K}^{-1}$ is the Boltzmann constant, and T is the temperature taken to be 300 K. The gas density at a point in space away from the opening of the nozzle would fall off as a function of the distance. We approximate this fall off using a Lorentzian function developed empirically from Monte-Carlo simulations for a collisionless gas based on the kinetic model, which is described in Appendix F section F.1. This function is given by:

$$\rho_{gas}(\Delta R) = \frac{\rho_0}{\left(\frac{\Delta R}{R_f}\right)^2 + 1} \quad (4.13)$$

where ΔR is the distance from the orifice and $R_f \approx 0.32 \pm 0.08$ mm is the fall off length scale determined from the simulations, with the uncertainty given by the 95% confidence interval from the fits to the simulation results. Figure 4.11 shows the relative gas density as a function of

distance based on Eq. 4.13.

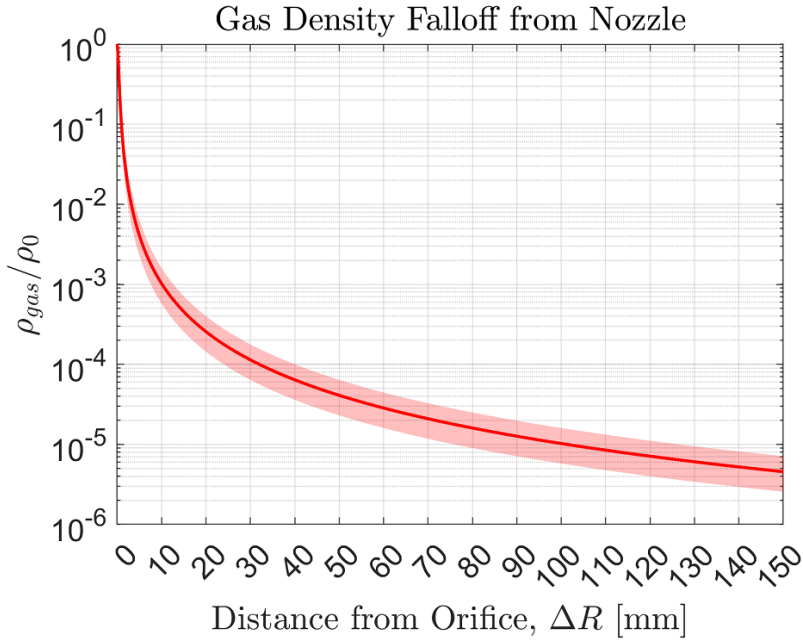


Figure 4.11: Plot of predicted gas density per unit reservoir density as a function of position from the nozzle. This is based on Eq. 4.13, which is determined from Monte Carlo simulations described in Appendix section F.1. The shaded region includes the 95% confidence interval for the best fit parameter of R_f .

At 2 cm from the nozzle, Eq. 4.13 predicts that the gas density is on the order of a factor of $\sim 10^{-4}$ to 10^{-3} of the backing density. Since the pressure and density of an ideal gas are linearly proportional, this would correspond to a density of 10^{12} to 10^{13} cm^{-3} (or 10^{-3} to 10^{-2} mbar) at the laser focus. Table 4.2 shows the molecular density at various pressures. A molecule will experience a laser intensity depending on the precise location of the molecule within the laser distribution. At sufficient intensities, a nitrogen molecule may donate up to 10 electrons, so that one may approximate roughly that the electron density is on the order of 10^{13} to 10^{14} at the peak of the laser. However, the ionization and scattering dynamics of the electrons due to the laser may result in complex distributions deviating from this approximation.

Table 4.2: List of molecular densities, ρ_{mol} , at various gas pressures P_{gas} , assuming an ideal gas.

P_{gas}	ρ_{mol} [1/cm ³]
1 atm (\approx 1 bar)	2.4×10^{19}
10 mbar	2.4×10^{17}
10^{-3} mbar	2.4×10^{13}
10^{-5} mbar	2.4×10^{11}

4.9 Image Readout

As previously mentioned, images captured by the E_{\perp} and $E_{||}$ objectives were refocused from infinity using lenses of focal lengths of 300 mm onto camera sensors, respectively the Andor DV440-BU2-2492 and Zyla 4.2 MP PLUS, with an overall magnification of $15\times$ for both imaging paths. The Zyla camera has a scientific Complementary Metal-Oxide-Semiconductor (sCMOS) sensor with 6.5 μm square pixels and a resolution of 2048×2048 , implying a field-of-view region of $877 \mu\text{m} \times 877 \mu\text{m}$. The Andor camera has a CCD sensor with 13.5 μm square pixels and a resolution of 2048×512 of which the software at the time only reads a 1024×255 sub-field, implying a field-of-view region of $922 \mu\text{m} \times 230 \mu\text{m}$.

Due to obstructions in the transport optics for the $E_{||}$ objective, likely as a result of the beam path exiting the chamber through a port at an oblique angle and through a bellows, visibility of the focal region was limited, as shown in Fig. 4.12a of the imaged region of the chamber interior illuminated by laser scattering. Nevertheless, with the use of a BG39 optical filter (Fig. 4.12b), which cuts off wavelengths above 650 nm while passing through visible wavelengths below 650 nm, the laser beam was visible and confirmed by changing the orientation of the OAP mirror and observing a shift in the imaged location of the beam, as shown in Fig. 4.12c-e.

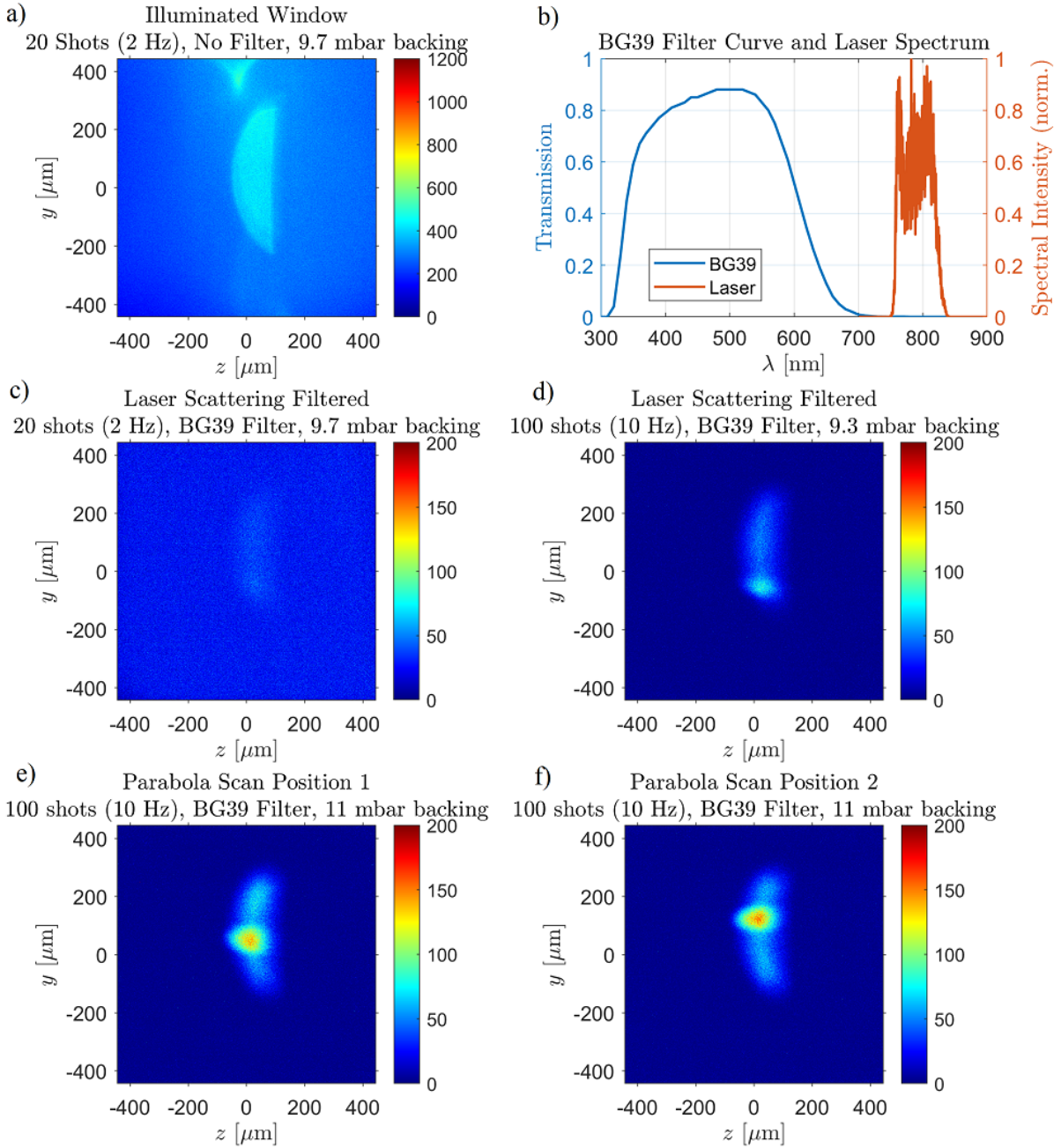


Figure 4.12: Images of the focal region captured during live shots by the $E_{||}$ objective under varying conditions. The images were read out by the Zyla 4.2 MP Plus camera ($15\times$ overall magnification) for shots at full laser energy (2.67 J on target), integrated over 10 s during the firing of the shot batches. The illuminated window a) is shown for unfiltered light comprising of scattered laser radiation inside the chamber. A BG39 filter, b), was then added to filter the laser light (Wizzler spectrum shown) and capture light primarily from plasma recombination and second harmonic RTS. The shot number was also scaled up from c) 20 shots 2 Hz to d) 100 shots at 10 Hz. The parabola orientation was adjusted and corresponding images were captured at different parabola settings e) and f). Each image was processed with a background subtraction followed by a median filter and the colorbar values correspond to net counts.

The imaging system for the E_{\perp} objective did not suffer the same obstructions as that for the $E_{||}$ objective, thereby the light produced by the laser beam can be clearly seen, as shown in Fig. 4.13. Although there were no clear single shot images, there are images from multi-shot runs that show distinct streaks, likely correlating with individual shots and provides observations of the pointing stability. There appeared to be a drift in the laser pointing correlated more with time of the shot and less so with the shot number. For example, comparing the 5-shot (0.5 Hz) image in Fig. 4.13a with the 100 shot (10 Hz) image in Fig. 4.13f, where both images were captured over 10 s, the overall excursion is comparable. Adding optical filters which cut off laser radiation while allowing visible (BG39) or near-infrared (RG850) radiation allow the radiation produced by the laser to be more clearly seen and show that there is radiation at both the visible and infrared.

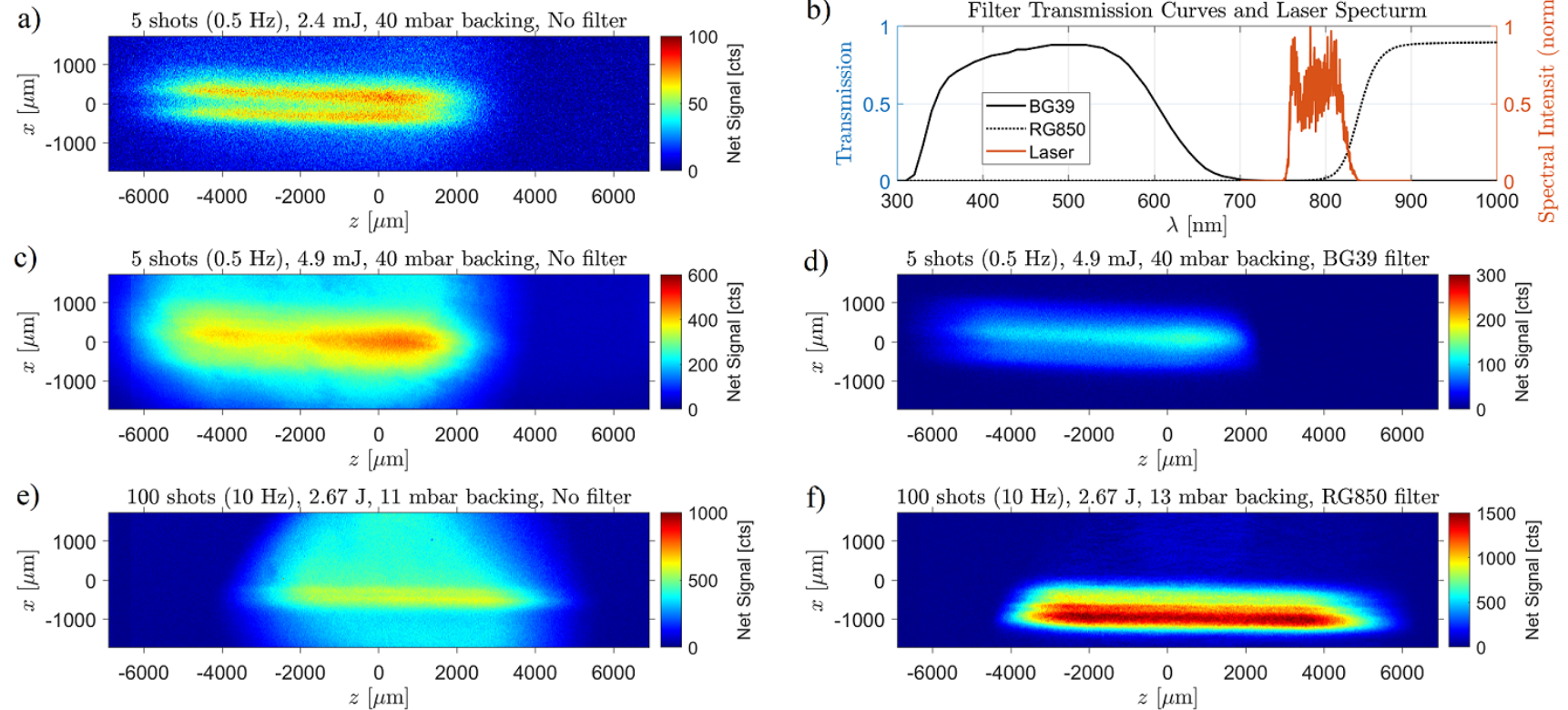


Figure 4.13: Images of the focal region captured during live shots by the E_{\perp} objective at various conditions. The images are shown in a) and c)-f) while b) shows a plot of the filter transmission curves and laser spectrum. Initially, images were captured at a) low energy (2.4 mJ on target), low repetition rate, moderately-low gas pressure (~ 40 mbar), and no filter, then c) double the energy. Images were also captured using d) a BG39 filter. At a later day, images were captured at full energy (2.67 J on target), low pressure (~ 10 mbar), e) without and f) with an RG850 filter. Note that the imaging system was continuously adjusted, therefore image f) has a stronger signal than e) likely due to better imaging optimization.

Figure 4.14 show examples of images captured during the live shots and cropped over the region around the laser radiation. These images were each generated by averaging over 5 images, each image being an accumulation of a run (100 shots at 10 Hz), for a total of 500 shots. The cameras' shutters stayed open during each run and, having no gating capability, captured essentially all of the light generated from the focal region during the laser interaction; therefore, the signal on represented on the images are dominated by plasma recombination. Figure 4.14a, specifically, shows a structure containing multiple overlapped beams, indicating a pointing instability whose total excursion, $h = 66 \mu\text{m}$, is about 4.4 times the beam width, $b = 15 \mu\text{m}$.

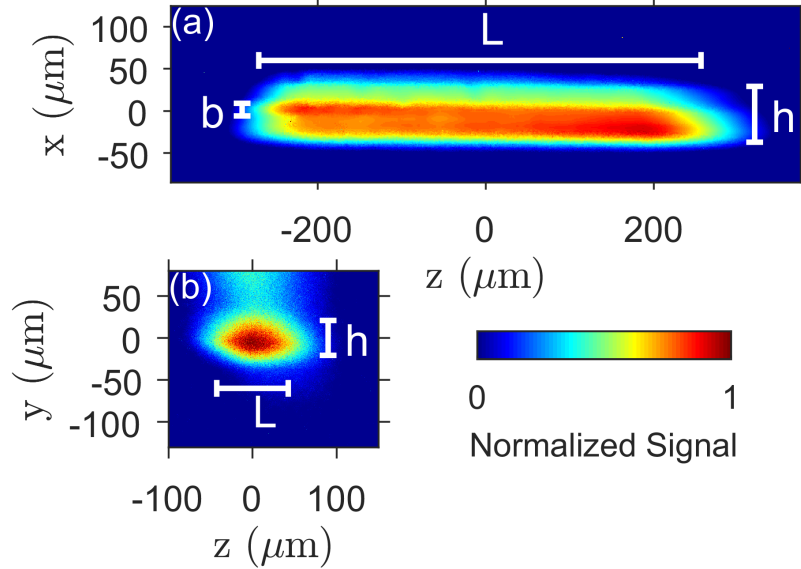


Figure 4.14: Cropped taken during the live shots emphasizing the location of the laser beam. The images shown were integrated over 500 shots and captured by the a) \mathbf{E}_\perp objective and b) $\mathbf{E}_{||}$ objective. In a), $L = 526 \mu\text{m}$, $h = 66 \mu\text{m}$, $b = 15 \mu\text{m}$. In b), $L = 85 \mu\text{m}$, $h = 41 \mu\text{m}$.

4.10 Spectrum Measurement

The spectrometer was an Oriel MS260i [87], based on the Czerny-Turner [4] optical design with a 0.25 m focal length (see Fig. 4.15), and output to an intensified CCD camera (Andor iStar

DH 720-25U-03 ICCD), which allowed for temporally gated measurement of light from either the E_{\perp} objective or the $E_{||}$ objective for any given run. The ICCD is discussed in more detail in section 4.10.5. The incoming light from the microscope objective was focused onto the adjustable entrance slit of the spectrometer using a 2 inch diameter lens. An optical filter may be placed in front of the slit to cut down on the scattered laser light at around 800 nm, in order to allow the RTS light in the visible band to be resolved without saturating the camera. The spectrometer houses a triple grating assembly, allowing three gratings to be installed and selected during operation via motorized rotation, with an angular separation of $\sim 120^{\circ}$ between gratings. The gratings installed in the spectrometer were ruled gratings produced by Richardson Gratings consisting of 150 lines/mm [88], 1200 lines/mm [89], and 2400 lines/mm [90], all of which were designed for the visible (and some UV) band. The selected grating disperses incoming light into multiple spectral orders, one of which is captured and collimated with a mirror and sent through an exit port and onto the ICCD camera for acquisition, effectively passing a spectrum band determined by the field of view of the readout camera and the grating setting. Light from spectral orders not sent to the output port are absorbed within the spectrometer. Slight rotation of the triple grating assembly allowed offset of the central wavelength.

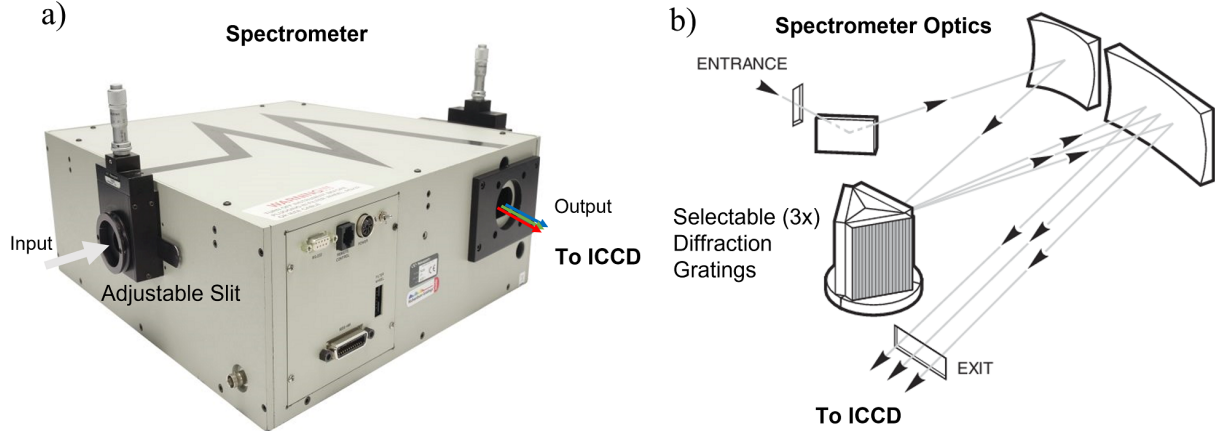


Figure 4.15: Diograms of the Oriel MS260i spectrometer showing a) exterior photo and b) schematics of internal optics, which is based on the Czerny-Turner design [4]. The input light goes through a micrometer-adjustable slit (widths ranging from closed to 5 mm), redirected by a turning mirror and then focusing mirror onto a diffraction grating selected from a triple grating assembly [88–90]. The dispersed light is finally collimated by a focusing mirror and sent through an exit port. Essentially, the illuminated slit is reimaged via a 0.25 m focal length system at the output with a spectral dispersion. Diagrams adapted from [87].

4.10.1 Physics of Diffraction Gratings

While diffraction gratings come in different varieties (for example there are transmissive and reflective gratings, both of which have various groove shapes and densities), the physical principles behind their function are the same. Diffraction gratings consist of spatially periodic reflective or transmissive elements through which light emitted from them result in an interference pattern that varies with the light wavelength. Take for example the blazed grating (Fig. 4.16a), also known as the echelle grating, which is the class of diffraction gratings used in Oriel MS260i spectrometer during the experiment [91] (Fig. 4.16b), a type of reflective grating whose ruling pattern resembles a series of steps with a spatial periodicity of length, d .

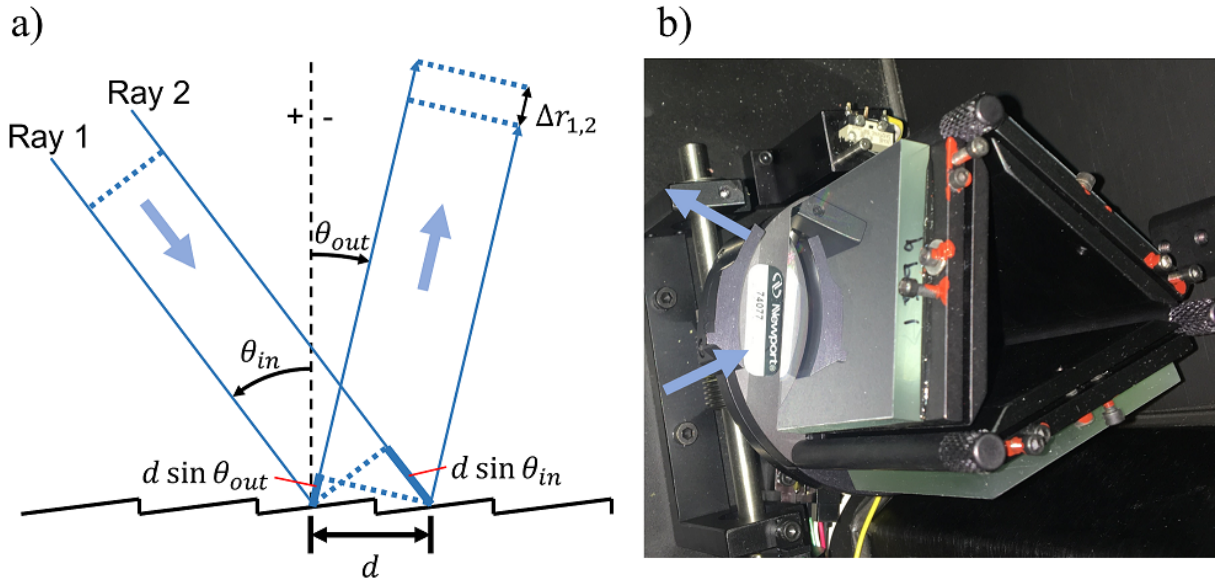


Figure 4.16: Diagram of a) the ray geometry of a blazed diffraction grating and b) photo of the physical diffraction gratings used in the experiment. Shown in the ray diagram are two parallel rays incident on a blazed diffraction grating at an angle θ_{in} relative to the grating normal, landing on adjacent rulings a distance d apart equal to the ruling period, and reflecting off at an angle θ_{out} with an overall path difference of $\Delta r_{1,2}$. The photo shows the triple diffraction grating assembly in the Oriel MS260i spectrometer with the 150 lines/mm (model 74077) grating surface in view.

Consider broadband parallel light rays from the source incident at an angle θ_{in} relative to the grating normal, landing on the grating surface profile at separate rulings and points spaced sequentially a distance, d , apart. These light rays arrive at the same relative points to each ruling (e.g., at the horizontal centers of each ruling, or a quarter of a period from the left, etc.). These rays reflect off of the grating surface at some outgoing angle, θ_{out} . They interfere constructively when the path difference between two adjacent rays, $\Delta r_{1,2}$, from the source to the observer is equal to an integer multiple, m , of the wavelength of light, λ , in other words, $\Delta r_{1,2} = m\lambda$. In this example, the observation point is taken to be far from the diffraction grating. Taking the convention where an angle referenced counterclockwise relative to the grating normal is positive, while an angle referenced clockwise is negative, the constructive interference condition results in

the well-known grating equation:

$$d(\sin \theta_{in} + \sin \theta_{out}) = m\lambda \quad (4.14)$$

In a spectrograph, the incoming rays are collimated and therefore all have the same unique value of θ_{in} , while the outgoing dispersed radiation will have values of θ_{out} determined by their wavelength and spectral order, m . For outgoing directions close to the grating normal, the small angle approximation can be made ($\sin \theta_{out} \approx \theta_{out}$) so that the relationship between θ_{out} and λ is linear. More generally, θ_{out} may not be small, and the dispersed light is projected onto a plane whose normal is at an angle, θ_{obs} , from the normal of the grating, so that the position, x_{obs} , along the observation plane depends on $\tan(\theta_{out} - \theta_{obs})$, therefore the relationship between λ and x_{obs} involves higher order terms in x_{obs} from a Taylor expansion.

A more detailed description of the light produced from a diffraction grating requires a more mathematically rigorous treatment using the Fresnel-Kirchhoff diffraction integral. Without getting into the full derivation (which the reader may find in [92]), the Fresnel-Kirchhoff integral describes the monochromatic field, $U(P)$, at an observation point P after the field has passed through an aperture represented by a planar surface \mathcal{A} , containing the origin O , from a point source at P_0 , as shown in Fig. 4.17. The Fresnel-Kirchhoff integral may also be used to describe the field reflected off of a mirror represented by \mathcal{A} by simply taking the reference point P to be on the same semi-space as P_0 . We define a Cartesian coordinate system centered at origin O with unit vectors $\hat{\mathbf{x}}$, $\hat{\mathbf{y}}$, and $\hat{\mathbf{z}}$, the coordinates of P_0 to be (x_0, y_0, z_0) , and that of P to be (x, y, z) . Furthermore, the planar surface \mathcal{A} has a unit normal vector $\hat{\mathbf{n}}$ along $\hat{\mathbf{z}}$ and a point Q on \mathcal{A} is defined with coordinates $(\xi, \eta, 0)$.

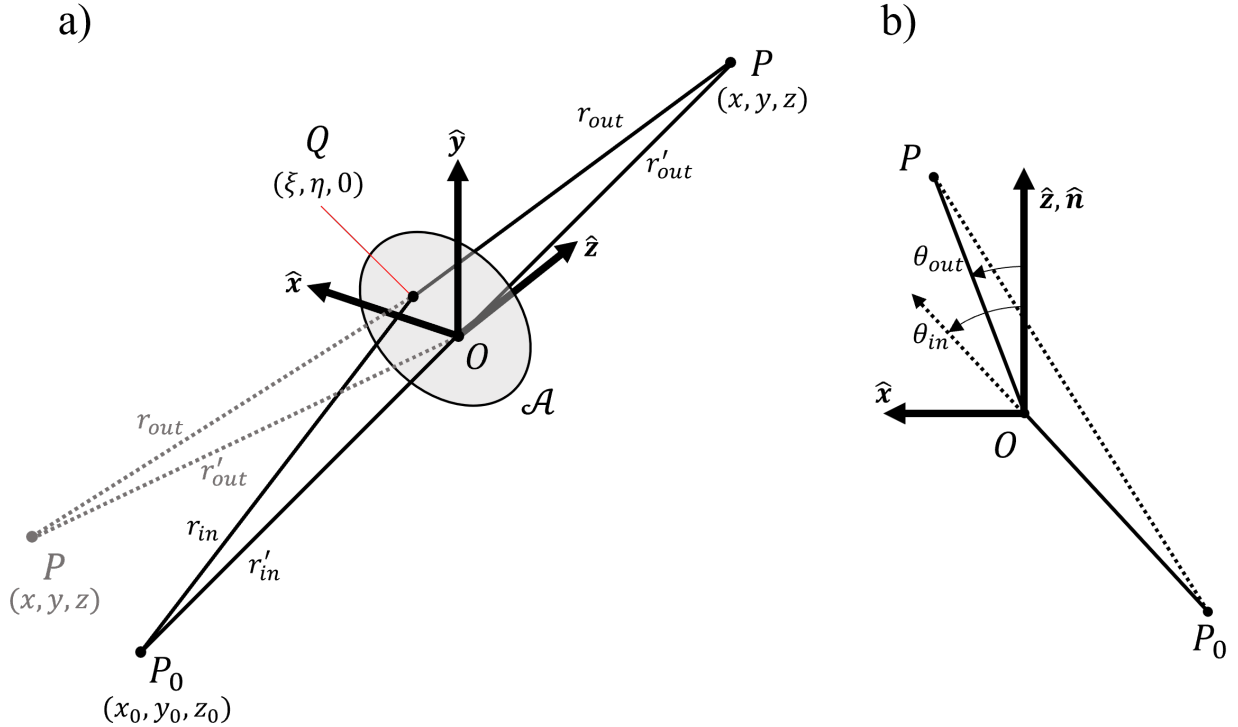


Figure 4.17: Diagrams showing the coordinate system used in the Fresnel-Kirchhoff integral from two perspectives. Shown in a) includes a point source P_0 emits radiation which passes through an aperture defined by surface \mathcal{A} and is observed at point P . Alternatively, if the surface \mathcal{A} is reflective, the Fresnel-Kirchhoff integral is applicable if P is located in the same semi-space as P_0 (gray point with dotted lines). Shown in b) is a top view clarifying the relative positions of points P_0 , P , and O , which are not necessarily all colinear, as well as θ_{in} and θ_{out} for a transmitting system. The diagrams are not drawn to scale.

In the limit where the dimensions of \mathcal{A} is small compared to the distances from any point on \mathcal{A} (say Q) to P_0 and P , and where the angles made by lines \overline{PO} and $\overline{P_0O}$ with $\overline{PP_0}$ is not too large, the Fresnel-Kirchhoff integral takes on a simple form:

$$U(P) = C \iint_{\mathcal{A}} F(\xi, \eta) \exp [ik(r_{in} + r_{out})] dS \quad (4.15)$$

Here, the integral is taken over the surface \mathcal{A} and the quantities r_{in} and r_{out} are the distances of $\overline{P_0Q}$ and \overline{PQ} , respectively, where Q is the point on the surface over which the surface integral

is evaluated and dS is the differential surface area element. The function $F(\xi, \eta)$ is a complex transmission function, which accounts for the losses (real part) and phase shifts (imaginary part) after the light has interacted with the media at surface \mathcal{A} . For a transmitting medium, this accounts for medium thickness and index of refraction, while for a reflective medium, this accounts for the reflectivity as well as offsets from the plane defined by \mathcal{A} . The quantity $k = 2\pi/\lambda$ is the wave vector magnitude and C is a constant which depends on the locations of P_0 and P and the wavelength λ . In physical terms, Eq. 4.15 states that the field at point P is equal to the total contribution of waves from all the paths taken from point source P_0 to \mathcal{A} and from \mathcal{A} to observation point P while accounting for the material effects on light due to \mathcal{A} .

If we denote r'_{in} and r'_{out} to be the lengths of line segments $\overline{P_0O}$ and \overline{PO} respectively, we may rewrite r_{in} and r_{out} in terms of the coordinates of Q (ξ, η), in the aperture, as well as the coordinates of P (x, y, z) and P_0 (x_0, y_0, z_0):

$$r_{in}^2 = r'^2_{in} - 2(x_0\xi + y_0\eta) + \xi^2 + \eta^2 \quad (4.16)$$

$$r_{out}^2 = r'^2_{out} - 2(x\xi + y\eta) + \xi^2 + \eta^2 \quad (4.17)$$

Due to the small dimensions of the aperture, we may expand 4.17 over the variables ξ/r'_{in} , ξ/r'_{out} , η/r'_{in} , and η/r'_{out} to obtain:

$$r_{in} \sim r'_{in} - \frac{x_0\xi + y_0\eta}{r'_{in}} + \frac{\xi^2 + \eta^2}{2r'^2_{in}} - \frac{(x_0\xi + y_0\eta)^2}{2r'^3_{in}} \quad (4.18)$$

$$r_{out} \sim r'_{out} - \frac{x\xi + y\eta}{r'_{out}} + \frac{\xi^2 + \eta^2}{2r'^2_{out}} - \frac{(x\xi + y\eta)^2}{2r'^3_{out}} \quad (4.19)$$

For the purposes of this thesis, the quadratic and higher order terms in ξ and η are ignored.

Keeping the linear terms in ξ and η , from eq. 4.19, the Fresnel-Kirchhoff integral (Eq. 4.15) may be rewritten as:

$$U(p, q) = C \iint_{\mathcal{A}} F(\xi, \eta) \exp[-ik(p\xi + q\eta)] d\xi d\eta \quad (4.20)$$

where

$$p \equiv \frac{x}{r'_{out}} + \frac{x_0}{r'_{in}} \quad (4.21)$$

$$q \equiv \frac{y}{r'_{out}} + \frac{y_0}{r'_{in}} \quad (4.22)$$

and the factor $\exp[ik(r'_{in} + r'_{out})]$ had been absorbed into the constant C .

For a diffraction grating with N rulings spaced distance d apart and oriented along $\hat{\mathbf{y}}$, the rulings are centered at the coordinates $(\xi_0, \eta_0), (\xi_0 + d, \eta_0), \dots, (\xi_0 + (N - 1)d, \eta_0)$, as shown in Fig. 4.18a. We set $y = 0$ and $y_0 = 0 \Rightarrow q = 0$ to consider only light which travel perpendicular to the orientation of the rulings. The dispersion, therefore, is along $\hat{\mathbf{x}}$, so that

$$p = \sin \theta_{out} - \sin \theta_{in}. \quad (4.23)$$

The Fresnel-Kirchhoff integral becomes a summation over the N integrals of each ruling:

$$U(p) = C \sum_{n=0}^{N-1} \exp(-ikpnd) \iint_{\mathcal{A}'} F(\xi, \eta) \exp(-ikp\xi') d\xi' d\eta' \quad (4.24)$$

$$= U^{(0)}(p) \frac{1 - \exp(-iNkd p)}{1 - \exp(-ikd p)} \quad (4.25)$$

where \mathcal{A}' is the surface of a single ruling, (ξ', η') are the coordinates along this surface. The choice of ruling does not matter, since it was assumed that points P and P_0 are far from the

diffraction grating compared to the linear dimensions of \mathcal{A} . Using the first ruling for example (Fig. 4.18b), the primed coordinates may be related to the un-primed coordinates via $\xi' = \xi - x_0$ and $\eta' = \eta - \eta_0$. The function $U^{(0)}(p) \equiv C \iint_{\mathcal{A}'} F(\xi', \eta') \exp(-ikp\xi') d\xi' d\eta'$ represents the single ruling diffraction pattern and depends on the pattern of the rulings. A blazed grating, for example, will have surface offsets from \mathcal{A}' which are accounted for as phase shifts due to the imaginary part of $F(\xi', \eta')$.

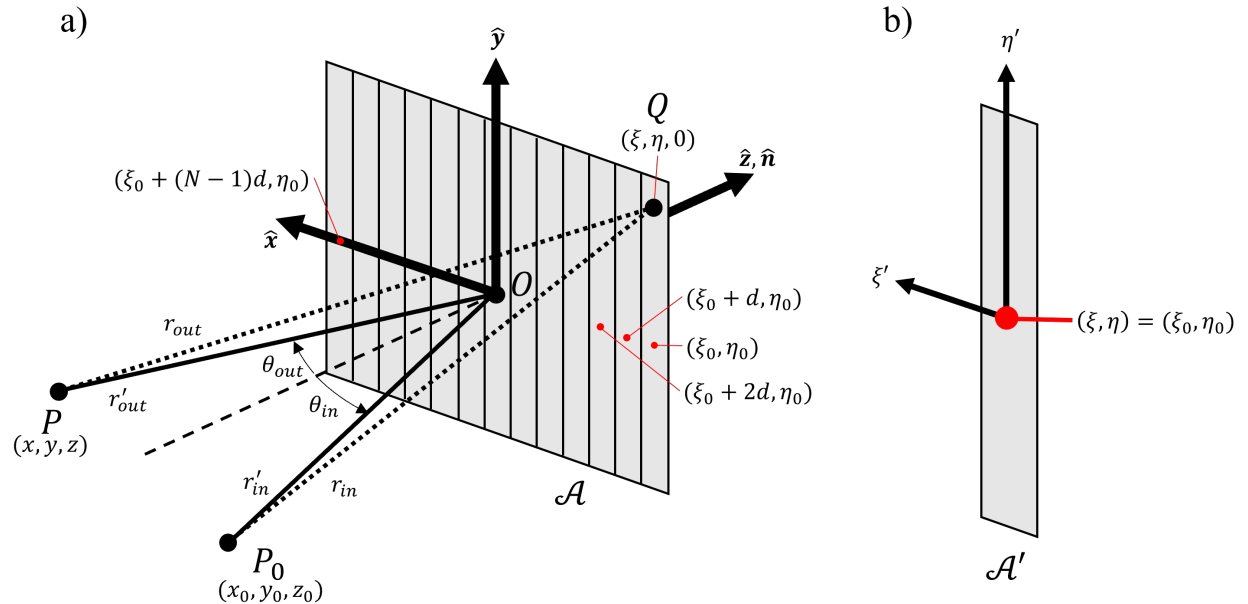


Figure 4.18: Diagrams of the coordinate system used in the Fresnel-Kirchoff integral applied to a diffraction grating. See Eq. 4.25. Shown in a) is a diffraction grating with N rulings and in b) is the coordinate system for a single ruling representing the integral expression for $U^{(0)}(p)$. The centers of individual rulings are indicated by red dots. The points P and P_0 are drawn assuming $y = y_0 = 0$, while Q is a point anywhere on the grating. The figures are not drawn to scale (in a realistic setup, P and P_0 would be much further away from the grating, and the grating ruling density would be much higher than what is illustrated).

The intensity, $I(p)$ is then given by:

$$I(p) = |U(p)|^2 = I^{(0)}(p) \left(\frac{\sin(Nkdp/2)}{\sin(kdp/2)} \right)^2 \quad (4.26)$$

where $I^{(0)}(p) \equiv |U^{(0)}(p)|^2$. We focus our attention on the second factor in Eq. 4.26, which we write as in terms of a function $H(N, X)$ such that

$$H(N, \frac{kdp}{2}) \equiv \left(\frac{\sin(Nkdp/2)}{\sin(kdp/2)} \right)^2 \quad (4.27)$$

The peaks of this distribution occurs when $kdp/2 = m\pi$, which is equivalent to the grating equation (Eq. 4.14). The offset in adjacent peaks is $\Delta p = \lambda/d$. The integer N appearing in the argument of the sine function in $H(N, kdp/2)$ determines the width of the peaks, as well as the number of smaller, secondary peaks between the primary peaks, as shown in Fig. 4.19a.

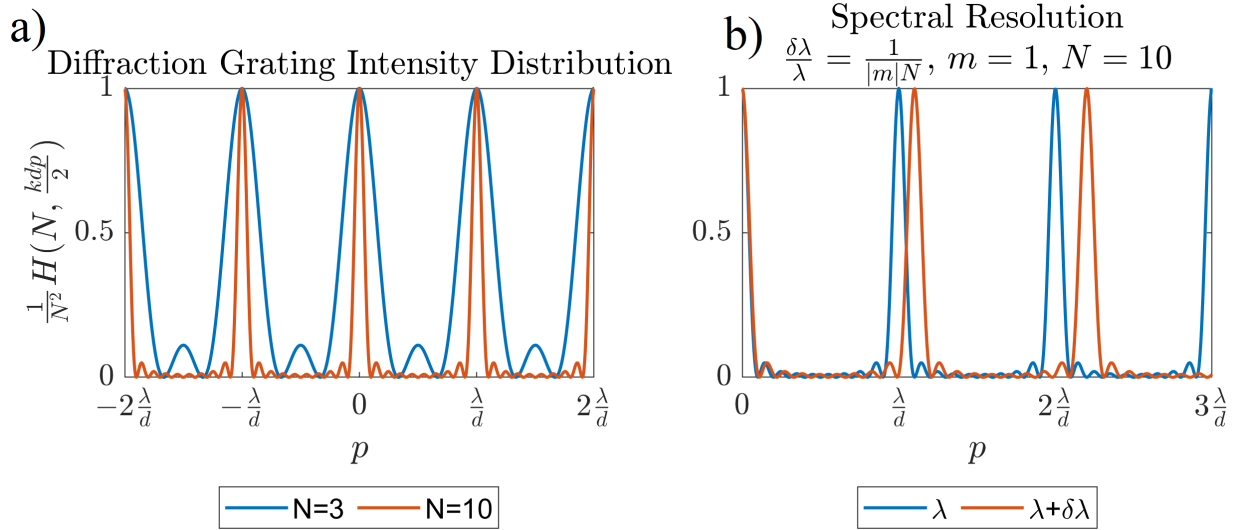


Figure 4.19: Plots of $H(N, kdp/2)$ for a) two different values of N and b) two wavelengths differing by $\delta\lambda$. The expression for $H(N, kdp/2)$ is given in Eq. 4.27, while in b) the value of $\delta\lambda$ is determined from Eq. 4.30 with $m = 1$ and $N = 10$. Plot a) shows the inverse relationship between N and the peak width and the presence of secondary peaks proportional to N . Plot b) shows the Rayleigh criterion for order $m = 1$, as well as better line separation at $m = 2$. The line separation between different wavelengths, in fact, increases with m .

The locations of the minima are given by $p = m'\lambda/(Nd)$ (m' an integer not divisible by

N). The distance between each primary peak to its adjacent minima is therefore

$$\delta p = \frac{\lambda}{Nd} \quad (4.28)$$

while the width of a primary peak is equal to $2\delta p$. When the wavelength is varied by a small amount, $\delta\lambda$, the distribution is shifted by an amount

$$\delta p_\lambda = \frac{|m|\delta\lambda}{d} \quad (4.29)$$

Letting $\delta p = \delta p_\lambda$ be the condition in which the two adjacent lines of wavelength λ and $\lambda + \delta\lambda$ are just resolved (i.e. the Rayleigh criterion - see Fig. 4.19b for an example with $m = 1$), we determine the following expression for the spectral resolution for a *diffraction limited* system:

$$\delta\lambda = \frac{\lambda}{|m|N} \quad (4.30)$$

Eq. 4.30 states that the spectral resolution is better for shorter wavelengths and larger number of grating rulings (both of which reduce the peak width at a given wavelength) and for higher magnitude order numbers (which increases the dispersion). In practice, N is limited by the size of the diffraction grating and collimating optics, while $|m|$ is limited by the fact that the intensity in single ruling diffraction pattern generally falls off at higher orders. Typically, modern diffraction gratings are designed to maximize efficiency for a range of spectral orders and reduce efficiency in others.

4.10.2 Spatial Calibration

In order to understand the spatial properties measured by the spectrometer, a calibration in the number of pixels per unit length at the slit, both along the slit length as well as the slit width, was conducted. This was done with the 1200 lines/mm grating and carried out by placing a strip of grid paper, whose square boxes are 1 mm in width, along the length of the entrance slit, as illustrated in Fig. 4.20a, as close to the slit as possible via masking tape. The grid paper strip was illuminated with a 635 helium-neon (HeNe) laser source, and the resulting images, for slit widths set at 1 mm and 2 mm, were captured by the spectrometer readout camera, appearing in a region along x from 565 to 615 pixels (in a 1024 wide by 255 high image), as shown in Fig. 4.20b. The vertical and horizontal profiles (summed over the rows and columns respectively) for the grid paper images captured for two different slit settings are shown in Fig. 4.20c and d. Analysis of the locations of the troughs (local minima) in the vertical lineouts, summarized in Table 4.3, determined the spatial calibration to be 63 px/mm. The full length of the visible slit in the camera image is therefore 4.0 mm.

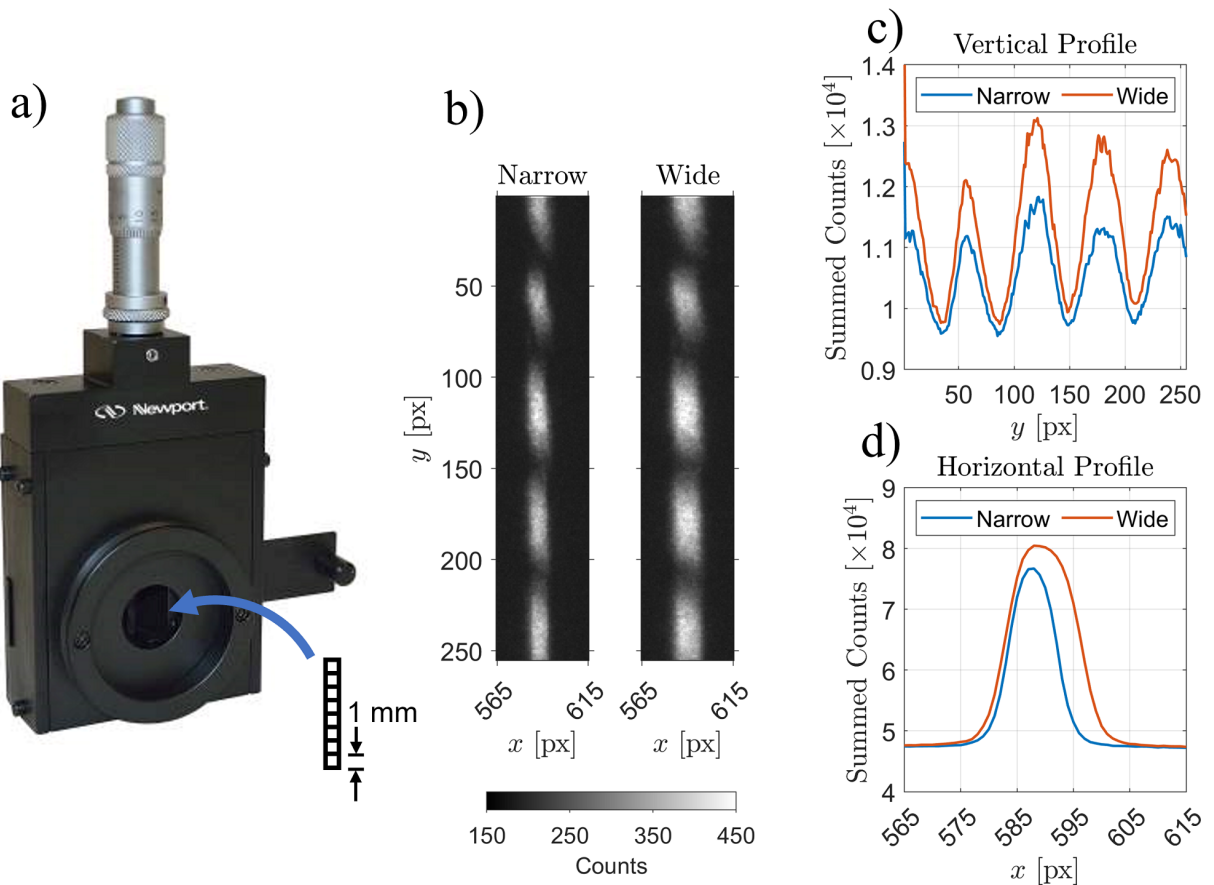


Figure 4.20: Diagrams showing the calibration of the entrance slit to the spectrometer. Shown are a) photo of the micrometer-adjustable slit module for the Oriel MS260i spectrometer with an illustration of a strip of 1 mm square grid paper (not to scale with the photo), b) images captured by the Andor iStar DH 720-25U-03 ICCD readout camera with the grid paper strip illuminated with a 635 nm HeNe laser and the slit widths set at two different widths, c) vertical profiles (summed over the rows) of the images shown in b), and d) horizontal profiles (summed over columns) of the images shown in b). The 1200 lines/mm grating set to a central wavelength of 635 nm was used.

Table 4.3: Table of the y-pixel locations of the troughs (local minima), y_{\min} , in the vertical profiles of the imaged 1 mm grid paper strip along with the differences between adjacent troughs, Δy_{\min} . The imaged grid paper is shown in Fig. 4.20. The outliers are indicated in red, possibly owing to the strip not being fully flat at the top end. Excluding the outliers, the average of the remaining set of values of Δy_{\min} is 63 px/mm with an standard deviation of 3 px/mm.

Narrow Slit		Wide Slit	
y_{\min} [px]	Δy_{\min} [px]	y_{\min} [px]	Δy_{\min} [px]
34	52	34	46
86	63	80	69
149	60	149	61
209		210	

The spatial calibration of the slit width was performed by varying the slit width using the micrometer adjustment, illuminating the slit with a continuous-wave (CW) laser light, capturing the image, and determining the width of the horizontal profile, defined in two ways: the full-width at half-maximum ($\Delta x_{0.5}$) and the full-width at 10% maximum ($\Delta x_{0.1}$), as shown in Fig. 4.21. The micrometer reading, w_{mic} , was not zeroed to the slit width, therefore the real width value, w_{real} , was taken in reference to the "Closed" position shown in Fig. 4.21a, which shows a narrow line due to limited machine tolerance, backlash, and possible damage to the slit. Linear fits to the expressions $a\Delta x + b$ and $a\Delta x$ using the images in Fig. 4.21b-d were performed, where a and b are fitting parameters, and Δx is equal to either $\Delta x_{0.5}$ or $\Delta x_{0.1}$. The expressions represent fits without and with the y-intercept, b , forced to 0. The fit results are displayed in Fig. 4.22 and Table 4.4.

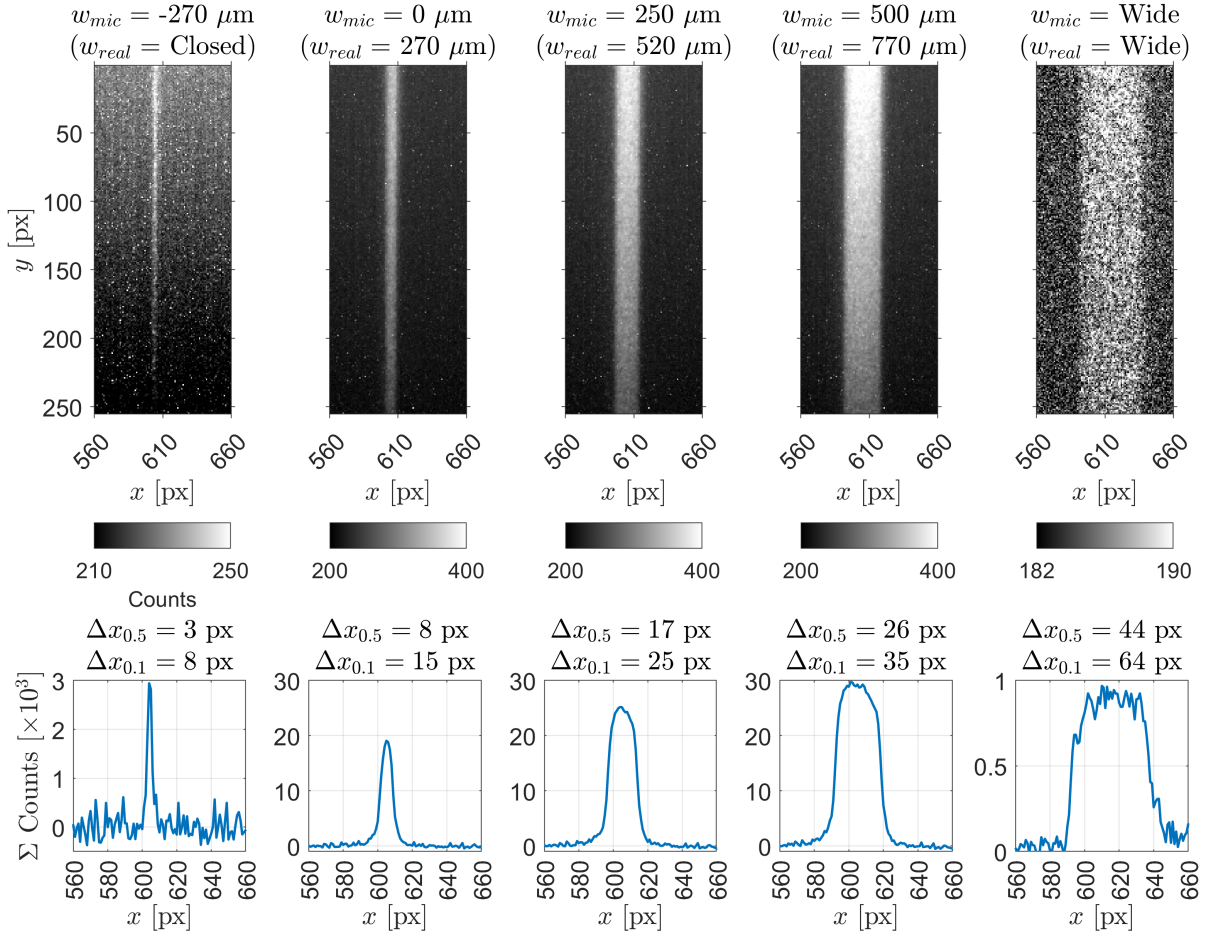


Figure 4.21: Images of the laser-illuminated entrance slit captured by the spectrometer readout camera at varying slit widths and their horizontal profiles. The "closed" slit, a), shows a line due to the limited machine tolerance of the slit assembly, but is taken to have effectively 0 width. The real slit width, w_{real} is equal to the micrometer reading, w_{mic} , plus 270 μm due to the micrometer not being zeroed to the slit width. The slit was open fully wide in e). 635 nm laser was used to illuminate a) through d), while a 530 nm laser was used to illuminate e). The 1200 lines/mm grating was used with a central wavelength set equal to the nominal laser wavelength used for illumination. The horizontal profiles were obtained by summing over each column, and subtracting the background (which was taken to be the average of the column sums from $x = 275$ to $x = 500$). The full-widths at half maximum, $\Delta x_{0.5}$ and the full-widths at 10% maximum, $\Delta x_{0.1}$ of the profile peaks are given.

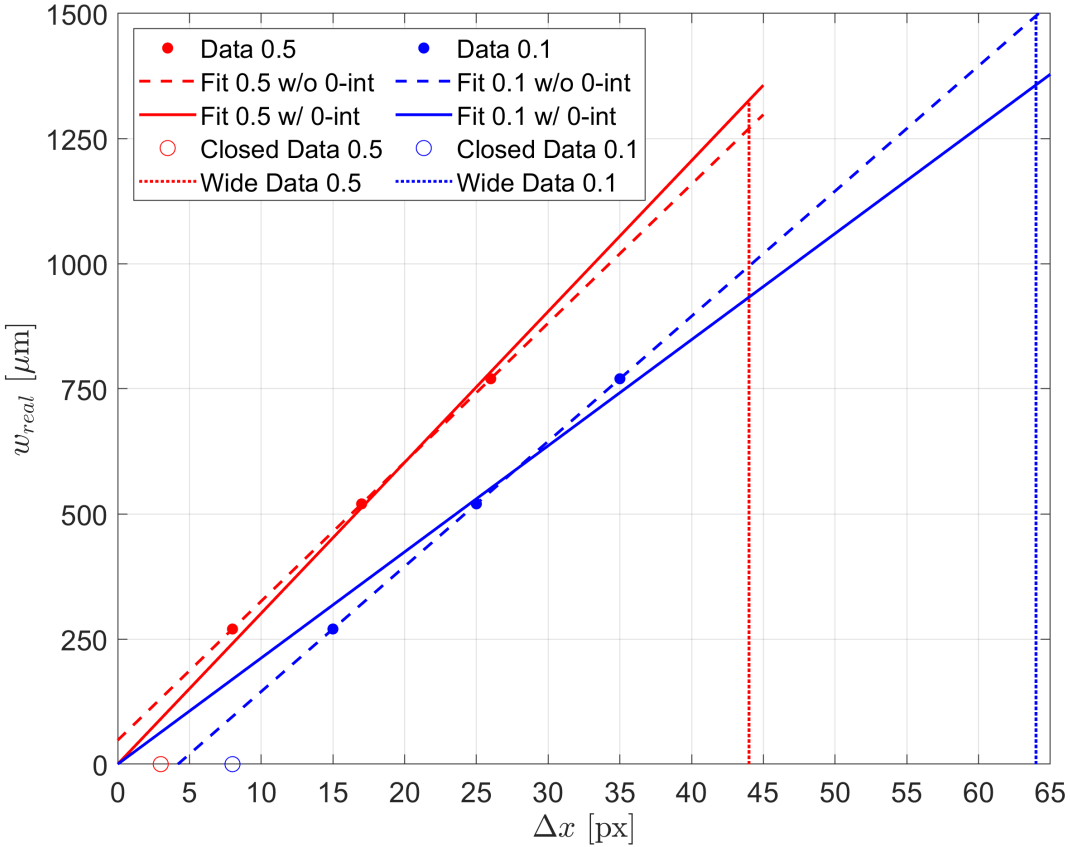


Figure 4.22: Plot of the data and linear fits to the slit width, w_{real} , based on the micrometer reading as a function the width of the horizontal profile, Δx , from the slit image captured by the spectrometer readout camera. The data comprises of profile widths measured at half maximum ($\Delta x = \Delta x_{0.5}$), represented in red, and 10% maximum ($\Delta x = \Delta x_{0.1}$), represented in blue. The solid data points were used in their respective fits, while the open data points represent the Δx measurement when the slit is in the "closed" configuration. For each set of data points, fits with and without the y-intercept set to 0 were carried, with the results summarized in Table 4.4. The vertical dotted lines represent the measured results of the slit when it is open wide (see Fig. 4.21e), where the micrometer setting was not recorded.

Table 4.4: Table of the fit results of the horizontal spatial calibration of the spectrometer based on the slit width. See Fig. 4.22. The values in parentheses in the column for a represent the half width of the 95% confidence interval. Parameters without parenthetical values attached have 95% confidence intervals of 0. The values after \pm in the column for $1/a$ are the propagated uncertainties from the column for a using the 95% confidence intervals.

Model	a [$\mu\text{m}/\text{px}$]	b [μm]	$1/a$ [px/mm]
$w_{real} = a\Delta x_{0.5} + b$	27.78	47.78	34
$w_{real} = a\Delta x_{0.5}$	30.15 (3.1)	N/A	33 ± 3.4
$w_{real} = a\Delta x_{0.1} + b$	25	-105	40
$w_{real} = a\Delta x_{0.1}$	21.2 (3.8)	N/A	47 ± 8.5

The fit results show a considerable difference in the parameter a between using $\Delta x_{0.5}$ as opposed to $\Delta x_{0.1}$ when the y-intercept is forced to 0, and a small difference when the y-intercept is not forced to 0. The parameter b , on the other hand, varies substantially depending on whether the $\Delta x_{0.5}$ or $\Delta x_{0.1}$ values were used. Both linear models work well down to slit widths as small as 270 μm , but eventually break down as the slit approaches fully-closed. The wide open slit (Fig. 4.21e) was predicted to be ~ 1.3 mm using the fit based on $\Delta x_{0.5}$ and ~ 1.5 mm using the fit based on $\Delta x_{0.1}$ where the y-intercept was not forced to zero in both cases.

Finally, it should be noted that these fits predict horizontal calibration values ($1/a$ in px/mm) which are smaller than the vertical calibration value of 63 ± 3 px/mm obtained from the grid paper, which is expected since the Oriel MS260i spectrometer has a specified 1.1 horizontal and 1.6 vertical magnification (a ratio of 0.6875). Using this ratio and the vertical spatial calibration, we should expect the horizontal calibration, $1/a$, to be 43 ± 2 px/mm, which agrees with the fits using $\Delta x_{0.1}$.

The final topic on the spatial calibration is the orientation of the laser propagation axis as it is imaged onto the slit. Fig. 4.23a and b together show a collapsed optical diagram of the imaging system capturing the laser focal region and relaying it to the spectrometer slit. Due to the combination of lenses used to relay the image from the objective to the slit, the final image of the laser axis has orientations which are shown in Fig. 4.23c and d, where the propagation vector, \mathbf{k}_\perp , from the E_\perp -objective is perpendicular to the slit, and the propagation vector, \mathbf{k}_\parallel , from the E_\parallel -objective is parallel to the slit.

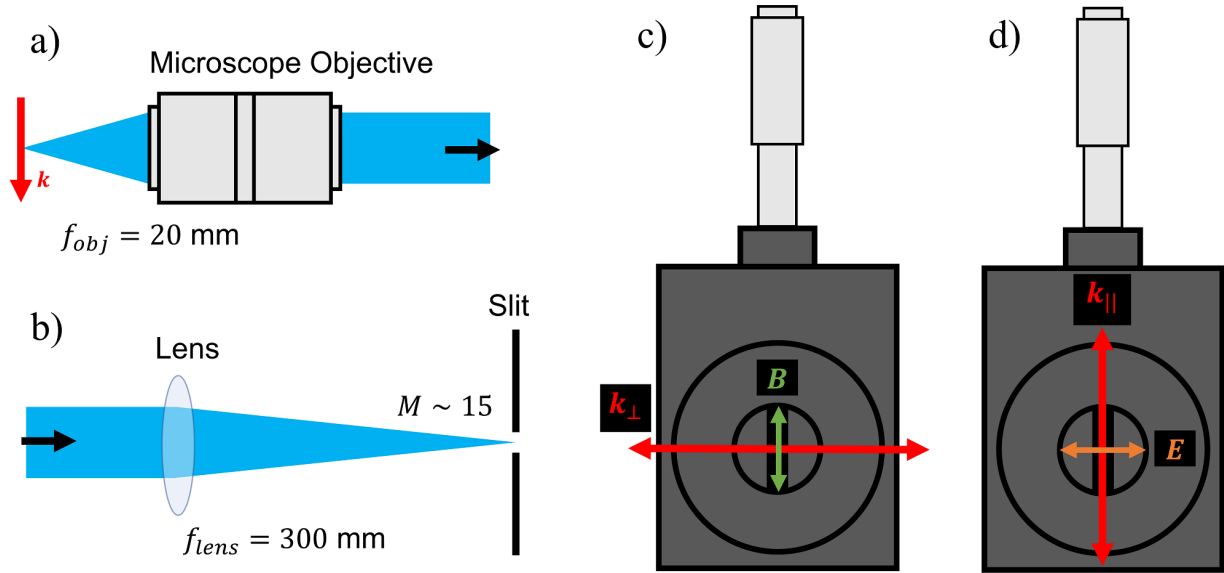


Figure 4.23: Diagrams illustrating the orientation of the laser and field polarizations as they are images onto the entrance slit. Shown are a) the infinity-corrected microscope objective capturing light from the laser focus, b) the lens focusing the light from the microscope objective onto the spectrometer slit, imaging with a magnification of ~ 15 , and c)-d) the entrance slit with the orientations of the laser axis imaged onto the slit by the c) E_{\perp} objective (k_{\perp}) and d) E_{\parallel} objective (k_{\parallel}). The lengths of the red arrow-tipped lines are not representative of the scale of the real images of the laser focal region at the slit.

4.10.3 Wavelength Calibration

The wavelength calibration of the spectrometer for the desired grating (150 lines/mm [88]) at various central wavelengths, λ_c , were performed by collecting mercury (Hg) spectra from a UV lamp (generic brand UV-C U-60) as well as room lights, as shown in Fig. 4.24.

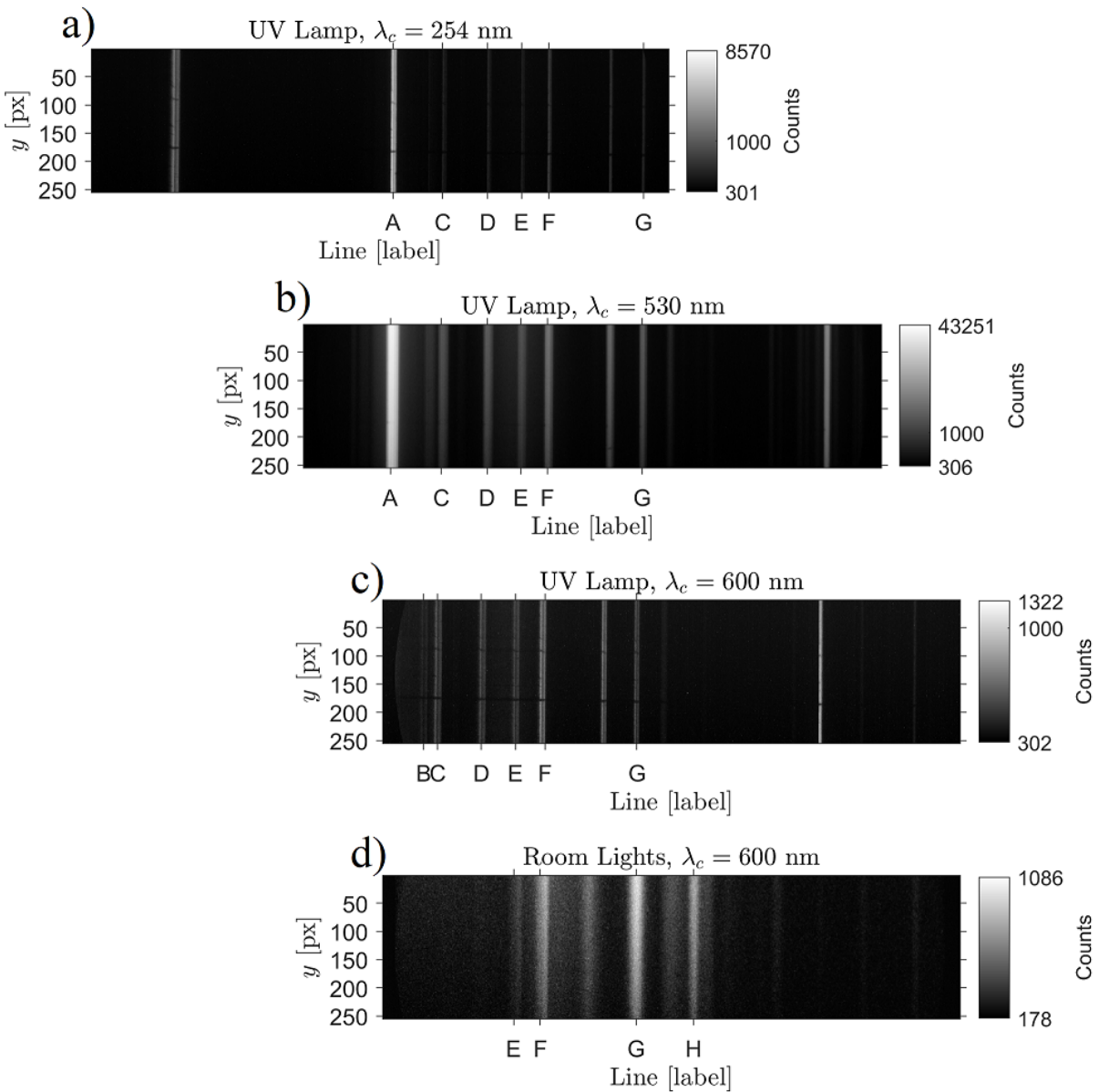


Figure 4.24: Spectrum images (1024 wide by 255 high) of mercury emission lines from a) - c) a UV lamp at various central wavelength, λ_c , settings of the spectrometer and of d) the room lights. The lines labeled "A" through "H" were identified with strong emission lines found in the tables of strong emission lines in the NIST Handbook of Basic Atomic Spectroscopic Data [2] and have their x [px] coordinate listed in Table 4.5. The images were offset horizontally in order to align the common Hg lines vertically.

The pixel positions of select lines measured from the Hg spectra (where the spectrum images were 1024 pixels across) were matched with the wavelengths of strong emission lines from

the tables of strong emission lines in the NIST Handbook of Basic Atomic Spectroscopic Data [2], as shown in Table 4.5.

Table 4.5: Table of the pixel positions, x , of select Hg emission lines measured by the spectrometer, their corresponding wavelengths from the NIST tables of strong lines [2], λ_N .

		Line							
		A	B	C	D	E	F	G	H
NIST Hg Lines		λ_N [nm]							
Source	λ_c [nm]	253.7	296.7	313.2	365	404.7	435.8	546	614.9
UV Lamp	254 nm	535.5		623	703	763	811	979	
	530 nm	154		244	325	385	432	600	
	600 nm		73.5	98	175.5	236.5	288.5	451	
Room Lights	600 nm					233	280	450	552

Linear fits (Fig. 4.25) were done for each data set to the equation $\lambda_i = p_1x_i + p_2$, where λ_i are the line wavelengths from the NIST tables in nm, x_i are the x position in px, and p_1 and p_2 are fitting parameters.

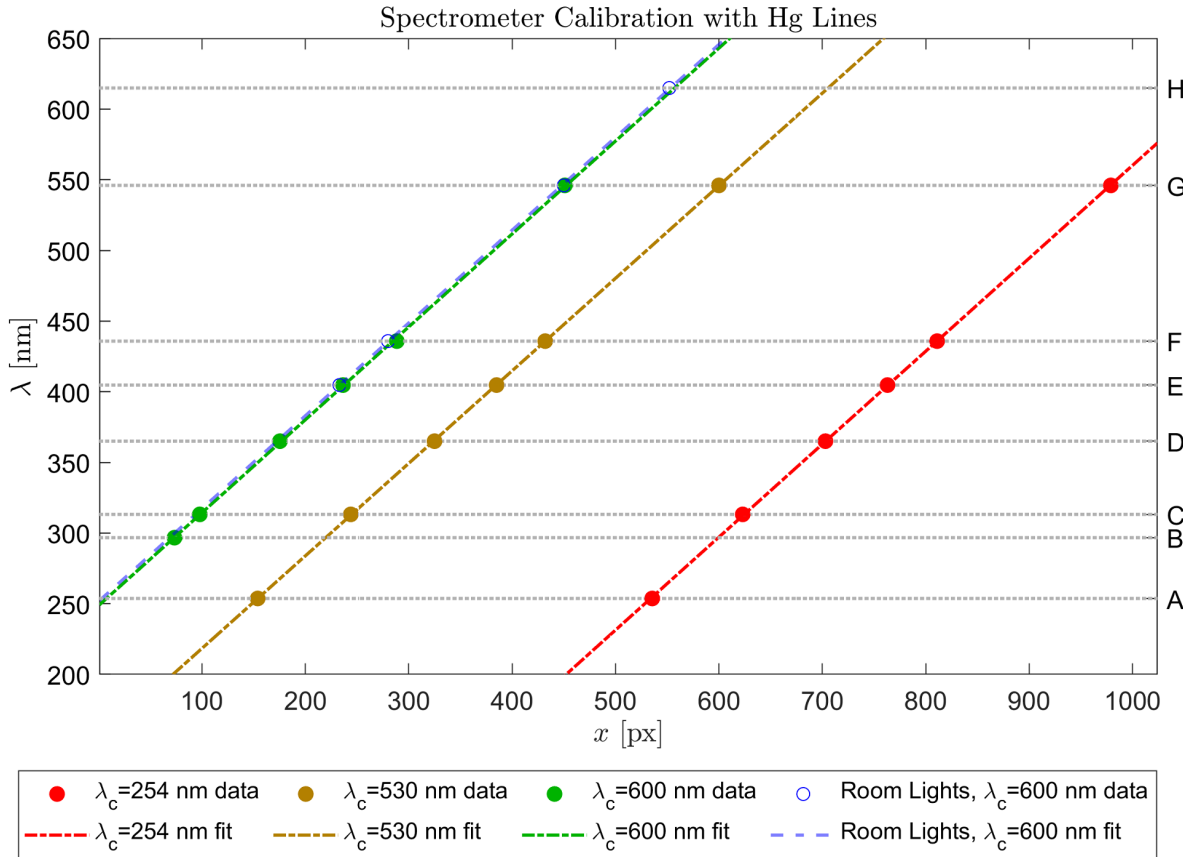


Figure 4.25: Plots of the NIST tabulated wavelengths as a function of the measured pixel positions, x , of mercury (Hg) strong lines, at various central wavelengths, λ_c . The measurements were spectrometer images of the Hg strong lines obtained from the UV lamp (green, yellow, and red solid circles) and room lights (blue open circles) along with their linear fits (dot-dashed lines for the UV lamp and dashed line for the room lights). The NIST tabulated wavelengths are also represented with horizontal dotted lines labeled from A-H. See Table 4.5 for the data point values and Table 4.6 for the fit results.

Table 4.6: Results of the linear fits to the NIST wavelengths, λ_i , as a function of measured x pixel positions, x_i , for a given central wavelength setting, λ_c . The fit equation is given by $\lambda_i = p_1 x_i + p_2$, where p_1 and p_2 are the fitting parameters. The equation may also be written in a more physically intuitive form as $\lambda_i = \lambda_c + \delta_\lambda^x (x_i - x_0)$, where δ_λ^x and x_0 were re-parameterized from p_1 and p_2 . The entry in red indicates an outlier for the fit value of $\lambda_c - p_2$ (and therefore p_2) and was ignored in the determination of the final values of δ_λ^x and x_0 .

Source	λ_c [nm]	p_1	p_2	$\lambda_c - p_2$
UV Lamp	254	0.658 ± 0.006	-97.5 ± 4.5	351.5 ± 4.5
UV Lamp	530	0.651 ± 0.004	152.8 ± 1.5	377.2 ± 1.5
UV Lamp	600	0.658 ± 0.013	248.6 ± 3.3	351.4 ± 3.3
Room Lights	600	0.657 ± 0.017	251.5 ± 6.7	348.5 ± 6.7
Mean		0.656 ± 0.006	N/A	350.5 ± 2.9
		$\delta_\lambda^x \equiv 1/p_1$		$x_0 \equiv$
				$(\lambda_c - p_2)/p_1$
		1.524 ± 0.014		534 ± 7

The results of the fits are shown in Table 4.6. The parameter p_1 represents the slope of the linear fit; its reciprocal, $\delta_\lambda^x \equiv 1/p_1$, is the calibration in the wavelength dispersion in units of pixels per nm, which was found to be 1.524 ± 0.014 px/nm. The parameter p_2 is related to the centering of the image for a given central wavelength, λ_c . The quantity $p_2 - \lambda_c$ is expected to be the same if the setting of λ_c rotates the diffraction grating by the correct amount corresponding to λ_c , however, it was found that for $\lambda_c = 530$ nm, this offset was off by 26.7 nm relative to the other settings (red text on Table 4.6). This discrepancy, along with the fact that the RTS data was taken exclusively at $\lambda_c = 600$ nm, was the reason this value was treated as an outlier and not included in the determination of the mean value of $p_2 - \lambda_c$. The quantity $x_0 \equiv (\lambda_c - p_2)/p_1$ is the x position, in pixels, where the measured wavelength is equal to the central wavelength setting for any given λ_c , and was found to be 534 ± 7 .

The best fit parameters give the following relation between the wavelength and pixel number:

$$\lambda[\text{nm}] = p_1 x_{\text{px}} + p_2 = \frac{x_{\text{px}} - x_0}{\delta_\lambda^x} + \lambda_c = \frac{x_{\text{px}} - 534}{1.524} + \lambda_c \quad (4.31)$$

where x_{px} is the horizontal pixel number of the spectrum image. The uncertainty in λ may be estimated by adding the uncertainties in x_{px} , δ_λ^x and x_0 in quadrature, and noting that $x_{\text{px}} - x_0$ is at most x_0 :

$$\sigma_\lambda[\text{nm}] = \sqrt{\left(\frac{\sigma_{x_{\text{px}}}}{\delta_\lambda^x}\right)^2 + \left(\frac{\sigma_{x_0}}{\delta_\lambda^x}\right)^2 + \left(\frac{(x_{\text{px}} - x_0)\sigma_{\delta_\lambda^x}}{(\delta_\lambda^x)^2}\right)^2} \quad (4.32)$$

$$\leq \sqrt{0.43 \times \sigma_{x_{\text{px}}}^2 + 31.5} \quad (4.33)$$

An uncertainty in x_{px} of, for example, 10 px therefore corresponds to $\sigma_\lambda \leq 8.6$ nm, while knowing x_{px} perfectly results in $\sigma_\lambda \leq 5.6$ nm. Comparing the residuals between the calibrated wavelengths and the NIST tabulated wavelengths, however, we find that the average error is only 1.1 nm when ignoring the outliers, as shown in Table 4.7.

Table 4.7: The residuals between the calibrated wavelengths, λ , and NIST tabulated wavelengths, λ_N , defined by $\Delta_\lambda \equiv \lambda - \lambda_N$. The entries in red text correspond to outliers due to an issue related to the offset not correctly corresponding to the central wavelength at 530 nm. The absolute value of the residuals, $|\Delta_\lambda|$, not including the outliers, were averaged to determine the typical experimental uncertainty in the wavelength, $|\Delta_\lambda|_{\text{avg}}$, from the calibration.

		Line							
		A	B	C	D	E	F	G	H
NIST Hg Lines		λ_N [nm]							
		253.7	296.7	313.2	365	404.7	435.8	546	614.9
Source	λ_c [nm]								
	254 nm	1.3		-0.8	-0.1	-0.4	-0.04	-0.01	
	530 nm	27		27	28	28	27	27	
UV Lamp	600 nm		1.1	0.7	-0.2	0.09	3.1	-0.5	
	600 nm					-2.2	-2.5	-1.1	-3.1
$ \Delta_\lambda _{\text{avg}}$ [nm]		1.1							

4.10.4 Recombination Spectra

Plasma recombination spectra for helium (He), argon (Ar), and nitrogen (N_2) ionized by the VEGA-2 laser were measured and are shown in Fig. 4.26. The He spectra was captured during a preceding campaign using the same laser system, target chamber, and spectrometer. The calibrated wavelengths of various lines were compared with the wavelengths in the NIST tables and found to agree within 3.5 nm at most and 2.1 nm on average, as shown in Table 4.8. This is larger than the value of 1.1 nm for $|\Delta_\lambda|_{avg}$ determined from the Hg data, but within the uncertainty, σ_λ , from error propagation (Eq. 4.33). This serves as a validation for the wavelength calibration from the Hg data for the error tolerance predicted by error propagation.

The spectra shows that, among the three species of gas available, nitrogen is most suitable for producing and measuring second harmonic RTS radiation. Nitrogen's recombination spectra consists of strong lines around 380 to 450 nm and weak emission from 450 to 550 nm. Above 550 nm, recombination lines were not observed, providing a clean region up to 750 nm (where the laser light and 1st harmonic RTS would begin to appear) over which the Doppler shifted RTS radiation may be analyzed. Helium, on the other hand, has a strong line at 587.5 nm, while argon has lines which are observed from 375 nm up to 525 nm, as well as weaker lines from 650 nm and above. Furthermore, continuum emission was observed for both He and Ar throughout the 375 to 750 nm band, whereas for N_2 , such emission from 550 to 750 nm was not evident.

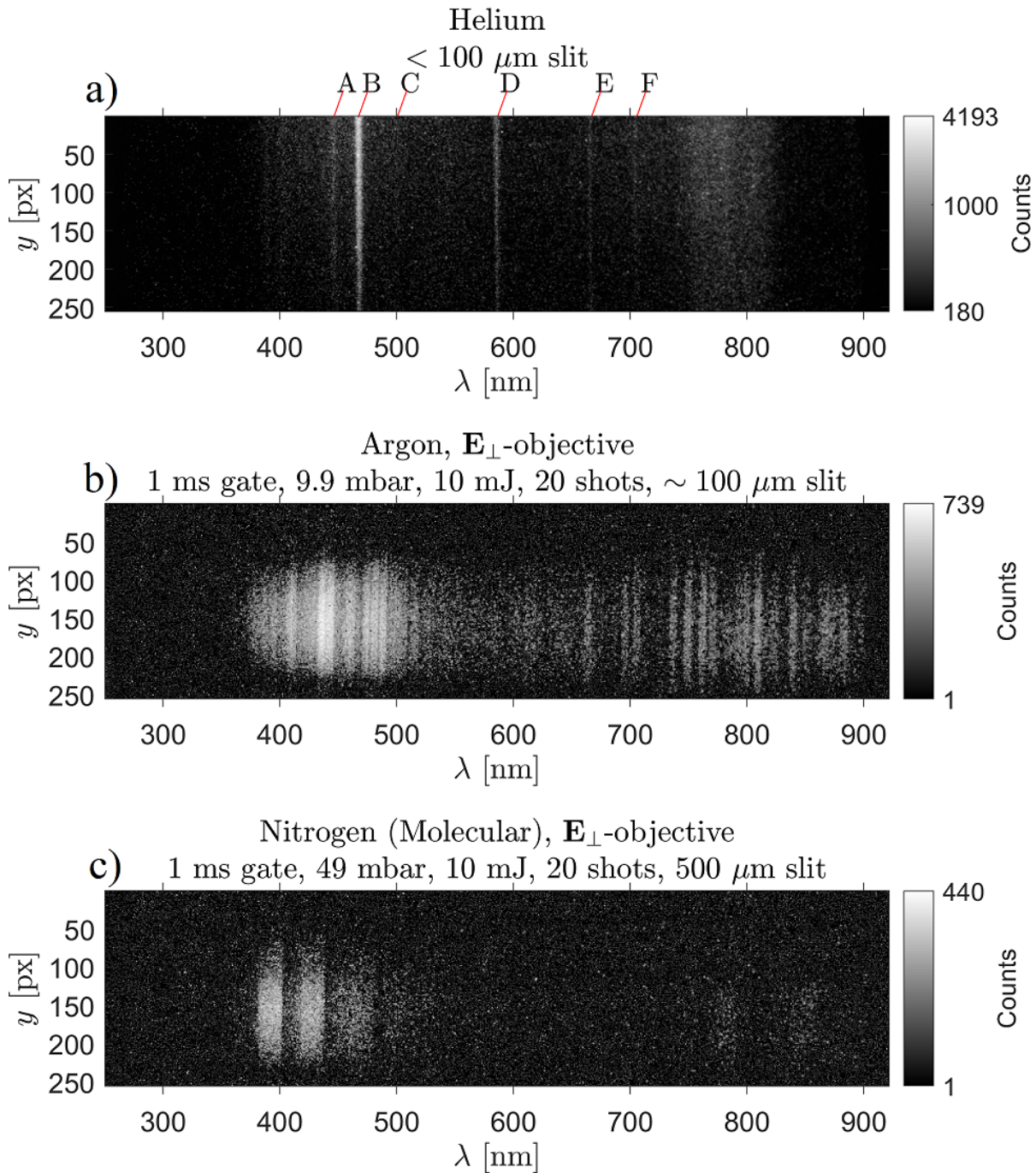


Figure 4.26: Recombination spectra of a) helium (w/ 1% nitrogen mix), b) argon, and c) nitrogen. The images were captured using the 150 lines/mm grating with $\lambda_c = 600$ nm, and are plotted on a log scale. The helium spectrum was captured during a previous experiment using a lens imaging in the \mathbf{E}_\perp direction and mirrors. The various He emission lines used for validating the calibration are indicated by the labels "A" through "F" (see Table 4.8). The argon spectrum was captured during the RTS experiment using the \mathbf{E}_\perp objective. The nitrogen spectrum was captured using the \mathbf{E}_\parallel objective. The argon and nitrogen spectra were background subtracted. The horizontal axis is the wavelength from the mercury lines calibration (eq. 4.31).

Table 4.8: Summary values for the selected helium (He) recombination lines measured by the spectrometer. See Fig. 4.26. The values include: 1) the NIST tabulate wavelengths, λ_N , 2) x pixel position, x , 3) Hg calibrated wavelength, λ (from Eq. 4.31), 4) residual in calibrated wavelength, $\Delta_\lambda \equiv \lambda - \lambda_N$, and 5) the average error, $|\Delta_\lambda|_{\text{avg}}$.

	Line					
	A	B	C	D	E	F
λ_N [nm]	447.1	468.5	501.6	587.5	667.8	706.5
x [px]	299	332	381	511	634	691
λ [nm]	445.8	467.5	499.6	584.9	665.6	703.0
Δ_λ [nm]	-1.3	-1.0	-2.0	-2.6	-2.2	-3.5
$ \Delta_\lambda _{\text{avg}}$ [nm]	2.1					

4.10.5 Temporal Gating

The temporal gating is facilitated by the built-in intensifier tube (Fig. 4.27a) integrated inside the ICCD camera [93] (Fig. 4.27b) attached to the output of the spectrometer, where the dispersed spectrum image is sent. The intensifier tube consists of an input window, where incoming light enters and hits a photocathode. Photoelectrons are generated at the photocathode, which are accelerated toward a microchannel plate (MCP). The voltage across the MCP amplifies the electron signal through an electron multiplication process. The electrons generated at the MCP then hit a phosphor screen, leaving a fluorescent afterimage that is captured by a CCD camera sensor which is coupled to the phosphor via a fiber optic bundle. The ICCD camera is controlled via the Andor Solis software, which provides options for delay and gate width. The temporal gating is ultimately controlled by the time duration of the applied voltage across the MCP, in a manner analogous to the flash duration in high speed photography. By delaying and reducing the gate duration, the light signal can be temporally filtered to isolate emission produced primarily by RTS, as shown in Fig. 4.27c.

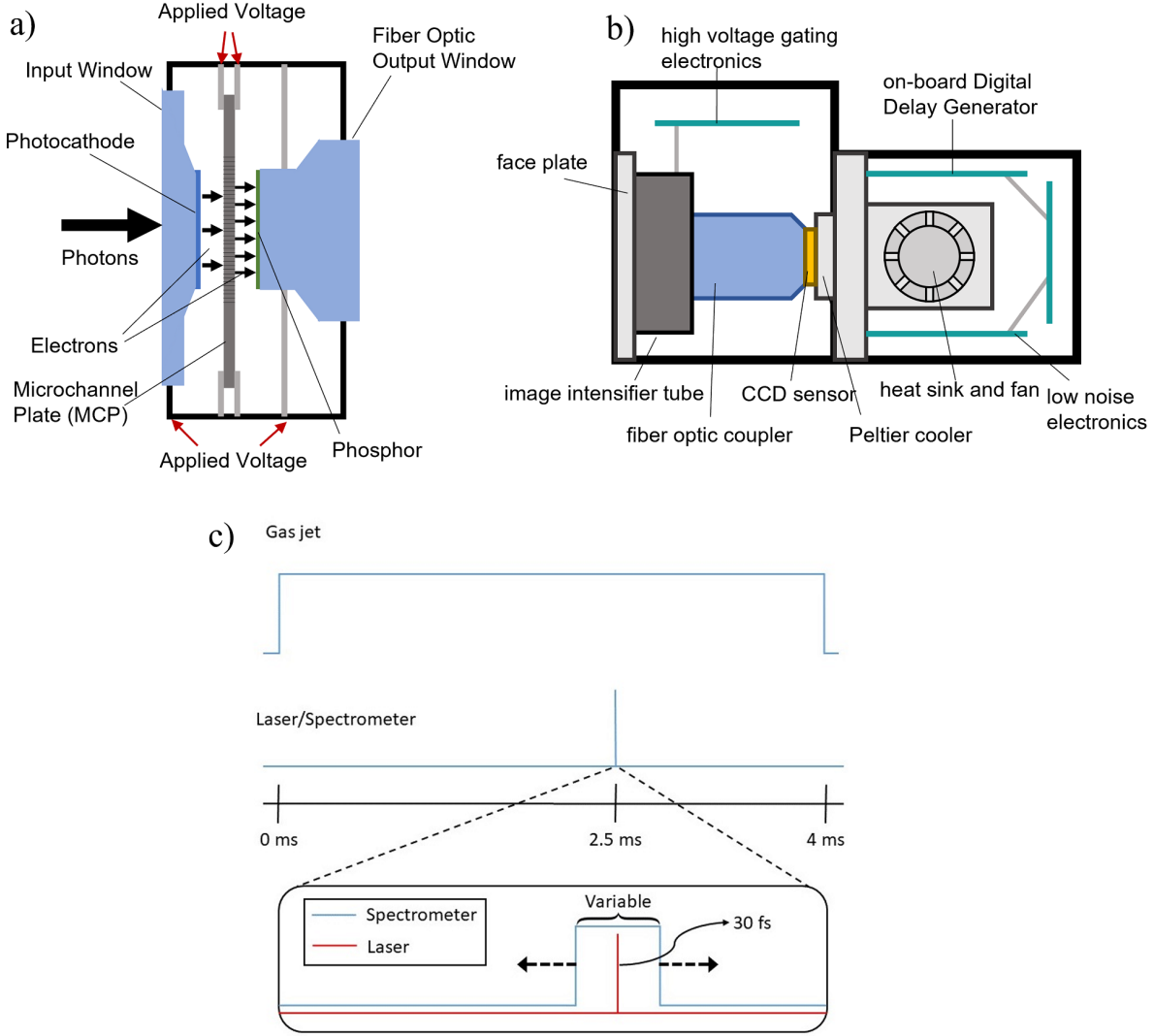


Figure 4.27: Diagrams of illustrating the intensified CCD camera and its gating operation. Shown are a) the image intensifier tube, b) the intensified CCD camera system containing the image intensifier, and c) timeline of the relative timing of the opening of the gas nozzle, laser arrival at focus, and time duration observe by the gated spectrometer. Diagrams a) and b) were adapted from [93].

The RTS signal was found in time by starting with a large gate width to capture the plasma recombination light, and then over a series of shots, reducing the gate width and adjusting the delay until a broadband signal is captured window 5 ns gate window. Fig. 4.28 shows the captured spectrum for various gate durations, τ_{gate} , around the arrival of the laser pulse, while Fig 4.29 shows that for varying delay shifts, Δt_{delay} , at $\tau_{gate} = 5$ ns.

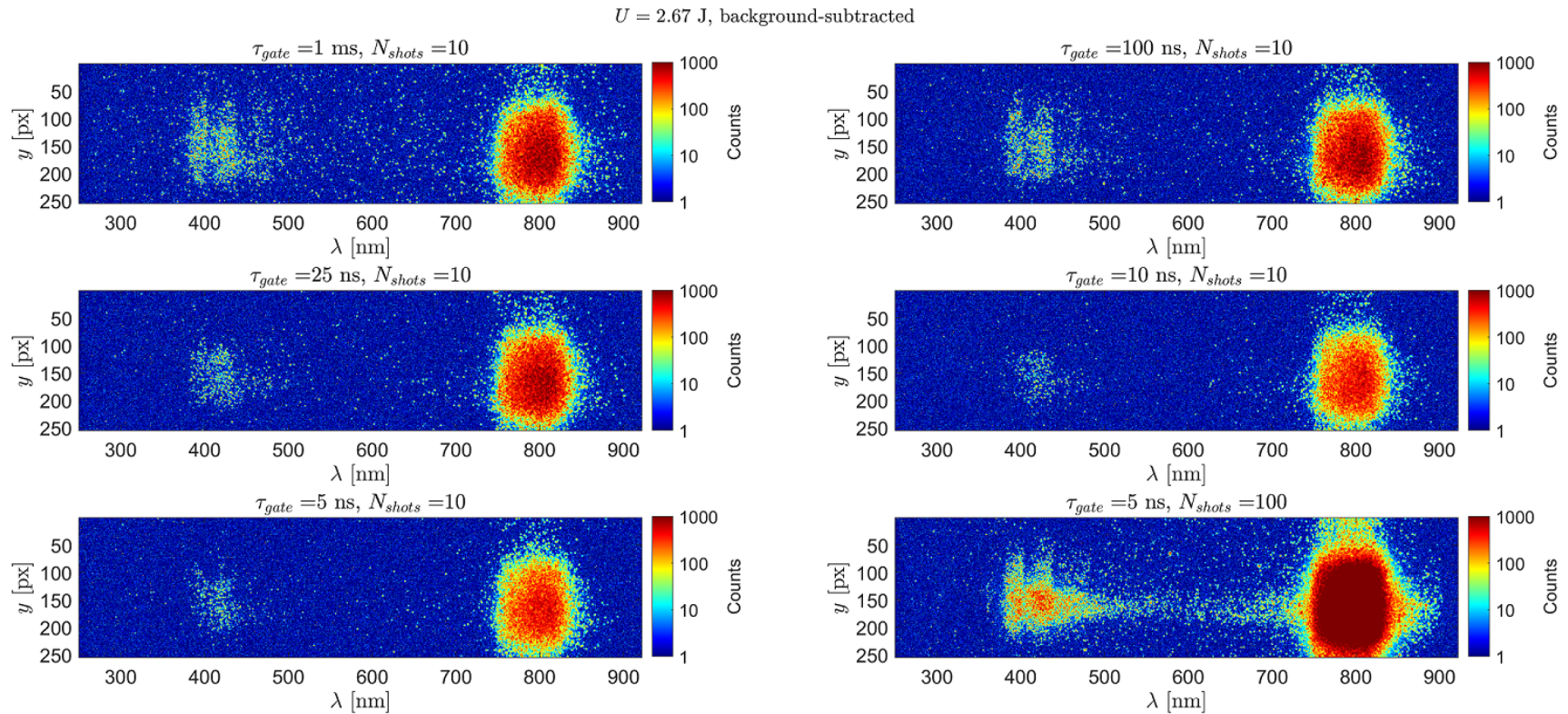


Figure 4.28: RTS spectra (background-subtracted) taken using the E_{\perp} objective over subsequently smaller gate durations, τ_{gate} . The images were captured with $U = 2.67 \text{ J}$ and the signal strength are plotted in a log scale. After achieving the smallest gate duration of 5 ns, an acquisition was taken for 100 shots (last image). For $\tau_{gate} = 1 \text{ ms}$ and 100 ns, the plasma recombination lines can be observed. For $\tau_{gate} \leq 25 \text{ ns}$, the plasma recombination light (380 to 550 nm) vanish for the $N_{shots} = 10$ data, but reappear as N_{shots} is raised to 100 shots, possibly owing to the overall increase in signal as well as the accumulated jitter and drift in the timing between the ICCD gate and laser pulse arrival time. The large patch of light from 750 to 850 nm comes from the scattered laser light. The y dimension on the images corresponds spatially to the displacement along the E polarization. The fact that the plasma recombination signal extends further out in y on the images than does the RTS is evidence that the ionization occur at lower intensities (including the fringes of the laser pulse) than that needed to generate an observable RTS signal, as expected physically.

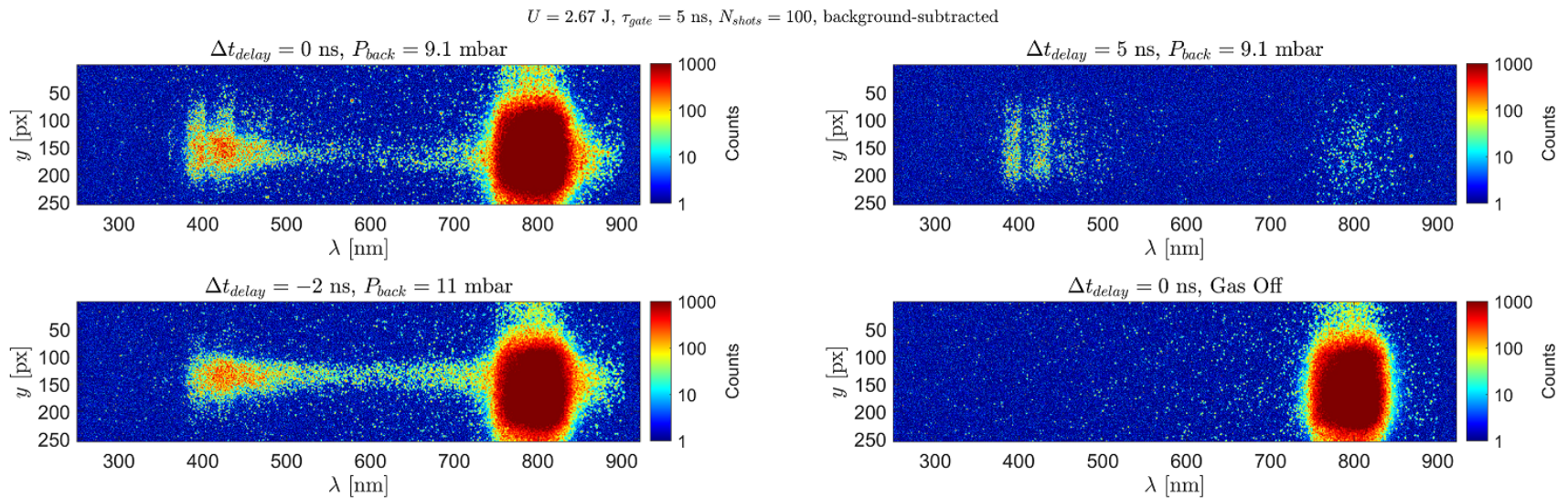


Figure 4.29: RTS spectra taken using the E_{\perp} objective with $\tau_{gate} = 5$ ns over various gate delay offsets, Δt_{delay} as well as a background spectrum. The images were taken for $U = 2.67$ J and integrated over 100 shots. The background spectrum (bottom right image) was taken by turning the pulsed nozzle off so that only the scattered laser radiation can be seen. The RTS radiation and scattered laser light all but vanishes for $\Delta t_{delay} = 5$ ns, leaving primarily the plasma recombination. For $\Delta t_{delay} = -2$ ns, the RTS signal is better optimized, as the plasma recombination is more filtered out. We note, however, that this optimization does not remain throughout all of the subsequent acquisitions, and eventually the recombination light does leak back in, owing perhaps to a drift in the ICCD gate trigger and pulse arrival.

The spectral data measured for varying values of τ_{gate} and Δt_{delay} show that the second harmonic RTS can be captured, albeit not without some contamination of plasma recombination light as well as scattered laser light. There is nevertheless a clean region from 550 to 700 nm over which the RTS spectrum can be observed and analyzed.

4.11 Results and Analysis

During the experiment, multiple spectrum images were captured over several shot batches at relativistic pulse energies. On 07/11/2018, measurements from the E_{\perp} -objective was taken at full pulse energy (2.67 J on target) and \sim 10 mbar backing pressure. On 07/13/2018, measurements were taken from the $E_{||}$ -objective were taken at three pulse energy settings (0.99, 1.73, and 2.67 J on target) and \sim 10 mbar backing pressure. While images without the use of a BG39 filter were captured for the E_{\perp} -objective, the filter was later implemented, via placement in front of the spectrometer slit, in order to cut down on the capture of scattered laser light. Each shot batch consisted of 100 shots, and background images (gas nozzle turned off) were also taken over several shot batches whenever parameters (energy, and placement of BG39) were changed. Spectrum images, averaged over 5 shot batches (5×100 shots) and background subtracted, are shown in Fig. 4.30.

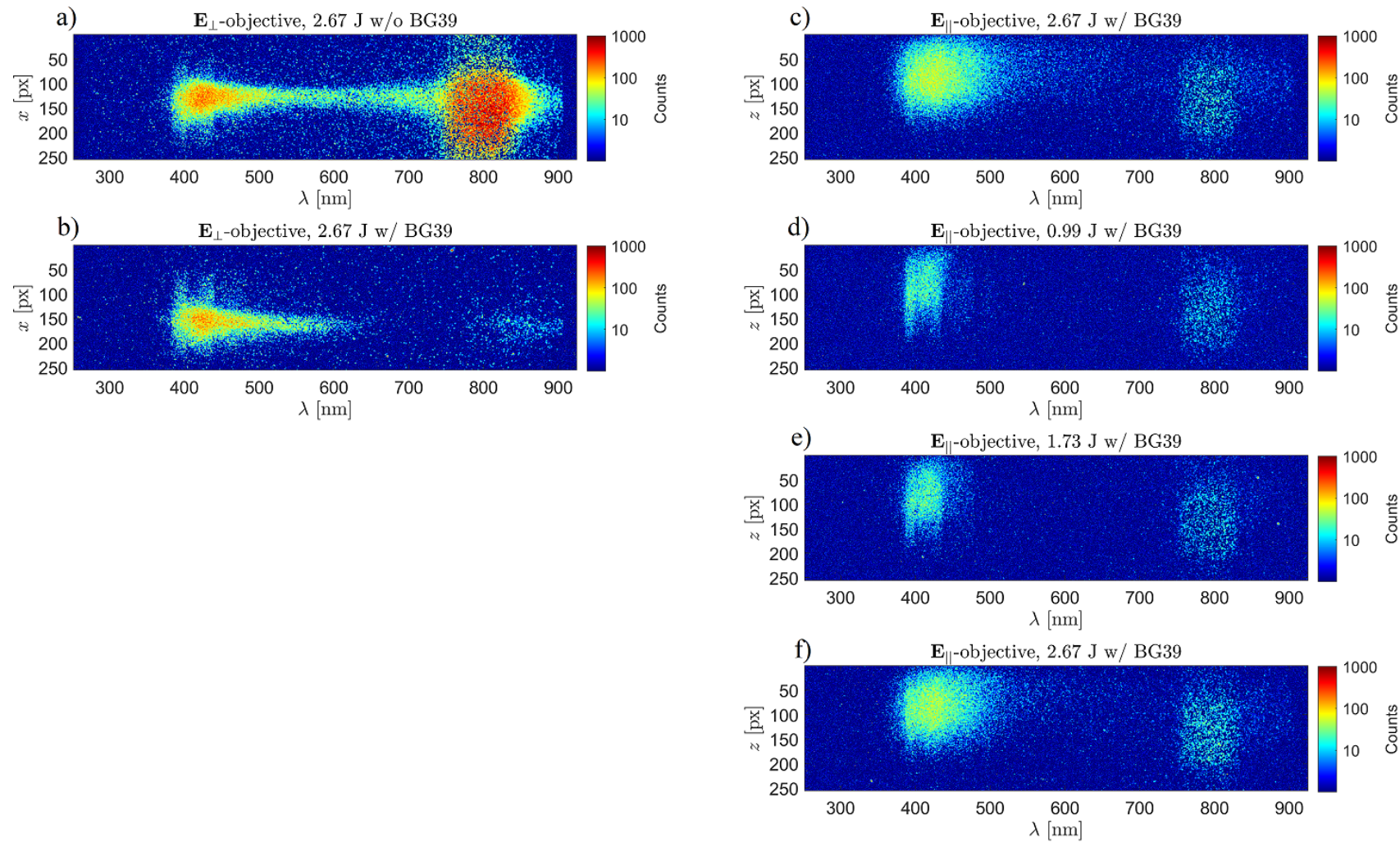


Figure 4.30: Spectrum images captured during the live laser shots by the E_{\perp} -objective (a-b) on 07/11/2018 a) with and b) without the use of a BG39 filter. Spectrum images captured by the E_{\parallel} -objective (c-f) on 07/13/2018 at different energies with the use of a BG39 filter, plotted in the chronologically order in which the data was taken. In all cases, the spectrometer slit width was open to 500 μ m.

There are several observations that can be made from the spectrum images. The first is that, for the E_{\perp} objective at the highest laser energy (2.67 J), the Doppler shifted second harmonic is strong and overlaps with the fundamental emission at the laser band. The second is that when the BG39 filter is applied, the Doppler shifted second harmonic signal at highest laser energy goes to background at around 650 – 700 nm. The third is when the energy is reduced (to 1.73 J and 0.99 J), the RTS signal along with the wavelength of the Doppler shifted tail diminishes. Finally, it can be seen throughout the spectrum images the presence of plasma recombination light, which contaminate the RTS signal. For the E_{\perp} -objective in particular, where the image of the laser is such that the propagation direction of the laser is orthogonal to the input slit, the plasma recombination light extends further out spatially (in this case, x) from the laser axis.

To determine a quantitative result for the onset wavelength, $\lambda_r^{(2)}$, the spectral images were first averaged over their vertical dimension to produce a spectral profile at each wavelength. The resulting spectral profiles from the $E_{||}$ -objective spectral images are shown in Fig. 4.31.

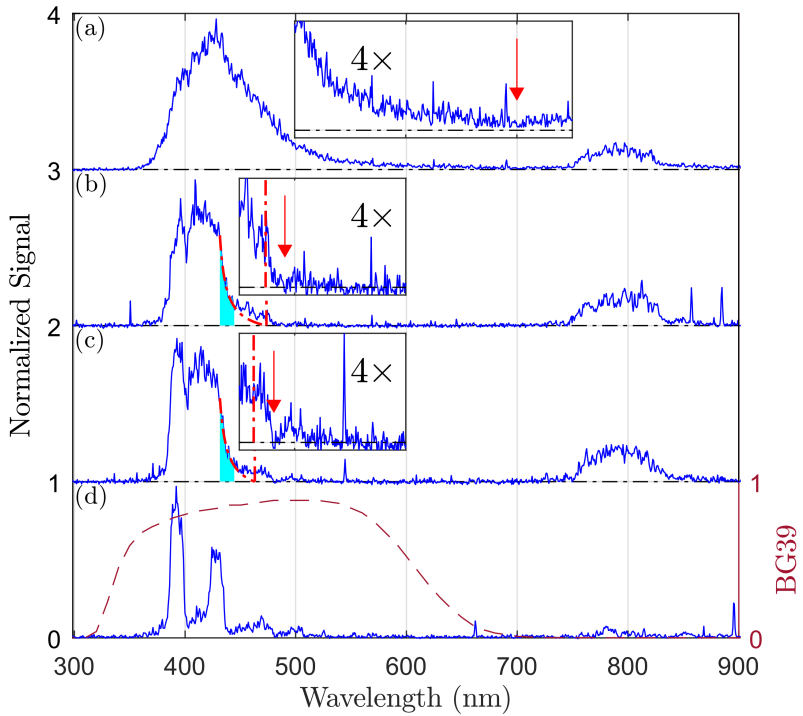


Figure 4.31: Plots of spectral profiles of the spectrum images for three values of pulse energy: a) 2.67 ± 0.08 , b) 1.73 ± 0.05 , and c) 0.99 ± 0.03 J and d) plasma recombination light with BG39 transmission curve. The spectral profiles correspond to the right column of Fig. 4.30 reordered from highest to lowest pulse energy.

After column averaging, $\lambda_r^{(2)}$ was determined by combining two approaches. In the first approach, $\lambda_r^{(2)}$ was determined by picking the longest wavelength extending from the second harmonic that goes to background, indicated by the red arrow. The second approach involves fitting a rational polynomial, $f(\lambda) = a + b/(\lambda + c)$ with a , b , and c being fitting parameters, over the region indicated by the shaded blue and finding the intercept of this function with background, indicated by the dash-dotted vertical lines. The final estimates of $\lambda_r^{(2)}$ are the average of the two approaches. For the high energy case of 2.67 J in Fig. 4.31a, the fact that $\lambda_r^{(2)}$ coincides with the tail of the BG39 transmission curve suggests that this method predicts, at best, a lower bound of the peak intensity. Using Eq. 4.1, with $\theta = 90^\circ$ and $\lambda_0 = 790$ nm, the corresponding peak

intensities for the various pulse energies used on target, U , are calculated and summarized in Table 4.9.

Table 4.9: Summary of the results of the second harmonic spectrum onset wavelength determined versus pulse energy on target, U . The uncertainty in U is based on a fluctuation of $\sim 2.65\%$ reported by the laser bay. The "Label" columns indicate the corresponding subplots in Fig. 4.30 and 4.31. The onset wavelength from using the two methods of the rational polynomial fit, $\lambda_r^{(2)}$ (fit), and the intercept of the signal with background, $\lambda_r^{(2)}$ (bg), are provided separately. Their average and standard deviation is given in the " $\lambda_r^{(2)} (\sigma_{\lambda_r^{(2)}})$ " column. The final calculated peak intensity using Eq. 4.1 is given in the " I_{pk}^{RTS} " column.

Label ¹	Label ²	U [J]	$\lambda_r^{(2)}$ (fit) [nm]	$\lambda_r^{(2)}$ (bg) [nm]	$\lambda_r^{(2)} (\sigma_{\lambda_r^{(2)}})$ [nm]	I_{pk}^{RTS} [W/cm ²]
c	a	2.67 ± 0.08	N/A	700	700 (0)	$(6.8 \pm 0.7) \times 10^{18}$
d	c	1.73 ± 0.05	474	481	472 (9)	$(1.7 \pm 0.4) \times 10^{18}$
e	b	0.99 ± 0.03	463	472	482 (9)	$(1.9 \pm 0.4) \times 10^{18}$
f	N/A	2.67 ± 0.08	640	625	632.5 (7.5)	$(5.3 \pm 0.6) \times 10^{18}$

¹ See Fig. 4.30, ² See Fig. 4.31

4.11.1 Comparison with Indirect Method

As a sanity check, we compare the intensities, I_{pk}^{RTS} , determined from $\lambda_r^{(2)}$ against the method used for estimating the peak intensities, I_{pk}^{Im} , based on using the focal spot images, as described in section 4.3. Using $\Delta t = 30$ fs, the estimated peak intensities for the corresponding pulse energies U for RTS spectra are $I_{pk}^{\text{Im}} = (2.2 \pm 0.4, 3.9 \pm 0.6, 6.0 \pm 1.0) \times 10^{18}$ W/cm². Fig. 4.32 shows the values of I_{pk}^{RTS} (data points) compared with those of I_{pk}^{Im} , plotted as a linear function of the laser energy U , at two values of Δt (30 fs and 60 fs).

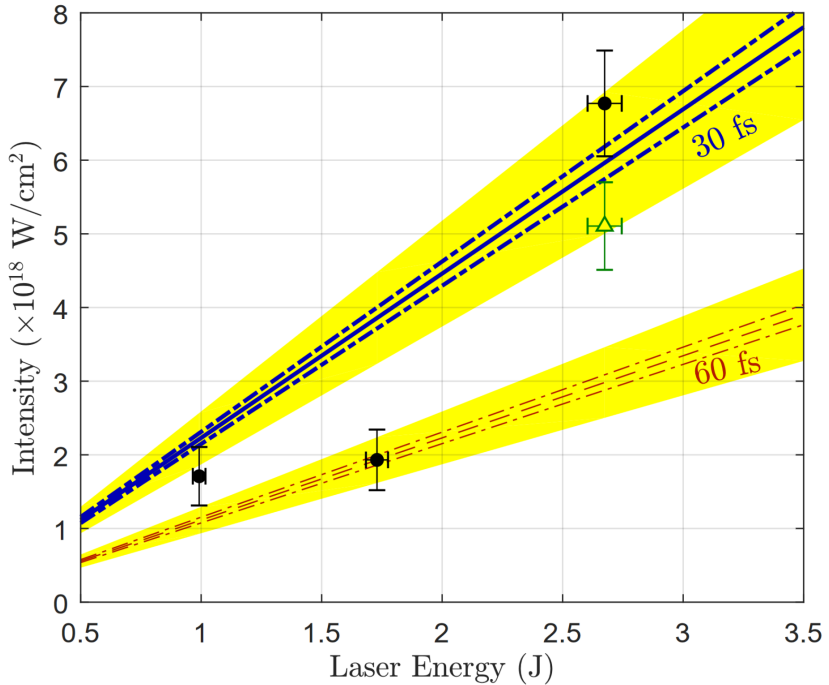


Figure 4.32: Plot comparing the predicted peak intensities from measurement of the second harmonic spectrum onset wavelengths (data points) to the peak intensities estimated from the focal spot images. The peak intensities calculated from the focal spot image assume a 30 fs (blue-solid) and 60 fs (red-dashed) pulse duration. The dot-dash indicates the uncertainty in the peak intensity from the focal spot image assuming the camera spatial calibration is known exactly (i.e., uncertainty in A_{pix} is 0). The shaded yellow indicates the uncertainty with the uncertainty in A_{pix} is taken into account. The data point represented by the green triangle was chronologically after the data points represented by the black dots.

4.12 Discussion and Conclusion

Given the uncertainties in $I_{\text{pk}}^{\text{RTS}}$ and $I_{\text{pk}}^{\text{Im}}$, the two methods are in general agreement. The data points with $U = 0.99$ and 2.67 J statistically agree with $I_{\text{pk}}^{\text{Im}}$ with $\Delta t = 30$ fs, while $U = 1.73$ J is in better agreement with $\Delta t = 60$ fs. There are several contributions to this. First, the RTS spectra is contaminated with plasma recombination light, making determination of $\lambda_r^{(2)}$ difficult. Second, the pulse width was known to drift by as much as a factor of 2 based on past experiments by another group using the same laser. This is corroborated by the fact that

the intensities predicted by the RTS spectra tends to decrease over time, as the order in which the data was taken was 2.67, 0.99, 1.73, and 2.67 J (the last in this list represented by the green triangle) over several hours. There was not a means to monitor the laser pulse duration during this experiment, and the laser was therefore not re-optimized after the initial optimization done at the beginning of the day. Changing the pulse energy typically requires re-optimization of the pulse duration for peak performance. It is evident that the method using RTS is capable of detecting changes in the peak intensity whereas the indirect method does not. Real-time monitoring of the laser characteristics is necessary for the indirect method to be viable for determining peak intensity.

Capturing RTS spectrum to use as an intensity gauge at $(\theta, \phi) = (\pi/2, 0)$ is useful between 10^{18} to 10^{19} W/cm². At some point $\sim 10^{19}$ W/cm², the harmonics begin to overlap, making it difficult to determine $\lambda_r^{(2)}$ as we have done here. Based on Eq. 4.1, the overlap between the harmonics may be offset to higher intensities by observing the radiation at smaller θ . This would run into issues, however, when the angle gets too small, as the laser itself would be collected by the detector. For the microscope objectives used in this experiment, for example, the full diameter of front face of the objective is 34 mm, which subtends a 32.5° half angle when placed at its working distance. In order to have a, say, 10° clearance from the laser axis for the laser pulse after focus, the minimum angle at which the objective's axis can be placed is 42.5°. To observe at shallower angles, it would be necessary to work with detectors with smaller numerical apertures. Downsides of going to smaller numerical apertures include the reduction of collected light and a longer depth-of-field.

Chapter 5

Experiment 2: Angular Distribution

Introduction

The premise behind measuring the RTS angular distribution stems from the idea that the angular emission pattern is expected to change with laser intensity. The overall emission would be more forward scattered, as expected, due to the forward component of electron motion that increases with the laser field strength and due to the effects of relativistic beaming. This would be true for electrons experiencing the peak of the field if the plane wave model derived by Sarachik and Schappert [55] is applicable to the real laser. Electrons outside of the peak of the field would still be expected to experience a higher intensity if the overall intensity distribution increases with the laser energy, however, ponderomotive scattering [58, 60] of the electron due to the laser gradient would need to be considered. Short of developing a full model of RTS scattered by a realistic laser, an experiment measuring the angular distribution could nevertheless still be carried out to probe an answer from nature.

In this chapter, we discuss the initial experiment in measuring the RTS angular distribution using 0.05 numerical aperture (NA), fiber-based light detectors mounted in a rotation stage to achieve angular variation while keeping the detectors at a constant radial distance from the focus. The light captured by the fiber is routed out of chamber and coupled into a spectrometer, as in the first experiment, consisting of an intensified charge-coupled device (ICCD) camera featuring a 5 ns minimum temporal gate. The RTS light is produced from free electrons ionized by a puff of

gas from a flared gas nozzle oriented from the side. Schematics of the main features are shown in Fig. 5.1.

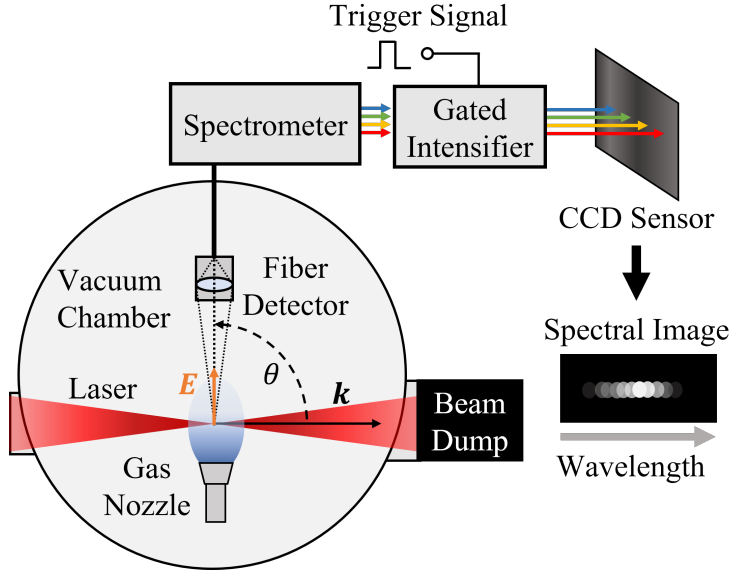


Figure 5.1: Diagram of experimental layout, with the target chamber viewed from the top. Relativistic Thomson scattering is produced at the focus of the VEGA-2 laser within a gas jet. The scattered radiation is captured by a fiber-based detector at an angle θ relative to k , rotating along the $E-k$ plane, and sent to a spectrometer with a gated intensified CCD camera. Figure is not to scale.

5.1 VEGA-2 Characteristics

As in the first experiment, the VEGA-2 beam of 11 cm diameter of a roughly supergaussian distribution (see Fig. 5.2a) of the near-field measurement) was focused in an $f/13$ geometry using an $f = 130$ cm off-axis parabolic mirror. The temporal intensity profile remained roughly Gaussian with small shoulders with a ~ 30 fs FWHM. The spectrum, on the other hand, as shown in Fig. 5.2b, is more strongly weighted towards the lower end of the ~ 755 to 825 nm distribution compared to the first experiment (see Fig. 4.6), but maintaining a strong subpeak at ~ 760 nm. This skewing in the spectrum relative to that from 2018 was observed throughout 10 days from

11/12/2019 to 11/26/2019.

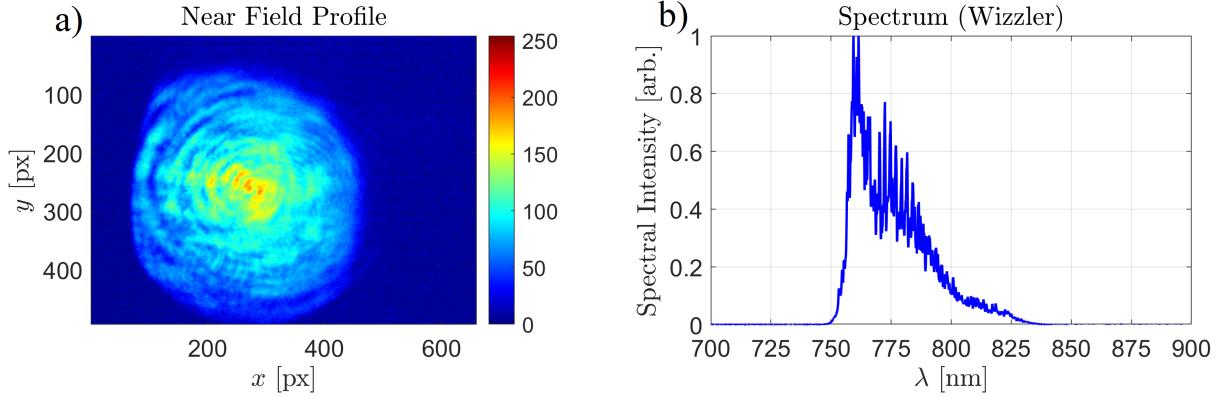


Figure 5.2: Plots of diagnostic measurements of the VEGA-2 beam from the laser bay metrology bench. Shown are the a) near-field beam profile, reduced in size with a non-aberrating telescope before captured with a camera, and b) the spectrum from the Wizzler, both at the metrology bench after the compressor. The near-field image has structure due to imperfections in the transport optics, and therefore only provides a general shape of the true profile. These measurements were taken on 11/26/2019.

The focal spot was imaged directly using an infinity-corrected microscope objective mounted on a pair of linear translation stages allowing for translation transverse and longitudinal to the beam. The image is routed outside of the chamber using a motorized mirror and focused onto a camera sensor. These components are shown in Fig. 5.3. The stages have a sufficiently long travel distance to move the microscope objective and mirror away from the beam path during the full power shots.

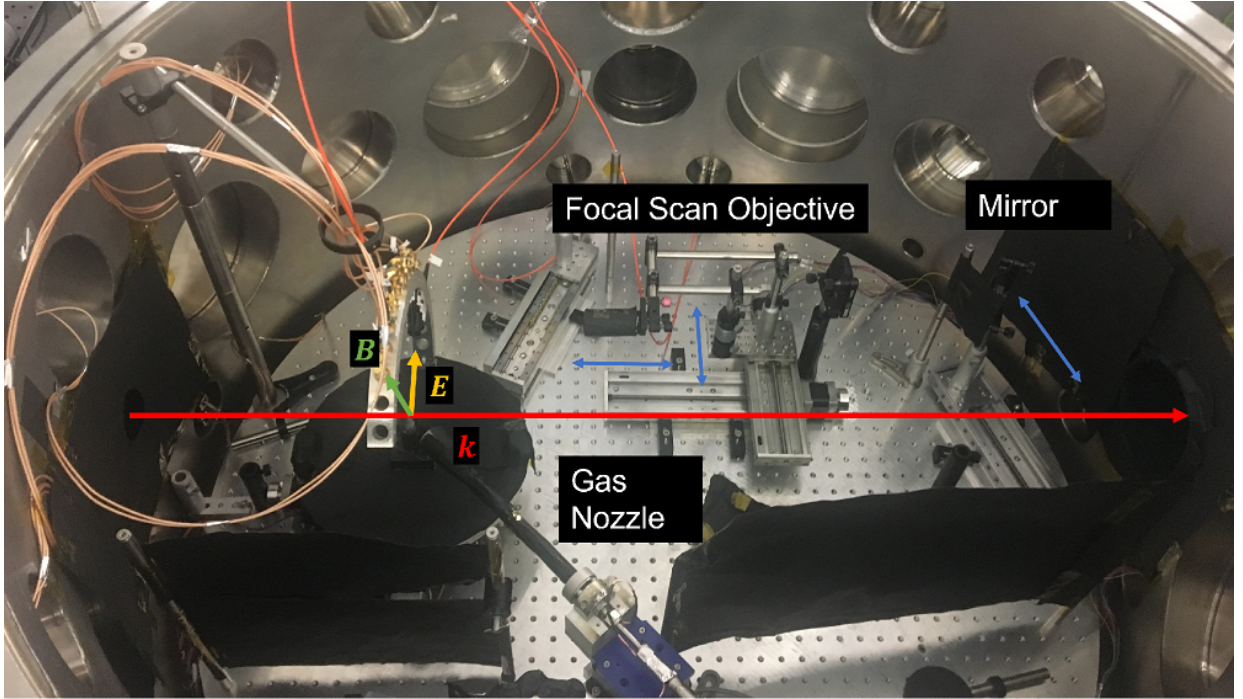


Figure 5.3: Annotated photo of the interior of the vacuum chamber containing experimental components, including the focal spot imaging system. The focal spot imaging system consists of an objective microscope and mirror mounted on motorized translation stages. The direction of the propagating beam is indicated, along with the E and B polarizations at the focus, around where the detectors and gas nozzle are centered.

The spatial calibration of the focal spot imaging system is accomplished using an United States Air Force (USAF) test pattern placed in the field of view and illuminated with a 850 nm diode, as shown in Fig. 5.4a. One can see that there is a spatial distortion of the image, however, since the image focal spot is confined within a small region of the image, as shown in Fig. 4.3b, it suffices to use the first illuminated pattern line closest to the central spot and along the horizontal line centered on the central spot $y = 0$ (see the lineout curve on Fig. 5.4c) as the fiducial. This illuminated line is 62.5 μm based on the known data for group 3, element 1 (G3E1) having 8 line pairs per mm. It measured 142 pixels across (in a 1920 px wide by 1200 px high image), resulting in calibration a of 0.44 $\mu\text{m}/\text{px}$. Assuming this calibration holds also in the y direction, the focal spot image is plotted in Fig. 5.4d in physical dimensions. As in the

first experiment, the distribution in the focal plane contains an approximately Gaussian central spot surrounded by a ring-shaped diffraction structure, but with imperfections resulting perhaps from the nonuniform structure in the near-field profile and aberrations in the beam transport and focusing optics. One can see a modulation structure in the azimuthal coordinate having 3 lobes over 2π . Furthermore, the laser light extends further than the imaging system allows, as can be seen in the log scale images of the background light having a sudden falloff, likely from clipping in the imaging system.

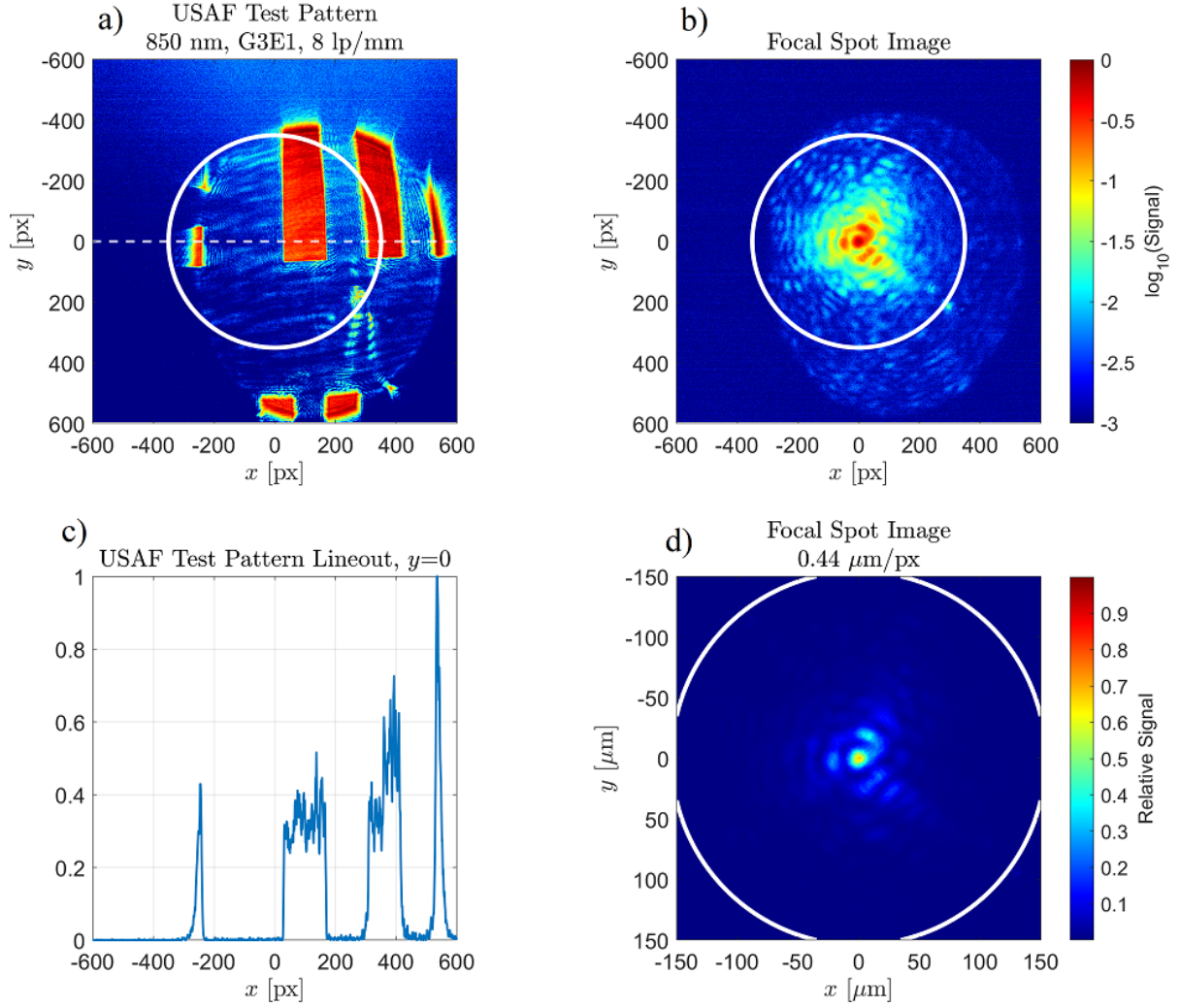


Figure 5.4: Images showing the focal spot and spatial calibration method. Shown are a) the USAF test pattern and b) focal spot image color-coded in a log scale; c) plot of the horizontal lineout centered on the focal spot (i.e., along white dashed line in a); and d) image of the focal spot image plotted in physical coordinates in linear scale. The white circles indicate the same region in the image containing the main focal spot distribution for comparison between images.

5.2 The All-Around Radiation Collector (AARC)

Measurement of the photon emission rates in various angles around the sphere required development of a new diagnostic. This diagnostic requires the directions, parameterized by the spherical-coordinate variables θ and ϕ , to be variable. Here, θ is the polar angle such that the

pole $\theta = 0$ is located along the \mathbf{k} direction relative to the focus and ϕ is the azimuthal angle such that $(\theta = 90^\circ, \phi = 0)$ corresponds to the $\hat{\mathbf{x}}$ direction, or direction of \mathbf{E} polarization and $(\theta = 90^\circ, \phi = 90^\circ)$ corresponds to the $\hat{\mathbf{y}}$ direction, or the direction of \mathbf{B} . While there are different ways to achieve this, a preferred design would be simple to calibrate and operate, cover a wide range of angles, be compact so as to allow other components to be used around the focus without obstruction, and be compatible with different types of detectors. These features were built into the design of our apparatus, which we call the All Around Radiation Collector (AARC), whose CAD drawing is shown in Fig. 5.5.

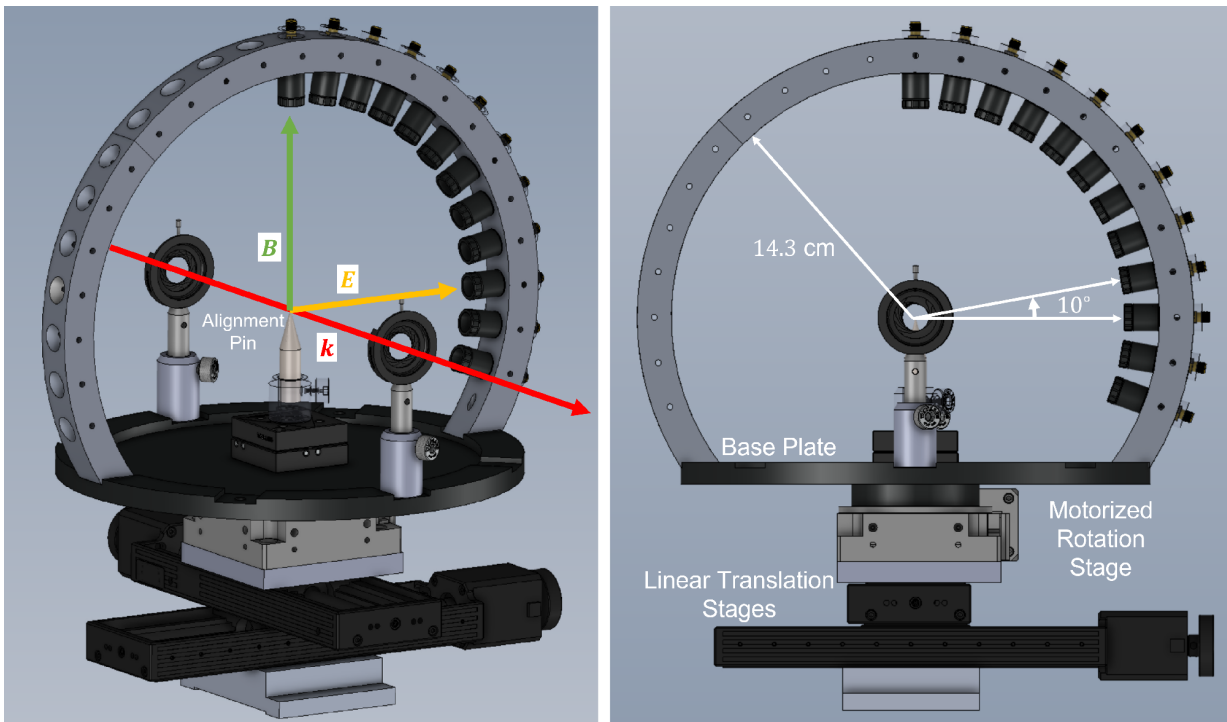


Figure 5.5: Models of the AARC showing an isometric (left) and front (right) view. The AARC was designed by Andrew Longman and machined at the University of Alberta.

The AARC consists of pieces of aluminum structure, in the shape of an arc machined to different lengths and consists of 5/8 inch slots separated by 10° that allow for the mounting of detectors consisting of 1/2 inch optics. Each arc piece is designed to attach to a mounting base,

so that each detector is oriented looking towards the laser focus at a uniform distance from the focus (~ 14 cm, determined by the arc piece's radius of curvature). The arc piece fits into a 25 mm wide slot machined to a tight tolerance in the mounting base. The base itself is in the shape of a disc and mounted on a motorized rotation stage (Standa 8MR191V) which rotates about an axis perpendicular to the chamber floor and parallel to \mathbf{B} . The motorized rotation stage allows the detectors mounted in the arc to scan through different values of θ and ϕ , which can be calculated from the angular position of the rotation stage and the angular position of the slot occupied by the detector.

The AARC pieces were machined by first cutting out the arc shapes (inner radius 143 mm, outer radius 163 mm) with a water jet out of a 1 inch thick plate made of high grade hardened aluminum. Each piece was then fitted a jig and mounted on a Haas 5-axis CNC rotary table, which finished the shape of the piece and ream the holes for the detector slots. The diameter of the 5/8 inch detector slots had a tolerance that was over-specified by 2 thou to allow for expansion of brass inserts. The tolerance of each dimension was on the order of 1 thou.

Since the rotation of the AARC is about $\hat{\mathbf{y}}$ whereas the definitions of θ and ϕ are relative to the pole directed along $\hat{\mathbf{z}}$, a conversion is necessary from a detector mounted at arc position, ϕ_{Arc} , with AARC rotation angle, θ_{Arc} . The relationship is given by:

$$\theta = \left| \text{atan2} \left(\sqrt{\cos^2 \phi_{\text{Arc}} \cos \theta_{\text{Arc}}^2 + \sin^2 \phi_{\text{Arc}}}, \cos \phi_{\text{Arc}} \sin \theta_{\text{Arc}} \right) \right| \quad (5.1)$$

$$\phi = \text{atan2} (\sin \phi_{\text{Arc}}, \cos \phi_{\text{Arc}} \cos \theta_{\text{Arc}}) \quad (5.2)$$

where atan2 is the four-quadrant inverse tangent function (defined over the range $-\pi$ to π) given in terms of the ordinary inverse tangent (defined over the range $-\pi/2$ to $\pi/2$) by:

$$\text{atan2}(y, x) = \begin{cases} \tan^{-1}(y/x) & (x \geq 0) \\ \pi - \tan^{-1}(y/x) & (x < 0, y \geq 0) \\ -\pi - \tan^{-1}(y/x) & (x < 0, y < 0) \end{cases} \quad (5.3)$$

The mapping between $(\theta_{\text{Arc}}, \phi_{\text{Arc}})$ and (θ, ϕ) is illustrated in Fig. 5.6.

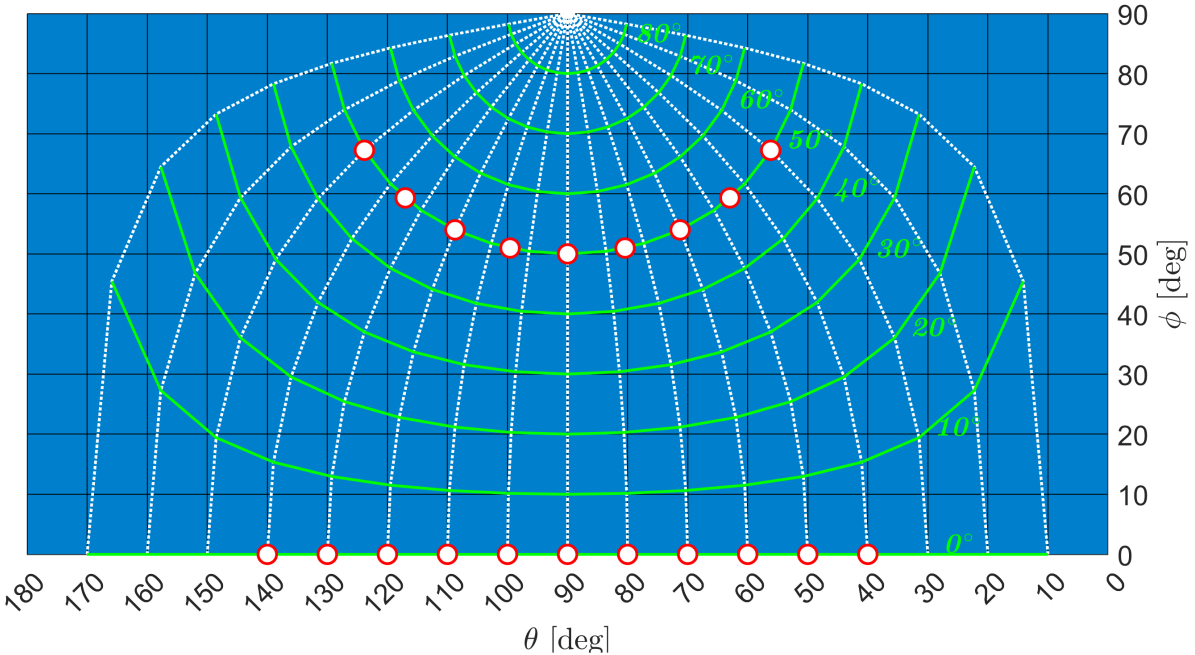


Figure 5.6: Plot of the mapping between $(\theta_{\text{Arc}}, \phi_{\text{Arc}})$ and (θ, ϕ) . The green contours represent the paths each mounted detector (fixed values of ϕ_{Arc} from 0° to 90° at 10° intervals) traverses when the AARC is rotated to an angle θ_{Arc} equal to θ at $\phi_{\text{Arc}} = 0^\circ$. Fixed values of θ_{Arc} are traced out by the dotted white lines. The red circles indicate detector positions used in the experiment.

5.3 Fiber Optic Detectors

Our detectors, as shown in the diagram in Fig. 5.7, each consists of an AC127-019-A ($f = 19$ mm) doublet lens of 1/2 inch diameter [94] inside an S-Mount filter holder (Edmund Optics 63-952) [95] that is threaded onto a 5/8 inch diameter cylindrical brass housing with

a HASMA SMA adapter [96] and an SMA fiber optic cable (M114L02) [97] attached at the opposite end. The fiber optic cable has a 600 μm core and a 0.22 numerical aperture. This detector is designed to image the focus \sim 13 cm from the lens onto the aperture of the optical fiber located on the imaging plane behind the lens. A visible band, interference shortpass filter, with a cutoff wavelength of 725 nm is placed in front of the lens to reject scattered laser light. A 3D printed shim of a length calibrated to maximize the detector efficiency is placed between the filter holder and the HASMA adapter to keep the fiber aperture at the right distance.

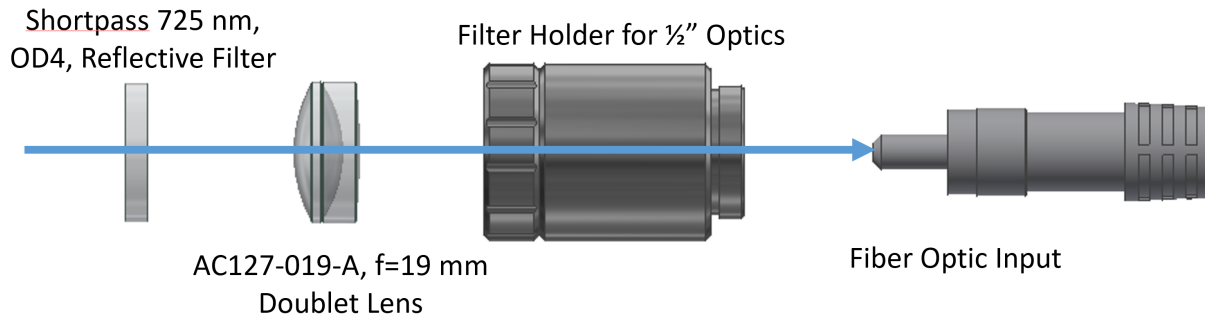


Figure 5.7: Exploded diagram of the fiber-based detection optics. Shown are a shortpass filter, doublet lens, filter holder, and fiber optic input. The brass housing, fiber shim, and HASMA adapter are not shown.

5.3.1 Coupling to Spectrometer

The light captured by the fiber adapter was coupled out of the vacuum chamber and then into a spectrometer (Oriel MS260i) with a gated intensified CCD camera (Andor iStar DH 720-25U-03 ICCD). The spectrometer grating was rotated to reflect light from \sim 200 – 900 nm onto the camera sensor, which has a horizontal (vertical) pixel resolution of 1024 (255), producing an image whose horizontal pixel position is linearly proportional with the wavelength (\approx 1.5 nm per pixel). The ICCD camera has a 5 ns gate, which serves as a temporal filter that removes plasma recombination light occurring during the few hundred ns following laser ionization.

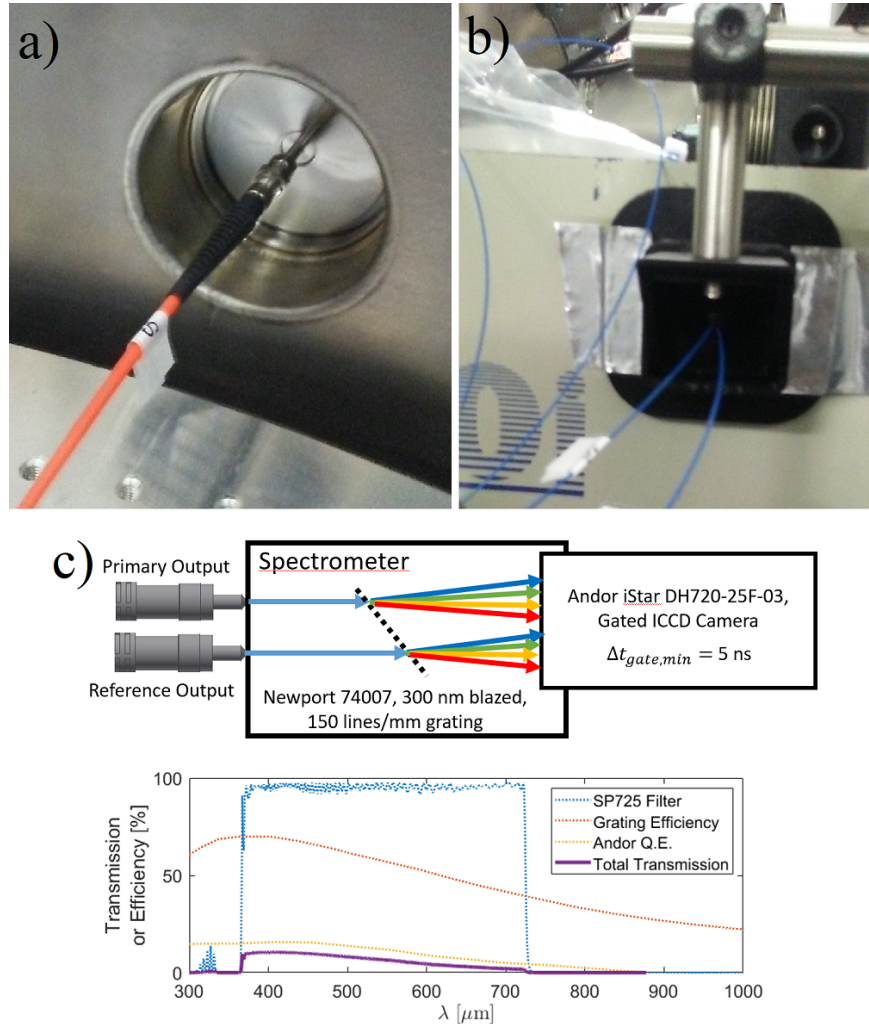


Figure 5.8: Photos of a) the fiber connected to a vacuum fiber feedthrough, b) bare fibers coupled into the spectrometer input via a 3D printed mount. Diagram, c) of the two coupled fibers into the spectrometer with a plot of the spectral responses of various components, including the total response.

5.3.2 Wavelength Calibration

The wavelength calibration is done, as in the first experiment, by capturing room lights into the spectrometer, this time using the two fiber lines. The 150 lines/mm grating was used and set to a 500 nm central wavelength. From the room light spectrum, as shown in Fig. 5.9, the pixel locations of four peaks are selected and compared with the NIST tables of strong mercury (Hg)

emission lines at 404.6, 435.8, 546, and 614.9 nm, producing a calibration equation (for a 1024 pixel wide image) given by:

$$\lambda[\text{nm}] = 196.59 + 0.6657 \times x_{\text{px}} \quad (5.4)$$

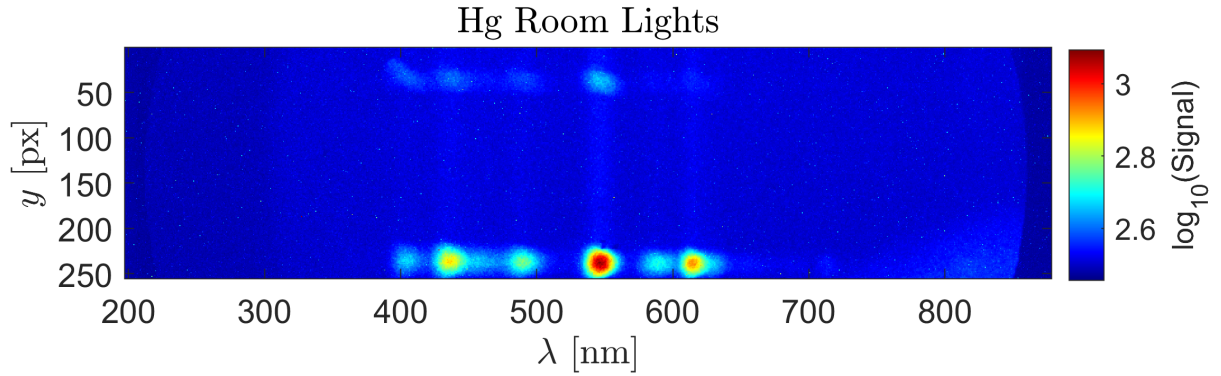


Figure 5.9: Spectrometer image of the mercury (Hg) room lights captured by two optical fiber lines from the detectors mounted in the AARC. One fiber contributes to the signal in the image above $y = 50$ px, while the other fiber contributes to the signal below $y = 200$ px. The difference in signal strength is due to one fiber oriented downwards and away from the room lights, while the other fiber oriented horizontally and towards the room lights.

5.3.3 Alignment of Detection Optics

To facilitate the centering of the AARC, an alignment pin with a cone-shaped end is placed using a magnetic mount at the center of the base of the stage so that the tip of the cone end is located at the center of curvature of the arc pieces. The rotation stage is mounted on two linear translation stages (PI VT-80 series with 150 mm travel), allowing translation of the AARC parallel as well as perpendicular to the laser beam, in a plane parallel to the chamber base. The focal plane is found using an imaging system looking at the best focus of the laser beam. The translation stage of the AARC that is longitudinal to the laser is moved so that the best focus of

the alignment pin overlaps with the best focus of the laser. A glass bead pre-adhered to the tip is illuminated by a 400 nm blue diode laser, similar to what's shown in Fig. 5.10a, through a beam traveling the reverse path of the imaging system, and the translation stage transverse to the laser beam is moved so that the signal from the illuminated bead is optimized. For the fiber detectors, this signal is shown in the spectrometer as a spot centered around 400 nm, as in Fig. 5.10b. The home position of the rotation stage is established using two irises placed diametrically apart.

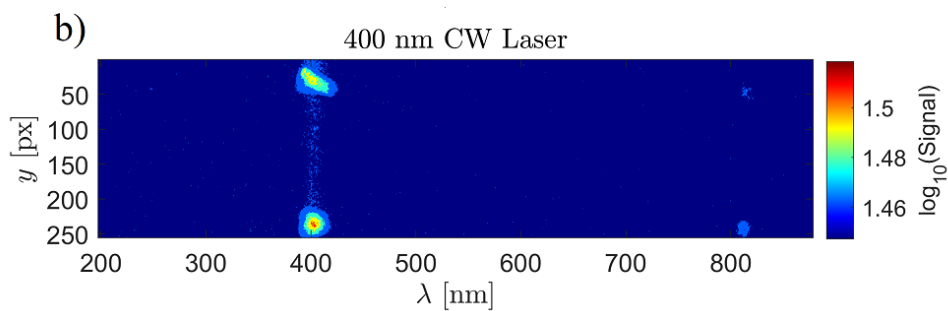
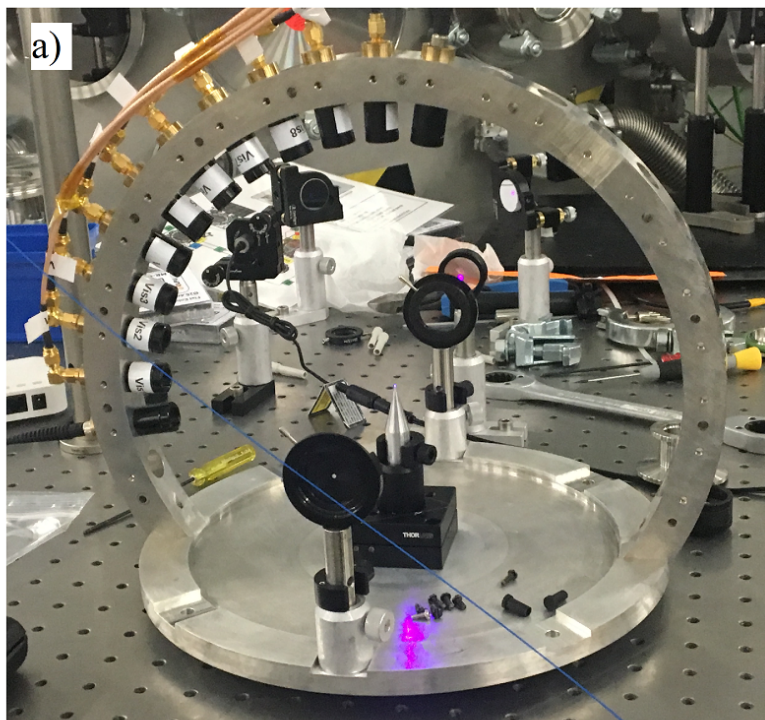


Figure 5.10: Photo, a), of the AARC assembly with a blue diode laser illuminating the glass bead mounted on the alignment tip, and b) the signal of the illuminated bead captured by the fiber detectors and spectrometer system.

5.4 Scattered Light Mitigation

After the focus, the beam was sent through a port into a beam dump chamber, as shown in Fig. 5.11. The beam dump chamber consists of a 5×3 array of 2" square neutral density (ND) filters of optical density (OD) 5, mounted on an aluminum frame to form a 10" \times 6" rectangular filter. The ND filters were glued to the frame using Torr-seal and the gaps between the filters were filled with NOA 88 optical adhesive using a syringe and UV cured at 365 nm. The mounted filter set was oriented at Brewster's angle relative to the laser to minimize the proportion of reflected laser light at the filter's front surface. The transmitted laser light travels through the filter twice, the second path occurring after reflecting off of the aluminum frame. The result is attenuated laser light that gets scattered within the beam dump chamber, whose walls are covered with black aluminum foil secured with Kapton tape. This beam dump arrangement helps reduce the amount of scattered laser light that end up being transmitted into the detectors.

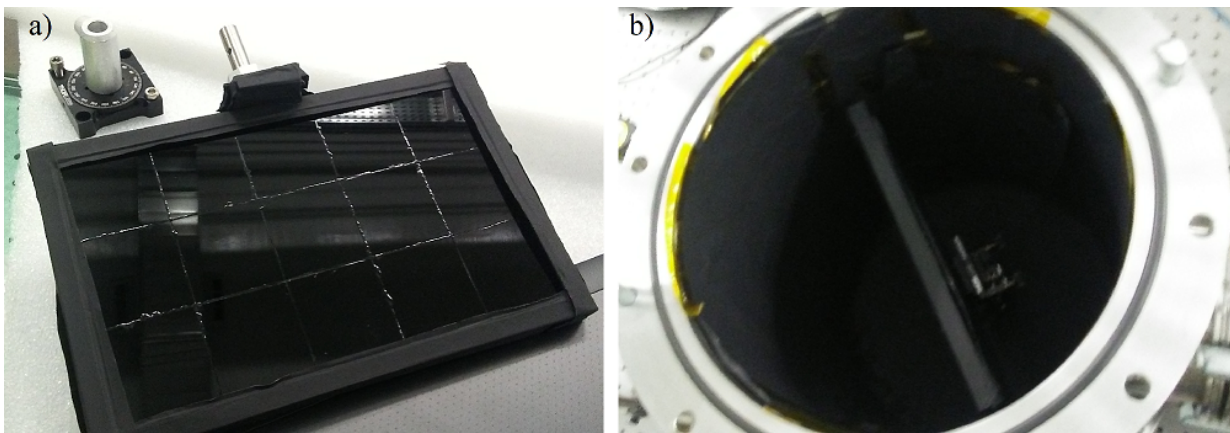


Figure 5.11: Photos of a) the beam dump consisting of an array of ND filters glued to an aluminum frame and b) the beam dump chamber with the beam dump mounted at Brewster's angle relative to the beam. Credit: Andrew Longman for the original design of the beam dump frame.

5.5 Gas (Electron) Source

To introduce the nitrogen gas used to produce electrons from laser ionization in focal region, we used a pulsed gas nozzle connected to a reservoir chamber back-filled with nitrogen, both shown in Fig. 5.12. The gas pulse duration was ~ 4 ms, producing a quasistatic gas cloud at the focus during the short (~ 30 fs) duration of the laser pulse including the prepulse (\sim ps). The reservoir chamber ensured that the backing pressure of the gas nozzle remained constant over subsequent pulses. The gas nozzle is mounted on a motorized translation stage to allow the distance from the laser focus to be varied. For the results discussed in this paper, a pressure of 200 mbar was maintained in the reservoir chamber and the mouth of the nozzle was located at a distance of 4.5 cm from the focus, leading to an estimated $\sim 10^{-3}$ mbar, at the laser focus based on simulations modeling the gas nozzle using MolFlow, which predicts $\sim 10^{-5}$ mbar at focus per mbar backing pressure. After each gas pulse, the focal region equilibrates to the background chamber pressure of $\sim 4.6 \times 10^{-6}$ mbar before the next pulse.

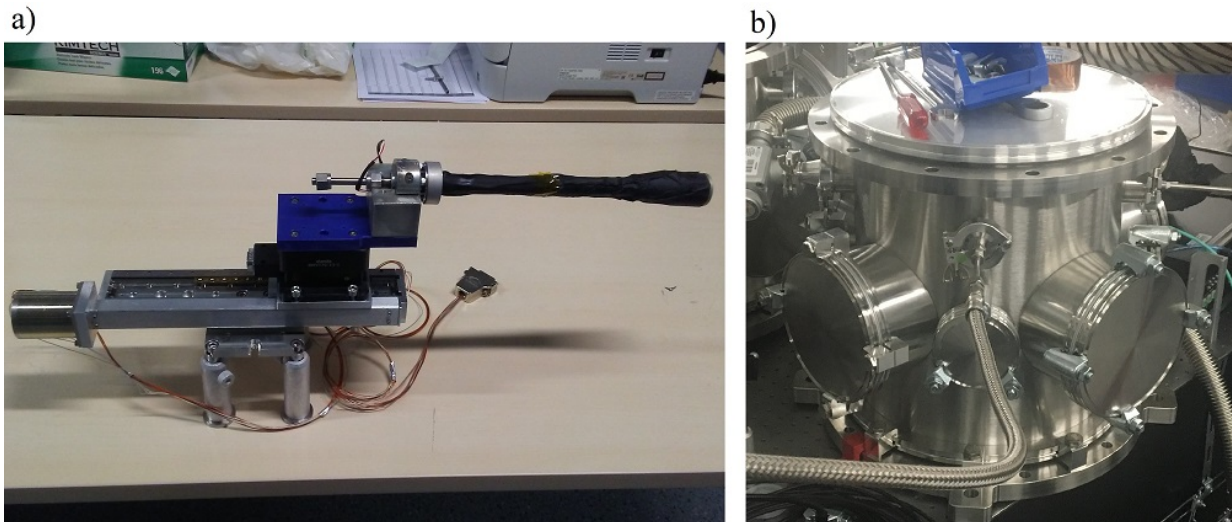


Figure 5.12: Photo of a) the gas nozzle and b) the reservoir chamber. Credit: Andrew Longman for the original design of the gas nozzle system.

5.6 Experimental Procedure

The AARC was scanned over a range of angles from $\theta = 40^\circ$ to 140° , in increments of 10° , for the primary detector mounted in the $\vec{E} - \vec{k}$ plane, capturing, for each angle, a spectrometer image from the accumulation of 256 laser shots fired at 1 Hz with the gas nozzle pulsing at each shot. Background images were also captured under the same conditions for a limited set of angle positions by keeping the gas nozzle closed during the laser shots and data acquisition. Two sets of scans were conducted: one for a laser pulse energy of 3.4 J at the focus and another for 1.9 J.

5.7 Analysis

5.7.1 Image Processing

The first part of analysis involves processing the image to produce the best representative spectrum. This includes 1) hot spot removal, 2) background subtraction, and 3) image rotation. An example of the process is shown in Fig. 5.13, which is explained in the paragraphs below.

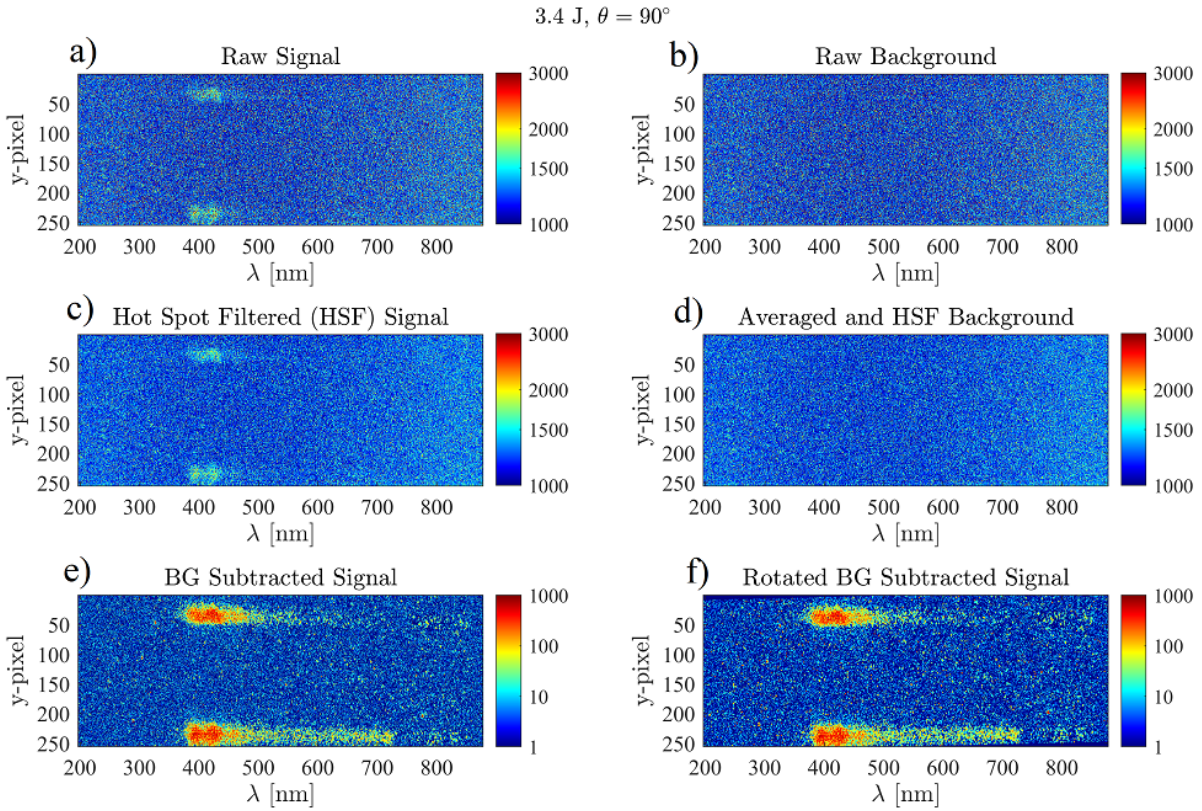


Figure 5.13: Spectrometer images showing the image processing steps. The raw signal, a), is applied a hot spot filter producing c). The raw background, b) is also applied the same hot spot filtering technique, and the average over all backgrounds in a set is shown in d). The signal image is then subtracted by the averaged background image, resulting in e), and then rotated and re-cropped, f).

Starting with the raw signal and background images, examples shown in Fig. 5.13a and b, the first step of image processing involves removal of "hot spots," which are pixels on the camera sensor that consistently read anomalously high counts. This could be due to damage to the pixels themselves, or the inherent pattern noise of the pixels. Whichever the case, a map of such pixels can be obtained by correlating the set of background images to locate pixels whose counts were above the threshold of 2000 and appeared in every background image in the set. This map is then used on each individual raw image (including signal and background) to find and remove the mapped hot spots by replacing each hot spot with the average of the set of pixels within the

3×3 region around the hot spot with counts < 2000 . This is then followed up by locating pixels, for each image, whose counts are greater than a threshold of 3000 and removing those hot spots in the same below-threshold, 3×3 pixel region averaging method. Finally, we deal with the individual hot spots that are between 2000 and 3000 counts but did not appear in every image. We found one such hot spot and eliminated it from our calculations. An example of the resulting hot spot filtered image is shown in Fig. 5.13c, where upon a close inspection, it can be seen that many pixels whose values were previously > 3000 in Fig. 5.13a have been replaced with values closer to their surrounding pixels.

In the next stage of image processing, an average background for each image set, like that shown in Fig. 5.13d for the 3.4 J , $\phi_{\text{Arc}} = 0^\circ$ set, is generated from the set of background images (also hot spot filtered) by performing a simple average on each pixel. Averaging over the set of backgrounds gets rid of fluctuations between individual backgrounds, which would otherwise affect the final result, due to the low signal-to-noise levels of the RTS signal. Each signal image in a set is subtracted by the averaged background image. This is followed by a subtraction of the residual background, which was a small bias in the regions outside of the signal distribution. The result is a background subtracted image, of which an example is shown in Fig. 5.13e.

The final stage of image processing involves rotating the background subtracted images by 1° in order to square up the spectral distributions, using the cubic interpolation method for the imrotate() function in MATLAB. Additionally, we crop the image produced by the rotation function back to the original dimensions of 1024×255 . An example of the rotated image is shown in Fig. 5.13f.

5.7.2 Region of Interest

The spectral images, having signal extending from 400 to 725 nm, provides flexibility in choosing the wavelength band for calculating the angular distribution. The plasma recombination spectra obtained in Experiment 1 (Chapter 4) had shown that there are plasma recombination in the range around 400 to 500 nm. We observe in the spectra captured by the fibers that there is signal extending as far towards the infrared as ~ 700 nm, petering out at the longer end. The wavelength band from 601 – 650 nm was therefore chosen for its lack of plasma recombination light and presence of Doppler shifted RTS signal.

The selection of 601 – 650 nm as the wavelength band to be analyzed requires a determination of a region of interest (ROI) from which to calculate a representative value for the number of emitted photons at each angle of measurement. In the case of the spectrometer images, the ROI was simply defined as a box of pixels centered on the RTS signal and wavelength band. The height of the box was determined by analyzing the distribution of the signal strength along the y coordinate, with the goal of sampling the signal while avoiding background. The height was chosen to be 10 pixels, which provides the largest sampling of the signal without sampling into the regions of the distribution where the signal strength drops off substantially. The width of the box was determined by the pixel range corresponding to the 601 – 650 nm band based on the wavelength calibration. Figure 5.14 shows the ROI annotated over a spectrum image.

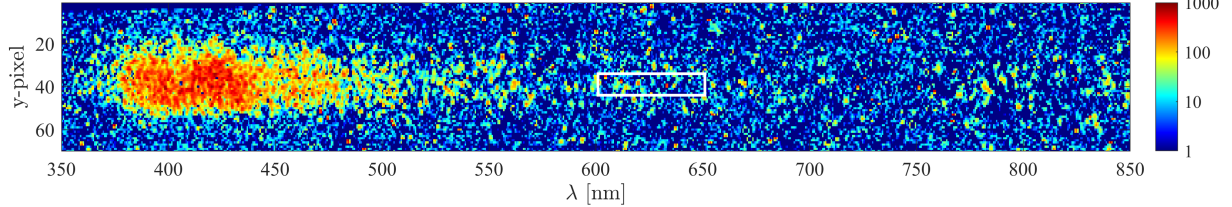


Figure 5.14: Cropped image of the RTS spectrum captured by the fiber mounted at $\phi_{\text{Arc}} = 0$. The region of interest used for calculating the signal strength as the AARC is rotated is indicated in the white box.

From each image, we take the mean of the pixels in the region of interest as the value representing the photon emitted at the corresponding angle. For the uncertainty in this value, we considered two sources: 1) statistical uncertainty, i.e., the square root of the total number of counts divided by the number of pixels in the ROI, and 2) the fluctuation of the ROI mean when we shift the ROI horizontally by about ± 10 nm, quantified by the standard deviation. It turns out that the statistical uncertainty is at least two orders of magnitude smaller than the fluctuation from the wavelength shift. To obtain a final uncertainty, we averaged over the set uncertainties obtained from the ROI of each set of images (each set containing acquisitions at all angles for the same laser pulse energy). This uncertainty is used for all data points, as it is a representative of the real uncertainty that includes scattered light, residual hot spots, etc., and which we expect to be uniform.

5.8 Results

The feature of interest in the angular distribution is the angular location of the dip, we call θ_{\min} , appearing between 60° and 90° . Theoretically, this dip corresponds to the hole of the donut-shaped distribution from Thomson scattering bending forward as a result of relativistic distortions as the laser intensity increases. Since the experimental data had an angular resolution

of 10° and contain signal contributed by substantial noise sources, it is difficult to determine a value of θ_{\min} . Figure 5.15 shows the angular distribution data obtained from the spectrometer images along with parabolic fits to select data points and fitting metrics. One can see that the general shape of the distributions show the existence of dips between 60° and 90° .

In an attempt to model the dip, the range of data points around where the dip is apparent were fitted to parabolas. The parabolic fits were performed by minimizing the χ^2 value between the data and the model, $M(\theta_i) \equiv A(\theta_i - B)^2 + C$, by varying the parameters, A , B , and C in the model, and choosing the best fit values. The formula for χ^2 is given by:

$$\chi^2 = \sum_i \frac{(S_{\text{RTS}}(\theta_i) - M(\theta_i))^2}{\sigma_S^2} \quad (5.5)$$

where $S_{\text{RTS}}(\theta_i)$ is the relative RTS signal measured at θ_i and σ_S is the uncertainty in the RTS signal (taken to be uniform across all θ_i). The value of θ_{\min} is equal to the parameter B from the model which minimizes the χ^2 value and corresponds to the parabola vertex. Using the vertices of the parabolic fits as an estimation of θ_{\min} as shown in Fig. 5.15c, there is a trend towards smaller angles at higher pulse energies. Values of χ^2 are shown in 5.15d and the corresponding p values in 5.15e.

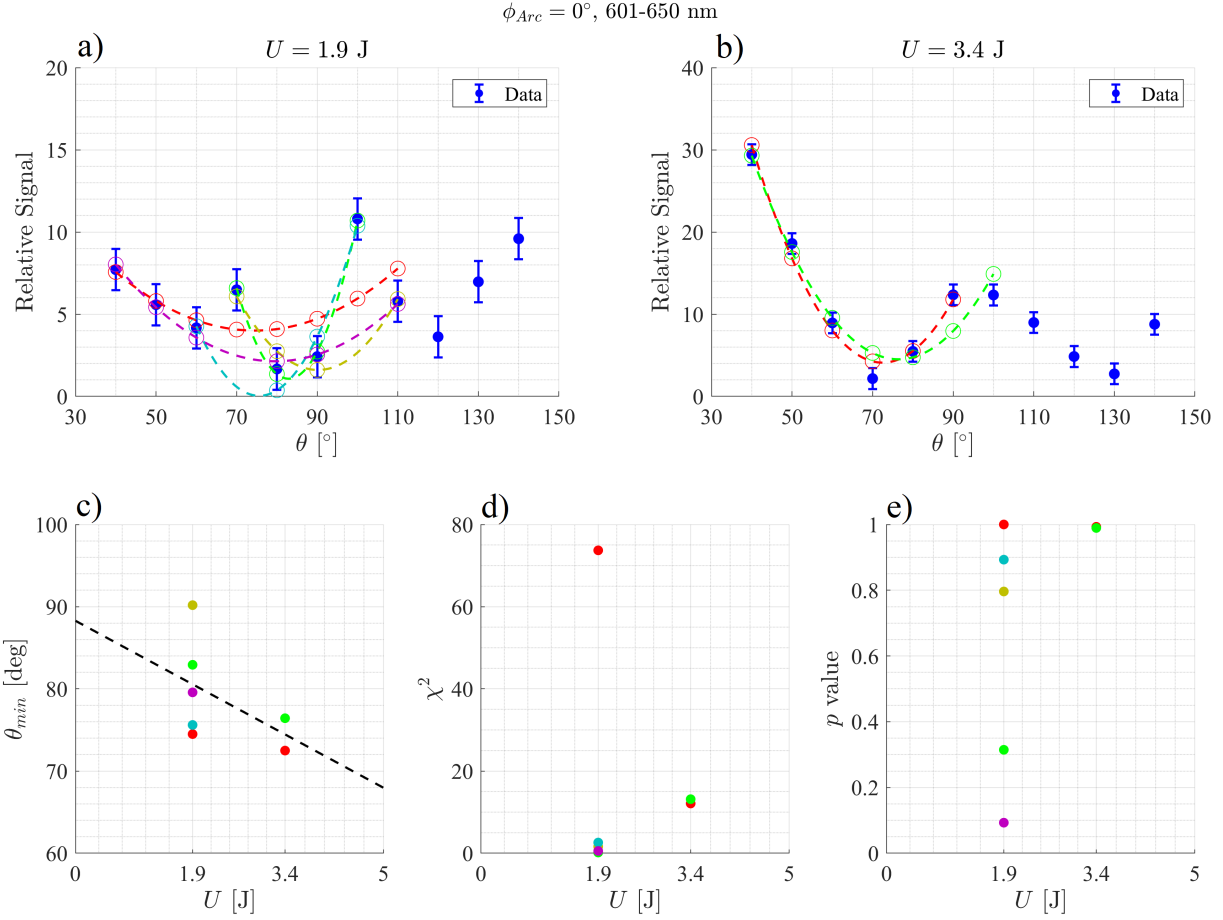


Figure 5.15: Plots showing the results of the angular distribution measurement. Shown are the angular distribution data (blue dots w/ error bars) for pulse energies of a) 1.9 J and b) 3.4 J on target along with fitted parabolic curves (dashed lines) over various selected data points (open circles). Plots of the c) parabola vertex representing θ_{min} along with a trendline fit over all data points, d) the χ^2 value of the parabolic fits, and e) the p value for the given χ^2 value and degrees of freedom (number of data points - 3). The colors for c) to e) are coded to match the parabolas in a) and b).

The variability of the parabolas from the different choices of data points used for fitting illustrate the difficulty in interpreting the data and quantitatively extracting a precise value for θ_{min} . For the 1.9 J data set, the parabola fitting all data points from 40° to 110° (red) predicts the lowest value of θ_{min} being 74.5° . If we assume that the data points at 70° and 100° are outliers and exclude them in the fit, the resulting parabola (purple) predicts a larger value of θ_{min} at 79.6° . The remaining three parabolas assume that the dip is defined more locally, with a smaller range

of θ used for fitting. For the 3.4 J data set, two parabolic fits were performed, one which fits over the well-defined parabolic shape from 40° to 90° (red) and the other which includes an additional data point at 100° (green) implying that the data point at 90° may be an outlier. The predicted values of θ_{\min} for the red and green parabolas for the 3.4 J data set are, respectively, 72.5° and 76.4° .

5.9 Discussion

Our experimental data show promising qualitative agreement, although quantitatively, we cannot use this data to determine the value of θ_{\min} to an accuracy from which the peak intensity can be determined. There are a number of issues that, if addressed in the future, would help make our method a robust quantitative characterization of the laser intensity.

The first issue is the lack of a complete set of background images. Taking background images after each signal image would allow us to track any changes in the background signal over time. Taking background images over different angles would allow us to map out the real background anisotropy. The same can be said about taking a measurement of the plasma anisotropy in the absence of RTS light.

The second issue is the presence of random noise, which results in hot pixels that are not consistent across all images, a number of which are due to cosmic rays. While our hot spot filter removed hot spots whose counts exceed our set threshold, which we determine to be the smallest threshold we can use before clipping real signal, hot spots whose counts falling below the threshold remain. At low count values, it becomes difficult to discern real signal from unwanted noise.

The third issue, which is closely related to the second issue, is the presence of scattered light. Reducing scattered light would improve our signal to noise ratio and unwanted signal contamination. The scattered light can be filtered from the detectors spatially, temporally, spectrally, or through some combination.

The fourth issue is the low angular resolution (every 10°) of our data set. This raises the question of whether it is appropriate to determine a value of θ_{\min} based on the behavior of the data that includes a large range of θ around where θ_{\min} appears to be or if it is necessary to examine the trend more locally and over a smaller range of θ . A better angular resolution and greater density of data points would allow us to better judge the overall behavior of the distribution around the dip, whether data points are outliers or indeed real RTS structure, and more precisely quantify θ_{\min} .

5.10 Conclusions

We propose improvements to our detector setup as well as experimental ideas to address some of the previously mentioned issues. One improvement we can make is to switch from using the gated ICCD with the spectrometer to using a streak camera, which would improve the temporal resolution from 5 ns to an order of 100 ps. This would allow us to sample light during a shorter time period encapsulating the RTS event, and reduce light from plasma recombination. Another improvement is to mount an arc piece sideways in order to allow detection from multiple directions in the \vec{E} - \vec{k} plane. Having multiple simultaneous detectors capturing data would improve data acquisition efficiency, resulting in the ability to achieve better angular resolution and statistics over the limited laser time typically allotted during campaigns. During the experiment,

we may also take measurements while using a pulse that is stretched by, for example, introducing a chirp via rotating the compressor grating. A stretched pulse would reduce the peak intensity of the beam and therefore the RTS light as well, while retaining plasma recombination light. This allows us to map the background anisotropy, which includes any changes in the detector efficiency associated with the geometry.

Chapter 6

Experiment 3: High Resolution Angular Distribution

Introduction

The goal of this experiment was to address the issues encountered in Experiment 2 (Chapter 5) by taking RTS angular distribution data at finer angular steps, larger sample sizes, and better signal-to-noise conditions. In addition, this experiment is done alongside measurements of the electron ejection distribution as well as the ions produced, although the RTS emission remains the focus of this thesis. Given that the rotation stage (Standa 8MR191V) holding the AARC has angular resolutions of 0.01° degrees per motor step, while the numerical aperture of the fiber detectors correspond to a 3° collection half-angle, angular resolutions $\sim 5^\circ$ is possible. The primary concern is the limited time available to conduct the measurements.

The decision therefore was made to focus only on the angular distribution in the E-k plane. The AARC was modified to hold multiple detectors at $\phi = 0$, to allow for larger coverage and more sampling along the E-k plane. Related to this emphasis on larger sampling was the decision to send the light into a streak camera as opposed to a spectrometer. This was due to the fact that only at most two fibers could be coupled into the spectrometer in the previous experiment, whereas it was possible to couple four fibers into the streak camera. Furthermore, the streak camera provided temporal resolution of the signal, allowing the gate window to be reduced below 500 ps so as to filter out plasma recombination light much more effectively. The spectral selection was handled using optical filters transmitting from 600-650 nm. A diagram of the experimental

layout is shown in Fig. 6.1.

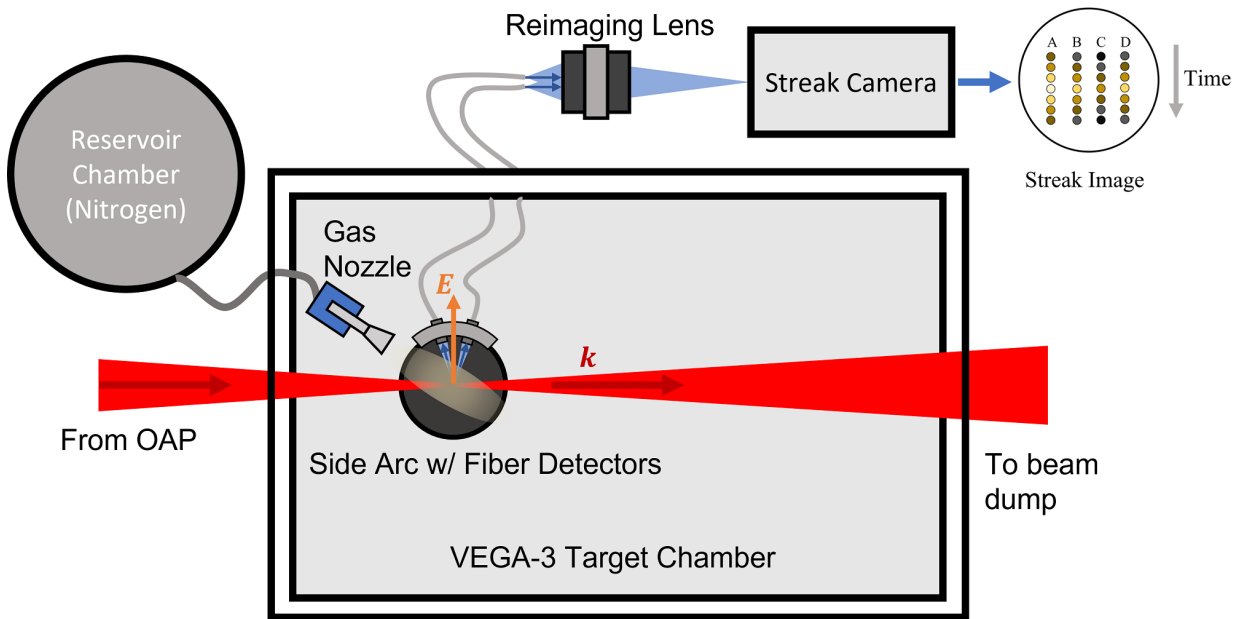


Figure 6.1: Diagram of the experimental layout for the 2022 RTS experiment. The AARC modified so that it was flipped on its side, hence the name side arc, such that the detectors were aligned within the $E - k$ plane, is used to capture RTS light produced from electrons ionized from a pulsed nitrogen gas by the VEGA-3 laser. The detectors comprised of fiber optic cables which routed the light outside and reimaged using a lens onto a streak camera for temporal gating.

6.1 VEGA-3 Characteristics

The VEGA-3 laser was chosen as part of the push for the higher intensities required for the electron and ion experiments planned in parallel with the RTS experiment, while maintaining a long focal length geometry for comparing the RTS results with previous experiments. As already mentioned in Chapter 3, the VEGA-3 beamline consisted of a 22 cm collimated beam which is focused using a 250 cm focal length OAP (f/11 geometry) down to a $11 - 13 \mu\text{m}$ diameter FWHM. A schematic of the beam in the target area is shown in Fig. 6.2. Characterization of this beam is done in the metrology bench (see section 3.1) as well as images of the focal spot at low

powers in the target chamber, as was done in the previous experiments for the VEGA-2 laser. During this experiment, an autocorrelator to measure the pulse duration was also provided in the target area, by taking a leaked portion of the beam from the OAP chamber and taking it outside to the autocorrelator device.

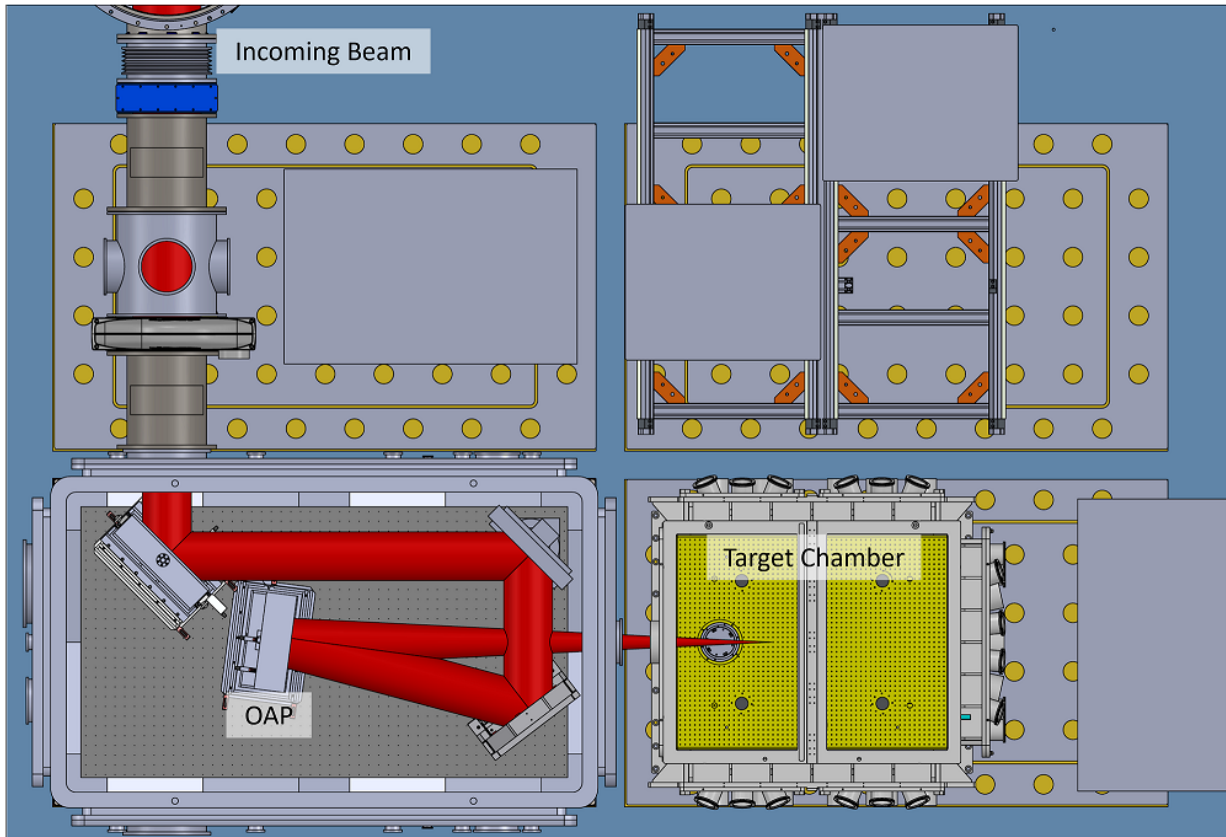


Figure 6.2: Top view of the CAD model of the VEGA-3 target area. Shown is the VEGA-3 beam entering after being transported from the laser bay and then hitting turning mirrors before being focused by an off axis parabolic mirror into the target chamber. CAD model courtesy of Centro de Láseres Pulsados.

6.1.1 Focal Scan

Images of the focal spot was captured in a manner similar to the procedure carried out in the first experiment (Chapter 4). A wedge was used to reflect an attenuated portion of the beam onto a reference focal plane. A 20 \times Mitutoyo Plan Apo near-infrared (NIR) microscope

objective was used to image the reflected focal distribution onto a camera at various offsets for best focus. The $20\times$ objective was used for imaging as opposed to the $10\times$ objective (used in the first experiment) since the $20\times$ objective was undamaged, whereas the $10\times$ objective was damaged likely due to unprotected exposure to the VEGA laser. The $10\times$ objective was reserved for alignment of the laser to the AARC, which will be discussed in section 6.4. Figure 6.3 shows a schematic including the two focal spot imaging systems and Fig. 6.4 shows a series of images of the focal scan captured by the $20\times$ objective.

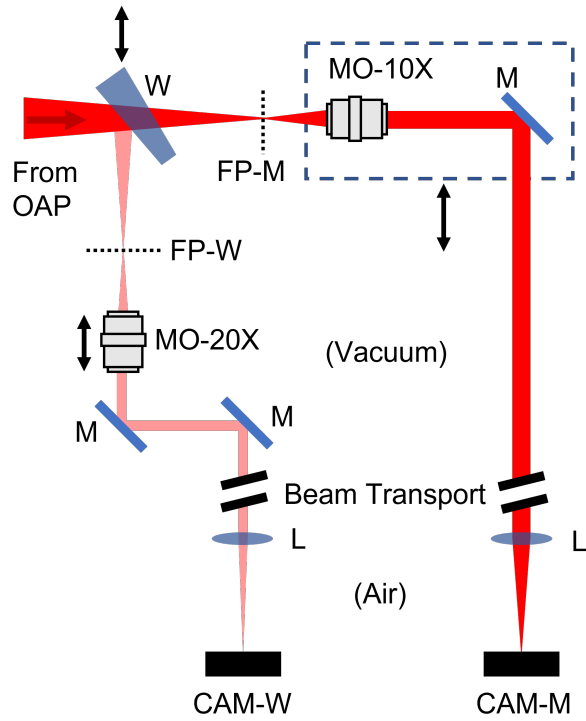


Figure 6.3: Schematic (not drawn to scale) of the two focal spot imaging systems. The main imaging system consisted of a $10\times$ microscope objective (MO-10X) imaging around the main focal plane (FP-M), whose beam was transported out of the chamber with mirrors (M) and focused with a lens (L) onto a camera sensor (CAM-M). The wedge imaging system consisted of a $20\times$ microscope objective (MO-20X) imaging around the reference focal plane produced by the wedge (FP-W), whose beam was transported and focused on to a separate camera sensor (CAM-W). In the main imaging system, the microscope objective and mirror were mounted on a translation stage that moved the assembly into and out of the main beam for measurement and live shots. In the wedge imaging system, a wedge is moved into and out of the main beam path for measurement and live shots.

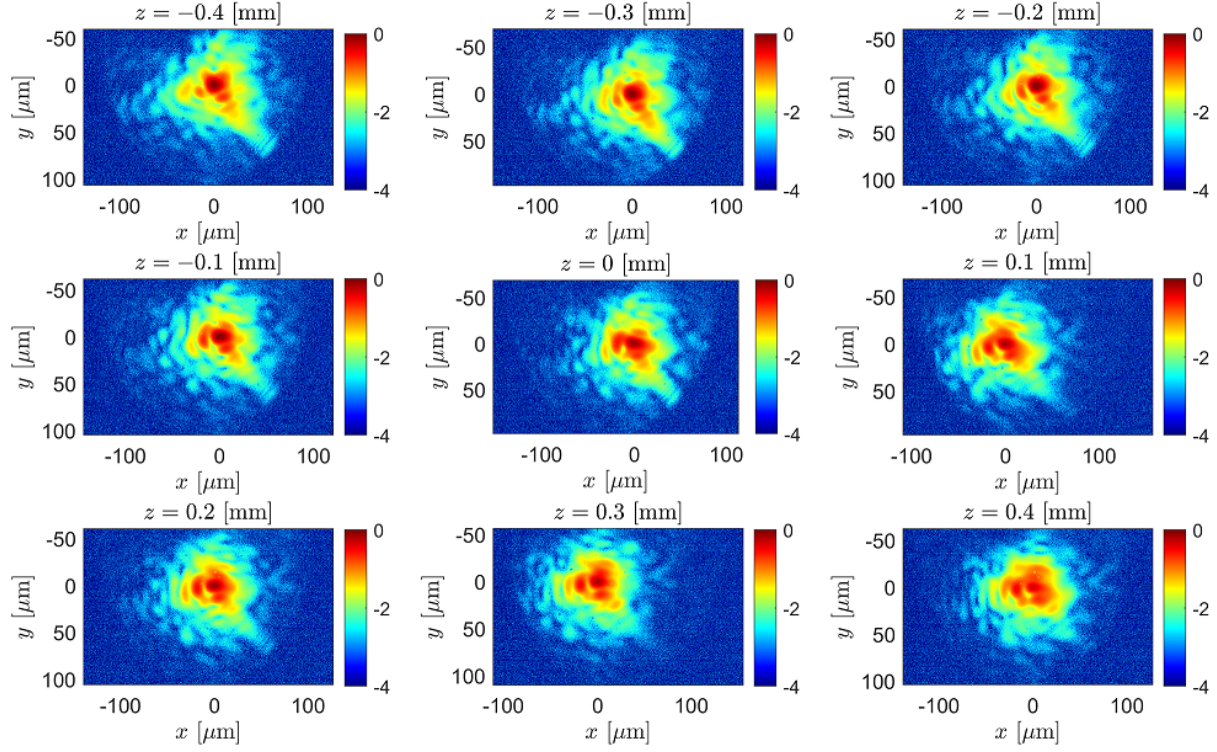


Figure 6.4: Images of the focal spot captured by the wedge imaging system at various offsets from the plane of best focus. The images are normalized to the peak pixel value out of all images in the set and plotted are the \log_{10} of the values, showing the relative order-of-magnitude fall off from the peak.

The spatial calibration was based on measurements of the lines in various elements on a United States Air Force (USAF) 1951 test pattern, images shown in Fig. 6.5. Each image contains multiple elements in a group, of which one element was used for sampling the horizontal and vertical lineouts (red dotted lines) whose values are shown in Fig. 6.6. Threshold values between 1×10^4 to 1.8×10^4 counts, in 0.8×10^4 increments, were used for determining the line edge positions, which are used to calculate the line widths (in pixels) shown in Fig. 6.7. Aggregating these values through averaging, as shown in Table 6.1, an overall calibration of 7.2 ± 0.5 pixels per μm was determined for the wedge imaging system. The code for performing the calibration analysis as well as a detailed example of the calibration steps is given in appendix D.1.

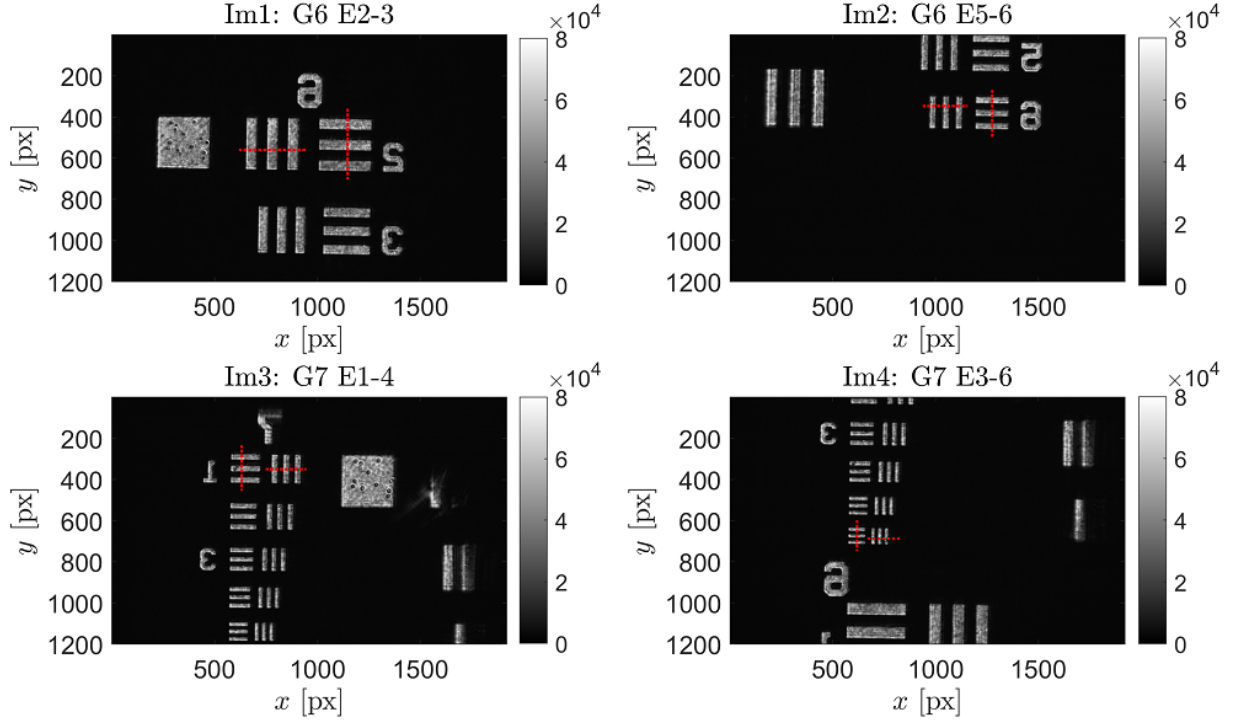


Figure 6.5: Images (labeled Im1 to Im4) of various groups and elements of the USAF test pattern used. In each image, a horizontal as well as a vertical dotted red line are shown, indicating locations of lineouts (Fig. 6.6) taken for calibration analysis.

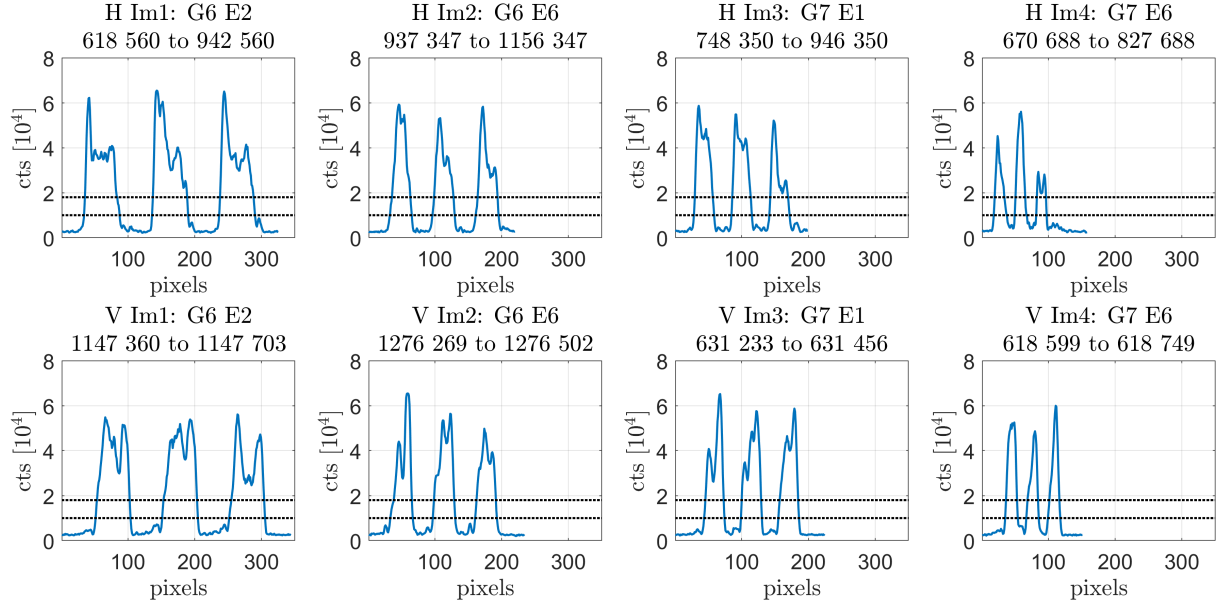


Figure 6.6: Plots of the lineouts sampled from the images of the USAF test pattern images. See Fig. 6.5. The dotted horizontal lines indicate the bounds of the threshold values (1×10^4 – 1.8×10^4 in 0.8×10^4 increments) used for determining the locations of the pattern line edges.

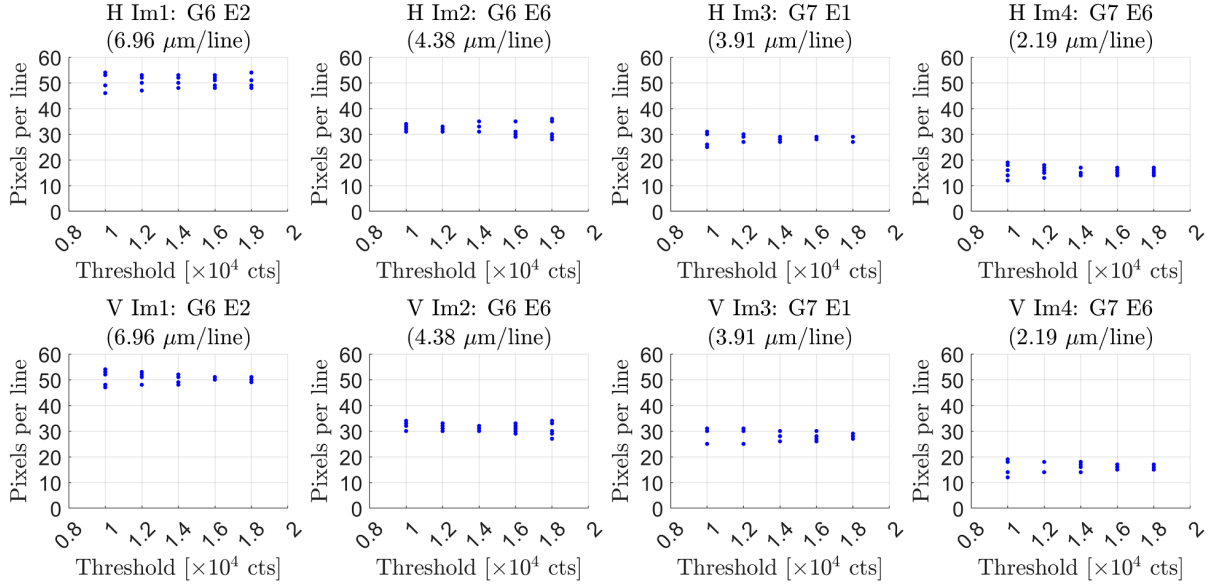


Figure 6.7: Plots of the pattern line widths calculated from taking the difference between the locations of the pattern line edges determined from their intersections with various threshold values (within the horizontal dotted lines in Fig. 6.6). The known line widths of each pattern element are given in parenthesis.

Image	Element	Horizontal [px/μm]	Vertical [px/μm]
1	G6E2	7.3 (0.3)	7.2 (0.3)
2	G6E6	7.3 (0.5)	7.1 (0.4)
3	G7E1	7.2 (0.4)	7.2 (0.5)
4	G7E6	7.1 (0.8)	7.4 (0.8)
Overall		7.2 (0.5)	7.2 (0.6)

Table 6.1: Spatial calibration results determined from each lineout. The pixels per line values from Fig. 6.7 are divided by their corresponding element line widths to obtain calibrated values in units of px/μm. The samples over all threshold values for each element are aggregated and their average (standard deviation) are given.

6.1.2 Temporal and Spectral Measurements (Wizzler)

The temporal profile and spectrum of the VEGA-3 compressed pulse measured by the Wizzler in the laser bay metrology bench (see section 3.1) is shown in Fig. 6.8. The measurements show very similar characteristics as the VEGA-2 pulse in terms of pulse width and spectral band-

width and central wavelength. An autocorrelator was also set up in the target area near the OAP to measure the pulse duration closer to the target and is discussed in more detail in the next section, section 6.1.3.

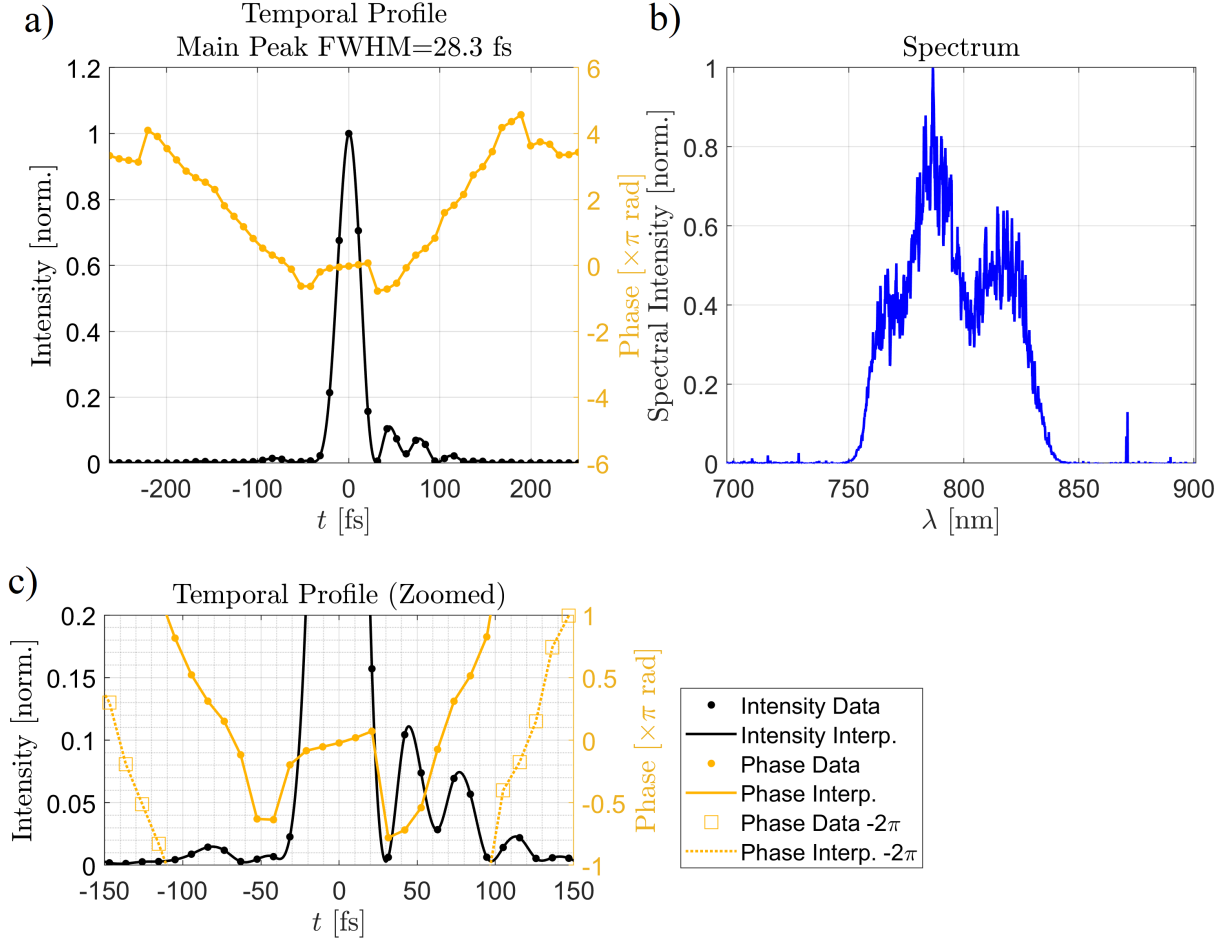


Figure 6.8: Plots of a) the reconstructed temporal pulse shape and phase and b) the spectrum measured from the VEGA-3 laser by the Wizzler at the laser bay metrology bench. See section 3.1 for a description of the metrology bench. A zoomed in plot of the temporal profile and phase c) is shown including a phase curve offset by -2π to show the phase variation for one of the the smaller peaks. A cubic interpolation was used to connect the intensity data, while a linear interpolation was used to connect the phase data.

6.1.3 Energy and Temporal Measurements (Live Shots)

During the live shots, the energy and pulse duration were both monitored. The energy was monitored using the calibrated pyroelectric energy meters in the laser bay (see section 3.1). This energy was then multiplied by 0.89 to account for transmission losses at the laser bay to the target chamber. The pulse duration was monitored using an autocorrelator near the OAP, which measures a picked off portion of the beam and taken out of the vacuum chamber. The autocorrelator measurements of the pulse duration averaged over each run, as well as the laser energies on target (last shot of the run) are reported in the Figures 6.9, 6.10, 6.11, and 6.12 for nominal pulse energies of 2, 6, 10, and 30 J respectively. The autocorrelator measurements have not been corrected for dispersion due to the exit port window and glass filters, therefore do not represent the pulse duration in the vacuum chamber (which require further analysis to be discussed).

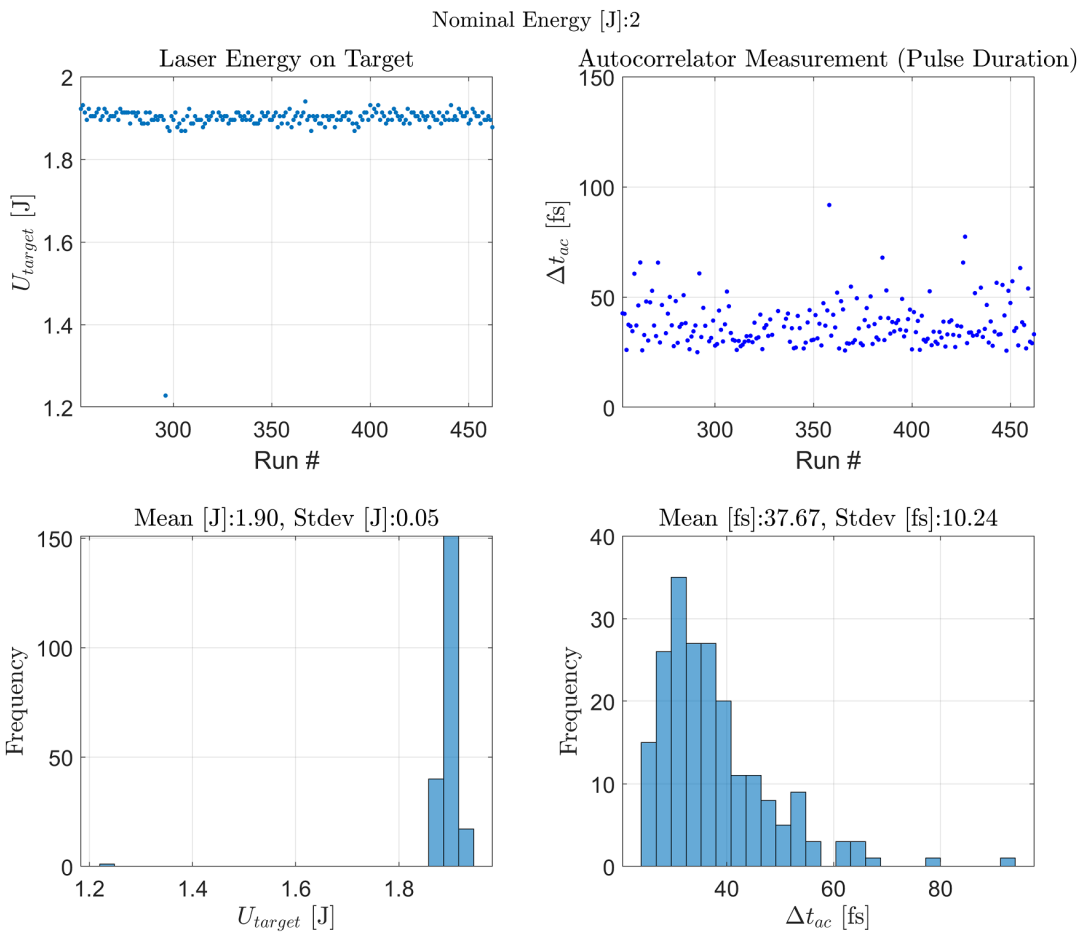


Figure 6.9: Laser energy (last shot of run) and autocorrelator-measured pulse duration data (averaged over each run) for each run number for the runs operating at 2 J nominal energy, 8 shots per run at 1 Hz. Also shown are corresponding histograms of the datasets distributed over 25 bins.

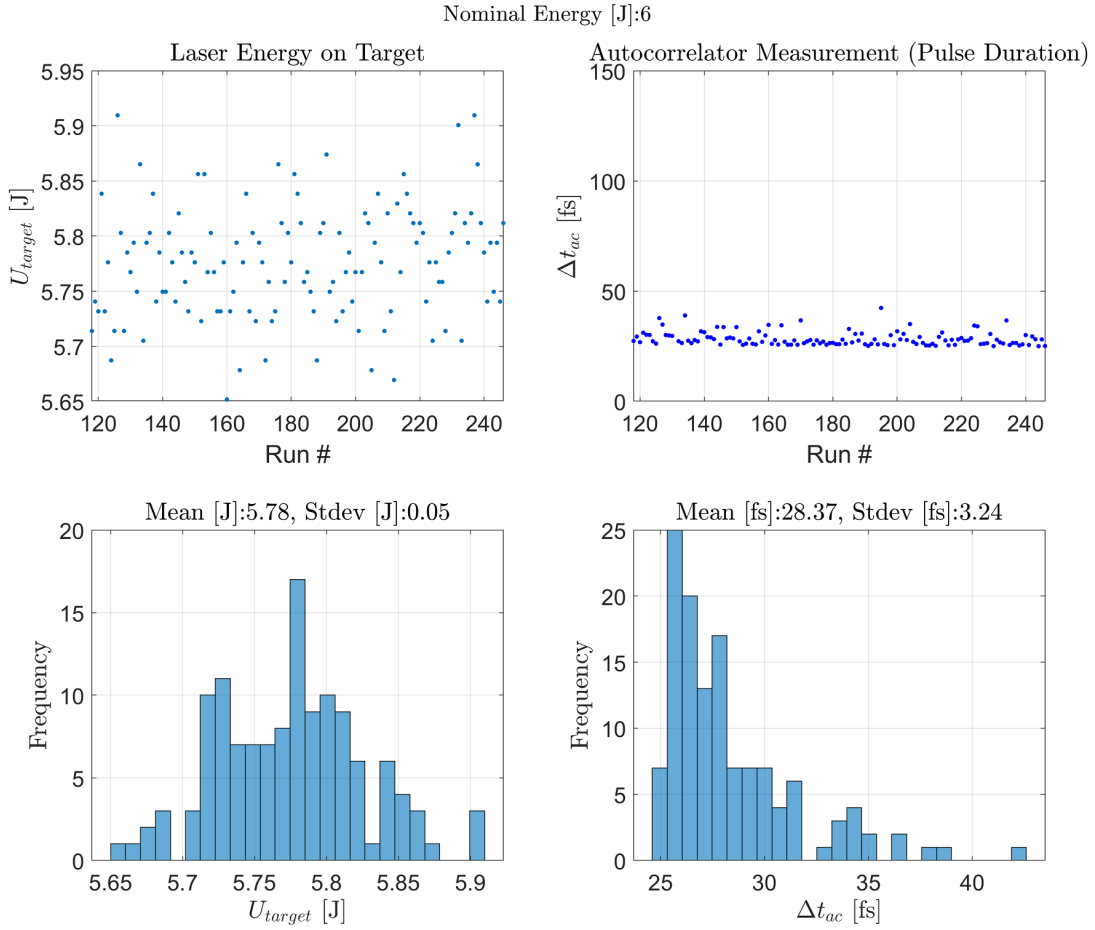


Figure 6.10: Laser energy (last shot of run) and autocorrelator-measured pulse duration data (averaged over each run) for each run number for the runs operating at 6 J nominal energy, 8 shots per run at 1 Hz. Also shown are corresponding histograms of the datasets distributed over 25 bins.

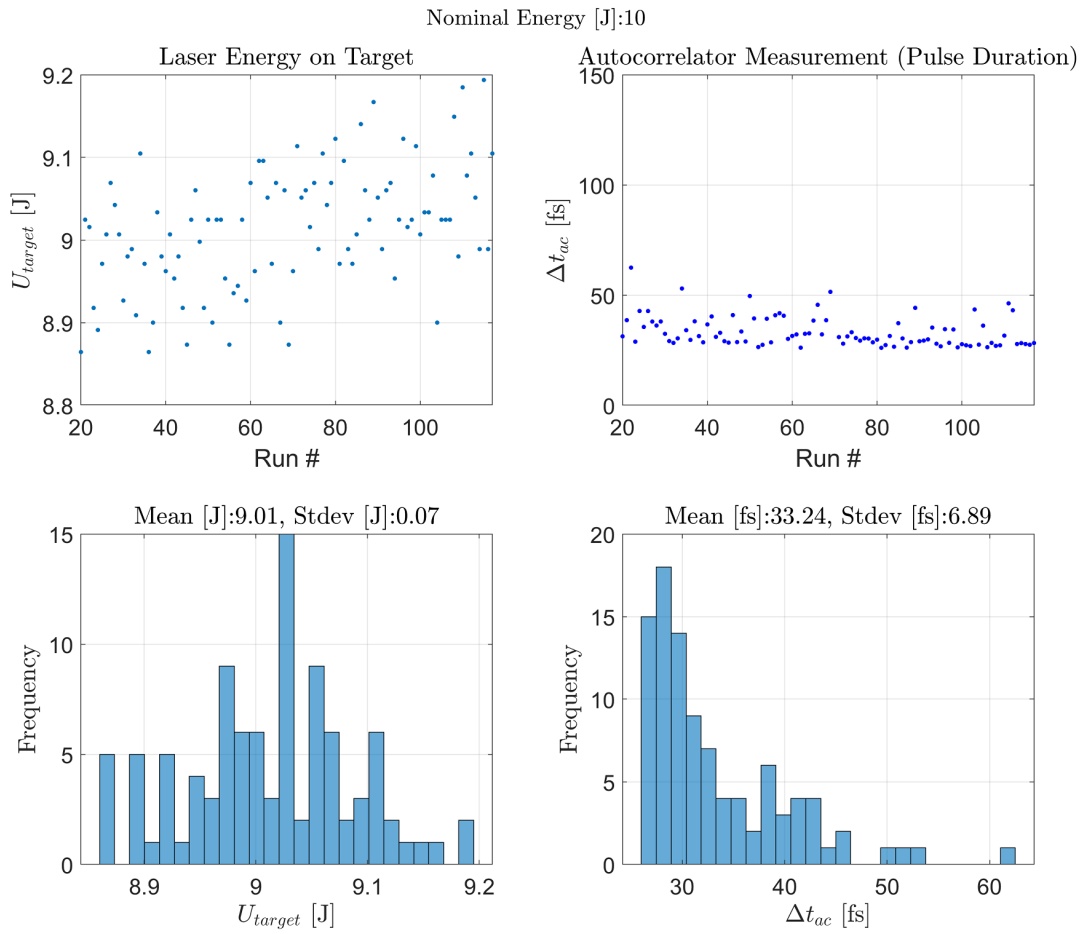


Figure 6.11: Laser energy (last shot of run) and autocorrelator-measured pulse duration data (averaged over each run) for each run number for the runs operating at 10 J nominal energy, 8 shots per run at 1 Hz. Also shown are corresponding histograms of the datasets distributed over 25 bins.

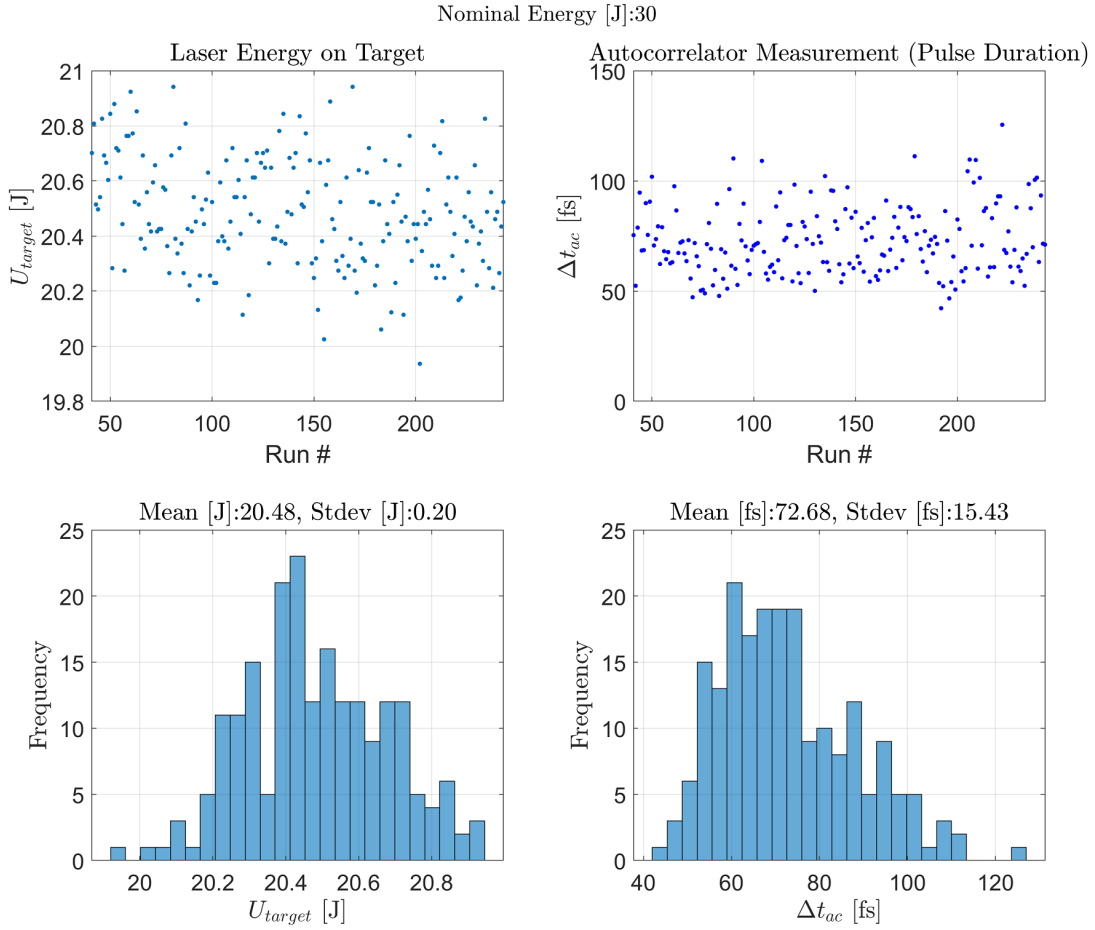


Figure 6.12: Laser energy and autocorrelator-measured pulse duration data for each run number for the runs operating at 30 J nominal energy, single-shot. Also shown are corresponding histograms of the datasets distributed over 25 bins.

In order to correct for the dispersion effects on the pulse due to the exit port window, which was 5 mm in thickness, as well as the sets of neutral density (ND) filters placed in front of the autocorrelator at various nominal energies, we first determine the second order group delay dispersion (GDD), denoted as $\frac{\partial^2 \phi}{\partial \omega^2}$, from the autocorrelator-measured pulse duration based on the

following relationship between pulse duration, Δt , and GDD:

$$\Delta t = \Delta t_{TL} \sqrt{1 + \left(\frac{4 \ln 2 \frac{\partial^2 \phi}{\partial \omega^2}}{\Delta t_{TL}^2} \right)^2} \quad (6.1)$$

Here, Δt_{TL} refers to the pulse duration of the transform-limited pulse if dispersion was completely removed (i.e. GDD=0).

Assuming a $\Delta t_{TL} = 28.3$ fs unchirped pulse (based on the pulse duration measured by the Wizzler - see section 6.1.2), the GDD, $\left(\frac{\partial^2 \phi}{\partial \omega^2} \right)_{ac}$, corresponding to the autocorrelator-measured pulse duration can be determined by setting $\Delta t = \Delta t_{ac}$ and solving for $\frac{\partial^2 \phi}{\partial \omega^2}$. The duration of the pulse in vacuum, Δt_{vac} , and before passing through glass to reach the autocorrelator can be determined by assuming that its corresponding GDD, $\left(\frac{\partial^2 \phi}{\partial \omega^2} \right)_{vac}$, follows

$$\left(\frac{\partial^2 \phi}{\partial \omega^2} \right)_{vac} = \left(\frac{\partial^2 \phi}{\partial \omega^2} \right)_{ac} - \Delta \frac{\partial^2 \phi}{\partial \omega^2} \quad (6.2)$$

where $\Delta \frac{\partial^2 \phi}{\partial \omega^2}$ is the change in dispersion due to the total glass thickness traversed by the pulse, and is related to the glass thickness L_{glass} by

$$\Delta \frac{\partial^2 \phi}{\partial \omega^2} = (\text{GVD}) \times L_{glass} \quad (6.3)$$

where GVD is the group velocity dispersion. For fused silica, the GVD is equal to 36.70 fs²/mm. The rationale behind eq. 6.2 is that light traversing through glass, where its speed is inversely proportional to frequency, can only gain a net positive chirp. The value of $\left(\frac{\partial^2 \phi}{\partial \omega^2} \right)_{vac}$ can then be plugged into eq. 6.1 to determine Δt_{vac} . The results of this calculation are shown in Table 6.2.

Table 6.2: Table summarizing the measured energy, measured pulse duration, and corrected pulse duration. Included are the average (standard deviation) of the measurements of energy on target, U_{target} , and autocorrelator-measured pulse duration, Δt_{ac} , for each of the nominal energies, $U_{nominal}$, along with the number of runs, N_{runs} , as well as the total glass thickness traversed by the pulse in reaching the autocorrelator (including exit port window and ND filters) and the corresponding change in second-order group delay dispersion (GDD), $\Delta \frac{\partial^2 \phi}{\partial \omega^2}$ (see eq. 6.3). Also shown are the predicted values of the pulse in vacuum Δt_{vac} calculated by shifting the GDD at the autocorrelator by $-\Delta \frac{\partial^2 \phi}{\partial \omega^2}$ (see eq. 6.1 and 6.2, as well as Fig 6.13). Uncertainties shown after the \pm symbol were derived from taking the standard error in Δt_{ac} (standard deviation divided by $\sqrt{N_{runs}}$) as the uncertainty and propagating to their values via the corresponding equations.

$U_{nominal}$ [J] N_{runs}	2 207	6 128	10 97	30 203
U_{target} [J]	1.9 (0.05)	5.78 (0.05)	9.01 (0.07)	20.48 (0.20)
Δt_{ac} [fs]	37.67 (10.24)	28.37 (3.24)	33.24 (6.89)	72.68 (15.43)
$\left(\frac{\partial^2 \phi}{\partial \omega^2}\right)_{ac}$ [fs ²]	254 \pm 22	20 \pm 58	178 \pm 27	683.3 \pm 24
L_{glass} [mm]	5.0	8.3	9.6	9.0
$\Delta \frac{\partial^2 \phi}{\partial \omega^2}$ [fs ²]	183.5	304.6	352.3	330.3
Δt_{vac} [fs]	29.1 \pm 1.0	39.7 \pm 8.0	33.1 \pm 2.8	44.7 \pm 3.6
$\left(\frac{\partial^2 \phi}{\partial \omega^2}\right)_{vac}$ [fs ²]	70.3 \pm 22	-384.3 \pm 58	-174.3 \pm 27	353 \pm 24

The effects of dispersion due to the window can be understood as moving along the Δt versus GDD curve defined by eq. 6.1 and is illustrated in Fig. 6.13. Since the curve is not one-to-one, one may in principle choose either side (positive or negative GDD) as the starting point for Δt_{ac} . In our case, the positive side was chosen since we expect the the vacuum pulse to be close to optimally compressed, since the laser operators have precalibrated the grating positions at each operating energy, and choosing the negative side would result in larger values in both Δt_{vac} and $\left(\frac{\partial^2 \phi}{\partial \omega^2}\right)_{vac}$.

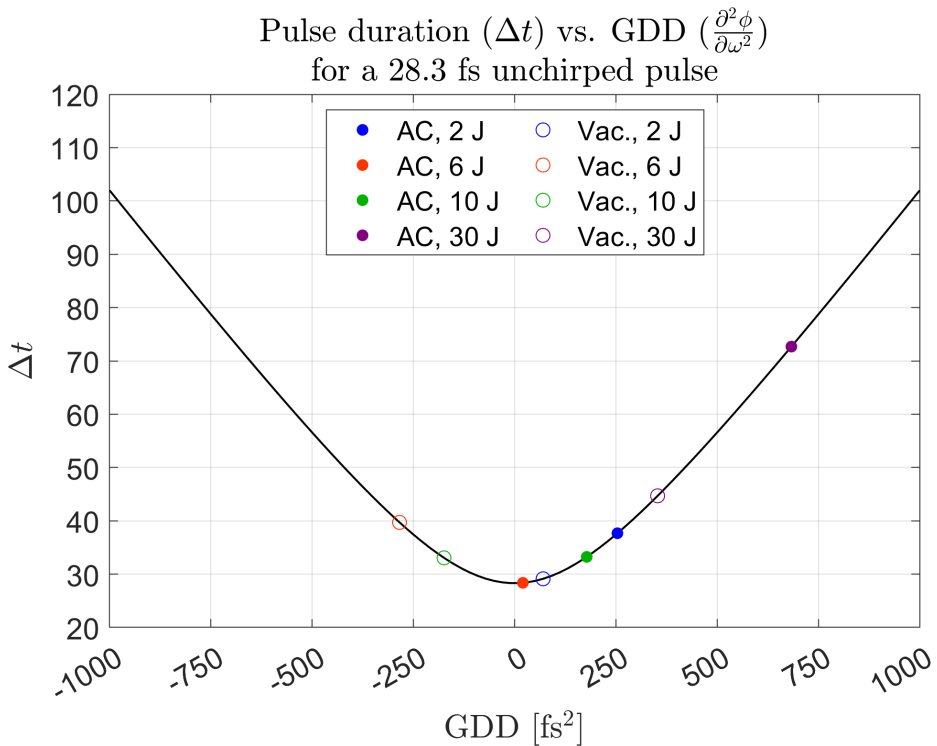


Figure 6.13: Plot of the Δt versus GDD curve along with measured and corrected values of pulse duration. See Eq. 6.1 for the curve, which assumes a 28.3 fs unchirped pulse. The values include those the pulse duration and GDD at the autocorrelator (AC) and predicted values in vacuum (Vac.) shown in Table 6.2.

6.1.4 Peak Intensity Estimation

The peak intensity can be estimated from the values of U_{target} , Δt_{vac} , and the spatially calibrated focal spot images using the method described in section 4.3. This was done by first computing the peak intensity per unit power, $I_{pk}^{Im}/(U/\Delta t)$, which can then be easily scaled to the peak intensity for a given set of values of U_{target} and Δt_{vac} via multiplication by $U_{target}/\Delta t_{vac}$. The data acquired at the nominal energy of 30 J was done on 03/28/2022, and a set of 3 focal spot images at best focus were taken at lower power. The data acquired at the nominal energies of 2, 6, and 10 J were all done on the same day (03/30/2022), and a set of 10 focal spot at best focus were taken at low energy. The values of $I_{pk}^{Im}/(U/\Delta t)$ from each focal spot image was computed

and averaged for each day. The results of the analysis are shown in Table 6.3 and plotted in Fig. 6.14.

Table 6.3: Values involved in the estimate of the peak intensity using the focal spot images, and measured energy and pulse duration. The uncertainty in $I_{\text{pk}}^{\text{Im}}/(U/\Delta t)$ is defined as the standard deviation in the mean from the computed $I_{\text{pk}}^{\text{Im}}/(U/\Delta t)$ values in each of the 3 and 10 images taken on 03/28/2022 (30 J) and 03/30/2022 (2, 6, and 10 J) respectively. The standard deviation in U_{target} was used as the uncertainty in propagating to the uncertainty in $I_{\text{pk}}^{\text{Im}}$, since the standard deviation is a better estimate of the overall error in U_{target} than the standard deviation in the mean.

U_{nominal} [J]	2	6	10	30
$I_{\text{pk}}^{\text{Im}}/(U/\Delta t)$ [e5 W/cm ² /J/s]		2.67 ± 0.20		2.65 ± 0.77
U_{target} [J]	1.9 (0.05)	5.8 (0.05)	9.0 (0.07)	20.5 (0.20)
Δt_{vac} [fs]	29.1 ± 1.0	39.7 ± 8.0	33.1 ± 2.8	44.7 ± 3.6
$I_{\text{pk}}^{\text{Im}}$ [e19 W/cm ²]	1.7 ± 0.2	3.9 ± 0.5	7.2 ± 0.9	12.2 ± 1.3

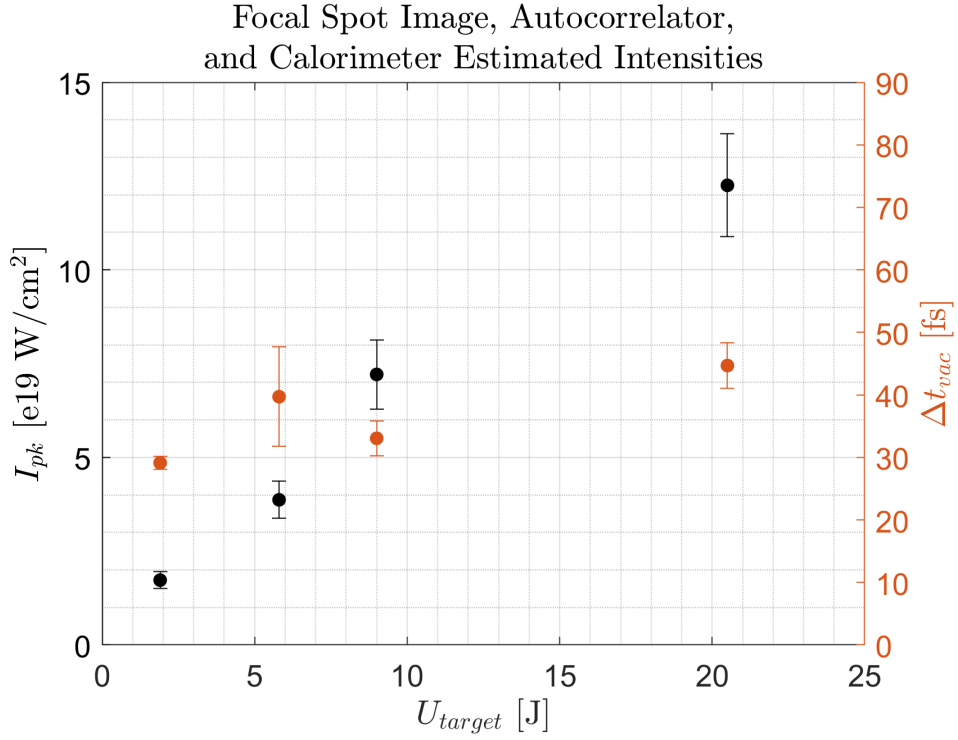


Figure 6.14: Plot of the estimated peak intensity (left vertical axis) versus energy on target as well as the pulse duration (right vertical axis) versus energy on target. The estimated pulse duration over the range of energies used while varying by as much as 15 fs ($\sim 54\%$) does not show a strong correlation with energy, thus the estimated peak intensity scaled roughly linearly with the energy.

6.2 The Side Arc

In order to mount the detectors in the E-k plane, a new design of the arc piece was necessary while using the same rotary base and motorized stages. The new design's imaging focus also needed to be centered at the same reference point as the original arc. Therefore, the new design needed to have the detectors mounted at the correct height, radial distance from focus, and orientation. Furthermore, the machining tolerances needed to be within acceptable error (the pointing accuracy needed to be within the 3 mm detector field of view). While outsourcing the machining work to a third party with a 5-axis CNC was originally considered, there were many concerns associated with the third party not fully understanding the design application that would lead to longer turnaround times, costs, and inadequate tolerances. After extensive discussion with the machinist, Lester Putnam, at the Institute for Physical Science and Technology (IPST), the final design, shown in Fig. 6.15, was developed and machined in-house at the University of Maryland using a 3-axis CNC and manual rotary table.

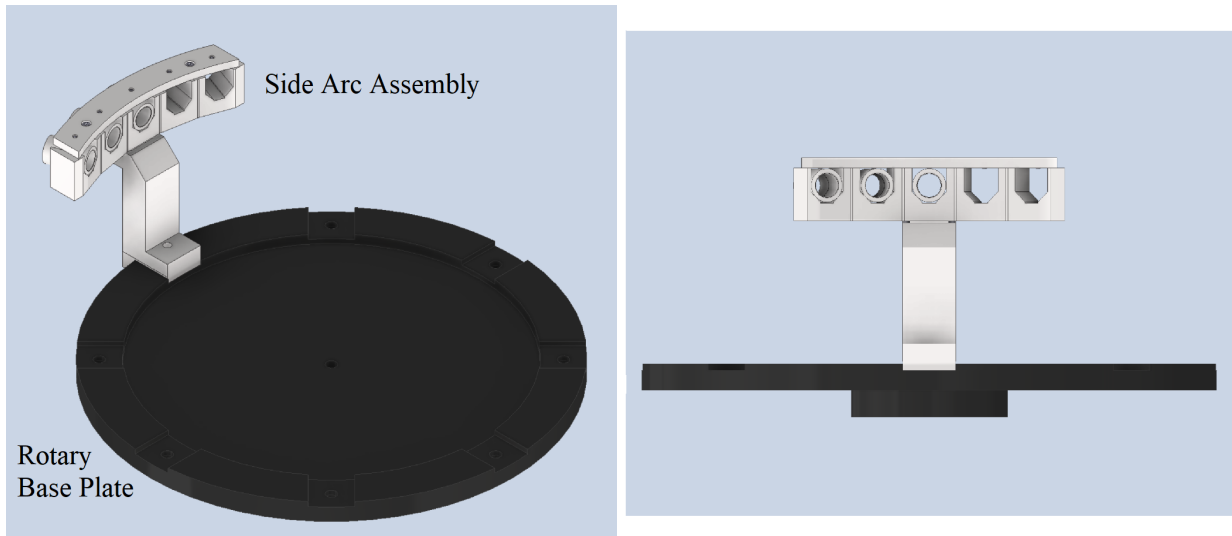


Figure 6.15: CAD images of the side arc assembly mounted on the rotary base in isometric view and side view. The nylon-tipped set screws on the top plate were originally 4-40 and had been modified to 8-32 last minute as a result of set screw availability. The securing screws for the riser are 1/4"-20. Credit: Lester Putnam for the final design and model of the side arc assembly and for the original idea of using V-grooves.

This new assembly consists of an arc with 90° V-shaped grooves cut in the radial direction relative to the center point of the arc to allow the mounting of up to 5 detectors spaced 10° apart. The shape of the V-grooves orient the detectors towards the same center point (with an error on the order of 1 mm) via two edges of contact with the 5/8" cylindrical detector housings. A top plate is affixed over the arc, providing a fixture for nylon-tipped 8-32 set screws to hold the detectors in place from the top. Each detector slot on the side arc has a front flat surface for registering the edge of the detector housing to achieve the same detector distance from the arc center. The detector's radial distance is constrained by the filter holder attached in front of the 5/8" cylinder, which has a slightly larger diameter than 5/8". The side arc is mounted over a riser designed to position the side arc vertically at the correct height. Optional shims are available to place in between the side arc and riser for varying the height by 0.5 to 1.5 mm in steps of 0.5 mm, depending on the shim thickness and number of shims used. Two alignment pins determine

the orientation of the arc relative to the riser. The riser is mounted on the rotary base, with its orientation at this contact surface determined by registering one side of the riser's flat side surface with that of the flat side of the groove on the arc rotary base. The riser's radial position is determined by a protrusion at the back from the bottom of the riser being in contact with the outer edge of the rotary base.

6.3 Fiber Optic Detectors

The fiber optic detectors largely remained unchanged from the 2019 experiment (see section 5.3). The main differences were in the specific models of fiber optic cables and optical filter combinations used. Inside the vacuum chamber, vacuum compatible fibers from Thorlabs (MV64 UHV, 0.22 NA, 600 μm core, SMA to SMA) 2 m in length were used. These fibers were not jacketed, therefore aluminum foil was wrapped as protection against abrasion during rotation of the side arc. Outside of the vacuum chamber, jacketed fibers from Thorlabs (UM22-600, 0.22 NA, 600 μm core, SMA to Flat-Cleaved) 2 m in length were used, with the SMA end connected to the vacuum feedthrough and the bare flat-cleaved end coupled to the streak camera. In each detector, a 600 – 650 nm (FWHM) interference filter was added on top of the shortpass 725 nm filter, their transmission curves shown in Fig. 6.16. Based on the transmission data, which was provided by the manufacturer, the combined filter would provide at least 10^{-5} attenuation outside of 500 – 700 nm and at least 10^{-10} attenuation above 775 nm.

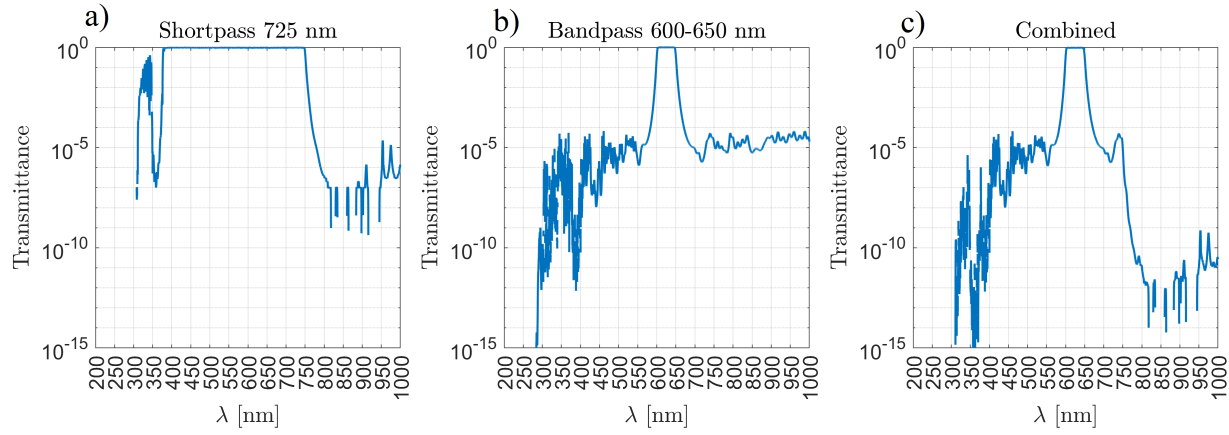


Figure 6.16: Transmission curves of a) the shortpass 725 nm filter, b) the bandpass 600-650 nm filter, and the combined (shortpass 725 nm and bandpass 600-650 nm) filter set plotted in log scale. The transmission curve data was representative data obtained from the manufacturer and there may be slight differences from the curves for the filters used in the experiment.

6.4 Alignment of Detectors

6.4.1 Fiber Alignment to AARC Center

In order to work as intended, the fiber detectors must all be viewing towards the focal point over all angles of data collection. This is facilitated by the machining of the AARC components such that the mounted detectors are looking at the center point of the AARC, which is referenced using a bead epoxied onto the conical tip machined into a $\frac{1}{2}$ " rod mounted on a kinematic magnetic base. An imaging system consisting of a long focal length camera lens viewing the bead was used for alignment, as shown in Fig. 6.17.

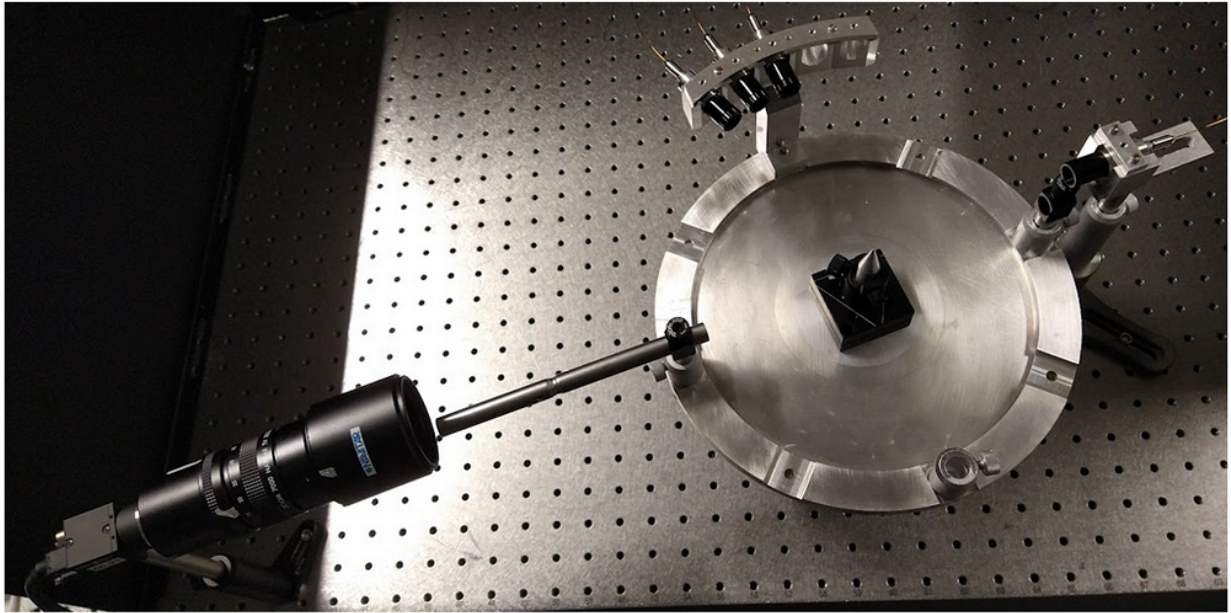


Figure 6.17: Photo of the setup used for detector alignment. A Blackfly PGE-23S3M camera with a Navitar zoom lens mounted was focused on the alignment bead. Directly opposed was a fiber based detector, which was back-illuminated. The profile of the projected light from the back-illuminated fiber detector at the plane of the bead marks the field of view (see Fig. 6.19, 6.20 and 6.22).

First, the imaging system was used to characterize the deviation of the bead from the rotational axis as the AARC rotary base was rotated over 360 degrees, as shown in Fig. 6.18. This deviation was found to be 1 bead diameter (about 250 μm) at best, and 2-3 bead diameters (500-750 μm) at worst. It was verified that the largest excursion of the bead within the image (bead appearing furthest to the left and furthest to the right) corresponds to angular difference of 180 degrees.

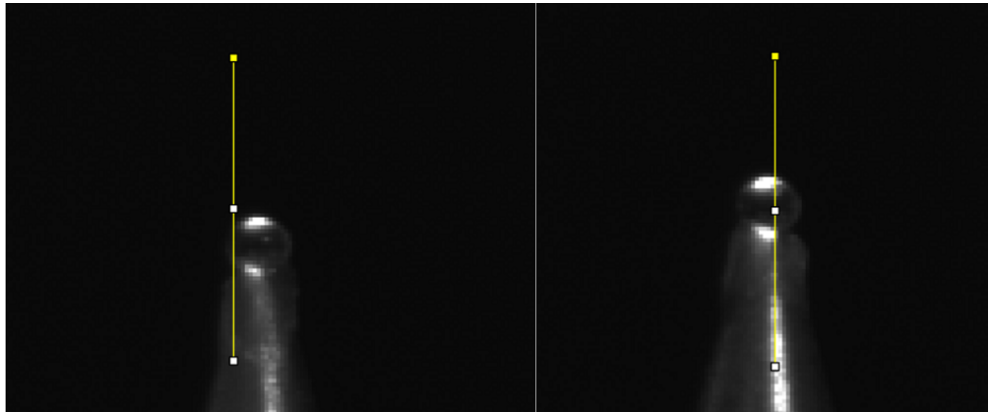


Figure 6.18: Images of the bead at maximum excursion to the left and right of the image out of a set of images captured every 10° over a full rotation of the rotary base. The vertical line indicates the same pixel x position, 1150, on both images. On average, the full excursion is on the order of one bead diameter ($\sim 250 \mu\text{m}$) .

The deviation is caused by an off centering of the tip due to the play in the M6 screw in the through holes of the magnetic base and AARC rotary base. There are also other machine tolerances in the mounting of the conical tip that contributes to this offset. Nevertheless, using the bead will allow the laser focus to be aligned within 750 microns of the rotational axis at worst and within 250 microns when a more careful mounting of the tip is performed. A careful mounting would entail centering the through holes by eye viewing from the top before placement of the M6 bolt, and ensuring proper technique is utilized to minimize excessive shifting of the components from the tightening of the bolt. This deviation is tolerable given that the field of view of the fiber detectors is 3 mm in diameter, if we can ensure that each detector's field of view is centered at the bead.

While the V-shaped grooves carved into the side arc were done to tight tolerance, it may have not been enough, and the centering of the individual fiber detectors relative to the center of the AARC needed to be checked. To accomplish this, the optical fibers are back illuminated, and an imaging system captures the projected illumination at the focal plane of the bead from

opposite to the detector. The projected illumination marks the fiber detector field of view and is centered around the bead when the detector is properly aligned.

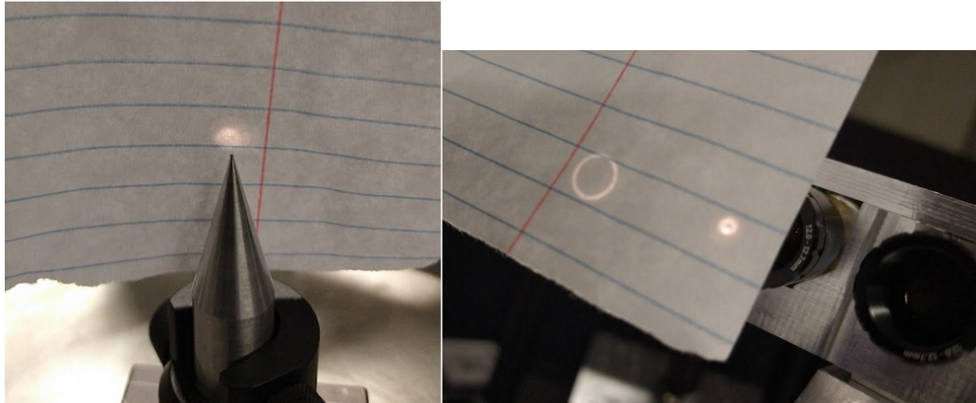


Figure 6.19: Photos showing the profiles of the back illuminated light from the fibers at different locations. Left: Back illuminated fiber light from multiple detectors near the plane of the bead. The light from the different detectors are somewhat overlapped. Right: The back illuminated fiber light just as it leaves the detector. Note that light from the detector on the left is a ring due to the narrow range of angular modes coupled at the opposite end, but the exit surface is filled, which is also the case when projected into the plane at the bead.

It was found that the different detectors mounted on the Side AARC do not all project back illuminated spots that were centered around the bead.

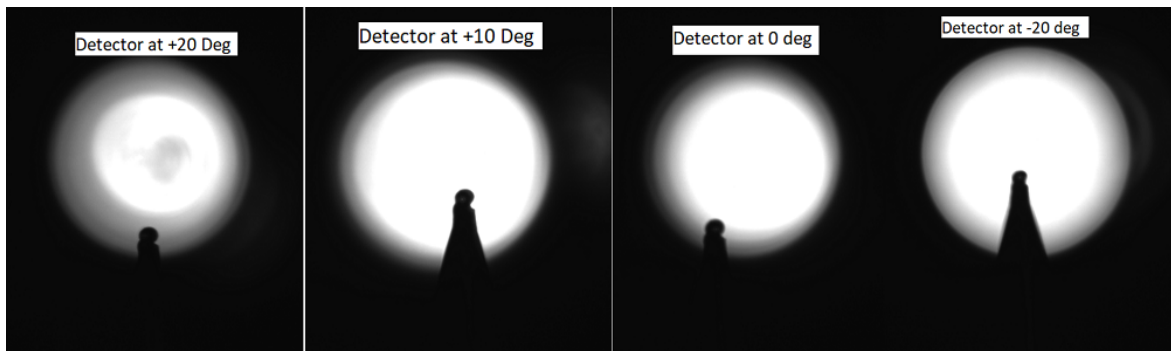


Figure 6.20: Images of the bead (in focus) and projection of the back illuminated fiber light for each of the four detectors mounted at different positions on the side AARC. The detector at -20 deg (and possible +10 deg) appear well-centered. For reference, the shutter time for these images is 0.5 ms.

Fortunately, extra space around the V-grooves lateral to and above the cylindrical housings

allow the detectors to be shimmed to adjust pitch and yaw. A simple method for shimming can be done by folding aluminum foil into steps, like a ladder, and placing it between the bottom of the aluminum housing and V-groove. Placing the steps of the shim behind the vertical axis of the 8-32 set screw creates a downward pitch. Placing the shim diagonally across a V-groove allow slight adjustment in the yaw. This was primarily a trial-and-error process, and once the desired alignment is established, the detector and shim were kept in place, and periodically rechecked by back illumination for alignment.



Figure 6.21: Photos of the aluminum foil shims at different stages of the application process for ever-so-slight pointing adjustment of the detector toward the desired direction. A small piece of aluminum foil, about 2" in length was folded up in a staircase pattern to provide sub-millimeter sized steps and then wrapped around the detector's aluminum housing before affixing onto the side arc.

The imaging system is mounted in a fixed position separate from the AARC assembly. This process is therefore easily repeated for a subsequent detector by rotating the AARC to align the next detector to the same imaging system. After applying shims to the misaligned detectors, these detectors are now centered around the bead.

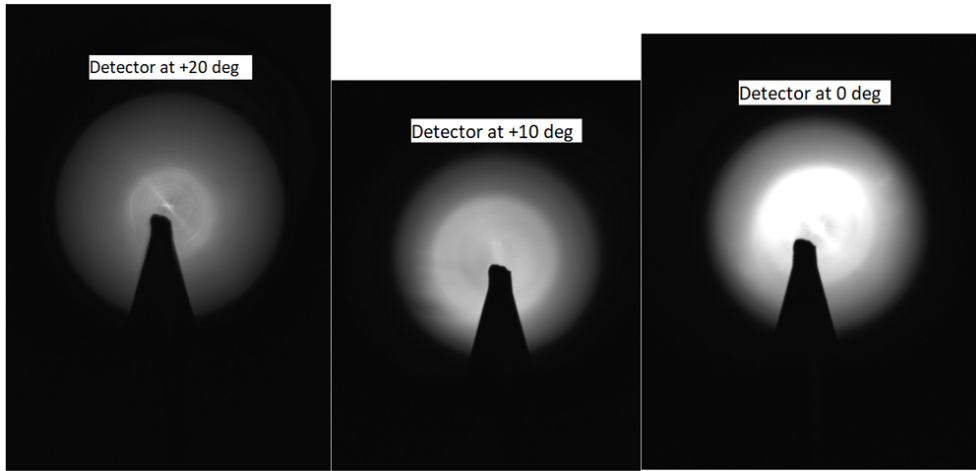


Figure 6.22: Images of the alignment tip (bead missing) and projected back illuminated fiber light after these detectors have been shimmed. In these images, the shutter time was reduced to 0.1 ms (from 0.5 ms in Fig. 6.20). The bead had been knocked off.

The single detector holders are mounted separate from the AARC assembly, but nevertheless are intended to also have their fields of view centered at the laser focus (or equivalently the bead) from the same radial distance as the side AARC detectors. Features of the AARC can be used as references for positioning the single detector radially and azimuthally, while imaging of the back illumination projected at the bead can be used to position the single detector in height as well as orient its yaw. The freedom to adjust the single detectors independently through their height and rotation adjustments eliminate the need to use shims.

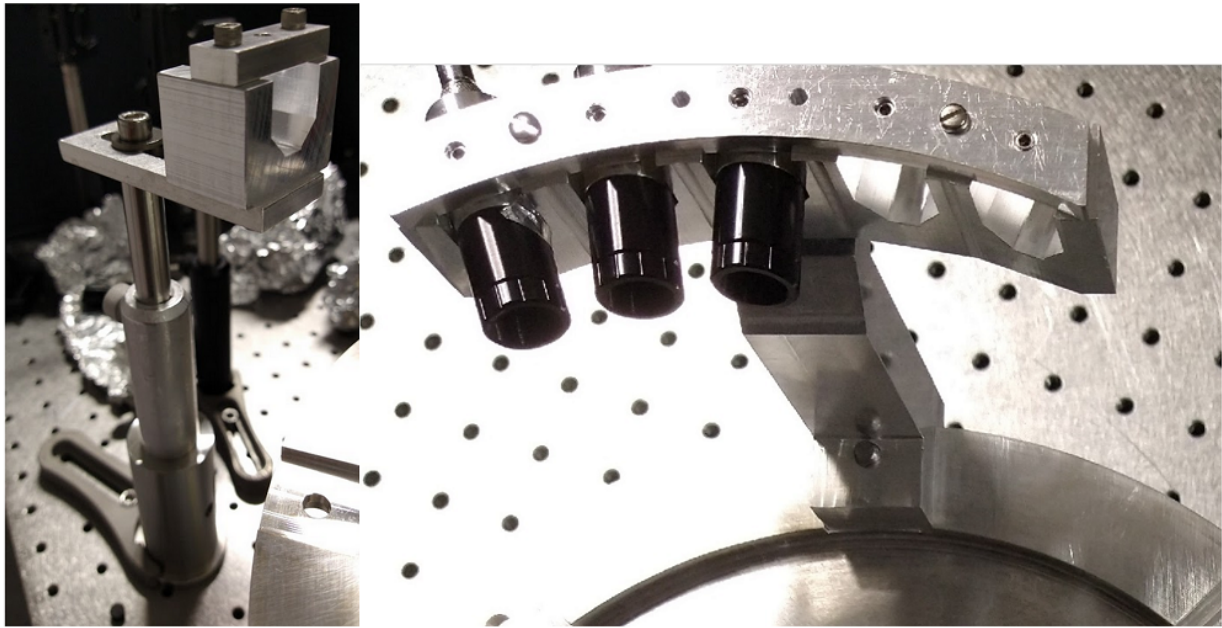


Figure 6.23: Images showing two types of detector holders. Left: A single detector holder. It is mounted on a $\frac{1}{2}$ " post inserted in a post holder, which is mounted on top of a 1.5" post with a bottom pedestal. The front face of the V-groove registers the radial distance. Right: A close up of the side AARC showing the front flats for each detector position.

The procedure to align one of the single detectors is described as follows:

1. The single detector was positioned azimuthally by rotating the AARC base so that one of the slots is located at the desired angle and then placing the single detector behind the slot and pointing the detector at the bead.
2. the single detector was positioned radially by rotating the AARC so that the side AARC was positioned adjacent to the single detector. The single detector holder's front face was moved to match the radial distance of the front detector flats of the side AARC. This was iterated with the previous step to correct for errors in moving the single detector. Once the single detector was positioned, the pedestal under the 1.5" post was clamped down.
3. Using the diametrically opposed slot to the one used to align the single detector holder,

an imaging system was set up to image the bead 180 degrees from the detector. Before back illuminating the fiber, the imaging system needed to be set to an appropriate exposure to prevent saturation. We used a Blackfly PGE-23S6M camera with a Navitar Zoom 7000 TV lens set at 108 mm focal length, which required the minimum shutter time and gain when back illuminating the fiber with a desk lamp. The imaging system did not need to be exactly precise - as long as it was able to clearly see the bead in focus as well as the projection of the back illuminated fiber.

4. Once the bead and back illumination was visible, the height of the $\frac{1}{2}$ " post underneath the single detector holder could be adjusted simultaneously with the yaw rotation to achieve optimal signal and centering of the illumination around the bead.

When repeating this process for other detectors, the imaging system would need to be moved. Fortunately, we had only used two fixed fiber detectors and, as mentioned above, the precision of the imaging system was not critical.

Given the limited space in the target chamber, a procedure was needed to align the fiber detectors in both the side AARC and single detector holders without creating a gridlock. The procedure to align the entire set of single detectors and AARC detectors is described as follows:

1. The fixed fiber detectors were to be aligned first before putting fiber detectors in the side AARC, because the fixed fiber detectors require rotation of the AARC base over large angles. The side AARC would be moved out of the way (for example, where the 0 deg detector aligns with $\theta = 20^\circ$) and the inspection imaging system would be set up (blue dots in Fig. 8) and alignment be done for each of the two fixed fiber detectors.

2. After the fixed fiber detectors are aligned, the imaging system was relocated (red dot in Fig. 8) looking through a gap in the array of fixed detectors (for example, $\theta = -75^\circ$) to allow the side AARC detectors to be inspected near their nominal positions during the experiment (for example $\theta = 105^\circ$).

This system will require the fixed electron detectors to be arranged so as to allow a gap in order for the fiber detectors in the side AARC (positioned at the +10 deg and -10 deg positions) to be inspected without colliding into the gas nozzle. When the -10 deg detector is at $\theta = 105^\circ$, the right edge of the side AARC would be at 140 deg.

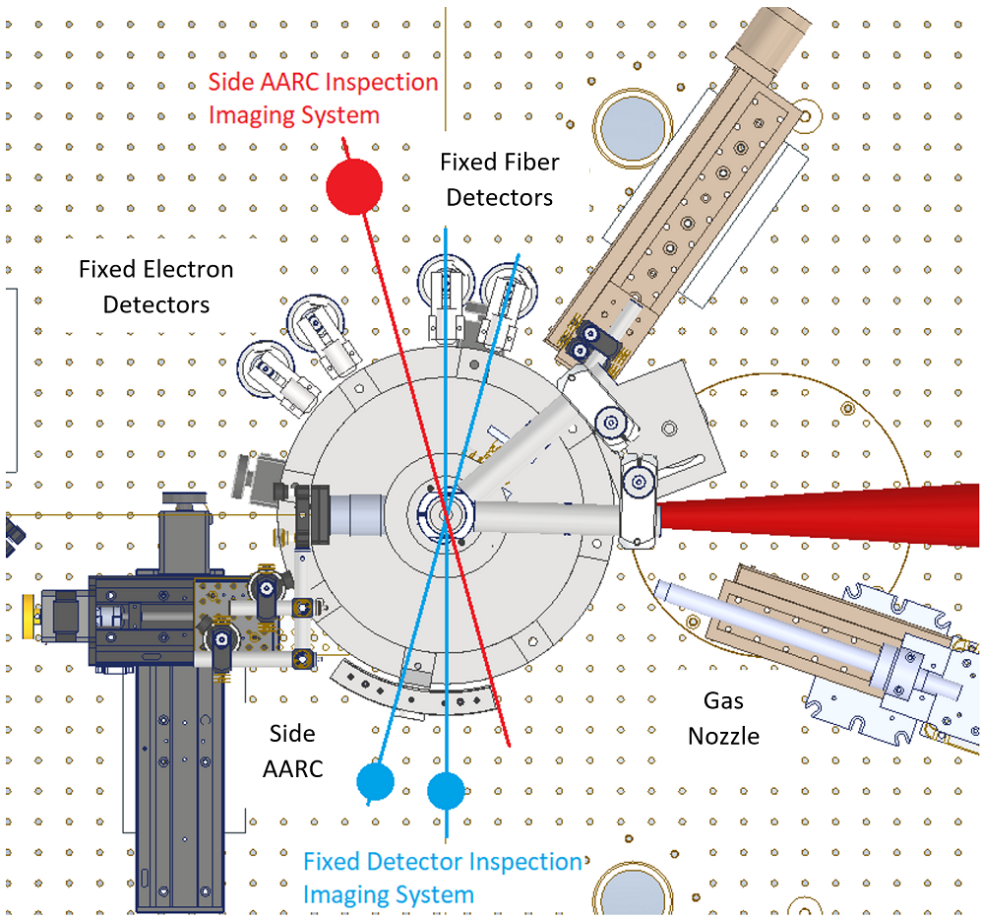


Figure 6.24: Diagram of the placement of the inspection imaging system during alignment. The red dot indicates the location of the camera which was made to focus on the alignment bead through a gap between the fixed detectors. The red line indicates this camera's line of sight across the opposite side of the bead where the movable detector, mount on the side arc, must be positioned for inspection. The blue dots indicated the positions for where the camera needed to be placed to inspect each of the two fixed fiber detectors across the bead. The side arc was rotated out of the way to allow a clear line of sight to the fixed detector.

6.4.2 AARC Alignment to Laser Focus

There were three lasers involved in the alignment. The first was a green diode laser (532 nm) in the target area, that passed through the TCC at an angle. The second was a diode laser from the laser bay made available on Week 2. The third was the VEGA-3 laser running at low power. The intention would be that all three lasers overlap at the focus, and that the diode laser

was collinear with the VEGA-3 laser. While there was likely some deviation between the beams, they were small due to their sharing of a common imaging system for imaging the focal spot. Due to time constraints, the green laser was used for aligning the AARC.

The AARC had two linear translation stages, one more-or-less along the laser axis and the other transverse to it. The exact parallelism and perpendicularity was not critical, since these stages spanned a plane containing the laser \mathbf{k} vector, and their home positions referenced by the bead. The bead of the AARC was determined to be well-aligned in the transverse direction relative to the green laser when transmitted light through the bead (which acts like a lens), captured by the focal spot imaging system, displayed a symmetrical pattern on the image, as shown in Fig. 6.25b. Since the field-of-view (FOV) of the imaging system (around 200 microns – based on a calibrated tip size of 9.5 microns) was smaller than the size of the bead itself (450 microns), the AARC transverse linear stage needed to be translated in order for the edges of the bead to come into view, as shown in Fig. 6.25a and c. The bead was determined to be well-aligned longitudinally to the beam when the edges of the bead appeared in focus on the imaging system. After the imaging system was aligned, the bead was removed, and the motorized tip was moved into the field-of-view of the imaging system and adjusted until it was centered and in focus, as shown in Fig. 6.25d.

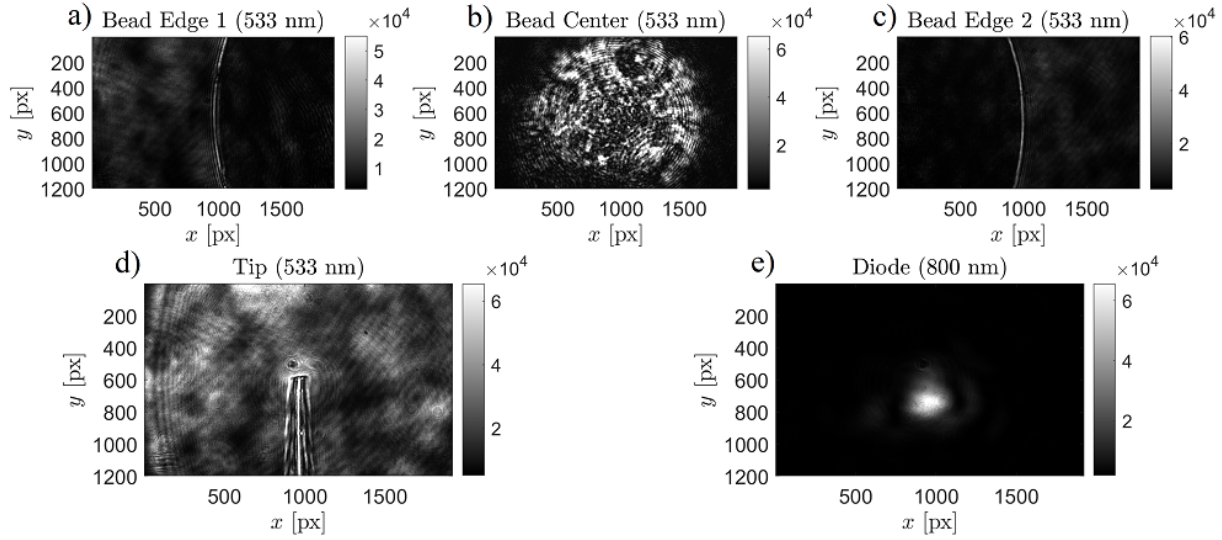


Figure 6.25: Images captured by the microscope objective imaging system oriented along the main beam during alignment. See Fig. 6.3 for schematic. Shown are images of the a) left edge, b) center, and c) right edge of the bead. Also shown are d) the alignment tip and e) the diode laser. A 533 nm laser was used for illumination of the bead and tip, whereas the diode laser was 800 nm.

It turned out that the physical height of the laser, instead of the nominal 230 mm provided to us prior to the experiment, was 227 mm. To address this realization, the AARC assembly, being mounted on a 23 mm rising block and four 2 mm thick shims beneath the block corners, was lowered by removing the shims, lowering the bead to 228 mm. The remaining 1 mm offset in height was compensated by raising the beam height of the laser by adjusting the alignment mirrors. The diode and VEGA-3 beams were also raised by 1 mm by adjusting the focusing parabola. The imaging system, which captures the image of the diode laser as shown in Fig. 6.25, was used to fine tune the parabola adjustment.

The AARC rotation stage was referenced to the laser axis using diametrically opposed pupils set at the height of the bead. The AARC was rotated so that the alignment laser passed through both pupils while scattering off the bead. The rotation stage had a physical home corresponding to the limit switch, which was disabled during operation, but may be enabled when

referencing was required. It turned out that simply mounting the AARC rotation base onto the rotation stage by eye was enough for the pupils to be aligned to the laser without further fine tuning in the rotation of the stage. The home position of the rotation stage was therefore the same position for positioning the Side AARC's center detector at 90 degrees relative the laser propagation axis. Since the pupil diameter was 2 mm and located 125 mm from the rotation axis, the rotational calibration was correct to within $\pm 0.5^\circ$.

6.5 Reimaging of Fiber Array

The streak camera was designed to accept light through its input slit, which is delicate and prone to damage from physical contact. To avoid this, it would be necessary to couple the light from the flat cleaved fibers into the streak camera without attempting to place the fibers at the plane of the slit. A reimaging system, illustrated in Fig. 6.26, was therefore designed for this purpose. The lens comprising the reimaging system (Nikon F-mount 50 mm f/1.4), the fibers, as well as the streak camera input slit needed to be placed at distances relative to one another so as to optimize the f/# matching of the system while keeping all four fibers within the field of view.

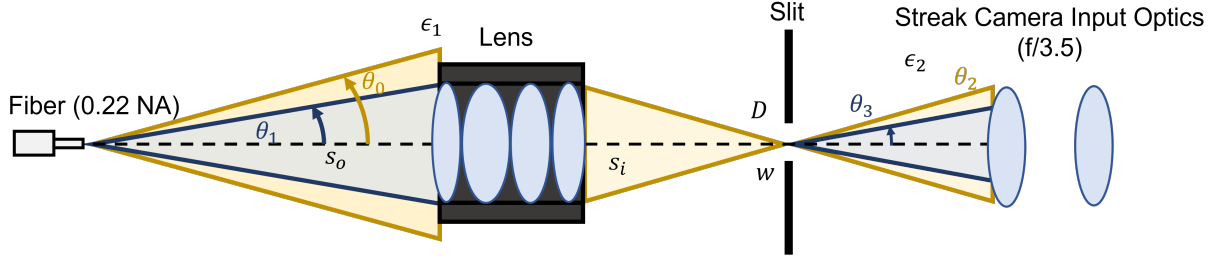


Figure 6.26: Diagram of the reimaging system used for coupling the output fibers onto the input slit of the streak camera, showing the geometric quantities used for calculating coupling efficiency. The output fiber emits light with a cone half-angle θ_0 based on its NA specification. The lens ($f = 50$ mm) with a front surface distance s_o from the fiber collects a half-angle of θ_1 . The collection efficiency at the lens, ϵ_1 depends on θ_0 relative to θ_1 . The lens and focuses the light onto the slit at a distance s_i from the lens back surface. The image of the fiber face has a diameter D at the slit, set to a width w (which during the experiment was open all the way, allowing the entire fiber image through). The output half-angle, θ_2 , is determined by s_i as well as the lens output aperture diameter. The streak camera input optics captures with a half-angle θ_3 . The collection efficiency at the streak camera input depends on θ_2 relative to θ_3 . The total collection efficiency is $\epsilon_1 \times \epsilon_2$.

The collection efficiency of the reimaging system is given by $\epsilon = \epsilon_1 \times \epsilon_2$ where ϵ_1 and ϵ_2 are the collection efficiencies at different stages of the reimaging system, and are equal to either the ratio of the solid angles of the output light and the collection aperture, that is $\epsilon_1 = \Omega_1/\Omega_0$ and $\epsilon_2 = \Omega_3/\Omega_2$ (overfilled condition), or unity (under-filled condition). The solid angle is related to the half-angle via $\Omega_i = \int_0^{2\pi} \int_0^{\theta_i} \sin \theta d\theta d\phi = 2\pi(1 - \cos \theta_i)$, hence:

$$\epsilon_1 = \begin{cases} \frac{1 - \cos \theta_1}{1 - \cos \theta_0} & \theta_0 > \theta_1 \\ 1 & \theta_0 \leq \theta_1 \end{cases} \quad (6.4)$$

$$\epsilon_2 = \begin{cases} \frac{1 - \cos \theta_3}{1 - \cos \theta_2} & \theta_2 > \theta_3 \\ 1 & \theta_2 \leq \theta_3 \end{cases} \quad (6.5)$$

The angles themselves were determined as follows:

- θ_0 is determined by the fiber numerical aperture (0.22) and is equal to $\sin^{-1}(0.22) = 12.7^\circ$.

- θ_1 is determined by the object distance, s_o , and the input clear aperture of the lens, which is measured to be 34 mm, and is equal to $\tan^{-1}(34 \text{ mm}/(2s_o))$.
- θ_2 is determined by the image distance, s_i , and the output clear aperture (in reality, it may be smaller, but this is a conservative approximation), measured to be 32 mm, and is equal to $\tan^{-1}(32 \text{ mm}/(2s_i))$.
- θ_3 is determined by the f/# of the streak camera input optics, which comprises of a pair of f/3.5 lenses located such that the slit is one focal length away from the first lens, and is equal to $\tan^{-1}(1/(2 \times 3.5)) = 8.13^\circ$.

The object and image distances, s_o and s_i , were defined as the distances from the front and back flange of the lens respectively, as shown in Fig. 6.28. Their relationship is one-to-one, and was characterized by measuring the distance of the best-focus image formed of a 1 cm section of a ruler for each lens distance from the object. The size of the corresponding image, D_{image} was also measured to obtain the magnification.

The quantities s_o and s_i are not to be confused with the object and image distances relative to the principal planes, $s_{o,pp}$ and $s_{i,pp}$, which approximately follows the thin lens relationship:

$$\frac{1}{f} = \frac{1}{s_{o,pp}} + \frac{1}{s_{i,pp}} \quad (6.6)$$

Nevertheless, these distances are related by offsets, i.e., $s_o + h_o = s_{o,pp}$ and $s_i + h_i = s_{i,pp}$ where h_o and h_i are constants equal to the displacement between the physical back and front of the lens and the back and front principal planes respectively. The lens was characterized by measuring s_i and the magnification, M , as a function of s_o , and then determining h_o and h_i by

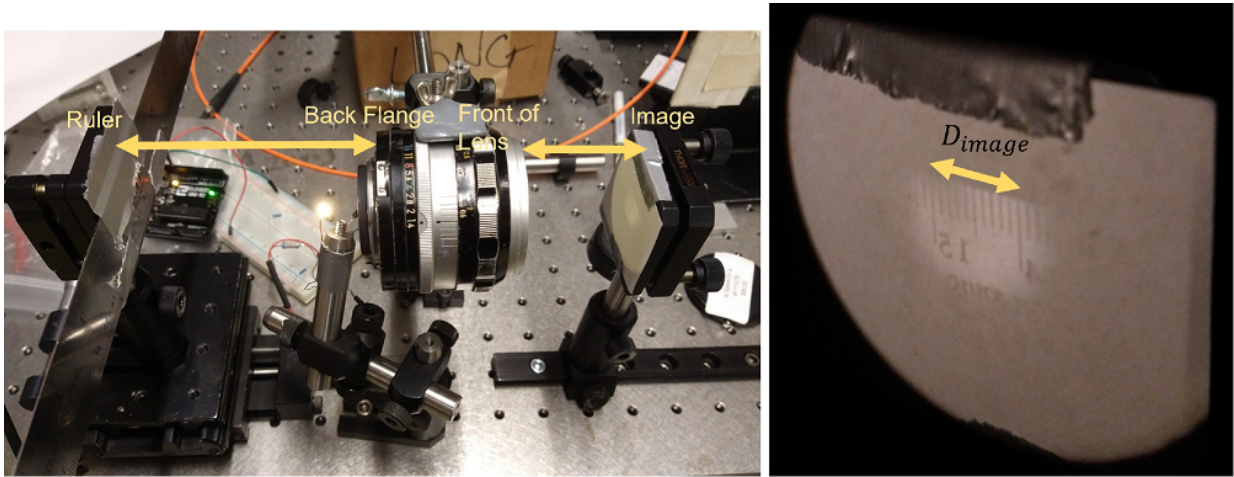


Figure 6.27: Photos showing the setup used for measuring image distance s_o versus object distance s_i of the reimaging lens. The reimaging lens is a Nikon F-mount 50 mm f/1.4 camera lens with its focus ring set to the minimum focus distance. The image on the right shows the imaged ruler section used for determining the location of the image plane as well as magnification, via the image size D_{image} , over a set of distances.

fitting Eq. 6.6 to the data, with h_o and h_i as the fitting parameters, as shown in Fig. 6.28a. The result is $h_o = 10.5$ mm and $h_i = 51.47$ mm. These values were also used to calculate M using $M = (s_i + h_i)/(s_o + h_o)$ and plotted against the data points in Fig. 6.28b.

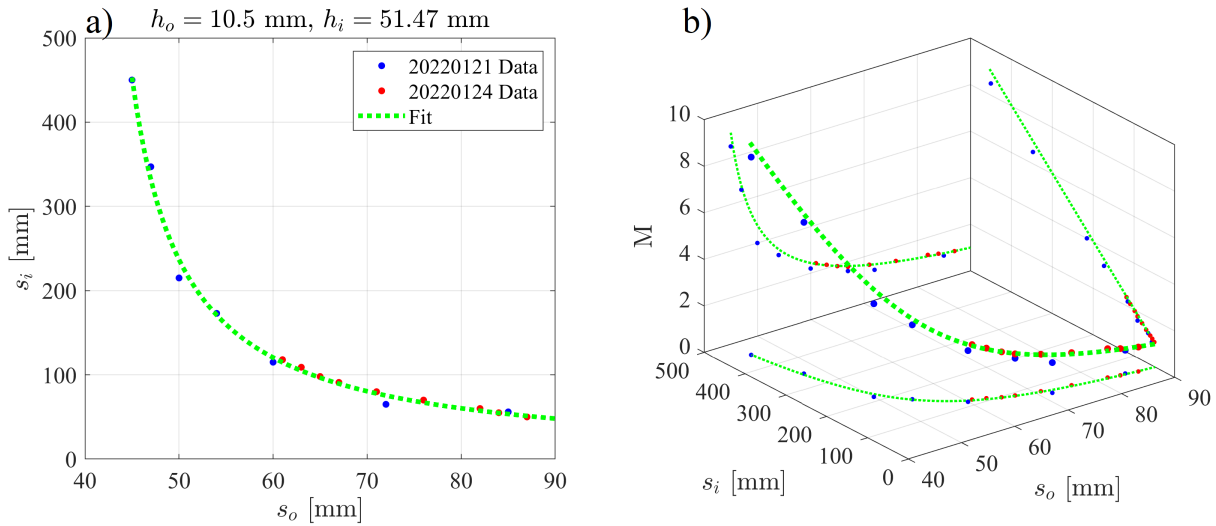


Figure 6.28: Plots of a) the image distance versus object distance datasets taken over two different days along with a fit over the combined dataset and b) same as a) but with the magnification measurements included.

The conclusion based on the previous discussion is that the total light collection efficiency ϵ of the reimaging system has a one-to-one relationship with the magnification M of the imaging setup (via their mutual relationship with s_o and s_i). Figure 6.29 shows that ϵ increases with M up to a certain value ($M \sim 2$) after which no more efficiency can be gained from increasing the magnification. This can be understood intuitively from the fact that the magnification is proportional to the image distance, which is inverse related with the solid angle entering the streak camera slit such that at a sufficient image distance, all of the light is collected by the streak camera input optics and none is lost to overfilling. Meanwhile, the light from the fiber end, which is placed close to the lens, are completely captured by the lens.

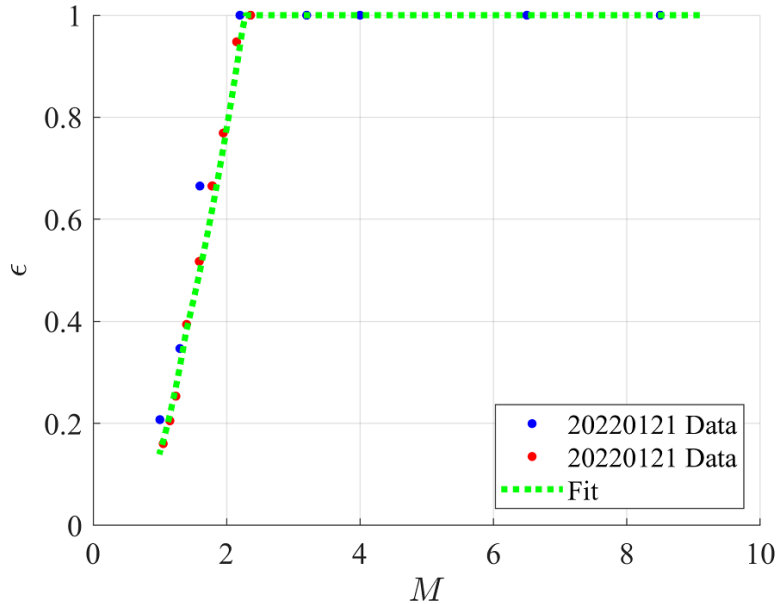


Figure 6.29: Plot of the overall efficiency versus magnification from the dataset as well as the curve based on the fit parameters. The overall efficiency is a function of s_i and s_o via $\epsilon = \epsilon_1(s_o) \times \epsilon_2(s_i)$ as is the magnification ($M = (s_i + h_i)/(s_o + h_o)$, where h_i and h_o are fit parameters). The requirement that the image is in focus provides a constraint between s_i and s_o .

The choice of M is limited by size of the fiber array and the length of the streak camera input slit (~ 17 mm), which would clip the image of the fiber array if the magnification is too

large. The fiber array consisted of the four flat cleaved fiber ends oriented horizontally in order to produce individual streaks in the final streak camera image. The spacing of the fibers needed to be small enough in order for the magnified image to fit within the streak camera input slit, while large enough where light from one fiber does not bleed into another. This was accomplished by designing a support consisting of a block of material with through holes just large enough for the fibers to be threaded. The initial prototype involved a 3D printed support as well as right angle clamps (normally used for post holders) used for cinching the jacketed portion of the fiber via bubble wrap, as shown in Fig. 6.30. The right angle clamps allowed the individual fibers to be adjusted for focus.

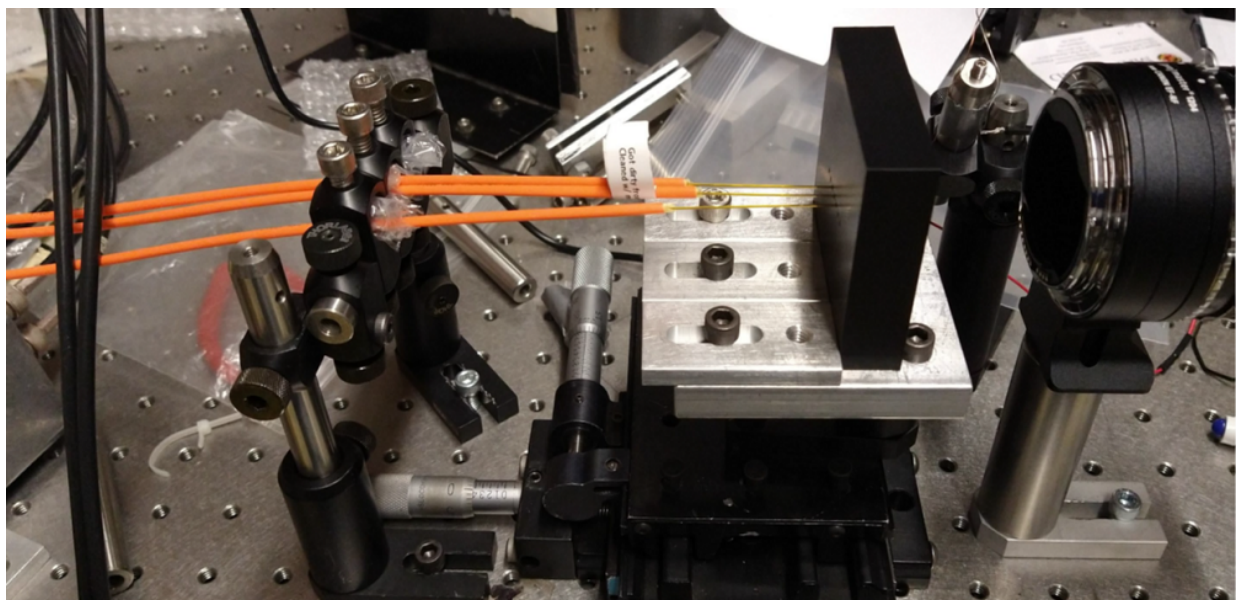


Figure 6.30: Photo showing initial prototyping of a system for holding mounting multiple bare fibers. A 3D printed block with ~ 2 mm holes was used to position the bare fiber ends, while an improvised cinching system consisting of right angle post clamps and bubble wrap over the jacketed (orange) portion of the fibers was used to position and secure the fiber ends longitudinally.

Later, the design was switched over to a 1 in. diameter cylindrical holder, which can be mounted on a mirror mount for adjustability. The final mounting system, shown in Fig. 6.31, consisted of an aluminum cylindrical holder mounted to a breadboard and block over which the

jacketed portions of the fibers were lightly clamped.

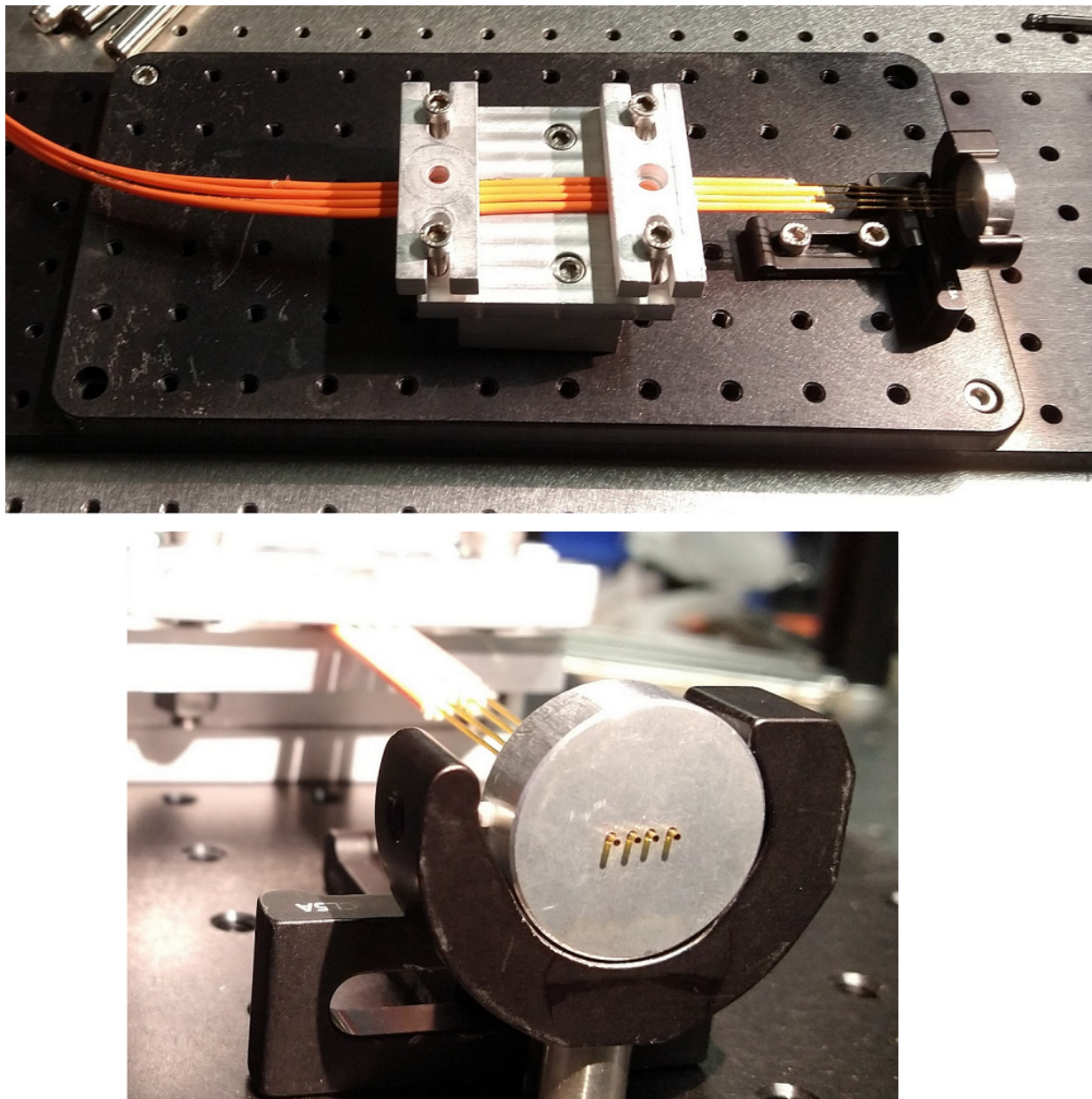


Figure 6.31: Photos showing the final assembly used to mount the output fibers. The fibers were secured using clamps over their jacketed regions, while the bare ends were threaded through ~ 1 mm diameter holes drilled through a custom-machined 1" diameter aluminum disc designed for compatibility with 1" optical mounts.

This mounting system was designed to be modular and easily integrated into the reimaging system shown schematically in Fig. 6.32. A light tight shroud made of black construction paper

and black anodized aluminum foil taped together was built to prevent ambient light from being collected by the streak camera.

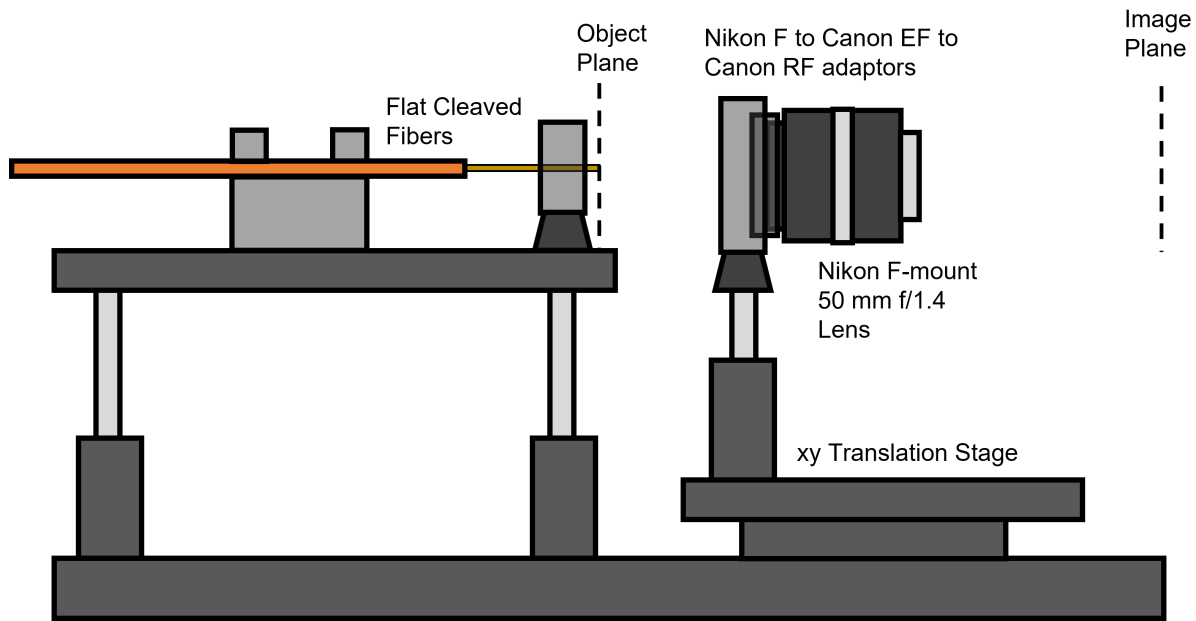


Figure 6.32: Diagram of the full assembly for output fiber mounting and reimaging. The Nikon lens was mounted on an xy translation stage for position adjustment to reimaging the bare fiber ends at the object plane onto the streak camera input slit located at the image plane. This assembly was put together, installed in front of the streak camera and covered in a light-tight shroud on short notice, therefore a photo is not available.

The final reimaging system had a magnification of ~ 1.7 as can be seen by the 1 mm size images of the fibers, which are physically $600 \mu\text{m}$ in diameter, in Fig. 6.33. This would give a $f/\#$ matching efficiency of about 50%. While a better efficiency may have been obtained from additional fine tuning the reimaging system for a higher magnification, as there was apparently more room in the slit for the imaged fibers, this was not done in the interest of time.

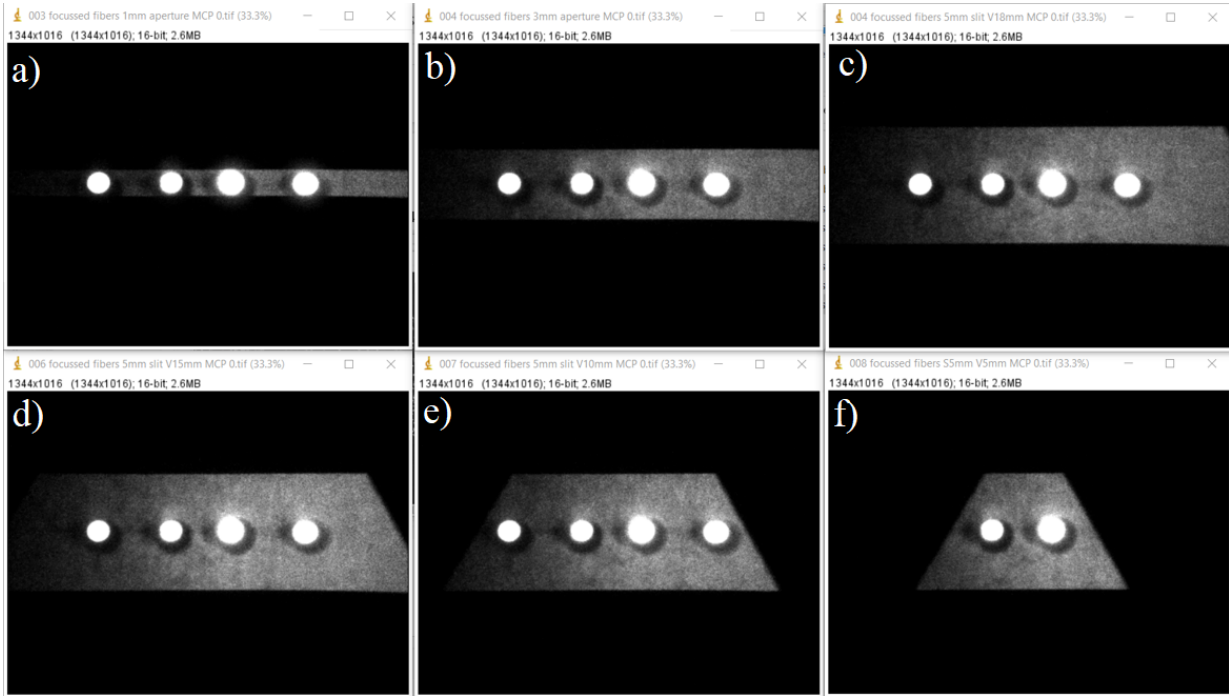


Figure 6.33: Images of the reimaged fibers along with ambient light collected at the input slit of the streak camera. The slit's width and length were set at a) 1 mm and 18 mm, b) 3 mm and 18 mm, c) 5 mm and 18 mm, d) 5 mm and 15 mm, e) 5 mm and 10 mm, and f) 5 mm and 5 mm.

6.5.1 Signal Bleeding and Ghosting

With the fibers setup, data was taken in order to characterize the bleeding of light from adjacent fibers as well as ghosting. Each fiber was individually illuminated to see these effects. As can be seen from Fig. 6.34, the individual fiber signals have coronas with a rather substantial extent ~ 2 mm, as well as ghost images appearing at roughly lateral reflection about the centerline of the image.

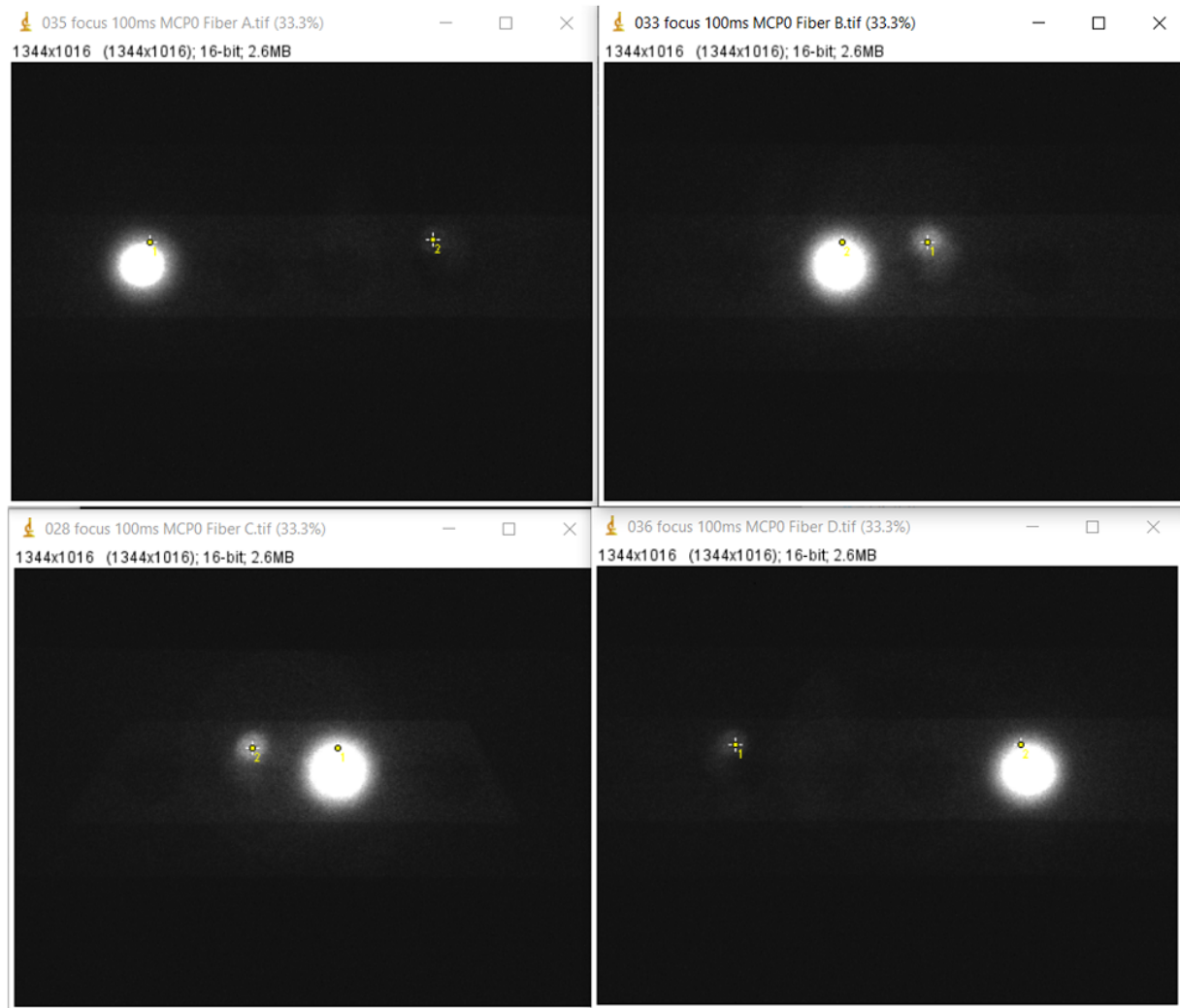


Figure 6.34: Images of individual illuminated fibers and their ghost images, captured by the streak camera. The ghost images are roughly located at a position horizontally-mirrored across the vertical bisector of the image and at a vertical distance higher than the center of the main spot by about a spot radius.

As shown in the lineouts in Fig. 6.35, the illuminated fibers produced a flat top distribution whose base extends 70-80 pixels (or 800 to 900 μm , based on the spatial calibration of 88 pixels per mm), while the tails extend to 150-250 pixels (1.7 to 2.8 mm). The ghost images have peak signals of 1% to 2% of the main signal peak and gaussian distributions whose base extends 75-100 pixels (850 to 1100 μm).

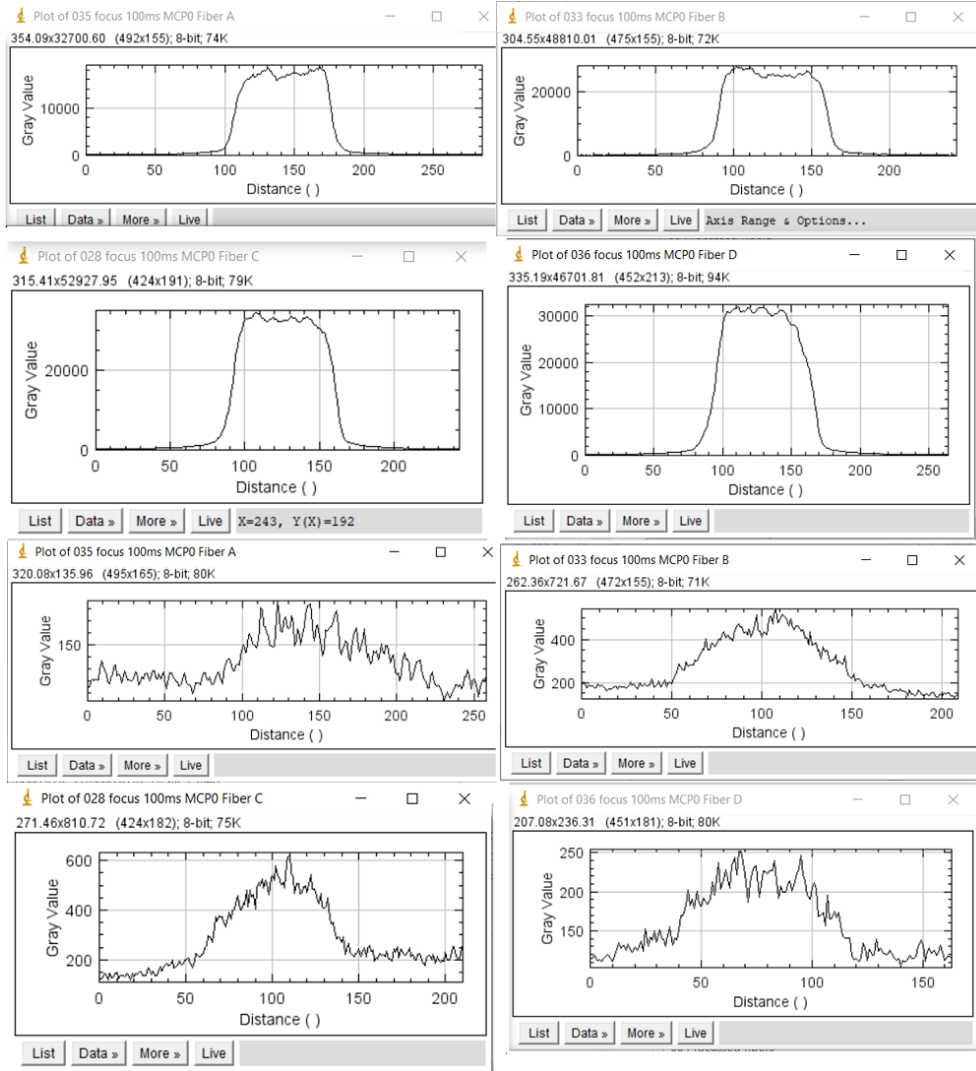


Figure 6.35: Plots of the lineouts of the illuminated fiber ends (top four images) and that of their corresponding ghost spots (bottom four images). See Fig. 6.34 for the image over which the lineouts were taken. The ghost spots peak at around a few hundred counts, while the main spots peak on the order of a few 10's of thousands of counts. The ghost spots therefore account for $\sim 1\%$ of the main spots and can be ignored if the signal strength between different fibers are within the same order of magnitude.

6.6 Measuring Temporally Resolved Signals with the Streak Camera

The streak camera's function was to resolve time varying light signals at resolutions as small as 10's of ps. This is accomplished by first converting the light into an electron flux propor-

tional to the light intensity at the photocathode via the photoelectric effect. The photoelectrons are accelerated through the gap between a pair of sweep electrode plates, where they are diverted in the transverse direction using a temporally ramped electric field produced by sweeping the voltage applied to the plates. The swept electrons then hit a phosphor screen and converted to light as they leave a fluorescent afterimage. This light is captured by a camera through an image intensifier. A diagram of the streak camera components is shown in Fig. 6.36.

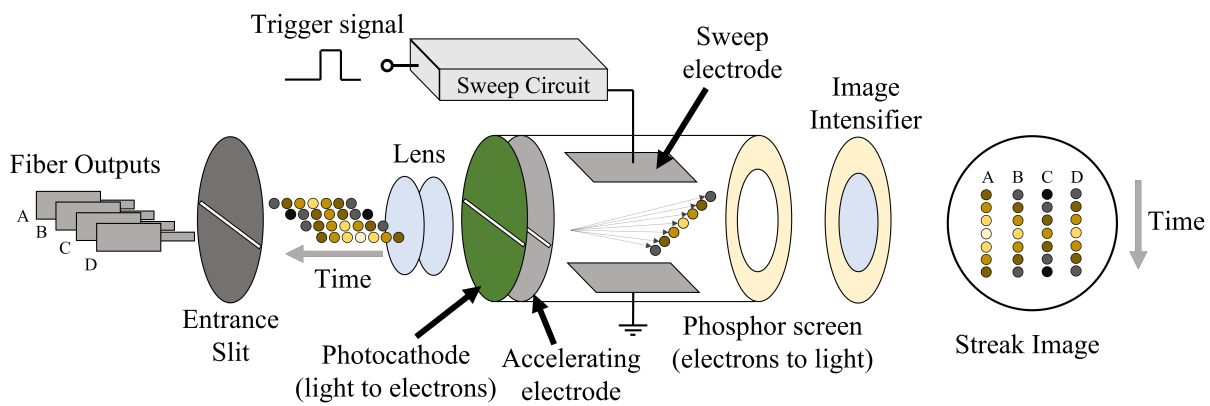


Figure 6.36: Diagram of components in a streak camera for converting temporal light signals into streak images. Light incident on a slit is collected by input optics which reimaging the slit onto a photocathode. Photoelectrons are generated at the photocathode and accelerated through the space between sweep electrodes. A temporally-ramped voltage across the electrodes causes the passing electrons to disperse vertically as a function of time. The dispersed electrons strike a phosphor screen, leaving a vertical streak whose vertical position is related to time. The image of the streak is captured through an image intensifier by a readout camera. Four fibers imaged on the entrance slit would result in four streaks in the readout image.

6.6.1 Streak Camera Timing

The streak camera (Hamamatsu C13410) timing system involves starting the sweep circuit on the streak unit (C13410) at least 17 ns prior to the arrival of the laser pulse at the target chamber center (TCC). The sweep circuit is normally held at a voltage that deflects electrons generated from the photocathode from the phosphor screen and image area. Sweeping this voltage over

time causes the electrons to hit the phosphor screen at a position correlated with time. A back sweep is necessary to reset the voltage to the starting conditions, during which the photocathode is automatically turned off to eliminate any conversion of light signal to electrons, and then turned back on again after the back sweep is completed. The afterimage of the streak left on the phosphor screen lasts on the order of milliseconds, during which fluorescent light is captured through an image intensifier (V12303-10) by a readout camera (C13440-20CU).

The sweep circuit may be run at a predefined repetition rate or triggered externally. In our experiment, it was triggered externally using a signal synchronized with the firing of the laser. The streak camera also allows the photocathode gate to be externally triggered (Trigger mode) as an alternate option to leaving it on (Normal mode). If the option to leave the photocathode on is selected, the photocathode will only turn off during the back sweep (as shown in Fig. 6.37).

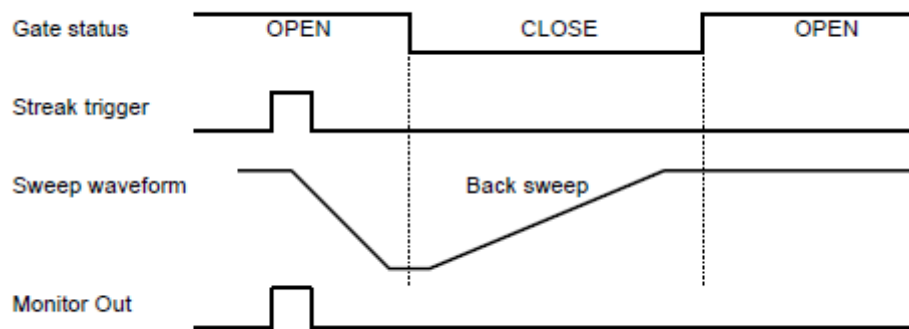


Figure 6.37: Timing diagram for normal mode operation. The gate status corresponds to voltage applied to the photocathode (active when open), while the streak trigger corresponds to the trigger to the sweep circuitry, which begins the application of the temporally ramped signal to the sweep plates (sweep waveform). After completing the sweep, the photocathode is deactivated and the voltage across the sweep plates are swept back to the initial voltage level, ready for the next trigger. Source: C13410 Instruction Manual.

To remove the capturing of light outside the time period of the desired streaked signal associated with leaving the photocathode on, the trigger mode can be selected so that the photo-

cathode is normally off and turns on only during sweep, including the period up to 10 μ s prior to the sweep (depending on delay settings), and turned off prior to the back sweep (see Fig. 6.38). While normal mode was used initially for diagnostics, we had later transitioned to trigger mode.

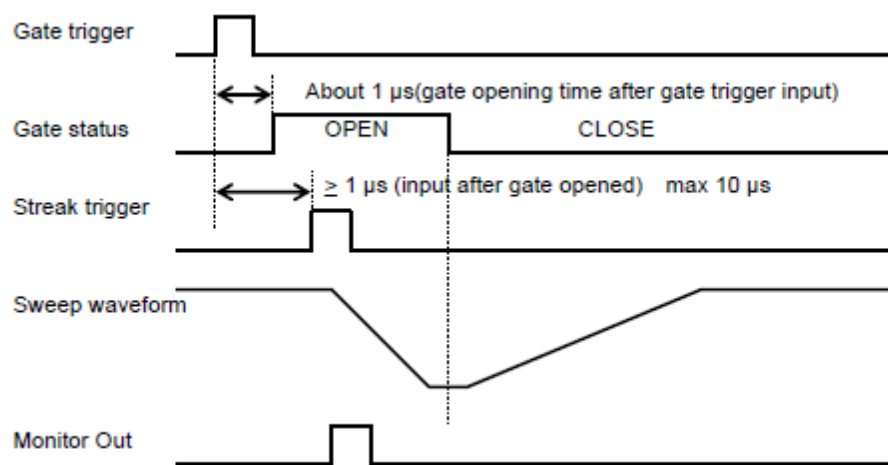


Figure 6.38: Timing diagram for trigger mode. The gate status, with "open" corresponding to the photocathode being active with voltage applied, in contrast to normal mode (Fig. 6.37), only occurs during the short window between the gate trigger and the end of the main sweep (before the back sweep). Source: C13410 Instruction Manual.

The trigger sources for the sweep circuit and photodiode gate are explained below. Variable delay generators, as shown in Fig. 6.39, were used to allow the operator to adjust the delay to find the value which matches the streak with the arrival of the light signal generated by the laser pulse.

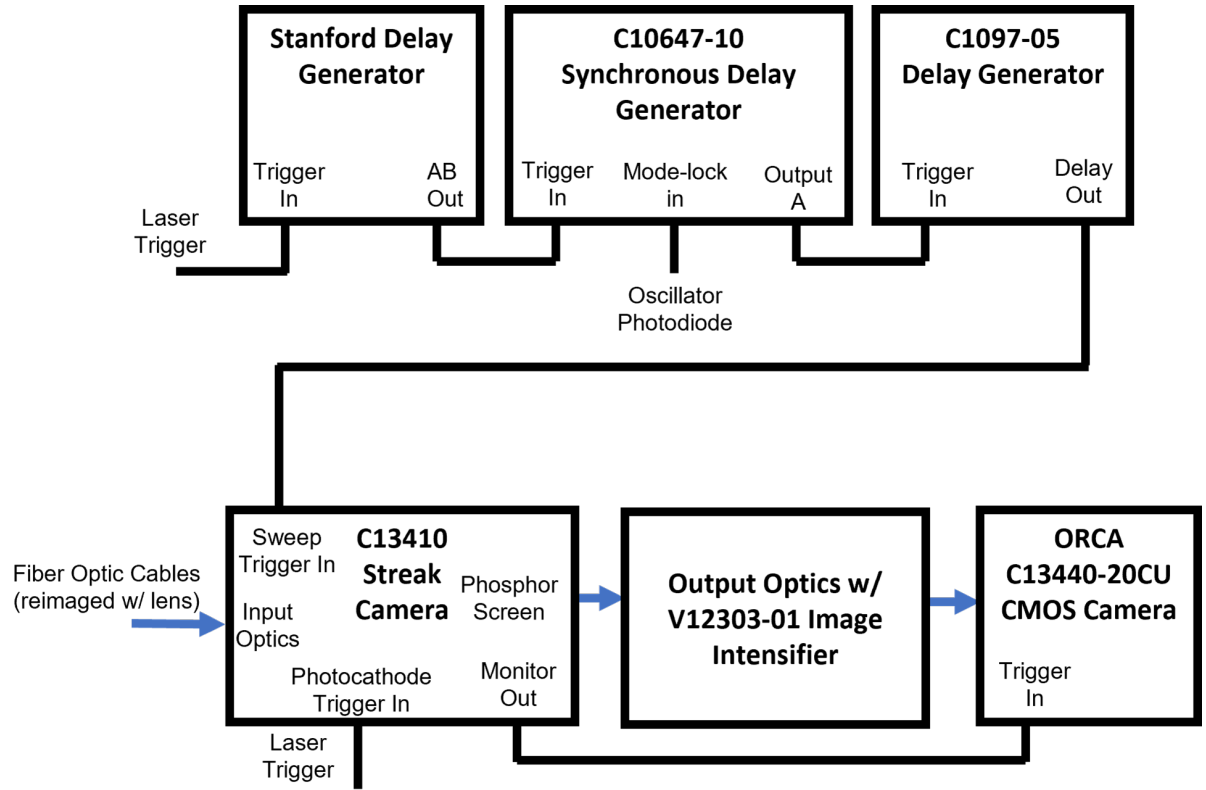


Figure 6.39: Diagram of trigger network for the streak camera in the target area. The Stanford and C1097-05 delay generators provided a fixed hardware controlled delay, while the C10647-10 Synchronous delay generator provided a trigger signal synchronized with the VEGA oscillator from a photodiode. The synchronous delay generator triggers off of the first oscillator pulse it sees after it receives a trigger from the laser trigger. The oscillator signal featured minimal jitter compared to the laser trigger (explained in Fig. 6.41), thereby providing more precise and stable trigger for the stream camera’s sweep electronics. The streak camera’s photocathode was triggered by the laser trigger since its timing precision requirements were not as demanding as the sweep electronics. The streak camera provides a delayed monitor out signal to trigger the ORCA readout camera.

A synchronous delay generator (C10647-10) utilizes a coarse gate and fine gate to output a low jitter trigger synchronized with the firing of the laser. The coarse gate receives a trigger that is synchronized with the firing of each laser pulse. The available sources provided for this trigger had jitters on the order of 350 ps, which would not be usable for fast streak speeds (e.g., 500 ps). To reduce the jitter to a usable level, a signal from the mode-locked oscillator is sent to trigger the fine gate. The synchronous delay generator outputs on the first oscillator pulse it sees after

receiving a trigger to the coarse gate. The resulting jitter at the streak camera is then around 10 or 20 ps.

The low jitter signal sent from the synchronous delay generator is then sent to the jitter-free C1097-05 delay generator, which can be controlled from a computer running Hamamatsu software (HPD-TA) to allow the operator to scan different delay values to find the signal. The streak camera provides a streak monitor out signal that is correlated with the timing of the streak to trigger the readout camera. The streak monitor out was also read out alongside the oscillator train, as shown in Fig. 6.40, to monitor the stability of the streak timing relative to the laser.

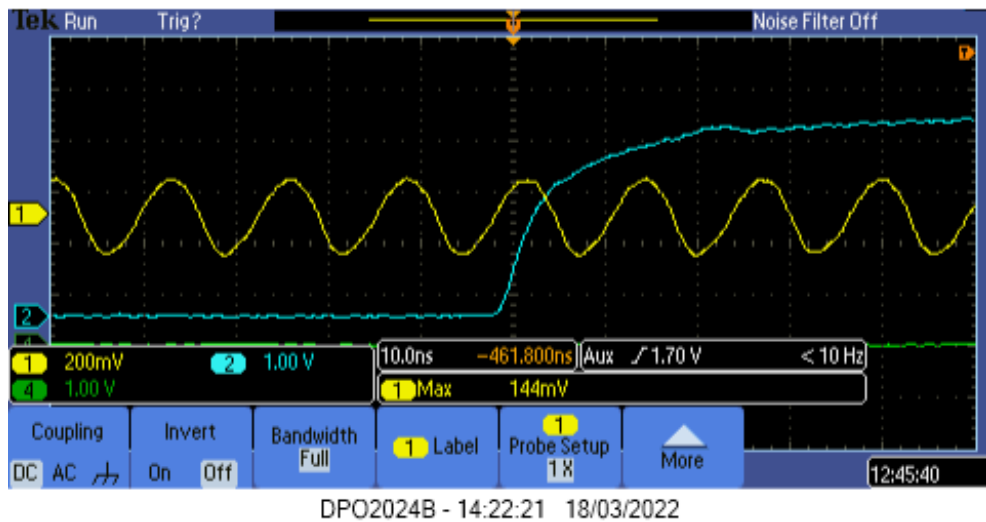


Figure 6.40: Scope image showing oscillator train and streak monitor out. The synchronous delay generator (Fig. 6.39) triggers off of the first oscillator pulse it sees after it receives a laser trigger. The streak monitor out is a signal synchronized with the laser trigger with some delay.

The signals for the triggers were generated in the laser bay as shown in Fig. 5. The oscillator signal comes from a fiber optic signal capturing the oscillator train, which has a 12.3 ns roundtrip time (78.125 MHz repetition rate) and sent to a photodiode. An FPGA-based device converts the oscillator signal into TTL clock signals of three different frequencies: 78.125 MHz

(same as the oscillator, 10 Hz, and 1 Hz. These TTL signals are distributed to five sites, each consisting of an FPGA-based delay generator, along the laser line for triggering various equipment. One such site is dedicated to triggering the VEGA-3 laser, including its Pockels cells. This is the site from which two triggers, synchronized with the firing of the laser, were provided for use in the target area (TA). The first of such triggers, which we call V3-1, is derived from the previous pulse during 1 Hz operation, and then delayed by about 800 ms, in order to provide a trigger that is sent earlier by 200 ms relative to the Pockels cells for triggering slow devices operating with the next pulse. The second of the triggers, which we call V3-2, is sent simultaneously (i.e., within a few hundred ns) with the firing of the Pockels cells. The exact delay timing of these triggers are shown in the inset table in Fig. 6.41 and their wave forms are shown in Fig. 6.42.

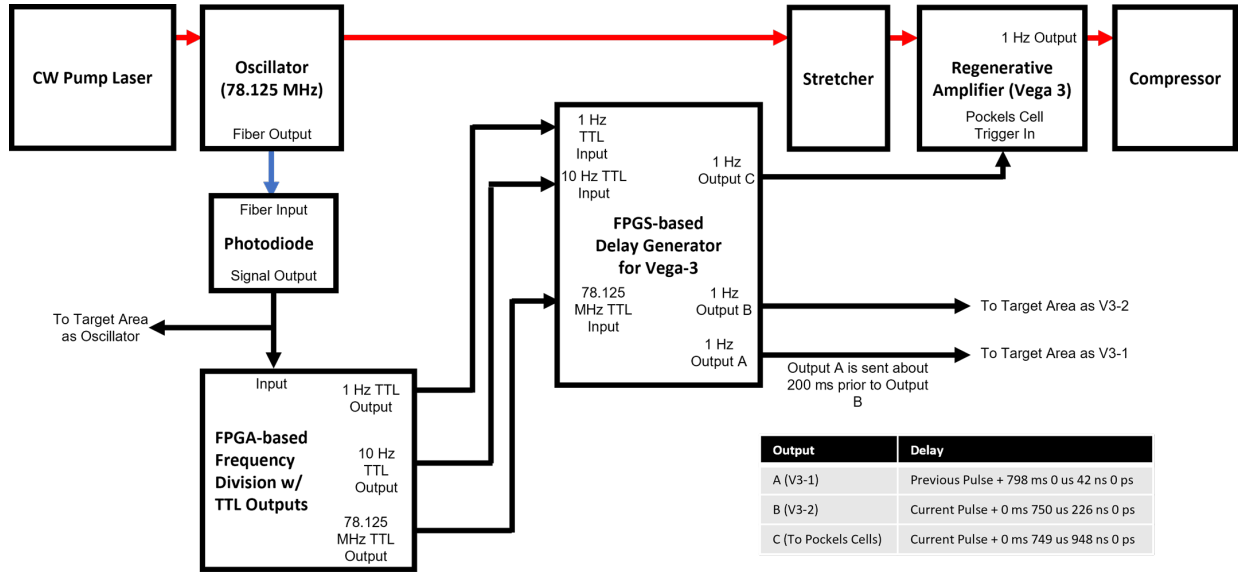


Figure 6.41: Diagram of the trigger sources in the laser bay. The signal from the oscillator (78.125 MHz) was sent to a FPGA-based frequency divider to generate 1 Hz, 10 Hz, and 78.125 MHz TTL outputs. These outputs were sent to an FPGA-based delay generator, which provide delayed 1 Hz outputs to the Pockels cells as well as to the laser bay. One such outputs, which we call V3-1, was a signal derived from the previous pulse (when operating in 1 Hz) with an added delay. Another output, which we call V3-2, was a signal derived from the current pulse and given a delay to closely match the timing to the output to the Pockels cell.

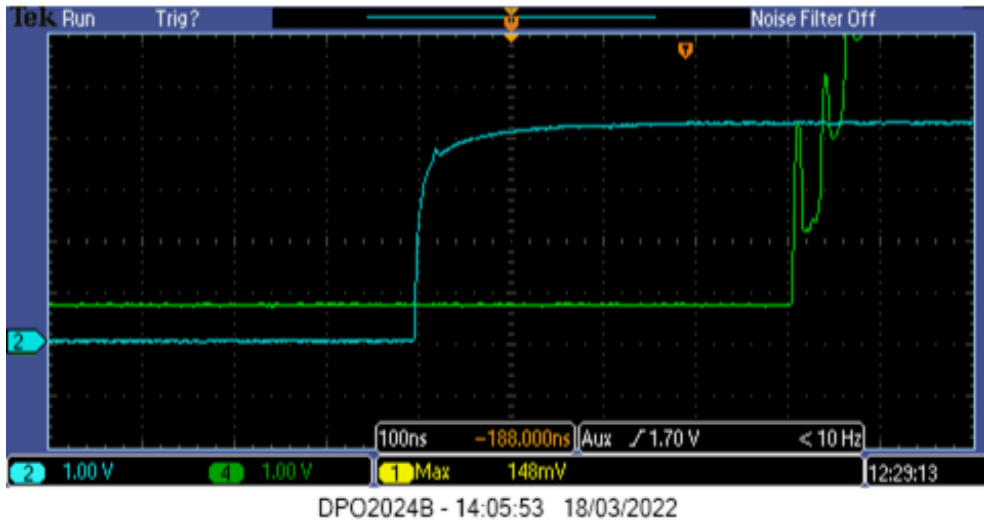


Figure 6.42: Scope image showing two triggers synchronized with the laser shots, CH2: V3-2 (blue) and CH4: V3-1 (green). These triggers are explained in Fig. 6.41. The V3-1 signal was initially used to trigger the synchronous delay generator for streak camera, but resulted in occasional jumps of 12.8 ns (one oscillator period) in the streak camera timing (see Fig. 6.43). When the V3-2 signal was used to trigger the synchronous delay generator, it resulted in no observed jumps.

During the testing of the streak camera, we had found that using V3-1 as the coarse trigger for the synchronous delay generator resulted in occasional jumps in the streak camera timing by one oscillator cycle (12.8 ns). Switching to using V3-2 for the coarse gate virtually eliminated this problem. Although we did not fully diagnose the cause, this was likely due to the arrival of V3-1 coinciding closely in time with the edge of an oscillator pulse, such that a small drift in time (a few ns) would result in an adjacent oscillator pulse being chosen for the fine trigger. The trigger V3-2 likely arrived far enough from the edge of an oscillator pulse that its drift was not enough to pass the edge.

In order to monitor the trigger stability, the signals from V3-1, V3-2, and the oscillator train were monitored with oscilloscopes. Additionally, the streak camera provides a streak monitor

output (STRK MON) signal correlated in time with the streaking of the camera and a photodiode was placed in the target chamber to capture the light from the laser when it reaches TCC. These were also monitored with oscilloscopes. As such, the drift and jitter in the relative time differences between these signals were monitored shot-to-shot. At finer time scales, the streaked images at 0.5 ns streak times were used to determine the shot-to-shot jitter.

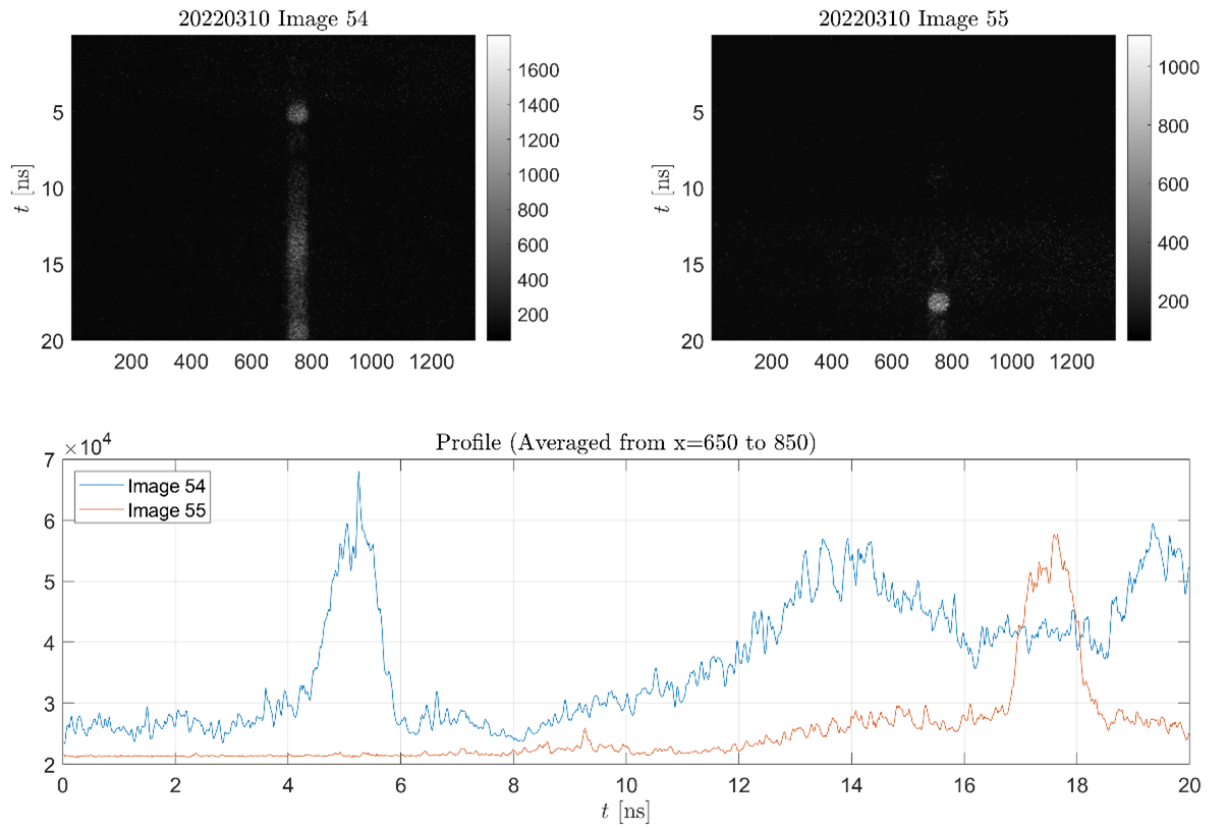


Figure 6.43: Streak camera images captured manually subsequently in time showing the evidence of jitter with jumps between adjacent oscillator pulses in the laser bay. The jump is 12.7 ns, which is consistent with the oscillator repetition period. The jumps occurred while the V3-1 signal (explained in Fig. 6.41 and Fig 6.42) was used as the laser trigger for the synchronous delay generator for the streak camera, and was removed upon switching to the V3-2 signal. Bottom: Temporal profiles averaged around the signal region for the two images shown in the top row.

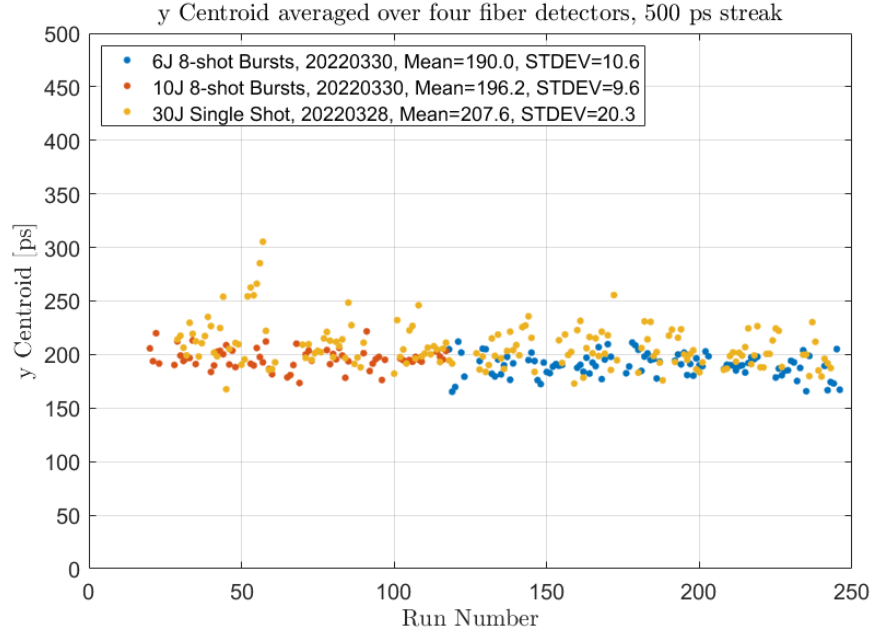


Figure 6.44: Centroids averaged over the four fiber detectors from the streak camera images at a 500 ps streak duration, taken during the live runs of the angular RTS scans at different energies. See, for example, Fig. 6.48 of a streak image with a 500 ps duration. The data points show stability in the streak camera signal throughout the live RTS measurements.

In order to determine the settings needed to capture the streaked image of the light produced when the laser pulse arrives at TCC, which we call t_0 , we ran the VEGA-3 laser at low powers (3 mJ) in atmospheric pressure order to produce light from air breakdown. This light is captured by the streak camera running at streak mode, at subsequently smaller streak durations with the delay adjusted to keep the streak signal centered, until it can be seen at the smallest streak duration, 0.5 ns. This delay setting was then used as the starting point for finding the RTS emission during the high power, live laser shots in vacuum.

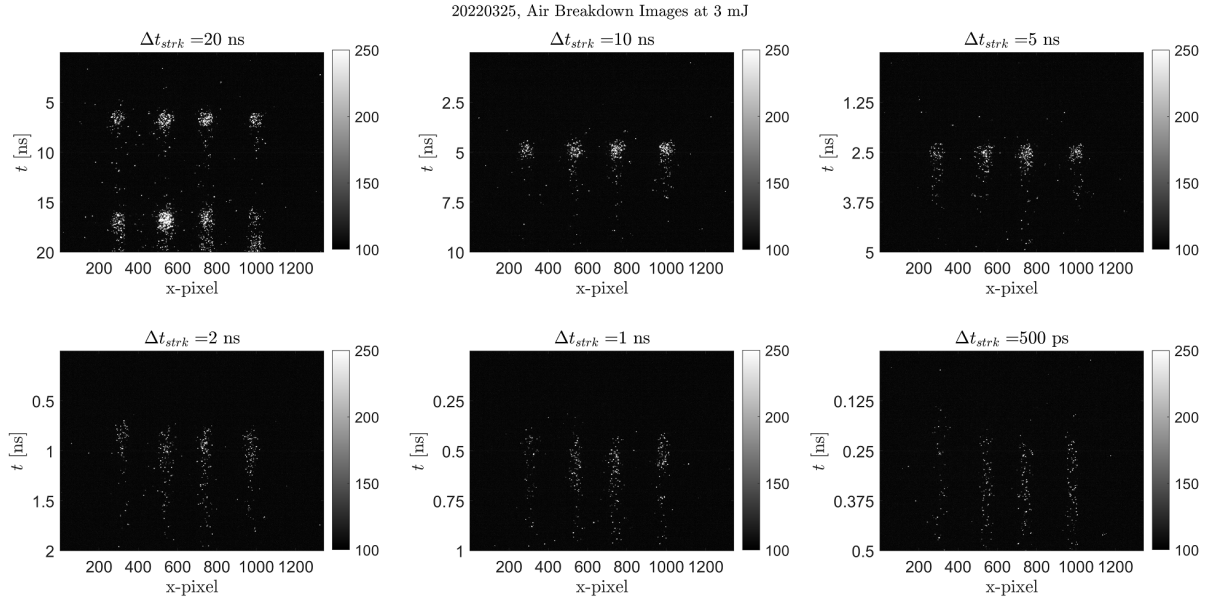


Figure 6.45: Streaked images from air breakdown from the laser at low power (3 mJ) at different streak times. Evident from the images, the air breakdown has a temporal duration of ~ 1 ns, which only begins to be resolved at the 5 ns streak time and lower. The second strong pulse in the image with a 20 ns streak time occurring ~ 10 ns after the initial signal was likely due to reflection from the chamber walls, consistent with the distance traveled by light over 10 ns (3 m) being on the order of the chamber dimensions. Images were taken on 03/25/2022.

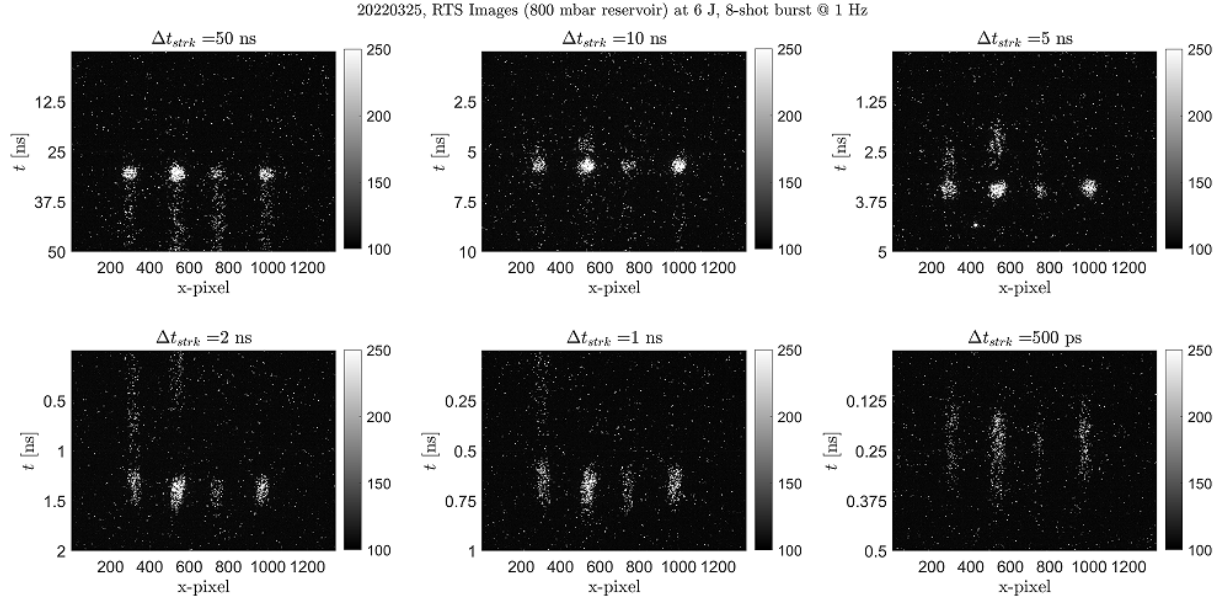


Figure 6.46: Streaked images from 6 J laser interaction with gas on (800 mbar reservoir pressure) at different streak times. The RTS signal begins to be temporally resolvable at 2 ns streak times, and is fully contained within the 500 ps streak time image, showing a signal duration of ~ 300 ps. Images were taken on 03/25/2022.

During streak mode operation, each streak duration has a different delay value needed for the streak camera to capture the same point in time. Hamamatsu has a table of recommended delay offsets for each streak duration relative to the delay for the 500 ps streak duration. During the experiment, these delay settings were used as starting points and adjusted as necessary to find the time of light emission of interest. Both the manufacturer recommended delays and experimental delays are shown in Table 6.4.

Sweep Duration [ns]	Spec Sheet Delay [ns]	Δ [ns]	Experimental Delay [ns]	Δ [ns]
100	279	121	585.0	0.0
50	158	110.6	585.0	3.0
20	47.4	16.3	588.0	16.0
10	31.1	13.4	604.0	13.6
5	17.7	15.7	617.6	13.9
2	2.0	1.9	631.5	1.9
1	0.1	0.1	633.4	0.1
0.5	0		633.5	

Table 6.4: Table of delays (from Hamamatsu spec sheet as well as experimental settings, recorded on 3/23/2022) versus sweep duration. The experimental delay is defined as the sum of the delay produced by the three delay generators between the laser trigger and the streak camera needed to observe the RTS signal, though not necessarily have the signal centered. It can be observed that the difference in delay, Δ , between sequential sweep duration settings for both the Hamamatsu recommended delays and the experimental delay settings are the same at 2 ns sweep time and smaller (highlighted in bold). At higher sweep times, it was not necessary for the experimental delay to be adjusted substantially to observe the RTS signal.

There are multiple factors determining the temporal resolution of the streaked fiber system:

1. The size of imaged fiber face on the readout camera
2. Dispersion in the fiber
3. Temporal dispersion in the streak camera optics and electronics

The size of the image fiber face at the readout camera while the streak camera is in focus mode and slit is open affects the temporal resolution in that light captured at the streak camera input during an instant in time, will have a temporal full-width at half maximum (FWHM) during streak mode given by:

$$\Delta t_{\text{im}} = \frac{D_{\text{pix}} \Delta t_{\text{strk}}}{1016} \quad (6.7)$$

where D_{pix} is the imaged fiber diameter in terms of pixels, Δt_{strk} is the streak time, and

1016 is used as the vertical image resolution. The full-width at half maximum diameter of the image of the fiber is about 60 pixels, corresponding to 30 ps when the streak camera is set to 500 ps streak mode.

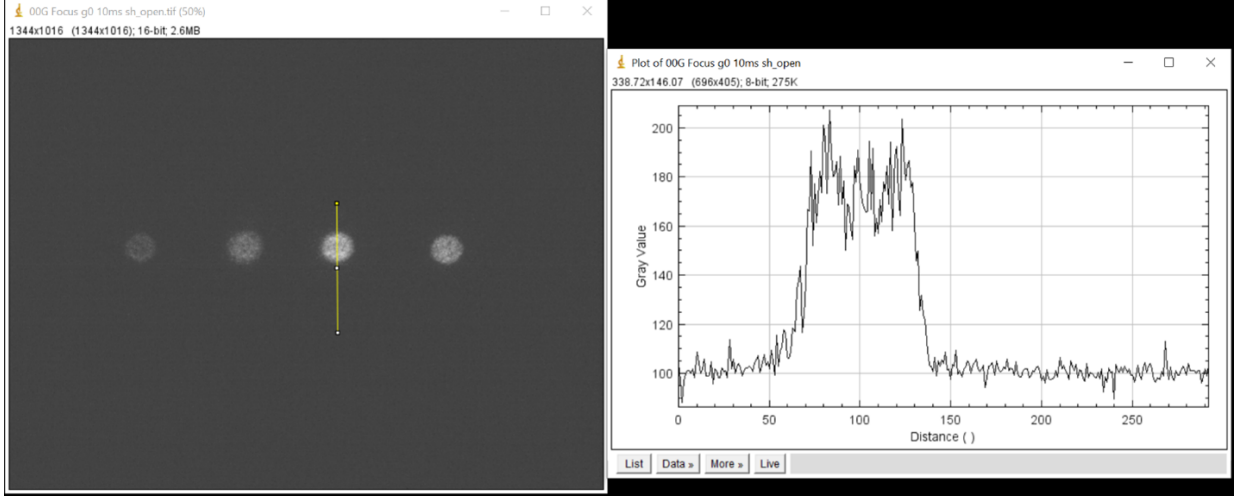


Figure 6.47: Image of fiber face on the readout camera in focus mode, as well as a vertical lineout of one of the fiber spots. In focus mode, the input slit of the streak camera is imaged directly without temporally streaking the signal. The FWHM of the spot is ~ 60 pixels, corresponding to 30 ps at 500 ps streak time.

As Thorlabs do not make measurements of the dispersion characteristics of their multi-mode fibers, their suggestion was to calculate for modal dispersion as the dominating contributor and add on a few ps to account for chromatic dispersion. Modal dispersion, which is the path difference of the fiber for rays incident at the maximum acceptance angle compared to a normally incident ray, is given roughly by [98]:

$$\Delta t_{\text{disp}} = \frac{L \times \text{NA}^2}{2n_{\text{core}}c} \quad (6.8)$$

which is about 221 ps for parameters based on the experiment, with $L = 4$ m, $\text{NA} = 0.22$, and $n_{\text{core}} = 1.46$. Combined with chromatic dispersion effects contributing another few ps, a

10 second light pulse, corresponding to the laser pulse transit time over the fiber detector's 3 mm field of view diameter, would result in a ≈ 235 ps signal at the end of the fiber output face. Parameters of the streak tube which contribute to the temporal resolution include space charge repulsion of electrons, as well as longitudinal components of momenta added to swept electrons by the real (nonideal) sweep electrodes.

6.7 Experimental Procedure

The first day of data acquisition for the high resolution RTS angular distribution took place on 03/28/2022. During this day, the laser operated at full power, single-shot, with an on-target energy of 20.5 ± 0.2 J. This was lower than the typical 23 J energy on-target provided by the VEGA-3 laser due to a failure in an amplifier for one of the pumps to the main amplifier, resulting in a shutdown of that pump for the day. The AARC was rotated at 5° increments from $\theta_{\text{Arc}} = -55^\circ$ to 20° , where $\theta_{\text{Arc}} = 0^\circ$ corresponds to the central detector on the side arc oriented perpendicular to the laser beam, and $\theta_{\text{Arc}} = -90^\circ$ corresponds to the central detector looking head on at the incoming beam. At each position, 10 – 12 acquisitions of the signal and 3 – 4 acquisitions of the background (gas nozzle off) were typically taken.

The second day of data acquisition for high resolution RTS angular distribution was 03/30/2022. Three energies were used: 9.01 ± 0.07 J, 5.78 ± 0.05 J, and 1.90 ± 0.05 J. As with the angular scan at 20.5 J on the previous RTS acquisition day, angular scans from $\theta_{\text{Arc}} = -55^\circ$ to 20° at 5° increments were performed at each of the three energies, taking typically 4 – 6 signal acquisitions and 2 – 3 background acquisitions per angle. For these lower energies, however, rather than running at single-shot, each acquisition consisted of 8-shot bursts at 1 Hz. Data capturing

the pulse energy and duration for both days are summarized in section 6.1.4.

6.8 Results and Analysis

In the end, 164 signal and 48 background runs were used in the analysis for the 20.5 J scan, 65 signal and 35 background runs for the 9.01 J scan, 95 signal and 33 background runs for the 5.78 J scan, and 159 signal and 48 background runs for the 1.90 J scan. A typical streaked image, example shown in Fig. 6.48, consists of four streaks each coming from a different fiber detector. Since only the F3 and F4 fibers were mounted on the side arc, whereas the F1 and F2 were on stationary mounts, only the F3 and F4 detectors were used to determine the final results of the analysis. Regions of interest (ROI) were chosen for streaked images to contain the F3 (red box) and F4 (blue box) detector streaks, even with jitter taken into account. The regions of interest were each 151 pixels in width and 813 pixels in height, corresponding to a duration of ~ 400 ps. The ROIs for the F3 and F4 detectors remain unchanged across signal and background and the entire range of angular positions and laser pulse energies

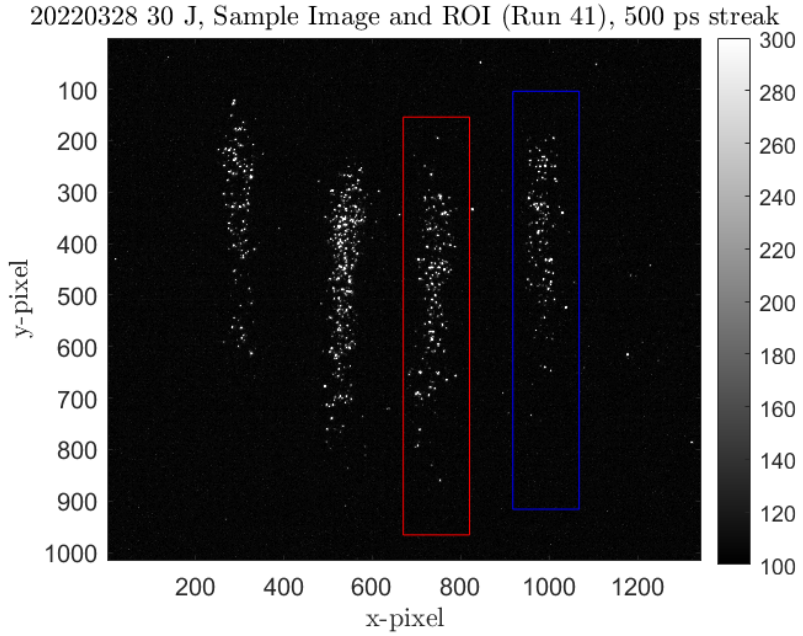


Figure 6.48: An example image of the streaked fibers (labeled from left to right: F1, F2, F3, F4) taken with a streak duration of 500 ps. The red and blue boxes indicate the regions of interest for the F3 and F4 fibers respectively, which were mounted on the side arc. The F1 and F2 fibers were fixed and were not included in the analysis.

In order to obtain relative angular RTS values, a sum over the counts were taken over the ROI and then divided by the total number of pixels, 122763. This value was then, for the days in which 8-shot bursts per run were acquired, divided by 8. This value was averaged over the different samples at the same angle for both the signal and background sets separately, and then the averaged background was subtracted from the averaged signal for each angle to ultimately get a value in the background-subtracted average counts per pixel per shot. Figure 6.49 shows log scale plots of the background-subtracted signals and the resulting angular distribution data, whose uncertainties are the standard errors (standard deviation divided by the square root of the number of data points) of the set of signal and background images added in quadrature.

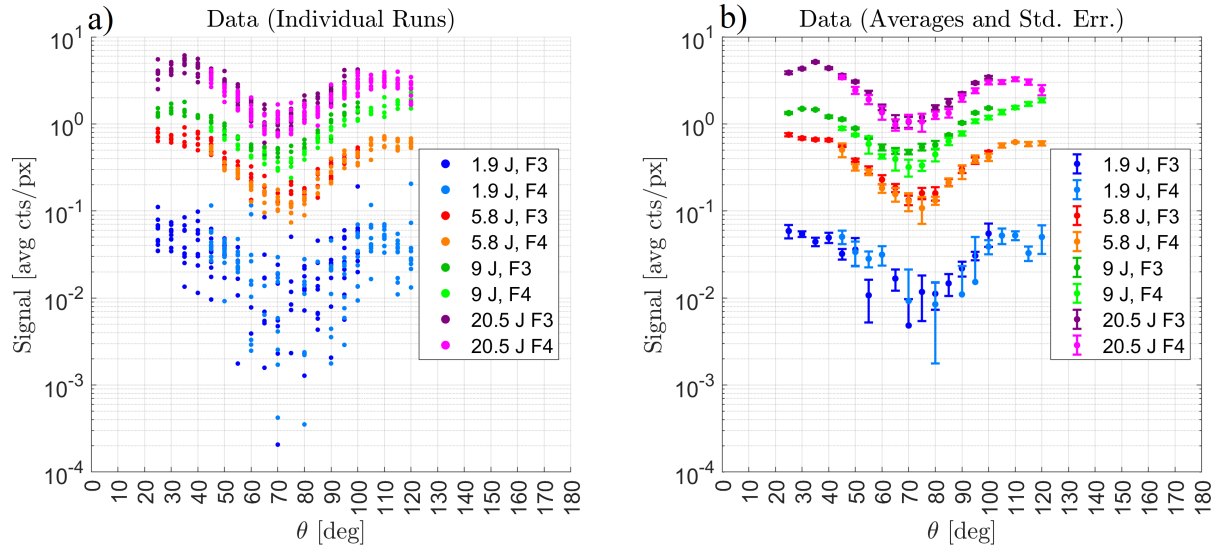


Figure 6.49: Plots of the angular distribution measurement data taken at different energies for both the F3 and F4 detectors in log scale. The sum over the region of interest of the signal minus the average background is shown in a) while the the mean of the data points for each angle is shown in b) with the standard deviation in the mean represented by the error bars.

One can immediately see that for all pulse energies used, a dip exists, bottoming at around 70° , roughly consistent with the 2019 experiment. At a glance, any shift in the dip of the angular distribution versus higher intensities is subtle at best, but there is a small shift between 5.8 J and the higher energies of a few degrees. The angular distribution for 1.9 is too noisy for a dip to be quantified, but the existence of a dip remains (note that there are some data points not visible in the log scale, as they have negative values after background subtraction). Figure 6.50 shows plots of the data in a linear scale along with parabolas fitted over the angular range of 50° to 90° . As in the analysis for the 2019 experiment, the parabola fits were performed by minimizing the χ^2 value (see Eq. 5.5) by varying the three parameters defining the parabolic expression, $A(\theta_i - B)^2 + C$, however, rather than using a uniform uncertainty averaged over all data points, the individual computed uncertainties for each data point were used.

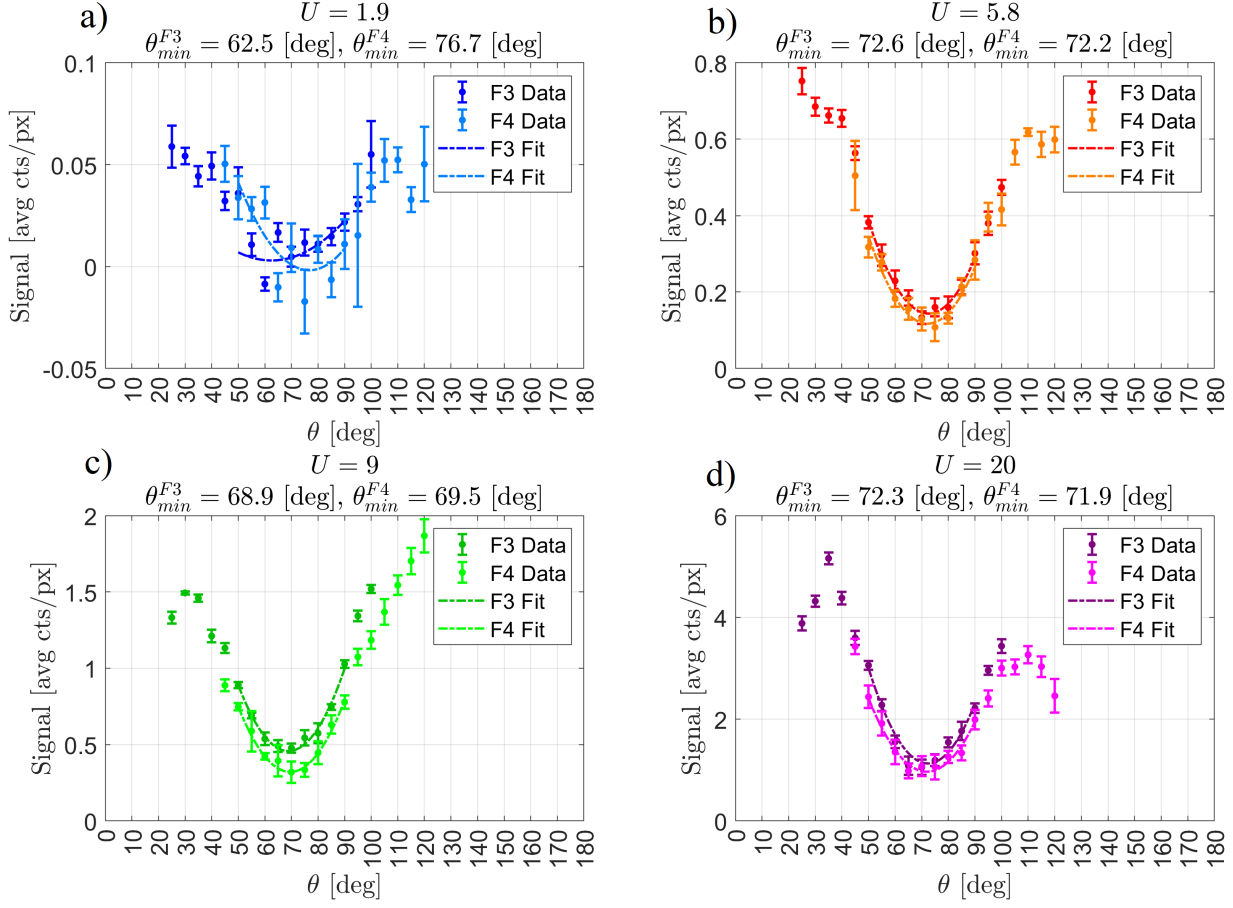


Figure 6.50: Plots of the angular distribution data in linear scale at various pulse energies along with parabolic fits over the data points in the angular range of 50° to 90° . The pulse energies include: a) 1.9 J, b) 5.8 J, c) 9 J, and d) 20 J, on target. Due to the noise for the 1.9 J dataset, the parabolas are not well defined over this angular region and the fits result in disagreeing parabolas. The parabolas for 5.8 J, 9 J, and 20 J data set, however, are well defined.

Several parabola fits were done for each energy over various ranges of angles around the dip. The results for the predicted dip angle, θ_{\min} , shown in Fig. 6.51a, show an overall, small trend towards smaller angles with increasing energy, but not a monotonic relationship. The values of θ_{\min} increased between 9.0 J and 20.5 J. This can be explained from the forward skewing in the overall radiation, parameterized by S_f , defined as the ratio between the average of the background subtracted signal data, $S(\theta_i)$, averaged over the angles 50° , 55° , and 60° (left of the dip) to the

data averaged over the angles 80° , 85° and 90° (right of the dip).

$$S_f = \frac{\{S(\theta_i) | \theta_i = 50^\circ, 55^\circ, 60^\circ\}_{\text{avg}}}{\{S(\theta_i) | \theta_i = 80^\circ, 85^\circ, 90^\circ\}_{\text{avg}}} \quad (6.9)$$

The larger backward skewing exhibited by the distribution at 5.8 J would have shifted θ_{\min} toward smaller values. Curiously, the distribution at 5.8 J shows as much, if not more forward skewing as the distribution at 20.5 J, which are both larger than the skewing for the distribution at 9 J. In other words, the data shows that the relative forward skewing of the radiation does not necessarily monotonically increase with energy.

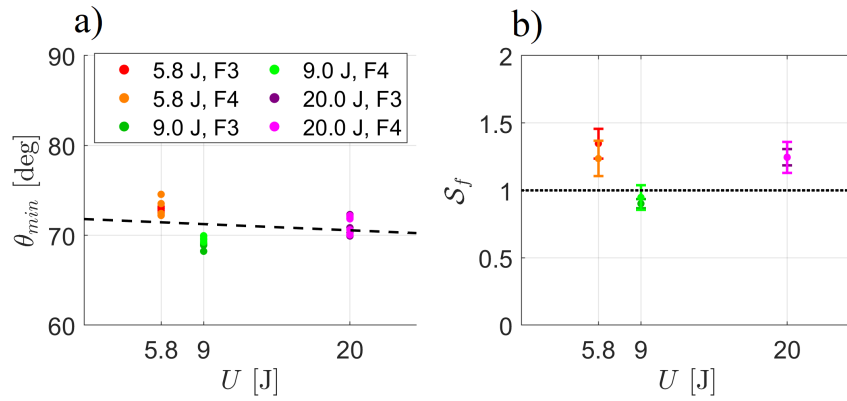


Figure 6.51: Plots of a) the parabola vertex position, θ_{\min} , from the fits to the angular distribution data using various ranges of angles (details in Table 6.5) and b) the forward skewing factor, S_f , for each angular distribution dataset defined as the ratio between the average of the signals in the angular range of 50° to 60° to that in the angular range of 80° to 90° (see Eq. 6.9).

Table 6.5 shows the results of the different parabola fits. Starting with a range of 50° to 90° , which has $n = 9$ data points resulting in a degree of freedom of $\nu = n - 3 = 6$, the range was reduced one data point at a time until the range contained 5 data points from 60° to 80° . The fits at 1.9 J have θ_{\min} values that systematically vary between the F3 and F4 detector data and are shown for reference only. The fact of the matter was that there was excess noise in the

1.9 J data set exacerbated by leakage of photons in background images. For the 5.8 J, 9.0 J, and 20.5 J data sets, there was enough signal-to-noise where parabolas can be clearly defined over the fitted regions. There were a couple of omitted outliers where the fits did not converge to a parabola with a dip located between 50° and 90° , but those were due largely in part to the fitting process itself and not the data. With additional tweaking, the fits in these outliers could be made to converge, but was not done out of interest in time.

Table 6.5: Summary statistical parameters of the fits to the angular distribution data, for various angular ranges. Shown are the χ^2 values define in Eq. 5.5 as well as the corresponding p values for the degree of freedom η determined by the number of data points subtracted by 3. The values for the fits which did not produce a parabola consistent with the dataset (for example, θ_{\min} that were outside of the 50° to 90° range) are treated as outliers and left blank.

	$\theta_{\text{range}} [\circ]$ ν	50 – 90 6	50 – 85 5	55 – 90 5	55 – 85 4	55 – 80 3	60 – 85 3	60 – 80 2
1.9 J, F3	χ^2	28.9	28.9					
	p	1.00	1.00					
	$\theta_{\min} [\circ]$	62.5	63.1					
1.9 J, F4	χ^2	15.5	15.4	14.5				
	p	0.98	0.99	0.99				
	$\theta_{\min} [\circ]$	76.7	77.5	76.0				
5.8 J, F3	χ^2	2.10	1.75	1.70	1.54	1.54	1.41	1.40
	p	0.09	0.12	0.11	0.18	0.33	0.30	0.50
	$\theta_{\min} [\circ]$	72.6	72.9	72.8	73.0	73.1	73.2	72.9
5.8 J, F4	χ^2	4.78	4.59	1.94	1.94	0.83	1.93	0.23
	p	0.43	0.53	0.14	0.25	0.16	0.41	0.11
	$\theta_{\min} [\circ]$	72.2	72.4	72.3	72.3	73.5	72.3	74.6
9.0 J, F3	χ^2	4.93	1.39	4.93	1.03	1.02		0.40
	p	0.45	0.07	0.58	0.09	0.20		0.18
	$\theta_{\min} [\circ]$	68.9	69.2	68.9	69.1	69.0		68.2
9.0 J, F4	χ^2	1.07	0.83	1.06	0.50	0.40	0.50	0.037
	p	0.02	0.02	0.04	0.02	0.06	0.08	0.17
	$\theta_{\min} [\circ]$	69.5	69.2	69.6	69.5	70.0	69.5	69.9
20.5 J, F3	χ^2	9.24	3.63		3.62	0.41	2.31	0.27
	p	0.84	0.40		0.54	0.06	0.49	0.12
	$\theta_{\min} [\circ]$	72.3	70.8		70.8	70.0	70.3	69.9
20.5 J, F4	χ^2	2.95	2.82	2.91	2.70	0.86	1.34	0.61
	p	0.18	0.27	0.27	0.39	0.16	0.28	0.26
	$\theta_{\min} [\circ]$	71.9	72.2	71.8	72.1	70.6	70.0	70.1

6.9 Discussion and Conclusion

The results have shown that the dip in the angular distribution does not vary significantly with the laser pulse energy (which correlates with the laser peak intensity and intensity distribution). There is a dip that persists at around 70° . For the detection setup used, operating the laser at lower energies will at some point result in a signal-to-noise ratio too small to quantify the dip. At the higher energy ranges, there was a very subtle shift in the dip towards lower angles. The relative amount of forward scattering compared to backward scattering between the dip did not show a clear trend versus the laser energy. As a laser intensity gauge, looking at the angular distribution along the $E\text{-}k$ plane does not appear to be a viable method, at least not over the energy ranges tested. It is possible, however, that at even higher laser energies, that the dip and/or the relative forward scattering will vary enough to observe a clear difference. Even then, the requirement for the detectors to be precisely aligned, the expense and complexity of using a streak camera, as well as the large number of shots needed to acquire sufficient sample sizes pose significant practical limitations in this method.

The RTS angular distribution data taken during this experiment is still a new observation of physics, and the results lead to the following questions:

1. What is the physics behind the existence of a dip at 70° ?
2. Why does the dip persist around 70° over an intensity range from 10^{19} to 10^{20} W/cm²?

The answer to the first question might possibly lie in the relative magnitudes of the longitudinal and transverse momenta of the electron trajectory as it is scattered by the laser, combined with the effects of relativistic beaming. The answer to the second question might be the RTS contributions

overwhelmingly originating from the corona of the laser beam, rather than the peak. Perhaps the choice of filtering the light over the range of 600 – 650 nm also resulted in a selection of intensities and emission directions as a result of the Doppler effect, leading to a complicated relation between the radiated light and the observed angular distribution.

Chapter 7

Modeling Relativistic Thomson Scattering for Realistic Laser Beams

In Chapter 2, we discussed the physics of relativistic Thomson scattering mainly of an electron interacting with an electromagnetic infinite plane wave, and in a few instances considered the case of a Gaussian temporal pulse. In Chapters 3 to 6, we presented the ultraintense laser experiments conducted looking at the optical spectrum as well as the angular distribution of radiated light produced from RTS and discussed their results which found that the onset wavelength in the spectrum is sensitive to the laser intensity, whereas the location of the dip in the angular distribution is not. This chapter is intended to expand upon Chapter 2 by discussing the physics of RTS due to a focused laser beam and explain some of the observations made from experiments.

7.1 Gaussian Beams

The simplest example of a focused beam is the Gaussian beam which may be derived by taking the paraxial approximation to the scalar wave equation. The intensity distribution in space is given by [99]:

$$I = I_0 \frac{w_0^2}{w^2(z)} \exp \left[-2 \left(\frac{r}{w(z)} \right)^2 \right] \quad (7.1)$$

where w_0 is the beam waist, $w(z) = \sqrt{1 + \left(\frac{z}{z_R} \right)^2}$ is the beam radius at z , and $z_R = \frac{\pi w_0^2}{\lambda}$ is the Rayleigh length. The complex fields are given by [100]:

$$\psi(x, y, z) = \frac{C}{w(z)} \exp \left[ik \frac{x^2 + y^2}{2R(z)} - i\phi_G(z) - \frac{x^2 + y^2}{w^2(z)} \right] \quad (7.2)$$

where C is a constant equal to the peak field amplitude, $R(z) = z + z_R^2/z$ is the radius of curvature and $\phi_G(z) = \tan^{-1}(z/z_R)$ is the Guoy phase. One might make the interpretation that the real fields are obtained by taking the real part of the complex fields, and in the case of linear polarization, that the field lies entirely along what is defined as the direction of polarization. This is approximately correct to first order. There are, however, additional components in the exact fields if one were to impose consistency with Maxwell's equations, which is addressed in the next section.

7.2 Maxwell-Consistent Fields

The Erikson-Singh model [101] provides a method to calculate Maxwell-consistent fields based on a given paraxial wave solution, $\psi(\mathbf{x})$, defined such that the propagating wave solution is $\psi(\mathbf{x})e^{i(kz-\omega t)}$, and $\mathbf{x} \equiv x\hat{\mathbf{x}} + y\hat{\mathbf{y}} + z\hat{\mathbf{z}}$ is a position of the field in space. The fields from the Erikson-Singh model is given by:

$$\mathbf{E}(\mathbf{x}, t) = E_0 \left[\hat{\mathbf{x}} + \frac{\hat{\mathbf{y}}}{2k^2} \frac{\partial^2}{\partial x \partial y} + \frac{i\hat{\mathbf{z}}}{k} \frac{\partial}{\partial x} \right] \psi(\mathbf{x}) e^{i(kz-\omega t)} \quad (7.3)$$

$$\mathbf{B}(\mathbf{x}, t) = B_0 \left[\frac{\hat{\mathbf{x}}}{2k^2} \frac{\partial^2}{\partial x \partial y} + \hat{\mathbf{y}} + \frac{i\hat{\mathbf{z}}}{k} \frac{\partial}{\partial y} \right] \psi(\mathbf{x}) e^{i(kz-\omega t)} \quad (7.4)$$

where $\psi(\mathbf{x})$ describes the spatial dependence of the wave amplitude, and may take on the form of spatial modes (e.g., Hermite-Gaussian or Laguerre-Gaussian modes). For the purposes of this thesis, we consider primarily two forms for $\psi(\mathbf{x})$: the standard Gaussian profile (known as the TEM_{0,0} mode, given in Eq. 7.2), and the Laguerre-Gaussian $p = 1, l = 0$ (LG_{1,0}) mode [102], given by:

$$\psi(\mathbf{x}) = \frac{C}{w(z)} \left[1 - \frac{2(x^2 + y^2)}{w^2(z)} \right] \exp \left[i \frac{k(x^2 + y^2)}{2R(z)} - i3\phi_G(z) - \frac{x^2 + y^2}{w^2(z)} \right] \quad (7.5)$$

where C is a constant, z_R is the Rayleigh range, $w(z)$ is the beam radius, and $\phi_G(z)$ is the Guoy phase defined for the Gaussian mode in the prior section. The $LG_{1,0}$ mode can be used to simulate profiles containing a strong primary Airy ring.

It can be seen from Eq. 7.3 and 7.4 that the electric and magnetic fields will have longitudinal components (along $\hat{\mathbf{z}}$) proportional to a first spatial derivative and orthogonal components proportional to a second mixed spatial derivative in $\psi(\mathbf{x})$.

7.3 Ponderomotive Scattering

A focused beam having a spatial dependence on its field amplitude means that an electron would see varying field strengths as it oscillates. The gradient it sees implies that the electron experiences a stronger field strength in one side of its oscillation compared to the other side, resulting in ponderomotive motion towards regions of lower intensity.

For low intensities, the ponderomotive force can be derived by considering the ponderomotive energy, U_p , of an electron oscillating in a laser field where the magnetic field is negligible, as described in section 2.2 on linear Thomson scattering. The position is given in Eq. 2.6 by $\mathbf{r}(t) = \frac{e}{m\omega^2} \mathbf{E}(\mathbf{r}, t)$ so that the ponderomotive energy, defined as the average potential energy in the system over a cycle, can be written as:

$$U_p = \frac{1}{2} m \omega^2 \overline{|\mathbf{r}(t)|^2} = \frac{1}{2} \frac{e^2}{m \omega^2} \overline{|\mathbf{E}(\mathbf{r}, t)|^2} = \frac{e^2 E_0^2(\mathbf{r})}{4m\omega^2} \quad (7.6)$$

where $\mathbf{E}(\mathbf{r}, t) = E_0(\mathbf{r}) \cos(\omega t)$ and $E_0(\mathbf{r})$ is the electric field amplitude at position \mathbf{r} . The pon-

deromotive force is defined as $\mathbf{F}_p = -\nabla U_p$ so that:

$$\frac{d\bar{\mathbf{p}}}{dt} = -\frac{e^2}{2m\omega^2} \nabla |\mathbf{E}|^2 = -\frac{e^2}{4m\omega^2} \nabla E_0^2(\mathbf{r}) \quad (7.7)$$

where $\bar{\mathbf{p}}$ is the slow component of the momentum, i.e., $\mathbf{p} = \tilde{\mathbf{p}} + \bar{\mathbf{p}}$, with $\tilde{\mathbf{p}}$ being the fast (oscillatory) component. Equation 7.7 states that the ponderomotive force is proportional to the intensity gradient (oriented from higher towards lower intensity).

The ponderomotive force for relativistic intensities is not as straightforward to derive, however, such derivations have been carried out [103–105] and a concise summary given in [106]. Furthermore, numerical calculations have been performed in [104] using their derived expression to establish agreement with integration of the full Lorentz force. This expression is presented below with a caveat that it was derived assuming $\lambda_0 = 1 \text{ }\mu\text{m}$, $w_0 = 10 \text{ }\mu\text{m}$, and $\Delta t \sim 300 \text{ fs}$:

$$\frac{d\bar{\mathbf{p}}}{dt} = -\frac{e^2}{2m\bar{\gamma}} \nabla \overline{|\tilde{\mathbf{A}}_\perp|^2} \quad (7.8)$$

Here $\tilde{\mathbf{A}}_\perp$ is defined to be the component of \mathbf{A} which includes the fast oscillations and $\bar{\gamma}$ is the average Lorentz factor of the particle trajectory. The difference between Eq. 7.8 and 7.7 is whereas the nonrelativistic expression involves a gradient of the spatial envelope, the relativistic expression involves the gradient of the time-average of the oscillatory field, along with a factor of $\bar{\gamma}$ in the denominator resulting in a suppression of the ponderomotive force. It can be argued that for a pulse that is not too short (as would be the case for the 300 fs condition used in the paper), that $\overline{|\tilde{\mathbf{A}}_\perp|^2} \approx |\overline{\mathbf{A}}_\perp|^2$, where $\overline{\mathbf{A}}_\perp$ is simply the spatial envelope of the traveling pulse. In this regime, the factor $\bar{\gamma}$ may be approximated by adding in quadrature the slow (total) and fast

(transverse, time averaged) components of the momentum, namely:

$$\bar{\gamma} \approx \sqrt{1 + \frac{|\bar{p}|^2}{m^2 c^2} + \frac{a^2(t, \mathbf{r})}{2}} \quad (7.9)$$

where, $a(t, \mathbf{r})$ is the value of the normalized vector potential at position \mathbf{r} at time t , and is related to the fast component of momentum via conservation of canonical momentum, $\tilde{\mathbf{p}}_\perp = e\tilde{\mathbf{A}}_\perp$, so that:

$$\frac{\overline{|\tilde{p}_\perp|^2}}{m^2 c^2} = \frac{e \overline{|\tilde{\mathbf{A}}_\perp|^2}}{m^2 c^2} \approx \frac{1}{2} \frac{e \overline{|\mathbf{A}_\perp|^2}}{m^2 c^2} = \frac{a^2(t, \mathbf{r})}{2} \quad (7.10)$$

To show the effects of ponderomotive scattering, we take an approach similar to [58] using a simple Gaussian distribution in the laser field (Eq. 7.2) so that the electric field is polarized along $\hat{\mathbf{x}}$ without any orthogonal or longitudinal components. In other words, we replace the definitions of the electric and magnetic fields from the equations of the plane wave modified with a Gaussian temporal pulse envelope in Eq. 2.78 and 2.79 with ones that include a Gaussian spatial mode:

$$\mathbf{E} = E_0 \cos \left[kz - \omega t + \frac{kx^2}{2R(z)} - \phi_G(z) \right] \frac{w_0}{w(z)} \exp \left[-\frac{x^2}{w^2(z)} \right] \exp \left[-\frac{(kz - \omega t)^2}{\tau^2} \right] \hat{\mathbf{x}} \quad (7.11)$$

$$\mathbf{B} = \frac{E_0}{c} \cos \left[kz - \omega t + \frac{kx^2}{2R(z)} - \phi_G(z) \right] \frac{w_0}{w(z)} \exp \left[-\frac{x^2}{w^2(z)} \right] \exp \left[-\frac{(kz - \omega t)^2}{\tau^2} \right] \hat{\mathbf{y}} \quad (7.12)$$

where $R(z) = z + \frac{z_R^2}{z}$ is the phase-front radius of curvature and $\phi_G(z) = \tan^{-1} \left(\frac{z}{z_R} \right)$ is the Gouy phase. The electron path of motion can then be calculated as usual using the Lorentz force differential equation. This is done for electrons in the E-k plane for various values of a_0 and plotted in Fig. 7.1.

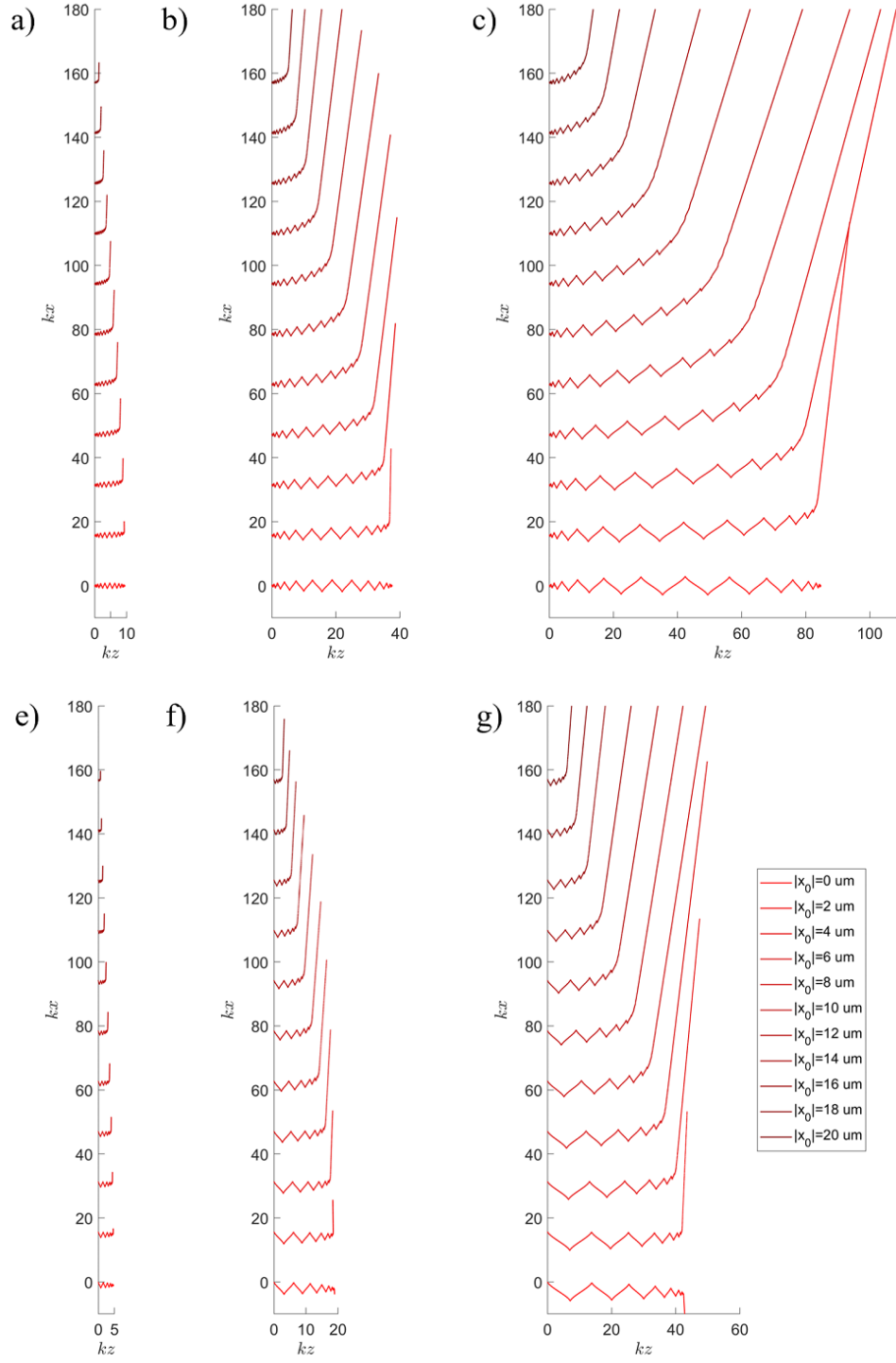


Figure 7.1: Plots of the electron motion born at $z(t_0) = 0$, $y(t_0) = 0$, and various locations in $x(t_0)$ from $x(t_0) = 0$ to $x(t_0) = w_0$, where $w_0 = 20 \mu\text{m}$ for a_0 values of 1 (a and e), 2 (b and f), and 3 (c and g). The electron is born prior to the arrival of the pulse ($t_0 \rightarrow -\infty$) for a-c and born at the peak of the pulse ($t_0 = 0$) for e-g.

The results show increased ponderomotive scattering relative to the forward drift along with an overall diminished relativistic Thomson scattering as the electron is born further away from axis. At some critical distance from axis, $x_{0,c} \sim w_0/2$, the Gaussian function reaches and inflection point so that the change in intensity gradient vs. x increases towards 0. As a result, the effects of ponderomotive scattering tapers off beyond $x_{0,c}$.

When the fields described by Eq. 7.11 and 7.12 are used to calculate the motion of an ensemble of electrons in 3 dimensions, the result is that the electron is only ponderomotively scattered with a component along the x direction, and never along the y direction, even if the electron is born at a location offset along y from the z axis, as shown in Fig. 7.2c and d. This turns out to be inaccurate, and that the real scattering electron distribution is affected by the longitudinal fields described by Erikson-Singh, which results in the scattering also having a y component, and a distribution over a cone. The Erikson-Singh model may be simplified, according to [107], and taking terms up to first order in $1/\mathbb{Z}$:

$$\mathbf{E}_{ES} = E_0 \left(\hat{\mathbf{x}} - i \frac{x}{\mathbb{Z}} \hat{\mathbf{z}} \right) \psi(\mathbf{x}) e^{i(kz - \omega t)} \quad (7.13)$$

$$\mathbf{B}_{ES} = \frac{E_0}{c} \left(\hat{\mathbf{y}} - i \frac{y}{\mathbb{Z}} \hat{\mathbf{z}} \right) \psi(\mathbf{x}) e^{i(kz - \omega t)} \quad (7.14)$$

where $\mathbb{Z} = z_R + iz$. After multiplying by the temporal envelope, $\exp[-(kz - \omega t)^2/\tau^2]$, and evaluating the real part, we find that the x component of \mathbf{E}_{ES} and y component of \mathbf{B}_{ES} are the same as Eq. 7.11 and 7.12; the longitudinal components along z , which are 90° out of phase with

the transverse components, and are given by:

$$\begin{aligned}\mathbf{E}_{ES} \cdot \hat{\mathbf{z}} &= E_0 \left(\frac{xz_R}{z_R^2 + z^2} \right) \sin \left[kz - \omega t + \frac{kx^2}{2R(z)} - \phi_G(z) \right] \\ &\quad \times \frac{w_0}{w(z)} \exp \left[-\frac{x^2}{w^2(z)} \right] \exp \left[-\frac{(kz - \omega t)^2}{\tau^2} \right]\end{aligned}\tag{7.15}$$

$$\begin{aligned}\mathbf{B}_{ES} \cdot \hat{\mathbf{z}} &= \frac{E_0}{c} \left(\frac{yz_R}{z_R^2 + z^2} \right) \sin \left[kz - \omega t + \frac{kx^2}{2R(z)} - \phi_G(z) \right] \\ &\quad \times \frac{w_0}{w(z)} \exp \left[-\frac{x^2}{w^2(z)} \right] \exp \left[-\frac{(kz - \omega t)^2}{\tau^2} \right]\end{aligned}\tag{7.16}$$

Including these components in the numerical solutions of the Lorentz force ODE results in the expected cone scattering behavior as shown in Fig. 7.2e and f.

$$a_0 = 2$$

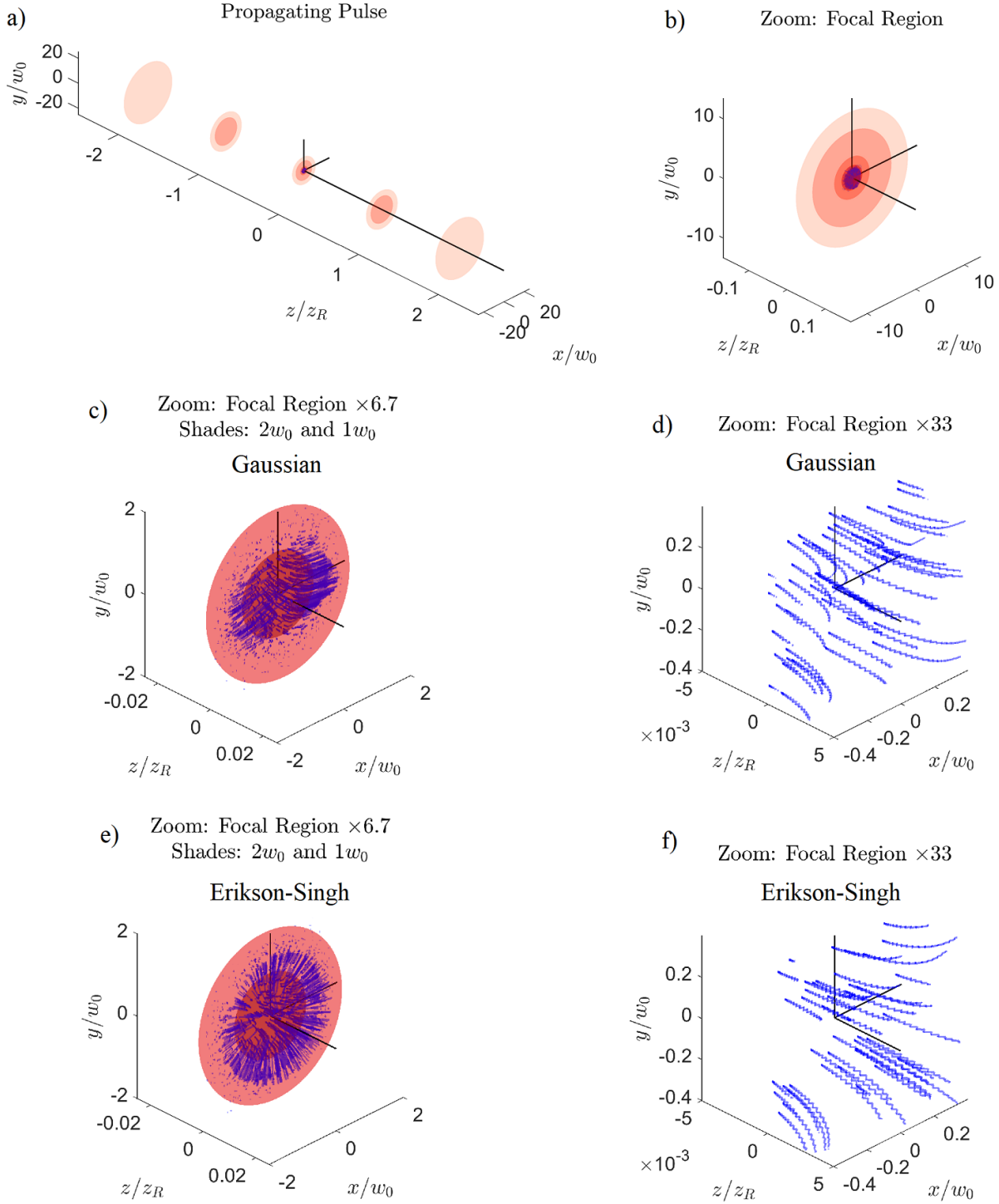


Figure 7.2: Plots of a traveling focused pulse ($w_0 = 20 \mu\text{m}$, $a_0 = 2$) and the resulting scattered electrons born at focus. The traveling pulse, a), at various time snapshots are superimposed, where the lightest pink shaded region are the surface contours corresponding to $I/I_0 = 10^{-100}$. The pulse at focused is shown in b). The pulse up to $2w_0$ is shown along with the paths of an ensemble of 1000 electrons calculated using the simple Gaussian model (Eq. 7.11 and 7.12) in c) along with a close up in d) and those for the Erikson-Singh model in e) and f).

7.4 Plane Wave Solutions Convolved with Gaussian Laser Distribution

In order to account for the laser's intensity distribution in space and its effect on the RTS radiation, as observed by a detector in an experiment, it would be necessary to sum up the contributions of a large number of electrons born throughout the focal region. This becomes a complex and computationally expensive ordeal. There is still knowledge to be gained about how the intensity distribution in space of a focused beam itself determines the overall radiated angular distribution. As the peak intensity of a beam increases, so does the region in the corona where electrons are accelerated to relativistic speeds and contribute to RTS radiation. This can be accounted for without including ponderomotive effects using the approach described in [59].

This approach involves convolving plane wave results of RTS radiation over a range of normalized vector potential values, a , with a weight distribution calculated from the spatial distribution $a(\mathbf{r})$. The quantity a is not to be confused with a_0 , which in the current context is defined as the normalized vector potential at the peak of the distribution. To be precise, a Gaussian beam has a spatial distribution given by:

$$a(\mathbf{r}) = a_0 \frac{w_0}{w(z)} \exp\left(-\frac{r^2}{w(z)^2}\right) \quad (7.17)$$

and when written in terms of coordinates normalized to the Gaussian beam parameters becomes:

$$a(\mathbf{r}) = a_0 \frac{1}{\sqrt{1 + \xi^2}} \exp\left(-\frac{\rho^2}{1 + \xi^2}\right) \quad (7.18)$$

where $\xi \equiv z/z_R$ and $\rho \equiv r/w_0$. In this approach, we ignore the temporal pulse shape, which is

adequate for our purposes considering that, to a reasonable approximation, electrons sample the entire intensity distribution in space at the peak of the pulse as it propagates.

The weight associated with a value of a over an interval size $\Delta a \equiv a_2 - a_1$ is proportional to the volume in space, ΔV , containing the interval of a values $\in [a_1, a_2]$. We may define $a \equiv a_1$ and $a_2 = a + \Delta a$, for example. Conveniently, Eq. 7.18 provides the spatial dependence of $a(\mathbf{r})$ in cylindrical coordinates, so that ΔV can be defined as a difference in the solids of revolution of the two volumes bounded by the surface contour defined by a_1 and a_2 respectively. In other words:

$$\frac{\Delta V}{\Delta a}(a; a_0) = \frac{1}{\Delta a} \left| \int_{-\xi_{max,2}}^{\xi_{max,2}} \pi \rho^2(a_2, \xi; a_0) d\xi - \int_{-\xi_{max,1}}^{\xi_{max,1}} \pi \rho^2(a_1, \xi; a_0) d\xi \right| \quad (7.19)$$

where $\rho(a, \xi)$ is a function that can be derived by solving Eq 7.18 for ρ :

$$\rho(a, \xi; a_0) = \sqrt{-(1 + \xi^2) \ln \left(\frac{a}{a_0} \sqrt{1 + \xi^2} \right)} \quad (7.20)$$

and $\xi_{max,i}$ is the positive endpoint of the volume along the axis, which is determined by setting $\rho = 0$ in Eq. 7.18 and solving for ξ :

$$\xi_{max,i} = \sqrt{\left(\frac{a_0}{a_i} \right)^2 - 1} \quad (7.21)$$

Due to symmetry, the negative endpoint is simply $-\xi_{max,i}$. Several contours are plotted using Eq. 7.20 in Fig. 7.3.

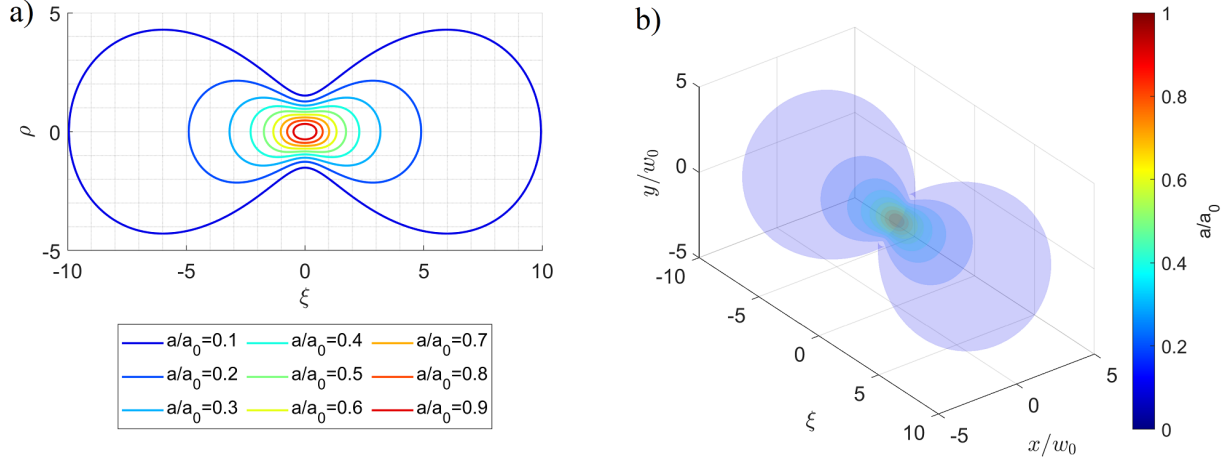


Figure 7.3: Plots of a) contour lines and b) surface contours of constant a for a Gaussian spatial distribution. The distribution is given by Eq. 7.18.

Since $a(\mathbf{r})$ extends over all space and never reaches a value of 0, a cutoff value, a_{cut} , must be established to prevent $\frac{\Delta V}{\Delta a}(a; a_0)$ from blowing up. As in [59], we choose $a_{\text{cut}} = 0.01$, which corresponds to $\sim 2 \times 10^{14} \text{ W/cm}^2$ just above the first appearance intensity of Nitrogen. Equation 7.19 was intended to be determined numerically, with an appropriate choice in the size of Δa , which defines a total number of a values, N_a , from a_{cut} to a_0 , that is, $N_a = \text{ceil}\left(\frac{a_0 - a_{\text{cut}}}{\Delta a}\right)$, where `ceil()` is a MATLAB function for rounding the argument to the next whole integer. After some trial and error, we have determined that $\Delta a \lesssim 10^{-5}$ is required for $\frac{\Delta V}{\Delta a}(a; a_0)$ to converge as Δa is varied for a_0 up to 10. The computed functions of $\frac{\Delta V}{\Delta a}(a : a_0)$ are plotted in Fig. 7.4 for a_0 from 1 to 10.

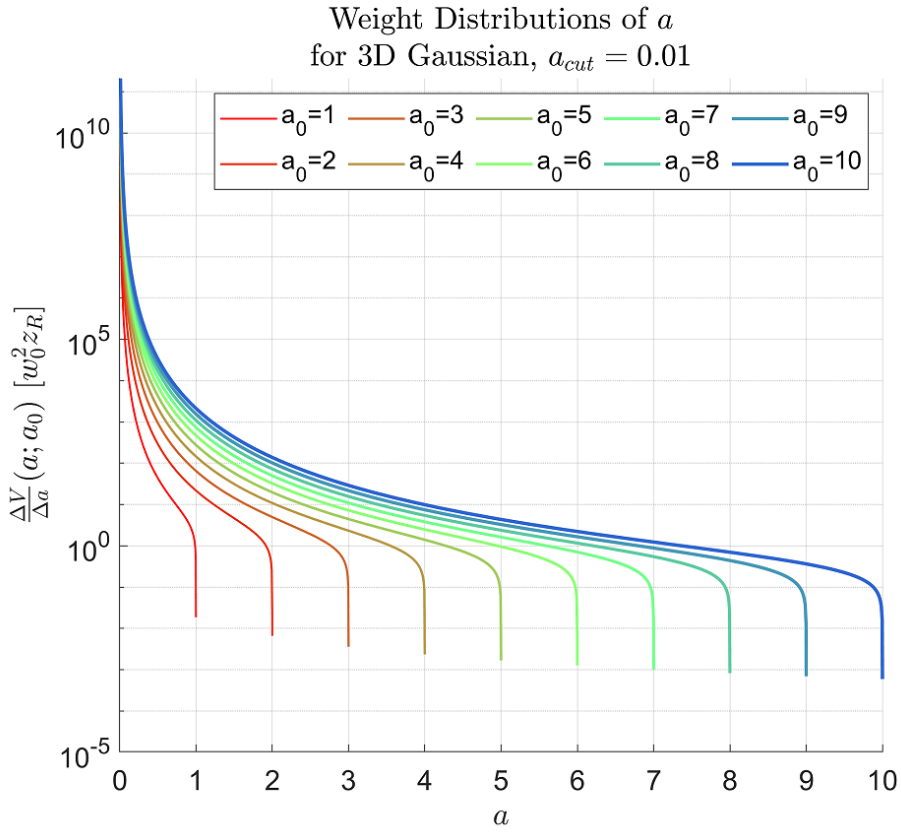


Figure 7.4: Plots of the weight distributions, $\frac{\Delta V}{\Delta a}(a; a_0)$, calculated numerically for various values of a_0 . The weight distributions are given by Eq. 7.19. A value of $\Delta a = 10^{-5}$ was used in the calculation.

It can be seen from Fig. 7.3 and 7.4 that as a decreases relative to a_0 , the total volume containing a fixed Δa interval increases quite dramatically. Going from the peak towards lower intensities, the surface contours begin as ellipsoids and transitions to a peanut or dumb bell shape.

The next step would be to calculate the plane wave angular distributions from the analytical formulas in [55] (Eq. 2.104) for each value of a for a given volume-weight distribution at a_0 , multiply with the corresponding weight, and sum the results. Since a value of $\Delta a = 10^{-5}$ was used to determine the volume-weight distributions, the number of data points in for a given distribution in the $a_0 = 1$ to 10 range is on the order of 10^5 to 10^6 . Therefore, to make calculations time efficient, it would be necessary to interpolate over the $\frac{\Delta V}{\Delta a}(a; a_0)$ curves and obtain a smaller

sample of $N \sim 100$ points. Suppose we have a list of a values, $a_i \in [a_{\text{cut}}, a_0]$, such that a_i and a_{i+1} are equally spaced for all i . The distribution in the total number of emitted RTS photons in the n th harmonic per unit time per unit solid angle, $\frac{d\Gamma_{\text{tot}}^{(n)}}{d\Omega}$, can then be written as a weighted sum of the plane wave RTS distributions at intensity a_i , $\frac{d\Gamma_{\text{pw}}^{(n)}}{d\Omega}$, with $\frac{\Delta V}{\Delta a}$ as the weights:

$$\frac{d\Gamma_{\text{tot}}^{(n)}}{d\Omega}(\theta, \phi) = \sum_{i=1}^N \frac{d\Gamma_{\text{pw}}^{(n)}}{d\Omega}(\theta, \phi; a_i) \times \frac{\Delta V}{\Delta a}(a_i; a_0) \quad (7.22)$$

Here, the photon rate per unit solid angle, $\frac{d\Gamma}{d\Omega}$, is used instead of the power per unit solid angle, $\frac{dP}{d\Omega}$. For plane wave solutions, they are related by a division in the radiated photon frequency $\hbar\omega = n\hbar\omega_0 [1 + \frac{1}{2}a_0^2 \sin^2(\theta/2)]$, so that distribution of higher frequencies being forward scattered due to Doppler effect, thus contributing to higher power in the forward direction, is canceled out:

$$\frac{d\Gamma_{\text{pw}}^{(n)}}{d\Omega} = \frac{1}{n\hbar\omega_0 [1 + \frac{1}{2}a_0^2 \sin^2(\theta/2)]} \frac{dP^{(n)}}{d\Omega} \quad (7.23)$$

Figure 7.5 shows the result of using Eq. 7.22 to calculate the second harmonic emission ($n = 2$) for plane wave solutions convolved with the Gaussian distribution for $a_0 = 1$ to 6. Furthermore, the same is plotted of angular distribution in the E-k plane in Fig. 7.6 for $a_0 = 1$ to 10.

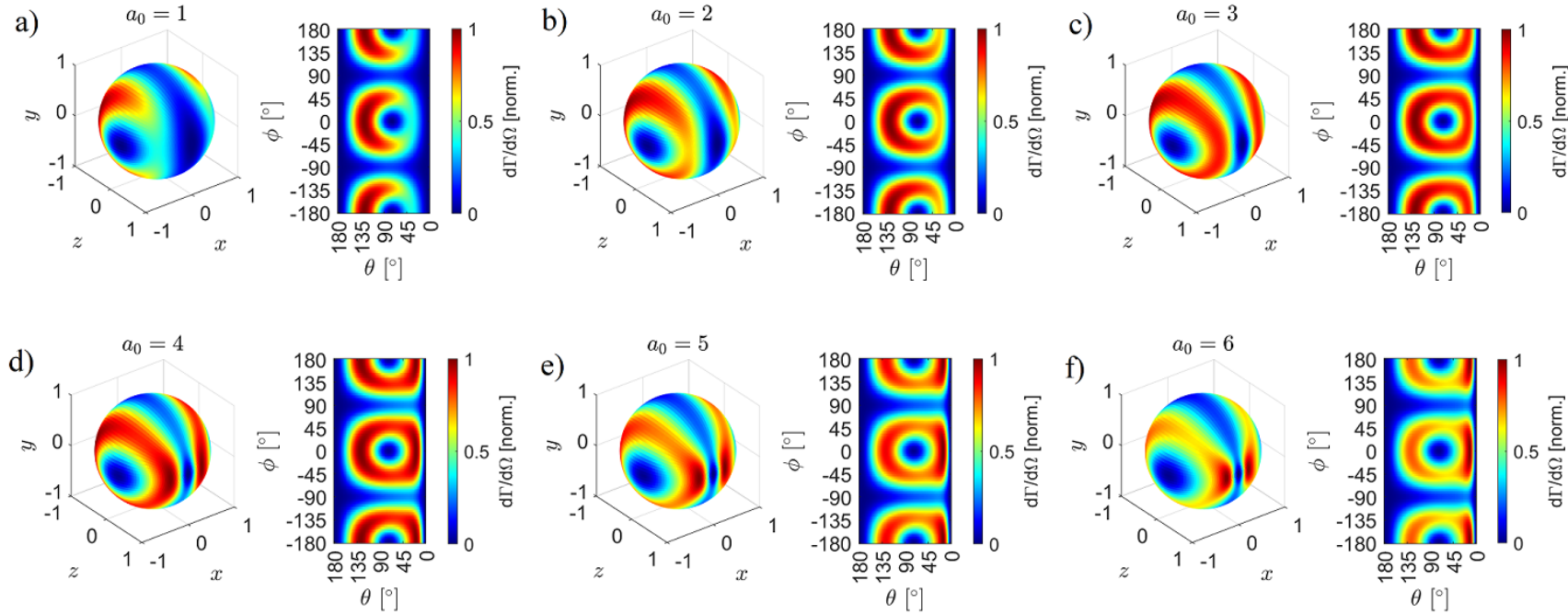
RTS Radiation Pattern ($n = 2$) of Plane Wave Convolved over Gaussian Spatial Distribution in Intensity

Figure 7.5: Plots of the total angular distribution of photons rate per unit solid angle in the second harmonic, $\frac{d\Gamma_{tot}^{(2)}}{d\Omega}$, calculated from the weighted sum of plane wave solutions. The weighted sum is given by Eq. 7.22, where the weights are derived from the intensity distribution in space of a focused Gaussian beam (Eq. 7.19). The plots include calculations for various values of a_0 : a) 1, b) 2, c) 3, d) 4, e) 5, and f) 6.

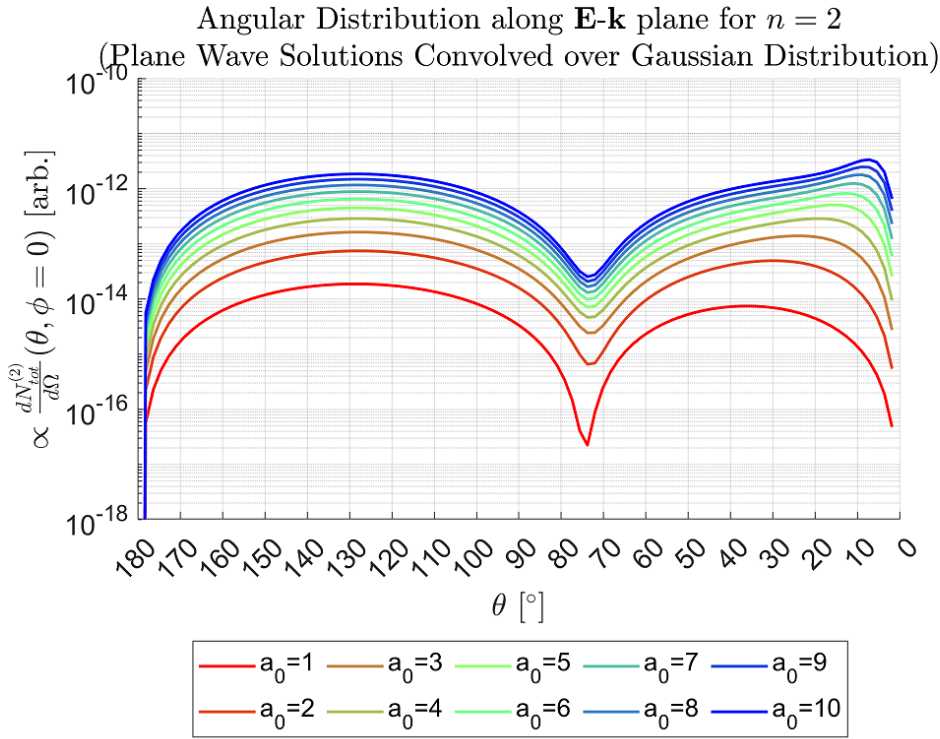


Figure 7.6: Plots of the total angular distribution of photon rate per unit solid angle in the second harmonic, $\frac{d\Gamma_{tot}^{(2)}}{d\Omega}$, from calculating the weighted sum of the plane wave solutions looking along the E-k plane. In other words, the E-k plane is along $\phi = 0$ in Fig. 7.5. The weight sum is given by Eq. 7.22), where the weights are derived from the intensity distribution in space of a focused Gaussian beam (Eq. 7.19). The calculation is done for a_0 from 1 to 10.

The results of these calculations show that when the intensity distribution in space is considered - rather than just the peak intensity - the overall angular distribution has a dip which does not vary significantly with a_0 . The electrons scattering at the corona of the laser experience RTS at lower intensities. Since the size of the corona grows with a_0 , the overall effect is that the dip is not as sensitive to a_0 as the plane wave models alone predict. This provides an explanation for the experimental observations described in Chapter 6 in the 2022 experiment where the dip did not shift very much with the pulse energy delivered to the target.

There are more details that may be added to this approach to further refine the model. For one, in the experiment, the field of view was limited to a diameter of ≈ 3 mm, whereas the

calculation was performed for as far as the contour for $a_{\text{cut}} = 0.01$ extended. Another detail is that in the 2022 experiment, measurements were made in the 600 to 650 nm band, which, considering the relationship between radiated frequency and scattering angle due to the the Doppler effect (Eq. 2.88), provides an angular bandpass filter for every value of a , and would likely change the overall angular distribution. At sufficiently large values of a_0 , the third and higher harmonics would begin to enter the 600 to 650 nm band. Lastly, the appearance intensities for various gas species may be included as a modification to the weight distribution. All of these details add complexity to the model, and would require careful consideration in order to be implemented.

Chapter 8

Conclusion

8.1 Summary of Thesis

We began with the premise that the growth in the number of ultraintense lasers worldwide created a need for laser diagnostics which have not kept up with the development of powerful lasers. Current methods of characterizing the intensity at focus are done by either sampling a leaked portion of the beam or performing measurements at low power and subsequently assuming such measurements hold at full power. This thesis explored the feasibility of using relativistic Thomson scattering (RTS) as an *in situ* intensity gauge for the focus of ultraintense lasers ($I \gtrsim 2 \times 10^{18} \text{ W/cm}^2$) as well as the physics of RTS at such intensities, of which few experiments have been conducted.

In Chapter 2, we discussed the physics of RTS, introducing the normalized vector potential, a_0 , as a parameter representing laser intensity and covered the equations of motion as governed by the Lorentz force as well as the radiation produced by the relativistic electron. We discussed how the measurement of the second harmonic spectrum looking specifically at the Doppler-shifted onset wavelength, λ_r , can be used to measure the laser's peak intensity. We also discussed the angular distribution and showed that the presence of a dip in the E-k plane shifting towards the laser propagation direction, \mathbf{k} , as a_0 increases motivated experiments in measuring the angular distribution.

In Chapter 3, we presented an overview of the experiments conducted at CLPU in mea-

suring the features of RTS deemed promising as diagnostics of the laser intensity. The spectrum measurements of the second harmonic emission of RTS were performed using the VEGA-2 300 TW laser in the 2018 experiment discussed in Chapter 4, which showed that the onset wavelength did, in fact, vary as the laser pulse energy delivered to the target was changed in a manner that agreed with indirect estimates of the peak intensity.

Measurements of the angular distribution were performed in the 2019 and 2022 experiment discussed in Chapters 5 and 6 respectively. In the 2019 experiment using the VEGA-2 laser, we showed that there is a dip which exists in the E-k plane which appeared to shift forward with laser energy; however, due to noise and limited angular resolution, it was not conclusive whether or not the location of the dip moved at all. In the 2022 experiment using the VEGA-3 laser, measurements of the angular distribution was done more carefully, achieving 5° resolution, larger statistical samples, and reduction of plasma recombination light by using a streak camera which provided temporal gating down to ~ 300 ps in duration. This experiment showed that the dip hardly moved at all with the laser energy.

In Chapter 7, we discussed the properties of RTS for the case of focused beams, which necessarily introduces a spatially dependent intensity profile. One consequence is the ponderomotive scattering of an electron over time from regions of higher to lower intensity proportional to the intensity gradient. Another is the fact that the corona region, in which electrons are scattered relativistically, grows with a_0 . Since there are a greater number of electrons that experience scattering at lower intensities in the corona than at the peak, they contribute significantly to the overall radiated angular distribution. A model convolving plane wave solutions with the intensity distribution in space shows that the dip in the angular distribution should not be very sensitive to a_0 , in stark contrast to the results from the plane wave models alone.

8.2 Conclusions from Results

We have found that the onset wavelength, λ_r , of the second harmonic spectrum being sensitive to the laser intensity makes a spectral analysis approach feasible in principle for characterizing the laser intensity. This was tested for a 800 nm central wavelength laser with a 30 fs temporal pulse duration and using a detector at ($\theta = 90^\circ, \phi = 0^\circ$). The spectral analysis of the second harmonic may be suitable as an intensity gauge in the 10^{18} to 10^{19} W/cm² range, although further work will be required to fully verify this technique as a diagnostic tool.

For the approach measuring the angular distribution, we have found that the location of the dip is not sensitive to the laser peak intensity. This may be due to the growing size of the corona as a_0 increases, where electrons undergoing lower intensity RTS contribute to the overall angular distribution and suppressing the movement of the dip location. Furthermore, measuring the angular distribution required multiple fiber detectors and numerous runs in order to capture the signal at high angular resolution. It may also be necessary to utilize a streak camera in order to gate out the plasma recombination light to distinguish the weak RTS signal. With the streak camera, the signal became too low to be reliable at pulse energies below about 2 J for a measurement band of 600 to 650 nm. Overall, the angular distribution does not appear to be a very viable approach for laser intensity characterization.

8.3 Future Research Possibilities on RTS

8.3.1 Verification of Spectral Analysis of Second Harmonic

A natural path ahead following the conclusion of this thesis is to fully develop the spectral analytical approach of measuring the second harmonic radiation. So far, we have verified sensitivity of the onset wavelength, λ_r , to the laser intensity in the direction of ($\theta = 90^\circ, \phi = 0^\circ$) only. This leaves a whole range of detection directions to be explored, such as ($\theta = 90^\circ, \phi = 90^\circ$), where the emitted RTS radiation is stronger, as well as $\theta < 90^\circ$, where theory predicts λ_r to be less sensitive to the laser peak intensity, allowing for higher intensities to be characterized before the second harmonic overlaps with the fundamental.

An important issue to address is the fact that the spectral data that allowed us to observe λ_r shifting with the delivered on target energy comes from a clipped portion of the beam (see Fig. 4.14b). The clipped portion included a captured beam length of $\sim 85 \mu\text{m}$, which was not clipped at the spectrometer input slit, given its orientation along the length of the slit (see Fig. 4.23). This raises a number of questions:

1. Does the spectrum change if a larger length of the beam was capture?
2. Does the spectrum change if we were to scan spatially along the beam, capturing a clipped portion of the beam?
3. Are we really looking at the focal plane of the laser in our spectral data?

In regards to question 3, we believe that we measured at the laser focus, since we had aligned our $E_{||}$ -objective imaging system with a diode laser scattering off of the alignment tip. It is possible,

however, that the focus of the real beam may have been outside of the field of view. On the other hand, since the VEGA-2 laser was focused with $f/13$ geometry, the exact location of the focus should not have been critical. Nevertheless, these are questions that future experiments can address. Images of the spatial distribution of the laser, without spectral dispersion, may be taken by turning the diffraction grating of the spectrometer to a reflector by setting it to 0th order.

Lastly, it may be worthwhile to study RTS from different gas species. Since different gas species have different sets of appearance intensities, there will be differences in the radiated light between species due to the varying effects of ponderomotive scattering on electrons born at different points in time relative to the peak of the pulse, as well as different locations in the spatial distribution of the laser. Whether and how these differences are consequential to the detected radiation are questions yet to be answered.

8.3.2 Spectral Analysis of Third Harmonic RTS

In our experiments, we did not intend to look for third harmonic radiation and have not found evidence of third harmonic in our data. Third harmonic radiation have been reportedly observed in [71] using a 10 nm bandpass filter centered at 310 nm, and in [68] also using 10 nm bandpass filters of an unspecified central wavelength. The measurements in [71] (see Fig. 3 in the paper) included polarization which were resolved along the $\hat{\theta}$ (polar) and $\hat{\phi}$ (azimuthal) directions. In regards to intensity characterization using spectral analysis, it may be possible to use polarization filters to suppress the detection of second harmonic so that the onset wavelength of the third harmonic may be resolved. For instance, the second harmonic radiation emitted in the direction of $(\theta = 90^\circ, \phi = 90^\circ)$ consists of primarily $\hat{\theta}$ (or \hat{z}) polarization, and may be

suppressed using polarizers oriented along $\hat{\phi}$ (or \hat{x}). On the other hand, the fact that the third harmonic is generally weaker than the second makes this approach quite delicate, requiring small detection numerical apertures, polarizers with high extinction ratios, lasers with high polarization purity, and may benefit from using large f-numbers in the laser's focusing geometry.

8.3.3 Spectral Analysis of Fundamental RTS

The advantage of using the fundamental in our spectral analytical approach is that it is not limited by the overlapping of harmonics as the laser intensity increases. However, this approach is not without difficulties. Looking at the first harmonic spectrum would require infrared detectors. Image intensifiers become nonsensitive to infrared light beyond the NIR as the low energy photons are no longer able to overcome the work function needed to convert into electrons at the photocathode. Detectors conventionally used for IR spectroscopy include InGaAs sensors with minimum exposure times on the order of 1 μs , which is not short enough to gate out plasma recombination light. A spectral analysis may be possible if there is an IR band free of plasma recombination.

8.3.4 RTS from Protons

At sufficient intensities, protons begin to move at relativistic speeds. This can be seen in the the normalized vector potential for protons, $a_p \equiv \frac{m_e}{m_p}a_0 \approx 0.0005a_0$, which reaches 1 when a_0 , the usual normalized vector potential for electron, is on the order of 2000, equivalent to an intensity of $9 \times 10^{24} \text{ W/cm}^2$. An experiment involving protons may be possible using hydrogen. The question would be whether or not the electrons ionized from hydrogen would produce RTS

that contaminate with the proton RTS. A possible path to alleviate this is to preionize and scatter away electrons using a second pulse prior to the primary pulse.

8.3.5 Further Studies of RTS Angular Distribution

Although measuring the angular distribution does not appear to be a viable means for characterizing the laser intensity, it may be studied for the sake of understanding the physics of RTS and support other methods of *in situ* intensity characterization. Our measurements of angular distribution focused on the emission along the E-k plane. Experiments conducted by other groups only looked at the distribution for fixed θ as a function of ϕ . A full map of the radiation pattern has yet to be measured, and doing so may serve as a useful verification of theoretical models and numerical simulations. However, without a clear purpose beyond gaining a general understanding of RTS, it may be difficult to justify conducting such studies considering the cost and complexity.

Appendix A: Formula Derivations

A.1 Angular Distribution of Radiation in Component Form

The quantity $\hat{\mathbf{n}} \times [(\hat{\mathbf{n}} - \beta) \times \dot{\beta}]$ appears in multiple equations for the radiated angular distribution, namely (in cgs units)

$$\frac{dP_{\text{rad}}}{d\Omega}(\hat{\mathbf{n}}, t) = \frac{e^2}{4\pi c} \left| \frac{\hat{\mathbf{n}} \times \{(\hat{\mathbf{n}} - \beta(t_{\text{ret}})) \times \dot{\beta}(t_{\text{ret}})\}}{(1 - \beta(t_{\text{ret}}) \cdot \hat{\mathbf{n}})^3} \right|^2 \quad (\text{A.1})$$

and

$$\begin{aligned} \frac{d^2U_{\text{rad}}}{d\omega d\Omega}(\hat{\mathbf{n}}) &= \frac{e^2}{4\pi^2 c} \left| \int_{-\infty}^{\infty} \frac{\hat{\mathbf{n}} \times [(\hat{\mathbf{n}} - \beta(t_{\text{ret}})) \times \dot{\beta}(t_{\text{ret}})]}{(1 - \beta(t_{\text{ret}}) \cdot \hat{\mathbf{n}})^2} \exp[i\omega(t_{\text{ret}} - \hat{\mathbf{n}} \cdot \mathbf{r}(t_{\text{ret}})/c)] dt_{\text{ret}} \right|^2 \\ &\quad (\text{A.2}) \end{aligned}$$

$$= \frac{e^2 \omega^2}{4\pi^2 c} \left| \int_{-\infty}^{\infty} \hat{\mathbf{n}} \times (\hat{\mathbf{n}} \times \beta(t_{\text{ret}})) \exp[i\omega(t_{\text{ret}} - \hat{\mathbf{n}} \cdot \mathbf{r}(t_{\text{ret}})/c)] dt_{\text{ret}} \right|^2 \quad (\text{A.3})$$

whose numerical implementation in code may be more conveniently written in terms of the individual components of $\hat{\mathbf{n}}$, β , and $\dot{\beta}$. Such is provided in this appendix.

Beginning with

$$\begin{aligned}
(\hat{\mathbf{n}} - \boldsymbol{\beta}) \times \dot{\boldsymbol{\beta}} &= \begin{vmatrix} \hat{\mathbf{x}} & \hat{\mathbf{y}} & \hat{\mathbf{z}} \\ n_x - \beta_z & n_y - \beta_y & n_z - \beta_z \\ \dot{\beta}_x & \dot{\beta}_y & \dot{\beta}_z \end{vmatrix} \\
&\quad [(n_y - \beta_y)\dot{\beta}_z - (n_z - \beta_z)\dot{\beta}_y]\hat{\mathbf{x}} \quad \mathcal{N}_x\hat{\mathbf{x}} \\
&= -[(n_x - \beta_x)\dot{\beta}_z - (n_z - \beta_z)\dot{\beta}_x]\hat{\mathbf{y}} \equiv +\mathcal{N}_y\hat{\mathbf{y}} \\
&\quad [(n_x - \beta_x)\dot{\beta}_y - (n_y - \beta_y)\dot{\beta}_x]\hat{\mathbf{z}} \quad +\mathcal{N}_z\hat{\mathbf{z}}
\end{aligned} \tag{A.4}$$

where \mathcal{N}_x , \mathcal{N}_y , and \mathcal{N}_z are shorthand for the components of $(\hat{\mathbf{n}} - \boldsymbol{\beta}) \times \dot{\boldsymbol{\beta}}$, we may then write

$$\begin{aligned}
\hat{\mathbf{n}} \times [(\hat{\mathbf{n}} - \boldsymbol{\beta}) \times \dot{\boldsymbol{\beta}}] &= \begin{vmatrix} \hat{\mathbf{x}} & \hat{\mathbf{y}} & \hat{\mathbf{z}} \\ n_x & n_y & n_z \\ \mathcal{N}_x & \mathcal{N}_y & \mathcal{N}_z \end{vmatrix} = -(n_x\mathcal{N}_z - n_z\mathcal{N}_y)\hat{\mathbf{y}} \\
&\quad +(n_x\mathcal{N}_y - n_y\mathcal{N}_x)\hat{\mathbf{z}} \\
&\quad \left\{ n_y[(n_x - \beta_x)\dot{\beta}_y - (n_y - \beta_y)\dot{\beta}_x] + n_z[(n_x - \beta_x)\dot{\beta}_z - (n_z - \beta_z)\dot{\beta}_x] \right\}\hat{\mathbf{x}} \\
&= -\left\{ n_x[(n_x - \beta_x)\dot{\beta}_y - (n_y - \beta_y)\dot{\beta}_x] - n_z[(n_y - \beta_y)\dot{\beta}_z - (n_z - \beta_z)\dot{\beta}_y] \right\}\hat{\mathbf{y}} \tag{A.5} \\
&\quad + \left\{ -n_x[(n_x - \beta_x)\dot{\beta}_z - (n_z - \beta_z)\dot{\beta}_x] - n_y[(n_y - \beta_y)\dot{\beta}_z - (n_z - \beta_z)\dot{\beta}_y] \right\}\hat{\mathbf{z}}
\end{aligned}$$

While we're at it, expressions for $\hat{\mathbf{n}} \times (\hat{\mathbf{n}} \times \boldsymbol{\beta})$ are provided:

$$\begin{aligned}
& [n_y(n_x\beta_y - n_y\beta_x) + n_z(n_x\beta_z - n_z\beta_x)]\hat{\mathbf{x}} \\
\hat{\mathbf{n}} \times (\hat{\mathbf{n}} \times \boldsymbol{\beta}) = & -[n_x(n_x\beta_y - n_y\beta_x) - n_z(n_y\beta_z - n_z\beta_y)]\hat{\mathbf{y}} \\
& +[-n_x(n_x\beta_z - n_z\beta_x) - n_y(n_y\beta_z - n_z\beta_y)]\hat{\mathbf{z}} \\
& [(n_y\beta_y + n_z\beta_z)n_x - (n_y^2 + n_z^2)\beta_x]\hat{\mathbf{x}} \\
= & +[(n_x\beta_x + n_z\beta_z)n_y - (n_x^2 + n_z^2)\beta_y]\hat{\mathbf{y}} \\
& +[(n_x\beta_x + n_y\beta_y)n_z - (n_x^2 + n_y^2)\beta_z]\hat{\mathbf{z}}
\end{aligned} \tag{A.6}$$

from which a desired form can be chosen. The expressions for $\boldsymbol{\beta} \cdot \hat{\mathbf{n}}$ and $\hat{\mathbf{n}} \cdot \mathbf{r}$ are left to the reader.

The components of $\hat{\mathbf{n}}$, which are Cartesian, may be written in terms of spherical coordinates of a unit sphere where θ is the polar coordinate relative to $\hat{\mathbf{z}}$ and ϕ is the azimuthal coordinate such that $(\theta = 90^\circ, \phi = 0)$ corresponds to $\hat{\mathbf{x}}$ and $(\theta = 90^\circ, \phi = 90^\circ)$ corresponds to $\hat{\mathbf{y}}$:

$$n_x = \sin \theta \cos \phi \tag{A.7}$$

$$n_y = \sin \theta \sin \phi \tag{A.8}$$

$$n_z = \cos \theta \tag{A.9}$$

A rectilinear 2D grid in θ - ϕ is mapped to positions on a sphere via Eq. A.7 to A.9, as illustrated in Fig. A.1. Each unique point (θ, ϕ) on the grid therefore corresponds to a unique set of values in the Cartesian directional coordinates (n_x, n_y, n_z) and point on the unit sphere.

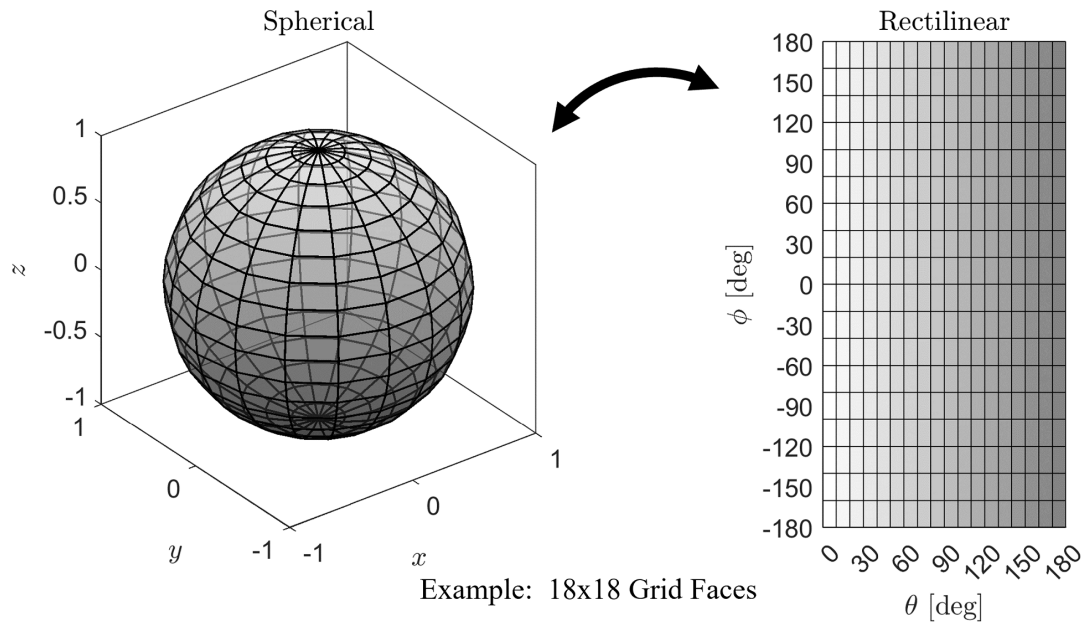


Figure A.1: Diagrams of a unit sphere with grid lines which are mapped to a rectilinear 2D grid in θ and ϕ . This diagram shows an example with 18×18 grid faces.

Appendix B: Units and Physical Constants

B.1 Conversion of Electric Charge and Fields between cgs and SI

Some of the expressions presented in this thesis were originally published in Gaussian units, also known as centimeter-grams-seconds (cgs), in their respective sources [55, 72]. The International System of units (SI) is currently the globally accepted system of units. We present an approach to convert key expressions from cgs to their SI counterparts in this thesis.

In this thesis, we are primarily concerned with the electric and magnetic fields, \mathbf{E} and \mathbf{B} , in free space, as well as the point charge, q , which for an electron is equal to $-e$, where e is the elementary charge (positive definite). A more thorough discussion on units used in electrodynamics is covered in the Appendix in Jackson [72]. For this Appendix specifically, we will use subscript SI to denote quantities in SI units and G to denote quantities in Gaussian (cgs) units. The relationships for the charge, electric and magnetic fields, as well as the electrostatic scalar and magnetic vector potentials, in SI and Gaussian units are given by:

$$q_{\text{SI}} = \sqrt{4\pi\epsilon_0}q_{\text{G}} \quad (\text{B.1})$$

$$\mathbf{E}_{\text{SI}} = \frac{\mathbf{E}_{\text{G}}}{\sqrt{4\pi\epsilon_0}} \quad (\text{B.2})$$

$$\mathbf{B}_{\text{SI}} = \sqrt{\frac{\mu_0}{4\pi}}\mathbf{B}_{\text{G}} \quad (\text{B.3})$$

$$\Phi_{\text{SI}} = \frac{\Phi_{\text{G}}}{\sqrt{4\pi\epsilon_0}} \quad (\text{B.4})$$

$$\mathbf{A}_{\text{SI}} = \sqrt{\frac{\mu_0}{4\pi}}\mathbf{A}_{\text{G}} \quad (\text{B.5})$$

where ϵ_0 is the vacuum permittivity and μ_0 is the vacuum permeability. Along with the vacuum speed of light, c , which is related to these constants via $c = 1/\sqrt{\mu_0\epsilon_0}$, the values of the constants are given by the following:

$$\epsilon_0 = 8.854\ 187\ 8 \dots \times 10^{-12} \text{ C}^2 \cdot \text{s}^2 \cdot \text{kg}^{-1} \cdot \text{m}^{-3} \quad (\text{B.6})$$

$$\mu_0 = 1.256\ 637\ 0 \dots \times 10^{-6} \text{ kg} \cdot \text{m}^2 \cdot \text{C}^{-2} \quad (\text{B.7})$$

$$c = 2.997\ 924\ 58 \times 10^8 \text{ m} \cdot \text{s}^{-1} \quad (\text{B.8})$$

The expression for \mathbf{E}_{SI} follows from Eq. B.1 and the fact that the electric field is defined as the force per unit charge. In SI units, the Coulomb force acting on point charge q_2 by q_1 is given by:

$$\mathbf{F}_E = \frac{q_{1,\text{SI}} q_{2,\text{SI}}}{4\pi\epsilon_0 r_{1,2}^2} \hat{\mathbf{r}}_{1,2} \quad (\text{B.9})$$

where $r_{1,2}$ is the distance between the two charges and $\hat{\mathbf{r}}_{1,2}$ is the unit vector directed from the location of $q_{1,\text{SI}}$ to $q_{2,\text{SI}}$. From the perspective of $q_{2,\text{SI}}$, which we may consider as a "test charge", the charge $q_{2,\text{SI}}$ produces a field in space, also known as an electric field, given by:

$$\mathbf{E}_{\text{SI}} = \frac{q_{\text{SI}}}{4\pi\epsilon_0 r^2} \hat{\mathbf{r}} \quad (\text{B.10})$$

where $q_{1,\text{SI}}$ is replaced symbolically with q_{SI} , $r_{1,2}$ with r and $\hat{\mathbf{r}}_{1,2}$ with $\hat{\mathbf{r}}$. In Gaussian units, the prefactor $\frac{1}{4\pi\epsilon_0}$ is absorbed into the charge terms $q_1 q_2$, so that:

$$\mathbf{F}_E = \frac{q_{1,\text{G}} q_{2,\text{G}}}{r_{1,2}^2} \hat{\mathbf{r}}_{1,2} \quad (\text{B.11})$$

with corresponding electric field:

$$\mathbf{E}_G = \frac{q_G}{r^2} \hat{\mathbf{r}} \quad (\text{B.12})$$

Using Eq. B.1, we can then derive Eq. B.2:

$$\mathbf{E}_{\text{SI}} = \frac{q_{\text{SI}}}{4\pi\epsilon_0 r^2} \hat{\mathbf{r}} = \frac{q_G}{\sqrt{4\pi\epsilon_0 r^2}} \hat{\mathbf{r}} = \frac{\mathbf{E}_G}{\sqrt{4\pi\epsilon_0}} \quad (\text{B.13})$$

Without going into a derivation for Eq. B.3, we discuss the physical interpretation between the magnetic fields in the two systems of units. In SI units, the magnetic force on a point charge, q_{SI} , is given by:

$$\mathbf{F}_B = q_{\text{SI}} \mathbf{v} \times \mathbf{B}_{\text{SI}} \quad (\text{B.14})$$

so that the magnetic field \mathbf{B}_{SI} may be interpreted as a force per unit charge per unit velocity (in a cross product relationship with the magnetic field) of the charge. Converting to Gaussian units, we then have:

$$\mathbf{F}_B = \frac{q_G}{\sqrt{4\pi\epsilon_0}} \mathbf{v} \times \sqrt{\frac{\mu_0}{4\pi}} \mathbf{B}_G = q_G \frac{\mathbf{v}}{c} \times \mathbf{B}_G \quad (\text{B.15})$$

In Gaussian units, the magnetic field can be interpreted as a force per unit charge per unit *normalized* velocity. The electric and magnetic fields in Gaussian units therefore have the same dimensions. Furthermore, the magnitudes of the electric and magnetic fields for an electromagnetic wave are the same in Gaussian units, whereas in SI the ratio is equal to c . In summary, the

Lorentz force in SI and Gaussian units are given by:

$$F_{\text{SI}} = q_{\text{SI}} (\mathbf{E}_{\text{SI}} + \mathbf{v} \times \mathbf{B}_{\text{SI}}) \quad (\text{B.16})$$

$$F_{\text{G}} = q_{\text{G}} \left(\mathbf{E}_{\text{G}} + \frac{\mathbf{v}}{c} \times \mathbf{B}_{\text{G}} \right) \quad (\text{B.17})$$

In view of Eq. B.4 and B.5, the electrostatic scalar potential, Φ , being related to the electrostatic field via $\mathbf{E}_{\text{stat}} = -\nabla\Phi$, has the same conversion factor between SI and Gaussian units as \mathbf{E} . The same can be said for the magnetic vector potential, \mathbf{A} , with its counterpart, \mathbf{B} , via the relationship $\mathbf{B} = \nabla \times \mathbf{A}$. If the vector potential has an explicit dependence on time, however, then the total electric field is related to \mathbf{A} in a way that varies depending on the units involved, specifically:

$$\mathbf{E}_{\text{SI}} = -\nabla\Phi_{\text{SI}} - \frac{\partial \mathbf{A}_{\text{SI}}}{\partial t} \quad (\text{B.18})$$

$$\mathbf{E}_{\text{G}} = -\nabla\Phi_{\text{G}} - \frac{1}{c} \frac{\partial \mathbf{A}_{\text{G}}}{\partial t} \quad (\text{B.19})$$

The factor of $\frac{1}{c}$ for the electric field expression in Gaussian units is due to the change in the ratio of the time varying (e.g., electromagnetic radiation) parts of $|\mathbf{E}|$ to $|\mathbf{B}|$ from SI to Gaussian units.

The normalized vector potential in SI and Gaussian units are given by:

$$a_{0,\text{SI}} = \frac{2e_{\text{SI}}^2 \langle |\mathbf{A}_{\text{SI}}|^2 \rangle}{m^2 c^2} \quad (\text{B.20})$$

$$a_{0,\text{G}} = \frac{2e_{\text{G}}^2 \langle |\mathbf{A}_{\text{G}}|^2 \rangle}{m^2 c^4} \quad (\text{B.21})$$

B.2 Conversion of Radiation Expressions from cgs to SI

Armed with the basic conversion formulas between SI and cgs, we may now derive formulas for the radiation expressions presented in 2.3.4. First we have the Liénard-Wiechert potentials:

$$\Phi_{\text{LW,G}}(\mathbf{x}, t) = \left[\frac{-e_G}{(1 - \boldsymbol{\beta} \cdot \hat{\mathbf{n}})R} \right]_{\text{ret}} \Rightarrow \Phi_{\text{LW,SI}}(\mathbf{x}, t) = \frac{1}{4\pi\epsilon_0} \left[\frac{-e_{\text{SI}}}{(1 - \boldsymbol{\beta} \cdot \hat{\mathbf{n}})R} \right]_{\text{ret}} \quad (\text{B.22})$$

$$\mathbf{A}_{\text{LW,G}}(\mathbf{x}, t) = \left[\frac{-e_G \boldsymbol{\beta}}{(1 - \boldsymbol{\beta} \cdot \hat{\mathbf{n}})R} \right]_{\text{ret}} \Rightarrow \mathbf{A}_{\text{LW,SI}}(\mathbf{x}, t) = \frac{\mu_0}{4\pi} \left[\frac{-e_{\text{SI}} \mathbf{v}}{(1 - \boldsymbol{\beta} \cdot \hat{\mathbf{n}})R} \right]_{\text{ret}} \quad (\text{B.23})$$

Next, we have the electric and magnetic fields derived from the Liénard-Wiechert Potentials:

$$\mathbf{E}_{\text{LW,G}}(\mathbf{x}, t) = -e_G \left[\frac{\hat{\mathbf{n}} - \boldsymbol{\beta}}{\gamma^2 (1 - \boldsymbol{\beta} \cdot \hat{\mathbf{n}})^3 R^2} \right]_{\text{ret}} - \frac{e_G}{c} \left[\frac{\hat{\mathbf{n}} \times \{(\hat{\mathbf{n}} - \boldsymbol{\beta}) \times \dot{\boldsymbol{\beta}}\}}{(1 - \boldsymbol{\beta} \cdot \hat{\mathbf{n}})^3 R} \right]_{\text{ret}} \quad (\text{B.24})$$

$$\Rightarrow \mathbf{E}_{\text{LW,SI}}(\mathbf{x}, t) = -\frac{e_{\text{SI}}}{4\pi\epsilon_0} \left[\frac{\hat{\mathbf{n}} - \boldsymbol{\beta}}{\gamma^2 (1 - \boldsymbol{\beta} \cdot \hat{\mathbf{n}})^3 R^2} \right]_{\text{ret}} - \frac{e_{\text{SI}}}{4\pi\epsilon_0 c} \left[\frac{\hat{\mathbf{n}} \times \{(\hat{\mathbf{n}} - \boldsymbol{\beta}) \times \dot{\boldsymbol{\beta}}\}}{(1 - \boldsymbol{\beta} \cdot \hat{\mathbf{n}})^3 R} \right]_{\text{ret}} \quad (\text{B.25})$$

$$\mathbf{B}_{\text{LW,G}}(\mathbf{x}, t) = [\hat{\mathbf{n}} \times \mathbf{E}_{\text{LW,G}}]_{\text{ret}} \Rightarrow \mathbf{B}_{\text{LW,SI}}(\mathbf{x}, t) = \frac{1}{c} [\hat{\mathbf{n}} \times \mathbf{E}_{\text{LW,SI}}]_{\text{ret}} \quad (\text{B.26})$$

from which we can extract the radiation terms:

$$\mathbf{E}_{\text{rad,G}}(\mathbf{x}, t) = -\frac{e_G}{c} \left[\frac{\hat{\mathbf{n}} \times \{(\hat{\mathbf{n}} - \boldsymbol{\beta}) \times \dot{\boldsymbol{\beta}}\}}{(1 - \boldsymbol{\beta} \cdot \hat{\mathbf{n}})^3 R} \right]_{\text{ret}} \quad (\text{B.27})$$

$$\Rightarrow \mathbf{E}_{\text{rad,SI}}(\mathbf{x}, t) = -\frac{e_{\text{SI}}}{4\pi\epsilon_0 c} \left[\frac{\hat{\mathbf{n}} \times \{(\hat{\mathbf{n}} - \boldsymbol{\beta}) \times \dot{\boldsymbol{\beta}}\}}{(1 - \boldsymbol{\beta} \cdot \hat{\mathbf{n}})^3 R} \right]_{\text{ret}} \quad (\text{B.28})$$

$$\mathbf{B}_{\text{rad,SI}}(\mathbf{x}, t) = \frac{1}{c} [\hat{\mathbf{n}} \times \mathbf{E}_{\text{rad,SI}}]_{\text{ret}} \quad (\text{B.29})$$

The Poynting vector is given by:

$$|\mathbf{S}_G(\mathbf{x}, t)| = \frac{c}{4\pi} E_{rad,G}^2(\mathbf{x}, t_{ret}) \Rightarrow |\mathbf{S}_{SI}(\mathbf{x}, t)| = \frac{1}{\mu_0 c} E_{rad,SI}^2(\mathbf{x}, t_{ret}) \quad (B.30)$$

The radiated power per unit solid angle is:

$$\begin{aligned} \frac{dP_{rad,G}}{d\Omega}(\hat{\mathbf{n}}, t) &= \frac{c}{4\pi} [RE_{rad,G}(\mathbf{x}, t_{ret})]^2 \\ &= \frac{e_G^2}{4\pi c} \left| \frac{\hat{\mathbf{n}} \times \{(\hat{\mathbf{n}} - \boldsymbol{\beta}(t_{ret})) \times \dot{\boldsymbol{\beta}}(t_{ret})\}}{(1 - \boldsymbol{\beta}(t_{ret}) \cdot \hat{\mathbf{n}})^3} \right|^2 \end{aligned} \quad (B.31)$$

$$\begin{aligned} \Rightarrow \frac{dP_{rad,SI}}{d\Omega}(\hat{\mathbf{n}}, t) &= \frac{1}{\mu_0 c} [RE_{rad,SI}(\mathbf{x}, t_{ret})]^2 \\ &= \frac{e_{SI}^2}{16\pi^2\epsilon_0 c} \left| \frac{\hat{\mathbf{n}} \times \{(\hat{\mathbf{n}} - \boldsymbol{\beta}(t_{ret})) \times \dot{\boldsymbol{\beta}}(t_{ret})\}}{(1 - \boldsymbol{\beta}(t_{ret}) \cdot \hat{\mathbf{n}})^3} \right|^2 \end{aligned} \quad (B.32)$$

The radiated energy per unit frequency per unit solid angle is:

$$\frac{d^2U_{rad,G}}{d\omega d\Omega}(\hat{\mathbf{n}}) = \frac{c}{4\pi^2} \left| \int_{-\infty}^{\infty} R(t_{ret}) \mathbf{E}_{rad,G}(\mathbf{x}, t_{ret}) \exp(i\omega t) dt \right|^2 \quad (B.33)$$

$$= \frac{e_G^2}{4\pi^2 c} \left| \int_{-\infty}^{\infty} \frac{\hat{\mathbf{n}} \times [(\hat{\mathbf{n}} - \boldsymbol{\beta}(t_{ret})) \times \dot{\boldsymbol{\beta}}(t_{ret})]}{(1 - \boldsymbol{\beta}(t_{ret}) \cdot \hat{\mathbf{n}})^2} \exp[i\omega(t_{ret} - \hat{\mathbf{n}} \cdot \mathbf{r}(t_{ret})/c)] dt_{ret} \right|^2 \quad (B.34)$$

$$= \frac{e_G^2 \omega^2}{4\pi^2 c} \left| \int_{-\infty}^{\infty} \hat{\mathbf{n}} \times (\hat{\mathbf{n}} \times \boldsymbol{\beta}(t_{ret})) \exp[i\omega(t_{ret} - \hat{\mathbf{n}} \cdot \mathbf{r}(t_{ret})/c)] dt_{ret} \right|^2 \quad (B.35)$$

$$\Rightarrow \frac{d^2U_{rad,SI}}{d\omega d\Omega}(\hat{\mathbf{n}}) = \frac{c\epsilon_0}{\pi} \left| \int_{-\infty}^{\infty} R(t_{ret}) \mathbf{E}_{rad,SI}(\mathbf{x}, t_{ret}) \exp(i\omega t) dt \right|^2 \quad (B.36)$$

$$= \frac{e_{SI}^2}{16\pi^3\epsilon_0 c} \left| \int_{-\infty}^{\infty} \frac{\hat{\mathbf{n}} \times [(\hat{\mathbf{n}} - \boldsymbol{\beta}(t_{ret})) \times \dot{\boldsymbol{\beta}}(t_{ret})]}{(1 - \boldsymbol{\beta}(t_{ret}) \cdot \hat{\mathbf{n}})^2} \exp[i\omega(t_{ret} - \hat{\mathbf{n}} \cdot \mathbf{r}(t_{ret})/c)] dt_{ret} \right|^2 \quad (B.37)$$

$$= \frac{e_{SI}^2 \omega^2}{16\pi^3\epsilon_0 c} \left| \int_{-\infty}^{\infty} \hat{\mathbf{n}} \times (\hat{\mathbf{n}} \times \boldsymbol{\beta}(t_{ret})) \exp[i\omega(t_{ret} - \hat{\mathbf{n}} \cdot \mathbf{r}(t_{ret})/c)] dt_{ret} \right|^2 \quad (B.38)$$

The analytical expressions from Sarachik and Schappert [55] describe the power as given by (Eq. 2.103):

$$\frac{dP^{(n)}}{d\Omega} = \frac{e_G^2 \pi c}{2\lambda_0^2} f^{(n)}(a_0, \theta, \phi) = \frac{e_{SI}^2 c}{8\epsilon_0 \lambda_0^2} f^{(n)}(a_0, \theta, \phi) \quad (\text{B.39})$$

where $f^{(n)}(a_0, \theta, \phi)$ is a dimensionless function.

B.3 Dimensional Analysis of Radiation Expressions

Alternatively, the radiation expressions in Gaussian units may be used directly in computation, followed by a conversion of the resulting values to SI units via dimensional analysis. In this section, we will use dimensional analysis to show that the radiation expressions in SI and Gaussian units agree. To do this, we start with the expressions in Gaussian units, then plug in the values of the given quantities in Gaussian units. The result will contain units of statC (Gaussian unit for charge), which may be converted to Gaussian base units (cm, g, s), then to the erg (Gaussian unit for energy) and finally to the Joule (SI unit for energy). We will need following definitions and conversion factors:

$$e_G = 4.8 \times 10^{-10} \text{ statC} \quad (\text{B.40})$$

$$1 \text{ statC}^2 = \text{cm}^3 \text{g/s}^2 \quad (\text{B.41})$$

$$1 \text{ erg} = \text{g} \cdot \text{cm}^2/\text{s}^2 = 10^{-7} \text{ J} \quad (\text{B.42})$$

It is useful to have the square of e_G on hand:

$$e_G^2 = (4.8 \times 10^{-10} \text{ statC})^2 = 2.3 \times 10^{-19} \text{ cm}^3 \text{g/s}^2 \quad (\text{B.43})$$

We focus on the expressions written out explicitly in terms of $\hat{\mathbf{n}}$, β , $\dot{\beta}$, and \mathbf{r}/c which are all dimensionless quantities, so that we only need to concern ourselves with the constant prefactors.

We begin with the prefactors in Eq. B.31 and B.32:

$$\begin{aligned} \frac{e_G^2}{4\pi c} &= \frac{(4.8 \times 10^{-10} \text{ statC})^2}{4\pi \times 3 \times 10^{10} \text{ cm/s}} = 6.11 \times 10^{-31} \frac{\text{cm}^2 \text{g/s}^2}{\text{cm/s}} = 6.11 \times 10^{-31} \text{ erg} \cdot \text{s} \\ &= 6.11 \times 10^{-38} \text{ J} \cdot \text{s} \end{aligned} \quad (\text{B.44})$$

$$\begin{aligned} \frac{e_{\text{SI}}^2}{16\pi^2\epsilon_0 c} &= \frac{(1.602 \times 10^{-19} \text{ C})^2}{16\pi^2(8.854 \times 10^{-12} \text{ C}^2 \text{s}^2 \text{kg}^{-1} \text{m}^{-3})(3 \times 10^8 \text{ m/s})} \\ &= 6.11 \times 10^{-38} \text{ J} \cdot \text{s} \end{aligned} \quad (\text{B.45})$$

The prefactors in Eq. B.34 and B.37 differ from Eq. B.31 and B.32 only by a factor of $\frac{1}{\pi}$, while the prefactors for B.35 and B.38 differ by a factor of $\frac{\omega^2}{\pi}$. It may be convenient to rewrite the prefactor in units of eV·fs to better understand the scale of the underlying physics:

$$6.11 \times 10^{-38} \text{ J} \cdot \text{s} \times \frac{1 \text{ eV}}{1.602 \times 10^{-19} \text{ J}} \times \frac{10^{15} \text{ fs}}{\text{s}} = 3.81 \times 10^{-4} \text{ eV} \cdot \text{fs} \quad (\text{B.46})$$

The remaining dimensions of $\frac{1}{\text{fs}^2}$ is contained within the $\dot{\beta}$ term inside the absolute value brackets (squared) in Eq. B.31 and B.32.

The analytical function from Sarachik and Schappert has a prefactor:

$$\begin{aligned} \frac{e_G^2 \pi c}{2\lambda_0^2} &= \frac{(4.8 \times 10^{-10} \text{ statC})^2 \pi (3 \times 10^{10} \text{ cm/s})}{2 \times (0.8 \times 10^{-4} \text{ cm})^2} = 1.70 \frac{\text{cm}^2 \text{g}}{\text{s}^3} \\ &= 1.70 \frac{\text{erg}}{\text{s}} \times \frac{10^{-7} \text{ J}}{\text{erg}} = 1.70 \times 10^{-7} \text{ J/s} \end{aligned} \quad (\text{B.47})$$

$$\begin{aligned} \frac{e_{\text{SI}}^2 c}{8\epsilon_0 \lambda_0^2} &= \frac{(1.602 \times 10^{-19} \text{ C})^2 (3 \times 10^8 \text{ m/s})}{8(8.854 \times 10^{-12} \text{ C}^2 \text{s}^2 \text{kg}^{-1} \text{m}^{-3})(0.8 \times 10^{-6} \text{ m})^2} \\ &= 1.70 \times 10^{-7} \text{ kg} \cdot \text{m}^2/\text{s}^3 = 1.70 \times 10^{-7} \text{ J/s} \end{aligned} \quad (\text{B.48})$$

Converting to units of eV/fs:

$$1.70 \times 10^{-7} \text{ J/s} \times \left(\frac{1 \text{ eV}}{1.602 \times 10^{-19} \text{ J}} \right) \left(\frac{1 \text{ s}}{10^{15} \text{ fs}} \right) = 1.06 \times 10^{-2} \text{ eV/fs} \quad (\text{B.49})$$

Appendix C: MATLAB Code (Numerical Calculations) from Chapter 2

Note: When copying and pasting code blocks onto MATLAB, the document compiler may add additional newline characters where a full line is broken in order to fit the document. These characters would need to be removed manually in the MATLAB editor. Furthermore, the caret character ^ produced by the document compiler may not be recognized by MATLAB, and would require manual replacement in the editor.

C.1 A Note on Double Precision

Double precision is MATLAB's default variable format for floating point numbers. The precision of a double variable is not uniform and depends on the value. The precision quantified by the distance between value of the number and its next adjacent number, and is typically around 10^{-15} the size of the value of the number itself. Figure C.1 shows a plot of precision determined using MATLAB's `eps()` function, which calls the "epsilon of the machine", vs. \log_{10} (order of magnitude) of the value.

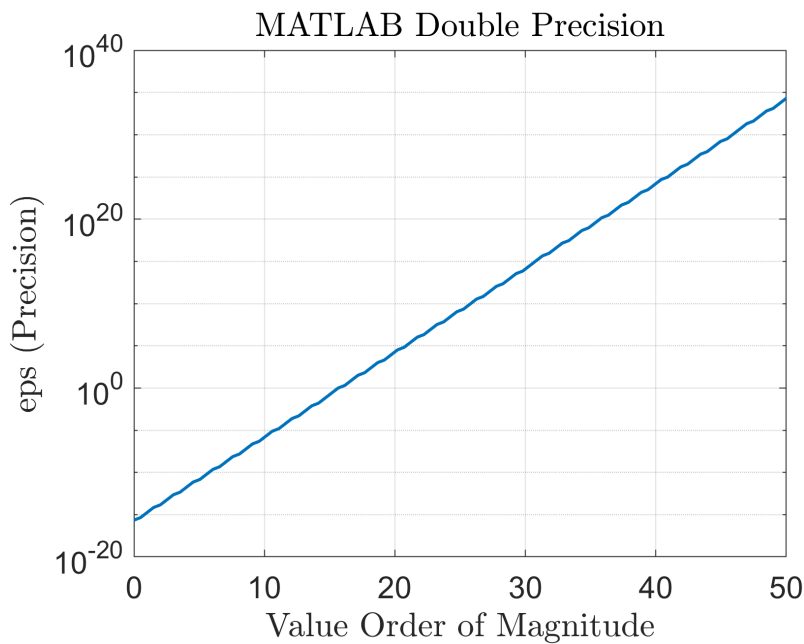


Figure C.1: Plot of eps (precision) as a function of the \log_{10} value. In other words, if the value is x then $y = \log_{10} x$ such that $x = 10^y$.

The range of values in physics calculations can vary by 10's or even more than 100 orders of magnitude depending on the units used. Arithmetic operations can lead to precision error and be accumulated. Furthermore, presentation of values with large exponents (whether positive or negative) can become difficult to interpret. It is therefore, good practice when performing numerical calculations to work with units whose typical values fall within the same order of magnitude, preferably an order of magnitude of 1.

C.2 Electron Motion under Lorentz Force by an Infinite Plane Wave

```
% Written and tested in MATLAB version R2022a
clear;

a0 = 1; % Normalized Vector Potential

% Normalized units are used in this script
% Initial Conditions
x0 = a0;
```

```

z0 = 0;
px0 = 0;
pz0 = 0;
delta0 = 0;

% ODE Parameters
y0(1) = x0;
y0(2) = z0;
y0(3) = px0;
y0(4) = pz0;
y0(5) = 0; % Used to facilitate calculating F_E and F_B separately
y0(6) = 0; % Used to facilitate calculating F_E and F_B separately
Nt = 8001;
tf = 2*pi*10*(1+a0^2/4); % 10 cycles
ti = 0;
tspan = linspace(ti, tf, Nt);

% ODE Solution
[t, y] = ode89(@(t, y) RTS_ODE(t, y, a0, delta0), tspan, y0);

% Extract Variables from Solution
for i=1:length(t)
    soln(i, :) = RTS_ODE(t(i), y(i, :), a0, delta0);
end

% Output Variables (Time Series) vs. t

x = y(:, 1);
z = y(:, 2);
px = y(:, 3);
pz = y(:, 4);
Fx = soln(:, 3);
Fz = soln(:, 4);
FEx = soln(:, 5);
FBx = soln(:, 6);

% Velocity and Acceleration in Normalized units
gamma = sqrt(1+px.^2+pz.^2);
vx = px./gamma;
vz = pz./gamma;
dt = t(2) - t(1);
ax = diff(vx)/dt;
az = diff(vz)/dt;

% Alternative Method to Determine Acceleration
betax = px./gamma;
betaz = pz./gamma;
betadotx = (1./gamma).* (Fx-px./ (gamma.^2).* (px.*Fx+pz.*Fz));
betadotz = (1./gamma).* (Fz-pz./ (gamma.^2).* (px.*Fx+pz.*Fz));

```

The previous script references the RTS_ODE() function which is defined below.

```
%% RTS ODE function
```

```

function dydt = RTS_ODE(t,y,a0,delta0)
    % This function uses normalized units
    %p -> p/mc
    %x -> kx
    %z -> kz
    %t -> omega*t

    % y variable element definitions
    %y(1) = x; dydt(1) = dxdt
    %y(2) = z; dydt(2) = dzdt
    %y(3) = px; dydt(3) = dpxdt
    %y(4) = pz; dydt(4) = dpzdt = F_B_z (magnetic force z component)
    %dydt(5) = F_E_x (electric force x component)
    %dydt(6) = F_B_x (magnetic force x component)
    dydt = zeros(6,1);

    % Lorentz integrator
    dydt(1) = y(3)/sqrt(1+y(3)^2+y(4)^2);
    dydt(2) = y(4)/sqrt(1+y(3)^2+y(4)^2);
    dydt(3) = (y(4)/sqrt(1+y(3)^2+y(4)^2)-1)*a0*cos(y(2)-t+delta0);
    dydt(4) = -y(3)/sqrt(1+y(3)^2+y(4)^2)*a0*cos(y(2)-t+delta0);
    dydt(5) = -a0*cos(y(2)-t+delta0);
    dydt(6) = y(4)/sqrt(1+y(3)^2+y(4)^2)*a0*cos(y(2)-t+delta0);
end

```

C.3 Electron Motion under Lorentz Force by a Gaussian Temporal Pulse

When a Gaussian temporal pulse is considered, we want a solution with a carrier-envelope phase (CEP) of 0 and where the electron is at its peak excursion during the peak of the laser. This is done by solving the Lorentz force differential equation in both directions of time, positive and negative, starting from $t = 0$, and combining the two-sided solutions. This is carried out in the script below.

```

% Written and tested in MATLAB version R2022a
clear;

a0 = 1;

% Initial Conditions
x0 = a0;
z0 = 0;
px0 = 0;
pz0 = 0;
delta0 = 0;

```

```

y0(1) = x0;
y0(2) = z0;
y0(3) = px0;
y0(4) = pz0;
y0(5) = 0; % For facilitating solving for F_Ex
y0(6) = 0; % For Facilitating solving for F_Bx
Nt = 8001;
tf = 2*pi*10*(1+a0^2/4); % 10 cycles (each side) of the infinite plane wave
at a0
ti = -tf; %
tspan1 = linspace(0,tf,Nt); % Positive side
tspan2 = linspace(0,ti,Nt); % Negative side

% Two sided RTS solution (mainly for gaussian)
[t1,y1] = ode89(@(t1,y1) RTS_ODE_gaussian_pulse(t1,y1,a0,delta0), tspan1,
y0); % Positive Solution
[t2,y2] = ode89(@(t2,y2) RTS_ODE_gaussian_pulse(t2,y2,a0,delta0), tspan2,
y0); % Negative Solution

% Combined Solution
t = [flipud(t2); t1(2:length(t1))];
y = [flipud(y2); y1(2:length(y1),:)];
for i=1:length(t)
    soln(i,:) = RTS_ODE_gaussian_pulse(t(i),y(i,:),a0,delta0);
end

% Output Variables (Time Series) vs. t
x = y(:,1);
z = y(:,2);
px = y(:,3);
pz = y(:,4);
Fx = soln(:,3);
Fz = soln(:,4);
FEx = soln(:,5);
FBx = soln(:,6);

gamma = sqrt(1+px.^2+pz.^2);
vx = px./gamma;
vz = pz./gamma;
dt = t(2) - t(1);
ax = diff(vx)/dt;
az = diff(vz)/dt;

```

The previous script references the RTS_ODE_gaussian_pulse() function defined below. The pulse width of the Gaussian envelope is defined to be 30 fs (intensity FWHM) within the function.

```

function dydt = RTS_ODE_gaussian_pulse(t,y,a0,delta0)
    c = 3*10^8; % m/s
    lambda0 = 0.8; % um

```

```

% y variable element definitions
% Quantities are in normalized units
%y(1) = x; dydt(1) = dxdt
%y(2) = z; dydt(2) = dzdt
%y(3) = px; dydt(3) = dpxdt
%y(4) = pz; dydt(4) = dpzdt = F_B_z
%dydt(5) = F_E_x
%dydt(6) = F_B_x
dydt = zeros(6,1);

t_fwhm = 30; %fs
tau = t_fwhm/sqrt(2*log(2))*2*pi*c/lambd0*10^-6*10^-15; % fs

% Lorentz integrator
dydt(1) = y(3)/sqrt(1+y(3)^2+y(4)^2);
dydt(2) = y(4)/sqrt(1+y(3)^2+y(4)^2);

carrier = cos(y(2)-t+delta0);
envelope_temp = exp(-(t-y(2)).^2/tau^2);

dydt(3) = (y(4)/sqrt(1+y(3)^2+y(4)^2)-1)*a0*carrier*envelope_temp;
dydt(4) = -y(3)/sqrt(1+y(3)^2+y(4)^2)*a0*carrier*envelope_temp;

dydt(5) = -a0*cos(y(2)-t+delta0);
dydt(6) = y(4)/sqrt(1+y(3)^2+y(4)^2)*a0*carrier*envelope_temp;
end

```

C.4 Electron Motion in the Drift Frame via Lorentz Transform

The script in C.2 is required to be run prior to running the following script. This script takes the electron motion infinite plane wave solutions, computes a Lorentz transform to the drift frame, and plots the resulting paths of motion.

```

gamma0 = sqrt(1+q^2/2);

% Lorentz Transformation from Numerical Results
vD = q^2/(4+q^2);
gammaD = 1/sqrt(1-vD^2);

tD = gammaD.* (t-vD/c*z);
zD = gammaD.* (z-vD*t);

tf_ci = find(abs(t-tf/10)==min(abs(t-tf/10))); % Search for index at the
% end of the first cycle
ti_c = 1:tf_ci;

```

```

% Figure-8 Analytical (Gibbon)
a = sqrt(q^2/(4+2*q^2));
kxmax = 2*a;
kx = linspace(-kxmax,kxmax,300);
kz = sqrt((1/16)*kx.^2.* (4*a^2-kx.^2));
c = 1;
vR = sqrt((1-4*(1-2*vD/(c+vD))*(2+2*(vD/(c+vD))-kx.^2).^-2));

for ti=1:length(t_lin)
    tvar = t_lin(ti);
    fun = @(zvar) myfun(zvar,a,tvar);
    z_RTS(ti) = fzero(fun,1);
    x_RTS(ti) = -q/sqrt(1+q^2/2)*cos(z_RTS(ti)-tvar+pi);
    px_RTS(ti) = -q*sin(z_RTS(ti)-tvar+pi);
    pz_RTS(ti) = -q^2/(4*sqrt(1+q^2/2))*cos(2*(z_RTS(ti)-tvar+pi));
end

% Plotting
grdlist = {[1],[2]};

figure('position',[1 1 1500 700]);
subplot(1,2,grdlist{1});
hold on;
p1(1)=plot(z(ti_c),t(ti_c),'linewidth',1.5,'color','blue',...
'displayname','Lab Frame');
p1(2)=plot(zD(ti_c),tD(ti_c),'linewidth',1.5,'color','red',...
'displayname','Lorentz Transform','linestyle',':');
p1(3)=plot(z_RTS,t_lin,'linewidth',1.5,'color','red',...
'displayname','Doppler Correction','linestyle','-');
xlim([-3 3]);
ylim([0 10]);
p1(4)=line([0 20],[0
20],'linestyle','--','color','black','displayname','Light Cone');
line([0 -20],[0 20],'linestyle','--','color','black');
xlabel('$kz$');
ylabel('$\omega_t$');
legend(p1,'location','north');

subplot(1,2,grdlist{2});
p2(1)=plot(z(ti_c),x(ti_c),'linewidth',1.5,'color','blue',...
'displayname','Lab Frame');
hold on;
p2(2)=plot(zD(ti_c),x(ti_c),'linewidth',1.5,'color','red',...
'displayname','Lorentz Transform','linestyle',':');
p2(3)=plot(kz,kx,'color','red','linestyle','-','linewidth',1.5,...
'displayname','Doppler Correction');
plot(-kz,kx,'color','red','linestyle','-', 'linewidth',1.5);
xlim([-0.5 2]);
ylim([-1 1]);
xlabel('$kx$');
ylabel('$kz$');
legend(p2,'location','north');

for i=1:2

```

```

    subplot(1,2,grdlist{i});
    daspect([1 1 1]);
    set(gca,'fontsize',15);
    grid on;
end

```

C.5 Electron Motion in the Drift Frame from Analytical Expressions

The following code computes and plots the electron motion in the drift frame from analytical expressions (see section 2.3.3).

```

clear;
set(0,'defaulttextinterpreter','latex');
figure('position',[1 1 1200 500]);

% Figure-8 momentum vectors

N = 1024*4;
N_cyc = 10; % Use 1 for default, 10 for FFT
tmax = 2*pi*N_cyc;
t_lin = linspace(0,tmax,N);
myfun = @(z,a,t) z-a^2/2*sin(2*(z-t+pi)); % parameterized function

% parameters
q = 1; % Normalized vector potential
a = sqrt(q^2/(4+2*q^2));
theta_obs = -atan(0.15/1);

for ti=1:length(t_lin)
t = t_lin(ti);
fun = @(z) myfun(z,a,t);
z_RTS(ti) = fzero(fun,1);
x_RTS(ti) = -q/sqrt(1+q^2/2)*cos(z_RTS(ti)-t+pi);
px_RTS(ti) = -q*sin(z_RTS(ti)-t+pi);
pz_RTS(ti) = -q^2/(4*sqrt(1+q^2/2))*cos(2*(z_RTS(ti)-t+pi));
end

dt = t_lin(2)-t_lin(1);
Fx_RTS = diff(px_RTS)/dt;
Fz_RTS = diff(pz_RTS)/dt;

gamma_RTS = sqrt(1+px_RTS.^2+pz_RTS.^2);
vx_RTS = px_RTS./gamma_RTS;
vz_RTS = pz_RTS./gamma_RTS;
ax_RTS = diff(vx_RTS)/dt;
az_RTS = diff(vz_RTS)/dt;

```

```

ticoarse = 1:N/8:N;
subplot(1,3,1);
plot(z_RTS,x_RTS,'linewidth',1.5,'color','blue','linestyle',':');
hold on;
plot(z_RTS(ticoarse),x_RTS(ticoarse),'linestyle','none','marker','.',...
'markersize',20,'color',[1 0 0]);
pscale=0.3;
quiver(z_RTS(ticoarse),x_RTS(ticoarse),pz_RTS(ticoarse)*pscale,....
px_RTS(ticoarse)*pscale,'linewidth',1.5,'autoscale','off','color',[1 0 0]);
xlim([-0.4 0.4]);
xticks(-0.4:0.4:0.4);
ylim([-1 1]);
title({'Figure-8 ($a_0=1$)',...
'and momentum'});

% Figure-8 vs. a0
qlist = [0.5, 1, 2, 10];

for qi = 1:length(qlist)
qtemp = qlist(qi);
a = sqrt(qtemp^2/(4+2*qtemp^2));
vD(qi) = qtemp^2/(4+qtemp^2);

kxmax(qi) = 2*a;

kx{qi} = linspace(-kxmax(qi),kxmax(qi),300);
kz{qi} = sqrt((1/16)*kx{qi}.^2.* (4*a^2-kx{qi}.^2));

c = 1;
vR{qi} =
sqrt((1-4*(1-2*vD(qi)/(c+vD(qi)))*(2+2*(vD(qi)/(c+vD(qi))-kx{qi}.^2).^-2)));
end

subplot(1,3,2);
for qi = 1:length(qlist)
colorval = [0 0 qi/length(qlist)];
lwval = qi/length(qlist)*2;
p(qi)=plot(kz{qi},kx{qi}, 'color',colorval,'linewidth',lwval, ...
'displayname',strcat('a_0=',num2str(qlist(qi))));
hold on;
plot(-kz{qi},kx{qi}, 'color',colorval,'linewidth',lwval);
end
legend(p,'location','eastoutside');
xlim([-0.5 0.5]);
zlim([-1.5 1.5]);
title('Figure-8 vs. $a_0$');

% Figure-8 proportions vs. a0
a0_lin = linspace(10^-2,100,10000);

zamp = a0_lin.^2./(4*(1+a0_lin.^2/2));
xamp = a0_lin./sqrt(1+a0_lin.^2/2);

subplot(1,3,3);

```

```

plot(a0_lin,zamp./xamp,'linewidth',1.5);
title('Figure-8 Proportions vs. $a_0$');
xlim([10^-2 10^2]);
xticks(10.^(-2:2));

```

C.6 Radiation Spectrum at $\theta = 90^\circ$

One of the scripts in either C.2 (plane wave) or C.3 (Gaussian pulse) is required to be run prior to running the following script. This script takes the electron motion solutions to either the infinite plane wave or Gaussian pulse and computes and plots the spectrum radiated at $\theta = 90^\circ$ (see section 2.3.4).

```

c = 3*10^8; % m/s
lambda0 = 800*10^-9; % m
omega0 = 2*pi*c/lambda0/10^15; % rad/fs

omega_FFT = linspace(0,4,1000); % units of omega0

% Components of Fourier Integral
for i=1:length(omega_FFT)
    FIx_E(i) = 0;
    FIz_E(i) = -sum(vz.*exp(1i*omega_FFT(i)*(t-x))*dt);

    FIx_B(i) = sum(vx.*exp(1i*omega_FFT(i)*(t-x))*dt);
    FIz_B(i) = -sum(vz.*exp(1i*omega_FFT(i)*(t-x))*dt);
end

e_cg = 4.8*10^-10; % statcoulomb
c_cg = 3*10^8*100; % cm/s
C1 = e_cg^2*omega0^2/(4*pi^2*c_cg)/10^7/(1.602*10^-19)/omega0^2*10^15; % eV/(rad/fs)/sr
C2 = C1/(2*pi*c_cg*10^-2*10^-15)*10^-9; % eV/(rad/fs)^2/nm/sr

lambda_FFT = 2*pi*c./(omega_FFT*omega0*10^15)*10^9; % nm

FI_E = abs(FIx_E.^2 + FIz_E.^2).^2;
FI_B = abs(FIx_B.^2 + FIz_B.^2).^2;

figure('position',[1 1 1400 500]);

subplot(1,2,1);
yyaxis left;
plot(omega_FFT,FI_E*C1,'linewidth',1.5,'Displayname','|| E');
ylabel('$\frac{d^2U}{d\Omega d\Omega} [eV/(rad/fs)/sr]$');

```

```

yyaxis right;
plot(omega_FFT,FI_B*C1,'linewidth',1.5,'Displayname','\perp E');
xlabel('$f/f_0$');
ylabel('$\frac{d^2U}{d\Omega} [eV/(rad/fs)/sr]$');
title('Frequency Spectrum');

subplot(1,2,2);
yyaxis left;
plot(lambda_FFT,FI_E*C2.*omega_FFT.^2*omega0^2,'linewidth',1.5,... 
'Displayname','|| E');
ylabel('$\frac{d^2U}{d\lambda} [eV/nm/sr]$');
yyaxis right;
plot(lambda_FFT,FI_B*C2.*omega_FFT.^2*omega0^2,'linewidth',1.5,... 
'Displayname','\perp E');
xlim([200 1200]);
xlabel('$\lambda [nm]$');
ylabel('$\frac{d^2U}{d\lambda} [eV/nm/sr]$');
title('Wavelength Spectrum');

for i=1:2
subplot(1,2,i);
legend('location','north');
grid on;
set(gca,'fontsize',15);
end

```

C.7 Total Energy Angular Distribution

The script in C.2 is required to be run prior to running the following script. This script computes the total energy angular distribution (Eq. 2.101) from the electron motion solutions to the Lorentz force differential equation.

```

e_cg = 4.8*10^-10;
c_cg = 3*10^8*100;

Ngrid = 50;
theta_lin = linspace(0,pi,Ngrid);
phi_lin = linspace(-pi,pi,Ngrid);
[theta,phi] = meshgrid(theta_lin,phi_lin);

nx = sin(theta).*cos(phi);
ny = sin(theta).*sin(phi);
nz = cos(theta);

denom = {};
int = zeros(size(nx));

```

```

for i=1:length(t)
    betay(i) = 0;
    betadoty(i) = 0;
    numx{i} = ny.*((nx-betax(i))*betadoty(i)-(ny-betay(i))*betadotx(i))
    ...
    + nz.*((nx-betax(i))*betadotz(i) - (nz-betaz(i))*betadotx(i));
    numy{i} =
    -nx.*((nx-betax(i))*betadoty(i)-(ny-betay(i))*betadotx(i)) ...
    + nz.*((ny-betay(i))*betadotz(i) - (nz-betaz(qi)(i))*betadoty(i));
    numz{i} =
    -nx.*((nx-betax(i))*betadotz(i)-(nz-betaz(i))*betadotx(i)) ...
    - ny.*((ny-betay(i))*betadotz(i) - (nz-betaz(i))*betadoty(i));

    denom{i} = (1-betax(i).*nx-betaz(i).*nz).^5;

    int = int + (numx{i}.^2+numy{i}.^2+numz{i}.^2)./denom{i};
end
int = omega0^2*e_cgs^2/(4*pi*c_cgs)*int*dt*10^-7/(1.602*10^-19)/omega0;

%% Plot Solution
figure('position',[1 1 1900 800]);

subplot(1,2,1);
surf(nx,nz,ny,int,'edgecolor','none');
set(gca,'ydir','reverse');
xlabel('$x$');
ylabel('$z$');
zlabel('$y$');

subplot(1,2,2)
imagesc(theta_lin*180/pi,phi_lin*180/pi,int{qi});
xlabel('$\theta$ [$^\circ]$');
ylabel('$\phi$ [$^\circ]$');
set(gca,'ydir','normal','xdir','reverse');
cb=colorbar;
cb.Label.String = 'eV/sr';
xticks(0:45:180);
yticks(-180:45:180);

for i=1:2
    subplot(1,2,i);
    colormap jet;
    daspect([1 1 1]);
    caxis([0 max(int,[],'all')]);
    set(gca,'fontsize',12);
end

```

C.8 Energy Angular Distribution over a Spectral Band

The script in C.2 is required to be run prior to running the following script. This script computes the energy angular distribution radiated over a spectral band from 400 - 700 nm (see Eq. 2.102) from the electron motion solutions to the Lorentz force differential equation. This script is written to allow either Eq. 2.72 ("Full Expression") or 2.73 ("By Parts Expression") to be used. The "Full Expression" is commented out so that only the "By Parts Expression" is implemented.

```
e_cg = 4.8*10^-10; % statC
c_cg = 3*10^8*100; % cm/s

Ngrid = 50;
theta_lin = linspace(0,pi,Ngrid);
phi_lin = linspace(-pi,pi,Ngrid);
[theta,phi] = meshgrid(theta_lin,phi_lin);

nx = sin(theta).*cos(phi);
ny = sin(theta).*sin(phi);
nz = cos(theta);

lambda0 = 800; % nm Laser central wavelength

lambda1 = 400; % nm Band Lower Bound
lambda2 = 700; % nm Band Upper Bound

c = 3*10^8; % m/s
omega0 = 2*pi*c/(lambda0*10^-9)*10^-15; % rad/fs
omega1 = 2*pi*c/(lambda1*10^-9)*10^-15; % rad/fs
omega2 = 2*pi*c/(lambda2*10^-9)*10^-15; % rad/fs

omegalist = linspace(omega2,omega1,500);
domega = omegalist(2) - omegalist(1);
lambdalist = 2*pi*c./omegalist*10^-15*10^9; % nm
dlambda = lambdalist(2) - lambdalist(1);

denom = {};
y= zeros(1,length(t)); % Clears out original assignment of variable y

intband_tot = zeros(size(nx));
for oi = 1:length(omegalist)
    omega = omegalist(oi);
```

```

intbandx{qi} = zeros(size(nx));
intbandy{qi} = zeros(size(ny));
intbandz{qi} = zeros(size(nz));
for i=1:length(t)
    msg = ['oi=', num2str(oi), '/', num2str(length(omegalist)), ...
    '; ti=', num2str(i), '/', num2str(length(t{qi}))];
    disp(msg);

    %
    betay(i) = 0;
    betadoty(i) = 0;

    % Full Expression
    %
    numx{i} =
ny.*((nx-betax(i))*betadoty(i)-(ny-betay(i))*betadotx(i)) ...
+ nz.*((nx-betax(i))*betadotz(i) -
(nz-betaz(i))*betadotx(i));
    numy{i} =
-nx.*((nx-betax(i))*betadoty(i)-(ny-betay(i))*betadotx(i)) ...
+ nz.*((ny-betay(i))*betadotz(i) -
(nz-betaz(i))*betadoty(i));
    numz{i} =
-nx.*((nx-betax(i))*betadotz(i)-(nz-betaz(i))*betadotx(i)) ...
- ny.*((ny-betay(i))*betadotz(i) -
(nz-betaz(i))*betadoty(i));

denom{i} = (1-betax(i).*nx-betaz(i).*nz-betay(i).*ny).^2;

fourargx{i} = numx{i}./denom{i};
fourargy{i} = numy{i}./denom{i};
fourargz{i} = numz{i}./denom{i};
%
% End of Full Expression

% By Parts Expression
%
fourargx{i} =
(ny*betay(i)+nz*betaz(i)).*nx-(ny.^2+nz.^2)*betax(i);
fourargy{i} = (nx*betax(i)+nz*betaz(i)).*ny -
(nx.^2+nz.^2)*betay(i);
fourargz{i} = (nx*betax(i)+ny*betay(i)).*nz -
(nx.^2+ny.^2)*betaz(i);
%
% End of By Parts Expression

fourkern{i} =
exp(li*omega/omega0*(t(i)-nx*x(i)-ny*y(i)-nz*z(i)));

intbandx = intbandx + fourargx{i}.*fourkern{i};
intbandy = intbandy + fourargy{i}.*fourkern{i};
intbandz = intbandz + fourargz{i}.*fourkern{i};
end
intband = (intbandx*dt).^2 + (intbandy*dt).^2 + (intbandz*dt).^2;

```

```

intband = abs(intband).^2;
intband =
e_cg$^2/(4*pi^2*c_cg$)*intband*10^-7/(1.602*10^-19)*10^15; %
eV/(rad/fs)/sr

intband_tot = intband_tot + intband;

end
intband_tot = intband_tot*domega; % eV/sr

%% Plot Solution
figure('position',[1 1 1900 800]);

subplot(1,2,1);
surf(nx,nz,ny,intband_tot,'edgecolor','none');
set(gca,'ydir','reverse');
xlabel('$x$');
ylabel('$z$');
zlabel('$y$');

subplot(1,2,2)
imagesc(theta_lin*180/pi,phi_lin*180/pi,intband_tot);
xlabel('$\theta$ [$^\circ$]');
ylabel('$\phi$ [$^\circ$]');
set(gca,'ydir','normal','xdir','reverse');
cb=colorbar;
cb.Label.String = 'eV/sr';
xticks(0:45:180);
yticks(-180:45:180);

sgtitle('Radiated energy per steradian (400-700 nm), 10 cycles, infinite
plane wave');

for i=1:2
    subplot(1,2,i);
    colormap jet;
    daspect([1 1 1]);
    caxis([0 max(intband_tot,[],'all')]);
    set(gca,'fontsize',12);
end

```

Appendix D: MATLAB Code (Data Analysis)

D.1 Calibration using USAF Test Pattern (Experiment 3)

The script in this appendix opens four images of the USAF test pattern captured by the wedge imaging system in Experiment 3, extracts a horizontal and vertical lineout from a chosen element in each image, calculates element line edges based on the lineout intersection to a set of threshold values (see Fig. D.1 and Table D.1). From the edge values, the element line widths in units of pixels [px] are calculated by taking the difference between adjacent edges (see Table D.2). The line widths are converted to spatial calibration values in units of px per μm by using the standard line widths for the corresponding group and element in the USAF test pattern. For example, the values in Table D.2, are multiplied by the standard line width of 6.96 μm for Group 6 Element 2, and are averaged to obtain a final value of 7.3 px/ μm with a standard deviation of 0.3 px/ μm . A chart of standard values of line pairs/mm are given in Table D.3. For example, for Group 6 Element 2, the standard value is 71.8 line pairs per mm, which corresponds to an element line width of $1/71.8/2 \times 10^3 = 6.96 \mu\text{m}$.

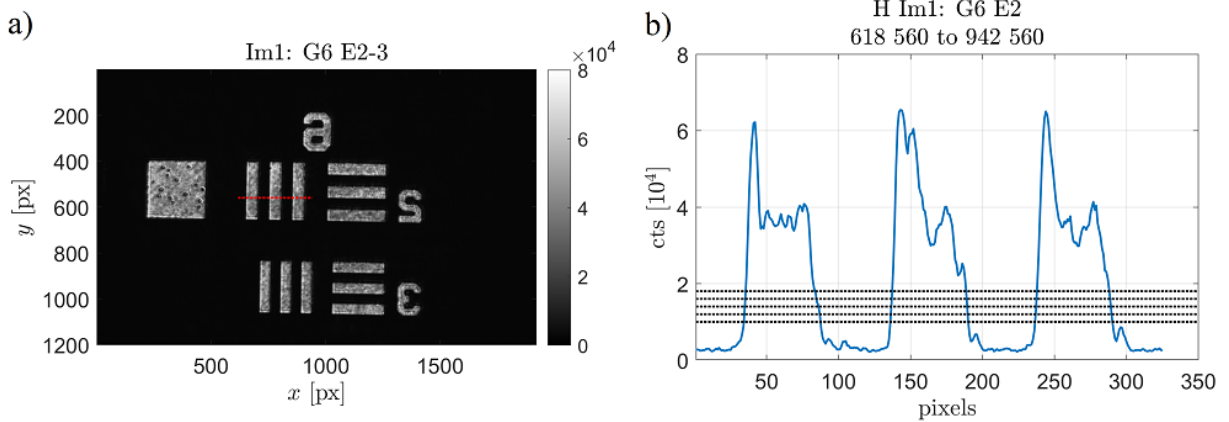


Figure D.1: Plots used to illustrate an example of the spatial calibration using a USAF test pattern. Shown are a) an image of the USAF test pattern, with the red dotted line indicating the lineout sample and b) the image lineout values in units of counts [cts], with the horizontal dotted lines indicating various thresholds used for calculating element line edges.

Table D.1: Positions of the element line edges determined from finding the intersection between the lineout and threshold values for Group 6 Element 2. See Fig. D.1 for the corresponding image. The edges are labeled x_i with i from 1 to 6.

	Threshold [cts]				
	10^5	1.2×10^5	1.4×10^5	1.6×10^5	1.8×10^5
x_1 [px]	34	34	34	35	35
x_2 [px]	87	86	86	84	83
x_3 [px]	136	136	136	137	137
x_4 [px]	190	189	189	189	188
x_5 [px]	236	236	237	237	237
x_6 [px]	290	289	289	288	288

Table D.2: Values of element line widths determined from taking the difference between adjacent edges. The widths are defined as $\Delta x_{j,i} = x_j - x_i$ with the corresponding values given in Table D.1.

	Threshold [cts]				
	10^5	1.2×10^5	1.4×10^5	1.6×10^5	1.8×10^5
$\Delta x_{2,1}$ [px]	53	52	52	49	48
$\Delta x_{3,2}$ [px]	49	50	50	53	54
$\Delta x_{4,3}$ [px]	54	53	53	52	51
$\Delta x_{5,4}$ [px]	46	47	48	48	49
$\Delta x_{6,5}$ [px]	54	53	52	51	51

Table D.3: Chart of line pairs per mm for the corresponding Group and Element in a 1951 USAF resolution test target. The width of a single line may be determined by dividing the inverse of these values by 2. The values were obtained from [108]. The Group and Element combinations used in Experiment 3 are highlighted in bold, while the Group and Element used in the example in Fig. D.1 and Tables D.1 and D.2 is highlighted in red.

Element	Group Number									
	-2	-1	0	1	2	3	4	5	6	7
1	0.250	0.500	1.00	2.00	4.00	8.00	16.00	32.00	64.00	128.00
2	0.280	0.561	1.12	2.24	4.49	8.98	17.95	36.0	71.8	144.0
3	0.315	0.630	1.26	2.52	5.04	10.10	20.16	40.3	80.6	161.0
4	0.353	0.707	1.41	2.83	5.66	11.30	22.62	45.3	90.5	181.0
5	0.397	0.793	1.59	3.17	6.35	12.70	25.39	50.8	102.0	203.0
6	0.445	0.891	1.78	3.56	7.13	14.30	28.50	57.0	114.0	228.0

```
% Written and tested in MATLAB version R2022a
clear;
% Load and organize image files
path = './wedge_calibration_USAF_20220401/';

file{1} = 'group6_2_3.tif';
file{2} = 'group6_5_6.tif';
file{3} = 'group7_element_1_2_3_4.tif';
file{4} = 'group7_element_3_4_5_6.tif';

pattern_element = {'Im1: G6 E2-3', 'Im2: G6 E5-6', 'Im3: G7 E1-4', 'Im4: G7 E3-6'};
lineout_element = {'Im1: G6 E2', 'Im2: G6 E6', 'Im3: G7 E1', 'Im4: G7 E6'};
pattern_linewidth = [6.96, 4.38, 3.91, 2.19];

for i=1:4
    image{i} = double(imread(strcat(path,file{i})));
end

% Define lineout coordinates
H{1} = [618,560; 942,560];
H{2} = [937,347; 1156,347];
H{3} = [748,350; 946,350];
H{4} = [670,688; 827,688];

V{1} = [1147,360; 1147,703];
V{2} = [1276,269; 1276,502];
V{3} = [631,233; 631,456];
V{4} = [618,599; 618,749];

% Assign Lineouts
for i=1:4
    lineoutH{i} = image{i}(H{i}(1,2):H{i}(2,2),H{i}(1,1):H{i}(2,1));
    lineoutV{i} = image{i}(V{i}(1,2):V{i}(2,2),V{i}(1,1):V{i}(2,1));
end
```

```

% Determine Edges and Linewidths vs. Threshold
thresholdlist = [1:0.2:1.8]*10^4;
for j=1:length(thresholdlist)
    for i=1:4
        edgesH{i,j}=find(diff(sign(lineoutH{i}-thresholdlist(j))));
        edgesV{i,j}=find(diff(sign(lineoutV{i}-thresholdlist(j))));
        dedgesH{i,j} = diff(edgesH{i,j});
        dedgesV{i,j} = diff(edgesV{i,j}');
    end
end

% Aggregate Data and Calculate Statistics
dedgesH_E = {[[],[],[],[],[]]};
dedgesV_E = {[[],[],[],[],[]]};
calibH_all = [];
calibV_all = [];
for i=1:4
    for j=1:length(thresholdlist)
        dedgesH_E{i} = [dedgesH_E{i}, dedgesH{i,j}];
        dedgesV_E{i} = [dedgesV_E{i}, dedgesV{i,j}];
    end
    calib_H(i) = mean(dedgesH_E{i})/pattern_linewidth(i); % px / mm
    calib_V(i) = mean(dedgesV_E{i})/pattern_linewidth(i); % px / mm
    calib_H_std(i) = std(dedgesH_E{i})/pattern_linewidth(i); % px / mm
    calib_V_std(i) = std(dedgesV_E{i})/pattern_linewidth(i); % px / mm

    calibH_all = [calibH_all, dedgesH_E{i}/pattern_linewidth(i)];
    calibV_all = [calibV_all, dedgesH_E{i}/pattern_linewidth(i)];
end
calib_H_tot = mean(calibH_all);
calib_V_tot = mean(calibV_all);
calib_H_tot_std = std(calibH_all);
calib_V_tot_std = std(calibV_all);

% Organize statistics into table
Tcalib = table(lineout_element', calib_H', calib_H_std', calib_V',
    calib_V_std',...
    'variablenames', {'Lineout Element', 'Horizontal', 'H Std. Dev.',
    'Vertical', 'V Std. Dev.'});
Tcalib = [Tcalib;{'Overall', calib_H_tot, calib_H_tot_std, calib_V_tot,
    calib_V_tot_std}];

```

Appendix E: MATLAB Code (Numerical Calculations) from Chapter 7

Note: When copying and pasting code blocks onto MATLAB, the document compiler may add additional newline characters where a full line is broken in order to fit the document. These characters would need to be removed manually in the MATLAB editor. Furthermore, the caret character ^ produced by the document compiler may not be recognized by MATLAB, and would require manual replacement in the editor.

E.1 Electron Motion under Lorentz Force by a Focused Pulse

This script computes the electron motion via the Lorentz force for a linearly polarized electromagnetic wave defined having a Gaussian beam spatial profile focused to $w_0 = 20 \mu\text{m}$, as well as a Gaussian temporal profile with a 30 fs intensity FWHM (Eq. 7.11 and 7.12). This is done for a set of electrons are born at various positions along \hat{x} , the polarization axis in the focal plane. The time in which the electron is born can be changed through the assignment of variable `ti` in the code.

```
clear;
set(0,'defaulttextinterpreter','latex');

c = 3*10^8;

lambda0 = 0.8; % um
k = 2*pi/lambda0; % 1/um
w0 = 20; % um
zR = pi*w0^2/lambda0; % um
z0 = k*zR; % Rayleigh Length in normalized units

omega0 = 2*pi*c/(lambda0*10^-6); % rad/s

t_fwhm = 30; % fs
tau = t_fwhm/sqrt(2*log(2))*2*pi*3*10^8/(800*10^-9)*10^-15;

q = 10;
```

```

Np = 21; % Number of particles

%x0max = k*w0*2;

x0max = 300;
x0list = linspace(0,x0max,Np);
z0list = zeros(1,Np);

alist = q*exp(- x0list.^2./(k*w0)^2);

for ei = 1:Np
    x0 = x0list(ei);
    z0 = z0list(ei);
    px0 = 0;
    pz0 = 0;
    delta0 = 0;

    y0(1) = x0;
    y0(2) = z0;
    y0(3) = px0;
    y0(4) = pz0;
    %y0(5) = 0;
    %y0(6) = 0;
    Nt = 16000;
    tf = 2*pi*25*(1+q^2/4);
    ti = 0; % Determines when electrons are aborn
    tspan1 = linspace(ti,tf,Nt);

    [t,y] = ode89(@(t1,y1) RTS_ODE_focused_gaussian_2D(t1,y1,q,delta0),
    tspan1, y0);

    clear('soln');
    for i=1:length(t)
        soln(i,:) =
            RTS_ODE_focused_gaussian_2D(t(i),y(i,:),q,delta0);
    end
    tp{ei} = t;
    x{ei} = y(:,1);
    z{ei} = y(:,2);
    px{ei} = y(:,3);
    pz{ei} = y(:,4);
    vx{ei} = soln(:,1);
    vz{ei} = soln(:,2);

    gamma{ei} = sqrt(1+px{ei}.^2+pz{ei}.^2);
    theta_s{ei} = atan(px{ei}(length(t))./pz{ei}(length(t)));
end

%%
figure;

hold on;
linspace(0,1,Np)';
for ei=1:Np

```

```

plot(z{ei},x{ei}, 'color',clist(ei,:),...
    'displayname',[ '|x_0|=' ,num2str(abs(x0list(ei)/k),'%1.0f'), ' um']);
daspect([1 1 1]);
end
legend('location', 'eastoutside');
xlabel('$kz$');
ylabel('$kx$');
title({{['$a_0=',num2str(q),'$', '$w_0=',num2str(w0),'$ um,'
$z_R=',num2str(zR,'%1.1f'),'$ um'],...
    ['$\Delta t_{fwhm}=',num2str(t_fwhm),'$ fs, $\omega_0
    $_i=',num2str(ti,'%1.1f'),'$ $\omega_0
    $_f=',num2str(tf,'%1.1f'),'$']});
set(gca, 'fontsize',15);

```

The previous script requires the function RTS_ODE_focused_gaussian_2D to be defined as follows:

```

function dydt = RTS_ODE_focused_gaussian_2D(t,y,q,delta0)
    % y variable element definitions
    %y(1) = x; dydt(1) = dx/dt
    %y(2) = z; dydt(2) = dz/dt
    %y(3) = px; dydt(3) = dpx/dt
    %y(4) = pz; dydt(4) = dpz/dt

    dydt = zeros(4,1);

    % Spatial Focusing Parameters
    lambda0 = 0.8; % um
    k = 2*pi/lambda0; % 1/um
    w0 = 20; % um
    zR = pi*w0^2/lambda0; % um
    z0 = k*zR; % Rayleigh Length in normalized units

    % Temporal Pulse Parameters
    t_fwhm = 30; %fs
    tau = t_fwhm/sqrt(2*log(2))*2*pi*3*10^8/(800*10^-9)*10^-15;

    % Intermediate Values
    gamma = sqrt(1+y(3)^2+y(4)^2);
    Rinv = y(2)/(y(2)^2 + z0^2); % 1 / Radius of Curvature (normalized
    % units)
    w = k*w0*sqrt(1+(y(2)/z0)^2); % Beam radius (normalized units)
    phi_G = atan(y(2)/z0); % Guoy phase

    % Field Components
    carrier = cos(y(2)) - t + delta0 + y(1)^2/2*Rinv - phi_G;
    envelope_spat = exp(-y(1)^2./w^2)/(w/k/w0);
    envelope_temp = exp(-(t-y(2)).^2/tau^2);
    Ex = q*carrier*envelope_spat*envelope_temp;
    By = q*carrier*envelope_spat*envelope_temp;

```

```

% Lorentz integrator
dydt(1) = y(3)/sqrt(1+y(3)^2+y(4)^2); % dx/dt
dydt(2) = y(4)/sqrt(1+y(3)^2+y(4)^2); % dz/dt
dydt(3) = y(4)/sqrt(1+y(3)^2+y(4)^2)*By - Ex; % dpx/dt
dydt(4) = -y(3)/sqrt(1+y(3)^2+y(4)^2)*By; % dpz/dt

end

```

E.2 Volume-Weight Distribution vs. a for a Focused Gaussian Beam (peak

$$= a_0)$$

This script calculates the weight distribution at each value of the spatially dependent normalized vector potential, a , based on the volume contained within an interval Δa centered at a (Eq. 7.19), for a defined in space to be a focused Gaussian beam with peak value of a_0 . This calculated multiple times, each for a different values of a_0 .

```

clear;
set(0,'defaulttextinterpreter','latex');
q0list = [1 2 3 4 5 6 7 8 9 10];

Nq0 = length(q0list);

qcut = 0.01;
Nz = 64;
dq1 = 10^-5;

qlist = {};
dV = {};
for q0i=1:length(q0list)
    q0 = q0list(q0i);

    Nq(q0i) = ceil((q0-qcut)/dq1);
    qlist{q0i} = linspace(qcut,q0,Nq(q0i));
    dq(q0i) = qlist{q0i}(2) - qlist{q0i}(1);

    disp(['q0i=',num2str(q0i), '/', num2str(Nq0), ',',
        'Nq=', num2str(Nq(q0i)), ', dq=', num2str(dq(q0i))])
    for qi=1:length(qlist{q0i})
        q = qlist{q0i}(qi);

        zmax = sqrt((q0/q)^2-1);
        z = linspace(-zmax,zmax,Nz);
    end
end

```

```

dz = z(2)-z(1);
rho{qi} = sqrt(-(1+z.^2).*log(q/q0*sqrt(1+z.^2)));
V(qi) = pi*sum(rho{qi}.^2*dz,'omitnan');
if qi > 1
    dV{q0i}(qi-1) = abs(V(qi)-V(qi-1));
end
end

Vmax{q0i} = V(1);
%dq = qlist(2)-qlist(1);
%dV = dV/sum(dV*dq)*Vmax;
dV{q0i} = dV{q0i}/dq(q0i);
end

for q0i=1:Nq0
    q0 = qlist(q0i);
    % Interpolation over 100 intensities
    qint{q0i} = linspace(qcut,q0,100);
    dVint{q0i} = interp1(qlist{q0i}(1:length(qlist{q0i})-1),...
        dV{q0i},qint{q0i}, 'cubic');
end

```

E.3 Angular Distribution Convolved with Gaussian Beam

The script in E.2 is required to be run prior to running this script. This script calculates the RTS angular distribution from the analytical expressions derived by Sarachik and Schappert (Eq. 2.103) for the second harmonic convolved with the Gaussian beam distribution using Eq. 7.22 and 7.23.

```

e = 1.602*10^-19;
c = 3*10^8;
lambda0 = 800*10^-9; % m
omega0 = 2*pi*c/lambda0; % rad/s

N = 101;

theta_lin = linspace(0,pi,N);
phi_lin = linspace(-pi, pi,N);
[theta,phi] = meshgrid(theta_lin, phi_lin);
cosalpha = sin(theta).*cos(phi);

dNdO_tot = zeros(N);
dNdO_band = zeros(N);

Nq0 = length(qlist);

```

```

for q0i=1:Nq0
    dNdO_band_tot{q0i} = zeros(N);
    dNdO_band_grand_tot{q0i} = zeros(N);
    for n=1:68
        dNdO_band_harm{q0i,n} = zeros(N);
    end
end

parfor q0i = 1:Nq0
    q0calc = q0list(q0i);
    qlist_lin_calc = qint{q0i};
    pdf_lin = dvint{q0i};
    n = 2;
    for qi = 1:(length(qlist_lin_calc)-1)
        disp(strcat('q0i=',num2str(q0i),', qi=',num2str(qi)));
        q = qlist_lin_calc(qi);
        dist = RTS_sarachik(n,q,omega0,'dNdO',N);
        dNdO_band = dist*pdf_lin(qi);
        dNdO_band_tot{q0i} = dNdO_band_tot{q0i} + dNdO_band;
    end
    %dNdO_band_harm{q0i,n} = dNdO_band_tot{q0i};
    dNdO_band_grand_tot{q0i} = dNdO_band_grand_tot{q0i} +
    dNdO_band_tot{q0i};
end

%% Plot Distribution

nx = sin(theta).*cos(phi);
ny = sin(theta).*sin(phi);
nz = cos(theta);

figure;
for q0i = 1:6
    subplot(2,6,2*q0i-1);
    surf(nx,nz,ny, ...
        dNdO_band_grand_tot{q0i}/max(dNdO_band_grand_tot{q0i},...
        [],'all'),'edgecolor','none');
    title(['$a_0$',num2str(q0list(q0i)),'$']);
    xlabel('$x$');
    ylabel('$z$');
    zlabel('$y$');
    set(gca,'ydir','reverse');

    subplot(2,6,2*q0i);
    imagesc(theta_lin*180/pi,phi_lin*180/pi, ...
        dNdO_band_grand_tot{q0i}/max(dNdO_band_grand_tot{q0i},...
        [],'all'));
    set(gca,'xdir','reverse','ydir','normal');
    xlabel('$\theta$ [$^\circ]$');
    ylabel('$\phi$ [$^\circ]$');
    xticks(0:45:180);
    yticks(-180:45:180);
    cb = colorbar;
    cb.Label.String = '$\Gamma/\Omega$ [norm.]';

```

```

end
colormap jet;

for i=1:12
    subplot(2,6,i);
    daspect([1 1 1]);
    set(gca,'fontsize',15);
end

sgtitle('RTS Radiation Pattern $(n=2)$ of Plane Wave Convolved over
Gaussian Spatial Distribution in Intensity');

```

The previous script calls the RTS_sarachik function defined below.

```

function [distout,theta_lin,phi_lin,theta,phi] =
RTS_sarachik(n,q,omega0,dist,N)
    %SARACHIK_RTS
    % Calculates angular distribution in an NxN theta-phi grid for a
    % given
    % harmonic, n, normalized vector potential, q, and incident laser
    % angular
    % frequency, omega0 [rad/s].
    % Options for distribution type (dist) are dPdO, dNdO, and
    % dNdthetadphi
    % Option for a wavelength band [nm]

    % Constants
    e = 1.602*10^-19;
    c = 3*10^8;

    if nargin <= 4
        N = 101; % Default: 101x101
        if nargin <= 3
            dist = 'dNdO'; % (Default: dNdO)
            if nargin <= 2
                lambda0 = 800*10^-9; % m
                omega0 = 2*pi*c/lambda0; % rad/s
                % (Default 375*2*pi Trad/s)
            end
        end
    end
end

% Grid Setup
theta_lin = linspace(0,pi,N);
phi_lin = linspace(-pi, pi,N);
[theta,phi] = meshgrid(theta_lin, phi_lin);
cosalpha = sin(theta).*cos(phi);

% Calculations
A = e^2*omega0^2*(1+(1/2)*q^2)*q^2/(8*pi*c);

```

```

M = (1+1/2*q^2*sin(theta/2).^2);

F1 = zeros(size(theta));
F2 = zeros(size(theta));

X = (1/4)*n*q^2*sin(theta/2).^2./M;
Y = q*n*cosalpha./M;

numax = max_besselnu_sarachik(n);
l_max = numax;
%l_max = 15; % Works for lower harmonics (need to determine exact boundary
l_list = -l_max:l_max;
for j=1:length(l_list)
    l = l_list(j);
    F1 = F1 +
        besselj(l,X).* (besselj(2*l+n+1,Y)+besselj(2*l+n-1,Y));
    F2 = F2 +
        besselj(l,X).* (besselj(2*l+n+2,Y)+besselj(2*l+n-2,Y));
end

T1 = (1 - (1+1/2*q^2)*cosalpha.^2./M.^2).*F1.^2;
T2 = -(1/2)*q*cosalpha.* (cos(theta)-(1/2)*q^2*sin(theta/2).^2)./...
    M.^2.*F1.*F2;
T3 = (1/16)*q^2*sin(theta).^2./M.^2.*F2.^2;

dPdO_L = A.* (n^2./M.^2).*n^2./M.^4.* (T1 + T2 + T3);
dNdO = dPdO_L.*M;
paredes = dNdO.*sin(theta);

omega_RTS = n*omega0./ (1+1/2*q^2*sin(theta/2).^2); % rad/s
lambda_RTS = 2*pi*c./omega_RTS*10^9; % nm
end

```

The function RTS_sarachik calls the function max_besselnu_sarachik defined below. This function determines where to truncate the Bessel function summation series.

```

function numax = max_besselnu_sarachik(nmax)
    %MAX_BESSELNU_SARACHIK Summary of this function goes here
    % Determines max Bessel function index for truncation of
    % infinite
    % series of Bessel functions
    nmax_list = [11,26,41,60,76];
    numax_list = [25,50,75,100,125];
    if nmax <= 11
        numax = 25;
    else
        numax = ceil(interp1(nmax_list,numax_list,nmax));
    end
end

```

Appendix F: Gas Nozzle Simulations

F.1 Gas Nozzle Simulations for a 1 mm Orifice

In this appendix, we describe simulations used to estimate the pressure of gas released from a nozzle as a function of distance from the nozzle. The simulation is based on kinetic theory, assumes collisionless particles for simplicity, and a species of molecular nitrogen. The collisionless assumption would be valid for low pressures ($\lesssim 10^{-2}$ mbar for nitrogen) where the mean free path, l_p , is larger than the linear dimension of length scales considered (in our case, on the order of ~ 1 to 10 cm) [109]. One may argue that at these lower pressures, conservation of momentum implies that the macroscopic results of a collisionless system is similar to those of a system with collisions. At higher pressures ($\gtrsim 10^{-1}$ mbar for nitrogen), the particles collide frequently, leading to collective motion, so that the kinetic theory breaks down. At these higher pressures, our model therefore serves only as a rough approximation of the gas density. Table F.1 shows the molecular density, average interparticle spacing, and mean free path for nitrogen over 9 decades of gas pressures from atmosphere to the typical background pressures in vacuum encountered in experiment. The average interparticle spacing is given by:

$$\overline{\Delta r} \equiv \frac{1}{\rho_{mol}^{1/3}} \quad (\text{F.1})$$

and can be used to estimate the Coulomb potential experienced by electrons born from different atoms. At a pressure of 1 atm, $\overline{\Delta r} = 3.5$ nm, corresponding to a Coulomb field of $E_{coul} = 1.2 \times 10^8$ V/m, which is equivalent to a laser with an intensity of $I_{eq} = 3.8 \times 10^9$ W/cm², many

orders of magnitudes smaller than relativistic intensities. The mean free path, l_p , is the average distance a molecule travels before colliding with another molecule, and depends on the size of the molecule parameterized by diameter, d_{mol} , the thermal velocity, v_{th} , and the molecular density. It is given by:

$$l_p = \frac{1}{\sqrt{2}\rho_{mol}\pi d_{mol}^2} \quad (\text{F.2})$$

where $d_{mol} \approx 3 \times 10^{-8}$ cm for molecular nitrogen.

Table F.1: List of molecular densities, ρ_{mol} , at various gas pressures P_{gas} , assuming an ideal gas, along with the average interparticle spacing, $\bar{\Delta r} \equiv \rho_{mol}^{-1/3}$, and mean free path, l_p , calculated for molecular nitrogen.

P_{gas}	ρ_{mol} [1/cm ³]	$\bar{\Delta r}$ [cm]	l_p [cm]
1 atm (≈ 1 bar)	2.4×10^{19}	3.5×10^{-7}	1.0×10^{-5}
100 mbar	2.4×10^{18}	7.5×10^{-7}	1.0×10^{-4}
10 mbar	2.4×10^{17}	1.6×10^{-6}	1.0×10^{-3}
1 mbar	2.4×10^{16}	3.5×10^{-6}	1.0×10^{-2}
10^{-1} mbar	2.4×10^{15}	7.5×10^{-6}	1.0×10^{-1}
10^{-2} mbar	2.4×10^{14}	1.6×10^{-5}	1.0
10^{-3} mbar	2.4×10^{13}	3.5×10^{-5}	1.0×10
10^{-4} mbar	2.4×10^{12}	7.5×10^{-5}	1.0×10^2
10^{-5} mbar	2.4×10^{11}	1.6×10^{-4}	1.0×10^3

In our kinetic, collisionless model, we initialize a set of $N_p = 10^6$ particles with a uniform-random distribution inside a 20 mm by 20 mm by 20 mm cube, which acts as our reservoir. The initial velocities of these particles have a probability distribution in their Cartesian components, denoted as v_i , given by the Maxwell-Boltzmann law [110]:

$$P(v_i) \propto \exp\left(-\frac{v_i^2}{2v_{th}^2}\right) \quad (\text{F.3})$$

where

$$v_{th} = \sqrt{\frac{k_B T}{m}} \approx 297.6 \text{ m/s} \quad (\text{F.4})$$

is the thermal velocity and also the standard deviation of the distribution, $k_B = 1.38 \times 10^{-23} \text{ m}^2 \cdot \text{kg} \cdot \text{s}^{-2} \cdot \text{K}^{-1}$ is the Boltzmann constant, T is the gas temperature taken to be room temperature of 300 K, and m is the mass of the gas species, which for molecular nitrogen is 28 amu or $4.68 \times 10^{-26} \text{ kg}$. An example of the initial particle distributions in position and velocity are plotted in Fig. F.1.

We define a coordinate system such that the origin is at the center of the cube. A circular hole of diameter $d_{\text{hole}} = 1 \text{ mm}$ is placed on the center of one side of the cube, namely the side in plane defined by $y = 10 \text{ mm}$. The simulation calculates the position at each iteration based on the simple Euler's method over 300 time steps from 0 ms to 1 ms, with step sizes of 6.7 μs . No forces are applied to the particles other than at the boundaries of the cube. At the time step where a particle pass outside of the cube through a wall, its position is reflected about the wall and its velocity component normal to the wall is flipped. However, if the particle passes through the hole, this calculation is ignored, and the particle is flagged as "outside" of the cube so that for the rest of time the particle does not interact with the boundary. The step size of 6.7 μs was chosen to avoid having particles with velocities large enough such that the particle travels a distance larger than the dimension of the box over one time step, resulting in leakage and nonphysical behavior.

A particle count of 10^6 was chosen due to memory limitations of the computer (32 GB). However, a larger particle count would be preferable in order to have a better statistical sample outside of the cube as well as for consistency with the particle densities of the reservoir used in experiment $\sim 10^{13}$ to 10^{15} cm^{-3} . Under the simulation parameters used, the number of particles leaked outside after 1 ms is about 1 percent of the total. The simulation results are shown in Fig. F.2.

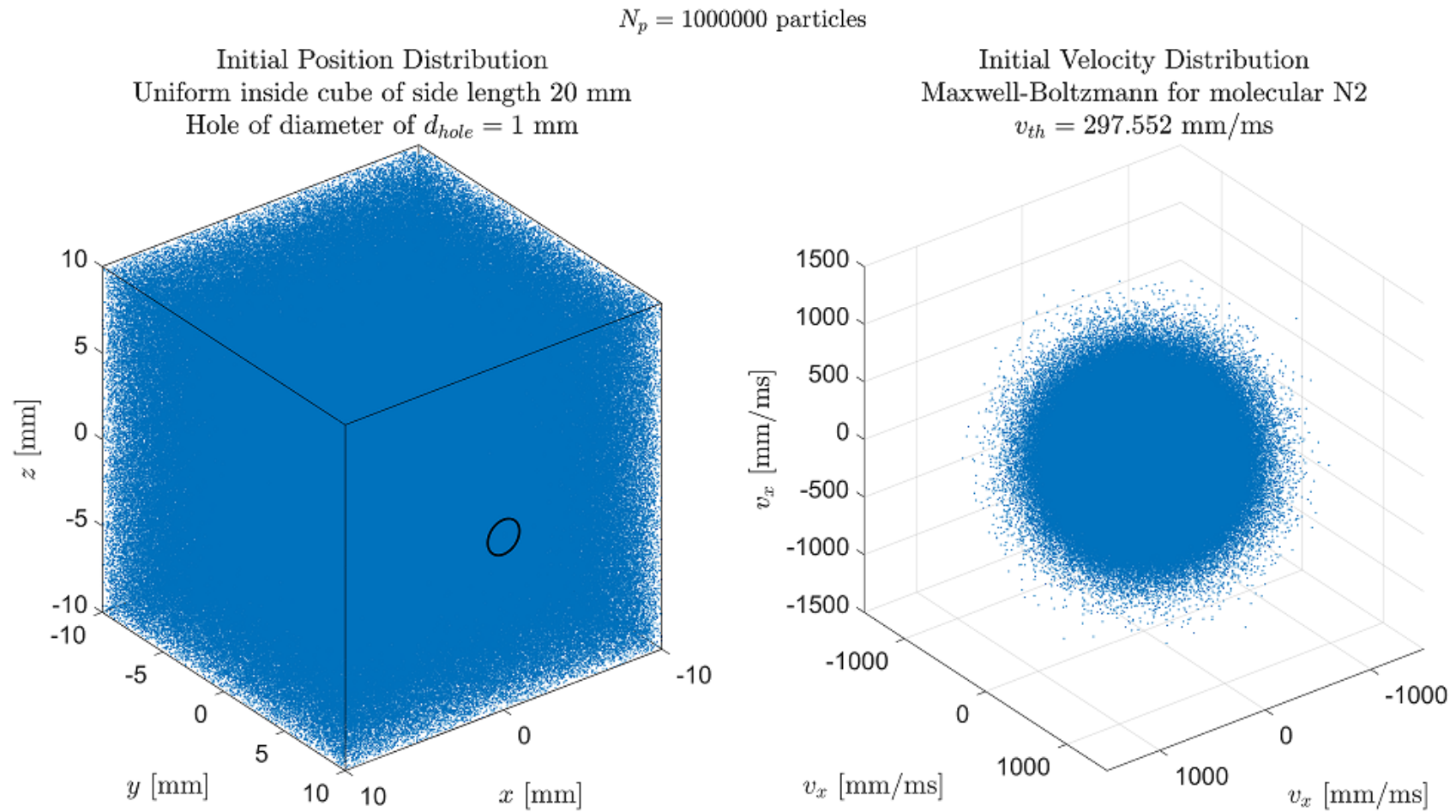


Figure F.1: Plots of the initial position and velocity distribution of particles used in the simulation. The particles are instantiated with a uniform spatial distribution inside of a 20 mm by 20 mm by 20 mm cube. The cube has a 1 mm diameter hole through which the particles can leak. The velocity distribution follows the Maxwell-Boltzmann distribution for molecular nitrogen at 300 K.

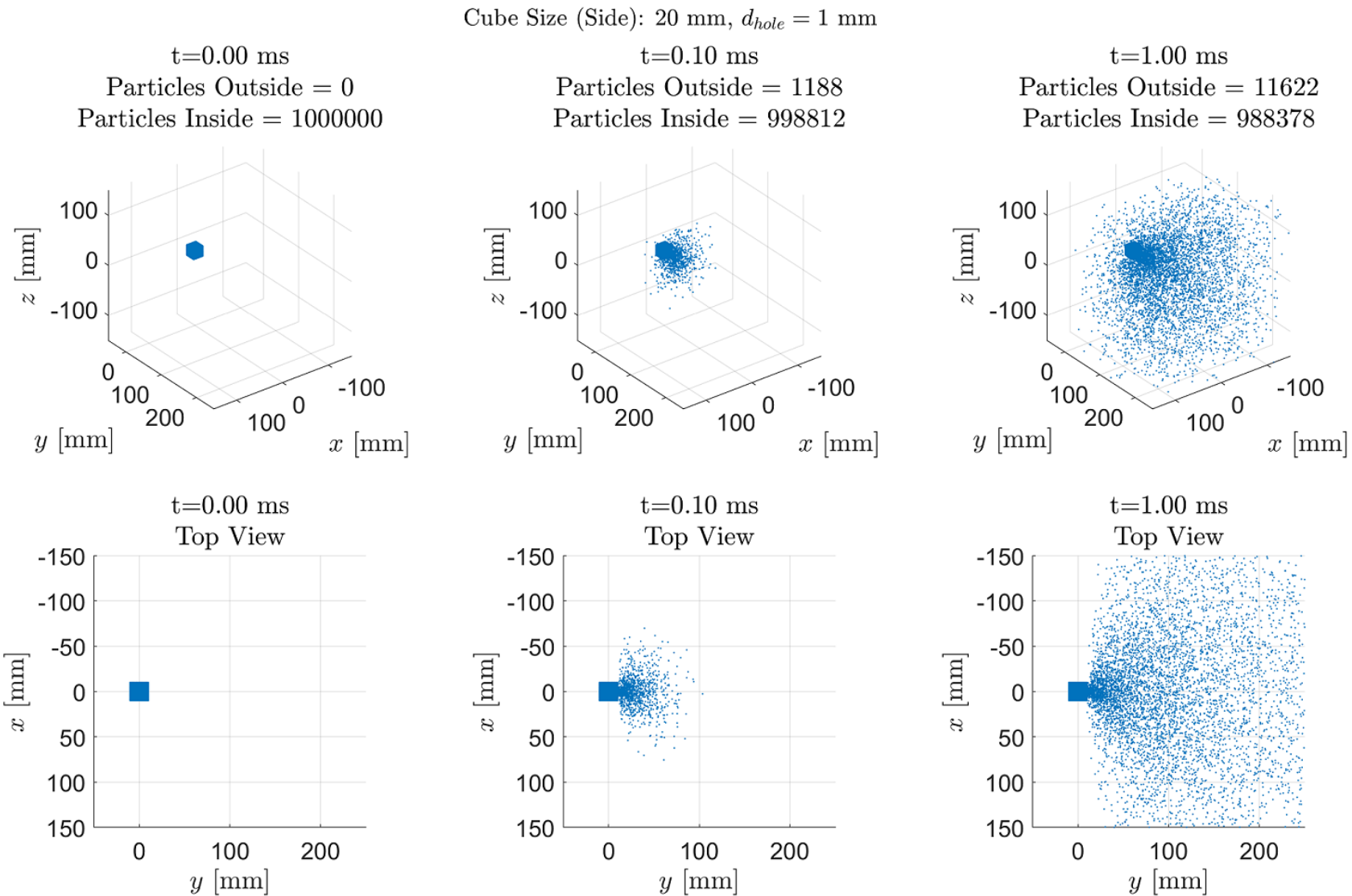


Figure F.2: Plots of the position distribution, shown in isometric as well as top view, of the simulated particles at various times. At $t = 0.10$ ms, the gas plume begins to fill the region up to about 100 mm. At $t = 1.00$ ms, the gas distribution up to 250 mm from the hole has reached a steady state.

In order to quantify the gas density from these simulations, we divide space into bins of size 10 mm by 10 mm by 10 mm and count the number of particles within. This is done in MATLAB using the `hist()` function for y position of particles inside the column defined by $|x| \leq 5$ mm and $|z| \leq 5$ mm, as well as using the `hist3()` function in a bivariate histogram in the y and x position for the layer defined by $|z| \leq 5$ mm. This is shown for select times are shown in Fig. F.3. In order to improve sampling, the simulation was run 10 times with different seeds, and the histogram data is averaged over these runs and shown in Fig. F.4.

The density distribution is expected to be continuous with the reservoir at the hole. At distances sufficiently far from the hole, such that the hole may be approximated as a point emitter, the density is expected to fall off proportional to the inverse square distance, $|\mathbf{R} - \mathbf{R}_0|$, from the hole, where \mathbf{R}_0 is the position of the hole center and \mathbf{R} is the position of the observation point. For an observation point along the y axis, this reduces to $R - R_0$. The density distribution can be described by a function of the form:

$$f(R) = \frac{c_1}{(R - R_0)^2 + c_2} \quad (\text{F.5})$$

for $R \geq R_0$, where c_1 and c_2 are parameters to be determined. In general, there would also be a factor of $\cos \theta$, where θ is the angle made from the normal axis to the hole, with the hole center as the point of origin, since a particle inside the box traveling towards the hole with direction θ sees a cross sectional area equal to $A \cos \theta$, where $A = \pi d_{hole}^2 / 4$ is the area of the hole. Here, we are interested in the density at $\theta = 0$, which also implies that $R = y$. When Eq. F.5 is used to fit the averaged histogram data, with c_1 , c_2 , and R_0 as fitting parameters, we determine the best fit

values (95% confidence half-interval) to be:

$$c_1 = 9000 \text{ (500)} \text{ mm}^2 \quad (\text{F.6})$$

$$c_2 = 0.10(0.05) \text{ mm}^2 \quad (\text{F.7})$$

$$R_0 = 9.8(0.3) \text{ mm} \quad (\text{F.8})$$

The ratio $c_1/c_2 = 90000$ corresponds approximately to the particle number per bin inside the cube (which should be closer to $1000000/8 = 125000$ given that bin volume is $1/8$ that of the cube) and R_0 is the fit-determined location of the hole along the y . In order for these parameters to be useful, we define the reservoir gas density by normalizing c_1/c_2 to the bin volume:

$$\rho_0 = \frac{c_1}{c_2 V_{bin}} \quad (\text{F.9})$$

where $V_{bin} = 10^3 \text{ mm}^3$ so that the gas density as a function of R becomes

$$\rho_{gas}(R) = \frac{f(R)}{V_{bin}} = \frac{\rho_0 c_2}{(R - R_0)^2 + c_2} \quad (\text{F.10})$$

where $V_{bin} = 10^3 \text{ mm}^3$. Equation F.10 can be written in a more physically intuitive form:

$$\rho_{gas}(\Delta R) = \frac{\rho_0}{\left(\frac{\Delta R}{R_f}\right)^2 + 1} \quad (\text{F.11})$$

where $\Delta R = R - R_0$ is the distance from the hole, and $R_f \equiv \sqrt{c_2} = 0.32 \text{ (0.08)} \text{ mm}$ is the parameter that controls the rate of density falloff with distance which we assumed to be independent of the reservoir density. One may recognize Eq. F.11 to be a Lorentzian function.

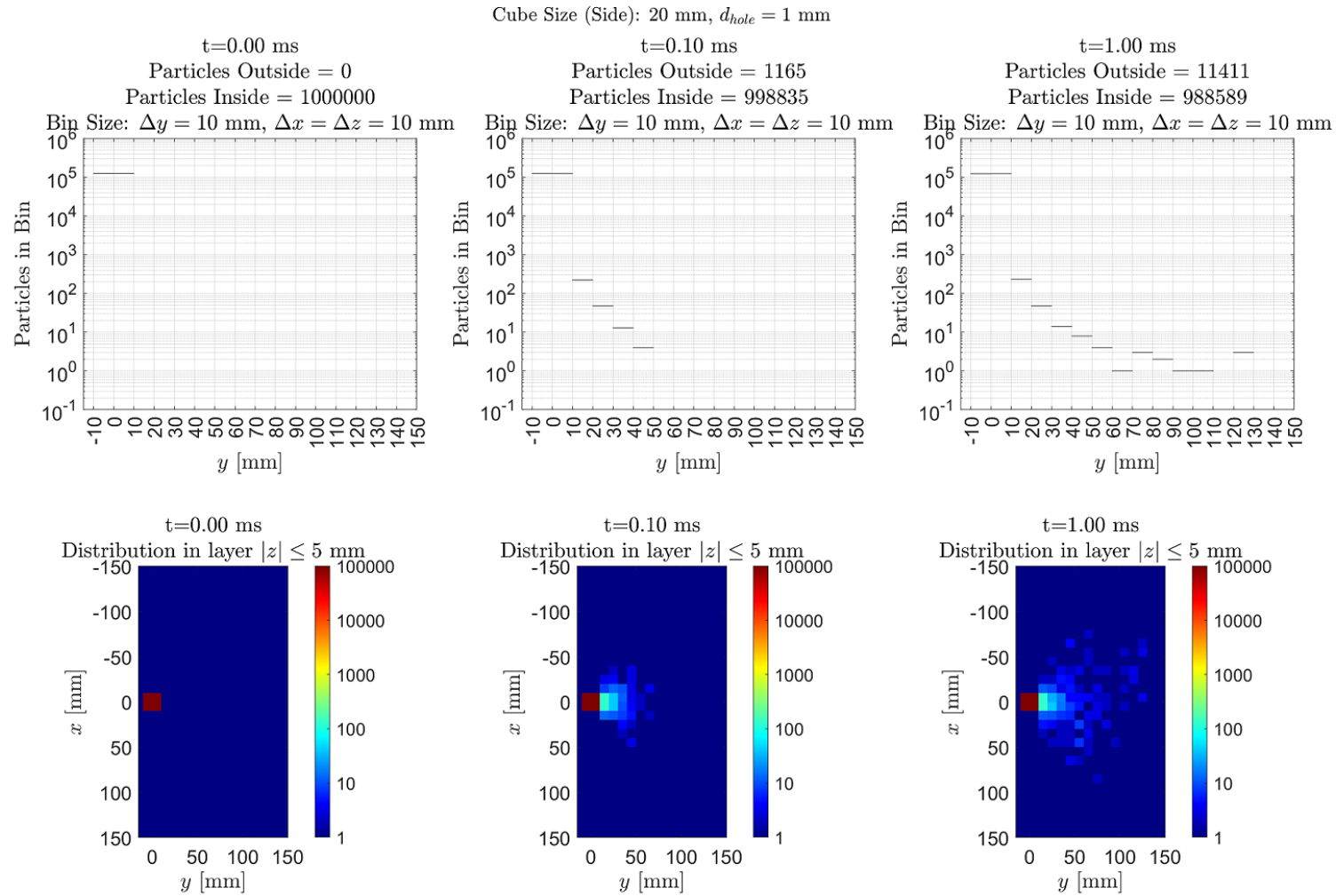


Figure F.3: Plots of single variable as well as two-variable histograms of simulated particle numbers. In the single variable histogram, the binning is conducted along a column with a 10 mm by 10 mm cross sectional area, and centered along the y axis. In the bivariate histograms the binning is done over a 10 mm thick layer centered on the x - y plane.

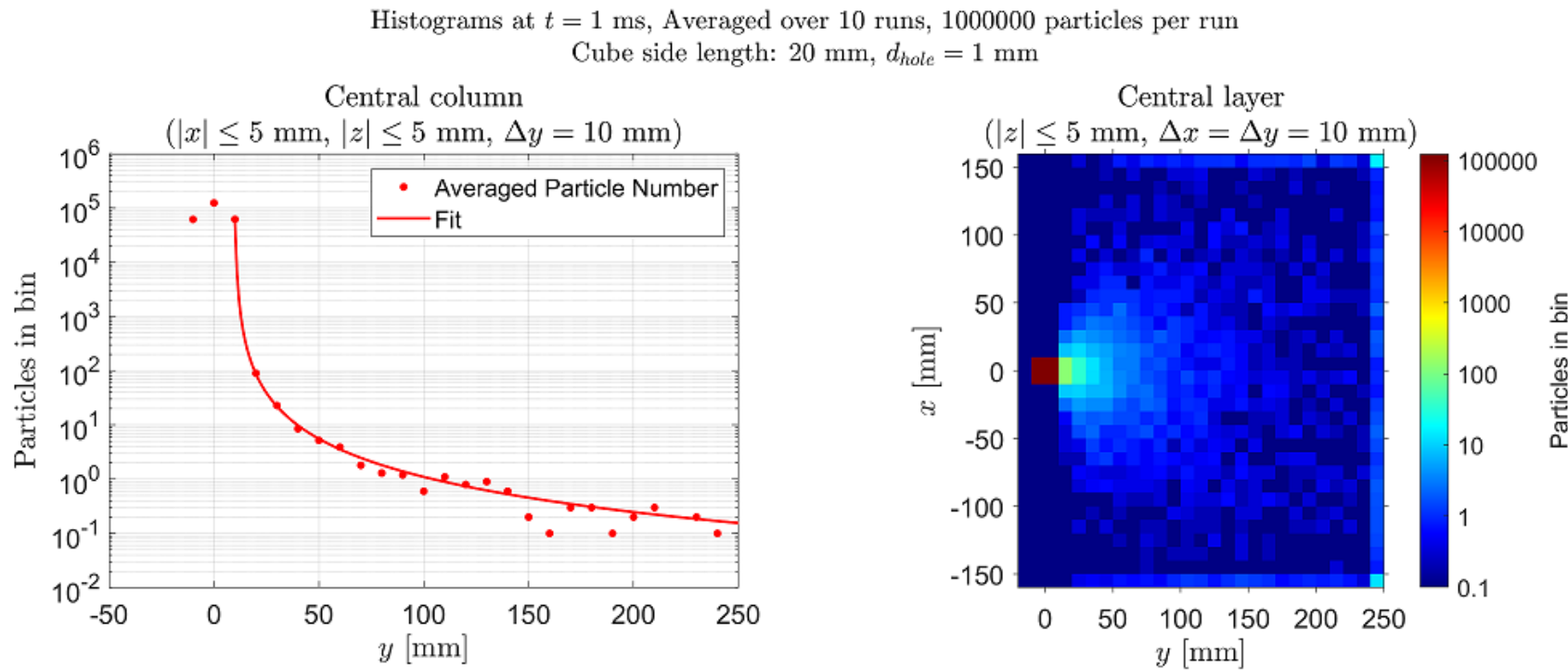


Figure F.4: Plots of histograms averaged over 10 simulation runs. In the single variable histogram, the data at $y \geq 10$ mm was fit with a Lorentzian with length scale $R_f \approx 0.32$ (see Eq. F.11). In the bivariate histogram, the bins at the edges include position values up to infinity, leading to artificial overcounting, and should be ignored.

Bibliography

- [1] ICUIL. Intense Laser Labs World Wide. <https://www.icuil.org/activities/laser-labs.html>.
- [2] NIST. Handbook of Basic Atomic Spectroscopic Data. <https://physics.nist.gov/PhysRefData/Handbook/periodictable.htm>.
- [3] C. Mendez, O. Varela, E. García, I. Hernández, J. Ajates, J. D. Pisonero, J. L. Sagredo, M. Olivar, and L. Roso. VEGA laser facility beamlines management for pump-probe experiments. page 151, October 2019.
- [4] M. Czerny and A. F. Turner. Über den Astigmatisus bei Spiegelspektrometern. *Zeitschrift für Physik*, 61(11):792–797, 1930.
- [5] A. L. Schawlow and C. H. Townes. Infrared and Optical Masers. *Physical Review*, 112(6), 1958.
- [6] T. H. Maiman. Stimulated Optical Radiation in Ruby. *Nature*, 187(4736):493–494, August 1960.
- [7] F. J. Mcclung and R. W. Hellwarth. Characteristics of giant optical pulsations from ruby. 33:828–831, 1962.
- [8] L. E. Hargrove, R. L. Fork, and M. A. Pollack. Locking of He–Ne laser modes induced by synchronous intracavity modulation. *Applied Physics Letters*, 5, July 1964.
- [9] National Academies of Sciences, Engineering, and Medicine. *Opportunities in Intense Ultrafast Lasers: Reaching for the Brightest Light*. The National Academies Press, Washington, DC, 2018.
- [10] G. A. Mourou and S. V. Bulanov. Optics in the relativistic regime. 78(2), 2006.
- [11] D. Strickland and G. Mourou. Compression of amplified chirped optical pulses. *Optics Communications*, 55(6):447–449, 1985.
- [12] E. Snitzer. Optical Maser Action of Nd+3 in a Barium Crown Glass. *Physical Review Letters*, 7(12):444–446, December 1961.
- [13] E. Snitzer. Glass Lasers. *Applied Optics*, 5(10):1487, October 1966.
- [14] P. Moulton. Ti-doped sapphire : laser may be the first of a series of broad- Gas-in-glass : new way tunable solid-state laser. *Optics News*, 8(9):9, 1982.
- [15] D. E. Spence, P. N. Kean, and W. Sibbett. 60-fsec pulse generation from a self-mode-locked ti:sapphire laser. *Opt. Lett.*, 16(1):42–44, January 1991.
- [16] J. T. Hunt and D. R. Speck. Present And Future Performance Of The Nova Laser System. *Optical Engineering*, 28(4), April 1989.
- [17] M. D. Perry, D. Pennington, B. C. Stuart, G. Tietbohl, J. A. Britten, C. Brown, S. Herman, B. Golick, M. Kartz, J. Miller, H. T. Powell, M. Vergino, and V. Yanovsky. Petawatt laser pulses. *Optics Letters*, 24(3):160, February 1999.

- [18] S.-W. Bahk, P. Rousseau, T. A. Planchon, V. Chvykov, G. Kalintchenko, A. Maksimchuk, G. A. Mourou, and V. Yanovsky. Generation and characterization of the highest laser intensities (10^{22} W/cm 2). *Optics Letters*, 29(24):2837, December 2004.
- [19] C. Hernandez-Gomez, D. Canny, I. O. Musgrave, and J. L. Collier. Picosecond contrast measurement of the Vulcan Petawatt facility. *Central Laser Facility Annual Report*, page 200, 2005.
- [20] B. C. Stuart, J. D. Bonlie, J. A. Britten, J. A. Caird, R. R. Cross, C. A. Ebbers, M. J. Eckart, A. C. Erlandson, W. A. Molander, A. Ng, P. K. Patel, and D. F. Price. The Titan laser at LLNL. In *2006 Conference on Lasers and Electro-Optics and 2006 Quantum Electronics and Laser Science Conference*, pages 1–2. IEEE, 2006.
- [21] V. Yanovsky, V. Chvykov, G. Kalinchenko, P. Rousseau, T. Planchon, T. Matsuoka, A. Maksimchuk, J. Nees, G. Cheriaux, G. Mourou, and K. Krushelnick. Ultra-high intensity- 300-TW laser at 0.1 Hz repetition rate. *Optics Express*, 16(3):2109, 2008.
- [22] U. Schramm, M. Bussmann, A. Irman, M. Siebold, K. Zeil, D. Albach, C. Bernert, S. Bock, F. Brack, J. Branco, J. Couperus, T. Cowan, A. Debus, C. Eisenmann, M. Garten, R. Gebhardt, S. Grams, U. Helbig, A. Huebl, T. Kluge, A. Köhler, J. Krämer, S. Kraft, F. Kroll, M. Kuntzsch, U. Lehnert, M. Loeser, J. Metzkes, P. Michel, L. Obst, R. Pausch, M. Rehwald, R. Sauerbrey, H. Schlenvoigt, K. Steiniger, and O. Zarini. First results with the novel petawatt laser acceleration facility in Dresden. *Journal of Physics: Conference Series*, 874:012028, July 2017.
- [23] J. W. Yoon, Y. G. Kim, I. W. Choi, J. H. Sung, H. W. Lee, S. K. Lee, and C. H. Nam. Realization of laser intensity over 10^{23} W/cm 2 . *Optica*, 8(5):630, 2021.
- [24] C. Bula, K. T. McDonald, E. J. Prebys, C. Bamber, S. Boege, T. Kotseroglou, A. C. Melissinos, D. D. Meyerhofer, W. Ragg, D. L. Burke, R. C. Field, G. Horton-Smith, A. C. Odian, J. E. Spencer, D. Walz, S. C. Berridge, W. M. Bugg, K. Shmakov, and A. W. Weidemann. Observation of Nonlinear Effects in Compton Scattering. *Physical Review Letters*, 76(17):3116–3119, April 1996.
- [25] D. L. Burke, R. C. Field, G. Horton-Smith, J. E. Spencer, D. Walz, S. C. Berridge, W. M. Bugg, K. Shmakov, A. W. Weidemann, C. Bula, K. T. McDonald, E. J. Prebys, C. Bamber, S. J. Boege, T. Koffas, T. Kotseroglou, A. C. Melissinos, D. D. Meyerhofer, D. A. Reis, and W. Ragg. Positron Production in Multiphoton Light-by-Light Scattering. *Physical Review Letters*, 79(9):1626–1629, September 1997.
- [26] C. Bamber, S. J. Boege, T. Koffas, T. Kotseroglou, A. C. Melissinos, D. D. Meyerhofer, D. A. Reis, W. Ragg, C. Bula, K. T. McDonald, E. J. Prebys, D. L. Burke, R. C. Field, G. Horton-Smith, J. E. Spencer, D. Walz, S. C. Berridge, W. M. Bugg, K. Shmakov, and A. W. Weidemann. Studies of nonlinear QED in collisions of 46.6 GeV electrons with intense laser pulses. *Physical Review D*, 60(9):092004, October 1999.
- [27] C. Radier, O. Chalus, M. Charbonneau, S. Thambirajah, G. Deschamps, S. David, J. Barbe, E. Etter, G. Matras, S. Ricaud, V. Leroux, C. Richard, F. Lureau, A. Baleanu, R. Banici,

- A. Gradinariu, C. Calderaru, C. Capiteanu, A. Naziru, B. Diaconescu, V. Iancu, R. Dabu, D. Ursescu, I. Dancus, C. A. Ur, K. A. Tanaka, and N. V. Zamfir. 10 PW peak power femtosecond laser pulses at ELI-NP. *High Power Laser Science and Engineering*, 10:1–5, 2022.
- [28] J. A. Bauer. Coulomb-corrected strong-field approximation for the two-electron atom. *Physical Review A - Atomic, Molecular, and Optical Physics*, 55(4):3261–3263, 1997.
 - [29] A. Gazibegovic-Busuladzic, D. B. Milošević, and W. Becker. High-energy above-threshold detachment from negative ions. *Physical Review A - Atomic, Molecular, and Optical Physics*, 70(5 B):1–14, 2004.
 - [30] J. M. Ngoko Djokap, S. X. Hu, L. B. Madsen, N. L. Manakov, A. V. Meremianin, and A. F. Starace. Electron Vortices in Photoionization by Circularly Polarized Attosecond Pulses. *Physical Review Letters*, 115(11):1–5, 2015.
 - [31] D. Pengel, S. Kerbstadt, D. Johannmeyer, L. Englert, T. Bayer, and M. Wollenhaupt. Electron Vortices in Femtosecond Multiphoton Ionization. 053003:1–5, February 2017.
 - [32] M. Lewenstein, P. Balcou, M. Y. Ivanov, A. L’Huillier, and P. B. Corkum. Theory of high-harmonic generation by low-frequency laser fields. *Physical Review A*, 49(3):2117–2132, March 1994.
 - [33] J.-Y. Zhang. Second-harmonic generation from regeneratively amplified femtosecond laser pulses in BBO and LBO crystals. 15(1):200–209, 1998.
 - [34] J. Koga, T. Z. Esirkepov, and S. V. Bulanov. Nonlinear Thomson scattering with strong radiation damping. *Journal of Plasma Physics*, 72(6):1315–1318, 2006.
 - [35] A. Di Piazza, K. Z. Hatsagortsyan, and C. H. Keitel. Strong signatures of radiation reaction below the radiation-dominated regime. *Physical Review Letters*, 102(25):1–4, 2009.
 - [36] P. Chen and T. Tajima. Testing Unruh Radiation with Ultraintense Lasers. *Physical Review Letters*, 83(2):256–259, July 1999.
 - [37] T. Heinzl, B. Liesfeld, K. Amthor, H. Schwoerer, R. Sauerbrey, and A. Wipf. On the observation of vacuum birefringence. *Optics Communications*, 267:317–321, 2006.
 - [38] D. Tommasini, D. Novoa, and L. Roso. Quantum Vacuum Polarization Searches with High Power Lasers Below the Pair Production Regime. In *Springer Series in Chemical Physics*, volume 86, pages 137–153. 2014.
 - [39] W. T. Hill, III and L. Roso. Probing the quantum vacuum with petawatt lasers. *Joint Physics: Conference Series*, 869:012015, 2017.
 - [40] H. Razmi, N. Baramzadeh, and H. Baramzadeh. Dispersive property of the quantum vacuum and the speed of light. *Modern Physics Letters A*, 34(4):1–6, 2019.

- [41] L. Roso, R. Lera, S. Ravichandran, A. Longman, C. Z. He, J. A. Pérez-Hernández, J. I. Apiñaniz, L. D. Smith, R. Fedosejevs, and W. T. Hill. Towards a direct measurement of the quantum-vacuum Lagrangian coupling coefficients using two counterpropagating super-intense laser pulses. *New Journal of Physics*, 24(2), 2022.
- [42] S. W. Hawking. Particle creation by black holes. *Communications In Mathematical Physics*, 43(3):199–220, August 1975.
- [43] W. G. Unruh. Notes on black-hole evaporation. *Physical Review D*, 14(4):870–892, August 1976.
- [44] W. Heisenberg and H. Euler. Folgerungen aus der Diracschen Theorie des Positrons. *Zeitschrift für Physik*, 98(11-12):714–732, 1936.
- [45] W. Heisenberg and H. Euler. Consequences of Dirac Theory of the Positron (Translated). May 2006. <http://arxiv.org/abs/physics/0605038>.
- [46] A. Di Piazza, L. Willingale, and J. D. Zuegel. Multi-Petawatt Physics Prioritization (MP3) Workshop Report. 2022.
- [47] R. Falcone, F. Albert, F. Beg, S. Glenzer, T. Ditmire, T. Spinka, and J. Zuegel. Workshop Report: Brightest Light Initiative. 2020.
- [48] G. A. Mourou, C. L. Labaune, M. Dunne, N. Naumova, and V. T. Tikhonchuk. Relativistic laser-matter interaction: From attosecond pulse generation to fast ignition. *Plasma Physics and Controlled Fusion*, 49(12 B), 2007.
- [49] C. N. Danson, C. Haefner, J. Bromage, T. Butcher, J. C. F. Chanteloup, E. A. Chowdhury, A. Galvanauskas, L. A. Gizzi, J. Hein, D. I. Hillier, N. W. Hopps, Y. Kato, E. A. Khazanov, R. Kodama, G. Korn, R. Li, Y. Li, J. Limpert, J. Ma, C. H. Nam, D. Neely, D. Papadopoulos, R. R. Penman, L. Qian, J. J. Rocca, A. A. Shaykin, C. W. Siders, C. Spindloe, S. Szatmári, R. M. Trines, J. Zhu, P. Zhu, and J. D. Zuegel. Petawatt and exawatt class lasers worldwide. *High Power Laser Science and Engineering*, 7, 2019.
- [50] D. D. Meyerhofer, S. W. Bahk, J. Bromage, D. H. Froula, D. Haberberger, S. X. Hu, B. E. Kruschwitz, R. L. McCrory, J. F. Myatt, P. M. Nilson, J. B. Oliver, C. Stoeckl, W. Theobald, L. J. Waxer, and J. D. Zuegel. OMEGA EP OPAL: A Path to a 100-PW Laser System. In *APS Division of Plasma Physics Meeting Abstracts*, volume 2014 of *APS Meeting Abstracts*, page UO5.006, October 2014.
- [51] J. Bromage, S.-W. Bahk, I. A. Begishev, C. Dorrer, M. J. Guardalben, B. N. Hoffman, J. B. Oliver, R. G. Roides, E. M. Schiesser, M. J. Shoup III, M. Spilatro, B. Webb, D. Weiner, and J. D. Zuegel. Technology development for ultraintense all-OPCPA systems. *High Power Laser Science and Engineering*, 7:e4, February 2019.
- [52] G. Pariente, V. Gallet, A. Borot, O. Gobert, and F. Quéré. Space-time characterization of ultra-intense femtosecond laser beams. *Nature Photonics*, 10(8):547–553, 2016.

- [53] A. Jeandet, A. Borot, K. Nakamura, S. W. Jolly, and A. J. Gonsalves. Spatio-temporal structure of a petawatt femtosecond laser beam. 2019.
- [54] Vachaspati. Harmonics in the Scattering of Light by Free Electrons. *Physical Review*, 128(2):664, 1962.
- [55] E. E. Sarachik and G. T. Schappert. Classical theory of the scattering of intense laser radiation by free electrons. *Physical Review D*, 1:2738–2752, 1970.
- [56] J. Gao. Thomson scattering from ultrashort and ultraintense laser pulses. *Physical Review Letters*, 93(24):18–21, 2004.
- [57] J. Gao. Laser intensity measurement by thomson scattering. *Applied Physics Letters*, 88(9):091105, 2006.
- [58] A. L. Galkin, V. V. Korobkin, M. Y. Romanovsky, and O. B. Shiryaev. Relativistic motion and radiation of an electron in the field of an intense laser pulse Relativistic motion and radiation of an electron in the eeld of an intense laser pulse. 2007.
- [59] A. Paredes, D. Novoa, and D. Tommasini. Measuring extreme vacuum pressure with ultraintense lasers. *Physical Review Letters*, 109(25):1–5, 2012.
- [60] G. Tarbox, E. Cunningham, R. Sandberg, J. Peatross, and M. Ware. Radiation from free electrons in a laser focus at 10^{18} W/cm²: modeling of photon yields and required focal conditions. *Journal of the Optical Society of America B*, 32(5):743, May 2015.
- [61] S. K. Ride, E. Esarey, and M. Baine. Thomson scattering of intense lasers from electron beams at arbitrary interaction. 52(5), 1995.
- [62] G. A. Krafft. Spectral Distributions of Thomson-Scattered Photons from High-Intensity Pulsed Lasers. *Physical Review Letters*, 92(20):204802, May 2004.
- [63] O. Har-Shemesh and A. Piazza. Peak intensity measurement of relativistic lasers via non-linear thomson scattering. *Optics Letters*, 37(8):1352–1354, 2012.
- [64] C. N. Harvey. In situ characterization of ultraintense laser pulses. *Physical Review Accelerators and Beams*, 21(11):114001, 2018.
- [65] D. J. Griffiths. *Introduction to Electrodynamics Fourth Edition*. Pearson, Illinois, 2013.
- [66] N. J. Peacock, D. C. Robinson, M. J. Forrest, P. D. Wilcock, and V. V. Sannikov. Measurement of the electron temperature by Thomson scattering in Tokamak T3. *Nature*, 224(5218):488–490, 1969.
- [67] T. J. Englert and E. A. Rinehart. Second-harmonic photons from the interaction. *Physical Review A*, 28(3), 1983.
- [68] S.-Y. Chen, A. Maksimchuk, and D. Umstadter. Experimental observation of relativistic nonlinear Thomson scattering. *Nature*, 396(6712):653–655, December 1998.

- [69] C. Z. He, A. Longman, J. A. Pérez-Hernández, M. D. Marco, C. Salgado, G. Zeraouli, G. Gatti, L. Roso, R. Fedosejevs, and W. T. Hill, III. Toward an in situ, full-power gauge of the focal-volume intensity of petawatt-class lasers. *Optics Express*, 27:30020–30030, 2019.
- [70] C. Fruhling, J. Wang, D. Umstadter, C. Schulzke, M. Romero, M. Ware, and J. Peatross. Experimental observation of polarization-resolved nonlinear Thomson scattering of elliptically polarized light. *Physical Review A*, 104(5):1–8, 2021.
- [71] B. Pratt, N. Atkinson, D. Hodge, M. Romero, C. Schulzke, Y. Sun, M. Ware, and J. Peatross. Experimental confirmation of electron figure-8 motion in a strong laser field. *Physical Review A*, 103(3):1–6, 2021.
- [72] J. D. Jackson. *Classical Electrodynamics Third Edition*. John Wiley & Sons, Inc., New York, 1999.
- [73] E. Carbone and S. Nijdam. Thomson scattering on non-equilibrium low density plasmas: principles, practice and challenges. *Plasma Physics of Controlled Fusion*, 57:014026, 2015.
- [74] P. Gibbon. *Short Pulse Laser Interactions with Matter: An Introduction*. Imperial College Press, London, 2005.
- [75] S. T. Thornton and J. B. Marion. *Classical Dynamics of Particles and Systems, 5th Edition*. Brookes/Cole Cengage Learning, Boston, MA, 2008.
- [76] E. M. L. L. D. Landau. *The Classical Theory of Fields 4th Edition*. Elsevier Ltd., Oxford, UK, 1980.
- [77] M. V. Ammosov, N. B. Delone, and V. P. Krainov. Tunnel Ionization Of Complex Atoms And Atomic Ions In Electromagnetic Field. In *High Intensity Laser Processes Proceedings*, volume 0664, October 1986.
- [78] A. Link, E. A. Chowdhury, J. T. Morrison, V. M. Ovchinnikov, D. Offermann, L. Van Woerkom, R. R. Freeman, J. Pasley, E. Shipton, F. Beg, P. Rambo, J. Schwarz, M. Geissel, A. Edens, and J. L. Porter. Development of an in situ peak intensity measurement method for ultraintense single shot laser-plasma experiments at the Sandia Z petawatt facility. *Review of Scientific Instruments*, 77(10), 2006.
- [79] E. A. Chowdhury, C. P. Barty, and B. C. Walker. "Nonrelativistic" ionization of the L-shell states in argon by a "relativistic" 10^{19} W/cm² laser field. *Physical Review A - Atomic, Molecular, and Optical Physics*, 63(4):1–6, 2001.
- [80] CLPU. Centro de Láseres Pulsados. <https://www.clpu.es>.
- [81] FASTLITE. Wizzler Single-shot, high contrast ultrafast pulse measurement. <https://fastlite.com/produits/wizzler-ultrafast-pulse-measurement/>.

- [82] E. Optics. 10X Mitutoyo Plan Apo NIR Infinity Corrected Objective. <https://www.edmundoptics.com/p/10x-mitutoyo-plan-apo-nir-infinity-corrected-objective/6833/>.
- [83] E. Optics. Blackfly PGE 23S6M. <https://www.edmundoptics.com/p/bfly-pge-23s6m-c-112-blackflyreg-poe-gige-monochrome-camera/2878/>.
- [84] E. Optics. 10X Mitutoyo Plan Apo Infinity Corrected Long WD Objective. <https://www.edmundoptics.com/p/10x-mitutoyo-plan-apo-infinity-corrected-long-wd-objective/6623/>.
- [85] Motic. Plan APO ELWD 10x Microscope Objective. <https://www.motic-microscope.com/p-1980-plan-apo-elwd-10x-microscope-objective.aspx>.
- [86] Parker. Pulse Valves Series 9. <http://www.parkerkuroda.com/japan/product/air/ls/Pulse%20Valve.pdf>.
- [87] Newport. MS260i High Resolution Imaging Spectrographs. <https://www.newport.com/f/ms260i-high-resolution-imaging-spectrographs>.
- [88] Newport. Diffraction Grating Assembly, Triple, 150 Grooves per mm, Model 74077. <https://www.newport.com/p/74077>.
- [89] Newport. Diffraction Grating Assembly, Triple, 1200 Grooves per mm, Model 74063. <https://www.newport.com/p/74063>.
- [90] Newport. Diffraction Grating Assembly, Triple, 2400 Grooves per mm, Model 74060. <https://www.newport.com/p/74060>.
- [91] Newport. The Grating Equation. <https://www.newport.com/n/the-grating-equation>.
- [92] M. Born and E. Wolf. *Principles of optics, 7th (Expanded) Edition*. Cambridge University Press, Cambridge, 2002.
- [93] Andor. An Introduction to Gated Intensified Cameras (ICCD Cameras). <https://andor.oxinst.com/learning/view/article/intensified-ccd-cameras>.
- [94] Thorlabs. AC127-019-A Achromatic Doublet. <https://www.thorlabs.com/thorproduct.cfm?partnumber=AC127-019-A>.
- [95] E. Optics. 12-12.7mm Diameter, S-Mount Thick Optic Mount. <https://www.edmundoptics.com/p/12-127mm-diameter-s-mount-achromatthick-lens-mount/18664/>.
- [96] Thorlabs. HASMA. <https://www.thorlabs.com/thorproduct.cfm?partnumber=HASMA>.
- [97] Thorlabs. M114L02 Fiber Patch Cable. <https://www.thorlabs.com/thorproduct.cfm?partnumber=M114L02>.
- [98] F. Mitschke. *Fiber Optics*. Springer, Berlin, Heidelberg, 2016.

- [99] S. A. Self. Focusing of spherical Gaussian beams. *Applied Optics*, 22(5):658, March 1983.
- [100] A. E. Siegman. *Lasers*. University Science Books, Sausalito, California, 1986.
- [101] W. L. Erikson and S. Singh. Polarization properties of Maxwell-Gaussian laser beams. *Physical Review E*, 49(6):5778–5786, June 1994.
- [102] L. Allen, M. W. Beijersbergen, R. J. C. Spreeuw, and J. P. Woerdman. Orbital angular momentum of light and the transformation of laguerre-gaussian laser modes. *Physical Review A*, 45:8185–8189, 1992.
- [103] E. A. Startsev and C. J. McKinstrie. Multiple scale derivation of the relativistic ponderomotive force. *Physical Review E - Statistical Physics, Plasmas, Fluids, and Related Interdisciplinary Topics*, 55(6):7527–7535, 1997.
- [104] B. Quesnel and P. Mora. Theory and simulation of the interaction of ultraintense laser pulses with electrons in vacuum. *Physical Review E - Statistical Physics, Plasmas, Fluids, and Related Interdisciplinary Topics*, 58(3):3719–3732, 1998.
- [105] A. J. Castillo and V. P. Milant’ev. Relativistic ponderomotive forces in the field of intense laser radiation. *Technical Physics*, 59(9):1261–1266, 2014.
- [106] J.-H. Yang, R. S. Craxton, and M. G. Haines. Explicit general solutions to relativistic electron dynamics in plane-wave electromagnetic fields and simulations of ponderomotive acceleration. *Plasma Physics and Controlled Fusion*, 53(12):125006, December 2011.
- [107] J. Peatross, M. Berrondo, D. Smith, and M. Ware. Vector fields in a tight laser focus: comparison of models. *Optics Express*, 25(13):13990, June 2017.
- [108] Thorlabs. Resolution Test Targets. https://www.thorlabs.com/newgroupage9.cfm?objectgroup_id=4338.
- [109] J. H. Moore, C. C. Davis, M. A. Coplan, and S. C. Greer. *Building Scientific Apparatus, 4th Edition*. Cambridge University Press, June 2009.
- [110] G. K. Batchelor. *An Introduction to Fluid Dynamics*. Cambridge University Press, February 2000.